Habitability of planets using numerical climate models. Application to extrasolar planets and early Mars

Martin Turbet

Sorbonne Université

Ecole Doctorale Astronomie et Astrophysique d'Ile de France

Laboratoire de Météorologie Dynamique

Habitabilité des planètes avec un modèle numérique de climat

Application aux planètes extrasolaires et à Mars primitif

Par Martin Turbet

Thèse de doctorat d'Astrophysique

Dirigée par François Forget

Présentée et soutenue publiquement le 3 Septembre 2018

Devant un jury composé de :

President :	Jacques Le Bourlot
Rapporteurs :	James Kasting
	Giovanna Tinetti
Examinateurs :	Raymond Pierrehumbert
	Emmanuel Marcq
	Jérémy Leconte
	Ha Tran
Directeur de thèse :	François Forget

Habitabilité des planètes avec un modèle numérique de climat : Application aux planètes extrasolaires et à Mars primitif.

Résumé : Avec la découverte d'anciens réseaux de rivières et de lacs sur Mars et la détection de planètes tempérées et de taille terrestre autour d'étoiles voisines, nous disposons à présent d'un terrain de jeu formidable pour explorer scientifiquement si la vie est abondante ou rare dans l'Univers. Mon travail de thèse vise à mieux comprendre les conditions dans lesquelles une planète peut maintenir de l'eau liquide - substrat essentiel de la vie - à sa surface. À l'aide de modèles numériques de climat 3D, et de calculs et mesures spectroscopiques, j'ai mené pendant ma thèse deux grandes enquêtes. Premièrement, j'ai exploré les environnements passés de la planète Mars, pour comprendre les conditions dans lesquelles se sont formées les énigmatiques rivières martiennes. À part la Terre, Mars est la seule planète qui a été habitable, mais nous ne savons toujours pas pourquoi. J'ai montré que les évènements extrêmes (formation des vallées de débâcle, impacts de météorites) qui ont pourtant profondément marqué la surface de Mars ne peuvent pas expliquer à eux seuls la formation de ces réseaux fluviaux. Mes travaux de thèse ont également permis d'établir que la présence de gaz à effet de serre réduits (hydrogène, méthane) offre une solution alternative prometteuse. Deuxièmement, j'ai étudié les atmosphères possibles des planètes extrasolaires solides et tempérées, notamment celles orbitant autour de petites étoiles comme Proxima du Centaure et TRAPPIST-1. J'ai montré que certaines de ces planètes ont des caractéristiques très favorables à la présence d'eau liquide en surface. Ce résultat est d'autant plus prometteur qu'il sera possible - comme démontré dans ma thèse pour le cas de la planète Proxima b - de caractériser l'atmosphère de ces planètes avec les futurs observatoires astronomiques JWST (James Webb Space Telescope) et ELTs (Extremely Large Telescopes)..

Mot clés: habitabilité, climat, exoplanètes, Mars, spectroscopie, modélisation

Habitability of planets using numerical climate models. Application to extrasolar planets and early Mars.

Summary: Ancient rivers and lakes discovered on Mars. Numerous temperate, Earth-sized extrasolar planets detected around nearby stars. Thanks to ground and space-based telescope observations and Solar System exploration missions, we now have a fantastic playground to explore scientifically how prevalent life is in the Universe. The main goal of my thesis work is to better understand the conditions necessary for a planet to maintain liquid water - a primary building block for life - on its surface. Using sophisticated 3D numerical climate models, as well as spectroscopic calculations and measurements, I conducted two major investigations during my thesis. First, I explored the environments of ancient Mars at multiple epochs in order to understand the conditions in which the enigmatic Martian rivers were carved. Apart from Earth, Mars is the only planet that has been habitable, but we don't know why. I showed that extreme events (outflow channel formation events, meteoritic impacts) that scarred the surface of Mars cannot by themselves explain the formation of these valley networks. Nonetheless, I showed that the presence of reducing greenhouse gases such as hydrogen and/or methane offers a promising alternative solution. Secondly, I studied the possible atmospheres of solid, temperate extrasolar planets, with a particular focus on those orbiting small stars such as Proxima Centauri and TRAPPIST-1. I showed that some of these planets have characteristics that are highly favourable to the presence of liquid water on their surface. This result is really promising as it will be soon become possible - as demonstrated in my thesis for Proxima b - to characterize the atmosphere of these planets with the future JWST (James Webb Space Telescope) and ELTs (Extremely Large Telescopes) astronomical observatories.

Keywords: habitability, climate, exoplanets, Mars, spectroscopy, modelling

Résumé long en français :

Avec la découverte d'anciens réseaux de rivières et de lacs sur Mars et la détection de planètes tempérées et de taille terrestre autour d'étoiles voisines, nous disposons à présent d'un terrain de jeu formidable pour explorer scientifiquement si la vie est abondante ou rare dans l'Univers. Mon travail de thèse vise a mieux comprendre les conditions dans lesquelles une planète peut maintenir de l'eau liquide - substrat essentiel de la vie telle que nous la connaissons - à sa surface. Ce manuscrit de thèse est décomposé en trois parties et douze chapitres retraçant mes différentes contributions à cette enquête. **Le premier chapitre** (introductif) donne tous les éléments au lecteur pour pouvoir comprendre le contenu, le contexte et les enjeux de cette thèse.

La première partie de mon manuscrit (Chapitres 2-4) est dédiée à l'étude des planètes extrasolaires. Nous avons maintenant la conviction (1) qu'il y a beaucoup de planètes extrasolaires, (2) qu'il y a de nombreuses planètes extrasolaires de la taille de la Terre et (3) qu'il y a une grande fraction d'entre elles qui sont "tempérées", c'est à dire recevant une insolation similaire à celle de la Terre. La prochaine étape est maintenant de savoir quelle fraction de ces mondes ont de l'eau liquide à leur surface, ou autrement dit sont "habitables".

Une première approche possible pour progresser dans cette enquête est de mieux contraindre les processus géophysiques et géochimiques qui régulent le climat et donc l'habitabilité des planètes. C'est ce qui a motivé l'écriture du **Chapitre 2**, dans lequel j'explore comment le cycle des carbonates-silicates - principal mécanisme de stabilisation du climat et donc de l'habitabilité de la Terre - se comporte sur d'autres planètes, en particulier sur des planètes qui sont distantes de leur étoile. En utilisant un modèle global de climat 3-D, prenant en compte simultanément les cycles de l'eau et du carbone, j'ai montré que le cycle des carbonates-silicates devient inefficace pour des planètes qui sont trop loins de leur étoile, car le dioxide de carbone - qui condense à la surface, sur les pièges froids de la planète - ne peut pas s'accumuler dans l'atmosphère et donc la réchauffer par effet de serre. Pour une planète similaire à la Terre (en masse, taille, composition, orbite, obliquité, étoile hôte), la condensation permanente du CO_2 sur les pôles (les pièges froids) est un frein pour le cycle des carbonates-silicates, pour des planètes au moins 30% plus distantes de leur étoile que ne l'est aujourd'hui la Terre du Soleil. Sur des planètes riches en eau, le CO_2 qui se condense à la surface sous forme de glace va progressivement couler sous la glace d'eau (car moins dense que la glace de CO_2) jusqu'a y être profondément enfoui. La condensation du CO_2 est donc un frein majeur à l'habitabilité de ces planètes extrasolaires.

Une deuxième approche est d'étudier l'habitabilité des planètes extrasolaires dont il sera bientôt possible de caractériser l'atmosphère par des observations télescopiques. En 2018, au moment où j'écris ces lignes, l'essentiel de nos connaissances sur l'habitabilité des planètes vient de trois planètes: Vénus, Mars et la Terre. Pourtant, la première caractérisation (imminente) de l'atmosphère de planètes extrasolaires, tempérées et de taille terrestre, est en passe de révolutionner tout ce que nous savons sur l'habitabilité de ces mondes. Les **Chapitres 3 et 4** de ma thèse présentent une analyse détaillée des climats possibles et de l'habitabilité de deux des systèmes planétaires parmi les plus favorables pour une caractérisation future de leur atmosphère: Proxima b, l'exoplanète la plus proche de la Terre. Et les 7 planètes en transit du système TRAPPIST-1. Ces planètes sont représentatives de planètes absentes dans notre système solaire, mais vraisemblablement abondantes

dans la galaxie. Dans le **Chapitre 4**, je montre qu'il est difficile pour ces planètes d'accumuler dans leur atmosphère de grandes quantités de dioxide de carbone (CO_2), de méthane (CH_4), d'ammoniac (NH_3) et même de diazote (N_2). Le CO_2 condense facilement sur les pièges froids de la planète, en particulier dans le cas où la planète est en rotation synchrone (état orbital le plus probable pour ces planètes). Le CH_4 et NH_3 sont sensibles à l'effondrement photochimique, produit par la photodissociation des molécules par le flux XUV intense émis par les étoiles de faible masse, comme TRAPPIST-1 et Proxima du Centaure. Dans une atmosphère chimiquement réduite, le N_2 peut également être photodissocié puis perdu dans de longues chaines carbonées qui sédimentent à la surface. Malgré la difficulté apparente des planètes orbitant autour de petites étoiles à maintenir une atmosphère, je montre dans les **Chapitres 3 et 4** que certaines de ces planètes - notamment Proxima b et TRAPPIST-1e - ont de grandes chances d'avoir de l'eau liquide à leur surface. En particulier, si ces planètes sont aujourd'hui (1) en rotation synchrone et (2) riches en eau (suffisamment riches pour que toute l'eau ne soit pas piégée sur les points froids de la planète), alors elles devraient avoir de l'eau liquide à leur surface, au moins dans la région sub-stellaire, et ce quelque soit l'atmosphère considérée. Ce résultat est d'autant plus prometteur qu'il sera possible prochainement de caractériser l'atmosphère de ces planètes avec le télescope spatial James Webb et la prochaine génération de télescopes au sol (type E-ELT, European Extremely Large Telescope). Dans le **Chapitre 3**, je montre notamment que Proxima b est une formidable candidate pour la caractérisation future de son atmosphère. D'abord, des courbes de phase thermique pourront être tentées avec le télescope James Webb afin de savoir si Proxima b a une atmosphère (ou non) et quelle est son épaisseur (si atmosphère il y a). Ensuite, et du fait de sa proximité à la Terre, Proxima b est une cible unique (tempérée, de la taille de la Terre) pour une caractérisation par imagerie directe, technique jusque là réservée aux planètes très jeunes (et donc chaudes) situées loin de leur étoile, avec la future génération de grands télescopes au sol. L'imagerie directe pourra être utilisée pour produire des courbes de phase en réflexion de Proxima b. Cela nous apporterait des informations sur les variations temporelles de l'albédo de Proxima b dans les longueurs d'onde du visible et du proche infrarouge, et donc des informations sur la nature de la surface et éventuellement des nuages de Proxima b. Proxima b pourrait devenir la première planète potentiellement habitable à être caractérisée et a ainsi le potentiel de révolutionner toutes nos connaissances sur l'habitabilité des planètes.

La deuxième partie de mon manuscrit de thèse (Chapitres 5-9) est dédiée à l'étude de la planète Mars primitive, pour tenter de comprendre les conditions dans lesquelles se sont formées les énigmatiques rivières martiennes. A part la Terre, Mars est la seule planète qui a été habitable, mais nous ne savons toujours pas pourquoi. Deux grandes hypothèses sont envisagées: (i) Mars aurait pu avoir de l'eau liquide à sa surface pendant des périodes de temps longues, grâce au puissant effet de serre de gaz hypothétiques, fournissant ainsi un environnement propice pour que la vie puisse émerger et se développer. (ii) Mars aurait pu avoir été réchauffée de manière transitoire par des évènements extrêmes, par exemple des impacts de météorites. Le résultat de cette enquête a des conséquences importantes pour notre compréhension de l'habitabilité des planètes du système solaire, et par extension des planètes extrasolaires. Ce travail est au coeur de la deuxième partie de ce manuscrit.

La première catégorie de scénario envisagée dans cette thèse est l'effet climatique d'évènements catastrophiques, tels que (i) les impacts de météorites et (ii) les écoulements d'eau brutaux qui ont conduits à la formation des grandes vallées de débâcle visibles aujourd'hui à la surface de Mars. Pour

cela, j'ai utilisé tout un arsenal de modèles numériques (hydrocode, modèles de climat 1-D et 3-D). Le première type d'évènement extrême considéré est l'effet climatique des écoulements d'eau brutaux sur les pentes des plaines du Nord de Mars. Dans le **Chapitre 5**, je modélise l'effet environnemental de tels écoulements, et ce pour une grande gamme de paramètres possibles (différents types d'écoulements, différents types d'atmosphères, différentes obliquités, différentes saisons). Le résultat est sans appel : quelque soit la gamme de paramètres considérée, la durée du chauffage induit par de tels écoulements est très courte. L'eau liquide produite par ces écoulements vient s'accumuler dans les plaines du Nord de Mars, pour y former un océan. Cependant, je montre dans le **Chapitre 5** que la durée de vie de cet océan est "géologiquement" très courte, d'abord (i) parce que l'océan va geler rapidement (en 10^3 ans maximum) et (ii) parce que l'océan va ensuite se sublimer rapidement vers les pièges froids de la planète (en 10^5 ans maximum). Dans le **Chapitre 6**, j'étudie en détails les conditions requises pour la formation et la survie d'un océan martien tardif (daté de l'Hespérien). Bien que la présence d'un océan tardif sur Mars ait été avancée pour expliquer la formation de tsunamis sur Mars pendant l'Hespérien, je montre dans ce chapitre que la présence d'un tel océan pose un certain nombre de paradoxes. Le deuxième type d'évènement extrême considéré dans cette thèse est l'effet climatique des impacts de météorites. Dans le **Chapitre 7**, j'explore - en utilisant une hiérarchie de modèles de climats - l'effet environnemental des plus gros impacts de météorites ayant frappé Mars primitif (impacteurs de diamètre supérieur à 50km), ceux qui sont suffisamment gros pour vaporiser dans l'atmosphère de Mars l'équivalent de dizaines de mètres d'eau précipitable. Je montre que l'effet de serre induit par la présence de grandes quantités de vapeur d'eau et de nuages ne peut pas maintenir Mars primitif dans un état "chaud" stable et durable. De plus, la nature des précipitations associées à de tels évènements (faible quantité de précipitations, précipitations diluviennes, précipitations non-corrélées spatialement avec la position des rivières martiennes) font des gros impacts de météorites de mauvais candidats pour expliquer la formation des réseaux de rivières martiennes. Dans le **Chapitre 8**, j'explore l'effet environnemental des impacts de météorite de taille modérée (impacteur de diamètre inférieur à 50km), en combinant les résultats d'un modèle numérique hydrodynamique (ou "hydrocode") avec ceux d'un modèle global de climat 3-D. Cette combinaison de modèles permet de simuler l'effet climatique des impacts de météorites, des toutes premières secondes jusqu'à des échelles de temps de plusieurs dizaines d'années. Je montre que l'érosion de surface induite par précipitations est très faible à la suite d'impacts de météorites de taille modérée. La quasi totalité de l'eau évaporée à la suite d'un impact recondense à la surface en quelques heures/jours. La principale source d'érosion vient de la fonte des réservoirs permanents de glace induite par le dépôt d'une couche très chaude d'éjecta produite par les impacts de météorites. Toutefois, je montre que la quantité totale et maximale d'eau liquide qui peut être produite par ce mécanisme est plusieurs ordres de grandeur en dessous de la quantité d'eau minimale requise pour éroder tous les réseaux de rivières martiens. Finalement, je montre dans les **Chapitres 5, 7 et 8** que les évènements extrêmes les plus violents de l'histoire de Mars (formation des vallées de débâcle, impacts de météorites) qui ont pourtant profondément marqué la surface de Mars ne peuvent pas expliquer à eux seuls la formation des réseaux fluviaux observés à la surface de Mars.

La deuxième catégorie de scénario envisagée dans cette thèse est l'effet à plus long terme de gaz à effets de serres additionnels, notamment des gaz chimiquement réduits comme le di-hydrogène (H_2) et le méthane (CH_4). A l'aide de simulations numériques de climat 3-D, j'ai exploré comment le climat de Mars primitif évolue en fonction de deux paramètres: (1) la quantité d'eau totale disponible à la surface (peu contrainte) et (2) la quantité de di-hydrogène dans l'atmosphère de Mars (très peu contrainte). Pour cela, j'ai implémenté dans le modèle de climat 3-D l'effet des rétroactions entre

géologie, hydrologie, glaciologie et climat, avec la prise en compte de l'effet (i) des lacs de cratères d'impacts, (2) des océans et (3) des glaciers. Je montre que l'inclusion de gaz à effet de serre réduits est une solution séduisante pour expliquer la formation des réseaux de rivières et lacs martiens. Dans les simulations contenant de grandes quantités de gaz réduits, le climat de Mars devient "chaud" et "humide", et la position des écoulements (induits par des précipitations) est en bon accord avec la position des réseaux de rivières observés aujourd'hui à la surface de Mars. Le meilleur accord est obtenu (i) en faisant l'hypothèse d'un évènement de "True Polar Wander", c'est à dire un basculement de la surface de Mars par rapport à son axe de rotation, suite à l'anomalie de masse produite par la formation du complexe volcanique de Tharsis et (ii) en ajustant la position des grands réservoirs d'eau (océans) présents à la surface de Mars. Toutefois, les quantités de di-hydrogène nécessaires pour atteindre un climat produisant des réseaux de rivière par précipitation sont bien plus importantes que celles requises pour réchauffer la température moyenne de surface de Mars primitif au dessus du point de congélation de l'eau.

La troisième et dernière partie de mon manuscrit (Chapitres 10-11) présente de nouveaux calculs et mesures spectroscopiques ayant pour but de mieux caractériser l'effet de serre de l'atmosphère de Mars primitif et des planètes extrasolaires, en particulier celles ayant une atmosphère dominée par le dioxide de carbone (CO_2). Dans le **Chapitre 10**, je discute des effets collisionnels de "line mixing", et en particulier de leur impact sur l'absorption dans l'aile lointaine des raies du CO_2. L'absorption dans l'aile lointaine (gauche, ou à faible nombre d'onde) des raies de la bande à 15 μm du CO_2 a un rôle important pour l'effet de serre de Mars primitif, et donc pour l'estimation de sa température de surface. Je montre dans ce chapitre que l'approche dite de "line-mixing" donne des résultats très similaires à l'approche plus traditionnelle dite du "facteur χ", renforcant par la même occasion les résultats de précédentes études montrant que la surface de Mars primitif ne peut pas être chauffée au dessus de 0°C avec du CO_2 uniquement. Ce résultat est confirmé dans le **Chapitre 11** à l'aide des premières mesures expérimentales de l'absorption dans l'aile gauche des raies de la bande à 15 μm du CO_2. Plus généralement, le **Chapitre 11** présente plusieures mesures expérimentales de l'absorption dans l'infrarouge lointain de mélanges gazeux composés (au moins en partie) de CO_2, réalisées dans la ligne AILES du synchrotron SOLEIL. Je présente dans ce chapitre les premières mesures expérimentales de l'absorption induite par collisions entre molécules de CO_2+CH_4 et CO_2+H_2. Ces mesures confirment des prédictions théoriques précédentes, montrant ainsi que l'absorption induite par collisions entre les molécules CO_2+X est plus forte qu'entre les molécules N_2+X. Ces mesures sont importantes car elles confirment que des atmosphères composées de CO_2/CH_4/H_2 peuvent produire un fort effet de serre sur Mars primitif, et par extension sur les planètes extrasolaires.

Pour finir, le **Chapitre 12** rassemble les conclusions principales de cette thèse, ainsi que mes perspectives personnelles.

Acknowledgments / Remerciements

Tout d'abord je remercie mon directeur de thèse François Forget sans qui cette thèse n'aurait jamais pu voir le jour. François, je te remercie pour ta confiance et surtout pour la grande liberté que tu m'as accordée pendant cette thèse. Liberté d'explorer mes propres pistes et sujets de recherche. Liberté de pouvoir démarrer des collaborations avec d'autres chercheurs. Liberté de pouvoir m'intégrer et trouver ma propre place au sein du laboratoire et de l'équipe de planétologie. Merci également pour tes nombreux conseils avisés qui m'ont aidé à me transformer progressivement, de jeune étudiant naif en chercheur chevronné ! Enfin, je voudrais te remercier de m'avoir donné les moyens de participer à de nombreuses conférences/écoles aussi bien en France qu'à l'étranger. Je sais que beaucoup de doctorants n'ont pas cette chance, et pour cela je te suis extrêmement reconnaissant.

Thank you to the official reviewers of this manuscript - James Kasting and Giovanna Tinetti - for their very positive, constructive feedbacks. I also thank the other members of my PhD jury - Ray Pierrehumbert, Jacques Le Bourlot, Ha Tran, Emmanuel Marcq and Jérémy Leconte - not only for agreeing to participate to my thesis committee, but also for their remarks on my manuscript. I must say that I am really honoured that you all accepted to be part of my PhD jury!!!

Je remercie aussi les relecteurs "non-officiels" de mon manuscrit: François, Papa, Noémie, Jean-Michel et Thomas. Merci beaucoup d'avoir pris le temps de relire ma thèse. Vous pourrez maintenant vous targuer d'avoir relu un jour un pavé d'un kilogramme. Défi réussi !!

Merci également à ceux qui ont participé aux répétitions de ma soutenance de thèse, à savoir François, Max, Margaux, Sébastien, Karine, André, Alexandre et Noémie. Vous m'avez donné beaucoup de bons conseils et surtout beaucoup de confiance pour engager sereinement ma soutenance. Rendez-vous le 3 Septembre 2018 à 14h pour en découdre une bonne fois pour toute !

J'aimerais ensuite remercier tous les développeurs (anciens et actuels) du modèle numérique de climat utilisé pendant ma thèse, entre autre: Robert Sadourny, Frédéric Hourdin, Ehouarn Millour, François Forget, Robin Wordsworth, Laurent Li, Francis Codron, Laurent Fairhead, Phu Le Van, Yann Wanherdrick, Jérémy Leconte, J.-B. Madeleine, B Charnay, A Spiga, Laura Kerber, Sandrine Guerlet, Sébastien Lebonnois, Richard Fournier, Jean-jacques Morcrette, Franck Montmessin, Ionella Musat, Christophe Hourdin, Mélodie Sylvestre, Michel Capderou, Thomas Navarro, M.-A. Filiberti, A. Armengaud, Jan Vatant, Maxence Lefèvre ... C'est grâce à vous tous que les 65000+ lignes du modèle générique de climat du LMD ont pu voir le jour. Et donc grâce à vous que les travaux réalisés pendant ma thèse ont pu voir le jour. Je voudrais également rendre un hommage à tous les chercheurs, postdoctorants, étudiants en thèse, stagiaires qui n'ont pas laissé leur nom dans les lignes de code du modèle du LMD et qui ont pourtant tant contribué à sa conception ... Sachez que pour cela, je vous suis très reconnaissant !

Merci plus particulièrement à Ehouarn Millour qui est aujourd'hui la pierre angulaire du modèle de climat du LMD. Ehouarn, c'est aujourd'hui grâce à toi si tous les modèles de climat du LMD sont aussi compétitifs, et grâce à toi si j'ai pu prendre autant de liberté pendant ma thèse avec ces mêmes modèles. Car en plus d'être la clé de voute du modèle du LMD, Ehouarn est une superbe personne qui n'hésite pas à donner de son temps pour aider les jeunes doctorants - comme moi - à mettre le pied à l'étrier. Beaucoup de laboratoires dans le monde ont de quoi nous envier notre Ehouarn 'national' !

J'aimerais maintenant remercier plusieurs personnes qui ont eu un rôle essentiel pendant ma thèse. Tout d'abord, Franck Selsis, l'homme qui est toujours dans les bons coups ! Merci Franck pour toutes

ces discussions que nous avons eu ensemble à propos des atmosphères planétaires et de leurs signatures spectrales. Cela m'a énormément fait progresser dans la compréhension de ma thèse ! Merci également de m'avoir donné ta confiance et d'avoir partagé avec moi tes meilleurs coups !!! J'espère pouvoir un jour te renvoyer l'ascenseur !

Merci également à Jérémy Leconte et Benjamin Charnay d'avoir pris le temps à de nombreuses reprises de répondre à mes questions sur les atmosphères (exo)-planétaires. Vous m'avez donné de nombreux précieux conseils quand j'en avais besoin. Vous m'avez également fait de nombreux retours sur mon travail qui m'ont aidé à mieux cerner ma thèse, et je vous en remercie beaucoup !!

Enfin, j'aimerais remercier Ha Tran et Jean-Michel Hartmann. Dès votre arrivée au LMD, vous avez joué le jeu de vous intéresser aux problèmes scientifiques soulevés par ma thèse, et pour cela je vous suis très reconnaissant ! J'ai appris énormément en travaillant à vos côtés sur un domaine qui - initialement - m'était plutôt étranger. Grâce à vous, j'ai connu la joie de pouvoir réaliser une belle expérience de laboratoire pour mieux comprendre le climat de Mars, et çà, çà n'a pas de prix !

Franck, Jérémy, Benjamin, Ha et Jean-Michel, j'espère très fort que j'aurai la chance de pouvoir continuer de collaborer avec vous dans le futur !

J'ai compris pendant ma thèse que la science ne se faisait pas seul. Que même le plus malin des génies n'est rien par rapport à la combinaison de talents et de savoirs-faire, surtout dans une discipline aussi inter-disciplinaire que celle de ma thèse. Ainsi, j'aimerais remercier très fort Emeline Bolmont, Gabriel Tobie, Vladimir Svetsov, Jim Head et Cédric Gillmann, de m'avoir justement fait profité de leurs talents et leur savoirs-faire sans lesquels mes résultats de thèse auraient été bien plus fades ...

Réciproquement, j'aimerais remercier Emmanuel Marcq, Thomas Fauchez, Sylvain Bouley, Michael Gillon, Loic Rossi, Edwin Kite, Franck Selsis, Ignasi Ribas, Jérémy Leconte de m'avoir accordé leur confiance, en collaborant sur leurs projets de recherche.

J'aimerais maintenant remercier les enseignants qui m'ont accordé toute leur confiance: Bérengère Villard, Aymeric Spiga, Jean-Baptiste Madeleine, Laurence Picon et Chrystèle Sanloup. J'aimerais également remercier Françoise Roques qui m'a donné la chance - enfin, au jeune doctorant que j'étais alors - de pouvoir participer à un cours formidable sur la science des exoplanètes. L'écriture de ce cours m'a été d'une aide formidable pour prendre du recul sur mon sujet de thèse, ce qui m'a été fort utile pour tout le reste de ma thèse.

Je remercie d'ailleurs tous les enseignants que j'ai eu la chance de rencontrer au cours de mes études et qui ont réussi à me donner le goût de la science et des études, suffisamment pour atteindre la thèse et le grade de docteur. Anne Thomazeau, Christian Cheminade, Jean-Marc Urbain et François Vandenbrouck, merci à vous !

Passons maintenant à mes collègues du laboratoire ! Merci aux informaticiens, d'abord à Karine Marquois pour son aide et sa bonne humeur si précieuses pour le laboratoire ! Ensuite à Franck Guyon, notamment pour avoir sauvé mon disque dur et les données qui vont avec, à un moment où - jeune innocent que j'étais - je n'avais aucune sauvegarde de mon travail ... Merci également à Evelyne, Molyka et Martine pour toute l'aide administrative que vous m'avez apporté pendant ma thèse, et qui m'a épargné tant de stress !!!

Plus généralement, merci à tous les permanents du labo - que je n'ai pas encore remercié - qui m'ont fait profité de leurs bons conseils et de leur expérience, à savoir Sébastien, André, Sandrine G, Jean-Louis, Frédéric, Caroline, Frédérique, Michel, Philippe, Laurent, Solène, Geneviève, Jean-Louis,

Marie-Pierre, Sandrine B., Ariana, Jean-Yves ... C'est d'abord grâce à vous - les "permanents" - que l'ambiance au LMD est si agréable ! Merci également au trio de choc de l'IPSL - Isabelle, Marie, Catherine - ainsi qu'à Venance pour vos conseils en communication toujours au top !

Merci à tous les doctorants, post-doctorants et ingénieurs de passage du laboratoire - tous dans le même bateau, comme on dit - Tanguy, Thomas, David, Margaux, Jan, Kevin, Chao, Gabriella, Fuxing, Chiku, Maxence, Vladimir, Binta, Sonia, Alexandre C, Flo, Can, Emmanuel, Alexandre B, Yuan, Mélody, Sylvain, Paul, Roland, Maxime, Yue, Jean, Habib, Marine, Max, Mikel, Itziar, Addisu, Sofia, Manu, Lluis, Duc, Alizée, Simon, ... pour tous les bons moments passés ensemble, aussi bien au coin café qu'autour d'une bière au bar l'Inévitable, ou bien en conférence à l'autre bout du monde, ou encore chez moi pour fêter le nouvel an martien ! Merci également aux invités de passage Mike Wolff, Takanori Kodama, Thomas Fauchez, avec qui j'ai passé de très bons moments ! J'espère très fort que nous pourrons rester en contact par la suite, et que nous aurons des occasions de nous retrouver !

Je voudrais maintenant faire un triomphe pour notre groupe "La Résonance de Laplace", groupe de rap qui a commencé sur les planches un certain 19 Octobre, composé de Laura Kerber aka Lo'rap, Tanguy Bertrand aka Fresh diggy ice, Apurva Oza aka King Osa, David Dubois aka Whaledave et Aymeric Spiga aka Habitable Z; et qui a mal tourné un certain premier Avril 2017 ... Merci pour ces moments gravés dans mon esprit !

Mention spéciale à Habitable Z pour tous les conseils que tu m'as prodigué pendant la thèse, aussi bien du côté professionnel que personnel ! Surtout, ne change pas d'un pouce !

Merci maintenant à tous mes amis pour tous les moments passés ensemble - à côté de la thèse - et qui m'ont fait vraiment beaucoup de bien !! Merci à vous Vincent, Bastien, Sébastien, Guillaume, Alan, Ileyk, Félix, Bilal, Olivier, Valentin, Greg, Lester, Laurent, Pierrick, ...

Merci également à l'équipe de France de football d'avoir gagné la coupe du monde 2018, merci car vous m'avez bien fait galérer dans l'écriture de ma thèse ...

J'aimerais maintenant remercier ma famille. D'abord mes soeurs, Daphné et Marion. Ça y est, votre petit frère est maintenant dans la cour des grands ! Merci à Sébastien, Nicolas, Elisabeth, Philippe, Clément, Jean, Audrey, et Claire pour les bons moments passés ensemble en famille ! Un big up pour mon petit Basile. Un jour peut-être, quand tu seras grand, tu pourras lire ces lignes. Sache que, quelques jours après le départ de ton arrière-grand mère, alors que je revenais d'une conférence à l'autre bout du monde ... ta naissance m'a fait le plus grand bien !

Je voudrais également remercier mes oncles, tantes, cousins, cousines qui m'ont soutenu si gentillement dans les épreuves difficiles de la fin de ma thèse ... Merci à vous ! Malheureusement, et malgré mon titre de docteur, je ne pourrai pas vous faire d'ordonnances ...

Papa, Maman, merci pour tout, vous êtes vraiment les meilleurs ... Merci de m'avoir soutenu dans ce que j'ai entrepris, merci de m'avoir donné la liberté de continuer les études qui me plaisaient, merci de m'avoir soutenu dans les moments difficiles, et d'avoir été à mes côtés dans les moments heureux. J'espère que l'accomplissement de cette thèse de doctorat vous rendra fiers ! Papa, si tu lis ces lignes, sache que je te lance un défi ! Celui - une fois ta retraite prise - de te lancer dans une thèse et d'obtenir toi aussi le grade de docteur ! Comme je te l'ai toujours dit, si je l'ai fait, tu peux le faire !!

Enfin, je dois remercier la personne qui a été la plus importante pour moi pendant toute la durée de cette thèse. Mon trésor, mon soutien, mon équilibre, mon courage, ma motivation, ma force, et

tellement plus encore ... Oui oui, c'est bien de toi dont je veux parler, ma Noémie. Sans toi, rien de tout cela n'aurait été possible ...

Contents

Chapter 1

Introduction

Contents

1.1 Motivation and organization of the manuscript

Ancient rivers and lakes discovered on Mars. Geysers spotted on the icy moons Enceladus and Europa. Tens of temperate, Earth-sized planets detected around other stars. Thanks to ground and space-based telescope observations and Solar System exploration missions, we now have a fantastic playground to explore scientifically how frequent life is in the Universe. Several approaches have been undertaken to make progress on this long-standing investigation, listed below by decreasing order of luck and increasing order of patience:

- **Detect signals emitted by an extraterrestrial civilization.** In the 60's, American scientists started the SETI (Search for ExtraTerrestrial Intelligence) program, designed to search for extraterrestrial signals with the help of radiotelescopes. As of 2018, this approach has remained unsuccessful.

- **In situ search for life in the Solar System.** This investigation started more than 40 years ago with the Viking 1 and 2 landers[1] sent on the surface of Mars to look for evidence of life. Even though this investigation remains fruitless, space exploration missions have demonstrated that there are (and were) many habitats in the Solar System where life could emerge and develop.

- **Look for biomarkers in the atmosphere of distant planets.** On Mars, this investigation is focusing on the detection of atmospheric methane sources[2]. On extrasolar planets, this consists in detecting remotely combinations of molecules that - we think - should only be produced by life as we can imagine it.

- **Find the best planet(s) to look for life, and then look (in situ or remotely) if there is life or not.**

My PhD is mostly focused on this last, long-standing investigation. We are now confident that (1) there are a lot of extrasolar planets, (2) there are a lot of terrestrial planets (in size) and (3) there is a large fraction among them that are temperate (e.g. that receive an insolation similar to the Earth). The next step is to know what fraction of these worlds do have liquid water on their surface. Being at the heart of my thesis's work, this investigation is the topic of the **Part I** of my manuscript.

A first approach to make progress on this investigation is to better characterize the geophysical and geochemical processes playing a major role in the regulation of the habitability of planets. This is what motivated the work presented in **Chapter 2**, where I explore how the carbon cycle - the major mechanism of regulation of the climate and habitability on Earth - behaves on distant planets. In particular, in this chapter I focus on the effect of carbon dioxide surface condensation as a possible limit to the habitability of extrasolar planets.

A second approach is to better characterize the habitability of potentially habitable extrasolar planets that are and/or will soon be amenable to atmospheric characterization. For now, most of our knowledge on planetary habitability comes from the study of three planets: Venus, Mars and Earth. Yet, the first (imminent) characterization of atmospheres of Earth-sized, temperate extrasolar planets is likely to revolutionize all what we know about planetary habitability. **Chapters 3 and 4** present deep investigations of the possible climates and habitability as well as the observability (with existing techniques of exoplanet atmospheric characterization) of the best candidates that we now have: Proxima Centauri b, our closest neighbour, and the seven transiting planets of the TRAPPIST-1 system. These planets are likely representative of planet types that are not found in the solar system, but which should be abundant in the galaxy.

In the Solar System, the only example of a planet (except Earth) that hosted surface liquid water is Mars. However, it is still unclear whether Mars had surface liquid water for long periods of time - and thus provided a suitable environment for life to develop - or whether Mars had surface liquid

[1] Viking 1 and 2 were equipped with several scientific instruments designed to detect life.

[2] The detection of methane is one of the goal of the Trace Gas Orbiter (TGO) probe currently in orbit around Mars.

water episodically in response to extreme events such as meteoritic impacts. The outcome of this pending question has strong consequences for the search of life in the Solar System, and indirectly for the search of life on extrasolar planets. This second investigation on Mars is explored in details in the **Part II** of my manuscript.

The history of Mars can be decomposed in three epochs - Noachian, Hesperian and Amazonian - each of them being characterized by distinct pieces of evidence of fluvial activity. The Hesperian period was characterized by catastrophic water flows that carved the large outflow channels visible today on Mars. In **Chapter 5**, I explore the effect of these extreme events on the climate of Mars to know whether or not they could have induced the formation (through atmospheric precipitation) of contemporaneous mature valley networks. The Hesperian epoch is also thought to be the scene of tsunami events, suggesting the existence of an ancient ocean potentially fed by the aforementionned catastrophic water flows. **Chapter 6** exposes the paradoxes that come with this scenario.

The Noachian period was characterized by the widespread formation of dendritic, mature valley networks and impact crater lakes. In **Chapters 7 and 8**, I use various kinds of sophisticated numerical models to investigate the environmental effect of meteoritic impacts for a wide range of impactor sizes, in order to estimate how much erosion could have been produced either by atmospheric precipitation (rainfall) or snowmelt. In **Chapter 9**, I instead focus on the long-term greenhouse warming produced by reducing atmospheres made of carbon dioxide and hydrogen.

Based on state-of-the-art 3-dimensions global climate model simulations, I provide in Part II new insights on the nature of the early Martian climate at multiple epochs.

The exploration of the surface habitability of planets relies on various assumptions about their atmospheric properties. The absorption of light by atmospheric gases is one of the most sensitive of them. **Part III** of my manuscript presents new insights on the spectroscopy of dense CO_2 atmospheres that have strong implications for the habitability of both early Mars and extrasolar planets. In **Chapter 10**, I discuss the impact of line mixing effects on dense CO_2 atmospheres. In particular, I focus on how this would affect absorption in the far wing of CO_2 band lines and - as a result - the calculation of the surface temperature of early Mars. **Chapter 11** is an experimental exploration of the collision-induced absorptions produced by methane and hydrogen when mixed with carbon dioxide. These results have strong implications for the greenhouse warming produced by reducing atmospheres.

Eventually, **Chapter 12** summarizes all the work presented in this manuscript. Possible avenues for future research - evidenced by my thesis's work - are also mentioned in this concluding Chapter.

This introductory Chapter is designed to give the reader the key elements needed to understand the content and relevance of the work presented in this manuscript. First, I give a general overview of our current understanding of the habitability of both Solar System and extrasolar planets (Sect. 1.2). I then introduce the mathematical and numerical tools used in this thesis to explore the surface habitability of planets, i.e. numerical climate models (Sect. 1.3) and spectroscopy (Sect. 1.4).

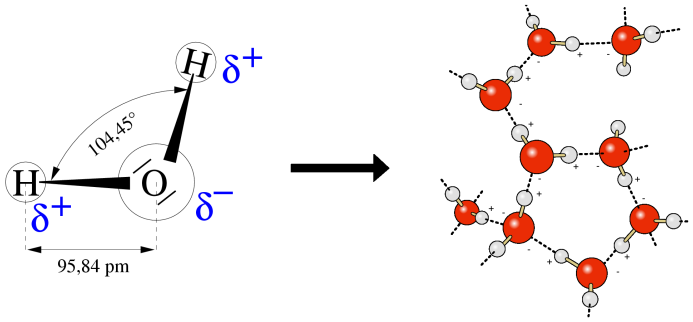

Figure 1.1: Water has an electric dipole moment equal to 1.83 Debyes. Water molecules can attract each other thanks to their large polarizability. The oxygen atom (O) is more electronegative than the hydrogen atom (H). Locally, the oxygen atom is charged negatively in the water molecule, and the hydrogen atom must be charged positively, by charge conservation. Water can thus form hydrogen bonds between other molecules, such as water or macromolecules. Credit: P.E. Zorner et R. Apfelbach.

1.2 The habitability of planets

1.2.1 Requirements for habitability

Life as we know it (and can recognize it) from our experience on Earth is based on carbon chemistry in liquid water solution, and evolves based on replication/reproduction. To be considered as "habitable", a planet must have (1) carbon, (2) liquid water, (3) a source of energy and (4) a solid or liquid surface.

- **Carbon:** Carbon is a chemical element that is essential for life. First, each atom of carbon can form four molecular bonds. Secondly, carbon atoms form with other abundant atoms (oxygen, hydrogen, and also carbon!) molecular bonds with a stability that is not too strong, not too weak, and that is similar for each possible bond (e.g. C-O, C-H, C-C). These two key properties are the reasons why carbon chemistry - also known as organic chemistry - is extremely rich and can form very diverse compounds.[3] In addition to carbon (and oxygen and hydrogen), additional nutrients (e.g. nitrogen, sulfur, phosphorus, potassium, etc.) are needed to enrich the diversity of chemical compounds.

- **Liquid water:** On Earth, liquid water is essential for life as we know it. Without water, biological activity cannot exist. Some organisms can survive as "spores" in extremely dry conditions, but their metabolism is stopped. Conversely, wherever and whenever liquid water is available, life is also present (Rothschild and Mancinelli, 2001). This holds at very large depth in the subsurface, or at very high temperature, or in acidic or very salty conditions, etc. Liquid water is the only solvent to date that can produce a chemistry as rich as biochemistry (Brack, 1993). Water molecules have a very large electric dipole moment and can thus form hydrogen bonds

[3] Other atoms such as Silicon (Si) are also able to form simultaneously four different chemical bonds. However, silicon forms with some atoms (in particular, oxygen) chemical bonds that are way too stable. This drastically reduces the diversity of compounds that can be produced with silicon-based chemistry, making it difficult for life to emerge and develop.

with other molecules (see Fig. 1.1). Hydrogen bonds are essential to (1) stabilize water molecules between each other and (2) stabilize macromolecules that can serve as building blocks of life. Last but not least, liquid water is stable for a very large range of temperatures and pressures, in particular at temperatures where chemical reactions are rather fast. Therefore, an habitable planet must have stable surface liquid water in the form of oceans or lakes at the surface, or in the form of aquifers in the subsurface. Even though liquid water is likely the best solvent for life - as we know it - to emerge and develop, experts are still investigating the ability of other solvents to do the same, e.g. methane and ethane in Titan's lakes and seas (McKay 2016 and references therein).

- **A source of energy:** A source of energy is essential to initiate the synthesis and the development of organic molecules that are the building blocks of life. On Earth, the main source of energy comes from the photons emitted by the Sun. This is the solar flux that feeds the photosynthesis.

- **A stable surface:** It is hard to conceive that life may have developed in the atmosphere of a gaseous planet. Without a liquid or solid surface, life would have to take advantage of cloud droplets to emerge. However, cloud droplets evaporate and re-form on very short timescales and provide thus a poorly stable environment for life to emerge and develop.

1.2.2 Classes of habitability

Life as we know it has to develop on a planetary body (e.g. planet or moon) that hosts liquid water. A moon or a planet is actually considered as being "habitable" if it hosts some liquid water. There are multiple types of environments that can provide stable liquid water; yet, they do not offer the same chances for life to emerge and evolve. We list below the four main classes of habitable planets/moons (Lammer et al., 2009; Forget, 2013):

- **Class I:** These are the planets/moons the most similar to the Earth in the sense that they are able to maintain surface liquid water on their surface. Life on these planets could use the photons emitted by the host star to initiate the mechanism of photosynthesis. On Earth, almost all living organisms depend directly or indirectly on the photosynthesis. This is the solar energy coupled with photosynthesis that have allowed life to modify Earth's atmosphere and surface.

- **Class II:** These planets/moons used to have similar characteristics than the Earth (class I) in the past but lost - in the course of their evolution - their ability to sustain surface liquid water. Life may have emerged and developed on the surface of these planets, and then may have penetrated deep in the subsurface. We recall that on Earth, life is now abundant down to several kilometers below the surface. When the surface of the planet becomes unhabitable, life may survive deep in the subsurface where liquid water is present. This might for example be the case on Mars.

- **Class III:** These are the planets/moons that have a subsurface liquid water ocean[4] and/or aquifers below the surface, and above a rocky core. Europa (natural satellite of Jupiter) and Enceladus (natural satellite of Saturn) are part of this category (see Fig. 1.3). On these two

[4]This subsurface liquid water ocean can be covered by an icy shell

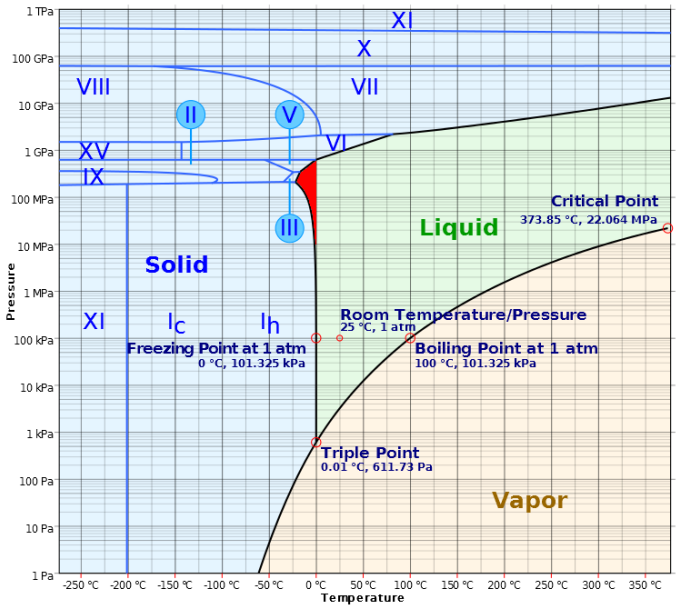

Figure 1.2: Phase diagram of water. Water is stable in liquid form for a large range of temperatures and pressures. On the surface of Earth, pure liquid water is stable between 0 and about 100°C. At high pressure, up to 200 MPa, the temperature of the solidus decreases with pressure. There is therefore a region in the diagram (here in red) where liquid water can be stable down to -20°. Salts can also significantly lower the freezing temperature of water. Credit: SESP.

planetary objects, the surface temperature is below -100°C, but liquid water is stable deep in the subsurface. The subsurface ocean is actually stabilized by the deep release of energy produced by the gravitational tidal friction exerted by the planet on the moon due to the eccentricity of the moons excited by moon-moon gravitational interactions.

- **Class IV:** These planets/moons have a subsurface liquid water ocean as class III objects. However, the ocean here is located between two layers of ice. The phase diagram of water (see Fig. 1.2) predicts in fact that - at deep pressures - liquid water should convert into ice. Classe III objects are mainly planets/moons that are extremely rich in water, such as Ganymede and Callisto (natural satellites of Jupiter) in the solar system (see Fig. 1.3).

Life on classes II/III/IV planetary objects

Photons emitted by the host star cannot reach the subsurface liquid water ocean on class II, III and IV planets, and photosynthesis cannot occur. On class II and III planets/moons, life can take advantage of the chemical energy and nutrients brought by hydrothermal and volcanic activity. On class IV objects, the liquid water ocean is trapped in "sandwich" between two layers of water ice. Experts used to believe that life would struggle to emerge and develop in this situation because of the lack of chemical energy and more importantly nutrients. However, it has been recently shown that heat and nutrients could be transported through the high-pressure lower icy shell thanks to solid-state convection (Choblet et al., 2017)

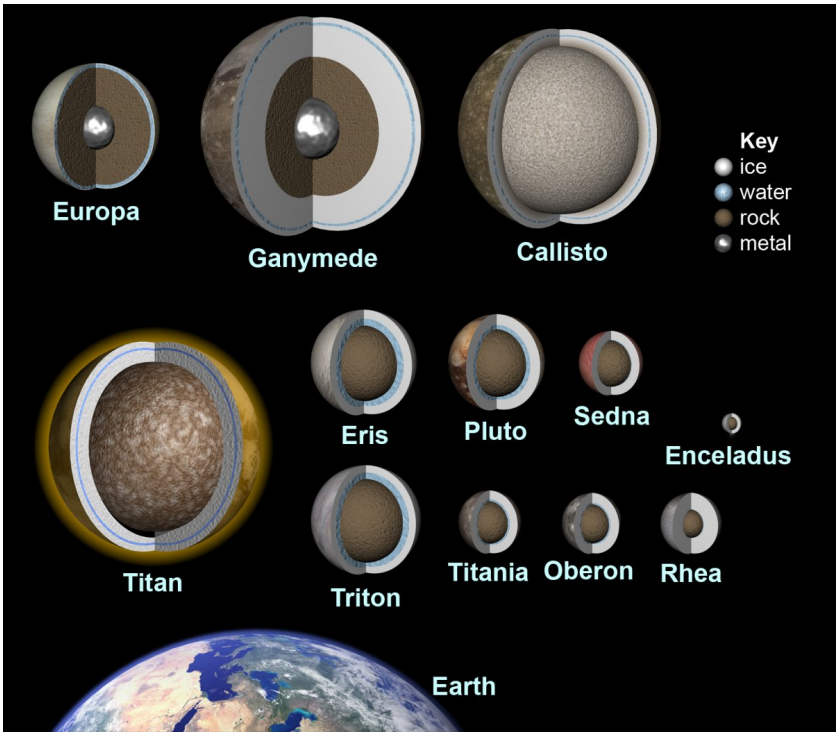

Figure 1.3: Internal models of various objects of the solar system. Liquid water is predicted to be abundant in the subsurface of many of these objects. Credit: D. Ellison, E. Lakdawalla, and B. Pappalardo.

In any case, life in the subsurface (class II, III and IV objects) would struggle to modify the surface and the atmosphere of its host planet/moon. Without the energy provided by photons (e.g. through photosynthesis), the biological activity is more limited and would have more difficulties to modify the chemical composition of the atmosphere in a way that it could be detectable remotely (Kaltenegger et al., 2010).

This is the main reason why my manuscript is focusing on the planets of class I habitability.

1.2.3 Sustaining surface liquid water

To host liquid water on their surface, class I planets must first accumulate liquid water on their surface. This means that such planets must first accumulate water, then keep it liquid and eventually prevent it from escaping to espace.

1.2.3.1 Get the water!

Water is abundant everywhere in the galaxy (Cernicharo and Crovisier, 2005), in molecular clouds, in protoplanetary disks, etc. Water could be a major primary component of numerous planets and moons and/or could have been brought by later accretion of comets and meteorites. In the solar system, water is abundant in many of the galilean moons and trans-neptunian objects.

In general, water could be a primary component of planets and moons that form beyond the

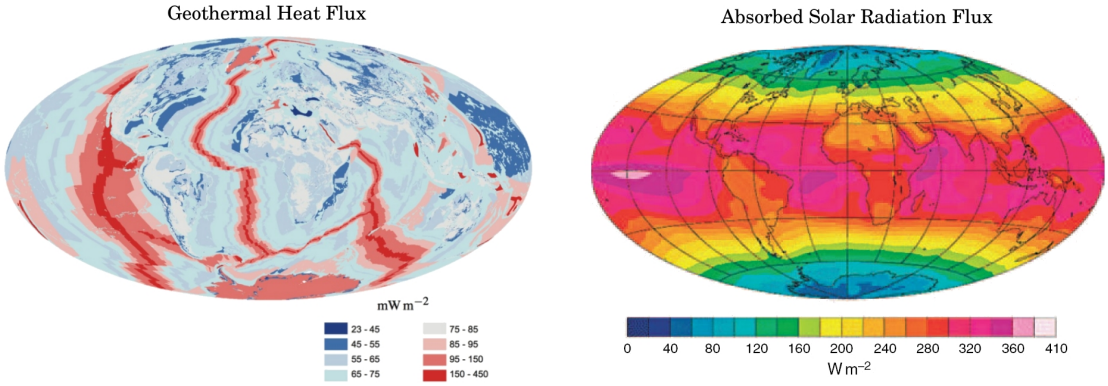

Figure 1.4: Annual mean geothermal heat flux and absorbed solar flux on Earth. The average geothermal heat flux is $\sim 8\times10^{-2}$ W m^{-2} and the average absorbed solar flux is 240 W m^{-2}. Credit: J.H. Davies and J. Michaelsen.

"iceline" (Ros and Johansen, 2013). The iceline is the distance to a star from which water becomes solid ice and can thus be accreted to become a major component of planetary embryos (Hayashi, 1981; Lecar et al., 2006).

1.2.3.2 Keep it liquid!

Water is probably very common in many planets and moons. Even liquid water could actually be widespread in the subsurface of many planetary bodies, as illustrated by our current knowledge of the interior structure and composition of icy moons and transneptunian objects (see Fig. 1.3) (Lunine 2017 and references therein). However, it is much more difficult for a planet to sustain liquid water on its surface because liquid water only exists for a limited range of temperatures (see Fig. 1.2). Surface temperatures depend on the energy balance of the system. The radiative cooling of the surface and oceans by thermal emission is compensated by external sources of energy. At the top of the atmosphere, the source of energy is the solar flux. At the bottom, this is the geothermal heat flux. On Earth, the solar flux dominates by at least 3 orders of magnitude any other source of energy in the radiative budget (see Fig. 1.4).

The stellar flux

To first order, it is the stellar flux that controls if the planet can keep liquid water on its surface. If the planet is too close from the host star, the surface temperature of the planet is too high for liquid water to be stable. If the planet is too far from the host star, the surface temperature of the planet is too low for liquid water to be stable.

The greenhouse effect of the atmosphere

The composition and the thickness of the atmosphere of a planet have a major role on the surface radiative budget. In particular, the presence of greenhouse gases usually contributes to increase the surface temperature of the planet. A greenhouse gas has the property to absorb light much more efficiently in the thermal infrared (where the peak of the thermal emission of the planet is) than in the spectral range where the peak of the stellar emission is. Greenhouse gases absorb thermal infrared

emission from the surface and emit radiations back to the surface, contributing to the warming of the surface.

On Earth, the major greenhouse gases are water (H_2O), carbon dioxide (CO_2), methane (CH_4) and ozone (O_3). Our experience in the solar system tells us that there is a wide variety of possible atmospheric compositions. The atmosphere of Jupiter is essentially made of dihydrogen (H_2) and helium (He); the atmosphere of Venus is dominated by CO_2; etc.

Note that the greenhouse warming power of a gas depends on the context (amount of gas, temperature of the planet, emission spectrum of a star). For example, on present-day Earth, small injections of methane (CH_4) in the atmosphere can have a huge greenhouse effect. Yet, on temperate planets orbiting cool stars, CH_4 can have a very strong anti-greenhouse effect, because (stratospheric) CH_4 absorbs light very efficiently in the near-infrared, where the peak of emission of cool stars is. This prevents stellar emission from reaching (and thus, warming) the low atmosphere and/or surface of the planet.

Note also that radiatively (almost) inactive gases such as N_2 or O_2 can play a very important role for greenhouse warming, through collisional broadening of absorption lines of greenhouse gases. This broadening can significantly increase the spectral range of absorption of greenhouse gases and therefore increase their warming power (see Section 1.4.3).

The geothermal heat flux

The geothermal heat flux on Earth is on average 3×10^3 times weaker than the solar flux. However, on other planetary objects, the geothermal heat flux can have a much more pronounced impact. Io, a volcanically active natural satellite of Jupiter, has a mean geothermal heat flux that is 25 times stronger than on Earth, because of the heating of the interior by tidal frictions (Spencer et al., 2000). It is possible that, in some very specific configurations, the geothermal heat flux could play an important role on the radiative budget of the planet and therefore on its habitability[5].

1.2.3.3 Protect it from escape!

An habitable planet can lose water through atmospheric escape. Surface liquid water is by definition in equilibrium with the atmosphere. Water that evaporates into the atmosphere can rise up into the upper layers and get photodissociated by the high energy photons (FUV [Far Ultraviolet] or more energetic photons, such as EUV [Extreme Ultraviolet] and X rays) emitted by the star, producing hydrogen and oxygen atoms. Hydrogen atoms are very light and can easily escape from the gravity of the planet. If the amount of water vapor in the upper atmosphere is high, and if the X/EUV/FUV flux emitted by the star is also high enough, then a planet that is initially habitable can lose the totality of its hydrogen - and thus of its water - to space in the long run.

There are actually numerous processes that can increase or reduce the atmospheric escape rates of water (hydrodynamical escape, meteoritic impacts-driven escape, solar wind-driven escape, etc.) (Pierrehumbert, 2010; Zahnle and Catling, 2017). Most of the atmospheric escape mechanisms involve very complex, non-linear processes that are very difficult to constrain even on present-day Earth. Space missions such as MAVEN currently in orbit around Mars (Jakosky et al., 2015) will hopefully

[5]For the very peculiar case of planets orbiting in the Habitable Zone of brown dwarfs, the internal heat flux produced by the tidal dissipation could actually be the dominant source of warming on the planet!

better constrain the atmospheric escape models so that we can start to safely apply them to planets or moons where no or almost no observations are available.

1.2.4 The "Habitable Zone"

Classically, The Habitable Zone defines the range of orbital distances for which a planet can sustain surface liquid water (Kasting et al., 1993), and can thus provide the environment for life to emerge and exploit photosynthesis, and potentially to modify the planetary atmosphere in a detectable way. The Habitable Zone (HZ)[6] is thus a very useful concept for astronomers to get an idea of where the planets to target or "hunt" to find life are. For this reason, it is sometimes nicknamed the Hunting Zone[7] (HZ) (see Fig. 1.5). The Habitable Zone is sometimes also known as:

- the "Surface Liquid Water Zone" (SLWZ). Very conventional, I agree.
- the "Surf Zone"[8] (SZ), for adventurers! The zone where you always get ocean waves and sunshine at the same time.
- the "Goldilocks Zone", a metaphorical reference to the children's fairy tale of "Goldilocks and the Three Bears".
- the "ecosphere" (Strughol, 1955), the historical definition.
- the "temperature zone" (Tasker, 2017).

Note that a planetary body that is inside the Habitable Zone is not necessarily habitable (e.g. the Moon is in the Habitable Zone but is not habitable).

1.2.4.1 Inner edge of the HZ

The inner edge of the Habitable Zone is defined as the minimal distance from a given star below which no planet can accomodate surface liquid water.

The "Runaway greenhouse" limit

Let's start with a thought experiment. Take the Earth and put it closer and closer to the Sun. As the Earth get closer to the Sun, the surface temperature and the amount of water vapor in its atmosphere will both increase. Although the Earth is much warmer than today, the radiative budget is still at equilibrium.

At some point however (e.g. from a given star-planet distance), the Earth reaches a tipping point from which the radiative budget becomes out of equilibrium. The amount of water vapor in the atmosphere is so large that the lower atmosphere becomes completely opaque at all infrared wavelengths. The infrared thermal emission emitted by the lower atmosphere and the surface cannot escape to space and the planet therefore cannot cool down. The surface temperature of the planet will progressively increase until the planet can reach a new equilibrium. This new "very hot" equilibrium state occurs when the surface temperature of the planet reaches $\sim$ 1800+ Kelvins (Kopparapu et al.,

[6] The Habitable Zone (HZ) should not be confused with the Habeertable Zone (also "HZ") (Turbo-King et al., 2017).
[7] Credit goes to Franck Selsis.
[8] Credit goes to the very same Franck Selsis.

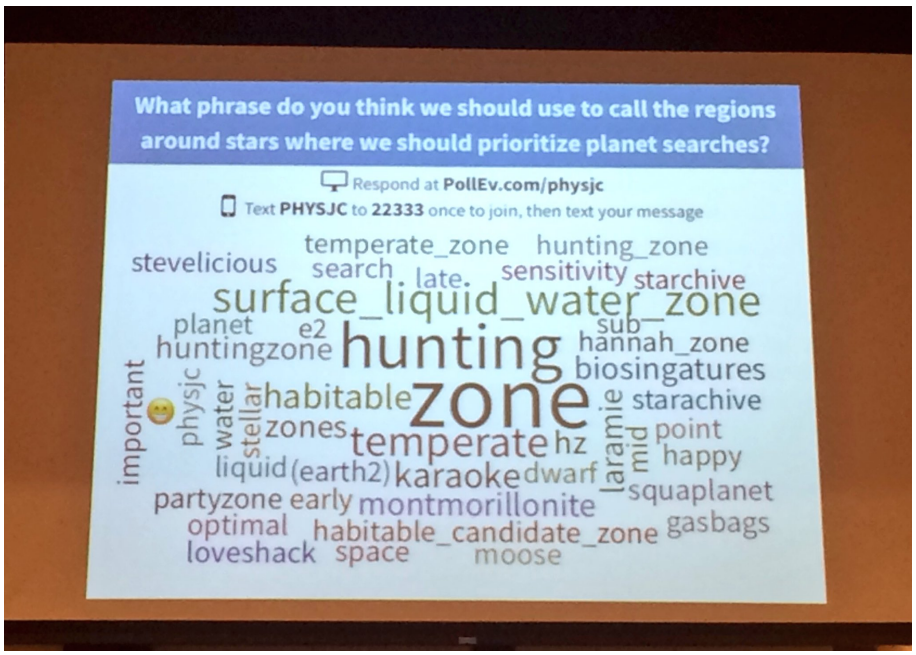

Figure 1.5: "What phrase do you think we should use to call the regions around stars where we should prioritize planet searches?". Results from a poll proposed to the participants of the Habitable Worlds 2017 conference, in Laramie (USA).

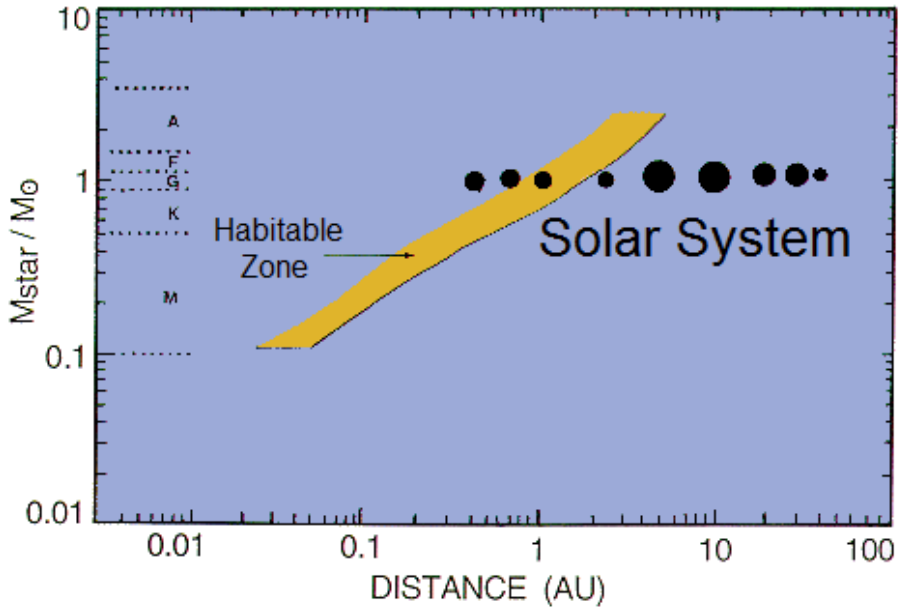

Figure 1.6: Classical Habitable Zone (in yellow) shown as a function of the star-planet distance (in astronomical unit [AU]) and the mass of the host star (with respect to the mass of the Sun $M_{\odot}$). The left part of the HZ was determined by the runaway greenhouse limit, whereas the right part was determined by the maximum greenhouse limit. From Kasting et al. (1993).

2013). At this extreme temperature, the planet is so hot that it starts to emit in the near-infrared / visible domains, where water vapor absorb light much less efficiently.

A planet that is too close from its host star would inevitably lose all its liquid water through evaporation into the atmosphere because of the "runaway greenhouse" mechanism (Ingersoll, 1969; Kasting, 1988; Nakajima et al., 1992).

Note that the exact position of the runaway greenhouse limit can be tricky to determine as it depends of a huge list of internal and external effects (some can be very subtle) such as the type of star, the mass and radius of the planet, the rotation rate of the planet, the amount of available surface water, the amount of additional greenhouse gases, the position and extension of continents, the size of cloud particles, etc.

The "Moist greenhouse" limit

Let's do a second thought experiment. Once again, take the Earth and push it closer and closer to the Sun. At 0.95 astronomical unit[9], the Earth would enter into the "runaway greenhouse" state depicted above. But before reaching that state, the Earth will transit progressively into warmer and warmer, wetter and wetter climate states. Similarly, the upper layers of the atmosphere will also become warmer and wetter. The solar X/EUV/FUV flux can reach the molecules of water in the upper atmosphere and break them into oxygen and hydrogen. Light hydrogen atoms can then easily escape from the gravity of the planet and be lost to space.

Through this mechanism, called the "moist greenhouse" (Kasting, 1988), the Earth could progressively lose all the hydrogen to space and therefore lose all its water.

Note that all the climate models do not currently agree on which of the two processes (a runaway greenhouse or a complete moist greenhouse, i.e. a moist greenhouse that leads to the loss of the entire present-day Earth surface/near-surface water content) will occur first on Earth (Kopparapu et al., 2013; Goldblatt et al., 2013; Leconte et al., 2013a; Wolf and Toon, 2015; Popp et al., 2016; Kopparapu et al., 2017). Although there are a lot of subtle differences between these models, it seems that the main source of discrepency is related to the convection scheme used in the models. The amount of water vapor that reaches the upper atmosphere is indeed strongly related to the strength and depth of the convective layers, as well as to possible overshoot processes. These processes occur at a very small (km) scale and cannot be spatially resolved by global climate models, which usually adopt schemes that mimic convection.

Another significant difference in the models also arises from the calculation of radiative properties of water vapor, i.e. from the switch between HITRAN and HITEMP H_2O line lists, as well as the switch between different H_2O continuum models (e.g. MT_CKD, BPS or CAVIAR). For instance, HITEMP includes many more weak lines of H_2O in the visible and near-infrared, so models that use it are more prone to a runaway greenhouse and have a harder time finding stable, moist greenhouse states (Kopparapu et al., 2013).

1.2.4.2 Outer edge of the HZ

The outer edge of the Habitable Zone is defined as the maximal distance from a given star beyond which no planet can accomodate liquid water. On a distant planet, water can easily freeze because of

[9]The distance between the Earth and the Sun is equal to 1 astronomical unit (AU), or 150 million kilometers.

the "runaway glaciation" mechanism. As water starts to freeze, the albedo of the planet rises, which creates even more freezing. This is a positive (destabilizing) feedback.

The position of the outer edge of the Habitable Zone can be calculated by finding the most efficient atmosphere to keep surface liquid water on a planet as far as possible from its host star. This is usually done by designing the best atmospheric cocktail of greenhouse gases (in both quantity and composition), and that is physically plausible. We call this limit the "maximum greenhouse".

The Maximum greenhouse

Greenhouse gases tend to warm the surface of planets. On Earth, greenhouse gases warm the surface in average by $\sim$ 33K. On Venus, the greenhouse warming rises several hundreds of Kelvins.

There are numerous greenhouse gases in nature, but there is only a limited number of them that we expect to be present in significant proportions in the atmosphere of habitable planets. The more plausible gases are carbon dioxide and water vapour (CO_2, H_2O). Other gases like ammonia (NH_3) or methane (CH_4) could be abundant in reducing atmospheres but would experience rapid photodissociation if they are not protected from the X/EUV/FUV flux emitted by the star, or if they are not replenished fast enough. H_2[10] is also a good candidate, but it is light and can escape very easily to space.

Traditionally, the Habitable Zone boundaries are calculated assuming CO_2 as the primary greenhouse gas. There are several reasons for that. First, because adding CO_2 into an atmosphere is in fact one of the most efficient way to warm the surface of a distant planet. Secondly, because CO_2 is a widespread greenhouse gas in the planets of the Solar System (Venus, Earth and Mars). Third, because we know that there are on Earth geochemical mechanisms (e.g. the carbonate-silicate cycle; see Section 1.2.6) that can regulate the amount of CO_2 in the atmosphere, stabilizing the climate in conditions where surface liquid water should be stable.

The Rayleigh scattering

Unfortunately, a planet cannot be warmed as much as wanted just by adding greenhouse gases such as CO_2 indefinitely. At some point, the opacity of the greenhouse gases starts to saturate in the infrared, while the fraction of the stellar emission absorbed by the surface and the atmosphere of the planet starts to decrease (Kasting et al., 1993; Kopparapu et al., 2013). This results from the Rayleigh scattering by gas molecules that tends to reflect incoming photons to space. A planet with a pure CO_2 atmosphere (without clouds) can keep liquid water on its surface until 1.67 Astronomical Units (around a Sun-like star). This distance is the outer edge of the Habitable Zone and was established for an atmosphere of 8 bar of CO_2, for planets with Earth radius and gravity (Kasting et al., 1993; Kopparapu et al., 2013). If the planet builds up more than 8 bar of CO_2, then it starts to cool down because of the Rayleigh scattering.

Note that the effect of Rayleigh scattering is lowered for planets orbiting cool stars, because most of the stellar emission occurs in the near-infrared spectral domain where the effect of Rayleigh scattering becomes negligible[11].

Atmospheric collapse

Surface condensation can also sometimes prevent a planet from building up an atmosphere as thick as wanted. Temperatures are not homogeneous on the surface of a planet. Whether atmospheric gases

[10] H_2 can produce a powerful greenhouse effect through collision-induced absorptions (see Sect 1.4.6).

[11] We recall that the cross section of Rayleigh scattering scales as λ^{-4}, with λ the wavelength

condense or not usually depends on the minimum surface temperature of the planet. This is why we usually call the regions of minimum temperature the "cold traps", because this is where gases that condense will get preferentially trapped. Usually, the cold traps are located either at the poles (on Earth, for instance) or on the nightside (for synchronously rotating planets; see Section 1.2.4.3).

Surface condensation or "atmospheric collapse" can prevent a planet to reach the theoretical "maximum greenhouse" limit. This possibility is discussed in details in Chapters 2 and 4.

The effect of clouds

Clouds play a major role to determine the edges of the Habitable Zone. Clouds can reflect a large part of the incident stellar light, but they can also produce a very strong greenhouse effect, by absorbing thermal infrared from the surface, and re-emitting part of it back to the surface at a lower brightness temperature. In some cases, clouds can even reflect (or scatter) the thermal infrared emission of the surface, back to the surface. Clouds, depending on their composition, thickness and spatial distribution can contribute positively or negatively to the radiative budget of a planet[12].

When CO_2 ice clouds start to form in a thick CO_2-dominated atmosphere, the surface of the planet can get warmer. CO_2 ice clouds are in fact made of thin particles of CO_2 ice that backscatter the thermal emission of the surface (Forget and Pierrehumbert, 1997). When taking into account the radiative effect of CO_2 ice clouds, the outer edge of the Habitable Zone can be theoretically pushed as far as 2.5 Astronomical Units from the Sun (assuming a 100% cloud cover) (Forget and Pierrehumbert, 1997)[13].

1.2.4.3 The effect of the rotation speed

The Earth rotates once in about 24 hours with respect to the Sun, and rotates around the Sun in about 365 days. The Moon, however, always shows the same face to the Earth. The rotation period of the Moon (with respect to the Earth) is equal to the orbital period of the Moon around the Earth. The Moon is in 1:1 spin-orbit resonance with the Earth. We usually tell that (i) the Moon is in synchronous rotation around the Earth or (ii) the Moon is tidally locked to the Earth. These three different wordings describe the same orbital configuration. Similarly, Mercury is in 3:2 spin-orbit resonance with the Sun. Every two orbits, Mercury has completed three rotations with respect to the Sun.

Generally, planets that orbit very close to their host star are influenced by gravitational tides exerted by the star on the planet. The tidal torque tends to lower the obliquity of the planet and tends to slow down the rotation of the planet, until the planet get trapped in a spin-orbit resonance state. Sometimes, the mechanism is so efficient that the planet ends up in synchronous rotation, like the Moon around the Earth.

Planets orbiting in the Habitable Zone of low mass stars are relatively close to their host (faint) star. As a consequence, gravitational tides should exert a significant influence on their rotation and

[12] On Earth for example, clouds are the main source of uncertainties in assessing how the climate will respond to an increase in carbon dioxide atmospheric levels.

[13] This number is in fact very likely overestimating the position of the outer edge of the Habitable Zone, because in reality, (i) the CO_2 ice cloud coverage can be much lower than 100% (Forget et al., 2013) and (ii) Kitzmann (2016) recently demonstrated that the greenhouse warming of CO_2 ice clouds had been overestimated in Forget and Pierrehumbert (1997) because of the way radiative transfer is handled in climate models (i.e. the widely used two-stream approximation can introduce significant error in the calculation of greenhouse warming produced by CO_2 ice clouds).

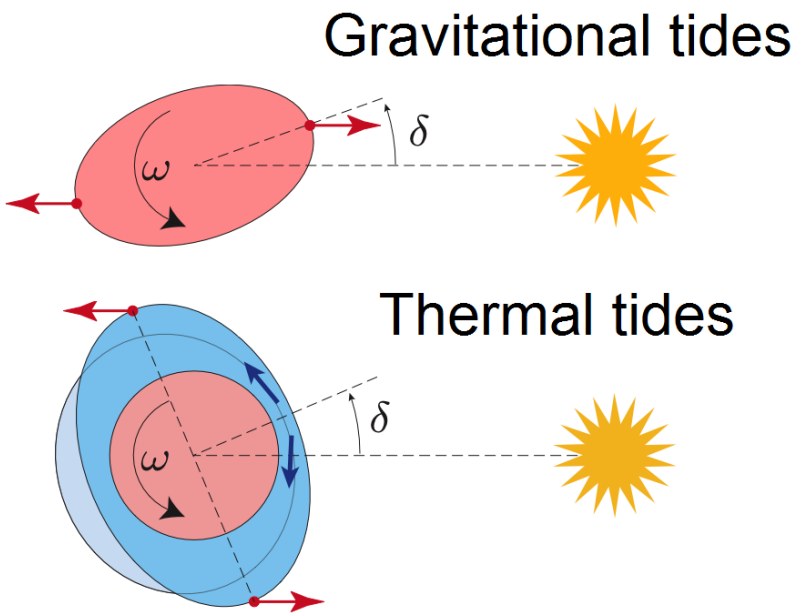

Figure 1.7: Mechanisms of the effect of gravitational tides (upper panel) and thermal tides (lower panel). ω and the corresponding black arrow indicate the direction of the rotation of the planet. δ refers to the angular lag created by the tides. The atmosphere is in blue. Credit: J. Laskar and A. Correia.

obliquity. Many of the planets orbiting in the Habitable Zone of low mass stars are expected to (1) have a near-zero obliquity, (2) have a near-circular orbit and (3) be in synchronous rotation around their host star.

Why do gravitational tides affect rotation?

The gravity force (that decreases as distance increases) exerted by a star on a planet is not the same everywhere on the planet. The part of the planet that is closer to the star is more attracted by gravity than the part of the planet that is the most distant to the star. As a consequence, the star distorts the planet and creates a bulge in the star-planet direction (Goldreich and Peale, 1966; Peale, 1977).

If the rotation period of the planet is shorter than its orbital period, the "tidal" bulge will be slightly shifted with respect to the star-planet axis. There is in fact a time lag before this tidal bulge disappears, because the planet is a non-elastic body.

As a consequence, there is a slight angular lag δ (see Fig. 1.7, upper panel) between the tidal bulge and the star-planet axis, creating a tidal torque that acts in the opposite direction of the rotation of the planet. This means that this tidal torque actually slows down the planet. This effect will persist until the rotation period of the planet is equal to the orbital period. In this situation, the most stable equilibrium state is the synchronous rotation.

Note that it is possible that the planet, depending on its eccentricity, may be trapped in higher orders of spin-orbit resonances (3:2, 2:1, etc.).

The effect of thermal tides

When a planet is endowed with a thick enough atmosphere, there is another tidal force that appears and that creates the opposite effect with respect to the gravitational tides. These are the "thermal" tides (Chapman and Lindzen, 1970; Leconte et al., 2015; Auclair-Desrotour et al., 2017a).

Take a planet with a thick atmosphere, like Venus for example. The Sun is going to warm preferentially the "substellar" region of the planet, the region of the planet where the Sun is at the zenith. The atmosphere in the substellar region will warm and thus expand. To equilibrate the pressure gradient in the atmosphere of the planet, this expansion will produce strong winds that will push atmospheric gases (and thus some mass) toward the terminators[14] of the planet. This creates a bulge of positive mass in the direction perpendicular to the star-planet axis.

If the rotation period of the planet is shorter than its orbital period, there will be an angular shift δ between the position of the "thermal tide" bulge and the direction perpendicular to the star-planet axis (see Fig. 1.7, lower panel). If δ is lower than 90°, the bulge will produce a thermal tide torque acting in the same direction than the planet, which will further accelerate the rotation speed of the planet.

If the thermal tides are strong enough, the period of rotation of the planet will converge in an equilibrium state that is different from the synchronous rotation, where gravitational tides and thermal tides offset each other. This is very likely what happened to Venus (Gold and Soter, 1969; Correia and Laskar, 2001).

Gravitational tides and thermal tides are the two main processes that control if a planet end up in synchronous rotation or not. In general, the lower the mass of the star, the thinner the atmosphere of the planet, the higher the chances for the planet to end up (rapidly) in synchronous rotation are. Planets that orbit in the Habitable Zone of very cool, small stars should very likely end up in synchronous rotation. This holds unless external factors come at play, such as outer massive planets that could excite the orbit of the planet in higher spin-orbit resonances.

A planet that is synchronously rotating receives the totality of the stellar emission on one face only. This has dramatic consequences for the type of climates and the habitability on these planets.

The inner edge of the Habitable Zone for synchronous planets

If you place the Earth at a distance of 0.95 Astronomical Unit from the Sun, the Earth is going to face a runaway greenhouse. Soon the Earth will not be habitable. Proceed now to the same experiment with a synchronously rotating planet. At 0.95 Astronomical Unit, the planet will remain habitable! As the planet get closer and closer to the Sun, the stellar flux received by the planet is getting higher and higher. This creates a strong convective region at the substellar point, producing a very thick, reflective cloud cover (Yang et al., 2013) as illustrated in Fig. 1.8. The cloud coverage of the irradiated face can be almost complete. The higher the stellar flux, the more efficient the convection is, the thicker and thus the more reflective the cloud cover is, and the higher the planetary albedo becomes. As a consequence, the inner edge of the Habitable Zone for synchronously rotating planets lies at much lower distance than (Earth-like) fast-rotating planets (see in Fig. 1.9 the difference between the pink and violet limits in the Habitable Zone diagram).

Synchronous planets that orbit in the Habitable Zone of very low mass (or "ultracool") stars can have a rotation period shorter than 10 days, and can enter in the "fast-rotating" regime (Edson et al., 2011; Carone et al., 2015, 2016), where winds can be so strong that the cloud cover is reduced and

[14] Terminators are the regions of transition between the dayside and the nightside of a planet.

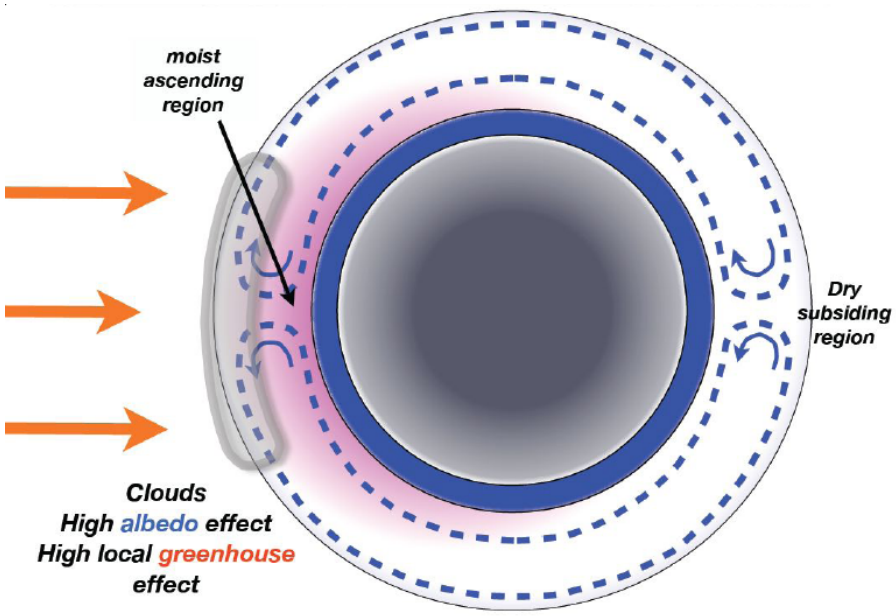

Figure 1.8: Schematic view of the stabilizing feedback of substellar clouds on synchronous planets. Credit: J. Leconte.

shifted away from the substellar point (Kopparapu et al., 2016). This drastically reduces the cloud negative (stabilizing) feedback described above, which pushes the inner edge of the Habitable Zone to lower irradiation as the mass of the star decreases (see in Fig. 1.9 how the pink limit evolves with the type of host star).

Note that there are still huge uncertainties related to how much clouds form (and how clouds are organized) at the substellar point of synchronously rotating planets. Most of these uncertainties come from the fact that current convection schemes are unable to represent how clouds can aggregate and form structures at much lower scales than the typical resolution of Global Climate Models (GCMs). The most efficient way to examine closely these effects is to use Large Eddy Simulations (LES) that can go to a low enough spatial (< 1 km) and thus temporal (~ 1 s) resolution that the convection processes can be explicitely resolved (Lefevre, Turbet et al., in preparation).

The outer edge of the Habitable Zone for synchronous planets

Cold planets are usually less affected by gravitational tides because they are more distant from their host star than the "hot" planets, e.g. planets near the inner edge of the Habitable Zone. In the Solar System, the typical timescale to synchronize the rotation of a planet at the inner edge of the Habitable Zone (0.95 AU) is roughly $30\times$ lower than a planet at the outer edge (1.67 AU). As a result, the timescale needed for a planet like Mars to reach the synchronous rotation state is much longer than the typical lifetime of a Sun-like star.

However, around very low mass stars, the Habitable Zone is much closer to the star, and even cold planets (e.g. planets near the outer edge of the Habitable Zone) are thus likely to end up in synchronous rotation. On such planets, the most efficient cold traps are usually located on the nightside. To sustain surface liquid water, the planet must first be able to sustain an atmosphere. For

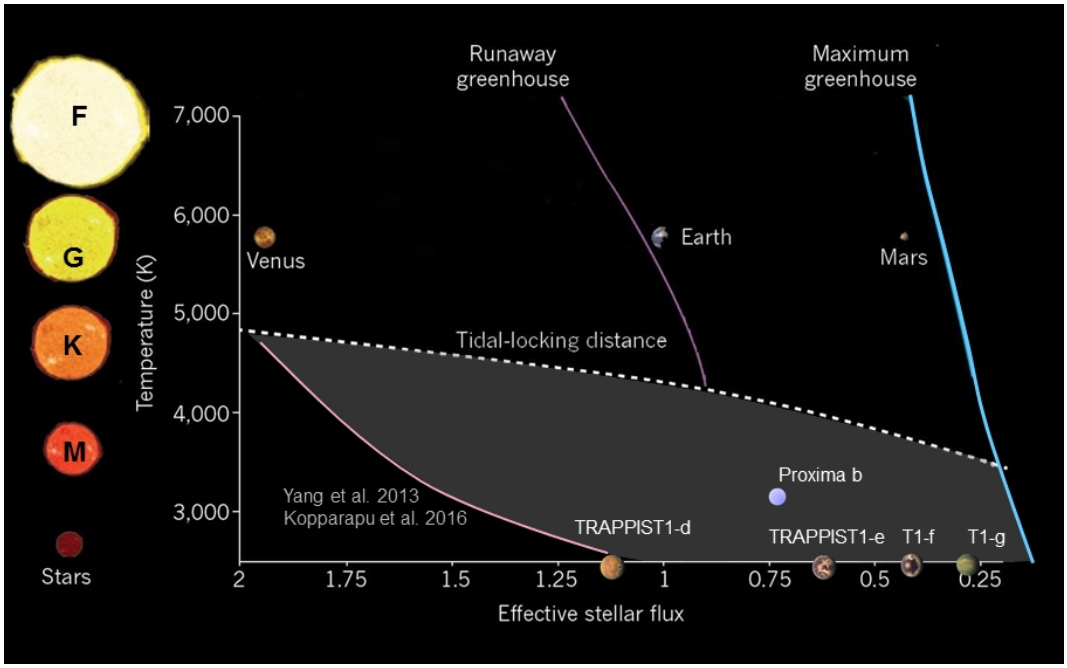

Figure 1.9: Habitable Zone (grey area) for synchronously rotating planets. The white dotted line (or "tidal-locking distance") is the typical time scale required to synchronise the orbit of a planet within a Gy timescale. Adapted from Kasting and Harman (2013).

example, a planet endowed with a thin enough atmosphere of $N_2/CO_2/H_2O$ could lose progressively all the gases by surface condensation on the night side. First, water vapor will condense on the night side, then CO_2, ... and even potentially N_2! As the atmosphere get thicker (by injecting more N_2 or CO_2 for example), (1) there is more greenhouse warming and (2) the heat transport between dayside and nightside becomes more efficient. These two effects combined tend to prevent atmospheric species from condensing on the nightside.

If the synchronous planet is able to sustain an atmosphere that is thick enough that atmospheric collapse is prevented, then the outer edge of the planet can be defined once again by the maximum greenhouse limit (see in Fig. 1.9 the pale blue limit). Note that other types of heat transport (e.g. oceanic transport) can also drastically increase the stability of synchronous planets to atmospheric collapse (Hu and Yang, 2014; Del Genio et al., 2017).

1.2.4.4 Influence of other effects on the boundaries of the Habitable Zone

There are many other effects that can actually affect the positions of both the inner and outer edges of the Habitable Zone.

Dry planets

Dry planets also known as "water-poor" planets or "land planets" are desert worlds with limited surface water (Abe et al., 2011). On these planets, water is expected to migrate to the cold traps of the planet (usually the poles). On such planets, the runaway greenhouse is much harder to trigger because of the low availability of surface liquid water. As a result, the inner edge of the Habitable

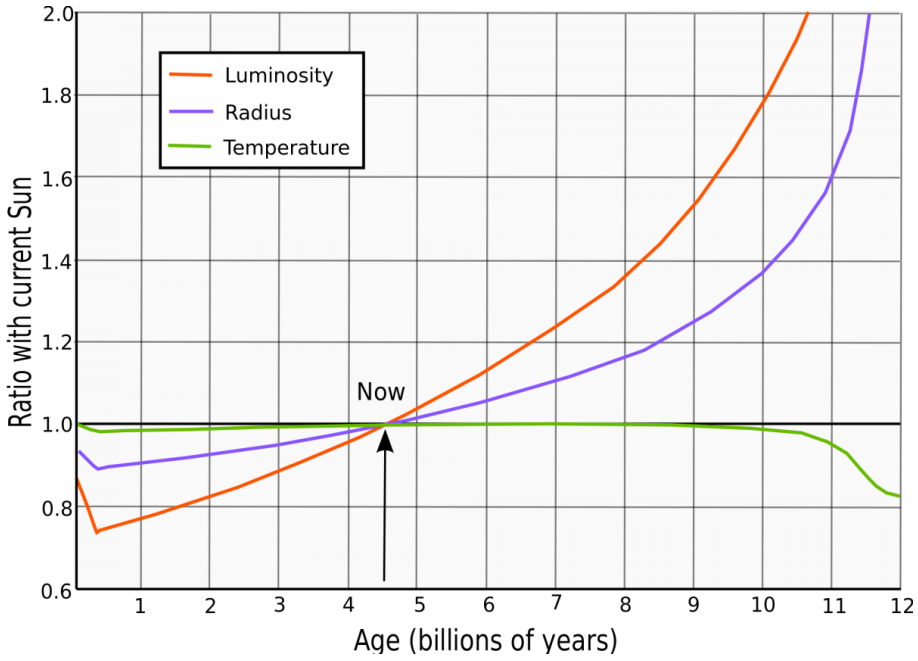

Figure 1.10: Evolution of the solar luminosity, radius and temperature from formation (Age = 0) to the exit from the Main Sequence phase (Age = 10.5 Gy). From Ribas (2010).

Zone of dry planets is expected to be much closer to the host star (Abe et al., 2011; Kodama et al., 2018).

Hydrogen-rich atmospheres

Hydrogen is a super efficient greenhouse gas due (i) to collision-induced absorptions (see Section 1.4.6) between H_2-H_2 and H_2-X pairs and due (ii) to the fact that it condenses only at extremely low temperatures. Theoretically, with a thick enough atmosphere of H_2, any distant terrestrial planet could sustain surface liquid water[15] (Stevenson, 1999; Pierrehumbert and Gaidos, 2011; Seager, 2013).

However, the main issue with the H_2 greenhouse warming is that H_2 is hard to sustain in the atmosphere of an Earth-sized planet because it can escape very easily to space (Ramirez and Kaltenegger, 2017).

1.2.5 Past and future of the Earth

The main source of production of energy in the Sun is nuclear fusion. Hydrogen atoms come together to form helium. As the mixing ratio of helium increases in the Sun, the Sun core gets denser and, as a consequence, warmer. Nuclear reactions are more and more intense, which increases the production of energy in the Sun's core. As a result, the solar luminosity is increasing with time.

The past of the Earth

[15] Even a free-floating planet (i.e. a starless planet) could sustain surface liquid water with a thick H_2 atmosphere and some geothermal heat flux (Stevenson, 1999).

Three billions years ago, the Sun was 20% fainter than today. If you suddenly reduce the solar flux on present-day Earth by 20%, oceans would rapidly freeze (Charnay et al., 2013). Yet, we have robust evidence that life was present on Earth at least from 3.5 billion years ago from stromatolites and microfossils (Schopf et al., 2007), and that surface or near-surface liquid water must have been present continuously on Earth from 3.5 Gya until now. This is usually known as the "faint young Sun paradox" (Sagan and Mullen, 1972).

There are several scenarios that could explain the continuous presence of life and liquid water on Earth since 3.5 Gya. The most common of these scenarios is that Earth had - at the time - an atmosphere dominated radiatively by CO_2 and potentially CH_4/H_2 that produced a strong greenhouse warming.

The future of the Earth

6 billions years from now, the Sun will leave the Main Sequence phase of stars to become a Red Giant. The radius of the Sun will increase by a factor of ~ 200 and the Earth will very likely end up swallowed by the Sun.

1-2 billion years from now, the Earth will receive 10% more radiation from the Sun, as the Sun get brighter and brighter with time. This should be enough to trigger a transition toward a Runaway Greenhouse (Leconte et al., 2013a; Wolf and Toon, 2015). All the water present in the surface and subsurface of the Earth will evaporate, forming a steam atmosphere with a temperature that could rise up to 1500°C (Kopparapu et al., 2013). The surface pressure of the Earth will then reach several hundreds of bar. The Earth will therefore become unhabitable.

900 millions years from now, the temperature of the Earth will be high enough for the CO_2 present in our atmosphere to get almost entirely weathered (see next subsection). The amount of CO_2 will go below 10 ppm (as a reminder, the present-day Earth concentration of CO_2 is ~ 400 ppm or 0.04%), which should stop the photosynthesis of terrestrial plants (Caldeira and Kasting, 1992). Without photosynthesis, life as we know it cannot subsist. Meanwhile, the Earth may have entered into a moist greenhouse state during which water is lost progressively to space.

More importantly, 100 years from now, the future climate change will cause a rise of mean surface temperatures by 1.5 to 4.5°C (IPCC, 2013: Climate Change 2013: The Physical Science Basis.). The main driver of this climate change is the production by us - humans - of greenhouse gases, and more particularly carbon dioxide (CO_2), a very powerful greenhouse gas. Although this is a terrible disaster for our planet, it is important to note that anthropogenic increased levels of CO_2 are unlikely to produce a transition toward a "runaway greenhouse" (Kasting and Ackerman, 1986; Goldblatt et al., 2013; Ramirez et al., 2014b).

Dangerous young stars

In general, the habitability of a planet is tightly linked to its host star and its temporal evolution. Before reaching the Main Sequence phase during which their luminosity increases slowly, stars have to go through the Pre-Main-Sequence (PMS) phase during which the star is warmer, brighter and larger. The PMS corresponds in fact to the phase during which a newly formed star is getting rid of the initial energy of its accretion, through the conversion of gravitational contraction to emissions of photons.

For a Sun-like star, the duration of the PMS - usually approximated by the "Kelvin-Helmoltz" timescale - is very short ($\sim 10^7$ years) compared to the typical lifetime of planets. However, the duration of the PMS phase can be much longer (up to 10^9 years) for smaller stars. During that period,

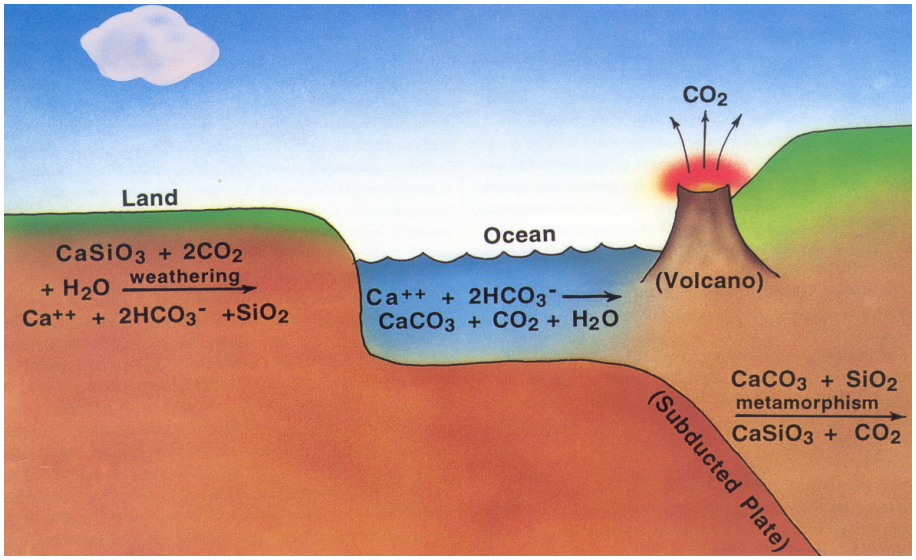

Figure 1.11: Mechanism of the carbonate-silicate cycle. Credit: J. Kasting.

planets orbiting around a PMS star could have faced a runaway greenhouse phase during which the most condensible species (e.g. water) would have been vaporized, and exposed to atmospheric escape.

1.2.6 The carbonate silicate cycle

The Earth is able to regulate the amount of carbon dioxide in the atmosphere (Walker et al., 1981) through the carbonate silicate cycle illustrated in Fig. 1.11. To put it in simple terms, atmospheric CO_2 can get dissolved in fresh water coming from precipitation. While flowing, liquid water can also dissolve silicated rocks (e.g. $CaSiO_3$) present on the surface of Earth. Products of the dissolution are transported through rivers to the oceans where they accumulate. Beyond a given concentration, dissolved ions combine to form carbonates. On Earth, the formation of carbonates is achieved by living organisms to make shells. The balanced chemical equation is typically: $CO_2 + CaSiO_3 \rightarrow CaCO3 + SiO_2$. Once they are formed, carbonates fall to the bottom of the oceans where they accumulate. Carbonates building up on top of the oceanic tectonic plates get slowly transported and eventually get subducted. At high depth, high pressures and temperatures reverse the chemical reaction, which releases CO_2. CO_2 is then outgassed by volcanoes and get returned into the atmosphere. That's it, the CO_2 cycle is complete.

The key element of the carbonate-silicate geochemical cycle is that the rate of rock dissolution reaction by CO_2 increases with temperature. As a result, if the Earth gets warmer, the amount of CO_2 in the atmosphere will decrease and the Earth will cool down. Similarly, if the planet gets cold, the CO_2 weathering rate decreases and CO_2 accumulates through volcanic outgassing. If the Earth gets so cold that it enters into a glacial era (Evans et al., 1997; Hoffman et al., 1998; Hoffman and Schrag, 2002), liquid water cannot weather continents anymore, and the layer of ice that will form between oceans and the atmosphere will prevent CO_2 to get dissolved. Meanwhile, volcanoes will keep outgassing CO_2 in the atmosphere. CO_2 will inevitably accumulate in the atmosphere until the amount of greenhouse gas is high enough for Earth to escape glaciation. The carbonate silicate cycle

is somehow a "geophysical thermostat" (Walker et al., 1981).

Note that the stabilizing feedback of the carbonate-silicate cycle acts on timescales on the order of million years, which is fast enough to influence the climate of our planet in the long term, but is way too slow to counteract the effect of the global warming induced by us, humans.

Several authors have recently explored how the carbonate-silicate cycle would behave on planets that harbour a different environment than the Earth (Kadoya and Tajika, 2014; Menou, 2015; Haqq-Misra et al., 2016; Abbot, 2016; Batalha et al., 2016; Paradise and Menou, 2017). I review recent advances below.

Limit cycles

We know from solar luminosity evolution models that the insolation on Earth was lower in the past. How did the carbonate-silicate cycle work at the time? And more generally, how does the carbonate-silicate behave on planets that are less irradiated than the Earth? A recent breakthrough to this question was made by Kadoya and Tajika (2014) and Menou (2015)[16].

The CO_2 atmospheric balance can be written:

$$\frac{d\, p_{CO_2}}{dt} = V - W(T_{surf}, p_{CO_2}) \tag{1.1}$$

with p_{CO_2} the partial pressure of CO_2, V the CO_2 outgassing rate by volcanoes, and W the CO_2 weathering rate. W can be estimated empirically by:

$$\frac{W}{W_\oplus} = \left(\frac{p_{CO_2}}{p_\oplus}\right)^\beta e^{\left(k_{act}(T_{surf}-288)\right)} \left(1 + k_{run}(T_{surf} - 288)\right)^{0.65} \tag{1.2}$$

This empirical expression is adapted by Menou (2015) from Earth studies (Berner and Kothavala, 2001). $p_\oplus = 0.33$ mbar is the pre-industrial p_{CO_2} level, $W{=}W_\oplus{=}V_\oplus$ (e.g. the present-day mean CO_2 outgassing rate) for a surface temperature $T_{surf} = 288$ K (i.e. 15°C). $k_{act} = 0.09$ K^{-1} is a coefficient proportional to the mineral dissolution activation energy. $k_{run} = 0.045$ K^{-1} is a coefficient expressing the effect of temperature on global river runoff. $\beta = 0.5$ is an exponent that determines how strongly weathering depends on atmospheric CO_2 partial pressure. β depends on the efficiency at which CO_2 is concentrated in the soil, and is thus highly dependent on the presence and type of plants (Berner and Kothavala, 2001). These coefficients can significantly vary depending on the planet considered, on if (very hypothetic) plants are present or not, on the position and elevation of continents, etc.

Whatever the choice of (physically plausible) coefficients, W is an increasing function of both temperature and CO_2 partial pressure. On pre-industrial Earth, CO_2 outgassing rate by volcanoes and CO_2 removal rate by weathering are roughly balanced (i.e. $W_\oplus = V_\oplus$), and the temperate climate of the Earth is stable. A planet that is less irradiated than Earth must have more CO_2 in the atmosphere than the Earth to sustain the same mean surface temperature (288 K) than present-day Earth. This means that, for a given surface temperature and CO_2 outgassing rate, the weathering rate should be higher for planets that are less irradiated, because W increases with p_{CO_2}.

Beyond a certain distance to the host star, the amount of atmospheric CO_2 required to keep the planet temperate becomes so large, and thus the weathering rate is so high that no solution exists

[16] James Kasting actually informed me that Eiichi Tajika had explored this idea more than a decade ago (Tajika, 2003, 2007) in the context of the early Earth and for scenarios of low CO_2 volcanic outgassing rates.

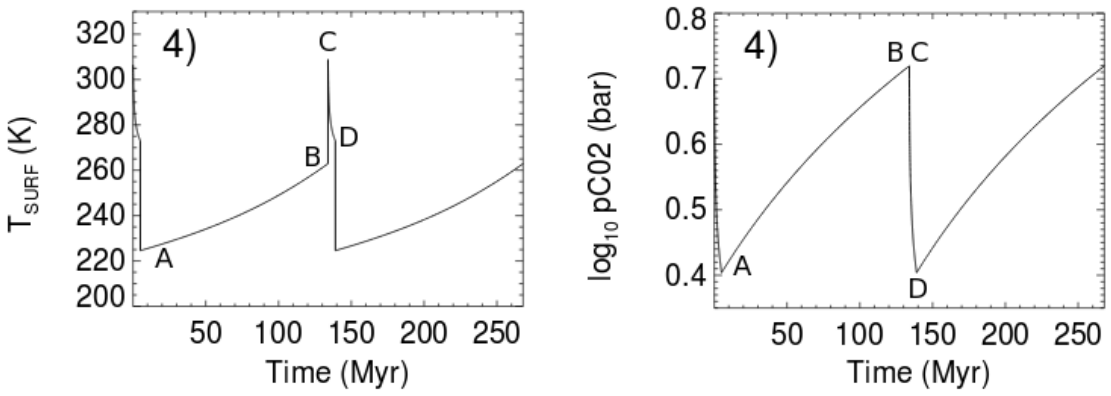

Figure 1.12: Temporal evolution of the surface temperature and CO_2 partial pressure on a planet located at 1.6 AU of a Sun-like star. It is assumed here that the CO_2 outgassing rate is 3 times that of present-day Earth. Adapted from Menou (2015).

to the equation 1.1. As a result, the planet will oscillate periodically between warm and cold states. This is illustrated in Fig. 1.12. Let's start at the point A. The planet is cold and glaciated and the weathering rate is zero. CO_2 accumulates through volcanic outgassing. Once the CO_2 partial pressure is high enough that the greenhouse warming of CO_2 can deglaciate the planet (B), the albedo of the planet suddenly decreases and the planet transitions into a warm state (C). Because the weathering rate is larger than the outgassing rate for temperatures above the melting point of water, the CO_2 partial pressure decreases, which reduces the surface temperature. CO_2 decreases until the surface temperature goes below 0°C (D) and the planet becomes entirely glaciated. This stops the weathering and brings us back to point A. This oscillation between warm and cold states, predicted on distant Earth-like planets[17], is called "limit cycle".

A direct implication of this result is that distant planets are expected to enter very easily in glaciation eras, where they could be trapped for extended periods of time because of (1) substantial seasonal weathering in localized deglaciated continental regions (Paradise et al., 2018) or (2) because atmospheric CO_2 could condense in the coldest regions (usually the poles) of the planet (Turbet et al., 2017b). This second possibility is the topic of Chapter 2.

The carbonate silicate cycle on water-rich and water-poor planets

Water-rich and water-poor planets can be considered as the two endmembers states of temperate Earth-like planets.

Water-rich planets are planets that have enough water for oceans (glaciated or not) to cover 100% of the planet. It has been shown that in this situation, it is the dissolution of CO_2 in the ocean - and obviously not the continental weathering - that controls the amount of CO_2 in the atmosphere and thus the habitability of the planet. The ability of oceans to dissolve CO_2 increases with decreasing temperature (Kitzmann et al., 2015), producing a positive feedback between temperature and CO_2 atmospheric concentration. As a result, water-rich planets could easily build up a thick CO_2-dominated atmosphere, whose thickness depends on the size of both H_2O and CO_2 reservoirs.

[17] Note that limit cycles have also been proposed as a possible scenario for the ancient climate of early Mars (Batalha et al., 2016).

Water-poor planets also known as "land planets" are desert worlds with limited surface water (Abe et al., 2011). On these planets, water is expected to migrate in the cold traps of the planet (usually the poles). Because water is expected to (1) cover a limited fraction of the surface and (2) stay in the coldest regions of the planet, the weathering rate is expected to be much reduced compared to a planet with an Earth-like surface water reservoir (Global Equivalent Layer[18] of 3 km) and that receives the same insolation. As a result, CO_2 should easily build up to high levels on land planets.

Venus is probably the best exemple of an extremely dry planet that was unable to equilibrate CO_2 levels through continental weathering.

1.2.7 Venus, a planet that faced a runaway greenhouse?

Venus is an exemple of what happens to a planet that is too close from its host star.

At first sight, Venus is a planet that is very similar to the Earth. It is a rocky planet, like the Earth, and its equatorial radius and mass are equal to 0.949 and 0.815 times that of the Earth, respectively.

Yet, the surface and the atmosphere of Venus are very exotic, with respect to the Earth. The mean surface temperature and pressure of Venus are $\sim 480°C$ and 90 bar, respectively. The atmosphere is essentially made of CO_2. Water vapor is a minor trace gas reaching concentration of 0.002% (20 ppm). If you take all the water of Venus and put it on the surface, this will produce a layer of 3 cm (e.g. a 3 cm GEL - Global Equivalent Layer) (Bougher et al., 1997; Bézard et al., 2009).

There are good reasons to think that Venus and the Earth formed in a similar manner, and that the two planets may initially have been composed with similar building blocks. But where did the water of Venus go? It is likely that water was abundant when Venus was a newly formed planet, but Venus was unable to keep its water. Because of the large surface temperature of Venus, all the water (initially potentially liquid) may have progressively been converted into water vapor (Way et al., 2016). Or alternatively, water may never had the chance to condense on the surface of Venus (Hamano et al., 2013). In both cases, atmospheric escape of hydrogen would have progressively transformed Venus into the dry planet that we see today.

In the early 90s, the Magellan space probe was sent to reach the orbit of Venus. Its radar instrument revealed the details of Venus topography with an unprecedented precision, indicating that liquid water did not flow on Venus for the last billion year (Solomon and Head, 1991; Solomon et al., 1991). This observation is crucial because it gives somehow an empirical constraint on the location of the inner edge of the Habitable Zone. One billion year ago, Venus received 1.76 times the present-day flux on Earth and was not habitable. One billion year ago, an intense volcanic activity completely resurfaced the surface of Venus, which prevents us from going back in time further that one billion year ago (Solomon and Head, 1991; Solomon et al., 1991). Until we go and dig on the surface of Venus, whether Venus hosted surface liquid water oceans in the past or not will remain a pending question.

Was Venus habitable one day? Is there life in the atmosphere of Venus[19]? Hopefully, future space missions of exploration will tell us more about these pending questions.

[18] The total water inventory is expressed here in global equivalent layer (GEL), which is the globally averaged depth of the layer that would result from putting all the available water in the system at the surface in a liquid phase.

[19] Venus might be part of class II habitability thanks to cloud droplets that could host primitive life.

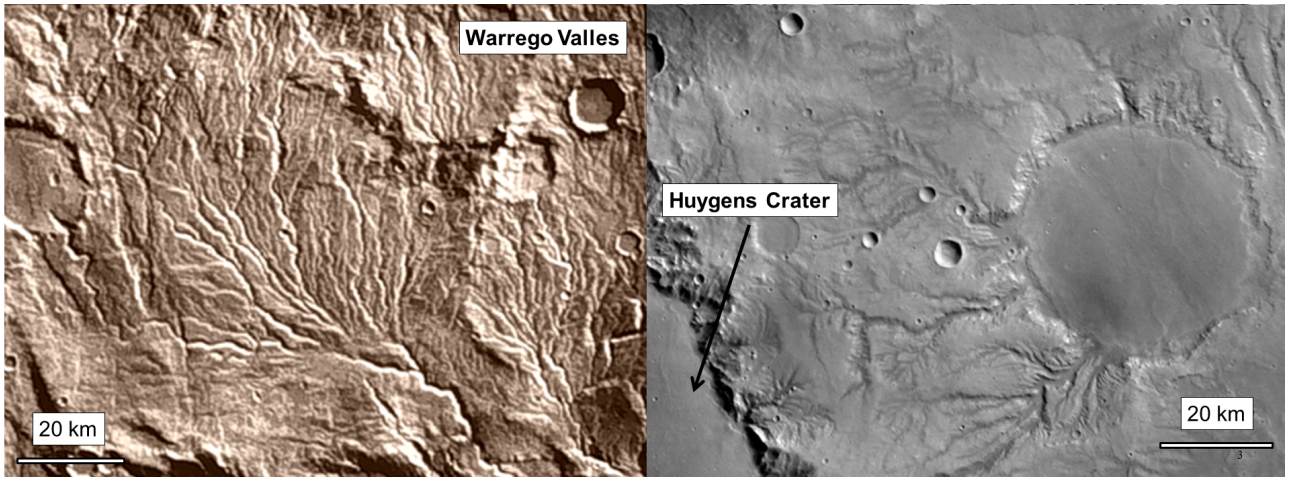

Figure 1.13: Two exemples of sites of dendritic valley networks. Both Warrego Valles (left panel, 42°S,93°W) and the valleys/impact crater lake in the east-rim of Huygens crater (right panel, 14°S,55°E) are located on Late Noachian terrains, in the southern highlands of Mars.

1.2.8 The early Mars enigma

Mars is the only example of planet - except our own Earth - where we know surface liquid water was present. Yet, we are still unable to understand why.

Today, Mars is a cold and dry planet. The mean surface temperature of the red planet is $\sim$ 200K and the mean surface pressure is $\sim$ 6 millibar. Within these conditions, water on present-day Mars can only exist as solid ice or as gas, and very anecdotally as liquid brines (McEwen et al., 2011, 2014; Ojha et al., 2015). Yet, we now have numerous pieces of evidence that ancient Mars was a planet that had many characteristics typical of an habitable planet.

Evidence for the presence of surface liquid water

In 1972, the Mariner 9 space probe discovered for the first time dry lakes and rivers on the surface of Mars. Their presence suggests that the surface of Mars was warm and the atmosphere thick enough in the past that liquid water was stable on the surface. The large majority of the martian rivers and lakes observed today on Mars (see Fig. 1.13) are located on terrains dated from $\sim$ 3.5-3.8 billion years ago (Fassett and Head, 2008a), based on the crater counting method.

Since then, the presence of stable surface liquid water on early Mars has been confirmed with the detection of multiple geomorphological and mineralogical evidence from both satellite and in-situ observations. The main pieces of evidence are:

- The discovery of mature, denditric valley networks (see Fig. 1.13) covering a large fraction of the ancient terrains of Mars (Carr, 1995; Hynek et al., 2010), as well as impact crater lakes (Cabrol and Grin, 1999; Fassett and Head, 2008b) and deltas (Malin and Edgett, 2003; Moore et al., 2003; Mangold and Ansan, 2006; Di Achille and Hynek, 2010).

- The discovery that old craters are much more eroded than young ones (Craddock and Howard, 2002; Mangold et al., 2012; Quantin et al., 2015). See Fig. 1.14.

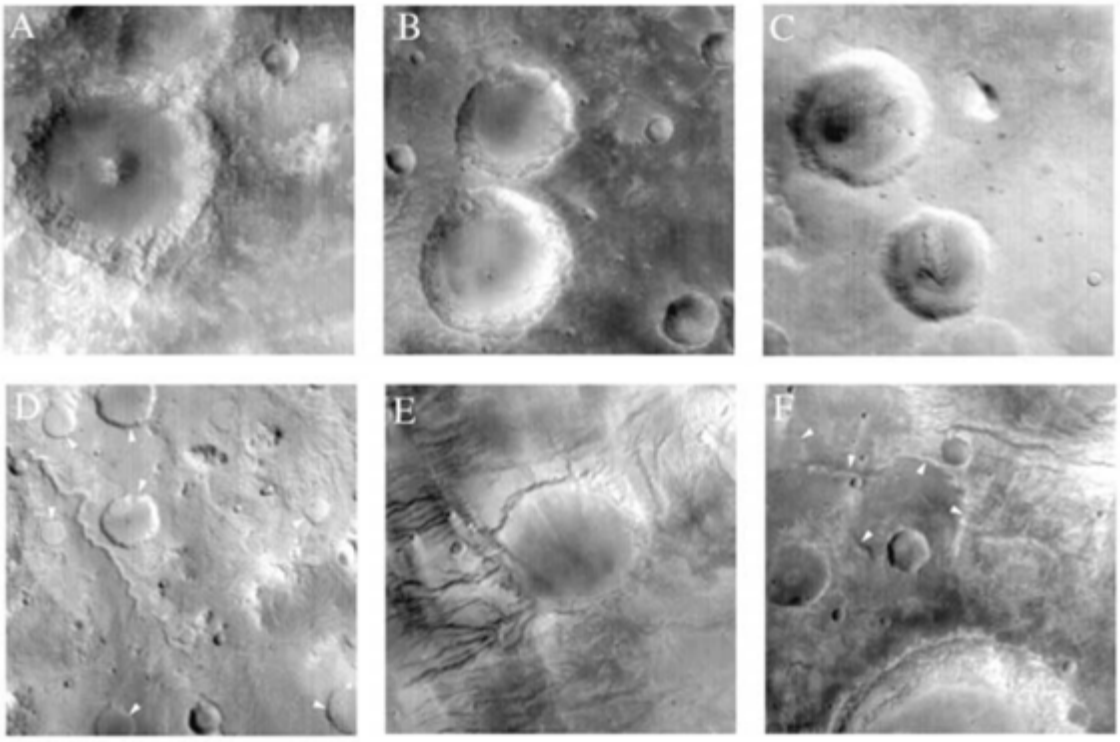

Figure 1.14: Various impact crater degradation stages, ranging from (A) to (F). Fresh, young craters (A) with a sharp central peak and irregular rim deposits get progressively eroded through time. First, (B) the central peak is eroded or buried. Then (C) the crater morphology is smoothed. (D) The crater rim is removed and the crater get progressively infilled. (E) The remaining flat-floored, rimless crater becomes breached by valley networks. Eventually (F) the crater is completely eroded/buried, producing a "ghost" crater (indicated by white arrows). Most of the Noachian impact craters are highly degraded, indicative of extended period of global erosion. From Craddock and Howard (2002).

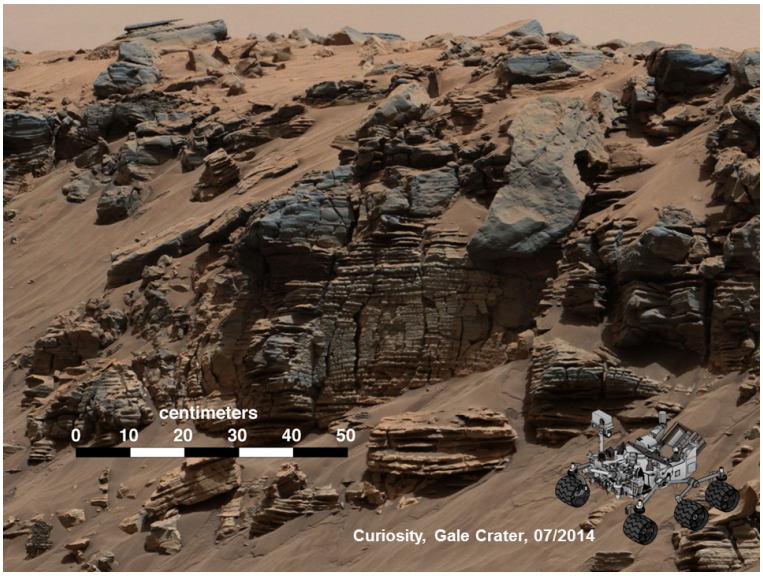

Figure 1.15: This evenly layered rock imaged in 2014 by the Mastcam on the Curiosity rover shows evidence for a lake-floor sedimentary deposit. This is a strong evidence that Gale crater - where Curiosity landed - is actually an ancient lake. From Grotzinger et al. (2015).

- The discovery of widespread hydrated minerals all over the Martian surface (Poulet et al., 2005; Bibring et al., 2006; Mustard et al., 2008; Ehlmann et al., 2011; Carter et al., 2013, 2015).
- The in-situ discovery of fluvial sedimentary conglomerates (Williams et al., 2013) and sedimentary deposits (Grotzinger et al., 2015) within the paleolake "Gale" by the Curiosity rover. See Fig. 1.15.

Note that evidence for ancient oceans on Mars are still very controversial (see the review in Head et al. 2018 and references therein). This possibility is discussed in details in Chapter 6 (and references therein).

Brief chronology of the Martian "liquid water" history for Dummies

Based on craters counting, the history of Mars is decomposed in four chapters:

1. **The Pre-Noachian epoch,** starting from the formation of Mars up to $\sim$ 4 Gya. This is when the largest impact craters formed, including Hellas and Argyre. The Pre-Noachian epoch very likely ended up with the last of the most extreme meteoritic impact events[20].
2. **The Noachian epoch,** from $\sim$ 4 to $\sim$ 3.6 Gya. The Noachian epoch is characterized by a very high meteoritic impactor flux. More importantly, the Noachian terrains are marked by by extensive fluvial activity, supported by (1) an extensive erosion, (2) an extensive formation of valley networks and impact crater lakes, and (3) widespread Al-rich phyllosilicates (clays) typical of wet environments. Evidence of fluvial activity in the Late Noachian epoch has been

[20]Because any of the impacts producing huge impact craters such as Hellas or Argyre would completely "reset" the surface Toon et al. (2010).

confirmed in situ by the Curiosity rover[21]. The end of the Noachian epoch is associated with (1) a sudden decrease of the erosion, (2) a sudden decrease in the formation of valley networks and impact crater lakes, (3) a change in the nature of formed minerals. Experts used to think that the main bulk of the Tharsis volcanic province [22] was emplaced before the formation of the valley networks, and that the associated release of volcanic gases (e.g. CO_2 or SO_2) may have subsequently contributed to a warmer Late Noachian Martian climate, favoring the formation of the valley networks (Phillips et al., 2001). We demonstrated in fact during my PhD thesis that the formation of Tharsis likely occured during or after the formation of the valley networks (Bouley et al., 2016). The volcanic activity associated to the rise of Tharsis may even have been at the origin of the end of the Noachian epoch, and the transition toward the Hesperian.

3. **The Hesperian epoch,** from $\sim$ 3.6 to 3 Gya. The Hesperian epoch is characterized by various evidence of intense volcanic activities, including (1) the rise of all the tallest Martian volcanoes (Olympus Mons, Arsia Mons, etc.), (2) extensive lava floods that resurfaced a large fraction of the Noachian terrains, (3) sulfate deposits and (4) large outflow channels (see Fig. 1.16). Outflow channels are thought to have been carved by episodic, sudden, warm, flowing water coming from subsurface aquifers, sourcing in regions of intense volcanic activity. The other pieces of evidence of the existence of surface liquid water during the Hesperian epoch are: (1) the formation of a few valley networks, (2) sulfate minerals. Eventually, evidence for warmer periods can be infered from the basal melting of thick ice sheets on terrains (e.g. the Dorsa Argentea Formation) dated from the mid-Hesperian (Head and Pratt, 2001; Scanlon et al., 2018). Evidence for tsunami events (hinting toward the presence of ancient ocean) have been reported, but I show in Chapter 6 that there are several issues with this hypothesis.

4. **The Amazonian epoch,** from $\sim$ 3 Gya until now. This is definitely the colder and drier era of Mars. Most of the Amazonian geological activity is restricted to glacial activity (induced by both water ice glaciers and carbon dioxide glaciers). Evidence of fluvial activities, such as few sites of (i) early Amazonian valley networks mostly located on the flanks of Martian volcanoes (Gulick and Baker, 1990; Baker et al., 1992) and (ii) outflow channels until Middle Amazonian (Rotto and Tanaka, 1995) and even Early Amazonian (Rodriguez et al., 2015), is very sparse.

In general, the history of Mars is characterized by a progressive decline of fluvial activity, which is hypothesized to result from a progressive decline of the atmospheric pressure[23].

The early Mars paradox

What is really intriguing is that despite all the pieces of evidence that liquid water was present on Mars for extended periods of time, we are still unable to understand why. 3.5 billion years ago, when most of the valley networks formed, the Sun was 25% dimmer than today. The insolation on Mars at the time was equal to 32% of the present-day Earth insolation, placing early Mars outside the Habitable Zone. This is really an issue, because the only exemple of habitable planet (e.g. early Mars) that we have - except Earth - should not be habitable, according to our general understanding

[21] Gale crater - where the Curiosity rover landed - is dated from the Late Noachian / Early Hesperian (Le Deit et al., 2013).

[22] Tharsis is the largest volcanic structure in the Solar System.

[23] That may have been lost to space, or in the subsurface as carbonates. Note however that the exact amount of CO_2 that could have been lost in carbonates is still very controversial.

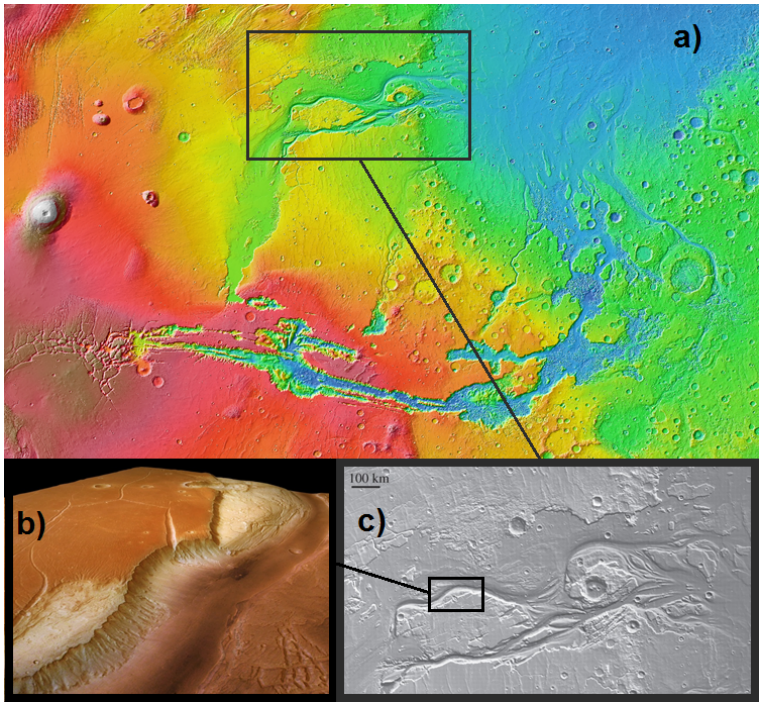

Figure 1.16: Various zooms on the Kasei Vallis outflow channel. Kasei vallis is the largest and longest outflow channel visible today on Mars. Outflow channels are thought to have been carved by sudden, warm, flowing water coming from subsurface aquifers (Clifford, 1993; Clifford and Parker, 2001). Credits: NASA/ESA.

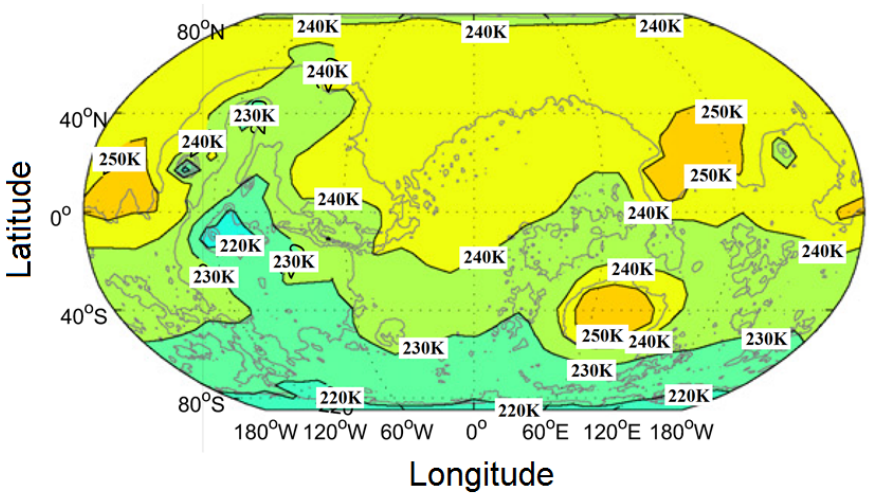

Figure 1.17: Annual mean surface temperature on early Mars, assuming a 1 bar CO_2 dominated atmosphere, a 25° obliquity, and a solar flux equal to 75% of the present-day value. Surface temperatures were calculated from a 3-D Global Climate Model (Wordsworth et al., 2013).

of planetary habitability. Therefore, any breakthrough in the understanding of the surface habitability of early Mars is of capital importance to understand the habitability of planets in general.

Various hypotheses have been explored to overcome this problem.

Dense CO_2 atmosphere

The first hypothesis is that the atmosphere of Mars was thicker in the past, and progressively escaped through time. Many scientists have explored, using numerical climate models, if a thick (multi-bar) CO_2 dominated atmosphere could produce enough greenhouse warming to raise the surface temperature of early Mars above the melting point of water. Although there were initially controversial results[24], we have now reached a consensus (Wordsworth et al., 2010a; Forget et al., 2013; Wordsworth et al., 2013; Kopparapu et al., 2013; Halevy and Head, 2014; Ramirez et al., 2014a; Turbet and Tran, 2017): The greenhouse warming produced by a thick CO_2 dominated atmosphere is insufficient to sustain surface liquid water on early Mars (see Fig. 1.17).

Note however that there are some remaining uncertainties on how much greenhouse warming a pure CO_2 atmosphere can produce on early Mars. This is discussed in details in Chapter 10.

This pushed many scientists to explore alternatives or sophisticated processes to solve the early Mars enigma.

CO_2 ice clouds

Forget and Pierrehumbert (1997) demonstrated that CO_2 ice clouds that form in a dense CO_2 atmosphere can produce a very strong greenhouse warming. CO_2 ice clouds can in fact scatter the thermal emission from the surface, back to the surface. Later, Forget et al. (2013) showed with a sophisticated 3-dimensions climate model that, although the greenhouse effect of CO_2 ice clouds can

[24] These discrepencies were related to (1) atmospheric CO_2 condensation not taken into account and (2) bad knowledge and practice on the spectroscopy of dense CO_2 atmosphere. See the review in Section 2 of Forget et al. (2013).

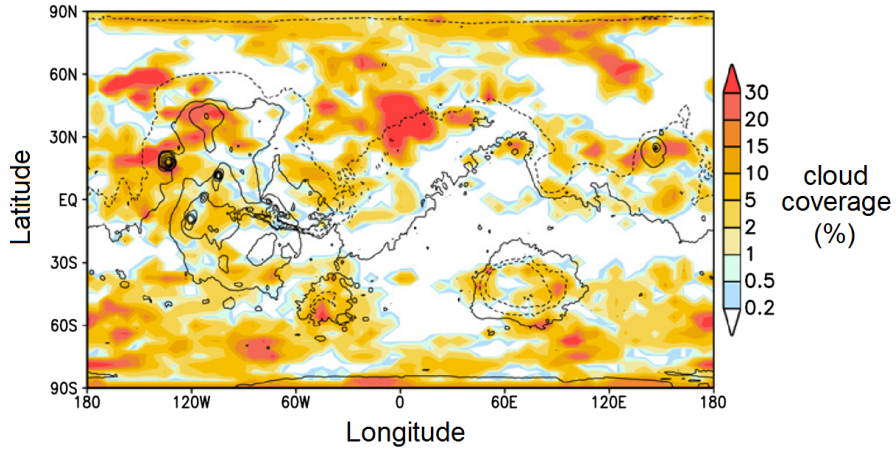

Figure 1.18: Snapshot of the CO_2 ice cloud coverage in a simulation of early Mars with a 2 bar CO_2-dominated atmosphere, at 25° obliquity. From Forget et al. (2013).

indeed be very strong, the effect is much weaker than initially thought (Forget and Pierrehumbert, 1997) because the effective CO_2 ice cloud partial coverage is limited (see Fig. 1.18). Even more recently, Kitzmann (2016) demonstrated that the greenhouse warming of CO_2 ice clouds had been overestimated in Forget and Pierrehumbert (1997) and Forget et al. (2013) because of the way radiative transfer is handled in the climate models (i.e. the widely used two-stream approximation can introduce significant error in the calculation of greenhouse warming by CO_2 ice clouds)[25].

H_2O ice clouds

Some scientists have explored the greenhouse warming of water ice clouds, and have suggested that it can be very efficient (Urata and Toon, 2013; Ramirez and Kasting, 2017), especially when located at high altitude (cirrus-like, cold clouds). However, for this mechanism to work, cloud properties (cloud coverage, cloud particle size, cloud content) must be tuned in a way that appears to challenge the laws of physics (Ramirez and Kasting, 2017). I discuss this process in more details in the Chapters 5, 8 and 7 of this manuscript.

Volcanic gases (e.g. SO_2 and H_2S)

Volcanic events (e.g. associated to the rise of the Tharsis volcanic province) could have injected large amounts of volcanic gases in the atmosphere, such as H_2S and SO_2. These gases can, when at high concentration, efficiently warm the atmosphere of early Mars (Tian et al., 2010; Mischna et al., 2013; Halevy and Head, 2014; Kerber et al., 2015). However, Tian et al. (2010) demonstrated using a 1-D climate model (and later confirmed by Kerber et al. (2015) using a 3-D Global Climate Model) that whenever large concentrations of SO_2 or H_2S are present, volcanic aerosols should be produced. Even small amounts of aerosols should dramatically cool down the surface of early Mars.

Reducing gases (e.g. CH_4 and H_2)

[25] Heng and Kitzmann (2017) recently proposed a viable solution to accurately model the radiative effect of CO_2 ice clouds in Global Climate Models without using a N-streams (with N>2) schemes which is computationally much more expensive.

Reducing gases have been proposed as an alternative solution to the early Mars enigma. Ramirez et al. (2014a) demonstrated that a thick CO_2+H_2 dominated atmosphere could raise the surface of Mars above 0°C, through efficient collision-induced absorptions between CO_2 and H_2. However, the issue is that it is difficult to maintain high levels of H_2 in the atmosphere, because H_2 is light and escapes rapidly to space.

Similarly, it has been argued that CO_2+CH_4 atmospheres could produce a strong greenhouse warming on Mars. However, the issue is that for high levels of CH_4, (1) highly reflective photochemical hazes (byproducts of the photodissociation of CH_4) form and (2) stratospheric CH_4 absorbs solar radiation (Haqq-Misra et al., 2008). These two effect combined produce a significant anti-greenhouse effect that would tend to cool down the surface of early Mars.

Wordsworth et al. (2017) recently calculated that CO_2+CH_4 and CO_2+H_2 collision-induced absorption had been underestimated by previous studies (e.g. Ramirez et al. 2014a) and that a few % of H_2 and/or CH_4 in a dense CO_2 atmosphere would suffice to warm early Mars above 0°C. This theoretical result is important because the new estimates of amounts of H_2 and CH_4 required to warm early Mars above the melting point of water are more compatible with the expected H_2 escape rate and CH_4 haze/statosphere cooling feedbacks.

During my PhD, I explored in details this hypothesis in two distinct ways. First, I measured experimentally the CO_2+H_2 and CO_2+CH_4 collision-induced absorptions to test the prediction of Wordsworth et al. (2017) (see Chapter 11). Then, I tested the greenhouse warming by reducing gases in a 3-D Global Climate Model (Chapter 9).

Extreme events

Mars exhibits numerous pieces of evidence that the red planet had to face numerous catastrophic events during its history. First, its surface is covered by meteoritic impact craters (see Fig. 1.19), some of them being very large. For example, the Hellas crater is a 2000-km diameter, 8-km deep meteoritic impact crater that may have been produced by an impactor as large as 500 km in diameter. This is tremendous! Several authors have argued that meteoritic impacts could have produced episodic periods of intense warming and precipitation that could be sufficient to explain the formation of valley networks, the mineralogy, etc (Segura et al., 2002, 2008; Toon et al., 2010; Segura et al., 2012). This hypothesis is discussed extensively in Chapters 7 and 8.

Later in the Martian history (during late Hesperian-early Amazonian era), large outflow channels were carved (see Fig. 1.16) by catastrophic release of warm, liquid water from subsurface aquifers (Clifford, 1993; Clifford and Parker, 2001). Some authors have argued that such events could have induced a global warming and precipitation on Mars which could explain the formation of the late valley networks. This hypothesis is discussed extensively in Chapter 5.

Implications of the early Mars enigma

There are two main classes of scenarios that could explain the various pieces of evidence that surface liquid water was present on early Mars.

First possibility: Mars was "warm" and "wet" for a long enough period of time that a stable hydrological cycle took place. Lake and rivers formed. Long-term greenhouse warming by SO_2 or CH_4 or H_2, etc. could favor this scenario. In this scenario, Mars provided a stable enough environment for life to emerge and develop.

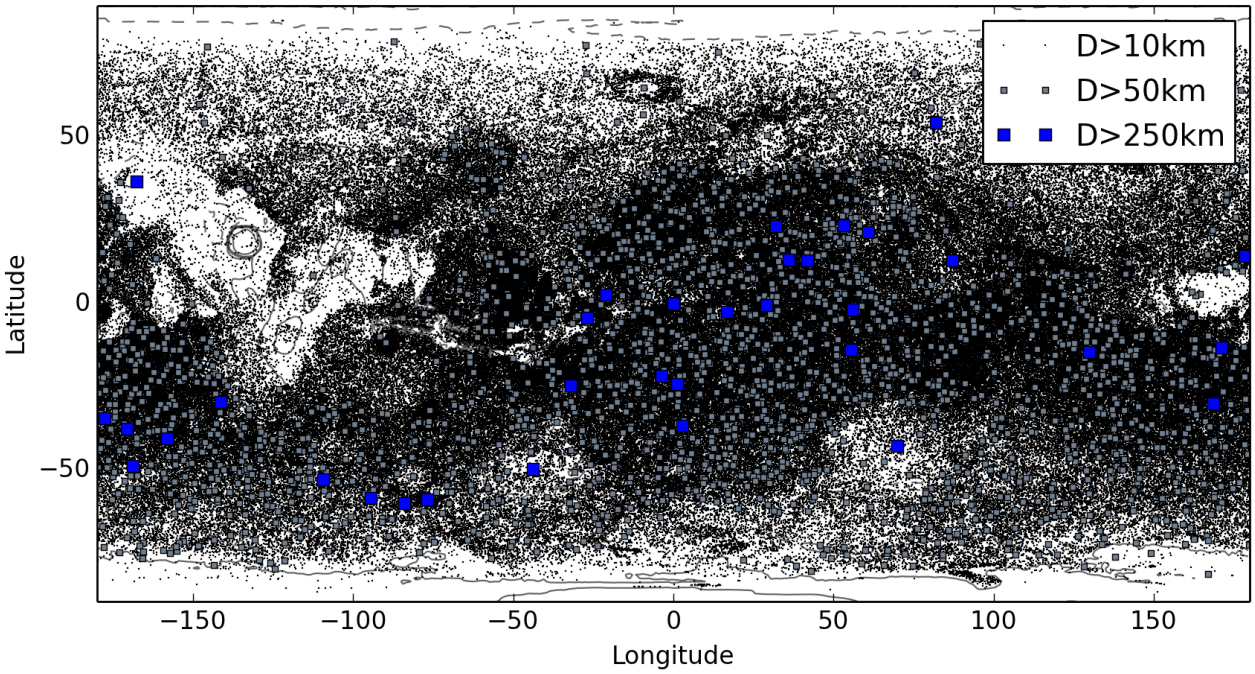

Figure 1.19: Map of craters visible today on the surface of Mars. Craters were separated in three categories: diameter > 250 km; 250 > diameter > 50 km; and 50 km > diameter > 5 km. This map was produced using the 1-km Robbins crater database (Robbins and Hynek, 2012), available on http://craters.sjrdesign.net/. Note that a majority of impact craters are not visible today on Mars because they have been eroded, or buried below subsequent volcanic deposits, ice, or erased by subsequent impact craters, etc.

Second possibility: Mars was a cold and dry planet but it was transiently warmed by brief, catastrophic events such as meteoritic impact, intense volcanism, etc. Cumulated, these events were conducive to the formation of valley networks and lakes visible today on Mars. In this scenario, liquid water was stable only episodically, and in a very extreme environment. It is much harder to conceive that life may have arose in such environment.

Catastrophic events? Or Long-term greenhouse warming? Which of these two scenarios is the leading source of extensive erosion early in the Martian history? The answer to this question has strong implications:

1. **On Mars.** Long-term greenhouse warming is definitely a much more favorable environment for life to arise and evolve. Instead, if all the pieces of evidence of surface liquid water can be explained by short, intense catastrophic events such as meteoritic impacts, it is then hard to conceive that life may exist. The result of this investigation has strong implications for the search of life on present-day Mars.

2. **On the habitability of extrasolar planets.** Calculations of the Habitable Zone indicate that Mars should not be habitable. If the solution to this paradox can be found with any source of long-term greenhouse warming, then our knowledge on the potential habitability of extrasolar planets should be revised accordingly.

1.2.9 Application to extrasolar planets

At the time I wrote my PhD (May 2018), the detection of 3767 extrasolar planets have been confirmed[26]. At the time you read my PhD, there will be potentially (and hopefully) orders of magnitude more[27].

Since 1995, the historical year of the discovery of the first planet found orbiting another Main-Sequence star than the Sun 51 Pegasi b (Mayor and Queloz, 1995), a lot of great discoveries have been made in the field. Thanks to successful space missions such as Kepler (Borucki et al., 2010) and intense monitoring from ground-based telescopes, we have discovered that not only extrasolar planets do exist, but they are also extremely numerous and diverse. Specifically to the field of planetary habitability, we have discovered that:

1. Earth-sized planets are numerous (Bonfils et al., 2013; Dressing and Charbonneau, 2013, 2015).

2. More specifically, Earth-sized planets orbiting in the Habitable Zone of their host star are numerous (Bonfils et al., 2013; Dressing and Charbonneau, 2013; Kopparapu, 2013; Dressing and Charbonneau, 2015).

This is really promising, because this tells us that there could be a lot of planets potentially habitable in our galaxy. As of 2015 (while I was starting my PhD), a few temperate Earth-sized extrasolar planets had been discovered, such as Kepler186f (Quintana et al., 2014) using the transit method or Gliese 667Cc (Bonfils et al., 2013) using the radial velocity method. See Fig. 1.20 for a reminder on the transit and radial velocity methods.

[26] source: `http://exoplanet.eu/`

[27] As I re-checked the website before submitting the manuscript, the number has already raised to 3786 ... 3791!

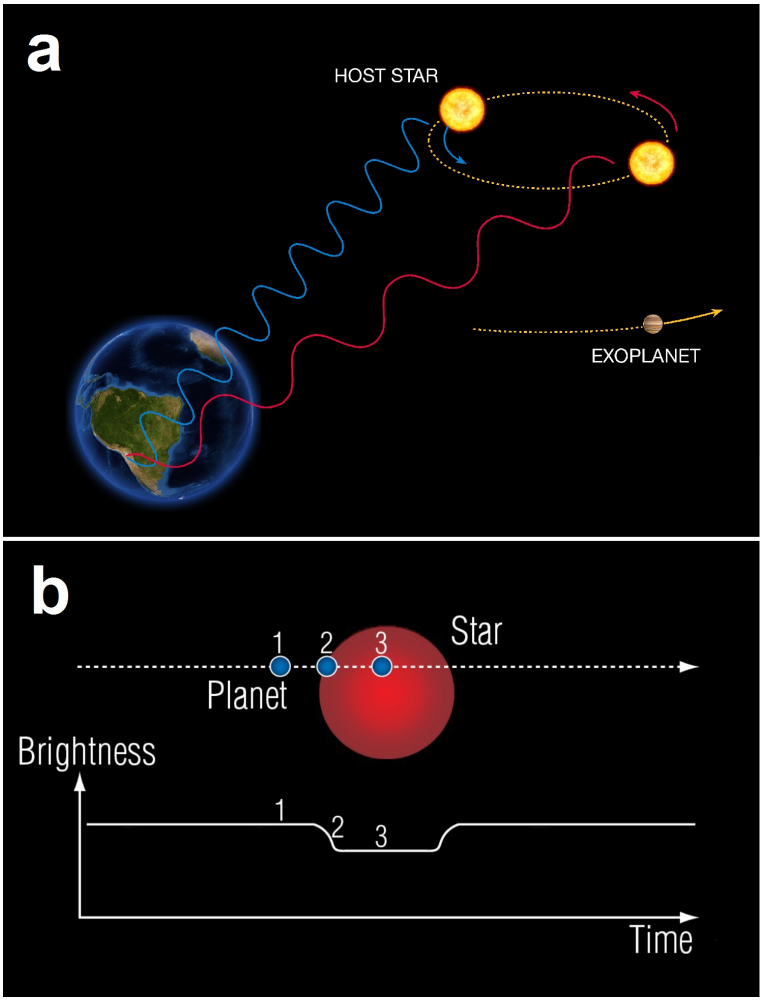

Figure 1.20: Illustration of the widely used radial velocity (a) and transit (b) methods to detect extra-solar planets. **The radial velocity technique (a):** Radial velocity technique consists in measuring the movements of a star perturbed by the gravitational pulls exerted by planets. The movements of the star translate into velocity changes, which produces Doppler shifts. With high resolution spectrographs, it is possible to detect Doppler shifts and thus infer the presence of planets and their basic properties (e.g. minimum mass and orbital period). **The transit photometry technique (b):** This method consists in monitoring the luminosity of a star. If by chance, a planet passes exactly between 1) observers on Earth and 2) the host star, then the planet will hide a fraction of the light emitted by the host star. The observed luminosity of the star will decrease during the "transit" of the planet. Analysis of the light curve (depth of the transit, time between two transits) of the star provides with various information such as the radius of the planet and its orbital period. Credit: ESO (a) and NASA, ESA, G. Bacon, STSci (b).

There were two common points between these planets. First, they are too far for existing and forthcoming techniques of atmospheric characterization (see Fig. 1.21) to work. For example, Kepler186f is $\sim$ 550 light years away from us. Gliese 667Cc is "only" $\sim$ 22 light years away but is not transiting[28]. Secondly, most of these Earth-sized, temperate planets are orbiting (cool, faint, low mass) small stars. We call them "M stars". The large majority of Earth-sized, temperate planets that we have detected so far are orbiting small stars because they are much more easy to find with existing exoplanet detection techniques, e.g. the transit and the radial velocity methods. We detail below why Earth-sized, temperate planets are much easier to detect around M-stars.

1.2.9.1 The M star opportunity

With the radial velocity technique

The semi-amplitude of the radial velocity (RV) of the star $K_{\rm RV} = \frac{V_{\star,\rm max} - V_{\star,\rm min}}{2}$ (with $V_{\star,\rm max}$ and $V_{\star,\rm min}$ the maximum and minimum radial velocity of the star, respectively) scales as (Lovis and Fischer, 2010):

$$K_{\rm RV} \propto \frac{M_{\rm p}}{\Big((M_\star + M_{\rm p})\ a\Big)^{1/2}} \sim \frac{M_{\rm p}}{\Big(M_\star\ a\Big)^{1/2}} \tag{1.3}$$

with $M_{\rm p}$ the mass of the planet, $M_\star$ the mass of the star and a the semi-major axis of the orbit of the planet. Because (1) M-stars have a low mass and (2) planets in the Habitable Zone of M stars are close to their host star (because M stars are faint), the semi-amplitude of the radial velocity of the star is amplified (compared to solar type stars). Moreover, because the orbital period of temperate, Earth-sized planets orbiting M stars is short[29], it is much easier to sample the amplitude of the RV at different orbital phase angles. Eventually, M stars are intrinsically better suited for radial velocity measurements (with respect to more massive stars):

1. because they display much more atomic spectral lines, used for the Doppler shifting measurements. The higher luminosity of more massive stars tends to ionize most atomic spectral lines.

2. because the rotation of M stars is usually slower than more massive stars. This reduces the contribution of the star rotation to the Doppler broadening of the spectral lines, and makes the radial velocity measurement easier.

In summary, there is a strong observational bias toward the detection of Earth-sized, temperate planets around M stars (with respect to more massive stars) with the radial velocity method.

With the transit technique

The amplitude of the transit depth $K_{\rm transit}$ of a planet transiting its host star is equal, in first approximation, to:

$$K_{\rm transit} = \left(\frac{R_{\rm p}}{R_\star}\right)^2 \tag{1.4}$$

with $R_{\rm p}$ the radius of the planet and $R_\star$ the radius of the star. Because M stars are smaller than other stars, the transit depth is significanty higher with respect to more massive stars.

[28] The existing atmospheric characterization techniques are much more favorable for transiting planets.

[29] We remind that the period T is proportional to $a^{3/2}$, with a the semi-major axis of the orbit of the planet.

Moreover, because the orbital period of temperate, Earth-sized planets orbiting M stars is short, the planet transits very frequently, favoring its detection and the characterization of its period (with additional transits).

Based on geometric arguments, it is also easier to find transiting Earth-sized temperate planets around M stars because the probability of transit is higher for planets close to their star[30]. The probability of a full (i.e. non-grazing) transit $P_{\rm transit}$ is (Winn, 2010):

$$P_{\rm transit} = \frac{R_\star - R_{\rm p}}{a} \sim \frac{R_\star}{a} \tag{1.5}$$

In summary, there is a strong observational bias toward the detection of Earth-sized, temperate planets around M stars (with respect to more massive stars) with the transit method.

Last but not least, there is a significant observational bias toward the detection of planets around M stars with all observational techniques, because M stars are the most common stars of the galaxy. Approximately 75% of stars are actually M stars, which considerably increases the chance to find planets around M stars.

A very important corollary is that there are much more M stars in the solar neighborhood than any other star. As an illustration, there are as much as 98 M stars in the 100 nearest stellar systems[31]! As a consequence, there are much more chance to find a temperate, Earth-sized exoplanet close to us around a M star (with respect to more massive stars).

Temperate Earth-size planets in our neighborhood

In August 2016, G. Anglada-Escude and his colleagues revealed the discovery of Proxima b (Anglada-Escudé et al., 2016), a temperate Earth-sized planet orbiting around the closest star from us, Proxima Centauri (4 light years away from us). In February 2017, we releaved the discovery of 7 transiting planets in the TRAPPIST-1 system (Gillon et al., 2017), 40 light years away from us. In April 2017, Jason Dittmann and colleagues revealed the discovery of the transiting planet LHS1140b also 40 light years away from us. In November 2017, Xavier Bonfils and his colleagues revealed the discovery of Ross128b (Bonfils et al., 2017) only 11 light years away from us. I summarize the properties of these newly discovered planets in Table 1.1.

The true reason why these very recent discoveries are so important is that these nearby planets should be the first potentially habitable planets amenable to future atmospheric characterization. And more importantly, this future characterization should be feasible with forthcoming astronomical observatories. From space, our best option will be the James Webb Space Telescope (JWST) and its 6.5 m mirror that should be launched to space by 2020[32]. From the ground, our best options are the large telescopes such as the E-ELT (39 m mirror) and the GMT (25 m mirror), both currently under construction in Chile.

As a result, there is now a huge interest (1) in better understanding the habitability of planets orbiting M-stars and (2) in detailed, specific investigations of newly discovered Earth-sized planets (listed in Table 1.1) to assess their potential habitability and observability with existing and forthcoming telescopes using various atmospheric characterization techniques detailed below. This is the topic of Chapters 3 and 4.

[30] We recall that the Habitable Zone becomes closer to the host star as the mass of the star decreases.

[31] source: `http://www.recons.org/` - list of the 100 nearest stellar systems.

[32] The launch date has already been postponed three times during my PhD thesis, from 2018 to 2021.

Name	Distance (ly)	Flux	Radius	Mass	Star type	Age (Gyo)	Date discovery
Proxima b	4.25	0.65	?	>1.27	M5.5	∼4.8	2016[a]
Ross128b	11.0	1.38	?	>1.35	M4	≥5	2017[b]
GJ1132b	39.3	19	1.2	1.6	M3.5	≥5	2015[c]
TRAPPIST-1b	39.6	3.91	1.12	1.02	M8	7.6±2	2016+2017[d]
TRAPPIST-1c	39.6	2.09	1.10	1.16	M8	7.6±2	2016+2017[d]
TRAPPIST-1d	39.6	1.05	0.78	0.30	M8	7.6±2	2016+2017[d]
TRAPPIST-1e	39.6	0.61	0.91	0.77	M8	7.6±2	2016+2017[d]
TRAPPIST-1f	39.6	0.35	1.05	0.93	M8	7.6±2	2016+2017[d]
TRAPPIST-1g	39.6	0.24	1.15	1.15	M8	7.6±2	2016+2017[d]
TRAPPIST-1h	39.6	0.14	0.77	0.33	M8	7.6±2	2016+2017[d]
LHS1140b	40.7	0.46	1.4	6.7	M4.5	≥5	2017[e]

Table 1.1: Best Earth-sized, temperate targets for future atmospheric characterization (as of May 2018). Parameters were derived and/or calculated based on references: Anglada-Escudé et al. (2016)[a], Bonfils et al. (2017)[b], Berta-Thompson et al. (2015)[c], Gillon et al. (2016)[d], Gillon et al. (2017)[d], Burgasser and Mamajek (2017)[d], Van Grootel et al. (2018)[d], Delrez et al. (2018)[d], Grimm et al. (2018)[d], Dittmann et al. (2017)[e]. Masses, radii, and stellar fluxes (received by the planets) are given in ratio to Earth values. Please keep in mind that there are still large uncertainties in some of these values. For instance, Kane (2018) recently demonstrated using the data provided by the satellite Gaia that some stellar distances may have been largely underestimated/overestimated, thus affecting the main properties of planets in these systems.

1.2.9.2 Atmospheric characterization

There are a lot of different techniques available to characterize the atmosphere of Earth-sized, temperate planets with forthcoming astronomical facilities, illustrated in Fig. 1.21.

Transit spectroscopy

Transit spectroscopy (see Fig. 1.21, row 1) has been the most widely used technique to characterize the atmosphere of hot, giant planets (Charbonneau et al., 2002; Tinetti et al., 2007; Sing et al., 2016). When a planet transits in front of its host star, the atmosphere of the planet blocks a fraction of the light emitted by its host star. Depending on the atmospheric thickness and composition, the planet absorbs light more or less efficiently at different wavelengths. Precised monitoring of the luminosity of the star at different wavelengths can therefore be used to infer the composition and thickness of the exoplanetary atmosphere.

Secondary eclipse

When a planet passes behind its host star, the thermal infrared emission of the planet is blocked by the host star (see Fig. 1.21, row 2). This technique has already been demonstrated on several very hot planets (Charbonneau et al., 2005; Deming et al., 2005; Demory et al., 2012). By comparing the luminosity measured (in the direction of the host star[33]) before and while the planet is occulted by the host star, it is possible to measure the termal emission of the planet. By doing this at different wavelengths, it is possible to infer the temperature of the planet, the composition and thickness of its atmosphere, etc.

Planet-planet occultation

If, by chance, at least two planets of the same stellar system are extremely coplanar with the host star and the observer on Earth, then from time to time a planet can occult another planet of the same system (see Fig. 1.21, row 3) (Ragozzine and Holman, 2010; Luger et al., 2017a). As a planet 1 occults a planet 2, the thermal emission of planet 2 is suddenly blocked. By measuring the luminosity in the direction of the star before and during a planet-planet occultation, it is possible to obtain the thermal emission of planet 2 and thus infer its temperature, atmospheric composition and thickness.

The technique (although it has never been successfully used) is promising because the Kepler mission has demonstrated that planetary systems with multi-transiting - and thus potentially coplanar - planets are numerous.

Thermal phase curves

The temperature and thermal emission is not uniform on a planet. On Earth, there are some seasonal, diurnal and other forms of variability. On synchronous planet, the temperature and thus thermal emission contrast can be extreme between the day and night sides.

As a planet rotates around its host star, it shows progressively a different face, and thus a different thermal emission, to a distant observer (see Fig. 1.21, row 4). The thermal emission of the planet will vary with time and these changes can be recorded throughout an orbit while observing the luminosity in the direction of the host star. This is what we call the "thermal phase curve".

Large day-night contrast on synchronous planets can potentially produce a strong signature using the thermal phase curve technique.

[33] The light coming from the star and the planet is spatially unresolved.

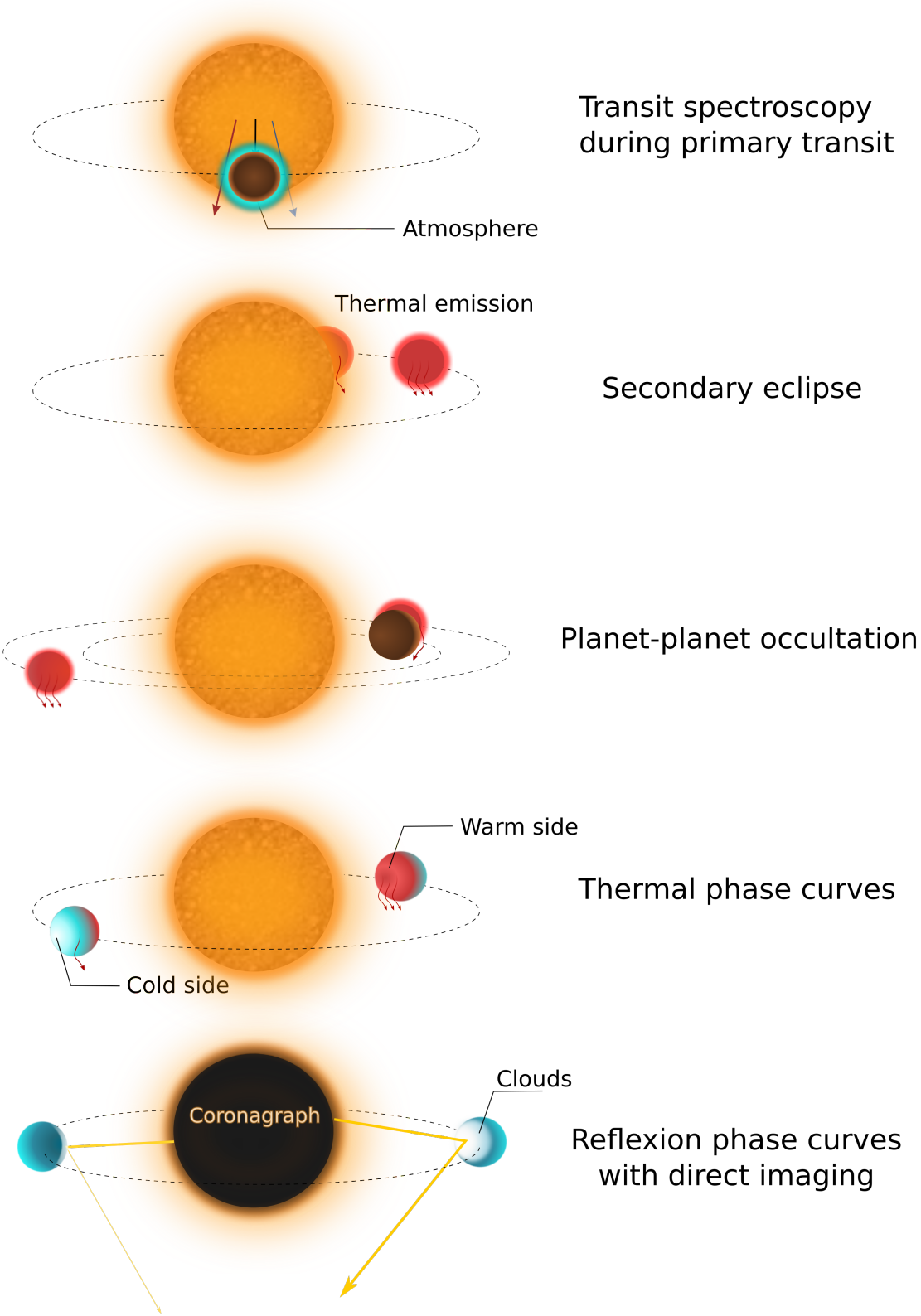

Figure 1.21: Illustration of the various methods that can be used with existing and forthcoming ground-based (e.g. E-ELT) and space (e.g. JWST) telescopes to characterize the atmosphere of nearby, temperate, Earth-sized extrasolar planets. Credit: N. Chaniaud.

This technique is very promising because it can be used on non-transiting planets, where previous techniques are not possible.

As of 2018, this technique has been restricted to warm planets with large temperature constrasts between day and night sides (Knutson et al., 2007; Demory et al., 2016).

Direct imaging and reflection phase curves

When a planet is far enough from its host star, and close enough to Earth (where we - observers - are), it is possible to spatially resolve the light emitted by the star from the light emitted and/or reflected by the planet.

The strict diffraction limit condition for a circular telescope ($1.22\lambda/\mathrm{D_{telescope}}$) can be used to assess if a planet can be spatially resolved or not. It can be written:

$$\frac{d_{\text{star-planet}}(\text{AU})}{d_{\text{star-Earth}}(\text{light years})} > 7.7 \times 10^{-2} \frac{\lambda(\mu\text{m})}{D_{\text{telescope}}(\text{m})} \tag{1.6}$$

with $d_{\text{star-planet}}$ the distance between the planet and its host star (in AU), $d_{\text{star-Earth}}$ the distance between the planetary system and observers on Earth (in light years), λ the wavelength of observation (in μm) and $D_{\text{telescope}}$ the diameter of the telescope (in m) used for the observation.

If the configuration of the planetary system is favorable according to the diffraction limit criterion[34], it is possible to separate the light emitted by the star from the one emitted or reflected by the planet[35]. Coronagraphs can then be used to hide a fraction of the light emitted by the star (see Fig. 1.21, row 5), and thus increase the planet/star luminosity contrast by several orders of magnitude.

As of 2018, the direct imaging technique has been mostly restricted to the detection and characterization of young planets (with a strong thermal emission) located far from their host star (because it provides a favorable angular separation) (Marois et al., 2008; Kalas et al., 2008; Chauvin et al., 2017).

But this technique could also be used to separate the light reflected by a planet from the one emitted by the host star, and thus to directly collect the light reflected by the planet in a telescope. This light can then be analyzed at several wavelengths[36]. The reflection phase curve consists in doing several direct imaging measurements of the same planet at different orbital phase angles. Variations in the reflected light can then be used to infer properties such as the albedo of the surface, atmosphere, aerosols and clouds of the planet.

Note on the high-contrast/high-resolution technique

Even after the operations described above, the planet/star contrast can remain too low to extract the photons reflected by the planet. Fortunately, several authors have proposed a technique, called "high-contrast/high-resolution" technique (or "cross-correlation") (Sparks and Ford, 2002; Riaud and Schneider, 2007; Snellen et al., 2010; Brogi et al., 2012; Snellen et al., 2014, 2015; Lovis et al., 2017), that can be used to further increase the planet/star contrast. Reflected light from the planet can be

[34] In practice, a very efficient Adaptive Optics (AO) system is required to reach the diffraction limit for ground-based observations. This AO system is usually composed of various optics such as deformable mirrors to correct for wavefront errors usually produced by atmospheric turbulence or mechanical vibrations in the instrument.

[35] In practice here, we are mostly interested in the light reflected by the planet because short wavelengths provide a much more favorable angular resolution

[36] Since direct imaging requires large aperture telescopes, the technique is usually restricted to ground-based observations. This indicates that direct imaging observations can only be performed at wavelengths corresponding to Earth atmospheric spectral windows.

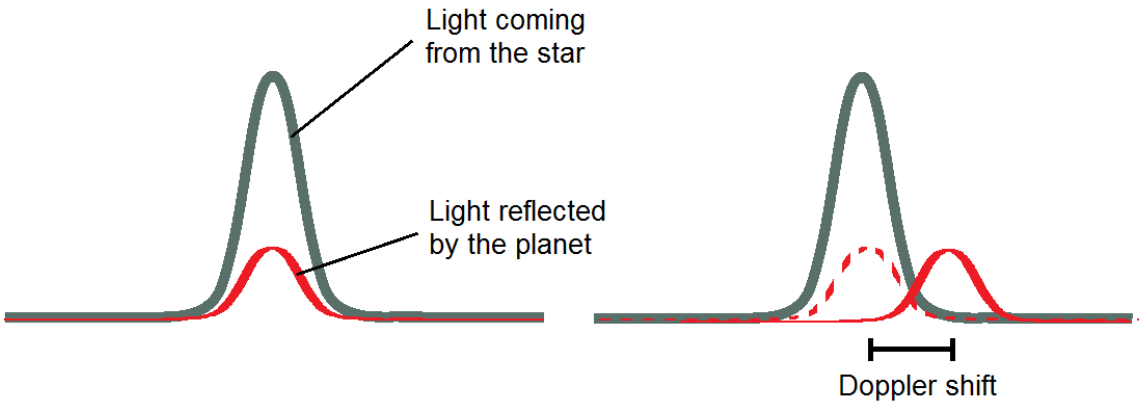

Figure 1.22: Principle of the cross-correlation technique. Emission lines from the star are Doppler-shifted away from planet reflected lines. As a result the planet/star contrast is locally increased.

collected and analysed with a high resolution spectrograph, i.e. with a resolution that is high enough that emission lines from the star (and that from the reflected light) can be spectrally resolved. The planetary orbital motion (relative to the host star) is maximal at maximal angular separation between the planet and the star, producing a Doppler spectral shift. It is then possible to take advantage of this Doppler spectral shift (see Fig. 1.22) to artificially increase the planet/star contrast.

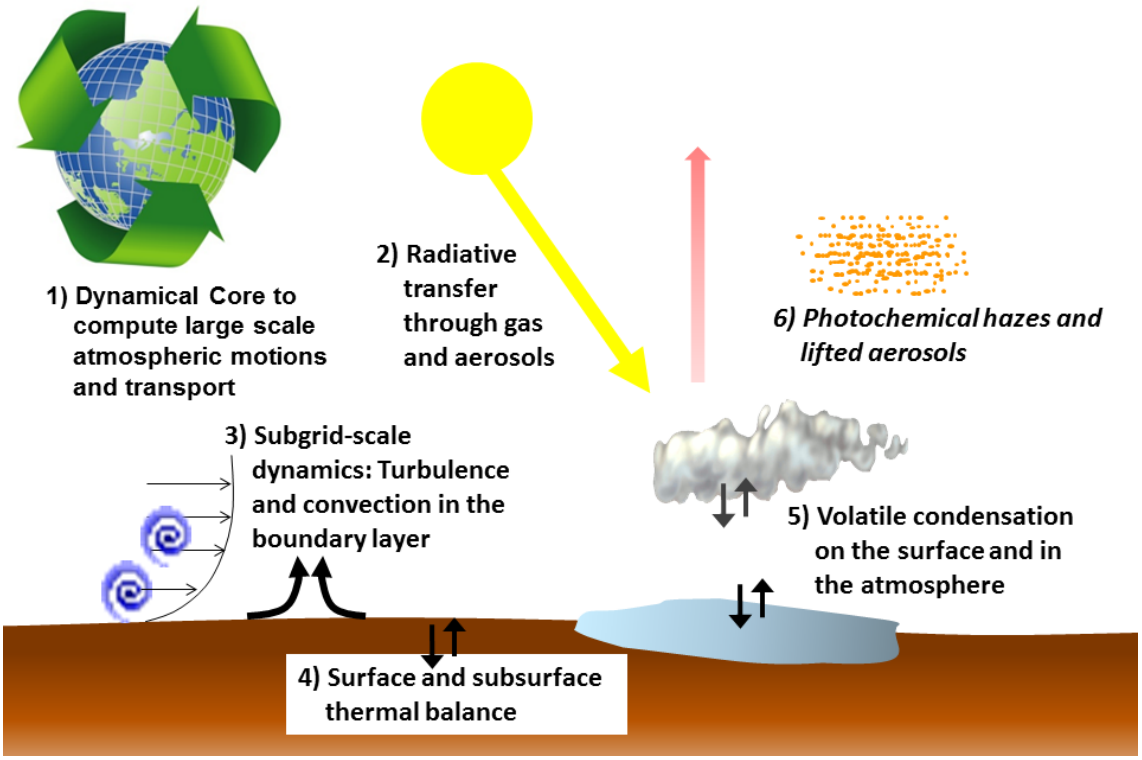

Figure 1.23: Description of the various physical processes involved to build a climate model (Forget and Lebonnois, 2013). Credit: F. Forget.

1.3 Numerical Climate Models to explore habitability

The surface habitability of a planet is tightly linked to the nature and behavior of its atmosphere.

There are numerous physical processes that are at play in the way a planetary atmosphere behaves, among them:

- Motions of air parcels, described with hydrodynamic equations (Navier-Stokes).
- Condensation, evaporation, sublimation and solidification of various volatile components of the planet, described with the thermodynamic equations.
- Formation and evolution of clouds, described with microphysics.
- Absorption, emission, scattering of the solar flux and thermal radiation of the atmosphere, clouds, and surface. These are described by the equations of radiative transfer.
- Atmospheric (photo-)chemistry, described with equations of chemical/photochemical kinetics.

Climate models are numerical codes designed to take into account as many as possible (and as accurately as possible) of all the physical processes described above (see Fig. 1.23). Numerical climate models have been initially developed to understand how the climate of the Earth works, and were then used to understand the effect of the anthropogenic greenhouse gas emissions on the climate of the

Earth. Motivated by various Solar System space exploration missions, scientists started to adapt these Earth-centered numerical climate models to the atmosphere of Solar System planets, such as Venus, Mars, giant planets, etc. Later on, and motivated by the detection of extrasolar planets, several teams all over the world created (or adapted, based on previous Earth numerical climate models) climate models to explore the whole diversity of extrasolar planets.

Numerical climate models are very useful tools to explore the climate(s) of both Solar System and extrasolar terrestrial planets. In particular, they can be used to explore the surface habitability of planets, by exploring the effect of greenhouse gases, atmospheric circulation, cloud formation, etc. on the surface environment of temperate, Earth-like planets. Numerical climate models simulations can also be used to provide synthetic observables for any of the atmospheric characterization techniques discussed in the previous chapter (transmission spectra, thermal emission occultation, thermal phase curves, etc.), to prepare and interpret atmospheric observations of extrasolar planets, including the temperate Earth-sized ones.

1.3.1 The hierarchy of climate models

There are a lot of different kind of climate models used in the scientific community, such as: 1-dimension reverse climate model, 1-dimension time-marching climate model, 2-D energy balanced models, 2-D energy balanced radiative convective models, 3-D General Circulation Models, 3-D Global Climate Models, 3-D Global Climate Models coupled with oceanic model, etc. I review below the three types of climate models that I used during my thesis to produce the results presented in this manuscript.

1.3.1.1 1-D reverse climate model

1-D reverse climate models or 1-D reverse radiative-convective models are - historically - the first models that were used to explore the habitability of extrasolar planets (Kasting, 1988; Kasting et al., 1993). These models are the simplest approach to simulate the mean thermal structure of an atmosphere. The entire atmosphere is modeled here by a single atmospheric column, receiving a flux equal to 1/4th of the stellar constant (i.e. the stellar flux at the zenith). Moreover, the solar zenith angle is usually fixed and taken equal to 60°[37]. In these models, the mean atmospheric thermal structure is constructed as follows:

1. The surface temperature and pressure of the planets are arbitrarily fixed.

2. The thermal structure is constructed from the surface to upper atmospheric layers by following the dry adiabatic thermal gradient[38].

3. If, at some point, the mixing ratio of a gas reaches the saturation level of any condensible gas, the gas condenses and we switch from a dry adiabatic thermal gradient to a moist adiabatic thermal gradient[39].

[37] This is the geometric average of the solar zenith angle.

[38] The dry adiabatic thermal profile describes a situation where vertical transport is controlled by dry convection (i.e. convection that does not involve the condensation of any atmospheric species). Whenever the vertical thermal gradient $\frac{dT}{dz}$ is steeper than $-\frac{g}{C_p}$, the atmosphere is unstable, and convection processes take place at least until $\frac{dT}{dz} = -\frac{g}{C_p}$

[39] The moist adiabatic thermal gradient is a sophisticated version of the dry adiabatic gradient, that takes into account the latent heat released by the condensation of gases. See equation 1.8.

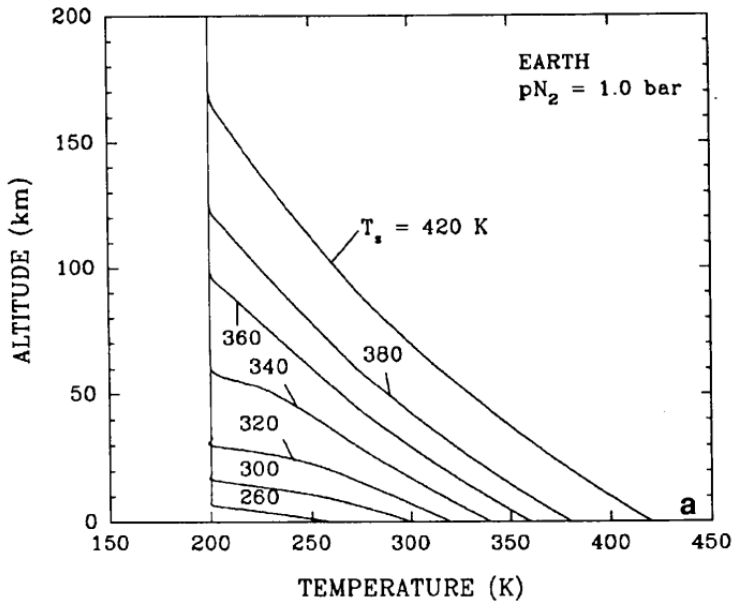

Figure 1.24: Temperature vertical profiles assumed for various surface temperatures. Here it is assumed that the thermal profile follows a moist (H_2O-driven) adiabatic gradient, i.e. that water vapour is at saturation everywhere, until the atmospheric temperature reaches the stratospheric temperature, arbitrarily fixed at 200 K. From Kasting et al. (1993).

4. Eventually, when the temperature reaches a fixed[40] stratospheric temperature, the atmospheric temperature is then assumed to be constant and equal to this fixed stratospheric temperature.

Once the thermal profile is constructed (see an exemple in Fig. 1.24), radiative transfer calculations are performed in both the solar emission (short-wave) and telluric emission (thermal infrared emission of the planet; long-wave) wavelengths to compute (i) the planetary albedo and (ii) the outgoing longwave radiation (OLR). From these radiative transfer calculations, it is then possible to calculate the incoming stellar radiation (ISR) required for the planet to be in radiative equilibrium. Because such calculation is (usually) computationally inexpensive[41], it is possible to perform calculations for a wide range of surface temperatures, and thus rapidly find, for a given instellation (or ISR), the corresponding surface temperature and thermal profile.

Pros

1-D reverse climate modeling is not only easy to implement, but it is also computationally inexpensive. Therefore, such climate models are well suited to explore a wide range of parameters, atmospheric compositions, etc.

Cons

However, 1-D reverse models rely on several assumptions that can be questioned. First, they usually assume a fixed stratospheric temperature, although it could drastically vary for different atmospheric composition or stellar spectrum. Secondly, they usually assume fixed (or a priori) saturation profiles.

[40] It is usually assumed that the temperature of the stratosphere T_{strat} is equal to the 'skin temperature' of the planet T_{skin}, which is equal to the effective radiating temperature divided by $2^{1/4}1/4$ (Kasting, 1988, 1991).

[41] at least, compared with the more sophisticated 3-D Global Climate simulations discussed later on.

Thirdly, there are not well suited to include clouds. Eventually, they are not well suited to explore temporal evolution of atmospheres.

Note that I used a 1-D reverse climate model in the Chapter 7 of this manuscript.

1.3.1.2 1-D time-marching climate model

1-D time-marching climate models or 1-D time-marching radiative-convective models are more sophisticated than reverse models, because they calculate self-consistantly (and through time) both the mean thermal structure and the radiative exchanges between the atmospheric layers. In these models, the atmospheric thermal structure is constructed as follows:

- At t=0, we assume arbitrarily a thermal profile (that can be constructed for example using the same method than for the 1-D reverse climate model) and an atmospheric composition.
- Then, for each timestep t, we compute the radiative transfer in both short-wave and long-wave spectral domains. From this calculation, we derive radiative heating (or cooling) rates, that are used to calculate, at t=t+Δt the new atmospheric vertical temperature profile. This is the "radiative" part of the calculation.
- We then check if the atmospheric thermal profile is stable to dry and moist convection. If not, the atmosphere is vertically mixed to ensure that the thermal profile is controlled by either the dry or moist adiabatic gradient (depending on if condensible species are present or not). This is the "convective" part of the calculation.

These calculations are then repeated a number of time, enough for the vertical temperature profile to reach radiative equilibrium.

Pros

The 1-D time-marching radiative-convective model provides a self-consistent calculation of the mean atmospheric thermal profile. It can be used to study the temporal evolution of a planet. It can be used globally or locally to derive a thermal structure at any position (latitude, longitude) on a planet. Eventually, 1-D time-marching models are useful because they can be used as a benchmark as well as can provide a coherent initial state for more sophisticated 3-D Global Climate Models described below.

Cons

1-D time-marching models are significantly more computationnally expensive than 1-D reverse models. More generally, 1-D models are unable to capture the effect of 3-D circulation, formation, evolution, and radiative feedback of clouds on the climate..

I used 1-D time-marching climate models in the Chapters 4, 7 and 10 of this manuscript. I also dedicated a significant amount of time during my PhD thesis to develop an online, interactive 1-D time-marching model[42] available on `http://laps.lmd.jussieu.fr/`. This model is designed to simulate the temporal evolution of any atmosphere of any terrestrial planet. This is a very useful tool to teach students principles of planetary habitability.

[42] This online model is based on the 1-D "generic" model used for research purposes.

1.3.1.3 3-D Global Climate Models

3-D Global Climate Models (GCMs)[43] are 3-dimensions numerical climate models designed to include all the physical and chemical processes (see Fig. 1.23) at play in planetary atmospheres and surfaces. These models are literally aiming at behaving like real planets.

GCMs can be seen as a network of 1-D time-marching radiative convective models connected to each other with a dynamical core, i.e. a numerical code solving the hydrodynamic equations on the (rotating) planetary sphere. This hydrodynamic core calculates the winds that transport atmospheric gases, clouds, aerosols, etc. from one atmospheric column to another.

Note on 3-D GCM with equilibrated volatile reservoirs

Recently, several "exoplanetary" 3-D Global Climate Models have reached a new gap, including now sophisticated feedbacks between atmosphere and volatile reservoirs:

1. For large volatile content, 3-D oceanic circulation models have been coupled to climate models (Hu and Yang, 2014; Del Genio et al., 2017). It has been demonstrated that oceanic circulation can drastically change the heat transport efficiency between cold and warm regions of the planet.

2. For small volatile content, numerical algorithms have been developed to calculate the preferential location of volatiles (Wordsworth et al., 2013). I used and developed extensively such algorithms to calculate for instance where ice would migrate or where lakes would form on both extrasolar planets (see Chapter 2, 3 and 4) and early Mars (see Chapter 5 and 9).

Pros

3-D Global Climate Models are the most accurate way to simulate the atmosphere of a planet.

Cons

3-D Global Climate Models can be computationally very expensive. Any sophisticated GCM simulation must be parallelized and run on computer clusters. Moreover, GCMs are based on heavy developments that require a lot of "human" time. There are only a few teams in the world that use such models, and there are usually based on tens of years of previous developments by tens to hundreds of scientists.

1.3.2 The 3-D LMD Generic Global Climate Model

At the Laboratoire de Meteorologie Dynamique, scientists have been developing for years 3-D Global Climate Models. Initially motivated by understanding the climate of the Earth and more specifically the anthropogenic global warming, they have developed a GCM to study the climate of our Earth. Later on, this GCM has been adapted to study the climate of Mars and later modified to simulate early Mars and extrasolar planets. This later model is now known as the 3-D LMD "Generic" Global Climate Model (see Fig. 1.25), or LMDG GCM. The ambitious goal of this model is to simulate as accurately as possible the climate of any planet, either inside or outside our Solar System. As of 2018, the LMDG GCM has been used to simulate the atmosphere of early Earth (Charnay et al., 2013,

[43] GCM can also refer to General Circulation Models. General Circulation Models are 3-dimensions numerical models that simulate the atmospheric circulation of a planet with very simplified equations to describe physical processes (usually represented by fixed heating rates). Instead, Global Climate Models are 3-dimensions numerical models whose goal is to model as accurately as possible all the physical processes (see Fig. 1.23) that shape the climate of a planet.

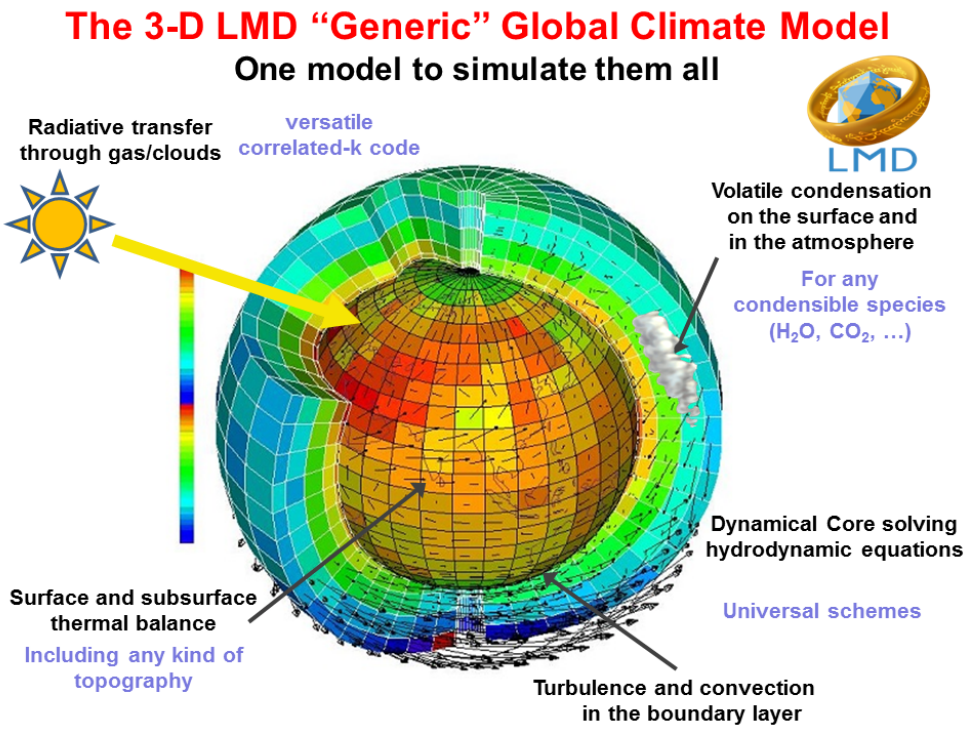

Figure 1.25: Description of the main building blocks of the 3-dimensions Laboratoire de Meteorologie Dynamique "Generique" Global Climate Model (LMD-G GCM).

2017), a highly irradiated "future" Earth (Leconte et al., 2013a), Pluto (Forget et al., 2017; Bertrand and Forget, 2017), Saturn (Guerlet et al., 2014; Spiga et al., 2015), Jupiter (Spiga et al., 2017), early Titan (Charnay et al., 2014), early Mars (Wordsworth et al., 2013; Forget et al., 2013; Kerber et al., 2015; Wordsworth et al., 2015; Turbet et al., 2017a), and exoplanets (Wordsworth et al., 2011; Leconte et al., 2013b; Forget and Leconte, 2014; Bolmont et al., 2016a; Turbet et al., 2016, 2017b, 2018a).

A large fraction of the work described in this manuscript is based on results obtained using the LMDG GCM. I describe below the different building blocks (see Fig. 1.25) of the model, with a particular focus on parts that I personnally contributed to during my PhD thesis. Additional information on the LMDG GCM as well as specific parameterizations can be found in the various Chapters of this work (and references therein), as well as in the PhD manuscript of Benjamin Charnay (Charnay, 2014). A paper describing in details the LMDG GCM is currently in preparation (Forget et al., in prep).

1.3.2.1 The dynamical core

The dynamical core is the part of the model that solves the primitive equations of meteorology (i.e. fluid dynamics around a rotating sphere) in a 3-dimensional grid that covers the entire planetary atmosphere. The dynamical core is based on a latitude × longitude × altitude grid, using the Arakawa C configuration, in which meridional wind, zonal wind and mass of air cells are calculated on staggered grids.

Simulations presented in this thesis have been performed with typical horizontal resolutions of 1-10° in latitude and longitude. The timestep of the simulations is adjusted to ensure that the CFL (Courant-Friedrichs-Lewy) condition is met, i.e. that:

$$\frac{u\,\Delta t}{\Delta x} < 1 \tag{1.7}$$

with u the typical wind speed amplitude (in m/s), Δt the timestep (in s) and Δx the horizontal resolution (in m) adopted in the model. In practice, I used typical dynamical timestep of a few minutes.

To satisfy the CFL condition at the poles (where the "longitudinal" resolution can become really high in the geometry of a latitude × longitude grid), a filter is applied.

The real power of our dynamical core is that it is common between all the models developed at the Laboratoire de Meteorologie Dynamique. Therefore, any improvement made by Earth, Venus or Jupiter scientists will directly benefit to Mars, Pluto ... or exoplanet scientists, and vice versa!

1.3.2.2 The radiative transfer

The radiative transfer is a major component of the 3-D LMDG GCM. The radiative transfer is performed in the model using (1) the plane parallel approximation and (2) the two-streams approximation. In other words, we assume that photons can either propagate upward or downward (with a fixed angle with respect to the surface for the incoming short-wave radiation) and in the same atmospheric column.

Our radiative transfer takes into account the absorption/emission by any gas, aerosols, clouds located at any altitude in the atmosphere. Details about how absorption/emission by gases are calculated are given in Section 1.4; details about how absorption/scattering by aerosols and clouds are calculated are given in the thesis manuscript of Jean-Baptiste Madeleine (Madeleine, 2011).

Assuming that the radiation absorption/emission/scattering properties of the atmosphere are known, the radiative transfer is then performed based on the large band approximation. In practice, both the visible (i.e. the range of wavelengths of solar/stellar emission) and the infrared (i.e. the range of wavelengths of telluric emission) channels are decomposed into 10 to 100 bands[44] in which the radiative transfer is performed. This decomposition in large bands is used to reduce the computational cost of the radiative transfer[45].

In the LMDG model, the large band approximation was complemented with the correlated-k method. Instead of using the approximation that the absorption is constant in each band, we assume that the absorption can reach a set of different values, each associated with a different probability. In practice, this is done by converting a high resolution spectrum (see Fig. 1.26, left panel) into a distribution of absorption expressed as a function of a cumulative probability (see Fig. 1.26, right panel). The distribution is much smoother than the absorption spectrum and can thus be interpolated by a limited number of points (usually between 10 and 30) as illustrated in Fig. 1.26 (right panel).

[44] The number, position, and width of each band can be adapted as wanted.

[45] The radiative transfer is often the major source of computational cost in our climate simulations. However, the large band approximation alone is often inaccurate to describe the absorption of gases, because absorption can vary a lot inside each band (see Fig. 1.26, left panel). The assumption that the absorption by gases in constant in each band is inaccurate and can lead to large errors in the radiative transfer. Absorption can for example be largely overestimated in bands where saturation of the absorption would normally be expected.

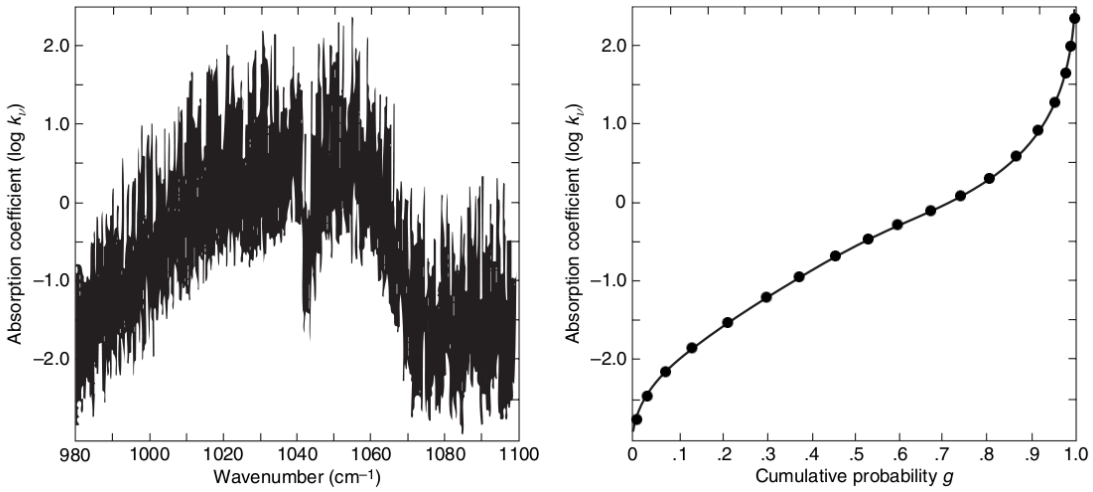

Figure 1.26: Illustration of the conversion of a high resolution spectrum (left panel) into an absorption distribution (right panel), also called "k-distribution". From Fu (2006).

The radiative transfer can then be performed in each band, and for each g-point (where g corresponds to the cumulative probability of absorption). Assuming that the number, position, and width of bands, as well as the number and positions of g-points have been smartly chosen, this approach gives in general an excellent compromise between radiative transfer accuracy and computational efficiency.

In practice, I first construct high resolution spectra, accounting for absorption near line centers, absorption in the far wings and absorption caused by transient dipoles (CIAs) and dimers (see Sect. 1.4). For my thesis, I used and adapted the numerical code *kspectrum* (Eymet et al., 2016) to generate the desired high resolution spectra for various mixtures of gases, such as N_2, O_2, CO_2, H_2O, H_2, CH_4, SO_2 and NH_3, depending on the scientific context. The high resolution spectra are calculated for a grid of temperatures, pressures, and mixing ratio to account for all the possible atmospheric configurations in the atmosphere. These high resolution spectra are then separated into a limited number (10-100, usually) of large bands. In each of the band, we calculate g the cumulative probability of absorption, from which we derive a look-up table giving the absorption of the band as a function of g, for each band, temperature, pressure and gas molecules mixing ratio of the grid. The absorption by GCM air cells in each spectral band is then computed by interpolating the temperature, pressure and mixing ratio of the cell within the pre-calculated values of the grid.

1.3.2.3 Turbulence and convection

Subgrid-scale dynamical processes (e.g. turbulent mixing and convection) are parametrized in the model as in Forget et al. (1999). The planetary boundary layer was accounted for by the Mellor and Yamada (1982) and Galperin et al. (1988) time-dependent 2.5-level closure scheme, and complemented by a convective adjustment (see below) which rapidly mixes the atmosphere in the case of unstable temperature profiles. Turbulence and convection mix energy (potential temperature), momentum (wind), and water vapor (and other trace species).

Vertical movements of air can be decomposed in two components. The first contribution comes

from the large scale circulation (e.g. Hadley cells) that produce ascending and descending flows at the planetary scale. The second contribution comes from the convection processes that take place whenever the atmosphere is unstable, i.e. whenever the air at low altitude is more boyant than the air at higher altitude. This unstable configuration triggers convection, i.e. vertical movements of air that lift warm air and drop cold air. Convection processes generally occur at horizontal scales that are small enough that they cannot be spatially resolved by 3-D Global Climate Models. Therefore, a sub-grid scale parameterization of the convection must be taken into account.

In the LMD-G, we used a simple (yet robust) approach called the "convective adjustment". Whenever the atmosphere is unstable (relative to the adiabatic profile criterion), the atmosphere is vertically mixed to get a stable temperature profile. The scheme that we use has been adapted to account for the effect (on the adiabatic, stable profile) of any condensation of any species, whatever their concentration (ever trace or dominant gas).

The adiabatic stable profile is written (Leconte et al., 2013a):

$$\frac{\mathrm{d}\ \ln T}{\mathrm{d}\ \ln P} = \frac{P}{P-P_v}\left([1-q_v]\ R_a + \frac{q_v L_v}{T}\right)\left(q_v C_{p,v} + q_a C_{p,a} + q_c C_{p,c} + q_v\ \frac{L_v}{T}\ \frac{P}{p-p_v}\ \frac{\mathrm{d}\ \ln P_{s,v}}{\mathrm{d}\ \ln T}\right)^{-1} \quad (1.8)$$

where T and P are the temperature and pressure of the atmosphere at at given altitude. P_i, q_i, $C_{p,i}$, and R_i[46] are the pressures, mass mixing ratios, specific heat capacities at constant pressure and specific gas constants of the species i, where i is:

1. equal to v, to denote a condensible species. On Earth, this is water vapour.
2. equal to a, to denote a non-condensible species. On Earth, this is N_2, O_2, etc.
3. equal to c, to denote condensed species (e.g. cloud particles, aerosols, etc.).

L_v is the specic latent heat of vaporization of the condensible species v, and $P_{s,v}$ is the saturation pressure of species v.

1.3.2.4 Cloud formation and precipitation

Both large scale and unresolved convections can lead to the condensation of water vapour (and other gases) into cloud particles. We summarize here the main properties of the numerical schemes used in the LMD-G GCM[47] to treat the cloud formation and precipitation.

Whenever water or any other species (e.g. CO_2) condense in the atmosphere, cloud particles are formed. Depending on the atmospheric temperature, the cloud particles are either solid or liquid. For water, the fraction of cloud particles $\alpha_{\mathrm{c,liquid}}$ (in %) in liquid phase is given by (Charnay, 2014):

$$\alpha_{\mathrm{c,liquid}} = \frac{T-(273.15-18)}{18} \quad (1.9)$$

where T is the atmospheric temperature of the corresponding GCM air cell[48]. Above 0°C, particles are fully liquid and below -18°C they are assumed to be fully solid.

[46] i.e. $R_i = \frac{R}{M_i}$, where R is the perfect gas constant and M_i is the molar mass of species i.

[47] The numerical schemes may differ from one chapter to another. For more information, we refer the reader to the Method section of each chapter.

[48] This formulation accounts for supercooling of liquid droplet down to -18°C.

We use a fix number of activated cloud condensation nuclei (CCNs) per unit mass of air N_c to determine the local H_2O cloud particle sizes[49], based on the amount of condensed material. The effective radius r_{eff} of the cloud particles is given by:

$$r_{\text{eff}} = (\frac{3\ q_c}{4\pi\rho_c N_c})^{1/3} \tag{1.10}$$

where ρ_c is the density of the cloud particles (1000 kg m^{-3} for liquid and 920 kg m^{-3} for ice) and q_c is the mass mixing ratio of cloud particles (in kg per kg of air). Typical values of N_c used in this work range between 10^4 and 10^6 kg^{-1}. The effective radius of the cloud particles is then used to compute both (1) their sedimentation velocity and (2) their radiative properties calculated by Mie scattering (or more sophisticated methods; see the PhD thesis of Jean-Baptiste Madeleine (Madeleine, 2011) for more details).

Water precipitation is divided into rainfall and snowfall, depending on the nature (and thus the temperature) of the cloud particles. Precipitation is considered to be "instantaneous" (i.e. it goes directly to the surface) but can evaporate while falling through sub-saturated layers. The re-evaporation rate of precipitation E_{precip} (in kg/m^3/s) is determined by (Gregory, 1995):

$$E_{\text{precip}} = 2 \times 10^{-5}(1 - \frac{q_v}{q_{s,v}})\sqrt{P} \tag{1.11}$$

where q_v and $q_{s,v}$ are the water vapour mixing ratios in the air cell and at saturation, respectively. P is the precipitation flux (in kg/m^2/s).

Rainfall is parametrized using two different schemes (depending on the Chapter considered):

- A simple cloud water content threshold scheme (Emanuel and Ivkovi-Rothman, 1999). Whenever the cloud content (in kg per kg of air) reaches a threshold value, precipitation occurs.
- A scheme from Boucher et al. (1995). Conversion of cloud liquid droplets to raindrops occurs by coalescence with other droplets.

Snowfall rate is calculated by the sedimentation rate of cloud particles in the atmospheric layer and is deduced from the sedimentation velocity of particles V_{sedim} (in m/s) assumed to be equal to the terminal velocity that we approximate by a Stokes law:

$$V_{\text{sedim}} = \frac{2\rho_c g {r_{\text{eff}}}^2}{9\eta} \tag{1.12}$$

where η is the viscosity of air and g the gravity of the planet. In practice, the velocity is multiplied in our model by the Cunningham "slip-flow" correction factor (Rossow, 1978) equal to $(1+\beta K_n)$, with β a constant equal to $\frac{4}{3}$ and K_n the Knudsen number that increases with decreasing atmospheric pressure.

[49] We use the same approach to determine the CO_2 ice cloud mean particle size (Forget et al., 2013).

1.3.2.5 Surface and subsurface schemes

The subsurface is decomposed in our model into various layers whose properties (thermal inertias and volumetric capacity) can be adapted to account for any kind of soil composition. The number and depths of the subsurface layers are carefully chosen to account for both the diurnal and seasonal thermal waves. Thermal exchanges (through conduction) between the subsurface layers are computed with a thermal diffusion soil model that originally derives from Hourdin et al. (1993) and that has been later modified to take into account soil layers with various conductivities both horizontally and vertically (Millour et al., 2009; Turbet et al., 2017a).

At the surface, evaporation and sensible heat exchanges are computed within the boundary layer scheme using the bulk aerodynamic formula described in Chapter 5 and Charnay (2014).

Calculations of the surface albedo is adapted as a function of the composition of the surface (rock, ocean, lakes, CO_2 ice, snow, sea ice, etc.). For example:

- When snow accumulates over rock, we use the numerical scheme of Le Treut and Li (1991).
- When sea ice forms over the ocean, we use the formulation of Charnay (2014).
- When CO_2 condenses on the surface, a thin layer of CO_2 frost is expected to cover the entire surface. Therefore, for a threshold value of 1 mm of CO_2 ice, the surface albedo is assumed to be equal to CO_2 ice albedo (equal to 0.5).
- etc.

I adapted the code during my PhD to account for the wavelength-dependency of the albedo of any type of surface. It is for instance crucial to account for the variation of the water ice/snow albedo across the visible/near-infrared spectrum, and study the ice albedo feedback on planets orbiting various types of stars.

The topography of the planet can be adapted as wanted (1) for a flat planet, (2) to match existing topography data on Solar System planets (Mars, Venus, Earth, etc.) or (3) create any kind of crazy looking planet.[50]

[50] Ask if you want me to create a virtual planet with your own name on it!

1.4 Spectroscopy for habitability

The climate and habitability of a planet is highly dependent on the radiative budget at the top of the atmosphere, and between the different atmospheric layers and the surface. These radiative exchanges are controlled by the absorptions/emissions and scatterings by gas molecules, lifted particles, condensates and photochemical aerosols. Similarly, to interpret measurements of atmospheres of extrasolar planets, we need to have a good knowledge of the absorptions/emissions/scatterings of gas/particles, and in various conditions.

To perform calculations of absorption and emission spectra of gas molecules, it is necessary to dig into detailed calculations of spectroscopy. There are sometimes misunderstanding and/or misuse of spectroscopy in the planetary science community. I give in this section some keys for a good practice of spectroscopy applied to the modeling of planetary atmospheres. This section also gives some background for the reader to understand the content of Chapters 10 and 11.

1.4.1 Radiative transfer equation

Let's consider a beam of light (of intensity I_ν) passing through a thin atmospheric layer of thickness dx[51]. For each kind of gas molecule and particle[52] that the beam encounters, the variation of intensity of the beam dI_ν at the wavenumber ν can be written:

$$dI_\nu = (B_\nu(T) - I_\nu)\, N\sigma dx \tag{1.13}$$

where N is the number of molecules/particles per unit volume (in molec cm^{-3} and part cm^{-3}, respectively), σ is the absorption or scattering cross section (in cm^2/molec and cm^2/part, respectively) of a single gas molecule and particle, respectively. dx is expressed in cm units. $B_\nu(T)$ is the Planck function at temperature T that characterizes the emission of gas and particles. B(T) can be written:

$$B_\nu(T) = \frac{2h\nu^3}{c^2} \frac{1}{e^{\frac{hc\nu}{k_B T}} - 1} \tag{1.14}$$

with h the Planck constant, c the speed of light in vacuum, k_B the Boltzmann constant.

The radiative transfer equation can be written in more details for any arbitrary mixture of gases and particles as follows:

$$\begin{aligned} dI_\nu = & \sum_{i=1}^{n_{\text{particles}}} \Big(N_i \left[B_\nu(T_i)\sigma_{\text{i,emis}} - I_\nu \left(\sigma_{\text{i,Mie scat}} + \sigma_{\text{i,abs}}\right)\right] \Big) dx \\ & + \sum_{i=1}^{n_{\text{gases}}} \Big(N_i \left[B_\nu(T_i)\sigma_{\text{i,emis}} - I_\nu \left(\sigma_{\text{i,Rayleigh scat}} + \sigma_{\text{i,abs}}\right)\right] \Big) dx \end{aligned} \tag{1.15}$$

with N_i is the number of gas molecules (particles, resp.) per unit volume in molec cm^{-3} (part cm^{-3}, resp.) at the temperature T_i[53]. $\sigma_{\text{i,Mie scat}}$ is the Mie scattering cross-section by particles. $\sigma_{\text{i,Rayleigh scat}}$ is the Rayleigh scattering cross-section by gas molecules. $\sigma_{\text{i,abs}}$ and $\sigma_{\text{i,emis}}$ are the absorption and

[51] The layer must be "thin enough" that absorption and scattering by gas molecules is weak.
[52] Particles can be cloud particles, lifted dust, sea salt, etc.
[53] At local thermodynamic equilibrium, T_i is the same for every particle and gas molecule.

emission cross-section of molecule gases (particles, resp.). The Kirchhoff's law of thermal radiation enforces that $\sigma_{\mathrm{i,abs}} = \sigma_{\mathrm{i,emis}}$.

The goal of the next subsections is to show how to calculate the absorption cross-sections of molecule gases[54], for any arbitrary mixture of gas, and at any temperature and pressure. This ambitious goal needs to be achieved to accuretaly model the radiative transfer in the atmosphere of any planet and thus its climate.

1.4.2 Absorption cross-sections near "line centers"

1.4.2.1 Energy levels and line positions

Each molecule has 3N degrees of freedom, with N the number of atoms in the molecule. These degrees of freedom are the movements of translation, rotation and vibration. Depending on the size and geometry of the molecule, the number of possible movements of translation, rotation and vibration can change[55]. Each mode of vibration and rotation[56] is associated to an energy level E[57]. A molecule can change from one vibrational and/or rotational mode to another by absorbing or emitting a photon[58] of wavenumber $\nu = \frac{\Delta E}{hc}$, with h the Planck constant, c the speed of light, and ΔE the difference of energy between two vibrational and/or rotational modes.

Likewise, electrons in a molecule can get excited from one energy level to a higher energy level by absorbing a photon of the right wavenumber.

Therefore, molecules can absorb and emit photons at very specific locations (i.e. wavenumbers) that correspond to all the possible energy level changes ΔE of the molecule (mostly electronic, vibrational and rotational). The locations of absorption are usually known as "line positions".

Knowing precisely the position (and intensity) of these transition lines (i.e. localized absorptions) is a difficult task that can be achieved by both calculations and experimental measurements. Fortunately, there are now many existing databases that provide detailed lists of position (and intensity) of transition lines, such as HITRAN, HITEMP, CDSD, ExoMol, GEISA, etc. I will focus in this Chapter on the use of the HITRAN database, because it is the most complete and accurate database for the various planetary atmospheres explored throughout this thesis.

Note that, whenever I introduce spectroscopic parameters provided by HITRAN, I add a $^{\#}$ symbol.

1.4.2.2 Intensity of lines

The total intensity of an absorption (or emission) line S(T) is given in HITRAN at 296 K only. S(T) can be calculated following:

$$S(T) = \frac{A\ g'\ e^{\frac{-hcE''}{k_{\mathrm{B}}T}}\ (1 - e^{\frac{-hc\nu_{c,0}}{k_{\mathrm{B}}T}})}{8\pi c\ {\nu_{c,0}}^2\ Q(T)} \tag{1.16}$$

where $\mathrm{A}^{\#}$ is the Einstein A-coefficient (coefficient for spontaneous emission, in s^{-1}), g'$^{\#}$ is the upper state degeneracy (number of transitions that have the exact same energy level), E$''^{\#}$ is the lower-state

[54] I focus in this chapter on the absorption/emission of gas molecules. For a detailed review on absorption/scattering by particles, the reader is refered to the thesis manuscript of Jean-Baptiste Madeleine (Madeleine, 2011).

[55] Although the sum of possible movements - or degrees of freedom - remains constant and equal to 3N.

[56] Translation energy levels are so close to each other that we can consider them as a continuum

[57] These energy levels are quantized.

[58] or by a collision with another molecule. See Section 1.4.5 on line mixing.

energy of the transition (cm^{-1}), $\nu_{c,0}{}^{\#}$ is the line position in vacuum, and Q(T) is the internal partition sum. The partium sum Q(T) is the sum over all the allowed transitions:

$$Q(T) = \sum_i g_i \, e^{\frac{-hcE_i}{k_B T}} \tag{1.17}$$

where g_i is the degeneracy for the transition of energy E_i. It is possible to calculate this sum, but I recommend rather to use the partition function sums calculated by Gamache et al. (2017), and provided at various temperatures and for many different gases by HITRAN[59].

By combining the expressions of $S(T)$ and $S(296K)^{\#}$, we derive:

$$S(T) = S(296K) \frac{Q(296K)}{Q(T)} \frac{(1 - e^{\frac{-hc\nu_{c,0}}{k_B T}})}{(1 - e^{\frac{-hc\nu_{c,0}}{k_B 296}})} e^{\frac{-hcE''}{k_B}(\frac{1}{T} - \frac{1}{296})} \tag{1.18}$$

All the parameters of this equation are provided by HITRAN: $S(296K)^{\#}$, $Q(T)^{\#}$, $Q(296K)^{\#}$, $\nu_{c,0}^{\#}$, and $E''^{\#}$. This gives a procedure to calculate accurately the line intensity of each possible transition.

1.4.2.3 Line broadening

The absorption produced by a transition line is not monochromatic. There are several processes that tend to "broaden" the absorption lines that can be put in two categories:

- A first source of broadening arises from the finite lifetime of excited levels of energy. The Heisenberg uncertainty principle dictates that $\Delta t \Delta E \geq \frac{\hbar}{2}$. Δt can be associated to the duration of the excited level, and ΔE to the uncertainty on the difference of energy between the ground and excited levels of energy. This relation demonstrates that $\Delta E \geq \frac{\hbar}{2\,\Delta t}$ and that a broadening must arise. The shorter the lifetime of the excited level, the larger is ΔE, and the broader the transition line is.

- A second source of broadening arises from the velocities of molecules, and because of the Doppler effect. Compared to a motionless molecule, a molecule with a speed v (in the light of sight of the source of photons) will absorb photons with a Doppler wavenumber shift equal to $\Delta\nu = (1 \pm \frac{v}{c})\,\nu_{c,0}$. Because the velocities of molecules are usually spread into a large range of values, this produces a broadening on the line transition.

In pratice, the most important sources of broadening are:

- **Natural broadening**. The lifetime of an excited state in an isolated molecule is not infinite, because of spontaneous emission[60]. This produces a small "natural" broadening of transition lines.

- **Pressure broadening**. In dense environments, gas molecules collide frequently with each other. The lifetime of the excited states of molecules is now controlled by the mean free path between

[59] on http://hitran.org.

[60] The lifetime of the excited state is controlled by the spontaneous emisson Einstein coefficient introduced in the previous subsection.

two collisions, which is (at least in dense environment) much shorter than the typical timescale of spontaneous emission. Therefore, collisions tend to reduce the lifetime of excited levels of energy, which produces a "pressure" broadening.

- **Doppler broadening**. The velocity distribution in a gas at temperature T follows a Maxwell distribution that can be converted in a spectral broadening, through the Doppler effect. This is the Doppler broadening of transition lines. The higher the temperature of the gas, the larger the spread of velocities is, and the broader the transition line is.

Note that there are a lot of other possible (minor) sources of broadening/narrowing such as the Dicke narrowing (Dicke, 1953) or the line mixing (discussed in Sect. 1.4.5).

In general (for planetary atmosphere applications), the broadening of transition lines is controlled by either the Pressure broadening or the Doppler broadening or both. This broadening can be described with a line shape (or line profile) $f(\nu - \nu_{c,0}, P, T)$ that depicts how the absorption of the transition line evolves with the distance to the line center $\nu - \nu_{c,0}$, the temperature T and the pressure of the gas P. The absorption cross-section $\sigma_{\rm abs}$ (in cm^2 molec^{-1}) of a gas can then be written:

$$\sigma_{\rm abs}(\nu - \nu_{c,0}, P, T) \;=\; S(T)\; f(\nu - \nu_{c,0}, P, T)\;. \tag{1.19}$$

S is the line intensity and gives the total absorption associated with the line. It is usually given in cm^{-1}/(molec cm^{-2}). f is the line shape or line profile, it gives the distribution of absorption around the center of the line, usually expressed in cm. We recall that $\sum_0^\infty f(\nu - \nu_{c,0})d\nu \;=\; 1$.

It is also convenient to introduce here the absorption coefficient $k_{\rm abs}$ (in cm^{-1}), defined as:

$$k_{\rm abs}(\nu{-}\nu_{c,0}, P, T) \;=\; N\,\sigma_{\rm abs}(\nu{-}\nu_{c,0}, P, T) \;=\; \frac{10^{-6}P}{k_{\rm B}T}\,\sigma_{\rm abs}(\nu{-}\nu_{c,0}, P, T) \;=\; \frac{10^{-6}P}{k_{\rm B}T}\,S(T)\,f(\nu{-}\nu_{c,0}, P, T)\,. \tag{1.20}$$

with N the number of gas molecules per unit volume in molec cm^{-3}. With the perfect gas low approximation, N can be replaced by $\frac{10^{-6}P}{k_{\rm B}T}$, with P (in Pa) and T (in K) the partial pressure and temperature of the gas, respectively.

For each of the broadening sources described above is associated with a line profile. For the collisional broadening, it is the Lorentzian profile:

$$f_{\rm L}(\Delta\nu, T, P) \;=\; \frac{1}{\pi}\,\frac{\gamma_{\rm L}(T,P)}{\gamma_{\rm L}^2(T,P) + (\Delta\nu - \delta(P_{\rm ref})P)^2}, \tag{1.21}$$

with $\Delta\nu$ the distance to the vacuum line center, $\delta(P_{\rm ref})^{\#}$ the pressure-induced shift of the line center (in cm^{-1}/atm) at $\rm T_{ref}$ = 296 K and $\rm P_{ref}$ = 1 atm, and $\gamma_{\rm L}(T,P)$ the half-width at half-maximum (HWHM) of the pressure broadening. $\gamma_{\rm L}(T,P)$ can be calculated for any temperature, pressure and mixtures, according to:

$$\gamma_{\rm L}(T,P) \;=\; \sum_{p=1}^{n_{\rm perturbers}} \left(\frac{T_{\rm ref}}{T}\right)^{n_{\rm p}} \gamma_{\rm p}(T_{\rm ref}, P_{\rm ref})\; P_{\rm p} + \left(\frac{T_{\rm ref}}{T}\right)^{n_{\rm self}} \gamma_{\rm self}(T_{\rm ref}, P_{\rm ref})\; P_{\rm self}, \tag{1.22}$$

with $\gamma_{\rm p}(T_{\rm ref}, P_{\rm ref})$ and $\gamma_{\rm self}(T_{\rm ref}, P_{\rm ref})$ the HWHM of the foreign and self pressure broadenings, respectively, and at the reference pressure and temperature. $n_{\rm p}$ and $n_{\rm self}$ are the temperature dependency

exponents for foreign and self pressure broadenings, respectively. $P_{\rm p}$ and $P_{\rm self}$ are the partial pressure of external gases and of the absorbing gas, respectively.

HITRAN database only provides the parameters $\gamma_{\rm self}(T_{\rm ref}, P_{\rm ref})^{\#}$, $\gamma_{\rm air}(T_{\rm ref}, P_{\rm ref})^{\#}$, and $n_{\rm air}^{\#}$, for the very particular case where the external perturber is a mixture that resembles the atmospheric composition of the Earth. Moreover, HITRAN does not provide the temperature dependency exponent for self pressure broadening, which forces to use the temperature dependency exponent of air.

This of course does not give satisfactory results in cases where the dominant atmospheric gas differ from air/N_2, and whenever the temperature of the gas is far from the reference temperature. Fortunately, there are a lot of scientific papers that record measurements of $\gamma_{\rm P}(T_{\rm ref}, P_{\rm ref})$ (for various perturbing molecules) and for $n_{\rm self}$ (for various absorbing molecules) that can be used instead of the parameters provided by HITRAN. We discuss for instance how to accurately model the mutual broadenings of multiple gases in mixtures of CO_2+H_2O in Turbet et al. (2017c) and Tran et al. (2018).

For the Doppler broadening, the absorption line can be described by a Gaussian profile:

$$f_{\rm G}(\Delta\nu, T) = \sqrt{\frac{\ln 2}{\pi \alpha_{\rm D}^2}}\, e^{(-\frac{\ln 2\, \Delta\nu^2}{\alpha_{\rm D}^2})}, \tag{1.23}$$

with $\Delta\nu = \nu - \nu_{c,0}$ the distance to the line center, and $\alpha_{\rm D}$ the half-width at half-maximum (HWHM) of the Doppler broadening that can be written:

$$\alpha_{\rm D}(T) = \frac{\nu_{c,0}}{c}\sqrt{\frac{2 N_{\rm a} k_{\rm B} T \ln 2}{M}}, \tag{1.24}$$

with M the molar mass of the absorber[61] (in g/mol) and $N_{\rm a}$ the Avogadro constant.

In practice, the most widely used profile in modeling of planetary atmospheres is the Voigt profile. The Voigt profile is a convolution of a Lorentz and a Gaussian profile that is designed to capture simultaneously the Doppler and collisional broadenings. Unfortunately, the Voigt profile cannot be explicitely calculated with usual mathematical functions. Various numerical algorithms exist to compute the Voigt profile (see Hartmann et al. 2008, Appendix III.A and references therein).

1.4.3 Far wing absorptions

Although the Voigt profile gives a relatively good description of the absorption near the line transitions, it usually does not give satisfactory results far from the position of the line center. Because the absorption in the far wings is weak, it is usually not an issue. However, it can play a huge role in thick atmospheres involving optically thick path; thick enough that the sum of the contributions from all the far wings can create a significant absorption (see the example of CO_2 far wings in Fig. 1.27). I see at least two implications of this:

1. Far wing absorptions can produced strong greenhouse effect by blocking atmospheric windows.

2. Because far wing absorptions can block atmospheric windows, the thermal emission of extrasolar planets (and thus their observability) can be significantly affected by far wing absorptions.

[61] The molar mass here depends on the considered isotopologue.

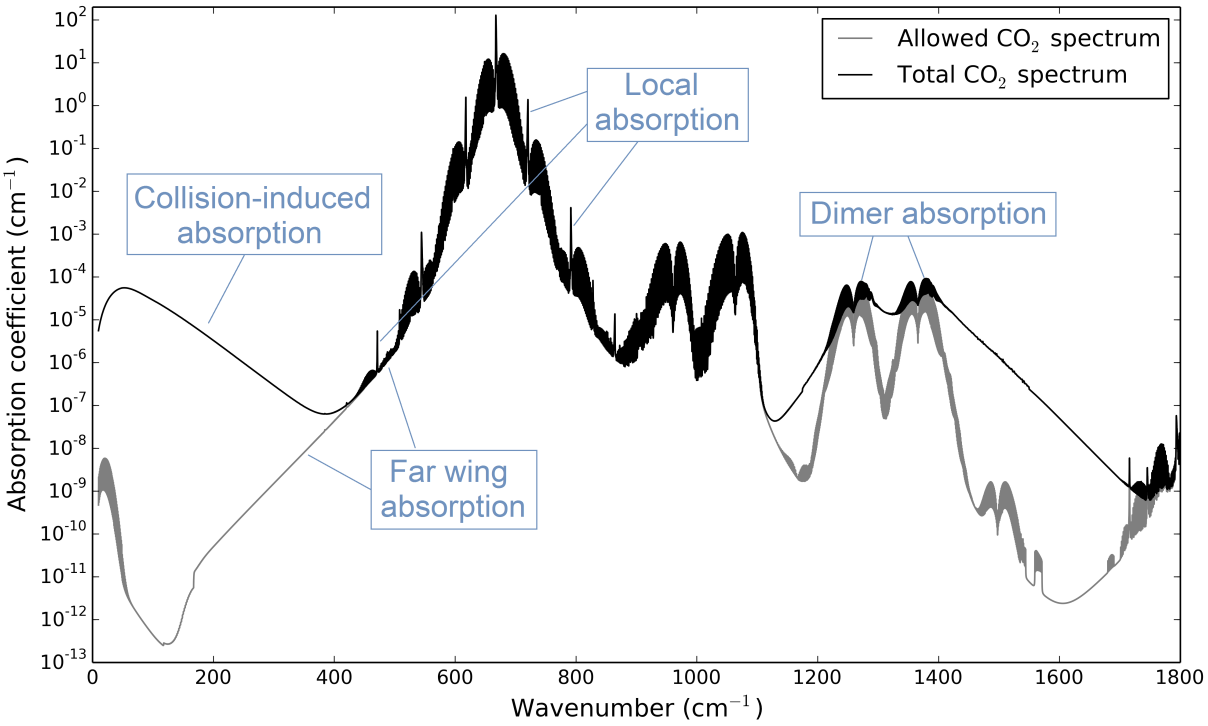

Figure 1.27: High resolution spectrum of pure CO_2 calculated at a pressure of 1 bar and a temperature of 300 K. This spectrum illustrates all the sources of absorption discussed in this introductory chapter. (1) Local absorption of lines, modeled using the Voigt profile. (2) Far wing absorptions of band lines, modeled using a χ-factor derived from experimental measurements (Perrin and Hartmann, 1989). (3) Collision-induced absorptions (Ho et al., 1971; Gruszka and Borysow, 1997, 1998; Hartmann et al., 2011) and (4) dimer absorptions (Baranov et al., 2004).

To my knowledge, there is currently no theory that can predict accurately the absorption far from the line centers. Instead, the approach that has been the most widely used is to add an empirical correction to the Voigt profile to account for differences between the Voigt profile (or Lorentzian profile, because the Voigt profile converges toward the Lorentz profile far from the line center) and experimental measurements. This correction is usually taken into account by introducing a χ-factor that is equal to 1 whenever the Voigt profile gives a good match with experimental results, and a value different to 1 otherwise. The behavior of the far wing is called "sub-lorentzian" for $\chi < 1$ and "super-lorentzian" for $\chi > 1$. Absorption cross-section (in cm^{-2}/molec) in the far wings of transition lines can then be written[62]:

$$\sigma_{\text{abs}}(\nu, N_{\text{a}}, N_{\text{p}}, T) = \sum_{l,\nu_l>0} N_{\text{a}}\ S(T) \left(\frac{\gamma_{\text{L}}(T,P)\ \chi_{\text{a+p}}(\nu-\nu_{c,0},T)}{\pi(\nu-\nu_{c,0})^2} + \frac{\gamma_{\text{L}}(T,P)\ \chi_{\text{a+p}}(\nu+\nu_{c,0},T)}{\pi(\nu+\nu_{c,0})^2} \right) \tag{1.25}$$

with $\gamma_{\text{L}}(T,P)$ the pressure-broadened HWHM (calculated following equation 1.22), $\chi_{\text{a+p}}$ the χ-factor measured experimentally in the far wing of the band lines of species "a" (absorber) and broadened by species "p" (perturber).

The reader should be careful when using χ-factors, because the definition of the χ-factor can vary from one publication to another, including sometimes asymmetric profiles (Menoux et al., 1991; Tran et al., 2018).

Ideally, and until we get a theory that can accurately predict absorption in the far wings, far wing absorption should be measured for a wide range of gas mixtures and temperatures[63] to adjust χ-factor for every absorption bands. In theory, far wing absorptions could be calculated using molecular dynamics numerical simulations (Hartmann et al., 2011). However, calculations very far in the wings are computationnally too expensive to be done with existing computing power (J-M Hartmann, personnal communication).

In practice, there is not enough available experimental data to adjust χ-factor everywhere. Instead, people usually use χ-factors measured in one band and apply it to other bands (where no experimental data is available).

Did you know for example that the absorption in the low frequency wing of the most famous CO_2 ($15\mu m$) band had never been measured until the experimental work presented in Chapter 11?

We actually show in Chapter 11, with the exemple of CO_2, that this approximation is generally not too bad, although small differences in χ-factor close to the line center can amplify, creating huge differences in absorption far in the lines. This can have a dramatic effect for exemple on the greenhouse effect of some gases (see Chapter 10).

1.4.4 Note on the line cutoff distance

My experience discussing with planetary scientists taught me that there is a lot of confusion on how to choose the line cutoff distance, i.e. the distance of the line center from which the absorption is assumed to be 0. There are actually two different situations where a line cutoff can/must be applied:

[62] Note the term in $(\nu + \nu_{c,0})$ comes from the contribution of "negative" transition lines. This term can contribute significantly only at very short wavenumbers

[63] Far-wing broadening can be strongly affected by the nature of the perturber. For example, absorption by the far wings of CO_2 band lines significantly differ when broadened by CO_2, N_2, or H_2O (Baranov, 2016; Turbet and Tran, 2017; Tran et al., 2018; Hartmann et al., 2018a).

The "computationally-driven" cutoff

Calculations of absorption of 10^6-10^9 of absorption lines over the entire spectrum can be computationnally extremely expensive. A common strategy to deal with this is to consider that the absorption far from a line center is equal to 0 whenever the distance to the line center is larger than a fixed cutoff distance d_{cutoff}. This trick reduces the range of distances where the calculation of absorption is performed, which reduces the computational cost.

The cutoff distance must be chosen carefully to be sure that significant far wing absorptions are not suppressed.

The "continuum-driven" cutoff

Several teams of scientists provide databases including the contribution of far wing absorptions. The most famous of these databases is the MT_CKD (Clough et al., 2005; Mlawer et al., 2012) that provides a state-of-the art tabulated continuum for water vapor[64]. This continuum has been tabulated taking into account the contribution of the far wings, starting 25 cm^{-1} from the line centers. Therefore, in this example, any calculation of a H_2O high resolution spectrum using the MT_CKD database must use the same convention. In other words, the water vapour spectrum must be calculated using a cutoff distance of 25 cm^{-1}[65].

There are two main reasons why this "tabulated" continuum approach is efficient:

- First, it is computationnally much more efficient. For the MT_CKD continuum for example, once the 25 cm^{-1} database is constructed, any calculation of water vapor spectrum can be made using a cutoff distance of only 25cm^{-1}.
- Second, the pressure dependency of the absorption is different between the line center and the far wings. By separating absorptions from the line center and from the far wings, it is possible to adapt the scheme of interpolation in radiative transfer to the P^2 dependency of the far wing absorptions, where P is the partial pressure of gases.

1.4.5 Collisional line mixing

It is often assumed that absorption spectra can be calculated assuming that the total absorption is equal to the sum of the absorption of each individual lines. In fact, this assumption can sometimes be hampered by a process called collisional "line-mixing" (Hartmann et al., 2008).

Spectra usually contain clusters of closely spaced transition lines. These clusters are almost always produced by different rotation modes of the same vibrational mode[66]. Lines within clusters can usually be considered as isolated (i.e. their contribution to the total spectrum is additive) for low atmospheric pressures, when collisions between molecules are rare. At high pressures, when collisions between

[64] This database includes the contribution of the absorption in the far wings, and probably other contributions coming from CIA and dimer absorptions (see next section).

[65] Ideally, the calculations near the line center should be calculated using the same spectroscopic database than the one used in MT_CKD. Another specifity of the MT_CKD and many other databases is that the pedestal absorption must be removed. The pedestal absorption calculated at 25cm^{-1} from the line center must be substracted everywhere between -25 and +25cm^{-1} from the line center, because the contribution of the pedestal is already included in the MT_CKD database.

[66] The difference of energy between two rotation modes is usually much lower than the difference of energy between two vibration modes

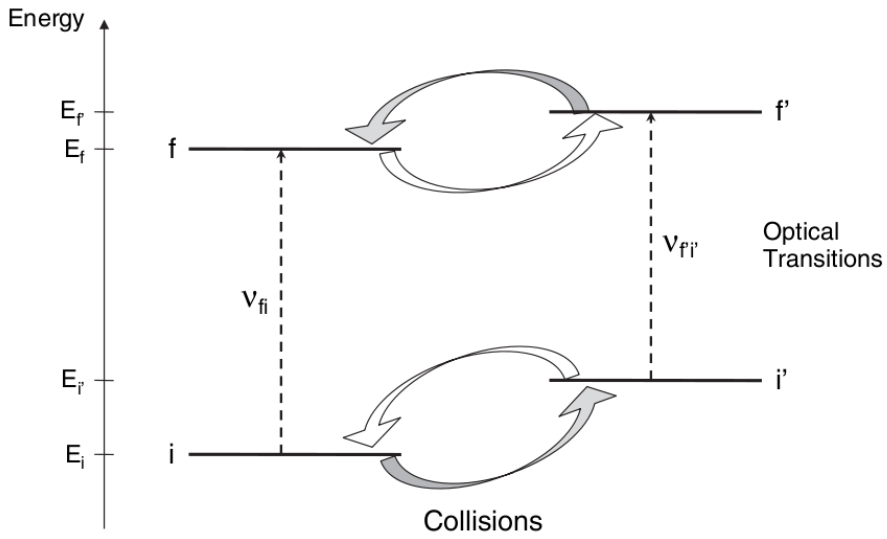

Figure 1.28: Schematic view of the line-mixing process in the case of two optical transitions. From Hartmann et al. (2008).

molecules become frequent, lines within cluster cannot be considered anymore as isolated, because of the collisional line mixing effect.

Let's consider two closely spaced transition lines (see Fig. 1.28) of levels i→f and i'→f' of wavenumbers $\nu_{\text{i-f}}$ and $\nu_{\text{i'-f'}}$, respectively. This means that $\nu_{\text{i-f}} \approx \nu_{\text{i'-f'}}$. If a molecule absorbs a photon of energy $hc\nu_{\text{i-f}}$, the level i can be excited to the level f. For isolated lines, this is the only possible way to go from level i to f. There is in fact another path to go from level i to f, through collisions with other molecules. A molecule in level i can transfer to level i' through a collision with another molecule, then absorbs a photon of energy $hc\nu_{\text{i'-f'}}$, and eventually transfer to level f through another collision. This demonstrates that a transition i→f can produce an absorption at a wavenumber $\nu_{\text{i'-f'}}$, instead of at wavenumber $\nu_{\text{i-f}}$ and that this transition line cannot be considered isolated whenever this second path becomes efficient enough. This second path changes the way energy levels of closely spaced lines are populated and changes therefore the shape of the absorption of closely spaced transition lines.

The effect of line mixing is illustrated qualitatively in Fig. 1.29, where absorption lines with line mixing and without (i.e. considering that absorption lines are isolated) are compared. At low pressure, the isolated line approximation gives satisfactory results. However, as the pressure increases, collisions are more and more frequent, and line mixing effects become dominant. Line mixing results in transfer of absorption from the wings to the line centers (Hartmann et al., 2008), thus leading to a sub-Lorenztian behavior in the wings. The effect of collisional line mixing is discussed in details in the context of early Mars atmosphere in the Chapter 10.

In order to account for the line mixing effects, theoretical approaches called ECS models (for Energy Corrected Sudden approximation) have been developed and successfuly tested near the line centers (see Tran et al. 2011 and references therein). However, these models are not yet designed to also give satisfactory results in the far wings. As of 2018, no model can accurately describe simultaneously absorptions in the line center and absorption in the far wings.

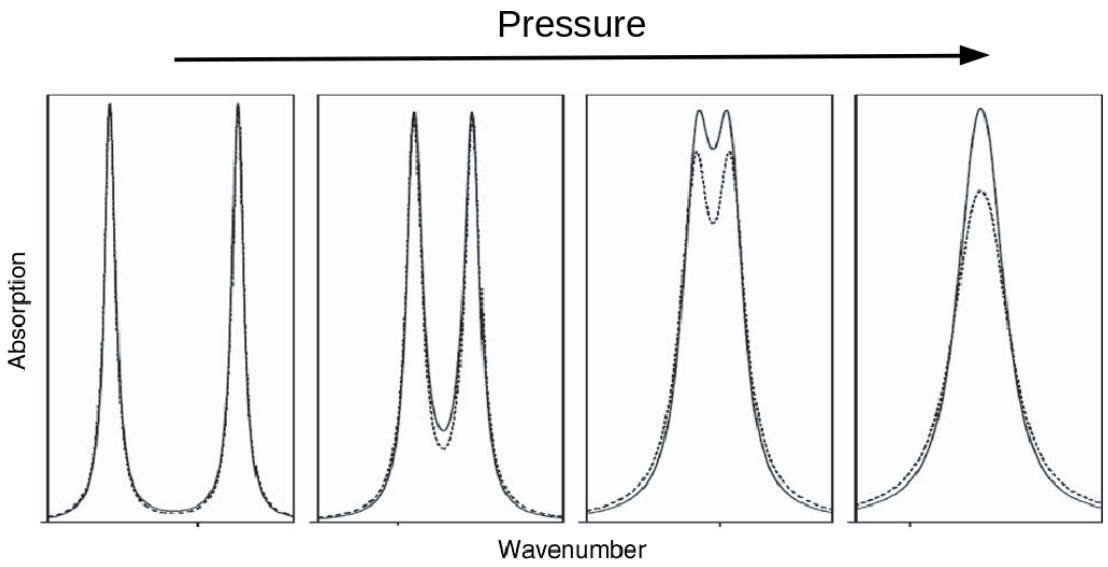

Figure 1.29: Typical evolution of the shape of a doublet of collisionally coupled transitions with increasing total pressure. Solid and dotted lines correspond to predictions made with and without the inclusion of line mixing, respectively. Adapted from Hartmann et al. (2008).

1.4.6 Collision-induced absorptions

In the previous sections, I only focused on the absorption coming from "allowed" line transitions, i.e. absorption corresponding to changes of mode of vibration and/or rotation. In fact, absorption can arise in spectral regions where quantum mechanics does not predict any "allowed" absorption, thanks to collisions between molecules. Whenever two molecules collide, electric interactions between the two molecules (during the collision) can change the distribution of electronic charges in each of the two molecules, thus producing transient dipoles.

We call the "forbidden" absorptions that arise from absorptions by transient dipoles the collision-induced absorptions (CIAs). These absorptions can arise from interactions of any pairs of molecules, even including symmetric ones (e.g. H_2, N_2, O_2, etc.).

The lifetime of excited states in transient dipoles is usually on the order of the duration of the collision, hence short. This is the reason why CIAs usually produce very broad absorptions (see the example of the CO_2-CO_2 CIA in Fig. 1.27). If the configuration of the collision is favorable, the two molecules can "stick" to each other and form a transient molecular complex that can also produce forbiden absorptions. Such molecular structure is called "dimer" and produce "dimer absorption" (see the example of the CO_2-CO_2 dimer in Fig. 1.27). Because dimer have a lifetime that is much longer than the duration of a collision, dimer absorptions usually produce a narrower absorption than CIAs.

Accurate ab initio calculations of CIAs is a difficult task to do, because this requires to know accurately (1) the potential of interaction between two colliding molecules at both short and large distances and (2) the dipolar/multipolar polarizabilities of the two colliding molecules. Therefore, laboratory measurements are crucial to determine accurately dimer absorptions and CIAs for various pairs of colliding molecules.

It is even more critical for binary CIAs (e.g. of the form X-Y with X being different than Y) where experimental measurements are lacking. An application of that for the CO_2-CH_4 and CO_2-H_2 pairs (with possible implications for the climate of early Mars) is tackled in Chapter 11.

Part I

Habitability of extrasolar planets

Chapter 2

CO_2 condensation and the habitability of distant Earth-like planets

Contents

2.1 Preamble

The carbonate-silicate cycle is a fascinating geochemical cycle that stabilizes the climate of our Earth on the long term (Walker et al., 1981). It has been speculated that such a carbon cycle could operate (or could have operated) on other planets, such as Mars, Venus or extrasolar planets (Pollack et al., 1987; Kasting et al., 1993; Batalha et al., 2016). Many studies have explored how such a carbon cycle would behave on Earth-like planets with various insolations, or orbiting various type of stars, most of them using simplified climate or energy balanced models (Menou, 2015; Abbot, 2016; Haqq-Misra et al., 2016).

I focus in this chapter on the ability of Earth-like planets to escape from a period of complete glaciation, depending on the insolation they receive. My main, original idea was that cold planets

orbiting far from their host star may not be able to escape from a period of complete glaciation - in the way Earth did, by the greenhouse warming produced by the CO_2 volcanic outgassing - because CO_2 can condense and thus accumulate on the cold regions of the planet. I realized soon that this idea had been previously proposed and published by Raymond Pierrehumbert (Pierrehumbert, 2005; Pierrehumbert et al., 2011) in the context of past episodes of glaciations of our own Earth. But no one has ever explored it quantitatively. For this, you need a 3-D Global Climate Model that is able to simulate both the water and carbon cycles. A model that can simulate the evaporation/sublimation/condensation of both H_2O and CO_2. A model that can simulate simultaneously the formation, evolution and precipitation of both H_2O and CO_2 clouds as well as their radiative effects. Fortunately, the LMD Generic Global Climate Model can simulate all these processes simultaneously, thanks to its historical ability to simulate the atmospheres of the Earth, ancient Earth, Mars, ancient Mars and extrasolar planets.

This chapter is based on a paper published in Earth and Planetary Science Letters in October 2017. The full reference is: Martin Turbet, Francois Forget, Jeremy Leconte, Benjamin Charnay & Gabriel Tobie, **"CO_2 condensation is a serious limit to the deglaciation of Earth-like planets"**, EPSL, 2017 (`http://adsabs.harvard.edu/abs/2017E%26PSL.476...11T`).

2.2 Abstract

It is widely believed that the carbonate−silicate cycle is the main agent, through volcanism, to trigger deglaciations by CO_2 greenhouse warming on Earth and on Earth-like planets when they get in a frozen state. Here we use a 3D Global Climate Model to simulate the ability of planets initially completely frozen to escape from glaciation episodes by accumulating enough gaseous CO_2. The model includes CO_2 condensation and sublimation processes and the water cycle. We find that planets with Earth-like characteristics (size, mass, obliquity, rotation rate, etc.) orbiting a Sun-like star may never be able to escape from a glaciation era, if their orbital distance is greater than $\sim$ 1.27 Astronomical Units (Flux $<$ 847 W m^{-2} or 62% of the Solar constant), because CO_2 would condense at the poles – here the cold traps – forming permanent CO_2 ice caps. This limits the amount of CO_2 in the atmosphere and thus its greenhouse effect. Furthermore, our results indicate that for (1) high rotation rates (P_{rot} $<$ 24 h), (2) low obliquity (obliquity $<$ 23.5°), (3) low background gas partial pressures ($<$ 1bar), and (4) high water ice albedo (H_2O albedo $>$ 0.6), this critical limit could occur at a significantly lower equivalent distance (or higher insolation). For each possible configuration, we show that the amount of CO_2 that can be trapped in the polar caps depends on the efficiency of CO_2 ice to flow laterally as well as its gravitational stability relative to subsurface water ice. We find that a frozen Earth-like planet located at 1.30 AU of a Sun-like star could store as much as 1.5, 4.5 and 15 bar of dry ice at the poles, for internal heat fluxes of 100, 30 and 10 mW m^{-2}, respectively. But these amounts are in fact lower limits. For planets with a significant water ice cover, we show that CO_2 ice deposits should be gravitationally unstable. They get buried beneath the water ice cover in geologically short timescales of $\sim 10^4$ yrs, mainly controlled by the viscosity of water ice. CO_2 would be permanently sequestered underneath the water ice cover, in the form of CO_2 liquids, CO_2 clathrate hydrates and/or dissolved in subglacial water reservoirs (if any). This would considerably increase the amount of CO_2 trapped and further reduce the probability of deglaciation.

2.3 Introduction

There are geological evidences that Earth had to face multiple episodes of global or quasi-global glaciation, at the end of the Archean 2.45-2.22 Gya and during the Neoproterozoic era, 710 and 650 Mya (Evans et al., 1997; Hoffman et al., 1998; Hoffman and Schrag, 2002).

It is widely believed that the carbonate−silicate cycle (Walker et al., 1981; Kasting et al., 1993; Kump et al., 2000) was the main agent to trigger deglaciations on ancient Earth. In particular, on a completely frozen planet, also called 'Hard Snowball', the weathering of CO_2 is stopped; continuous volcanic outgassing builds up atmospheric CO_2 that warm up the climate until liquid water is produced in the equatorial regions.

By extension, this mechanism may be crucial to stabilize the climate of Earth-like exoplanets. It is even central for the definition of the classical Habitable Zone (Kasting et al., 1993; Forget and Pierrehumbert, 1997; Kopparapu et al., 2013), which assumes that planets can build up CO_2 atmospheres (as massive as wanted) suitable for the stability of surface liquid water.

Planets near the outer edge of the Habitable Zone may suffer, as Earth did, episodes of complete glaciation. Recent work by Menou (2015) has even shown that, in the case of planets lacking land vascular plants, temperate climates may not be stable, because at high CO_2 partial pressure, the increased weathering rate does not allow temperate stable solutions. This effect, which is enhanced for planets weakly irradiated by their star, may systematically drive Earth-like exoplanets toward episodes of glaciation.

Can Earth-like planets in the Habitable Zone of their star always escape from episodes of glaciation? In this work, we use 3D Global Climate Model (GCM) simulations of snowball planets to study the ability of the increased CO_2 greenhouse effect resulting from volcanic outgassing to drive them out of glaciation. As the CO_2 outgassed by volcanoes accumulates in the atmosphere, the temperature of condensation of CO_2 can exceed the surface temperature of the poles. This leads to the trapping of extra outgassed CO_2, forming permanent CO_2 polar ice caps, and thus seriously limits the efficiency of the carbonate−silicate cycle. This possibility has already been suggested in Pierrehumbert (2005) and Pierrehumbert et al. (2011), but has never been explored yet. We propose in this paper a detailed study of this scenario.

2.4 Method

We use in this paper the 3-Dimensions LMD Generic Global Climate Model to study the deglaciation of Earth-like planets orbiting in a circular orbit around a Sun-like star (Sun spectrum and luminosity) in response to increasing amounts of atmospheric CO_2 (from 0.01 to 3 bar), and for orbital distances ranging from 1.10 to 1.45 Astronomical Units (AU). Detailed information on the model can be found in Appendix 2.8.1.

Our simulations were designed to represent completely frozen Earth-like planet characteristics. These include the radius (6370 km), the gravity field (9.81 m s^{-2}), the obliquity (23.5°) and the rotation speed (7.28×10^{-5} rad s^{-1}). The roles of obliquity, planetary mass and rotation rate on the ability of planets to escape glaciation episodes are discussed in sections 2.5.2 and 2.5.4. Eventually, most of the simulations were performed for a uniformly flat topography. The effect of topography is discussed in section 2.5.4.5.

All the simulations performed in this study were forced initially in a cold and dry state, assuming:

Explored parameters	Values
CO_2 partial pressures (in bar)	[0.01, 0.1, 0.4, 1.0, 1.5, 2.0, 3.0]
i) Stellar flux (in W m^{-2})	[1130, 1033, 949, 874, 808, 750, 697, 650]
ii) Flux compared to Earth (S_{eff})	[0.827, 0.756, 0.695, 0.640, 0.592, 0.549, 0.510, 0.476]
iii) Equivalent distance (in AU)	[1.10, 1.15, 1.20, 1.25, 1.30, 1.35, 1.40, 1.45]
Obliquity	0, 23.5°
CO_2 ice clouds	radiatively active, inactive

Table 2.1: Physical Parameterizations used for GCM calculations.

1. A uniform and complete ice cover.
2. Atmospheric and surface temperatures arbitrarily fixed to 230 Kelvins everywhere.
3. No water vapor, no clouds.

Depending on CO_2 partial pressure, obliquity, or parameterization of clouds, the simulations evolve in different steady state climate regimes that are discussed in the next section.

2.5 Glaciation escape limited by CO_2 atmospheric collapse

2.5.1 Reference case

We performed 40 simulations of Earth-like planets (as described in section 2.4 – with a 23.5° obliquity and radiatively inactive CO_2 ice clouds) starting from an initially cold (T = 230 K everywhere) and global glaciation state for multiple irradiation fluxes and CO_2 partial pressures (see table 2.1). We fix the N_2 partial pressure to be constant and equal to 1 bar, in order to be consistent with the case of Earth. All simulations were run long enough to reach equilibrium[1].

We find that, depending on the CO_2 partial pressure and the stellar flux, these simulations can evolve in three different climate regimes:

1. The greenhouse effect of CO_2[2] is sufficient to raise the surface temperatures in equatorial regions above the melting temperature of water ice[3]. In this case, the positive feedback due to the decrease of the surface albedo (from 0.6 to 0.07) and the greenhouse effect of water vapor drive the planet out of glaciation.

[1] up to 30 Earth years for the thickest atmospheric configurations.
[2] which is enhanced by the pressure broadening of N_2.
[3] 273 K, here.

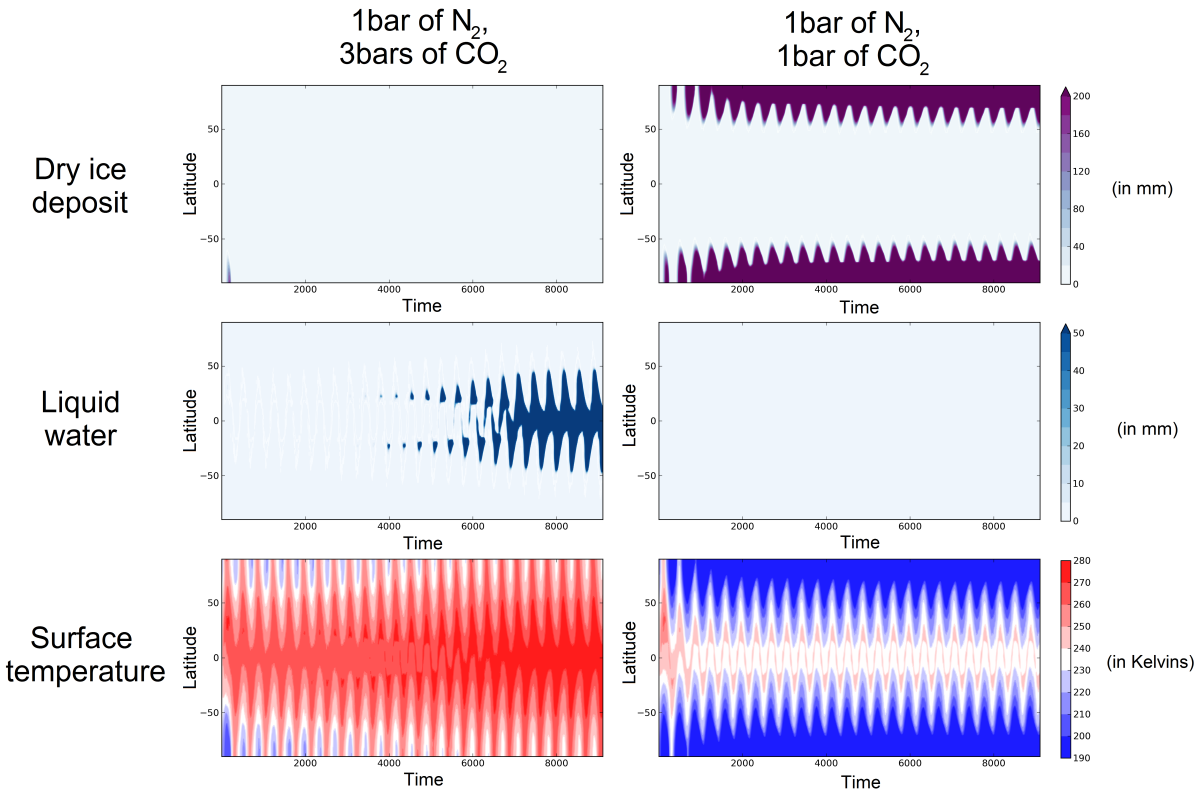

Figure 2.1: From top to bottom: Zonal means of (1) CO_2 ice deposit, (2) surface liquid water and (3) surface temperatures as a function of time (in Earth days), and for two different initial states. On left, the initially cold and dry planet starts with a CO_2 partial pressure of 3 bar and is able to escape glaciation. On right, the planet starts with a CO_2 partial pressure of 1 bar and ends up in atmospheric collapse. These simulations were run for planets with a 23.5° obliquity, radiatively inactive CO_2 ice clouds, and located at an equivalent orbital distance of 1.30 AU (F = 808 W m^{-2}).

2. The greenhouse effect of CO_2 is too weak to trigger a deglaciation. The planet stays in a snowball state.

3. The greenhouse effect of CO_2 is too weak to raise the surface temperatures of the poles above the condensation temperature of CO_2. In this case, atmospheric CO_2 collapses and the planet is locked in a global glaciated state, with two permanent CO_2 ice polar caps.

Figure 2.1 shows that, for a given solar flux (808 W m^{-2} here), the choice of the initial CO_2 partial pressure can either drive the planet out of glaciation (pCO_2 = 3 bar) or cause a permanent collapse of the atmosphere at the poles (pCO_2 = 1 bar).

These results are summarized in Figure 2.2b, for multiple stellar fluxes and CO_2 partial pressures. Each region of the diagram denotes a steady state climate regime reached by the planet:

1. In red, the planet is partially or totally deglaciated.

2. In white, the planet is entirely frozen.

3. In blue, the planet is entirely frozen and gaseous CO_2 has permanently collapsed at the poles. This situation actually occurs when winter CO_2 frost formation rate exceeds seasonal summer sublimation.

We now put these results in the context of an active carbonate-silicate cycle. A planet that enters in a global glaciation state must have initially a low CO_2 atmospheric content that places it in the lower part of the diagram (in Figure 2.2b). From this point, CO_2 is outgassed by volcanoes and accumulates in the atmosphere. As the CO_2 partial pressure increases, the planet moves up in the diagram until:

1. the planet reaches the red zone first. The planet is able to escape glaciation.

2. the planet reaches the blue zone first. All the extra CO_2 possibly outgassed by volcanoes condenses at the poles and the planet is locked in a perpetual glaciation state.

For an (Earth-like) 23.5° obliquity, we find this limit to occur for planets located at more than 1.27 AU from a Sun-like star (Flux < 847 W m^{-2}, S_{eff}[4] < 0.62), with an optimal CO_2 partial pressure around 1 bar (see Figure 2.2b).

However, if a planet starts with a large enough CO_2 atmospheric content so that it lies above the blue zone, then the CO_2 should resist atmospheric collapse and the deglaciation becomes possible.

2.5.2 Null obliquity case

For a 0° obliquity planet, because insolation in the polar regions is lowered, the equator-to-pole temperature contrast is amplified. Consequently, we find that permanent condensation of CO_2 at the poles happens for much lower equivalent distances (d > 1.13 AU, Flux < 1070 W m^{-2}, S_{eff} < 0.78; see Figure 2.2a).

[4]The effective flux S_{eff} is defined as the ratio between the incoming stellar flux on the planet and that on the Earth.

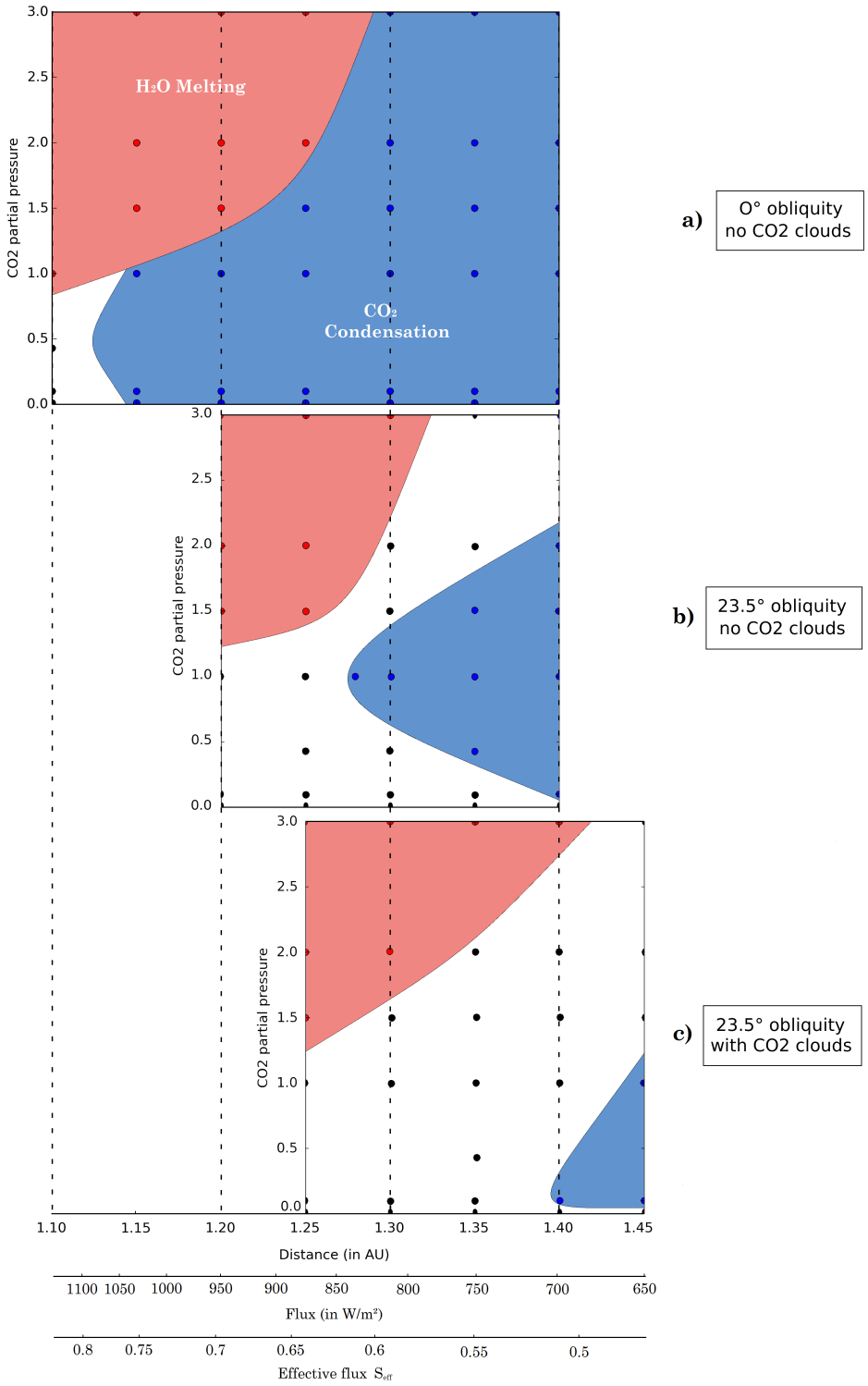

Figure 2.2: Climate regimes reached as function of the equivalent orbital distance from a Sun-like star (in AU) and the CO_2 partial pressure, assuming a cold start (i.e. snowball state without permanent CO_2 ice deposits). Diagrams a, b and c were constructed for Earth-like planets with 0° obliquity, 23.5° obliquity (reference simulation) and 23.5° obliquity with radiatively active CO_2 ice clouds, respectively. The red color roughly depicts the region where deglaciation is observed. The blue region represents glaciated states where CO_2 collapses permanently. The white region describes cases where none of this two previous conditions were reached.

2.5.3 Effect of CO_2 ice clouds

During polar nights, the temperatures at the poles are very low. CO_2 condenses at the surface but also in the atmosphere, forming CO_2 ice clouds that may have a significant warming effect (Forget and Pierrehumbert, 1997).

We performed multiple simulations for planets at 23.5° obliquity including radiatively active CO_2 ice clouds. For this, we used a constant cloud condensation nuclei [CCN] of 10^5 kg^{-1} designed to maximize the greenhouse effect of CO_2 ice clouds (Forget et al., 2013). This idealized configuration corresponds to an endmember description of the radiative warming effect of CO_2 ice clouds. In particular, Kitzmann (2016) has shown recently, using a more refined radiative transfer scheme, that a configuration like the one used in this section probably overestimates the warming effect of CO_2 ice clouds.

Our simulations (example in Figure 2.5.3) show that the CO_2 ice cloud distribution evolves significantly with seasons. In winter, CO_2 ice clouds form a quasi-complete polar cover and have a powerful greenhouse effect that limits the condensation of CO_2 at the poles. In summer, CO_2 clouds dissipate as insolation increases. As a result, CO_2 clouds have a very limited impact on the albedo and therefore do not contribute much to prevent polar CO_2 ice summer sublimation.

For these two reasons, CO_2 ice clouds seriously limit the collapse of CO_2 at the poles. Figure 2.2c shows that, with radiatively active CO_2 clouds, CO_2 condensation would occur for equivalent distance > 1.40 AU (Flux < 697 W m^{-2}, $S_{eff} < 0.51$).

2.5.4 Sensitivity study

2.5.4.1 The albedo of ices

The choice of water ice albedo can severely affect our results. For albedo higher than 0.67, we find that CO_2 condensation can occur on Earth-like planets (23.5° obliquity, radiatively inactive CO_2 ice clouds) for equivalent distance as low as 1.15 AU (Flux ~ 1033 W m^{-2}, $S_{eff} \sim 0.76$), corresponding to the reduced luminosity of the Sun 3.8 Gya calculated from standard solar evolution models (Gough, 1981).

We note that water ice albedo is considerably reduced around cool stars (Joshi and Haberle, 2012), making the scenario of CO_2 polar condensation less efficient. However, planets orbiting in the Habitable Zone of M-dwarfs are also subject to tidal locking. The temperature on the nightside of a synchronous planet can be extremely low, favoring the CO_2 condensation. This possibility is explored and discussed in details in Turbet et al. (2018a).

We also explored the effect of CO_2 ice albedo that could potentially be very high (see section 2.8.1.3, Kieffer et al. 2000) and we found it to be much less important.

Eventually, we acknowledge that a real Snowball might have regions of open continent not covered by water ice, which would lower albedo. These could act as sources of dust, and volcanic aerosols could also darken the surface (Abbot and Pierrehumbert, 2010).

2.5.4.2 The rotation rate

The rotation rate of Earth has evolved in time from 1.2×10^{-4} (4 Gya) to 7.3×10^{-5} rad s^{-1} (now) due to the effect of the Moon's tidal friction (Walker and Zahnle, 1986; Zahnle and Walker, 1987). More

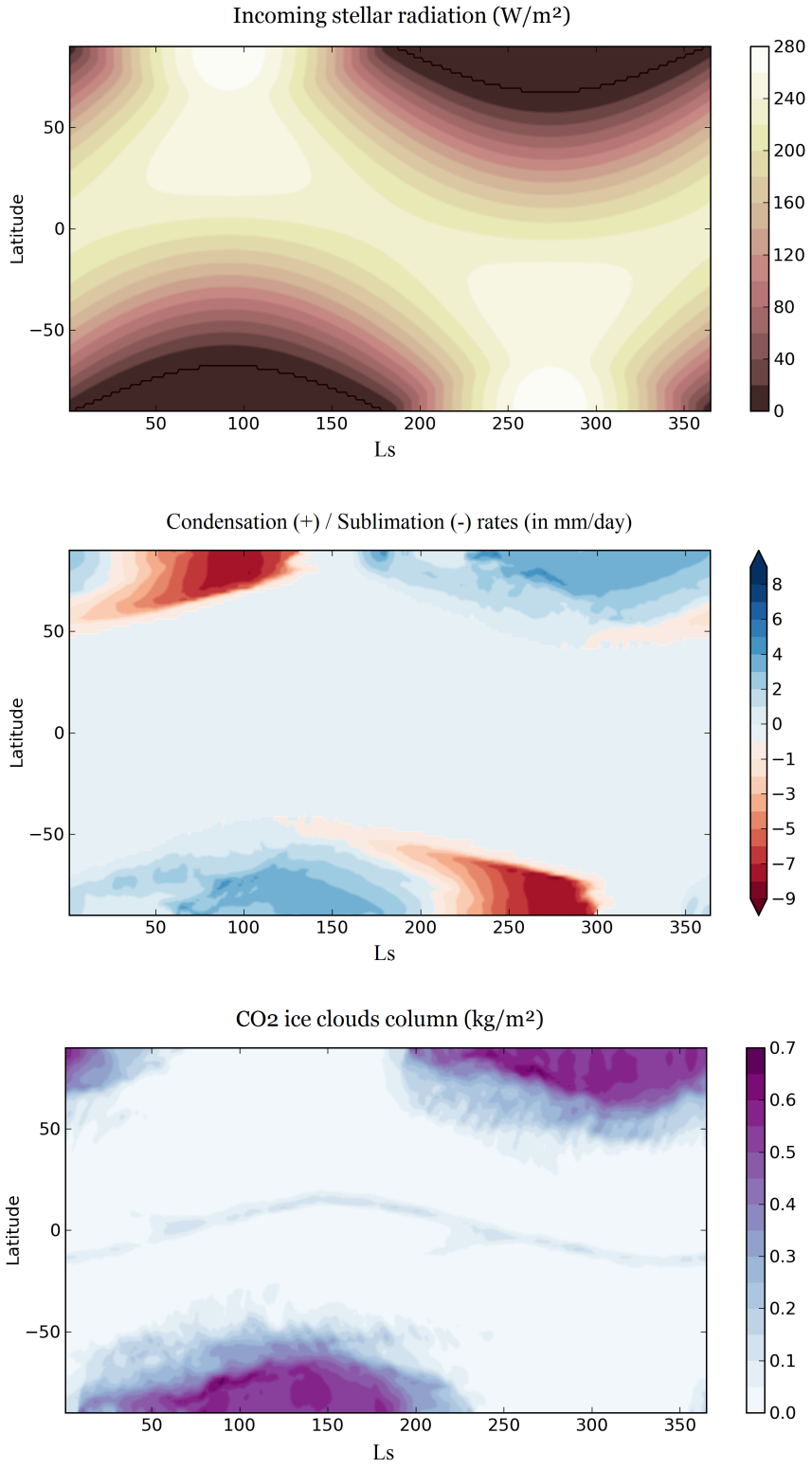

Figure 2.3: From top to bottom: (1) zonal mean of incoming stellar radiation (ISR) versus L_s, (2) zonal mean of CO_2 ice condensation(+)/sublimation(-) rates versus L_s, and (3) zonal mean of CO_2 ice cloud (column integrated) content versus L_s. These figures were computed for a planet with a 23.5° obliquity, active CO_2 ice clouds, located at an equivalent orbital distance of 1.40 AU (F = 697 W m^{-2}) and for a CO_2 partial pressure of 1 bar and a N_2 partial pressure of 1 bar.

generally, Earth-like planets could harbor a wide range of rotation rates.

In this study, we find that rotation rate is a very important parameter for CO_2 polar condensation. A high rotation rate reduces the latitudinal transport and thus increases the equator-to-pole surface temperature gradient (Kaspi and Showman, 2015), favoring CO_2 condensation at the poles. We find that, for a rotation rate $\Omega = 4\ \Omega_{\rm Earth}$ (23.5° obliquity, radiatively inactive CO_2 ice clouds), CO_2 can collapse as early as 1.15 AU (Flux $\sim$ 1033 W m^{-2}, $S_{\rm eff} \sim 0.76$).

To go further, we investigated the case of archean Earth, 3.8 Gya ($S_{\rm eff} \sim 0.76$), through simulations of a completely frozen planet, assuming a 23.5° obliquity, a rotation period of 14 hours and a water ice albedo set to 0.6. We find that CO_2 can condense at the poles seasonally, but never permanently.

2.5.4.3 The planetary mass

Massive planets also have a large radius that may be responsible for the weakening of the poleward heat transport, favoring the collapse of CO_2. For example, assuming an internal composition similar to the Earth, a 5 $M_{\rm Earth}$ planet would have a radius around 1.5 $R_{\rm Earth}$ or 10^4 km (Seager et al., 2007). We performed GCM simulations for a 5 $M_{\rm Earth}$ planet, for a CO_2 partial pressure of 1 bar and a N_2 partial pressure of 1 bar. In these conditions, we find that the collapse of CO_2 can occur for equivalent distances as low as 1.18 AU (Flux $<$ 981 W m^{-2}, $S_{\rm eff} < 0.72$).

However, because accretion of volatiles should increase with planetary mass, the atmospheric mass should also increase with it (see Kopparapu et al. 2014 section 2 for more details). Therefore, we expect a massive planet to have a greater content of background gas (e.g. N_2). For a 5 $M_{\rm Earth}$ planet, assuming that $P_{\rm surface}$ scales as ${R_{\rm planet}}^{2.4}$. (equation 3 in Kopparapu et al. 2014), we roughly get a partial pressure of N_2 equal to 3.3 bar [5]. Using GCM simulations, we find that in this more realistic case, CO_2 collapses for equivalent distances greater than 1.30 AU (Flux $<$ 808 W m^{-2}, $S_{\rm eff} < 0.59$).

2.5.4.4 The atmospheric composition: the role of N_2 partial pressure

The result of the previous section shows that N_2 partial pressure can have a significant impact on CO_2 collapse. As pN_2 increases, the atmosphere thickens and (1) the poleward heat transport increases and (2) the greenhouse effect of CO_2 increases because of pressure broadening of CO_2 by N_2. Both effects tend to prevent CO_2 condensation.

Quantitatively, our simulations show that, for an Earth-like planet with a CO_2 partial pressure of 1 bar (with 23.5° obliquity, radiatively inactive CO_2 ice clouds), doubling pN_2 from 1 to 2 bar leads to the condensation of CO_2 for equivalent orbital distances greater or equal to 1.35 AU (+0.08 AU difference).

2.5.4.5 The topography

To investigate the possible effects of topography on CO_2 polar condensation, we ran several simulations in which we emplaced a mountain range similar in size to the Himalaya (5 km altitude plateau, 10^6 km^2) at several latitudes (0°N, 30°N, 45°N, 60°N, 90°N). We find that CO_2 permanent condensation can occur on top of the mountain range for distances lower than 1.27 AU, only for latitudes greater than

[5] We remind the reader that volatile delivery to a planet is stochastic in nature and may be a weak function of planetary mass. By way of comparison, Venus (at $\sim$ 0.8 $M_{\rm Earth}$) has $\sim$ 3 bar of N_2 in its atmosphere.

45°N. For the 60°N latitude case, CO_2 condensation starts as low as 1.20 AU (Flux $\sim$ 949 W m^{-2}, $S_{eff} \sim 0.69$).

Nonetheless, the total amount of CO_2 that could condense and be trapped above a mountain range is rather low, because it is limited by the area of the mountain range.

2.6 How much CO_2 ice can be trapped?

In this section, we investigate two processes that should control the amount of CO_2 that can be trapped on the surface or subsurface: 1) flows of polar CO_2 ice to lower latitudes and sublimation; and 2) burial of CO_2 ice beneath the water ice cover due to higher density.

2.6.1 Maximum size of CO_2 ice glaciers

At first sight, the main limit of the trapping of CO_2 as ice instead of greenhouse gas is the size of the solid CO_2 polar reservoirs. When CO_2 is outgassed by volcanoes, the atmospheric pressure stays constant but the size of the CO_2 polar caps grows. At some point, the CO_2 ice caps form glaciers that can flow efficiently toward equatorial regions, CO_2 ice being much less viscous than water ice. In the process, CO_2 ice can be sublimated and reinjected in the atmosphere.

In this section, we give estimates of the maximum amount of CO_2 that can be trapped in steady state CO_2 ice polar caps, for a planet with a 23.5° obliquity, radiatively inactive CO_2 ice clouds, located at a distance of 1.30 AU (F = 808 W m^{-2}) and for both CO_2 and N_2 partial pressures set to 1 bar.

2.6.1.1 CO_2 ice caps radial extent

First, we get from our GCM simulations the radial extent of the two permanent CO_2 ice polar caps, defined for a positive annual mean CO_2 condensation rate. We note the corresponding radius of the ice cap $R_{cap,1}$. Then, in GCM simulations, we artificially extend (in the radial direction) the CO_2 ice caps to take into account the glacier flow, until the net globally averaged annual condensation/sublimation rate vanishes. In practice, we used the following algorithm:

1. We run the simulation until globally averaged annual mean rate of condensation/sublimation is constant.
2. If this rate is (roughly) null, CO_2 ice caps are in a dynamical equilibrium. We stop here.
3. If this rate is positive, we artificially increase the size of the CO_2 ice caps of one GCM grid (in the latitudinal direction, and for each longitude) by emplacing arbitrarily a large enough amount of CO_2 ice. We go back to step 1.

This method gives us a good estimate of the steady state maximal extent of the CO_2 ice polar caps. We note the corresponding radius of the ice cap $R_{cap,2}$. With and without glacier flow, we obtain polar cap radii $R_{cap,1}$ = 2070 km and $R_{cap,2}$ = 2800 km. This corresponds to a latitudinal extent down to 71.5°N and 65°N [6], respectively. Figure 2.4 shows zonal condensation/sublimation annual mean rates along the North Pole CO_2 glacier.

[6] By symmetry, results are identical in the southern hemisphere.

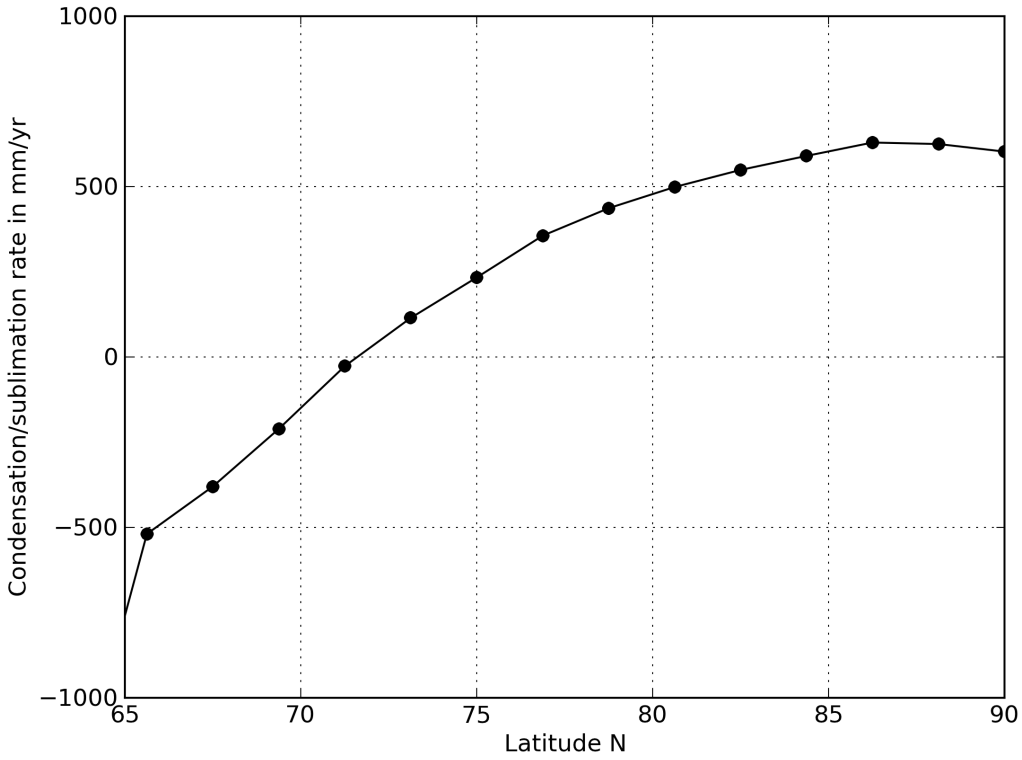

Figure 2.4: Zonal and annual mean CO_2 condensation/sublimation rates along the CO_2 northern ice cap, for the reference case (1.30 AU equivalent distance, 23.5° obliquity and radiatively inactive CO_2 ice clouds). It corresponds also to the a(r) function (see section 2.6.1.3). Positive values correspond to latitudes where the annual mean CO_2 condensation rate is positive. These are locations where CO_2 condenses permanently. Negative values are "potential" sublimation rates, i.e. it is assumed that CO_2 ice is available – following the algorithm described in section 2.6.1.1 – and can sublime all year long.

In total, the two CO_2 ice caps have an area of 27 millions of km^2 (respectively 49 millions of km^2 if considering the glacier flow). This corresponds to 5% (respectively 10%) of the total area of the (Earth-like) planet.

2.6.1.2 CO_2 ice cap inner region: a thickness limited by basal melting

In the region within the CO_2 ice caps with positive annual mean condensation rates, the CO_2 ice maximum thickness should be mainly limited by basal melting induced by the geothermal heat flux, noted F_{geo}.

Assuming that the temperature inside the CO_2 glacier rises linearly with depth, with a lapse rate fixed by the geothermal heat flux (conductive regime), the maximum CO_2 ice thickness h_{max} is given by:

$$h_{max} = \frac{\lambda_{CO_2} (T_{melt} - T_{surf})}{F_{geo}}, \tag{2.1}$$

where λ_{CO_2} is the thermal conductivity of CO_2 ice, T_{surf} is the temperature at the top of the glacier and T_{melt} is the melting temperature of CO_2 ice at the base of the glacier. As the latter is a function of the pressure below the CO_2 glacier, it implicitly depends on h_{max} so that the above equation must be solved numerically, once the local surface temperature is known (see Appendix 2.8.2 for details on the calculations). The resulting maximum CO_2 ice cap thickness h_{max} is plotted on Figure 2.5 as a function of the internal heat flux and the CO_2 partial pressure. For geothermal heat fluxes of 100/30/10 mW m^{-2} (red stars in Figure 2.5), basal melting condition gives CO_2 ice maximum thicknesses of 120/360/1200 m.

The exact latitude at which the glacier maximum thickness is determined by either basal melting condition or by glacier flow is difficult to determine. Moreover, in the region of transition between these two regimes, a basal liquid CO_2 flow could persist[7] and therefore speed up the glacier flow.

For simplicity, we fixed the thickness of the steady-state CO_2 glacier in the regions with positive annual mean condensation rate (regions of latitude $> 71.5°N$; see Figure 2.4) at the constant maximum thickness h_{max} derived from the basal melting condition. This maximum thickness serves as a boundary condition for the calculation of the glacier flow in regions with positive annual mean sublimation rate (see next section).

2.6.1.3 CO_2 ice cap outer region: a thickness limited by glacier flow and sublimation

To get estimates of CO_2 glacier profiles in the regions where sublimation dominates over condensation (latitude $< 71.5°N$, see Figure 2.4), we use a simple isothermal glacier model [8] (assuming no slip at the base of the glacier), following a similar approach than Menou (2013). The steady-state equation satisfied by a thin isothermal CO_2 glacier with a flat base and a no slip boundary condition at its bottom is (Fowler, 2011; Cuffey and Paterson, 2010)[9]:

$$\frac{1}{r}\frac{\partial}{\partial r}\left(r \, \frac{2A_0(\rho g)^n}{n+2} \, h^{n+2} \, | \frac{\partial h}{\partial r} |^{n-1} \, \frac{\partial h}{\partial r} \right) + a(r) = 0, \tag{2.2}$$

[7] Such basal flow could carry heat away from basal melting regions and thus also reduce the heat flux conducted through the CO_2 ice caps (Cuffey and Paterson, 2010; Menou, 2013).

[8] This is a simple approach that does not physically describe how the accumulating CO_2 ice spreads to feed the ablation zone. We acknowledge that a more physically complete model should be developed in the future.

[9] This is the classic solution for a glacier shape.

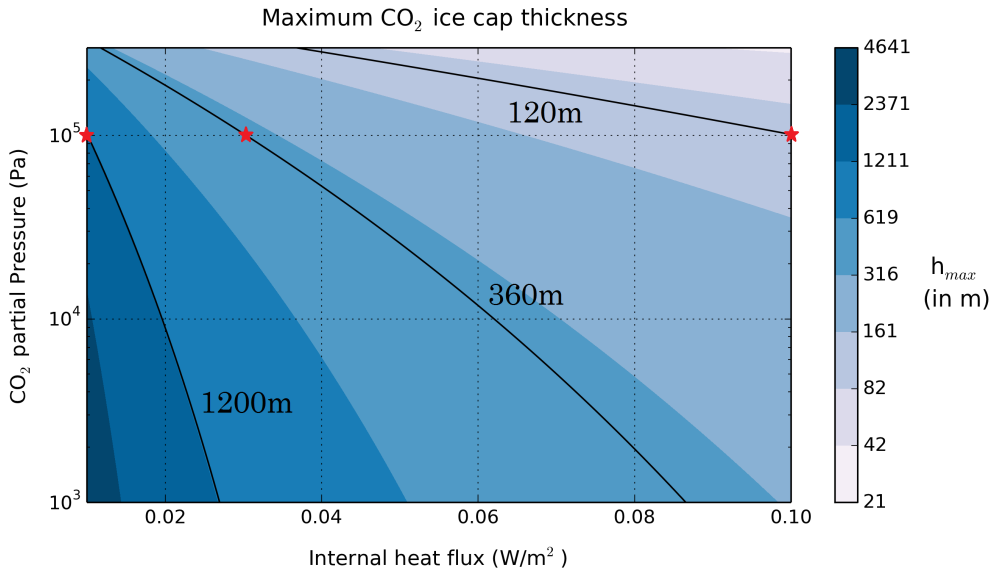

Figure 2.5: CO_2 ice cap maximum thickness (in m) calculated from the basal melting condition, as a function of surface CO_2 partial pressure and internal heat flux. The red stars correspond to three distinct cases, with pCO_2 = 1bar and F_{geo} = 10 / 30 / 100 mW m^{-2}, that are investigated in more details in the following sections.

with $h(r)$ the thickness of the CO_2 ice cap, assumed (for simplicity) radially symmetric, A_0 the flow rate constant (in Pa s^{-n}), n the power-law creep exponent, g the surface gravity, ρ the density of CO_2 ice and a(r) the annual mean condensation rate assumed (also for simplicity) to be a function of r only, and derived from our GCM simulations (see Figure 2.4).

First, assuming $\frac{\partial h}{\partial r} = 0$ for $r = R_{\mathrm{cap},1}$, we integrate equation 2.2 once. Then, assuming $h > 0$, $\frac{\partial h}{\partial r} < 0$ and $a(r) < 0$, we separate the variables h and r, and we integrate a second time, assuming $h(R_{\mathrm{cap},2}) = 0$ at the edge of the glacier. Eventually, assuming that $h(R_{\mathrm{cap},1}) = h_{\mathrm{max}}$, with h_{max} the maximum thickness of the glacier calculated using the basal melting condition, we can constrain the flow rate A_0 and get the following solutions for the thickness h of the CO_2 ice glacier:

$$h(r) = h_{\mathrm{max}} \text{ for } r \leqslant R_{\mathrm{cap},1}, \tag{2.3}$$

$$h(r) = h_{\mathrm{max}} \left(\frac{\int_r^{R_{\mathrm{cap},2}} \left(-\frac{1}{r_2} \int_{R_{\mathrm{cap},1}}^{r_2} r_1 \, a(r_1) \, dr_1 \right)^{\frac{1}{n}} dr_2}{\int_{R_{\mathrm{cap},1}}^{R_{\mathrm{cap},2}} \left(-\frac{1}{r_2} \int_{R_{\mathrm{cap},1}}^{r_2} r_1 \, a(r_1) \, dr_1 \right)^{\frac{1}{n}} dr_2} \right)^{\frac{n}{2n+2}} \text{ for } r > R_{\mathrm{cap},1}, \tag{2.4}$$

Figure 2.6 presents 9 possible steady-state CO_2 ice glacier profiles, for 3 different geothermal fluxes and 3 different flow laws (n = 1, 4.5 and 7) chosen consistent with previous experimental studies (Durham et al., 1999) and works about the martian CO_2 southern polar cap (Nye et al., 2000).

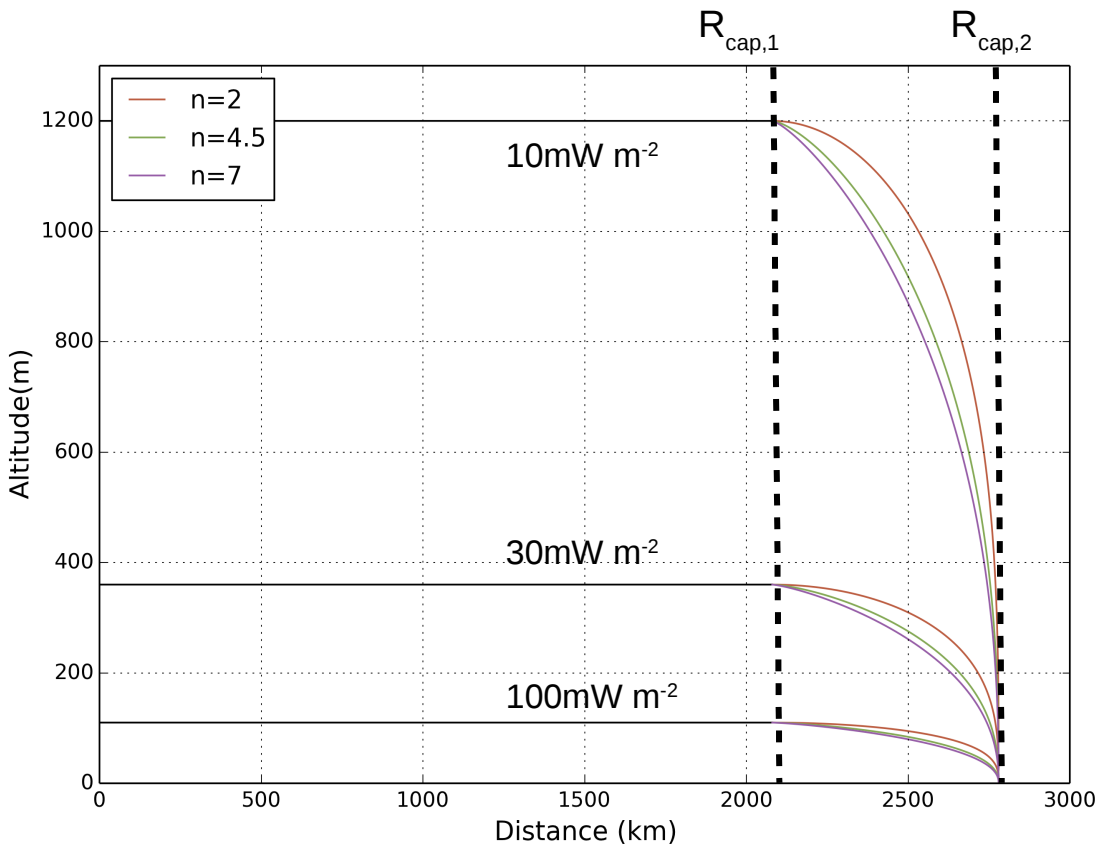

Figure 2.6: Possible radial profiles for the CO_2 ice polar glaciers. They correspond to solutions of equations 2.3 and 2.4, for 3 different internal heat fluxes (10/30/100 mW m^{-2}) and three different flow laws (n = 1, 4.5 and 7).

2.6.1.4 Calculation of the CO_2 maximum total reservoir

After integration of the steady state CO_2 ice radial profiles, we find that the maximum amount of CO_2 ice that can be stored in the two polar caps is approximately equal to 1.5/4.5/15 bar[10] for geothermal heat fluxes of 100/30/10 mW m^{-2}, respectively. On Earth, the current geothermal heat flux is $\sim$ 80 mW m^{-2} but can varies a lot, typically from 20 mW m^{-2} up to 400 mW m^{-2}, depending on the regions (Davies, 2013). Approximately 60% (respectively 40%) of CO_2 ice is trapped in region of $r < R_{cap,1}$ (respectively $r > R_{cap,1}$), meaning that the accumulation zone and the ablation zone contribute significantly and equally to the total size of the CO_2 ice reservoir.

It is now possible to calculate, for a given rate of CO_2 volcanic outgassing, the time required for a hard snowball planet to fill the CO_2 ice polar reservoirs and thus potentially escape glaciation. Assuming a present-day Earth CO_2 volcanic outgassing rate of $\sim$ 7 teramoles/year or 60 bar/Gy (Brantley and Koepenick, 1995; Jarrard, 2003), we get durations of glaciation periods of $\sim$ 42/93/270 My for internal heat fluxes of 100/30/10 mW m^{-2}. In fact, because CO_2 volcanic outgassing rate is dependant on the internal heat flux, the duration of the glaciation phases could be drastically increased for planets with low geothermal heat fluxes (typically lower than 80 mW m^{-2} as on present-day Earth). This suggests that planets near the outer edge of the habitable zone may need to be quite volcanically active in order to remain habitable.

When (and if) CO_2 ice caps become full, the system suddenly reaches a runaway phase, ending up with the complete vaporization of CO_2 polar ice caps and thus a hot atmosphere. This may have implications in the calculation and description of 'limit-cycles' (Menou, 2015; Haqq-Misra et al., 2016; Abbot, 2016) and more generally on the habitability of distant Earth-like planets. Detailed calculations of the stability of CO_2 ice caps when full can be found in Appendix 2.8.3.

It is also conceivable that catastrophic events such as meteoritic impacts could trigger deglaciation.

2.6.2 Gravitational stability and CO_2 sequestration

For planets covered by several hundred meters of water ice[11], owing to the high density of CO_2 ice ($\sim$1500 kg m^{-3}) or liquids ($\sim$1170 kg m^{-3}) compared to water ice ($\sim$930 kg m^{-3} at 200-220 K), the CO_2 deposits should rapidly become gravitationally unstable. This would result in a burial of the CO_2 deposits at the base of the H_2O ice layer. Such a density contrast should initiate Rayleigh-Taylor instabilities at a timescale that can be estimated at first order assuming two isoviscous layers using the following relationship (Turcotte and Schubert, 2001):

$$\tau_{RT} = \frac{13\ \eta}{\Delta\rho g b}, \tag{2.5}$$

with η the viscosity of the more viscous layer, $\Delta\rho$ the density contrast between the two layers and b the characteristic size of the domain. Depending whether CO_2 is liquid or solid at the interface with the H_2O layer, the density contrast would range between 240 and 570 kg m^{-3}. For a CO_2 ice deposit thickness of about 100 m, this density contrast results in a stress at the interface between the two layers of the order of 1 MPa. For such a stress level and temperature ranging between 200 and 220 K, the viscosity of the CO_2 ice layer is estimated between 10^{12}-10^{13} Pa s, based on available experimental data (Durham et al., 1999). At the same temperature and stress conditions, water ice has a viscosity $\leq$

[10] These quantities are not affected much by the choice of flow law (see Figure 2.6).

[11] We remind here that the Earth Global Equivalent Layer of surface water is $\sim$ 3km.

10^{16} Pa s, for grain size lower than 1 mm, based on experimental data (Durham et al., 2001; Durham and Stern, 2001; Goldsby and Kohlstedt, 2001). Therefore, this would be the layer controlling the Rayleigh-Taylor timescale. Assuming that a thickness of 100 m of CO_2 deposit is representative of the characteristics size of the domain, the R-T timescale is 7×10^3 yrs $\times$ ($\eta/10^{16}$ Pa s), which is geologically short. In the case of basal melting of the CO_2 layer, we should keep in mind that the generated CO_2 liquids will be unstable relative to the underneath water ice layer, but also relative to the overlying CO_2 ice layer as it has a density intermediate between those of CO_2 ice and water ice. When CO_2 melting occurs at the base of the CO_2 layers, a competition is expected between downward drainage through the water ice layer (similar to crevasse hydrofracturing in Earth glaciers; Krawczynski et al. 2009) and liquid injection in the overlying CO_2 ice layer and refreezing (similar to dike propagation). Assessing in details such complex processes are out of scope of the present paper. Nevertheless, based on these considerations, we can safely argue that the accumulation of a large volume of liquid CO_2 at the base of the CO_2 ice layer is unlikely.

Once gravitationally destabilized, the CO_2 ice deposit would sink at the base of the water ice shell at a rate that is determined mostly by the viscosity of water ice and the size of the CO_2 ice diapir. The time required for a CO_2 ice diapir to cross the water ice layer can be estimated using the Stokes velocity, the terminal velocity of a sphere falling through a constant viscosity medium (Ziethe and Spohn, 2007):

$$U_s = \frac{2}{9}\,\Delta\rho g\,(r^2/\eta) \tag{2.6}$$

For a diapir radius r of 100 m (comparable to thickness of the CO_2 deposit) and a viscosity of water ice of 10^{15}-10^{16} Pa s, this leads to a velocity of 0.04-0.4 m/yr. As temperature increases as a function of depth, the viscosity of water ice is expected to decrease with depth, resulting in an acceleration of the diapir fall. A 100-m diapir of CO_2 ice would thus not need more than $\sim 10^4$ yrs to reach the bottom of a 1-km thick water ice layer.

Even if the CO_2-H_2O interface is beneath the melting temperature of CO_2 ice, melting may occur during the diapir fall, which will reduce the density contrast and hence the fall velocity. However, as mentioned above, melting may promote fracturing of the water ice medium and rapid drainage of the CO_2 liquids due to its high density relative to the surrounding water ice. The rate of melting should also depend on the efficiency of heat transfer between the diapir and the surrounding ice. As the thermal diffusive timescale ($\sim r^2/\kappa$) for a 100-m-size diapir of CO_2 is of the order of 10^3 yrs and is thus $\leq$ to the expected diapir fall timescale, melting during the descent would be efficient. Detailed modelling would be required though to determine the exact volume of generated melt during descent.

CO_2 ice should completely melt and equilibrate thermally with the surrounding H_2O media once stabilized at the bottom of the water ice shell. The temperature and pressure conditions at the bottom of the water ice layer depend on its thickness and on the geothermal flow. For geothermal heat flux between 50 and 100 mW $^{-2}$, typical of the Earth, the melting of water ice would be reached for depth ranging between 1.5 and 3 km, corresponding to pressure of about 14 and 28 MPa. This pressure range is well above the saturation vapor pressure (3.5 MPa at 273 K; Lide 2004), so that CO_2 is highly stable in the liquid phase. Destabilizing the CO_2 liquids into gas phase would require the 273 K-isotherm at a depth of only 375 m, corresponding to abnormally high geothermal heat flux of 400 mW $^{-2}$, 5 times larger than the average heat flux on Earth. Even if the density of liquid CO_2 decreases with increasing temperature as it equilibrates with the surrounding water ice media, it remains always denser than water ice (Span and Wagner, 1996), and therefore should always accumulate at the bottom of the ice

shell. At T = 273 K and pressure between 14 and 28 MPa, CO_2 liquids have a density very close to that of liquid water (994 and 1048 kg m^{-3}, respectively, using the equation of state of Span and Wagner 1996), so that CO_2 coexists with H_2O at the ice-water interface.

Pressure and temperature conditions expected at the bottom of the ice layer are in the stability field of CO_2 clathrate hydrate (Sloan, 1998; Longhi, 2005), therefore CO_2 should rapidly interact with H_2O molecules to form clathrate hydrate. Clathrate hydrates are non-stoichiometric compounds consisting of hydrogen-bonded H_2O molecules forming cage-like structures in which guest gas molecules, such as CO_2, can be trapped (Sloan, 1998). Once formed, these clathrates are very stable and can be dissociated only if the temperature is raised about 5-10 K above the melting point of water ice. The storage of CO_2 in the form of clathrate should be particularly efficient in the case of warm bottom conditions as CO_2 liquids and liquid water coexist. In the cold bottom condition with no water ice melting, clathration is still possible but would be less efficient due to the physical separation between the two components. As CO_2 clathrate hydrate has a density of about 1150 kg m^{-3} (assuming full cage occupancy, Sloan 1998), they would rapidly sink at the bottom of the water liquid layer, ensuring an almost complete clathration of CO_2. Part of the CO_2 should dissolve in the liquid water during the clathrate sinking. The relative proportion of CO_2 trapped in the form of clathrate hydrate or dissolved in the water layer would depend on the volume of CO_2 that is buried at the base of the ice shell and on the volume (thickness) of the water layer.

In summary, as long as the water ice shell exceeds a few hundred meters, CO_2 should remain sequestered either in the form of CO_2 liquids, in the form of CO_2 clathrate hydrate or dissolved in the subglacial water layer. Release of gaseous CO_2 may occur only due to an increase of surface insulation and increase of geothermal flux resulting in a significant thinning and breaking-up of the water ice shell. The total amount of CO_2 that can be stored in the H_2O layer (by any of these three processes) depends on the total abundance of H_2O of the planet as well as CO_2/H_2O ratio. The CO_2 inventory on Earth, mostly in the form of carbonate rocks on the continents, is of the order of 10^2 bar (Walker, 1985). If the total CO_2 inventory exceeds the total amount of CO_2 that can be stored in the water layer, then the planet should be able at some point to escape from global glaciation, extra CO_2 being likely returned to the atmosphere through cryovolcanism.

Evaluating the maximum amount of CO_2 that can be trapped underneath the water ice cover require however a detailed description of the H_2O layer structure as well as thermodynamic models predicting the partitionning of CO_2 between the different phases.

2.7 Conclusions

We highlight in this paper a new scenario that would prevent distant Earth-like planets orbiting Sun-like stars from escaping episodes of complete glaciation. When a terrestrial planet reaches a Snowball state, CO_2 weathering ceases and CO_2 can accumulate in the atmosphere because of volcanic outgassing. As CO_2 builds up in the atmosphere, the temperature of condensation of CO_2 can exceed the surface temperature of the poles, which leads to the trapping of all extra CO_2 possibly outgassed.

Using LMD Global Climate Model simulations designed for Earth-like fully glaciated planets, we show that this mechanism can work from orbital distances as low as 1.27 AU (Flux $\sim$ 847 W m^{-2}, $S_{eff} \sim 0.62$). By comparison, the most recent estimate of the outer edge of the Habitable Zone (e.g. the maximum greenhouse limit) in similar conditions is 1.67 AU (Flux $\sim$ 490 W m^{-2}, $S_{eff} \sim 0.36$)

(Kopparapu et al., 2013).

This limit can occur at even lower distances for planets with 1) a low obliquity, 2) a low N_2 partial pressure, 3) a high rotation rate and 4) a high value of the water ice albedo (we chose in this work the conservative value of 0.6).

Conversely, this limit can occur at significantly higher distances when taking into account the radiative effect of CO_2 ice clouds. In winter, CO_2 ice clouds that form at the cold poles scatter back thermal infrared radiation of the surface. In summer, clouds are dissipated and therefore have almost no impact on the bond albedo. For these two reasons, CO_2 ice clouds can have a powerful warming effect at the poles, limiting CO_2 collapse at orbital distances greater than 1.40 AU (Flux < 697 W m^{-2}, $S_{eff} < 0.51$).

For each possible configuration, the amount of CO_2 that can be trapped in polar CO_2 ice caps depends on the efficiency of CO_2 ice to flow laterally as well as its graviational stability relative to subsurface water ice. The flow of CO_2 ice from polar to low latitudes regions is mostly controlled by its basal temperature (due to both the conductivity and melting temperature of CO_2 ice being low), and hence by the internal heat flux of the planet. We find for example that a frozen Earth-like planet located at 1.30 AU of a Sun-like star could store as much as the equivalent of 1.5/4.5/15 bar of CO_2 ice at the poles, for internal heat fluxes of 100/30/10 mW m^{-2}.

But these amounts are in fact lower limits. CO_2 ice being denser than water ice ($\sim 1.7 \times$ the volumetric mass of water ice), we find that CO_2 ice deposits should be gravitationally unstable and get buried beneath the water ice cover in a geologically short timescale of $\sim 10^4$ yrs, mainly controlled by the viscosity of water ice. If water ice cover exceeds about 300 meters (e.g. 10% of the Earth hydrosphere), then CO_2 should be permanently sequestered underneath the water ice cover, in the form of CO_2 liquids, CO_2 clathrate hydrates and/or dissolved in subglacial water reservoirs (if any). This would considerably increase the amount of CO_2 trapped and further reduce the probability of deglaciation.

2.8 Appendix

2.8.1 The LMD Generic Global Climate Model

2.8.1.1 Model core

This model originally derives from the LMDz 3-dimensions Earth Global Climate Model (Hourdin et al., 2006), which solves the primitive equations of geophysical fluid dynamics using a finite difference dynamical core on an Arakawa C grid.

The same model has been used to study many different planetary atmospheres of low-irradiated planets, including Archean Earth (Charnay et al., 2013), past climates of Mars (Forget et al., 2013; Wordsworth et al., 2013; Turbet et al., 2017a), or exoplanets (Wordsworth et al., 2011; Turbet et al., 2016, 2018a).

The simulations presented in this paper were all performed at a horizonal resolution of 96 × 96 (e.g. 3.75° × 1.875°) in longitude × latitude. In the vertical direction, the model is composed of 15 distinct atmospheric layers that were designed using hybrid σ coordinates (where σ is the ratio between pressure and surface pressure).

To account for thermal conduction in the icy ground, we used a 18-layers thermal diffusion soil model. Mid-layers depths range from $d_0 \sim 0.1$ mm to $d_{17} \sim 18$ m, following the power law $d_n = d_0 \times 2^n$ with n being the corresponding soil level, chosen to take into account both diurnal and seasonal thermal waves. We assumed thermal inertia of the ground ice to be constant and equal to 2000 J m^{-2} $s^{-1/2}$ K^{-1}.

We considered (in GCM simulations) the internal heat flux and/or the thermal heat flux F_{ground} conducted from an hypothetical underlying ocean to be zero[12].

2.8.1.2 Radiative Transfer

The GCM includes a generalized radiative transfer for a variable gaseous atmospheric composition made of a mix of CO_2, N_2 and H_2O (HITRAN 2012 database, Rothman et al. (2013)) using the correlated-k method (Fu and Liou, 1992; Eymet et al., 2016)) suited for fast calculation. For this, we decomposed atmospheric temperatures, pressures, and water vapor mixing ratio into the following respective 7 x 8 x 8 grid, similar to Charnay et al. (2013): Temperatures = {100,150, .. ,350,400} K ; Pressures = {10^{-6},10^{-5}, .. ,1,10} bar ; H_2O Mixing Ratio = {10^{-7},10^{-6}, .. ,10^{-2},10^{-1}} mol of H_2O / mol of air (H_2O+CO_2 here).

CO_2 collision-induced absorptions (CIA) and dimer absorption (Wordsworth et al., 2010a)) were included in our calculations as in Forget et al. (2013) and Wordsworth et al. (2013), as well as N_2-N_2 collision-induced absorption (Richard et al., 2012) and its role on the pressure broadening. We also added H_2O self and foreign continuums calculated with the CKD model (Clough et al., 2005), with H_2O lines truncated at 25 cm^{-1}.

For the computation, we used 32 spectral bands in the thermal infrared and 36 in the visible domain. 16 non-regularly spaced grid points were used for the g-space integration, where g is the cumulated distribution function of the absorption data for each band. We used a two-stream scheme (Toon et al., 1989) to take into account radiative effects of aerosols (CO_2 ice and H_2O clouds) and Rayleigh scattering (mostly by N_2 and CO_2 molecules), using the method of Hansen and Travis (1974).

[12] This is a reliable assumption for thick enough (typically > 100 m) water ice covers expected on hard Snowball Earth-like planets.

Physical parameters	Values
H_2O ice Albedo	0.6
H_2O ice thermal conductivity	2.5 W m^{-1} K^{-1}
H_2O ice emissivity	1.0
Ground H_2O ice thermal inertia	2000 J m^{-2} $s^{-1/2}$ K^{-1}
CO_2 ice Albedo	0.6
CO_2 ice thermal conductivity	0.5 W m^{-1} K^{-1}
CO_2 ice emissivity	0.9
CO_2 ice density	1.5
Surface Topography	Flat
Surface roughness coefficient	0.01 m

Table 2.2: Physical Parameterizations used for the GCM calculations.

We note that, for the calculation of absorption coefficients, we used only main isotopes: $^{12}C^{16}O_2$ and $^{1}H_2{}^{16}O$ and $^{12}N_2$. It has been shown in similar conditions (Halevy et al., 2009) that the radiative effect of isotopic composition should be small. Nonetheless, we take this opportunity to encourage dedicated studies about the influence of isotopic composition on the radiative properties of (thick) atmospheres.

2.8.1.3 H_2O and CO_2 physical properties

Both CO_2 and H_2O cycles are included in the GCM used in this work.

1. Melting, freezing, condensation, evaporation, sublimation and precipitation of H_2O physical processes are all included in the model. In the atmosphere, water vapor can condense into water ice particles clouds. At the surface, we fix the H_2O ice albedo at 0.6[13] and we use an emissivity of 1.

2. In our model, CO_2 can condense to form CO_2 ice clouds and surface frost if the temperature drops below the saturation temperature. Atmospheric CO_2 ice particles are sedimented and thus can accumulate at the surface. The CO_2 ice layer formed at the surface can sublimate and recycle the CO_2 in the atmosphere. The CO_2 ice on the surface contributes to the surface albedo calculation: if the CO_2 ice layer exceeds a threshold value of 1 mm thickness, then the local surface albedo is set immediately to the albedo of CO_2 ice (0.6 in this work). On Mars, the albedo of CO_2 ice can substantially vary (Kieffer et al., 2000) with insolation and presence of dust. Without dust, the albedo

[13] This is the standard value used in the Snowball Model Intercomparison (SNOWMIP) project (Pierrehumbert et al., 2011).

can become very high so that 0.6 is probably a lower estimate. For CO_2 ice, we use an emissivity of 0.9. The radiative effect of CO_2 ice clouds is discussed in details in section 2.5.3.

Physical parameters used for both CO_2 and H_2O ices are summarized in table 2.2.

2.8.2 Computation of maximal CO_2 ice thickness before basal melting

Compared to water ice, the temperature dependence of CO_2 ice thermal conductivity is rather flat in the 100-250 K range (Schmitt et al. 1997; Part I, Figure 4). We can thus estimate with a good approximation the maximum CO_2 ice thickness $h_{\max}$ (limited by basal melting) by:

$$h_{\max} = \frac{\lambda_{CO_2} \, (T_{\rm melt} - T_{\rm surf})}{F_{\rm geo}}, \tag{2.7}$$

where λ_{CO_2} is the thermal conductivity of CO_2 ice, $T_{\rm surf}$ is the temperature at the top of the glacier and $T_{\rm melt}$ is the melting temperature of CO_2 ice at the base of the glacier.

We derive then $T_{\rm melt}$ using the Clausius-Clapeyron relation (CO_2 solid-liquid equilibrium) at the base of the glacier:

$$T_{\rm melt} = T_{\rm ref} \, e^{\frac{(\frac{1}{\rho_{\rm liq}} - \frac{1}{\rho_{\rm sol}})}{L_{\rm fus}} \, (g \rho_{\rm sol} h_{\max} + P_{CO_2} + P_{N_2} - P_{\rm ref})}, \tag{2.8}$$

with $\rho_{\rm sol}$ and $\rho_{\rm liq}$ the volumetric mass of liquid and solid CO_2, $L_{\rm fus}$ the latent heat of fusion of CO_2 ice, $P_{\rm ref}$ and $T_{\rm ref}$ the coordinates of the triple point of CO_2, and P_{CO_2} and P_{N_2} the partial surface pressures of CO_2 and N_2, respectively. The pressure at the base of the glacier $P_{\rm melt}$ is estimated from the equation $h_{\max} = \frac{(P_{\rm melt} - P_{\rm surf})}{g \ \rho_{\rm sol}}$, with $P_{\rm surf} = P_{CO_2} + P_{N_2}$. We remind that we choose $pN_2 = 1$ bar for all our simulations.

We now derive the surface temperature $T_{\rm surf}$ as a function of the surface pressure $P_{\rm surf}$, using another Clausius-Clapeyron relation (CO_2 solid-gas equilibrium):

$$T_{\rm surf} = \frac{1}{\frac{1}{T_{\rm ref}} - \frac{R}{L_{\rm sub} \ M_{CO_2}} \ \ln(\frac{P_{CO_2}}{P_{\rm ref}})}, \tag{2.9}$$

with $L_{\rm sub}$ the latent heat of sublimation of CO_2 ice and M_{CO_2} the molar mass of CO_2. It is in fact assumed here that the global mean temperature at the top of the CO_2 polar ice caps is constant and equal to the temperature of condensation of CO_2. This approximation should remain valid as soon as there is enough CO_2 in the atmosphere (or CO_2 stays a dominant atmospheric species).

From the set of equations 2.7-2.9, we get a new equation on $h_{\max}$ of the form $h_{\max} = e^{h_{\max}}$, after several variable changes. We solve explicitely this equation using the lambert W function, and we obtain the following expression of the maximum possible CO_2 ice cap thickness $h_{\max}$:

$$\begin{cases} h_{\max} = \frac{\lambda_{CO_2}}{F_{\rm geo}} \left(\frac{1}{\frac{1}{T_{\rm ref}} - \frac{R}{L_{\rm sub} \ M_{CO_2}} \ \ln(\frac{P_{\rm surf}}{P_{\rm ref}})} \right) \\ \quad - \frac{L_{\rm fus}}{(\frac{1}{\rho_{\rm liq}} - \frac{1}{\rho_{\rm sol}}) \ g \rho_{CO_2}} \times W \left(\frac{-(\frac{1}{\rho_{\rm liq}} - \frac{1}{\rho_{\rm sol}}) \ g \rho_{CO_2} \ \lambda_{CO_2} \ T_{\rm ref} \ e^{\frac{(\frac{1}{\rho_{\rm liq}} - \frac{1}{\rho_{\rm sol}})}{L_{\rm fus}} \ (P_{\rm surf} - P_{\rm ref})}}{L_{\rm fus} \ F_{\rm geo}} \right. \\ \quad \left. \times \ e^{\frac{(\frac{1}{\rho_{\rm liq}} - \frac{1}{\rho_{\rm sol}}) \ g \rho_{CO_2} \frac{\lambda_{CO_2}}{F_{\rm geo}}}{L_{\rm fus}} \left(\frac{1}{\frac{1}{T_{\rm ref}} - \frac{R}{L_{\rm sub} \ M_{CO_2}} \ \ln(\frac{P_{\rm surf}}{P_{\rm ref}})} \right)} \right) \end{cases} \tag{2.10}$$

This equation is used to directly compute $h_{\max}$ as a function of the internal heat flux and CO_2 partial pressure (see Figure 2.5).

Note that we assumed a CO_2 ice volumetric mass density of 1500 kg m^{-3} and a CO_2 ice thermal conductivity of 0.5 W m^{-1} K^{-1} (Schmitt et al. 1997; Part I, Figure 4).

2.8.3 Stability of CO_2 ice caps

What happens once CO_2 ice caps have reached their maximum size, as calculated in section 2.6.1.4? Using calculations, we show in this appendix that, depending on a few parameters, the CO_2 ice caps when full may (or may not) be stable.

The total mass of CO_2 available at the surface and in the atmosphere is:

$$M_{\rm tot} = M_{\rm atm} + M_{\rm surf} = \frac{S P_{CO_2}}{g} + A h_{\rm mean} \rho_{CO_2}, \tag{2.11}$$

with A the area of the CO_2 ice caps, S the total area of the surface (i.e. $4\pi R_p^2$) and $h_{\rm mean}$ the thickness of the CO_2 ice caps averaged over A. When CO_2 ice caps are full, $h_{\rm mean} = h^{\max}_{\rm mean}$.

We assume now that the system – initially with full CO_2 ice caps – is slightly perturbated from $P_{CO_2} = P$ to $P + \delta P$. By conservation of CO_2 mass, the new mass of CO_2 ice caps is $M_{\rm surf}[P + \delta P] = \rho_{CO_2}\ A h_{\rm mean}[P + \delta P]$[14].

If this quantity is lower than the maximum mass of CO_2 ice caps, e.g. $\rho_{CO_2}\ A h^{\max}_{\rm mean}[P + \delta P]$, then the system is stable. Otherwise, the condition of unstability can be written formally:

$$\rho_{CO_2}\ A h_{\rm mean}[P + \delta P] > \rho_{CO_2}\ A h^{\max}_{\rm mean}[P + \delta P], \tag{2.12}$$

which can be rewritten, using mass conservation:

$$M_{\rm tot} - \frac{S\ [P + \delta P]}{g} > \rho_{CO_2}\ A h^{\max}_{\rm mean}[P + \delta P], \tag{2.13}$$

and using Taylor series:

$$M_{\rm tot} - \frac{S\ P}{g} - \frac{S\ \delta P}{g} > \rho_{CO_2}\ A h^{\max}_{\rm mean}[P] + \delta P\ \rho_{CO_2}\ \frac{d(A h^{\max}_{\rm mean})}{dP_{CO_2}}[P]. \tag{2.14}$$

Assuming that CO_2 ice caps were initially full, this yields to $h_{\rm mean}[P] = h^{\max}_{\rm mean}[P]$ and gives:

$$\left(M_{\rm tot} - \frac{S\ P}{g} - \rho_{CO_2}\ A h_{\rm mean}[P]\right) - \frac{S\ \delta P}{g} > \delta P\ \rho_{CO_2}\ \frac{d(A h^{\max}_{\rm mean})}{dP_{CO_2}}[P]. \tag{2.15}$$

For $\delta P > 0$, we have then:

$$A\ \frac{dh^{\max}_{\rm mean}}{dP_{CO_2}}[P] + h^{\max}_{\rm mean}\ \frac{dA}{dP_{CO_2}}[P] < -\frac{S}{\rho_{CO_2}\ g}. \tag{2.16}$$

We know first from GCM simulations that the area of the ice caps A is not a monotonic function of P_{CO_2} (see Figure 2.2). A is in fact extremely rich in information, because it depends on a subtle combination of the greenhouse effect of CO_2, the surface thermal emission, the condensation temperature of CO_2 and the global heat atmospheric redistribution. As P_{CO_2} grows, GCM simulations

[14] Hereafter, '[' and ']' are used to bracket variables.

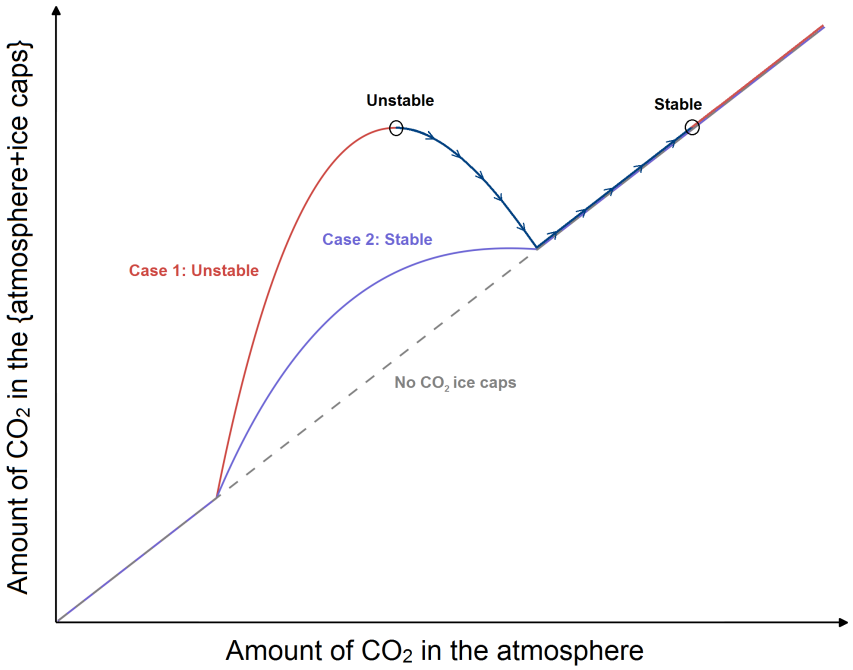

Figure 2.7: Qualitative estimates of the maximum amount of CO_2 in the {surface, atmosphere} as a function of the CO_2 partial pressure, for two different scenarios. In the first scenario (case 1), the CO_2 ice caps when full would be unstable. All the CO_2 ice get sublimed, forming a dense CO_2 atmosphere. In the second scenario (case 2), the CO_2 ice caps when full should progressively shrink as the CO_2 partial pressure increases, but would not be unstable. This configuration occurs when the decrease of the size of the CO_2 ice caps is offset by the increase of the CO_2 atmospheric mass.

tell us that $\frac{dA}{dP_{CO_2}}$ should vary from positive to negative values. Fortunately, we also know from the various GCM simulations shown in Figure 2.2b (23.5° obliquity, radiatively inactive CO_2 clouds) that the maximum of $A(P_{CO_2})$ should for example roughly lie at a CO_2 partial pressure of 1 bar in this specific configuration.

It is possible to derive an analytical - complicated yet - expression of $\frac{dh_{mean}^{max}}{dP_{CO_2}}$ using equations 2.10 and 2.4. It tells us that, whatever the configuration, $\frac{dh_{mean}^{max}}{dP_{CO_2}}$ is always negative. As pCO_2 increases, the temperature at the top of the CO_2 ice caps also increases, which limits the thickness of the CO_2 ice caps[15] (see equation 2.1).

We illustrate now the previous calculations with the experiment extensively described in this work (1.30 AU, 23.5° obliquity, radiatively inactive CO_2 ice clouds, CO_2 partial pressure of 1 bar). Based on GCM simulations, we assume that $\frac{dA}{dP_{CO_2}}|_{pCO_2=1bar} \sim 0$ m^2 Pa^{-1} and we have therefore (with

[15] Equation 2.4 shows that the mean thickness of the CO_2 ice caps is proportional to the maximum thickness calculated by basal melting.

$\frac{A}{S} \sim 0.1$; see section 2.6.1.1):

$$\frac{dh_{\text{mean}}^{\max}}{dP_{CO_2}} < -\frac{S}{gA\rho_{CO_2}} = \frac{-10}{9.81 \times 1.5 \times 10^3} = -7 \times 10^{-4} \text{ m Pa}^{-1}. \quad (2.17)$$

Our calculations indicate that this condition is valid for an internal heat flux roughly lower than 80 mW m^{-2} (case 1 in Figure 2.7). It means that, for an internal heat flux lower than 80 mW m^{-2}: (1) CO_2 ice caps when full would not be stable, and (2) the maximum amount of CO_2 that can be trapped in the {surface, atmosphere} system is attained for pCO_2 lower or equal to 1 bar.

Conversely, for an internal heat flux higher than 80 mW m^{-2} (case 2 in Figure 2.7), CO_2 ice caps when full would be stable (unless $\frac{dA}{dP_{CO_2}}$ term becomes somehow significant).

Chapter 3

Habitability and observability of Proxima Centauri b

Contents

3.1 Preamble

In May 2016, I got a phone call from my colleague Franck Selsis saying: 'Martin, I have great news for you! We have discovered a fantastic extrasolar planet. A planet that is very likely rocky, with a most probable mass of 1.4 times that of the Earth. A planet that is very likely temperate, with an insolation 0.7 times that of the Earth. But the most important fact is ... that this planet is orbiting the closest star from us: Proxima Centauri!!!".

That was it. The race had started. I had three months to explore all the possible climates of this planet, Proxima b, and more importantly, assess its observability with existing and forthcoming telescopes. On Wednesday August 24th 2016, Guillem Anglada-Escude and his colleagues publicly announced the discovery of Proxima b. The same day, I provided the entire scientific community with a complete review of the habitability and observability of the planet.

This chapter is based on a paper published in Astronomy & Astrophysics in December 2016. The full reference is: Martin Turbet, Jeremy Leconte, Franck Selsis, Emeline Bolmont, Francois Forget, Ignasi Ribas, Sean N. Raymond and Guillem Anglada-Escude, **The habitability of Proxima Centauri b. II. Possible climates and observability**, Astronomy & Astrophysics, 2016 (http://adsabs.harvard.edu/abs/2016A%26A...596A.112T).

3.2 Abstract

Radial velocity monitoring has found the signature of a $M \sin i = 1.3$ $M_\oplus$ planet located within the habitable zone (HZ) of Proxima Centauri. Despite a hotter past and an active host star, the planet Proxima b could have retained enough volatiles to sustain surface habitability. Here we use a 3D Global Climate Model (GCM) to simulate the atmosphere and water cycle of Proxima b for its two likely rotation modes (1:1 and 3:2 spin-orbit resonances), while varying the unconstrained surface water inventory and atmospheric greenhouse effect.
Any low-obliquity, low-eccentricity planet within the HZ of its star should be in one of the climate regimes discussed here. We find that a broad range of atmospheric compositions allow surface liquid water. On a tidally locked planet with sufficient surface water inventory, liquid water is always present, at least in the substellar region. With a non-synchronous rotation, this requires a minimum greenhouse warming ($\sim$10 mbar of CO_2 and 1 bar of N_2). If the planet is dryer, $\sim$0.5 bar or 1.5 bar of CO_2 (for asynchronous or synchronous rotation, respectively) suffice to prevent the trapping of any arbitrary, small water inventory into polar or nightside ice caps.
We produce reflection and emission spectra and phase curves for the simulated climates. We find that atmospheric characterization will be possible via direct imaging with forthcoming large telescopes. The angular separation of $7\lambda/D$ at 1 μm (with the E-ELT) and a contrast of $\sim 10^{-7}$ will enable high-resolution spectroscopy and the search for molecular signatures, including H_2O, O_2, and CO_2.
The observation of thermal phase curves can be attempted with the James Webb Space Telescope, thanks to a contrast of 2×10^{-5} at 10 μm. Proxima b will also be an exceptional target for future IR interferometers. Within a decade it will be possible to image Proxima b and possibly determine whether the surface of this exoplanet is habitable.

3.3 Introduction

Proxima Centauri b, recently discovered by Anglada-Escudé et al. (2016), is not only the closest known extrasolar planet but also the closest potentially habitable terrestrial world, located at only ~ 4.2 light years from the Earth (Van Leeuwen, 2007).

Proxima Centauri b, also called Proxima b, receives a stellar flux of ~ 950 W m^{-2} ($0.65-0.7\ S_\oplus$ at 0.05 AU based on the bolometric luminosity from Demory et al., 2009; Boyajian et al., 2012); this places Proxima b undoubtedly well within the so-called habitable zone (HZ) of its host star ($M_\star = 0.123$ M$_\odot$), which is defined as the range of orbital distances within which a planet can possibly maintain liquid water on its surface (Kasting et al., 1993; Kopparapu et al., 2013; Leconte et al., 2013a; Yang et al., 2013; Kopparapu et al., 2014, 2016). Indeed, for the effective temperature of Proxima (3050 K; Anglada-Escudé et al., 2016) climate models locate the inner edge between 0.9 and 1.5 $S_\oplus$, depending on the planet rotation (Kopparapu et al., 2016), and the outer edge at $\sim 0.2\ S_\oplus$ (Kopparapu et al., 2013). Nonetheless, surface habitability requires the planet to be endowed with a sufficient amount of water and atmospheric gases able to maintain a surface pressure and possibly a greenhouse effect (typically with CO_2).

Quantifying this last statement is the main goal of this study. While most previous studies on climate and habitability focused on estimating the edges of the habitable zone, here we rather investigate the variety of necessary atmospheric compositions and global water content to ensure surface liquid water. Using the limited amount of information available on Proxima b, we can already provide some constraints on its possible climate regimes as a function of a key parameter: the volatile inventory, which includes the amount of available water above the surface and the amount and type of greenhouse and background gases in the atmosphere. Investigating extreme inventory scenarios is especially important in our specific case because Proxima is an active M dwarf. This means that the atmospheric content of the planet has probably been dramatically influenced by various types of escape, especially during the pre-main-sequence phase in which the planet underwent a runaway greenhouse phase. See the companion paper by Ribas et al. (2016) for a detailed discussion.

Assuming a circular orbit, Proxima b should be in synchronous rotation with permanent dayside and nightside (1:1 resonance). However, Ribas et al. (2016) showed that the orbit of Proxima b might not have had time to circularize and that an eccentricity above $\sim$0.06 would be sufficient to capture the planet into a 3:2 spin-orbit resonance similar to Mercury. At higher eccentricities, higher resonances such as the 2:1 become possible as well. The climate on a tidally locked (synchronous) planet can dramatically differ from the asynchronous case. For a given volatile inventory, we will thus systematically try to infer the difference in behavior between a planet in a 1:1 and 3:2 resonance. The choice of the specific resonance order, however, has a much more subtle impact on the climate, so that the investigations of higher order resonances will be left for further studies.

Guided by various works on previously observed terrestrial exoplanets (Wordsworth et al., 2011; Pierrehumbert, 2011; Leconte et al., 2013b), this study thus explores the climate regimes available for Proxima b as a function of its spin state, atmospheric composition and thickness, and total amount of water available in the system. For this purpose, we use the LMD Generic Global Climate Model whose implementation for this specific study is detailed in Sect. 3.4.

For further reference, Figure 3.1 summarizes this attempt to quantify the possible climates of Proxima b for the two most likely spin states (1:1 and 3:2 spin-orbit resonance), as a function of the total water inventory and the greenhouse gas content (CO_2 here). The total water inventory is

expressed here in global equivalent layer (GEL), which is the globally averaged depth of the layer that would result from putting all the available water in the system at the surface in a liquid phase. Figure 3.1 serves as a guide throughout the various sections of this work.

To add a twist, Proxima b, as it is probably our closest neighbor, should be amenable to further characterization by direct imaging in the near future. With its short orbital period, multi-epoch imaging could then rapidly yield a visible and NIR phase curve of the planet. It could be one of our first opportunities to characterize a temperate terrestrial planet and its climate. We thus put a particular emphasis on quantifying observable signatures for the various type of atmospheres discussed here.

After presenting the details about the physical parameterizations used to model Proxima b, sections 3.5 to 3.7 contain our major findings about the climate regimes achievable on Proxima b. They are ordered following the global water inventory available from completely dry (Sect. 3.5), water limited planets (Sect. 3.6) to water-rich worlds (Sect. 3.7). Finally, in Sect. 3.8, we highlight potential observable signatures of these various climate regimes, and discuss how direct imaging with upcoming facilities could help us to constrain the actual climate of Proxima b.

3.4 Method - The LMD Generic Global Climate Model

This model originally derives from the LMDz three-dimensional Earth Global Climate Model (Hourdin et al., 2006), which solves the primitive equations of geophysical fluid dynamics using a finite difference dynamical core on an Arakawa C grid. The same model has been used to study very diverse atmospheres of terrestrial planets, ranging from (1) low irradiated planets as early Mars (Forget et al., 2013; Wordsworth et al., 2013, 2015; Turbet et al., 2017a), Archean Earth (Charnay et al., 2013), snowball Earth-like planets (Turbet et al., 2017b), or exoplanets like Gliese 581d (Wordsworth et al., 2011); (2) planets receiving stellar flux similar to the Earth (Bolmont et al. 2016a, this paper); and (3) highly irradiated planets such as future Earth (Leconte et al., 2013a) or tidally locked exoplanets like Gliese 581c / HD85512b (Leconte et al., 2013b).

Our simulations were designed to represent the characteristics of Proxima b, which include the stellar flux it receives (956 W m^{-2} / 0.7 $S_{\oplus}$), its radius (7160 km / 1.1 $R_{\oplus}$) and gravity field (10.9 m s^{-2}) which are calculated assuming a mass of 1.4 $M_{\oplus}$ (Anglada-Escudé et al., 2016) and the density of Earth (5500 kg m^{-3}); these characteristics also include a flat topography and various rotation speeds, namely $6.3{\cdot}10^{-6}$, $9.7{\cdot}10^{-6}$, and $1.3{\cdot}10^{-5}$ rad s^{-1}, for 1:1, 3:2, and 2:1 orbital resonances, respectively. All the simulations were performed assuming a circular orbit. Even if the maximum possible eccentricity of Proxima b is 0.35 (Anglada-Escudé et al., 2016), for dynamical reasons (Ribas et al., 2016) the upper limit of 0.1 would be more realistic. Therefore, the mean flux approximation seems reasonable (Bolmont et al., 2016a) here. We also worked with an obliquity of 0°, as expected for such a planet influenced by gravitational tides (see Ribas et al. 2016 for more details).

The simulations presented in this paper were all carried out at a horizontal resolution of 64 × 48 (e.g., 5.6 ° × 3.8°) in longitude × latitude. In the vertical direction, the model is composed of 26 distinct atmospheric layers that were built using hybrid σ coordinates and 18 soil layers. These 18 layers are designed to represent either a rocky ground (thermal inertia I_{rock} = 1000 J m^{-2} K^{-1} $s^{-\frac{1}{2}}$), an icy ground (I_{ice} = 2000 J m^{-2} K^{-1} $s^{-\frac{1}{2}}$) or an ocean (I_{ocean} = 20000 J m^{-2} K^{-1} $s^{-\frac{1}{2}}$ to take into account the vertical mixing) depending on the assumed surface. Oceanic heat transport is not

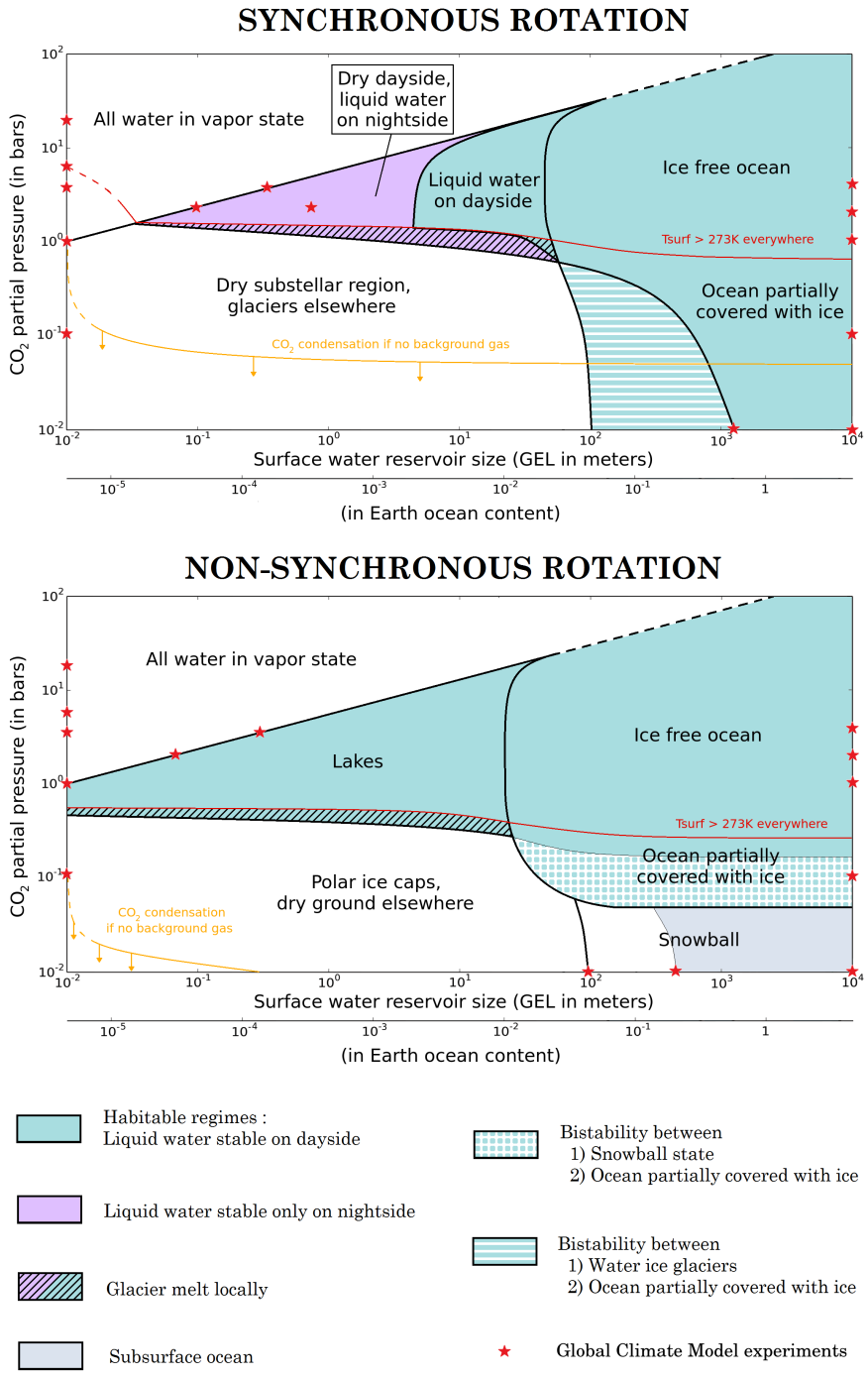

Figure 3.1: Schematic diagrams of the possible climate regimes reached as function of the CO_2 atmospheric content (in bar) and the H_2O content available at the surface (in global equivalent layer (GEL), in meters). The top and bottom panels describe the case of synchronous and asynchronous spin states, respectively. The red stars indicate the parts of the diagram that have been probed in this work using GCM simulations. The stars that lie on top of the left y-axis correspond to the case of a dry surface and atmosphere while those on the right y-axis consider planets completely covered by water. The presence of a background gas such as N_2 could significantly modify the lower part of the diagram ($pCO_2 < 1$ bar typically). It would favor the heat redistribution, which in turn could (1) prevent the CO_2 atmospheric collapse and (2) reduce the amount of ice possibly trapped in water ice glaciers.

Parameter	Value	Unit
$L_\star$	0.0017	$L_\odot$
T_{eff}	3000	K
Age	4.8	Gyr
$M_{\text{p}} \sin i$	1.27	$M_\oplus$
M_{p}	1.4	$M_\oplus$
R_{p}	1.1	$R_\oplus$
Semi-major axis	0.0485	AU
S_{p}	0.7	$S_\oplus$
Spin-orbit resonance	1:1 / 3:2 / 2:1	
Ω_p	$6.3{\cdot}10^{-6}$ / $9.7{\cdot}10^{-6}$ / $1.3{\cdot}10^{-5}$	rad s^{-1}
Stellar Day	∞ / 22.4 / 11.2	Earth days
Obliquity	0	$^\circ$
Eccentricity	0	
Surface types	Rock / Liquid water / Ice	
Thermal inertia	1000 / 20000 / 2000	J m^{-2} K^{-1} $s^{-\frac{1}{2}}$
Albedo	0.2 / 0.07 / wavelength-dependant (Figure 3.2)	

Table 3.1: Adopted stellar and planetary characteristics of the Proxima system. We also show the adopted parameters for various GCM parametrizations. The values for the stellar and planetary parameters are derived from Anglada-Escudé et al. (2016).

included in this study. Each of theses configurations is able to capture the diurnal waves for the non-synchronous orbital configurations. The planet day maximum explored duration is 22.4 Earth days for the 3:2 resonance orbital configuration. Table 3.1 summarizes all the parameterizations adopted in this work.

The GCM includes an up-to-date generalized radiative transfer (Rothman et al., 2009; Wordsworth et al., 2010a; Richard et al., 2012) for variable gaseous atmospheric compositions made of various cocktails of CO_2, N_2, and H_2O, using the correlated-k method (Fu and Liou, 1992; Eymet et al., 2016). Processes such as the radiative effect of clouds or Rayleigh scattering are taken into account. The emission spectrum of Proxima Centauri (see Figure 3.2, top panel) was computed using the synthetic BT-Settl spectrum[1] (Rajpurohit et al., 2013) of a M5.5 star with $T_{\text{eff}} = 3000$ K, $g = 10^3$ m s^{-2} and [M/H] = 0 dex.

Around a red dwarf like Proxima b, the bolometric albedo of ice and snow is significantly reduced (Joshi and Haberle, 2012) because of the shape of its reflectance spectrum. To account for this effect, the GCM computes the bolometric albedo of ice from a simplified law of the spectral albedo of ice and snow calibrated to obtain an ice and snow bolometric albedo of 0.55 around a Sun-like star (Warren and Wiscombe 1980; Warren 1984; Joshi and Haberle 2012; see bottom panel of Figure 3.2). Around Proxima b, our average bolometric albedo for ice and snow is 0.27. Yet, because of the varying spectral transmission of the atmosphere (due to variable water vapor and clouds), the bolometric albedo can locally reach values as high as 0.55.

Melting, freezing, condensation, evaporation, sublimation, and precipitation of H_2O are included

[1] Downloaded from https://phoenix.ens-lyon.fr

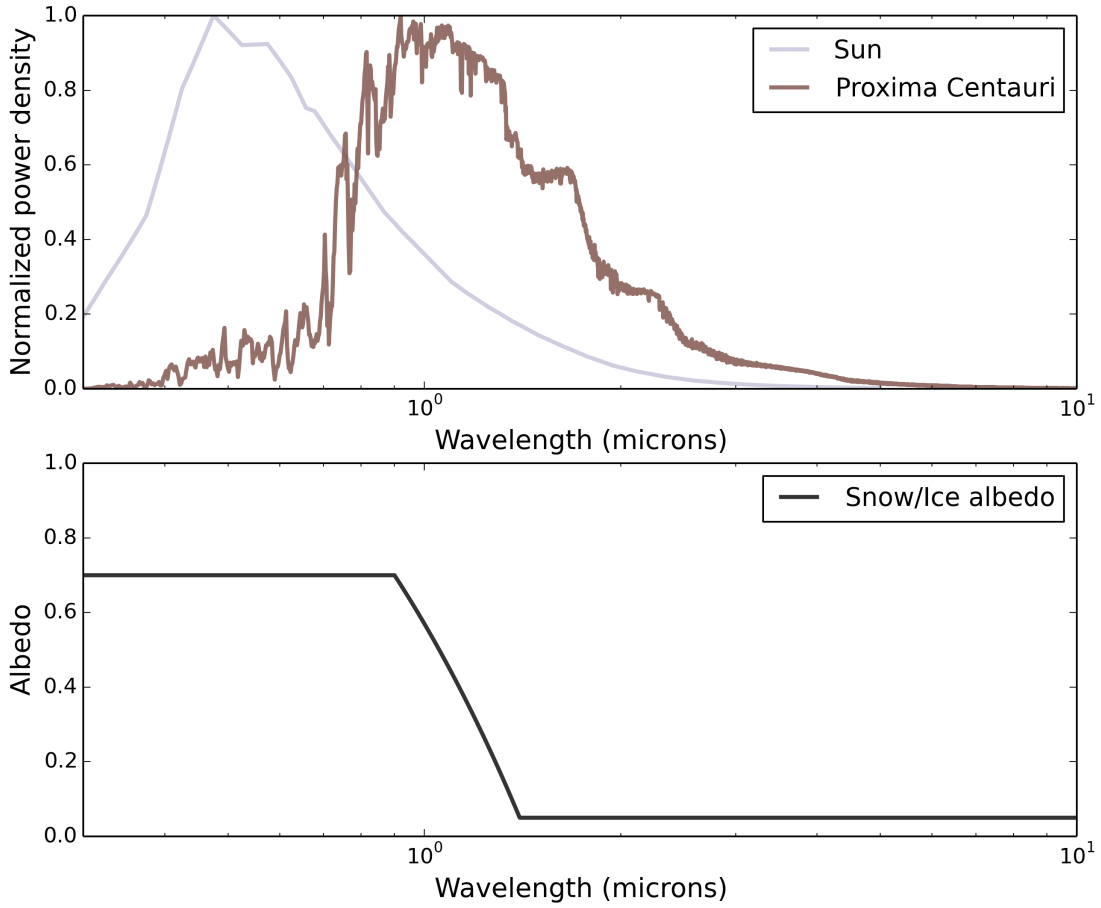

Figure 3.2: Top panel: Synthetic emission spectrum of a Proxima Centauri-like star (normalized by the peak value) used as input for the GCM calculations. For comparison, we put the spectrum of the Sun as usually computed in the LMD-GCM radiative transfer. Bottom panel: Spectral distribution of snow and ice surface albedo as computed in the GCM. Integrated snow and ice albedo values are 0.55 and 0.27 for the Sun and Proxima Centauri, respectively.

in the model. Similarly, we take the possible condensation and sublimation of CO_2 in the atmosphere (and on the surface) into account, but not the radiative effect of CO_2 ice clouds because their scattering greenhouse effect (Forget and Pierrehumbert, 1997) should not exceed 10 Kelvins in most cases (Forget et al., 2013; Kitzmann, 2016).

3.5 The case of a completely dry planet

Because Proxima b probably lost a massive amount of water during its early evolution around a pre-main sequence, active star (Ribas et al., 2016), we need to consider the possibility that the planet may now be rather dry. When water is in very limited supplies, its state is mostly determined by the temperatures of the coldest regions of the surface, the so-called cold traps (Abe et al. 2011; Leconte et al. 2013b; see next section).

To get some insight into the location and properties of these cold traps, we first consider the simple case of a completely dry planet. In this section, we focus on the greenhouse gas content needed to prevent the formation of a cold trap where ice could accumulate. Necessary conditions for the atmosphere to be stable are also discussed.

To evaluate this situation, we performed GCM simulations of rocky planets (surface albedo of 0.2) enveloped by pure CO_2 atmospheres with pressures ranging from 0.1 bar to 20 bar. Around a red dwarf like Proxima, CO_2 is a powerful greenhouse gas because it has stronger absorption lines in the near-infrared than in the visible and it does not contribute much to the stellar reflection by the Rayleigh scattering.

Figure 3.3 shows that the temperatures are very high across the surface even for CO_2 atmospheres of moderate thickness, and despite the low insolation compared to Earth ($S_p = 0.7\ S_\oplus$). In fact, GCM simulations show that, whatever the atmospheric pressure or the orbital configuration, surface temperatures are always greater than 273 K somewhere, although it is not the most relevant factor for the stability of liquid water (and therefore habitability), as indicated by the case of current day Mars (Read and Lewis, 2004; Millour et al., 2015).

3.5.1 Synchronous rotation

For the synchronous orbit case, surface pressures of 6 bar of CO_2 are required to warm the entire surface above the melting point of water. However, the surface temperature contrasts can be very high for lower atmospheric content. For example, as much as 150 K difference between the substellar and the coldest points in the 1 bar pure CO_2 simulation (see Figure 3.3, left bottom corner). In the synchronous configuration, the planet has two cold points located at symmetric positions around longitude $\pm 180°$ and latitude $\pm 60°$. The existence of these two cold traps persists in all the tidally locked simulations (dry, wet, down to 1 bar thin or up to 20 bar thick atmospheres, etc.) explored in this work, but their position can slightly vary, as a result of planetary-scale equatorial Kelvin and Rossby wave interactions (Showman and Polvani, 2011). In particular, our simulations show that thick atmospheres tend to move these two cold gyres toward the west direction and higher latitudes (see also Figure 3.6).

In addition, GCM simulations tell us that CO_2-dominated atmospheres that are thinner than ~ 1 bar are not stable at all because the surface temperature at the two cold points is lower than the temperature of condensation of CO_2 (see Figure 3.3, third row of left column, blue dashed line). We

identified here a positive feedback: when CO_2 starts to collapse because of the decrease in the total gas content, the heat redistribution becomes less efficient, which increases the temperature contrast between the substellar point and the gyres and therefore favors the CO_2 condensation at the cold points. In this case, the atmosphere would inevitably collapse until reaching an extremely low CO_2 atmospheric content in a regime of temperatures and pressures that are not well described by our model parametrizations.

In the process, CO_2 ice could be trapped for eternity, but also form glaciers that could flow efficiently to warm regions and resupply the atmosphere in gaseous CO_2 continuously (Turbet et al., 2017b). Moreover, the scattering greenhouse effect of CO_2 ice clouds (Forget and Pierrehumbert, 1997; Turbet et al., 2017b) that would form preferentially in the coldest regions of the planet could drastically limit the CO_2 atmospheric collapse.

In any case, this shows that having enough atmospheric background gas (main agent of the heat redistribution + additional pressure broadening) may favor the stability of the atmosphere and therefore the habitability of Proxima b. For example, for an atmosphere of 1 bar of N_2 – as could be more or less expected on an Earth-sized planet of $R_p \sim 1.1\ R_\oplus$ (Kopparapu et al., 2014) – and 376 ppm of CO_2, the dayside has mean surface temperatures above 273 K and the atmosphere does not collapse (see Figure 3.3, left bottom corner).

3.5.2 Asynchronous rotation

For non-synchronous cases, the substellar temperature "eye" pattern disappears and the atmospheric pressure at which surface temperatures are all strictly above 273 K is slightly lower because the stellar radiation is now distributed equally among the longitudes. For the 3:2 resonance case, Figure 3.3 shows that this condition is reached for atmospheric pressures greater or equal to 4 bar. 3:2 and 2:1 spin-orbit resonance configurations do not exhibit significant differences in term of surface temperature maps. The shorter stellar day in 2:1 (11.2 Earth days compared to 22.4), which weakens day and night contrasts is compensated by the higher rotation rate, which weakens equator-to-pole heat redistribution (Wordsworth et al., 2011; Kaspi and Showman, 2015).

Another crucial consequence of the efficiency of the heat redistribution relates to the CO_2 collapse, which occurs now at CO_2 atmospheric pressure as low as 0.1 bar in the 3:2 orbital resonance GCM simulations (this is a factor 10 lower than for the tidally locked configuration). Therefore, in such a configuration, asynchronous rotation would favor the stability of the atmosphere and thus the habitability of Proxima b.

3.6 Limited water reservoir

Another possibility is that Proxima b may have a limited, but non-zero, water inventory. In this case, the question is to know where this water is stored. To answer that question, Sect. 3.6.1 first makes an attempt at quantifying how much water vapor can be stored in the atmosphere without ever condensing at the surface. Then, in Sect. 3.6.2, we discuss what happens to the water reservoir when it condenses at the surface. In particular, we try to estimate how much water can be stored before it forms planetary scale oceans (this is discussed in Sect. 3.7).

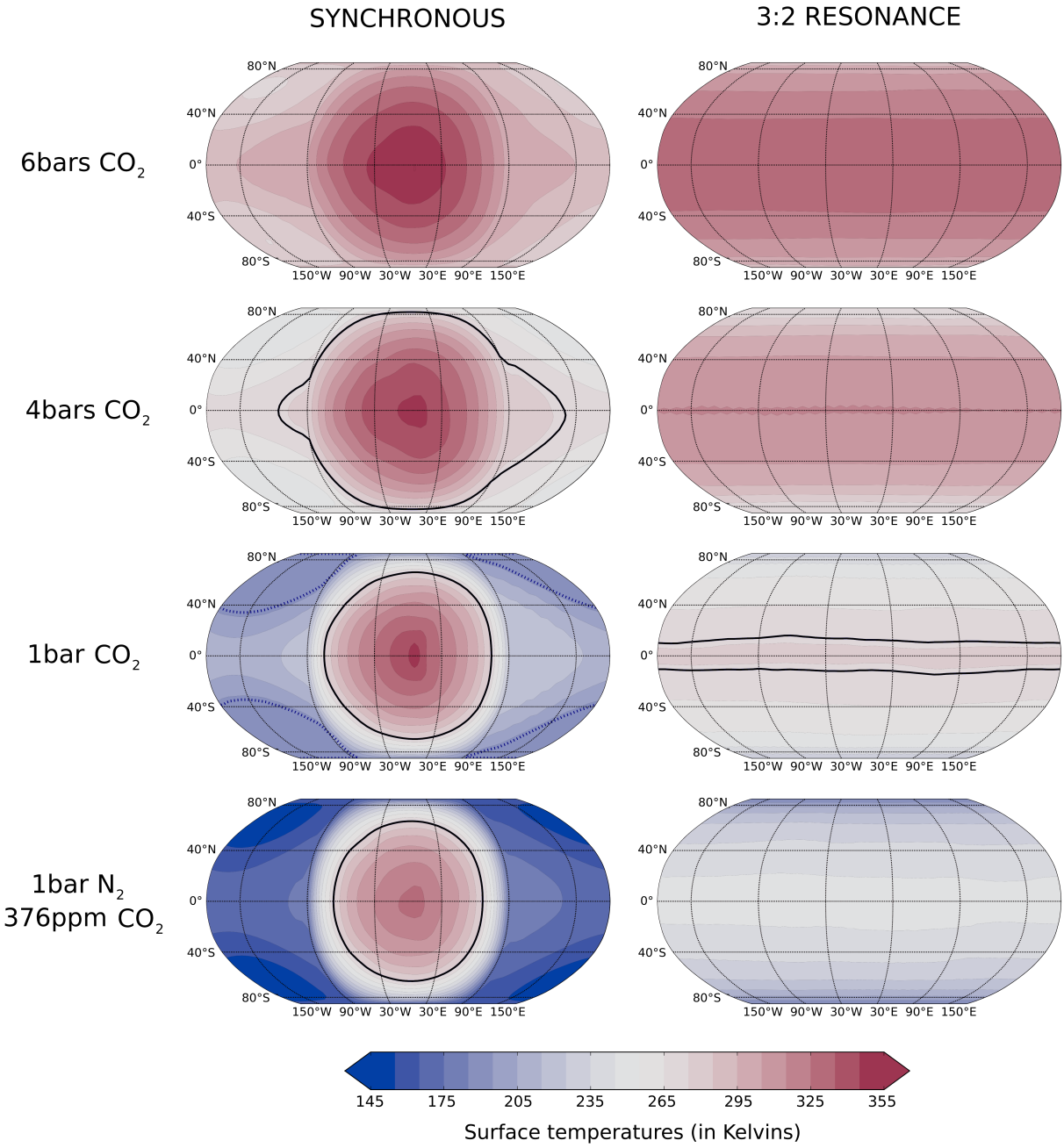

Figure 3.3: Biennal mean surface temperatures of completely dry atmospheres, for 2 orbital configurations (synchronous and 3:2 orbital resonance) and 4 atmospheric compositions and pressures (6 bar of pure CO_2, 4 bar of pure CO_2, 1 bar of pure CO_2 and 1 bar of N_2 + 376 ppm of CO_2 – Earth-like atmosphere). The solid black line contour corresponds to the 273.15 K isotherm; the dashed blue line contour indicates the regions where the atmospheric CO_2 collapses permanently into CO_2 ice deposits. The 1 bar pure CO_2 (synchronous) simulation is not stable in the long term since CO_2 would collapse at the two cold points.

3.6.1 Maximum amount of water stored in the atmosphere

The amount of water that can be maintained in a planetary atmosphere before it starts to condense at the surface depends primarily on the atmospheric temperatures. For example, Venus has a water GEL of ~2 cm (Bougher et al., 1997; Bézard et al., 2009) in its atmosphere that may form liquid water droplets in the atmosphere but never condenses at the surface. But it could store much more.

To quantify this possibility in the case of Proxima b, we perform a simulation with a 4 bar CO_2 dominated atmosphere, for a synchronous rotation, in aquaplanet mode (static ocean model, I = 20000 J m^{-2} K^{-1} $s^{-\frac{1}{2}}$, surface albedo of 0.07), and until equilibrium is reached (after $\sim$ 1000 orbits). Hereafter, water vapor is always included in the atmospheric calculations, expect when otherwise specified. When referring to a specific atmospheric composition, only the amount of background gases is specified.

Suddenly, we change the properties of the planet: first, we remove all the water available at the surface and, second, we use a rocky surface (I = 1000 J m^{-2} K^{-1} $s^{-\frac{1}{2}}$, surface albedo of 0.2), in place of the removed water at the surface. Then, at every orbit, we remove all the extra water that condenses from the planet. We repeat the process until precipitation completely stops for 50 consecutive orbits. Up to 45 cm GEL of water could be trapped in the atmosphere before it starts to condense (not shown). In this case, surface temperatures reach 370-450 K, which is a 45 K increase on average compared to the aquaplanet simulation.

Repeating this procedure for atmospheric pressures of 1 bar, 2 bar, and 4 bar, we obtained maximum amounts of water vapor (before it condenses permanently at the surface) of 1 cm, 10 cm, and 45 cm GEL. The corresponding simulations were reported in Figure 3.1 and define the black curve separating the region "All water in vapor state" from the rest of the diagram. The same GCM simulations, when taking the greenhouse effect of water vapor into account, show that surface pressures as low as 1.5 bar (and even lower for the 3:2 orbital resonance) are now sufficient to get surface temperatures above 273 K everywhere on the planet.

Thick, Venus-like atmospheres (pCO_2 typically > 10 bar) could potentially store very large amounts of water, although we did not perform the necessary simulations; these simulations would require a dedicated radiative transfer model. Interestingly, for atmospheres with a huge greenhouse effect, there is no reason for the partial pressure of water not to exceed that of the critical point. In this case, the temperature would also exceed the critical point so that discussing the transition to a liquid phase at the surface would not be very meaningful. The habitability of such environment seems largely unexplored.

3.6.2 Maximum amount of water stored on the surface

3.6.2.1 Cold climates: Limits on glaciers.

As soon as water is available in sufficient amounts, which depends on the atmospheric gas content (as detailed above), it can start to condense permanently at the surface. For a synchronous rotation, CO_2-dominated atmospheres with pressure typically lower than 1.5 bar exhibit surface temperatures that are lower than 273 K at their coldest points. Therefore, all the extra water available at the surface gets trapped at the two cold gyres forming inevitably stable water ice deposits. The range of water inventory for which such unhabitable climate regimes subsist depends on the atmospheric gas content and composition, but also possibly on the internal heat flux of Proxima Centauri b.

As the water inventory increases, the ice deposits thicken and start to form water ice glaciers that can at some point flow from the coldest regions of the planet toward warmer locations. There are in fact two distinct processes that can limit the growth of water ice glaciers (Leconte et al., 2013b; Menou, 2013):

1. The gravity pushes the glaciers to flow in the warm regions where ice can be either sublimated or melted. This limit depends mostly on the gravity of the planet and the mechanical properties of water ice (e.g., viscosity).

2. The internal heat flux of the planet causes the basal melting of the water ice glaciers. In such conditions, glaciers would slip and flow to warmer regions where, once again, ice could melt and sublimate. This limit depends primarily on the geothermal heat flux of the planet and the thermodynamical properties of water ice (e.g., thermal conductivity).

Menou (2013) has shown that for tidally locked terrestrial planets with Earth-like characteristics, the basal melting should be the condition that limits the thickness of the water ice glaciers. He finds maximum global equivalent ice thicknesses typically ranging from 320 m (for a 1 bar N_2, 3.6 % CO_2 atmosphere) and 770 m (0.3 bar N_2, 360 ppm CO_2 atmosphere).

In the same vein, we compute the maximum ice thickness before basal melting for four of our dry GCM simulations from Fig. 3.3. We use two distinct atmospheric compositions: 1 bar is pure CO_2 atmosphere; below that, the CO_2 can collapse permanently for synchronous rotation; 1 bar of N_2 + 376 ppm of CO_2), and two orbital configurations (synchronous and 3:2 resonance). This thickness, $h_{\rm ice}^{\rm max}$, is given by (Abbot and Switzer, 2011):

$$h_{\rm ice}^{\rm max} = \frac{A}{F_{\rm geo}} \ln \left(\frac{T_{\rm melt}}{T_{\rm surf}} \right), \tag{3.1}$$

where $F_{\rm geo}$ is the internal heat flux and $T_{\rm melt}$ is the melting temperature of ice at the base of the glacier. As the latter is a function of the pressure below the ice, it implicitly depends on $h_{\rm ice}^{\rm max}$ so that the above equation must be solved numerically, once the local surface temperature is known (Leconte et al. 2013b; see appendix 3.11.1 for details). This temperature is taken from the GCM outputs (see the third and fourth rows of Figure 3.3).

Assuming that it scales roughly with $M_{\rm p}^{1/2}$ (Abbot and Switzer, 2011), the geothermal flux can be extrapolated based on the Earth value (∼90 mW m^{-2}; Davies and Davies 2010), yielding $F_{\rm geo}$ = 110 mW m^{-2}. Of course, this estimate holds only because the Earth and Proxima are similar in age (Bazot et al., 2016). However, tidal heating could also take place. Ribas et al. (2016) showed that an initial eccentricity would not be damped significantly over the lifetime of the system. They also argue that, assuming the planet is alone in the system, it would be difficult to excite the orbital eccentricity above 0.1. This would correspond to an extra tidal heat flux of ∼ 70 mW m^{-2} for a tidal dissipation ten times lower than Earth. Therefore, for non-synchronous orbits, we arbitrarily set the geothermal heat flux $F_{\rm geo}$ to be equal to 110+70 = 180 mW m^{-2}. An upper limit on the tidal heating can also be derived from observations of Proxima b that put an upper limit of 0.35 on the eccentricity of the planet (Anglada-Escudé et al., 2016). This configuration produces a tidal dissipation heat flux of ∼ 2.5 W m^{-2}, which is similar to Io (Spencer et al., 2000). Yet, in this case, most of the heat would probably be extracted through convection processes (e.g., volcanism) instead of conduction, as on Io.

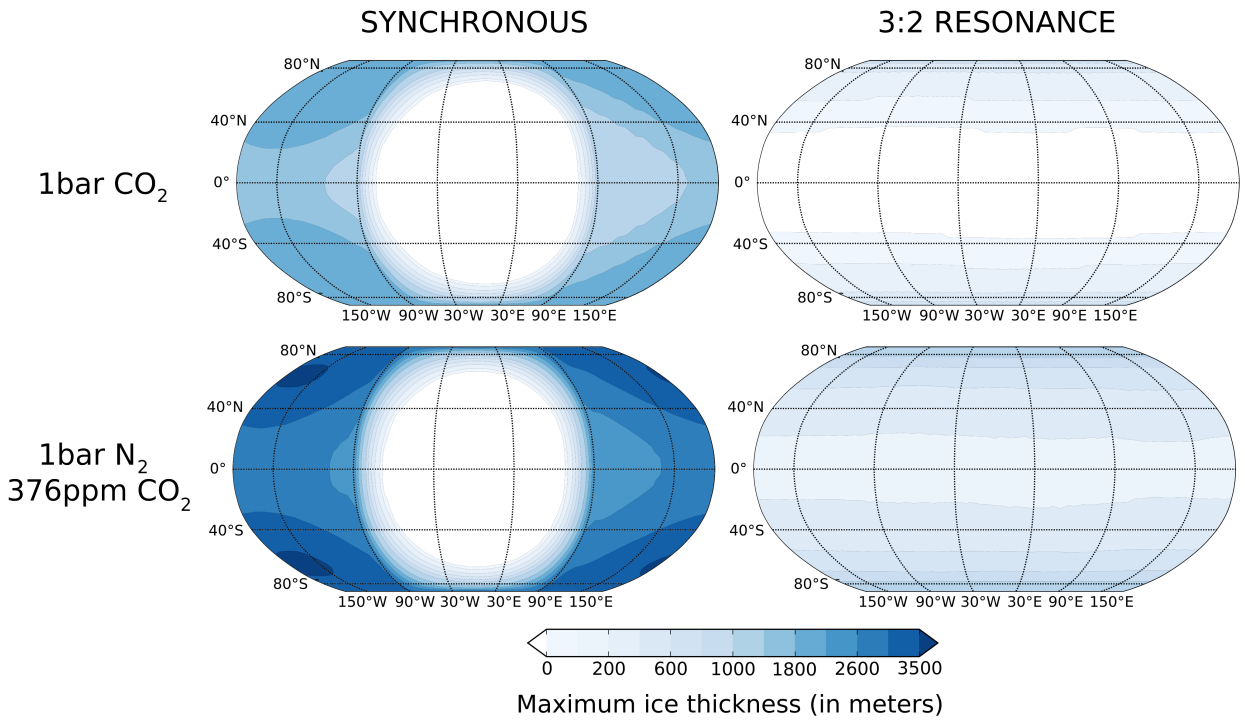

Figure 3.4: Maximum ice thickness calculated from 4 completely dry GCM simulations made of 2 different atmospheric compositions (1 bar pure CO_2 atmosphere, 1 bar N_2-dominated atmosphere with 376 ppm of CO_2) and 2 orbital configurations (synchronous and 3:2 resonance). The maximum ice thickness is calculated from the basal melting condition derived from the mean surface temperature from Figure 3.3. The internal heat flux is assumed to be 110 mW m^{-2} for the synchronous orbit cases and 180 mW m^{-2} for the asynchronous cases. The global equivalent thickness of ice is 940 m (1 bar of CO_2) and 1650 m (Earth atmosphere) for the synchronous rotation, and 115 m and 490 m for the 3:2 resonance, respectively. The amount of ice calculated from the 1 bar CO_2 simulation is probably a lower estimate since CO_2 would collapse, making the cold points even colder.

Thus only a (unknown) fraction of this flux should be used in Eq. (3.1). We thus decided to use a geothermal flux of 180 mW m^{-2} for our baseline scenario, but we note that an order of magnitude change could be possible.

Figure 3.4 shows the water ice maximum thickness maps derived for our four simulations. After spatial averaging, this yields maximum equivalent global thicknesses of ice of 940 m and 115 m for the 1 bar pure CO_2 atmosphere (respectively for sync. and async. rotations) and of 1650 m and 490 m for an Earth-like atmosphere.

On the one hand, very large amounts of ice (up to 61 % of Earth ocean content in the Earth-like atmosphere config.) can be trapped in the tidally locked case due to the high contrasts of temperature throughout the surface. *This is not an upper limit.* Thinner atmospheres (due to CO_2 collapse for example, see section 3.5) could entail much more extreme surface temperature contrasts. Such a *Pluto-like* planet could potentially trap tremendous amounts of water in the form of ice.

On the other hand, much more limited quantities of ice can be trapped in asynchronous simulations due to both a better heat redistribution and a higher geothermal heat flux. For an eccentricity of 0.35, the amount of trapped ice would be probably much less than 115 m and 490 m because of the increased internal heat flux.

We mention that these GCM simulations were performed with a dry atmosphere; the lack of water vapor, a powerful greenhouse gas, leads to an overestimate of the amount of ice possibly trapped.

Eventually, once the water ice glaciers start to spill, they can possibly melt at their edge, either on dayside or nightside. It has been shown by Leconte et al. (2013b) that such configuration could be long lived. We roughly put in Figure 3.1 (hatched region) the range of CO_2 and water inventory for which such scenario would happen. This is an exotic form of habitability.

3.6.2.2 Warm climates: Appearance of lakes

As discussed in Sect. 3.5, if the greenhouse effect of the atmosphere is sufficient, the coldest temperatures at the surface are above the freezing point of water. Although we might intuitively think that this situation is very different from above, from the point of view of the atmosphere, it is not. The atmosphere always tends to transport water from the hottest to the coldest regions. The fact that the cold-trap temperature is above the freezing point is irrelevant as long as there is not enough water at the surface to redistribute water more rapidly than it is brought in.

Liquid water thus first accumulates around the coldest regions of the planet. Interestingly, on a synchronous planet, these are located on the night side where no photons are available for photosynthesis. If the spin is non-synchronous, the volatiles would likely first concentrate toward the poles. This seems to be the case on Titan where methane lakes are mostly seen at high latitudes (Stofan et al., 2007).

The range of water inventory for which this configuration (liquid water on nightside) may subsist not only depends on the water inventory but also on the topography. In the case of a tidally locked planet, the topography features may not be randomly distributed because tidal locking could tend to favor the alignment of large-scale gravitational anomaly (correlated with topography anomaly) with the star-planet axis. For instance there is a clear difference between the near side and far side of the Moon (Zuber et al., 1994), and the deep Sputnik Planum basin on Pluto is located near the anti-Charon point (Moore et al., 2016). Thus it is conceivable that Proxima b may have its largest topographic basin either near the substellar point at the anti-stellar point.

Interestingly, as the water inventory grows, the response of the climate (amount of water vapor, atmospheric temperatures, ...) might be significantly different depending on the topography. Figure 3.5 illustrates qualitatively the fact that, depending on the topographic setup (basin at the substellar point, basin at the anti-stellar point, or no basin at all, i.e., a quasi-flat configuration), the distribution of water between the surface and the atmosphere might significantly differ. As significant amounts of water start to condense at the surface, liquid water would likely spill toward the main topographic depression of the surface. If this depression is for example located at the substellar point, where evaporation rates are the highest, the proportion of water in the atmosphere given a fixed total water inventory would be maximum and definitely much higher than in the extremely opposite case (a basin at the anti-stellar point).

Therefore, it is important to mention that assessing the proportion of water vapor in the atmosphere of Proxima b might not be sufficient to get information on the stability and location of surface liquid

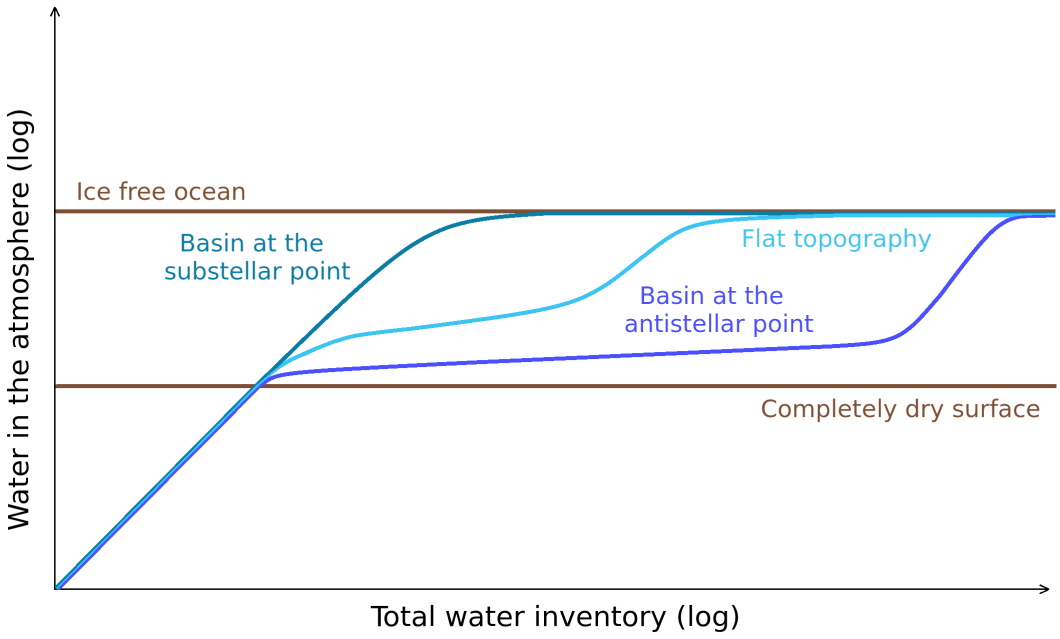

Figure 3.5: Qualitative evolution of the amount of water vapor in the atmosphere as a function of the total water inventory, assuming a synchronous rotation and a liquid water runoff activated, for three different scenarios: a quasi-flat topography, a basin at the substellar point, and a basin at the anti-stellar point. For high pCO_2, the range of water inventory for which the three scenarios diverge would flatten on a logarithmic scale because potentially high amount of water could be vaporized.

water, and vice versa, knowing the exact water inventory available on Proxima b would not be totally relevant to deduce its possible climatic regime.

3.7 Large water reservoir

Despite the large amount of hydrogen that could have escaped within the lifetime of Proxima b, the quantity of water now available on the planet also depends significantly on its initial water inventory. As argued by Ribas et al. (2016), if Proxima Centauri b formed beyond the ice line in a similar fashion to solar system icy satellites, it could still possess enough water to be an *aquaplanet*, the term aquaplanet refering here to a planet where water is abundant enough to flow efficiently on a planetary scale. In practice, in our simulations, this means that the surface acts as an infinite source of water.

In this section, we thus make an attempt at quantifying how much is *enough*. Then, we discuss the various climate regimes available to an aquaplanet and point out the main differences with the dry case.

3.7.1 Transition from small to large water inventory

The exact water inventory for which Proxima b would transition from a land planet (previous section) to an aquaplanet (this section) is difficult to define. In particular, the nature of the transition depends of the amount of greenhouse gas in the atmosphere.

For a low atmospheric greenhouse effect (meaning that ice is stable somewhere on the planet), there is a bistability between two possible climate regimes around the transition. To understand this bistability, we introduce a thought experiment in which we consider a planet with two very different initial conditions:

- Case 1: warm- and/or water-rich-start. We assume that the planet starts with a global ocean, possibly covered by sea ice wherever cold enough. This experiment has been carried out by Yang et al. (2014) with a 325 m deep ocean. They showed that in such a configuration, winds carry sea ice toward hot regions and the ocean carries heat toward cold regions, so that an equilibrium can be found with less than 10 m of sea ice in the coldest regions. They however acknowledge that the presence of continents could significantly alter this value. Yang et al. (2014) only looked at a synchronous planet, but the argument remains qualitatively valid for a non-synchronous planet, even though numerical values will surely change significantly.

  Therefore, water content as small as $\sim 10^2$ m GEL (and maybe even lower) is sufficient to maintain aquaplanet conditions. If water were to be removed or the temperature decreased, at some point, the oceanic transport would shut down and the planet would transition to a dry, cold regime with glaciers.

- Case 2: cold- and/or water-poor-start. As discussed in the previous section, if the planet started cold or dry enough, all the water would be trapped in ice caps and glaciers. Now, we demonstrated earlier that in this state, more than $\sim 10^3$ m GEL of ice could be stored this way. If the water inventory and/or the temperature were to be increased, glaciers would progressively spill toward hotter regions. This state could resist until the oceanic transport becomes more efficient than the atmospheric transport. After that, an ocean would accumulate and, in turn, warm the cold regions, speeding up the transition to the aquaplanet regime.

Therefore, between roughly $\sim 10^2$ and 10^3 m GEL, two distinct climate regimes coexist, depending on the history of the planet. As both the water inventory and the amount of greenhouse gases play a role, it is even possible for the planet to undergo hysteresis cycles between the two states. But the mechanism is rather different from that involved in snowball climates (which will be discussed later on). Indeed, here, the albedo feedback does not play a major role. What controls the transition between a water-rich and warm world toward a dry and cold one is now the oceanic transport. We note that on a non-synchronous planet, the upper limit of 10^3 m GEL would decrease as the cold traps are less efficient and at the same time, a smaller global ocean might be needed to efficiently warm the poles.

For warmer climates (in the sense that ice cannot form at the surface), the transition would happen whenever water were abundant enough to flow. Topography would thus be the key parameter (see Sect. 3.6.2.2).

A third situation can occur when the amount of greenhouse gases in the atmosphere is such that the partial pressure of water vapor at the surface can exceed that of the critical point. Then we expect

no transition at all as there is no phase transition between liquid and gaseous phase above the critical point.

Finally, we note that in any case another transition would occur at much higher water contents ($\sim 10^{5-6}$ m GEL) when high pressure ices form.

3.7.2 Necessary conditions to have surface liquid water

Assuming that Proxima b is in the aquaplanet regime, one may wonder what the minimal requirement is to maintain liquid water stable at the surface. Compared to the limited reservoir case, the requirements are much less stringent. There are two main reasons for this:

- There is too much water, by definition, for complete cold-trapping to occur. As a result, the lowest temperature at the surface is rather irrelevant. Instead, only the highest temperature matters. And it is much easier to have a planet with one region above freezing than a planet with no region below freezing.
- Because water is readily available for evaporation, the atmosphere, on average, is much closer to saturation compared to the dry case. As water vapor is a good greenhouse gas, this usually entails that for a given background atmosphere, the average surface temperature of the aquaplanet is higher than its dry counterpart. This can sometimes be mitigated by the ice albedo effect, but this effect is extremely weak around red stars such as Proxima (Joshi and Haberle, 2012), especially for synchronous spin states.

With that in mind, we performed a suite of aquaplanet simulations with various atmospheric compositions to assert the likelihood of surface liquid water. The results are shown in Fig. 3.6.

3.7.2.1 Synchronous rotation: Ubiquity of liquid water.

As can be seen on the left column of Figure 3.6, when the planet is synchronously rotating, temperatures are always high enough at the substellar point to have liquid water, whatever the atmospheric content (pure CO_2, Earth-like mixture, thin, 0.01 bar atmosphere). This would hold even without a background atmosphere; in this case, the atmosphere would be composed of water vapor. Indeed, because the substellar point permanently receives 956 W m^{-2}, it would take a surface bond albedo of 0.67 to cool this region below the freezing point. We recover the "Eyeball Earth" regime (Pierrehumbert, 2011) or "Lobster Earth" regime (Hu and Yang, 2014) (when deep ocean circulation is taken into account).

Starting from there, adding greenhouse gases to the atmosphere only (1) increases the mean surface temperature, (2) increases the size of the liquid water patch, and (3) reduces the temperature contrast. Eventually, above some threshold (~ 1 bar in our simulations), greenhouse is intense enough to deglaciate the whole planet.

3.7.2.2 Asynchronous rotation

In a non-synchronous spin-state, on the contrary, surface liquid water is not always possible. In fact, we recover a situation very similar to that on Earth: below some threshold amount of greenhouse gases, the planet falls into a frozen, snowball state.

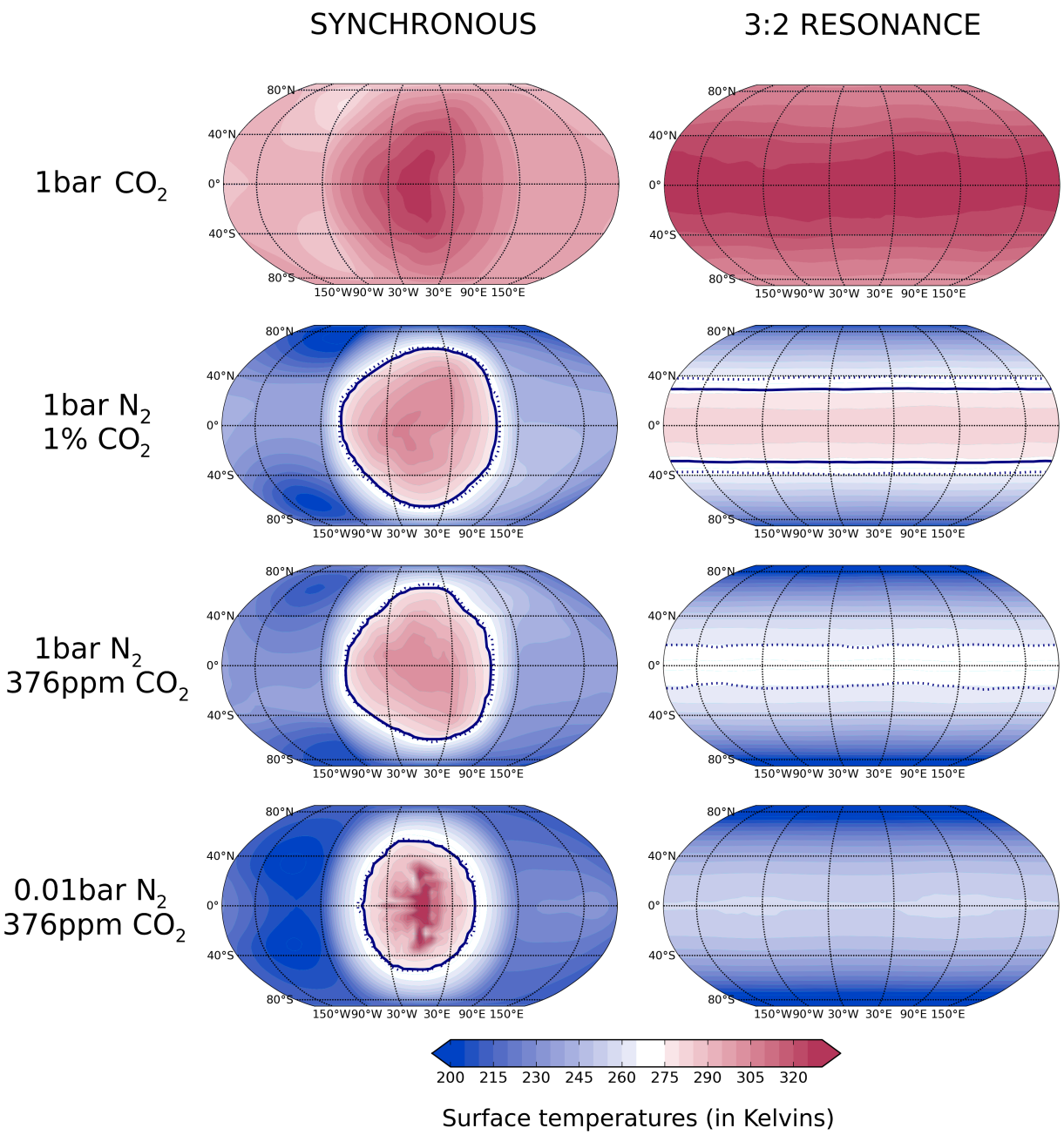

Figure 3.6: Biennal mean surface temperatures of atmospheres made of a variety of 4 cocktails of N_2 and CO_2 for 2 orbital configurations (synchronous and resonance 3:2), assuming planets initially completely covered by liquid water. Solid lines and dashed lines contours correspond to the location of permanent and seasonal surface liquid water, respectively.

The reason for this difference with the synchronous state is that any point at the equator now receives on average only $1/\pi$ of what the substellar point received at any time in the synchronous configuration. The zero-albedo equilibrium temperature corresponding to this mean flux is $\sim 270\,\mathrm{K}$. Some greenhouse effect is thus necessary to melt the equator, especially when the albedo and circulation effects are added.

Consequently, four different climate regimes can be reached on such an asynchronous planet, depending on the greenhouse gas content. These are depicted on the right column of Fig. 3.6. From top to bottom, we have:

1. For high CO_2 pressures (roughly above a few tenths of bar) the planet is covered by an ice-free ocean. We did not perform our simulations on a fine enough grid to be more precise, but the limit should be lower than 1 bar (see Fig. 3.6).

2. At lower levels of CO_2 (down to $\sim$0.01 bar with 1 bar N_2) the planet can keep a permanently unfrozen equatorial belt.

3. For lower greenhouse gas contents, diurnal patches of liquid water lagging behind the substellar point subsist.

4. For thin enough atmospheres, a completely frozen snowball state ensues.

The 0.01 bar atmosphere (on Figure 3.6, right column) is colder than 1 bar because, first, the pressure broadening of CO_2 absorption lines by N_2 is drastically reduced; and, second, the absolute amount of CO_2 in the atmosphere is 100 times lower. Both effects are responsible for the appearance of an equatorial band of relatively warmer surface temperatures for the 3:2 resonance, 1 bar of N_2 (+ 376ppm of CO_2) case.

The well known snowball hysteresis could potentially exist between our states 2, 3, and 4, although the weak ice-albedo feedback around M dwarfs certainly makes it less likely than on Earth (Shields et al., 2014). A confirmation of this would necessitate numerous additional simulations.

3.7.3 Subsurface oceans?

Whether or not surface liquid water is possible, we now try to assess the possibility of the presence of a subsurface ocean. Indeed, if Proxima b has been able to keep a large enough water inventory, the steady release of geothermal heat entails a rise in temperature with depth through the ice cap.

To assess a lower limit, we consider our coldest, and only fully glaciated case (0.01 bar of N2, 376 ppm of CO_2 and 3:2 resonance; see Figure 3.6, right bottom corner). Following a similar approach to section 3.6.2.1, we estimate that a subsurface ocean could exist for water GELs greater than 600 meters (assuming a geothermal heat flux of 180 mW m^{-2}). Any effect warming the surface would tend to lower this threshold.

Above such water inventories, Proxima b could thus be at least considered a class III or IV (if there is enough water to form high pressure ices) habitable planet (Lammer et al., 2009; Forget, 2013).

3.7.4 Thin atmospheres: Implication for water loss

When considering water loss around planets in the habitable zone of small stars, it is tempting to disregard water losses occurring after the end of the initial runaway greenhouse phase (which can be

important, e.g., Ribas et al., 2016). The reason for this is that the tropopause usually acts as an efficient cold trap. The amount of water vapor available for escape in the upper atmosphere is thus limited by diffusion (Kasting et al., 1993; Wordsworth and Pierrehumbert, 2013).

However, this conclusion is often based on calculation including a relatively massive, Earth-like background atmosphere. Because escape may have been very important for Proxima b in the past, early atmospheric escape may have removed an important fraction of the background atmosphere (Ribas et al., 2016). It is thus primordial to infer whether a less massive background atmosphere is still able to shield water vapor from escape once the planet has cooled down.

To that purpose, we performed simulations with an Earth-like atmospheric composition, but a lower background surface pressure (namely 0.1 and 0.01 bar; bottom panels of Figure 3.6). The substellar temperature and vapor mixing ratio profiles are shown in Figure 3.7, along with the reference 1 bar case.

The water vapor mixing ratio increases drastically in the atmosphere when the background pressure decreases, even at a given pressure level. This results from the fact that: (1) when the surface pressure decreases, the surface temperature cannot change drastically to remain in radiative equilibrium; (2) throughout the troposphere, the temperature follows a (moist) adiabat and is thus determined by the ratio of the local to the surface pressure. At a given pressure level, temperatures in the troposphere thus increase when the surface pressure decreases; (3) because of the Clausius-Clapeyron law, this increases the mixing ratio of water vapor throughout the troposphere; and (4) finally, the strong absorption bands in the near-infrared, i.e., the peak of the stellar spectrum, provide a positive feedback that tend to humidify the tropopause even more.

Moreover, the water vapor mixing ratio increases globally because it is advected by the large-scale circulation. As a consequence, hydrogen escape is not limited by the diffusion of water vapor anymore, even after the runaway phase. Low atmospheric background gas contents may thus lead to increased rates of hydrogen (and thus water) loss to space.

3.8 Observability

At the time of this study, the existence of planet transits or flares have not been established, which complicates the search. There is only 1.3% of chance that the inclination of the orbit of Proxima b produces transits, so we do not consider characterization by transit spectroscopy in this work.

3.8.1 Prospects for direct imaging

Proxima b may be the habitable-zone terrestrial exoplanet offering the best combination of angular separation and contrast for imaging. The angular separation between the planet and its star varies from 0 (for a 90° inclination) to 38 mas (0.05 AU at 1.29 pc). The planet/star contrast of a 1.1 $R_\oplus$ purely Lambertian sphere (surface albedo = 1) at 0.05 AU from Proxima is 2×10^{-7} when seen with a 90° phase angle and approaches 6×10^{-7} as the phase angle approaches 0°. Current instrumentation using adaptive optics and coronography on 10 m class telescopes (such as SPHERE/VLT, GPI/Gemini) aims to achieve a contrast of $10^{-6} - 10^{-7}$, but with an inner working angle of a few λ/D that is not smaller than 100-200 mas depending on the band (Lawson et al., 2012). Lovis et al. (2017) suggest

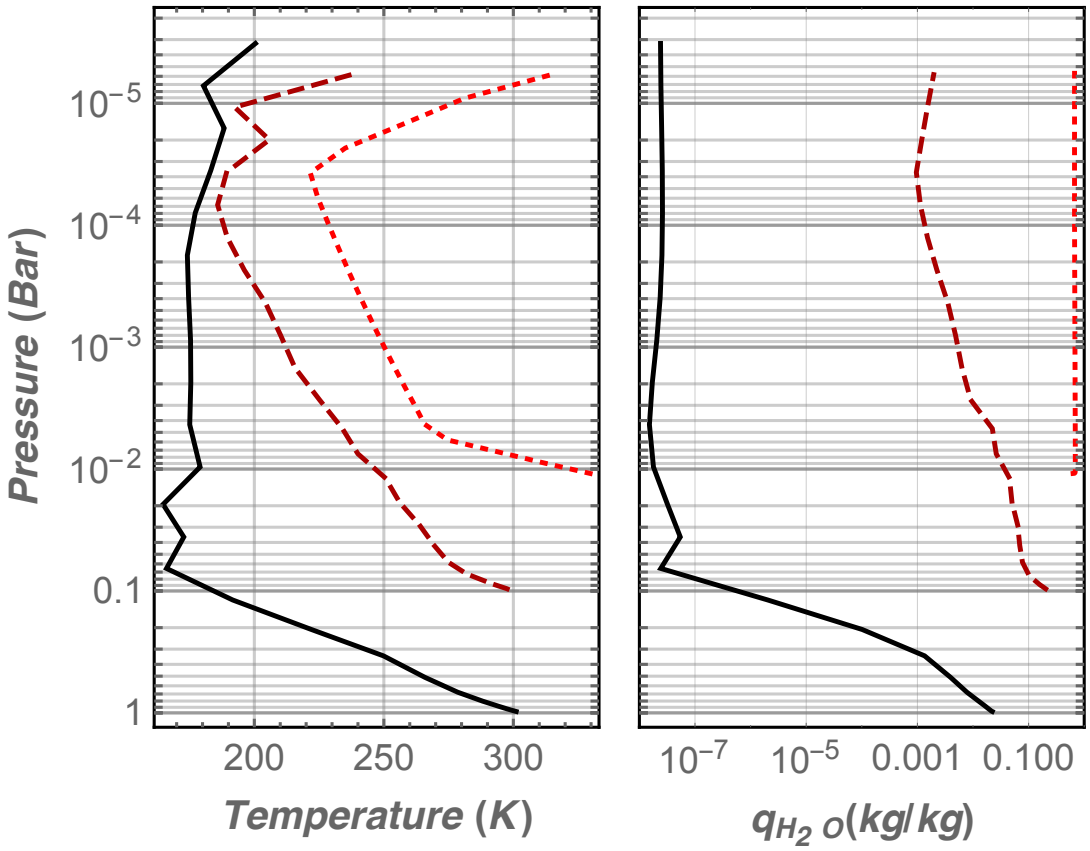

Figure 3.7: Annual mean atmospheric temperature (left) and water vapor (right) vertical profiles of atmospheres with different total surface pressure (solid black: 1 bar; dashed, dark red: 0.1 bar; dotted red: 0.01 bar). The composition of all three atmospheres is N_2 with 376 ppm of CO_2 and a variable amount of water vapor. The profiles are shown at the substellar point, but horizontal variations are fairly small above the 0.1 mbar level due to an efficient transport. Decreasing the surface pressure increases the water vapor ratio in the upper atmosphere drastically.

that the detection can actually be achieved with VLT by coupling SPHERE with the future high-resolution spectrometer ESPRESSO (first light expected in 2017). The idea is to first use SPHERE to reduce the stellar light by a factor $10^3 - 10^4$ at 37 mas from Proxima ($\sim 2\ \lambda/D$ at 700 nm) and then to search with ESPRESSO for the Doppler shifted planet signature on the $\sim$ 37 mas-radius annulus around the star when RV ephemeris predict maximal angular separation. The planet and stellar signals could indeed be separated thanks to cross-correlations with molecular high-resolution fingerprints, which could be specific to the planet, such O_2, or reflected and Doppler shifted in both cases by the planetary orbital motion. Such a planet-star disentangling was already achieved for non-transiting unresolved hot Jupiters with a contrast of $\sim 10^{-4}$ (Brogi et al., 2014). Lovis et al. (2017) expect a similar efficiency, which on top of the stellar extinction provided by SPHERE would allow them to reach the $\sim 10^{-7}$ contrast of Proxima b.
The combination of contrast and separation that is required to image Proxima b should be achieved with future larger telescopes such as the E-ELT (39 m) or the TMT (30 m). For the E-ELT, 37 mas corresponds to $7\lambda/D$ at 1 μm. At such angular separation, E-ELT instrumentation such as PCS (Kasper et al., 2013) is planned to achieve contrasts of $10^{-7} - 10^{-8}$, a performance that is sufficient to aim to directly characterizing Proxima b.

Following Selsis et al. (2011), we can use GCM simulations to compute disk-integrated fluxes in the spectral bands of the GCM and for any observing geometry. Figure 3.8 and 3.10 present synthetic observables at visible-NIR wavelengths obtained with a simulation for an aquaplanet with an Earth-like atmosphere (1 bar of N_2, 376 ppm of CO_2, and variable H_2O) and a synchronous rotation. Figure 3.8 shows reflection spectra at the spectral resolution of the GCM for different phase angles and the main bands observable through Earth's atmosphere. The thickness of the curves indicates the range of contrast values that is obtained for a given phase angle, depending on the inclination of the system. For instance, both polar and equatorial observers see the planet with a 90° phase angle but they do not receive the same spectral irradiance. In Figure 3.8 the radius of the planet is kept constant so the contrast variation at a given wavelength is only due to the observing geometry. However, the actual mass of the planet depends on the inclination of the orbit. In Figure 3.10, which shows reflection phase curves for three different inclinations and four spectral bands, we assumed the following relationship between radius and inclination of $R_\mathrm{p} \propto (M/\sin i)^{0.27}$.

We can see on these phase curves that low inclinations have the advantage of keeping the full orbit outside an inner working angle of twice the diffraction limit without losing contrast because of the increased planetary radius. Of course, for very low inclinations, the planet could no longer be considered "Earth-like". For instance, if $i < 10°$ (1.5 % of randomly oriented orbits) then the planet would be at least eight times more massive than the Earth. Small phase angles produce the highest contrast but imply small angular separations and short wavelengths. For phase angles smaller than 30°, imaging with a 39 m telescope is doable only in bands I and J, but with a contrast larger than 10^{-7}. For phase angles between 60 and 90°, the H and K bands can also be considered but with contrasts below 10^{-7}. Imaging seems out of reach in the L band ($3 - 4$ μm) with a 39 m aperture. Considering the wavelength dependency of the contrast, the diffraction limit and the fact that adaptive optics is challenging in the visible, the J band seems to represent a promising opportunity.

Sensitivity should not be an issue to directly detect Proxima b with the E-ELT. We calculated the exposure duration required to achieve a SNR of 10 per spectral channel with a spectral resolution of 100, assuming that the angular separation would be sufficient for the noise to be dominated by the sky

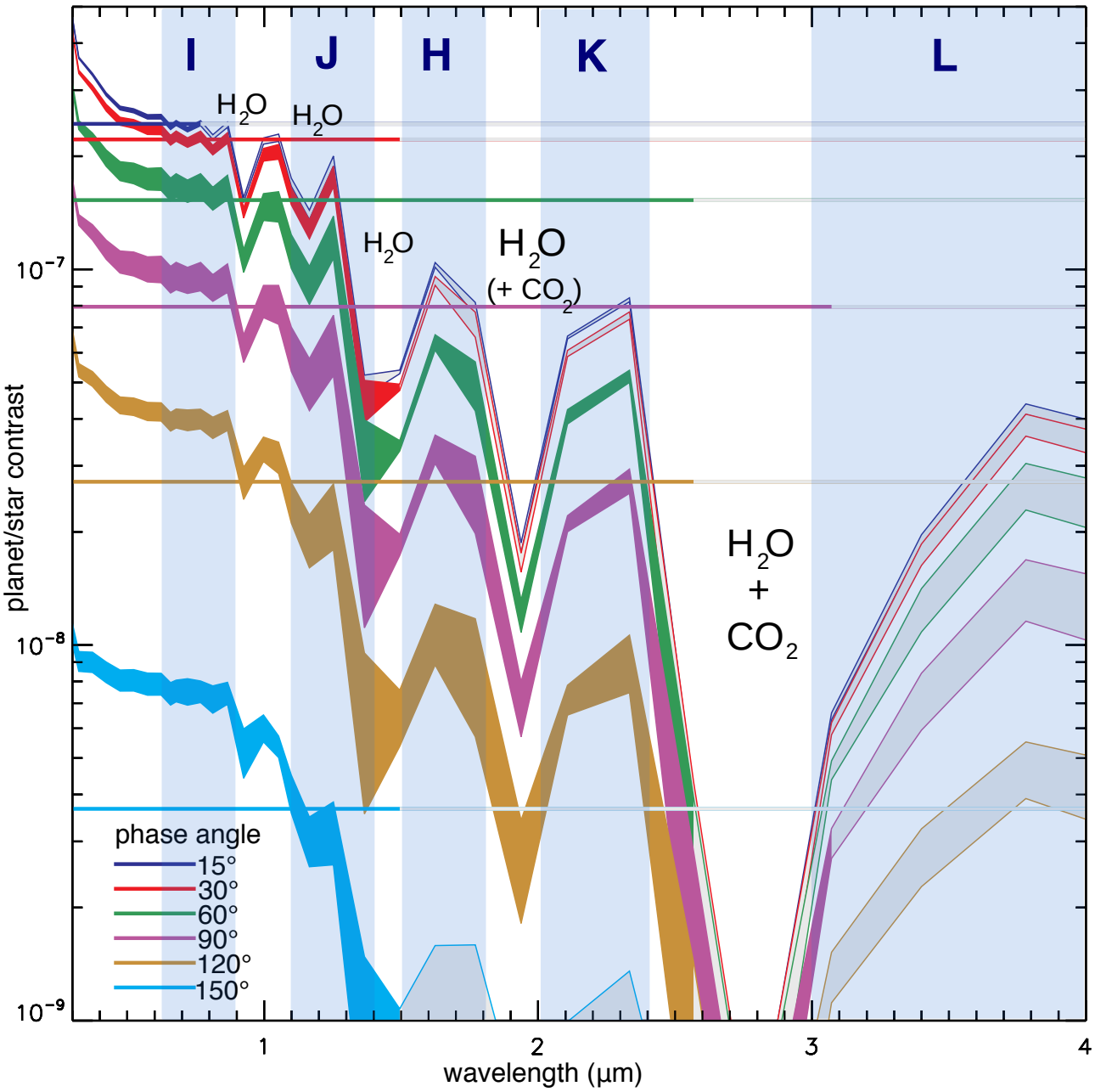

Figure 3.8: Reflection spectra computed for the synchronous case with an Earth-like atmosphere. Each color corresponds to a phase angle (0° meaning that the observer looks at the substellar point and 90° at a point on the terminator). The thickness of the curve indicates the range of possible values depending on the actual observing geometry (see text and Fig. 3.9). Straight lines are calculated for a constant surface albedo of 0.4. Curves are plotted in gray when the angular separation falls below twice the diffraction limit of the E-ELT ($2 \times 1.2\lambda/D$). These plots are obtained with a fixed planetary radius of 1.1 $R_\oplus$. Because these plots do not include the contribution from the thermal emission, the contrast at 3.5–4 μm is underestimated by a factor of ~ 2.

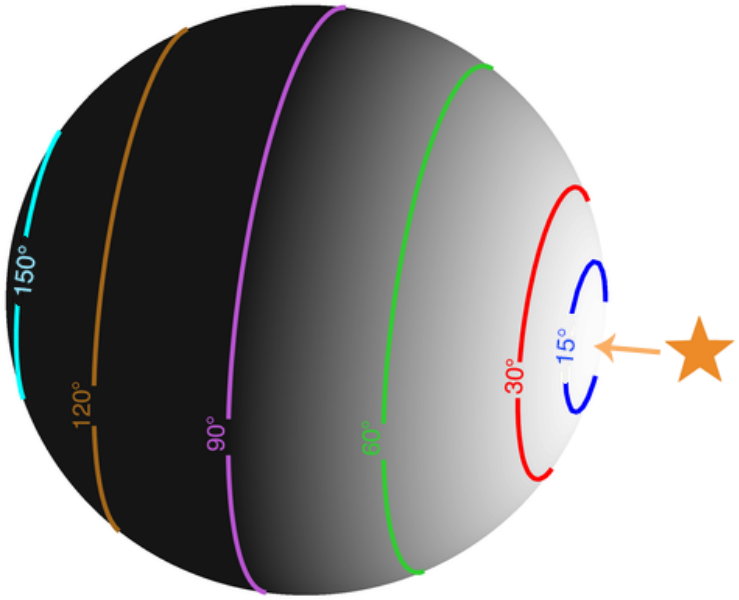

Figure 3.9: Observing geometries for spectra computation. Emission and reflection spectra are presented in this article for phase angles of 15, 30, 60, 90 120, and 150°.

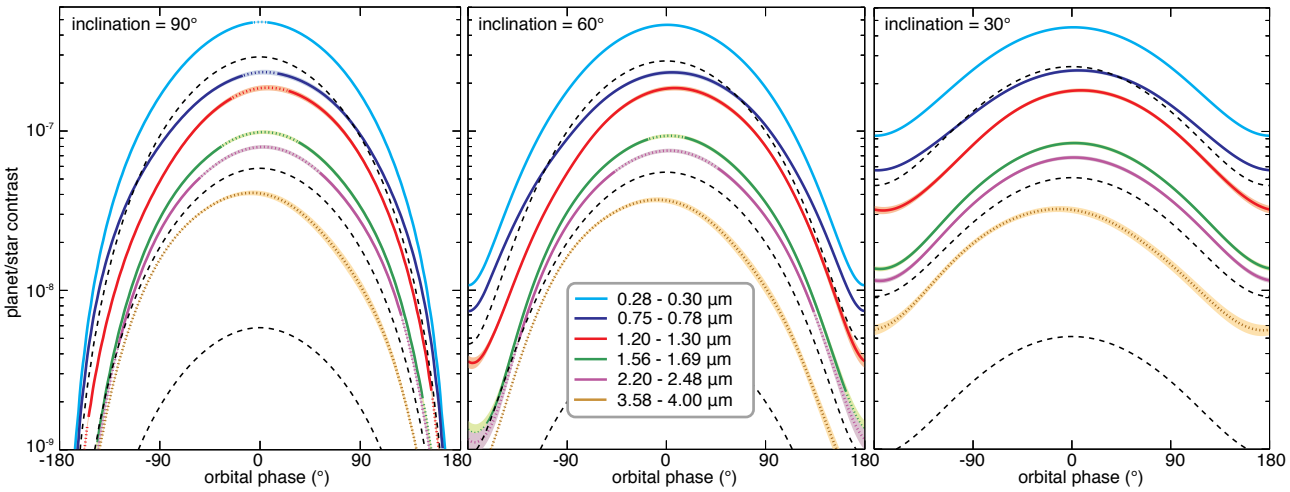

Figure 3.10: Reflection phase curves computed for the synchronous case with an Earth-like atmosphere for 4 spectral bands falling into the I, J, H K, and L windows. Shadowed areas indicate the 1-sigma variability due to meteorology (mainly changing cloudiness). The dashed curves are calculated with a constant surface albedo of 0.5, 0.1, and 0.01. Curves are dotted when the planet is inside an inner working angle of twice the diffraction limit of the E-ELT ($2 \times 1.22\lambda/D$). Contrary to Fig 3.8, these plots include a dependency of the planetary radius on the inclination of $R \propto (M_{min}/\sin i)^{0.27}$. We note that 60° is the median value for a random distribution of inclinations.

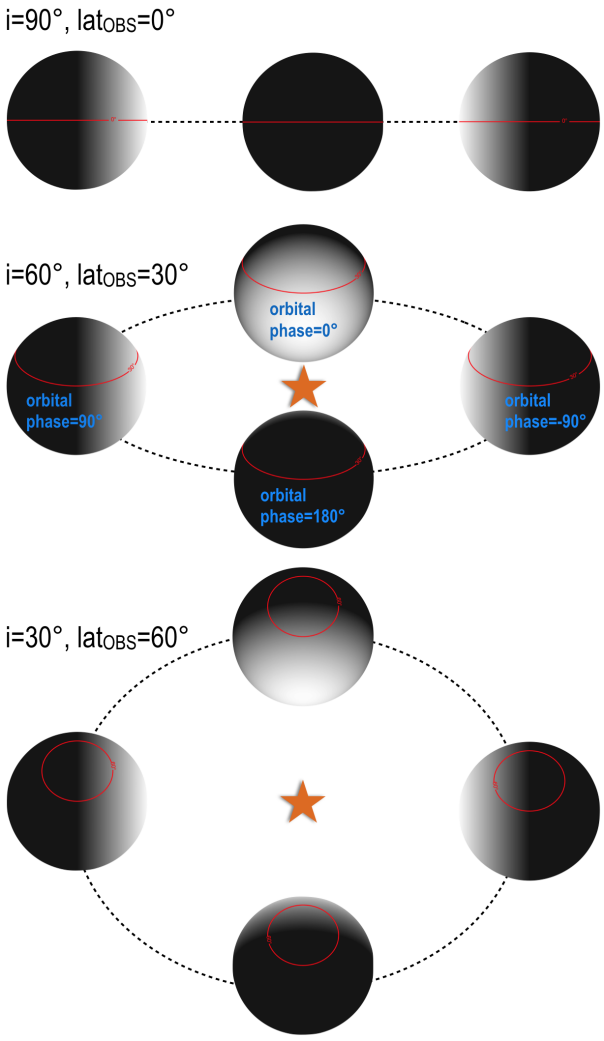

Figure 3.11: Phase curves and observing geometries. We computed reflected and emitted light curves for 3 inclinations as follows: 90, 60, and 30° corresponding to subobserver latitude of 0, 30, and 60°, respectively (as the we assumed a null obliquity). The subobserver latitude is indicated with a red line. In the Appendix 3.11.2, phase curves are shown only for an inclination of 60° (the median value for randomly oriented orbits).

background (continuum + emission lines[2]) and not Speckle noise. We assumed an overall throughput of 10%, integrated the background over an Airy disk and used the planetary signal derived from the GCM simulations for an inclination of 60° and a phase angle of 60°. We obtained integration times of 5 min at 0.76, 1.25, and 2.3 μm, and 30 min at 1.6 μm.

Assuming that adaptive optics would provide sufficient efficiency to reach the required contrast and angular resolution at such short wavelengths, an O_2 signature could be searched at 0.76 μm. This would require a high resolution to separate the planet lines from the telluric lines, taking advantage of the Doppler shift of the two components. Snellen et al. (2015) suggest that a resolution of 100,000 may be necessary for that, which matches that of the planned HIRES instrument[3]. This would imply tens of observing nights to reach a SNR of 10 per spectral channel, but previous observations (e.g., Snellen et al., 2010; Brogi et al., 2012; Snellen et al., 2014) have shown that a several σ detection of a high-resolution signature by cross-correlation can be achieved with a much lower SNR per channel (< 1) and hence a much shorter integration time. Snellen et al. (2015) estimated that it could be doable in ten hours with the instrument IFU/E-ELT.

At 3 μm, the maximum angular separation of 37 mas corresponds to twice the diffraction limit of a 39 m aperture. Above this wavelength, imaging Proxima b requires larger apertures and the Earth atmosphere (absorption and emission) becomes a major obstacle. The planet/star contrast at thermal wavelengths can, however, be orders of magnitude higher than the contrast produced by reflected wavelengths. The Earth/Sun contrast reaches $\sim 5 \times 10^{-7}$ at 10-12 μm, but Proxima is a star ~ 1000 times dimmer than the Sun while its planet b could emit about the same as Earth. Contrast values of up to $\sim 5 \cdot 10^{-4}$ could thus be expected. In addition, thermal wavelengths provide a unique way to constrain atmospheric properties (temperature mapping at different pressure levels, day-night heat redistribution, greenhouse effect, detection of IR absorbers such as H_2O, CO_2, O_3, and CH_4). For this reason, space telescopes using IR nulling interferometry have been considered in the past (Darwin, TPF-I) and will certainly have to be reassessed in the future as one of the main ways to characterize the atmosphere and climate of terrestial planets in nearby systems. In this context, we computed mid-IR spectra (Figure 3.12) and thermal phase curves (Figure 3.13) obtained with the same simulation used to produce short wavelength observables.

The phase curves we obtain are rather flat except in the 8–12 μm atmospheric window where the dayside emits significantly more than the nightside. Because the flux received by the planet is rather low, the updraft of clouds and humidity on the dayside remains moderate and restricted within a small region around the substellar point. For this reason we do not find that most of the cooling occurs on the nightside as found by Yang et al. (2013), Gómez-Leal et al. (2012), or Bolmont et al. (2016b) for planets with an Earth-like irradiation.

Considering the history of the planet, and in particular its hot past, an Earth-like atmosphere may not be the most relevant case to address observation prospects. In the Appendix 3.11.2 we present spectra and phase curves obtained with different compositions and rotations. As the planet could have experienced a fate similar to Venus (Ingersoll, 1969), we also present reflection spectra and phase curves for a Venus-like atmosphere (Lebonnois et al., 2015), including sulphur-bearing aerosols known to produce a high albedo at visible wavelength, and then exposed to the irradiance of Proxima at the

[2]We used the ESO documentation for the background: http://www.eso.org/sci/facilities/eelt/science/drm/tech_data/background/

[3]Documentation for E-ELT instruments HIRES and IFU can be found at https://www.eso.org/sci/facilities/eelt/docs/

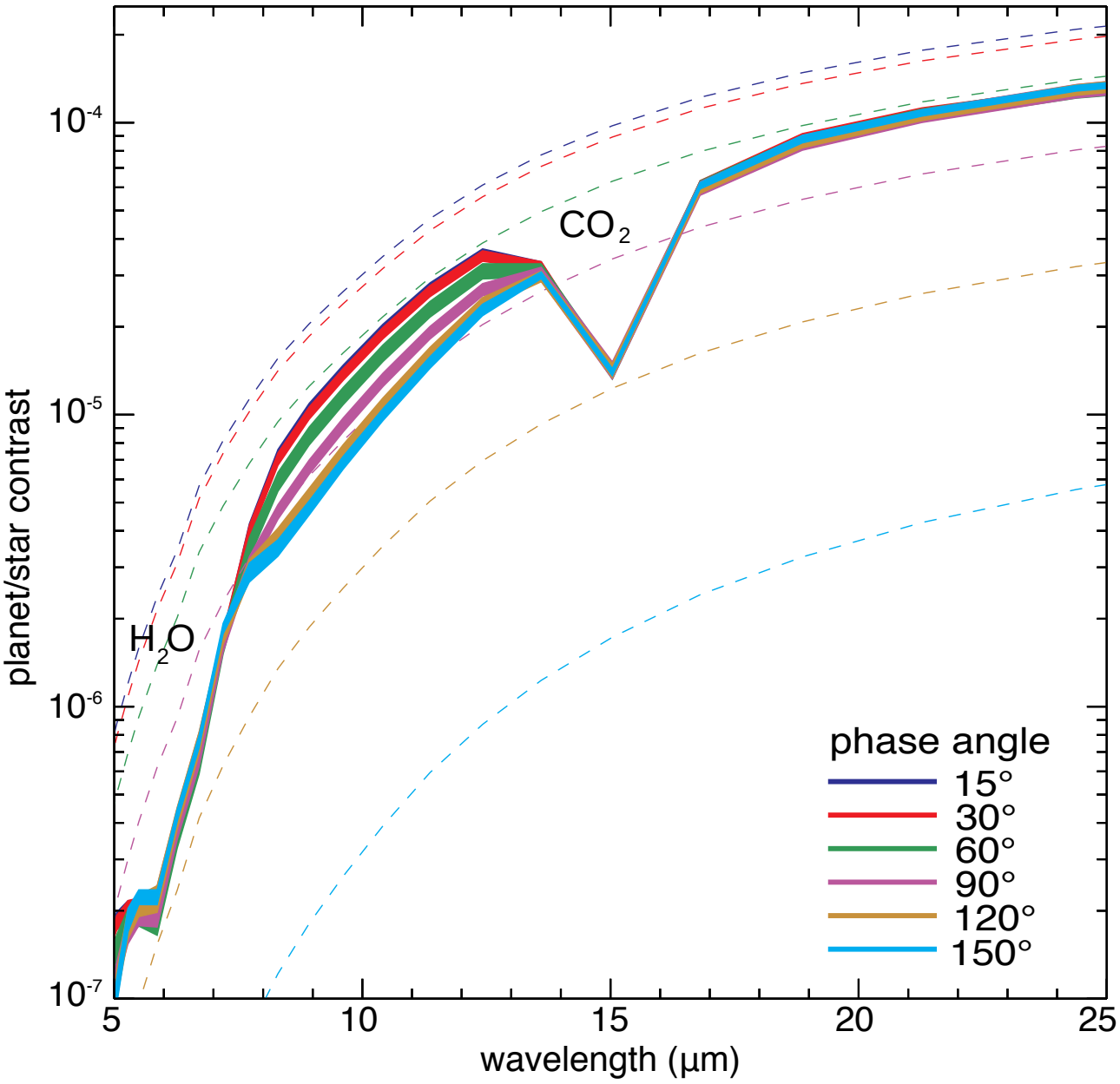

Figure 3.12: Emission spectra computed for the synchronous case with an Earth-like atmosphere. Each color corresponds to a phase angle. The thickness of the curves indicate the variability associated with inclination. Dashed lines are calculated for a planet with no atmosphere with a constant surface albedo of 0.2. These plots are obtained with a fixed planetary radius of 1.1 $R_\oplus$, whatever the inclination of the orbit.

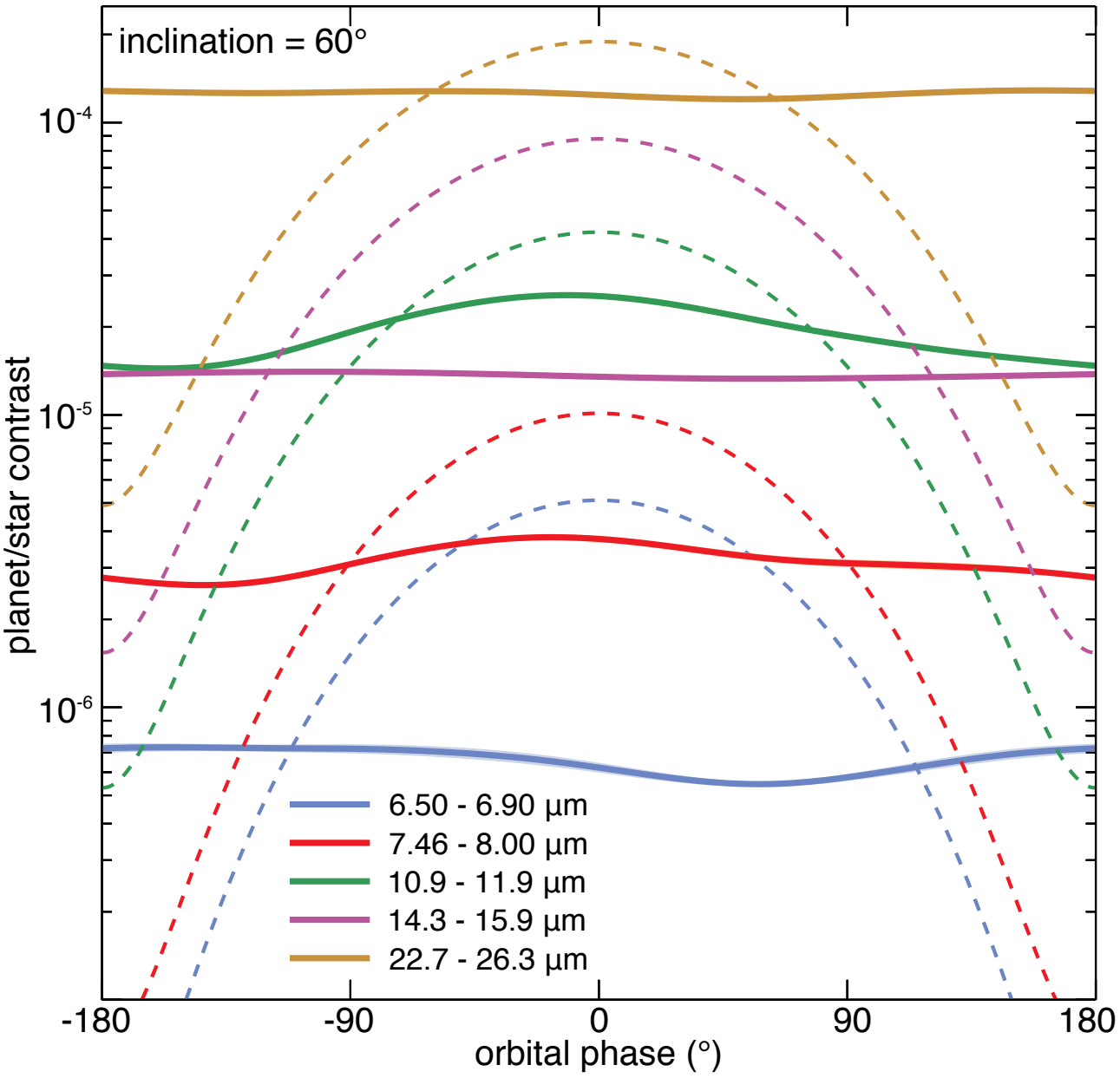

Figure 3.13: Emission phase curves computed for the synchronous case with an Earth-like atmosphere, for 4 spectral bands used in the GCM. Gray areas indicate the 1-sigma variability due to meteorology (mainly changing cloudiness). Dashed curves are calculated for a planet with no atmosphere with a constant surface albedo of 0.2. Contrary to fig 3.12, these plots include a dependency of the planetary radius on the inclination of $R \propto (M/\sin i)^{0.27}$.

orbital distance of Proxima b.

3.8.2 Prospects with James Webb Space Telescope

Observing the modulation due to thermal phase curves does not require a transit and has been achieved by photometry in the case of both transiting and non-transiting hot Jupiters (Crossfield et al., 2010). Although very challenging, in particular because of star variability, this observation can be attempted with James Webb Space Telescope (JWST). The planet-star contrast in the mid-IR can reach 10^{-4} but only the amplitude of the modulation can be detected. This amplitude depends strongly on the thickness of the atmosphere as shown by the phase curves presented in the Appendix 3.11.2. Dense atmospheres lower the day-night temperature contrast and therefore produce rather flat light curves and modulation below 10^{-5} in contrast. On the other hand, planets with no or a tenuous atmosphere (< 10 mbar) produce contrast amplitudes of $10^{-5}-10^{-4}$ in the wavelength range $8-15$ μm. Fig 3.14 shows the amplitude of the contrast modulation for a planet with no atmosphere, in radiative equilibrium, and for two inclinations. The modulation decreases with the inclination but this decrease is compensated by the increase of the mass and thus the radius. One can see that 1 hr exposure with the JWST at R=10 facilitates beating the stellar photon noise above 6 μm. According to Belu et al. (2011), the total noise is usually within 2-3 times the stellar photon noise for wavelengths below 15 μm; above this limit the thermal emission from the telescope dramatically degrades the observations. Detecting these modulations with JWST would be extremely challenging because of stellar variability and flares. But flux variations are smaller in the infrared and the orbital period and ephemeris of the planet are known, which considerably helps planning short exposure over several orbits, in particular near the peak at superior conjunction. Measuring a modulation would point to planets with no dense atmosphere such as Mercury or Mars. In theory, measurement at different wavelengths could be used to find atmospheric signatures (Selsis et al., 2011), constrain the radius, albedo, and inclination of the planet (Maurin et al., 2012) as well as its rotation (Selsis et al., 2013).

3.9 Discussions

The modeling work performed here to explore the possible climates and observability of Proxima b remains speculative. Major surprises in the composition of the atmosphere or the nature of the planet cannot be discarded. Within the known uncertainties, we can list the following points:

1. **The luminosity of Proxima Centauri is not perfectly known:** Using interferometry with two VLT telescopes, Demory et al. (2009) measured the radius of Proxima Centauri and its effective temperature and found R=0.141 $\pm$ 0.007 $R_\odot$ and T_{eff} = 3098 $\pm$ 56 K, which yields a bolometric luminosity of $0.00165 \pm 0.00012\, L_\odot$. In this study we used a value of $0.0017\, L_\odot$ while Anglada-Escudé et al. (2016) give $0.00155\, L_\odot$ as a median value that is derived from Boyajian et al. (2012). Both values are within the uncertainty of Demory et al. (2009) and Boyajian et al. (2012). Although changing the actual bolometric flux received by Proxima b would slightly alter surface and atmosphere temperatures found for a given atmospheric composition, this discrepancy does qualitatively not impact our results. Changing the actual bolometric flux received by Proxima b would of course alter the detailed relationship between atmospheric pressure and temperature. Considering the importance of this system, the community should agree on a standard

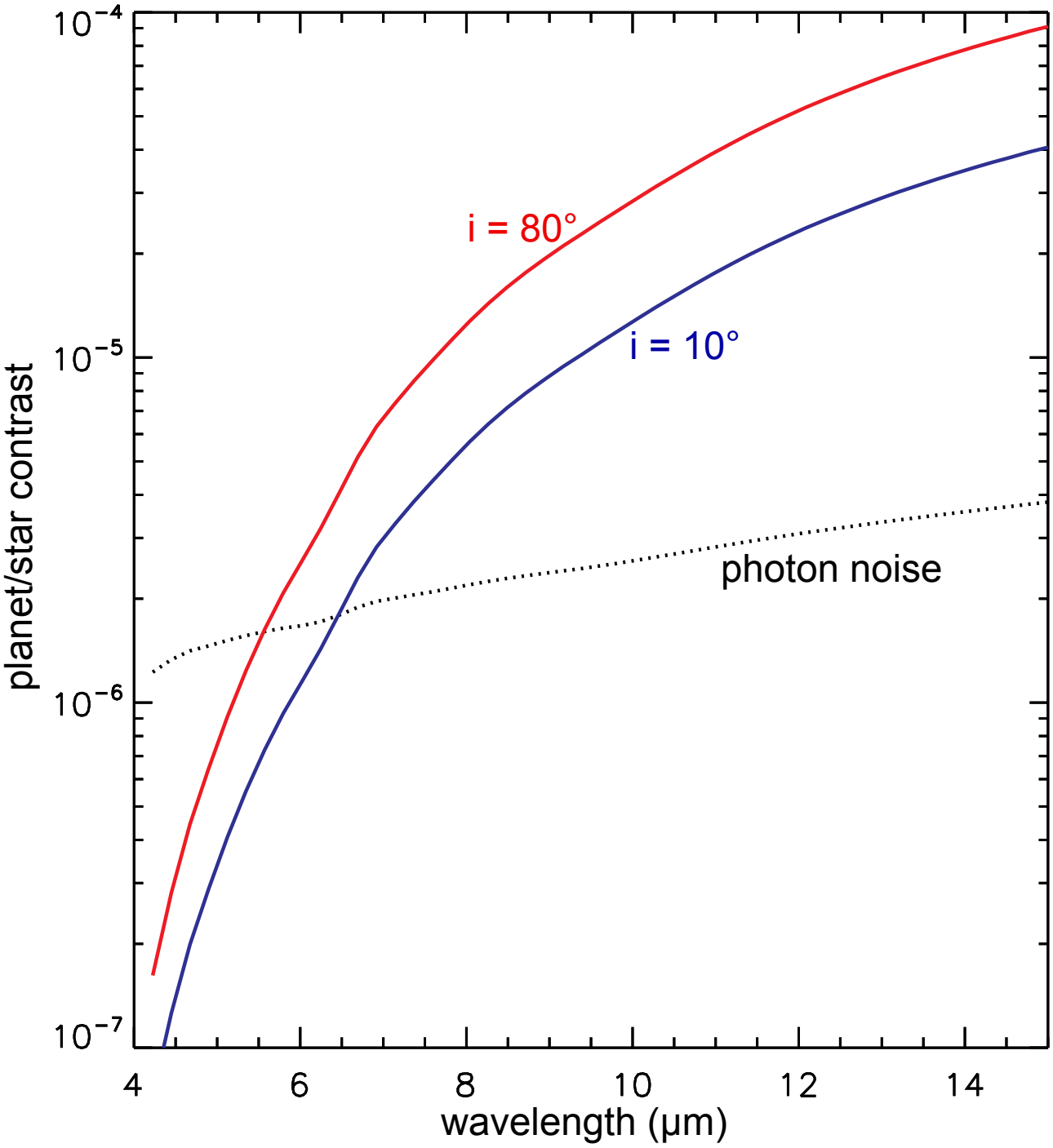

Figure 3.14: Observability of the photometric modulation due to thermal phase curves with JWST. The amplitude of the modulation is calculated for a planet with no atmosphere and a Bond albedo of 0.2 and with a radius that scales with the inclination as $R \propto (M/\sin i)^{0.27}$. The noise is computed for a 1 hr exposure, a spectral resolution of 10, and the collecting area of the JWST (25 m^2).

and calibrated irradiance spectrum of Proxima to be used for climate and habitability studies.

2. **The amount of background gas:** Some simulations in this work included background N_2 while others did not. It would require dedicated absorption coefficients to perform all the GCM simulations with a fixed N_2 partial pressure. Moreover, we have bad constraints on the amount of background gas available on the planet because of, first, uncertainties on the mass of Proxima b and, second, the possibility that the background gas was lost to space as a result of the high XUV flux of Proxima Centauri (Ribas et al., 2016).

3. **The convection scheme:** It should be kept in mind that models like Yang et al. (2013) find higher albedos in the substellar area owing to a different convection scheme and possibly different cloud parametrizations. As Proxima b is moderately irradiated, this discrepancy might not be as important as for the near-inner edge cases studied by Yang et al. (2013).

4. **The oceanic circulation:** We recall that our results in the aquaplanet regime neglected the effect of oceanic transport. This is an important era of future improvement, although it adds several new unconstrained ingredients, such as the presence and location of continents.

5. **Climate retroactions:** We assumed in this study that the amount of volatiles (H_2O, CO_2, and N_2) should be uncorrelated and therefore that each configuration of volatile inventory could be achievable by Proxima b. In fact, climate retroactions such as the carbonate-silicate cycle (Walker et al., 1981) could favor some of these configurations by linking the amount of carbon dioxide and water.

3.10 Conclusions

In this study, we explored the possible climates of Proxima Centauri b for a wide range of volatile inventories of water, carbon dioxide, and nitrogen. It appears from our results that the habitability of the planet is possible for a very broad range of atmospheric pressures and compositions, as shown by the size of the blue regions in Figure 3.1.

In a nutshell, the presence of surface liquid water requires either a large surface inventory of water (a global ocean able to resupply H_2O to the dayside by deep circulation) or an atmosphere with a strong enough greenhouse effect that increases surface temperatures above the freezing point of water *everywhere*.

Apart from receiving the necessary insolation, this study tells us that the key ingredient to the habitability of a planet is the retention of all volatiles, such as water, of course, but also non-condensible gases (with a greenhouse effect or not) to warm surface cold traps. Ribas et al. (2016) showed that it is possible that the planet lost large amounts of water. However, this work shows that even with extremely low amounts of water (a few 10^{-3} Earth ocean content for the synchronous case and less than 10^{-5} for the asynchronous case), there are CO_2 pressures that allow surface liquid water.

More generally, these conclusions are not restricted to the case of Proxima b. In fact, any low-obliquity planet within the classical habitable zone of its star should be in one of the climate regimes discussed here, although the limits between the various regimes would shift quantitatively with the planet parameters (e.g., the insolation).

Prospects for direct imaging with E-ELT are extremely promising: the star-planet separation reaches 9.5 λ/D at 760 nm (wavelength of the O_2 band) with a contrast of $0.9 - 5 \times 10^{-7}$ (depending on atmospheric and surface composition, and planetary radius) and 3.6 λ/D at 2 μm with a contrast of $10^{-7} - 10^{-8}$. J band (1.1-1.4 μm) offers a fine trade-off in terms of separation, contrast, and constraints on adaptive optics. The brightness of the planet should allow high-resolution spectroscopy and the search for a variety of molecular signatures, including O_2, H_2O, CO_2, and CH_4.

Thermal phase curve modulations are observable - in theory - with JWST, with a contrast of $\sim 10^{-5}$ at 10 μm but will be challenging because of stellar variability. More accurate mid-IR spectroscopy would probably require space-based interferometry. Most of our knowledge on planetary atmospheres and habitability come from the study of Venus, Mars, and Earth. Proxima b could potentially be the fourth terrestrial planet to confront all that we know on these domains.

3.11 Appendix

3.11.1 Computation of maximal ice thickness before basal melting

Because the ice thermal conductivity can vary substantially with temperature according to the relation $\lambda_{\rm ice}(T)=A/T$ with A=651 W m^{-1} (Petrenko and Whitworth, 2002), the temperature profile inside an ice layer in equilibrium follows an exponential law from which we derive a maximum thickness $h_{\rm ice}^{\rm max}$ before melting (Abbot and Switzer, 2011),

$$h_{\rm ice}^{\rm max} = \frac{A}{F_{\rm geo}} \ln \left(\frac{T_{\rm melt}}{T_{\rm surf}} \right), \tag{3.2}$$

where $F_{\rm geo}$ is the internal heat flux and $T_{\rm melt}$ is the melting temperature of ice at the base of the glacier. For pressure lower than 100 bar (ice thickness lower than $\sim$ 1 km), $T_{\rm melt}$ is roughly constant and equal to 273 K. However, this assumption does not work for higher pressures. Thus, we use the following parametrization for the melting curve of ice (Wagner et al., 1994):

$$\begin{aligned} P_{\rm melt}(T) = P_{\rm ref} \Bigg[& 1 - 0.626 \times 10^6 \left(1 - \left(\frac{T}{T_{\rm ref}} \right)^{-3} \right) \\ & + 0.197135 \times 10^6 \left(1 - \left(\frac{T}{T_{\rm ref}} \right)^{21.2} \right) \Bigg], \end{aligned} \tag{3.3}$$

where $T_{\rm ref}$ and $P_{\rm ref}$ are the temperature and pressure of the triple point of water.

Using the relation $h_{\rm ice}^{\rm max} = \frac{P_{\rm melt}-P_{\rm surf}}{\rho_{\rm ice}\ g}$ and following a similar approach to Leconte et al. (2013b), we can solve the system of equations (3.2, 3.3) implicitly (and numerically) and find the thickness at which melting occurs at the base of the glaciers.

3.11.2 Spectra and phase curves

We present here synthetic spectra and phase curves obtained with some of the GCM simulations. Reflected and emitted spectra are obtained as in Fig. 3.8 and Fig. 3.12, respectively. Reflection and thermal phase curves are computed as in Fig. 3.10 and Fig. 3.13, respectively, for a 60° inclination and a radius R= $(M_{min}/\sin 60°)^{0.27} = 1.11$ R$_\oplus$. Color codes for phase angles and wavelengths are the same as for figures in the main text.

To describe each different type of observables (reflected spectra, reflected lightcurves, thermal spectra, and thermal lightcurves), we start from dry cases with tenuous atmosphere, which exhibit the most simple features, and progress toward dense and humid atmospheres that combine more effects, including clouds.

3.11.2.1 Reflected spectra

Reflected spectra are shaped by Rayleigh scattering from the gas, Mie scattering from clouds, molecular absorption features, and surface reflectivity.

- Dry case, Earth-like atmosphere (Fig. 3.17): We can see the decrease of the albedo with increasing wavelengths in the UV-visible domain due to the combination of Rayleigh scattering and the constant surface albedo of 0.2. CO_2 absorption features can be seen at 1.9 and 2.6-2.7 μm. The rotation mode

of the planet does not affect the observables.
- Dry case, 1 bar of CO_2 (Fig. 3.18): same as above with more and deeper CO_2 features.
- Aquaplanet, mainly frozen, 10 mbar of N_2; 376 ppm of CO_2 (Fig. 3.19): Rayleigh scattering is negligible and the only atmospheric features are the H_2O bands. The drop of albedo between 1 and 1.5 μm is produced by the wavelength-dependent reflectivity of ice included in the model (Fig. 3.2). This drop is attenuated in the synchronized case because the dayside is partly covered by liquid water (Fig 3.6) whose reflectivity is constant with wavelength ($\sim 7\%$) and has a value close to that of ice in the infrared ($\sim 5\%$). For this reason, the overall albedo is also higher for the 3:2 rotation, the surface being mostly covered by ice.
- Aquaplanet, mainly frozen, 1 bar of N_2; 376 ppm of CO_2 (Fig. 3.20): In addition to the features described in the previous case, this configuration also exhibits signatures of the larger water vapor content due to higher temperatures: deeper H_2O absorption bands and a larger spatial and temporal variability due to meteorology. In synchronous rotation, the Rayleigh slope can be seen but not in the non-synchronous case because the albedo of the icy surface dominates over the albedo due to Rayleigh scattering.
- Aquaplanet, 1 bar of CO_2 (Fig. 3.21): This case exhibits the strongest molecular absorptions due to large columns of both CO_2 and water vapor. The low albedo of the liquid water surface reveals the atmospheric Rayleigh slope at wavelength lower than 600 nm. The spectrum of the synchronous case is very sensitive to the observing geometry for a given phase angle. As seen in Fig 3.16, this is due to the concentration of clouds at low latitude and eastward of the substellar point in the synchronous case, while the 3:2 case has very uniform cloud coverage.

3.11.2.2 Reflected phase curves

Departures between the observed phase curve and phase curve produced by a sphere with uniform surface albedo are due to longitudinal variations of reflectivity on the dayside, which, in our cases, can be due to cloud coverage or change in the nature of the surface (liquid versus icy).
- Dry case, Earth-like atmosphere (Fig. 3.23): The lightcurves are those expected for a sphere with a uniform albedo. As the atmosphere is very transparent at visible-NIR wavelengths, the value of this albedo is 0.2 (the wavelength-independent value attributed to the dry surface in the model) for all the bands except the one in the UV (cyan) that exhibits a higher albedo from Rayleigh scattering.
- Dry case, 1 bar of CO_2 (Fig. 3.24): same as above, except for the 1.6 (green) and 1.25 μm (red) bands that are attenuated by CO_2 absorption.
- Aquaplanet, mainly frozen, 10 mbar of N_2; 376 ppm of CO_2 (Fig. 3.25): We note again the overall decrease of albedo with increasing wavelength (a property of ice). While the phase curves of the asynchronous case present no longitudinal change of reflectivity, the phase curves of the synchronous case show a flattening at opposition at wavelength below 1.3 μm, which is due to the different albedo of ice and liquid water. This decrease in albedo at small phase angles is therefore a signature of the "eye ball" configuration that is observable here because the atmosphere and cloud cover are thin enough to give access to the surface reflectivity.
- Aquaplanet, mainly frozen, 1 bar of N_2; 376 ppm of CO_2 (Fig. 3.26): The "eye ball" signature of the synchronous case is still noticeable at wavelengths not absorbed by water vapor and not dominated by Rayleigh scattering, so typically between 0.5 and 0.8 μm. Clouds reduce the signature without hiding it completely as they cover the dayside ocean (see Fig. 3.15) only partially and because their

albedo is still lower than that of ice at these wavelengths. Because thick clouds tend to accumulate eastward of the substellar point, the phase curves are asymmetric except at UV wavelengths that are backscattered above the clouds. In the asynchronous case clouds are uniformly distributed in longitude and do not produce significant asymmetry.
- Aquaplanet, 1 bar of CO_2 (Fig. 3.27): Both the synchronous and asynchronous cases exhibit a high variability due to meteorology, which is a result of high temperatures and strong water cycle. The visible and NIR phase curves of the synchronous case are very asymmetric. The reason is the same as in the previous case but with a sharper transition in cloudiness with a clear sky west of the substellar point and a dense cloud patch east of the substellar point, as seen on Fig. 3.16.

3.11.2.3 Emission spectra

Thermal emission spectra are influenced by the temperature distribution at the surface at wavelengths where the atmosphere is transparent and by the thermal structure of the atmosphere at other wavelengths. In theory, emission spectra are also shaped by the surface emissivity but in our model it is fixed to unity in most cases.
- Dry case, Earth-like atmosphere (Fig. 3.29): In the synchronous case, the spectra are similar to those of sphere in radiative equilibrium except in the CO_2 band, which is emitted by a horizontally uniform layer of the upper atmosphere. At high phase angle and long wavelengths, differences from the sphere in radiative equilibrium appear owing to the transport of heat toward the nightside that contributes to the emission. In 3:2 rotation, the spectra are similar but more sensitive to the observing geometry at a given phase angle as the surface temperature map is no longer symmetric relative to the substellar point.
- Dry case, 1 bar of CO_2 (Fig. 3.30): In addition to the 15 μm band, high pressure CO_2 features including the hot bands at 9.5 and 11 μm and a CIA feature between 6.5 and 8 μm. These absorption features probe uniform high-altitude atmospheric layers and do not depend on the subobserver position, while windows probe the surface and exhibit a dependency on the observing geometry (synchronous) and variability (3:2).
- Aquaplanet, mainly frozen, 10 mbar of N_2; 376 ppm of CO_2 (Fig. 3.31): The spectra are featureless except for a shallow H_2O signature at 6-7 μm in the synchronous case. They depart from the spectra of a sphere in radiative equilibrium, in particular at long wavelengths, as the surface temperature does not drop below 200 K (synchronous) and 150 K (3:2) thanks to a redistribution of latent heat.
- Aquaplanet, mainly frozen, 1 bar of N_2; 376 ppm of CO_2 (Fig. 3.32): The spectra are similar to a present Earth spectrum, without the O_3 band and with shallower water vapor absorption due to lower temperatures.
- Aquaplanet, 1 bar of CO_2 (Fig. 3.33): There are no difference between the synchronous and 3:2 cases. All atmospheric windows are closed by either CO_2 or H_2O absorption and the emerging spectrum come from different but horizontally uniform layers.

3.11.2.4 Thermal phase curves

Emission light curves are controlled by the temperature longitudinal distribution at the surface if the atmosphere is transparent in the observed band or at the emitting atmospheric layer otherwise.

- Dry case, Earth-like atmosphere (Fig. 3.34): In both cases, the 15 μm CO_2 band is emitted from a uniform high altitude layer, which produces a flat phase curve. In the synchronous case, other bands exhibit phase curves that are similar to those of an airless planet except at high phase angle and long wavelengths, where the warming of the nightside by atmospheric circulation flattens the curves. In the 3:2 case, the flattening is more pronounced and is associated with a lag as surface temperature peaks in the afternoon.
- Dry case, 1 bar of CO_2 (Fig. 3.35): similar to the dry Earth case except that the 6.7 μm band is flattened due CO_2 CIA absorption.
- Aquaplanet, mainly frozen, 10 mbar of N_2; 376 ppm of CO_2 (Fig. 3.36): Here, the 15 μm CO_2 band is no longer opaque and exhibits the same behavior as the other bands. Compared with the previous case, and despite a more tenuous atmosphere, phase curves are more flattened because of the additional redistribution of latent heat (and the relatively high surface thermal inertia for the asynchronous case).
- Aquaplanet, mainly frozen, 1 bar of N_2; 376 ppm of CO_2 (Fig. 3.37): Efficient zonal heat redistribution flattens all the phase curves in the 3:2 case. In the synchronous case, the 11 and 7.7 μm bands coming from either surface or clouds show an increase at small phase angle with some asymmetry owing to the patch of clouds eastward of the substellar point (see Fig. 3.15. The 6.7 μm band emitted in the troposphere is flat with a slight decrease due to the clouds as well. The 15 and 24 μm bands are flat and not affected by clouds, emerging from higher levels.
- Aquaplanet, 1 bar of CO_2 (Fig. 3.38): There are no difference between the synchronous and 3:2 cases. All atmospheric windows are closed by either CO_2 or H_2O absorption and the emission comes from different but horizontally uniform layers. This produces flat light curves at different brightness temperatures with some shallow attenuation by the clouds at the most transparent wavelengths (11 and 7.7 μm).

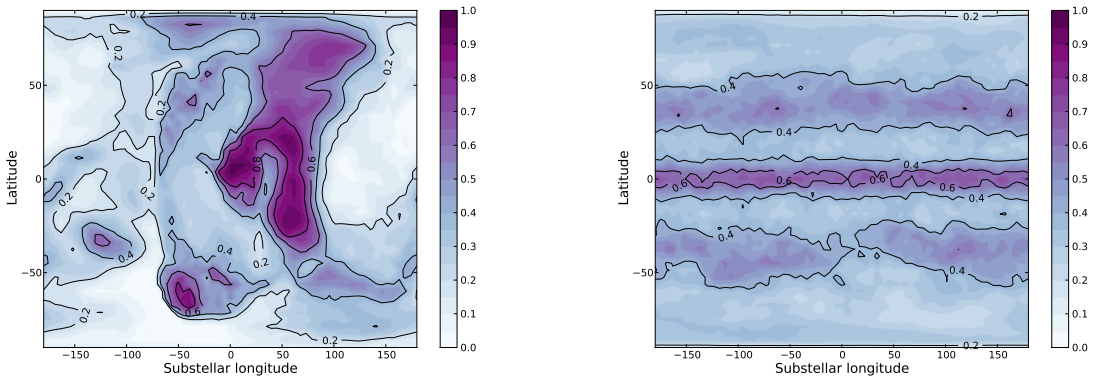

Figure 3.15: Cloud maps for an aquaplanet with an Earth-like atmospheric composition (1 bar of N_2, 376 ppm of CO_2). Left : synchronous rotation. Right : 3:2 spin-orbit resonance. In both cases, longitude is given relative to the substellar point. Colors indicate the fractional cloud cover, averaged over 2 orbits.

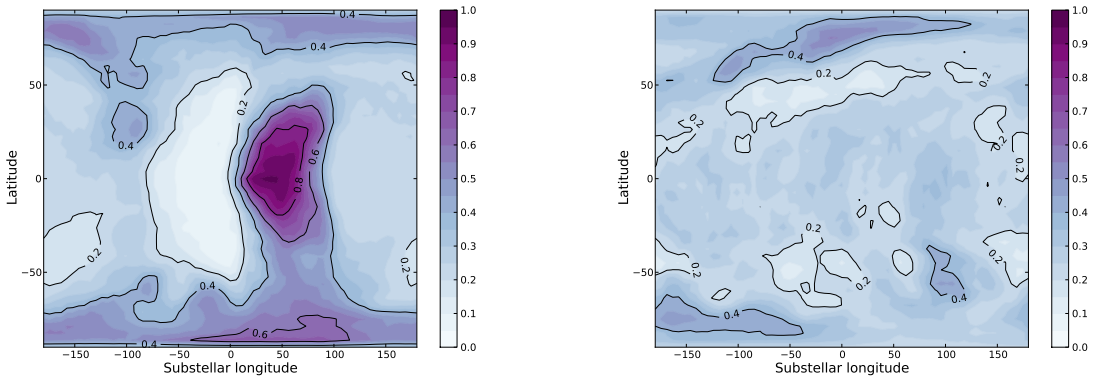

Figure 3.16: Cloud maps for an aquaplanet with a 1 bar CO_2 atmosphere. Left: synchronous rotation. Right: 3:2 spin-orbit resonance. In both cases, longitude is given relative to the substellar point. Colors indicate the fractional cloud cover, averaged over 2 orbits.

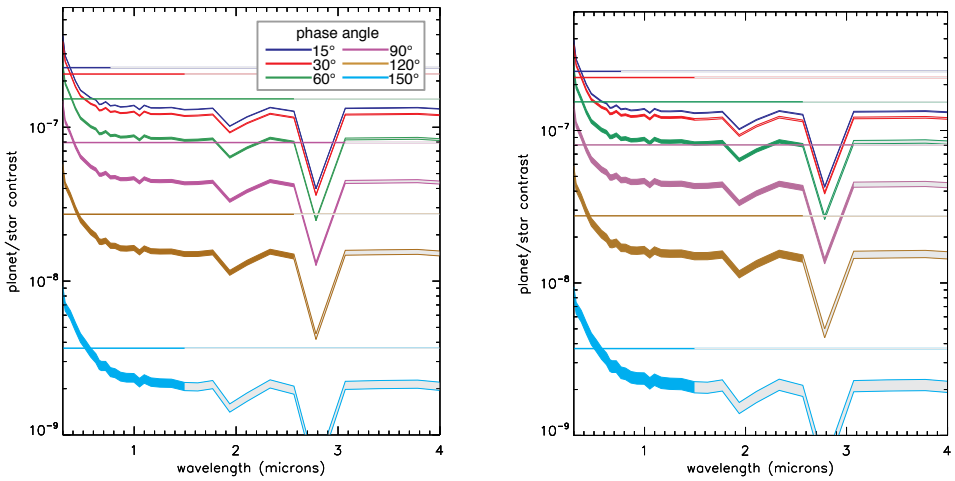

Figure 3.17: Reflection spectra computed for a dry planet with an Earth-like atmosphere in synchronous rotation (left) and 3:2 spin-orbit resonance (right).

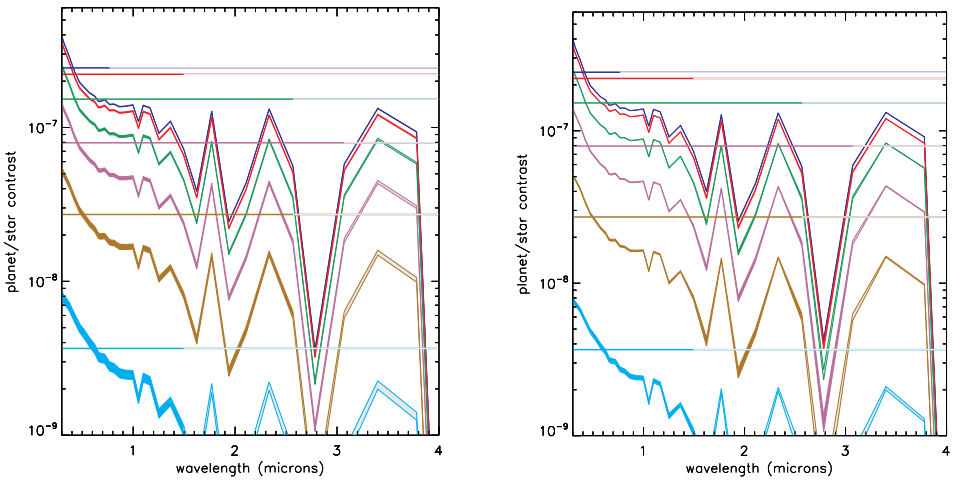

Figure 3.18: Reflection spectra computed for a dry planet with a 1 bar CO_2-dominated atmosphere in synchronous rotation (left) and 3:2 spin-orbit resonance (right).

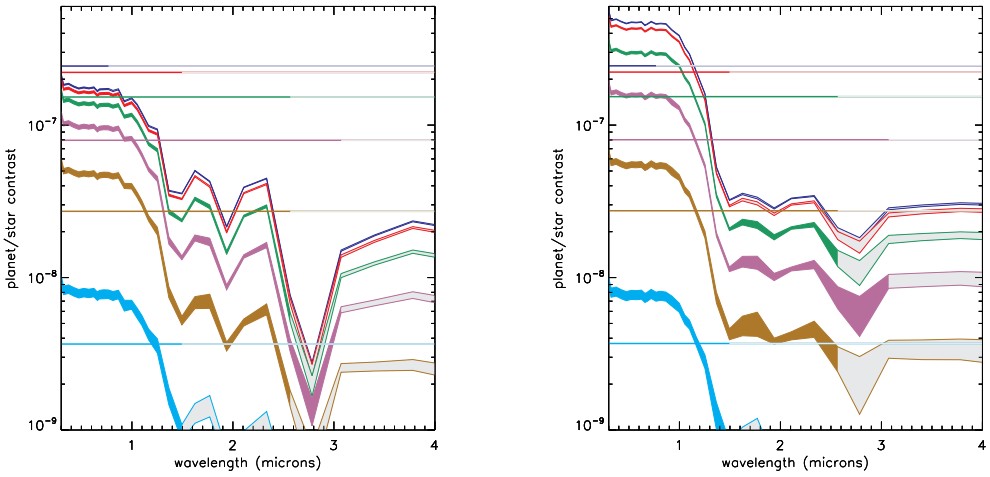

Figure 3.19: Reflection spectra computed for an aquaplanet with a 10 mbar N_2-dominated (+ 376ppm of CO_2) atmosphere in synchronous rotation (left) and 3:2 spin-orbit resonance (right).

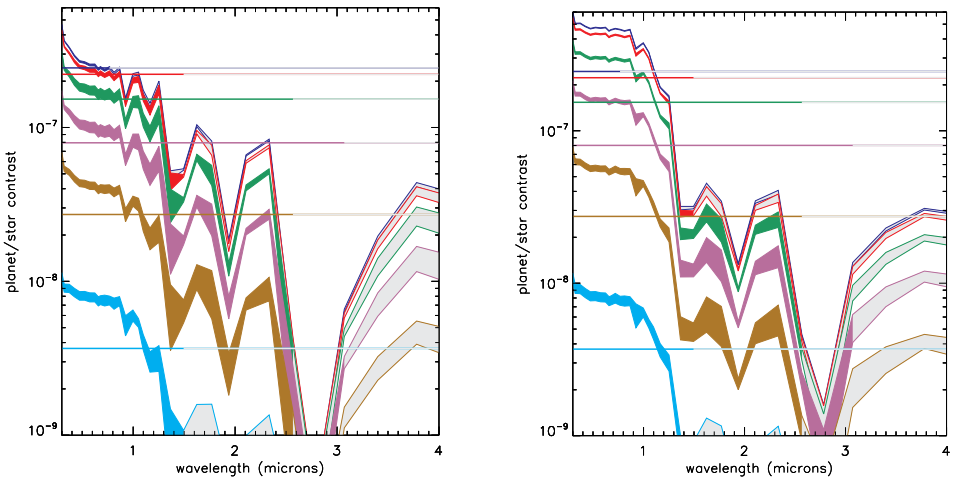

Figure 3.20: Reflection spectra computed for an aquaplanet with an Earth-like atmosphere in synchronous rotation (left) and 3:2 spin-orbit resonance (right).

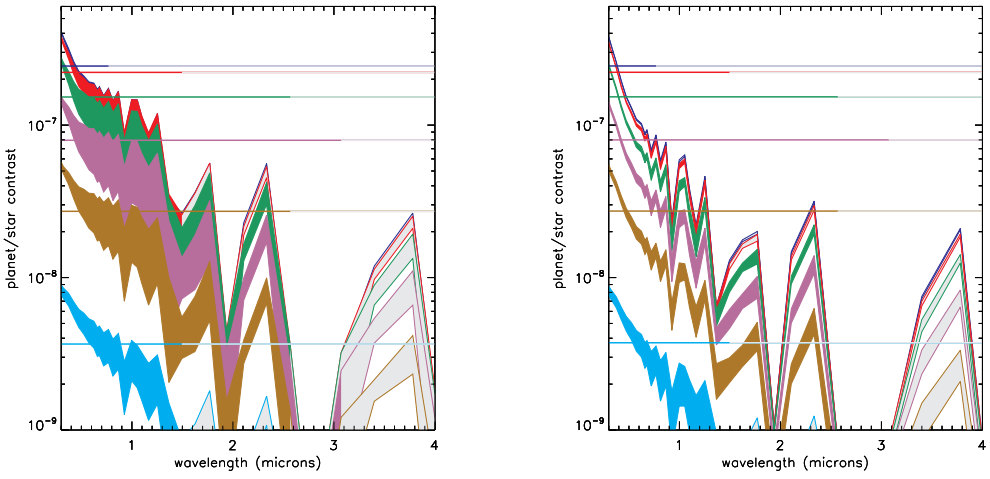

Figure 3.21: Reflection spectra computed for an aquaplanet with a 1 bar CO_2-dominated atmosphere in synchronous rotation (left) and 3:2 spin-orbit resonance (right).

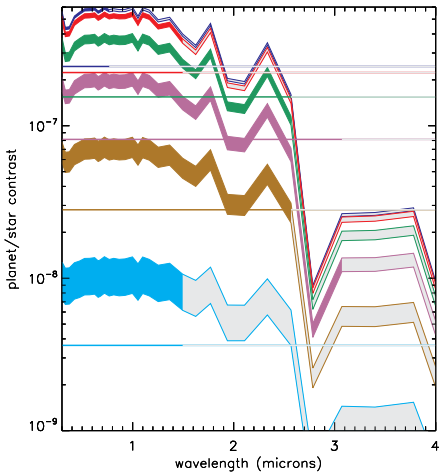

Figure 3.22: Reflection spectra computed for a dry planet with a Venus-like atmosphere (including aerosols).

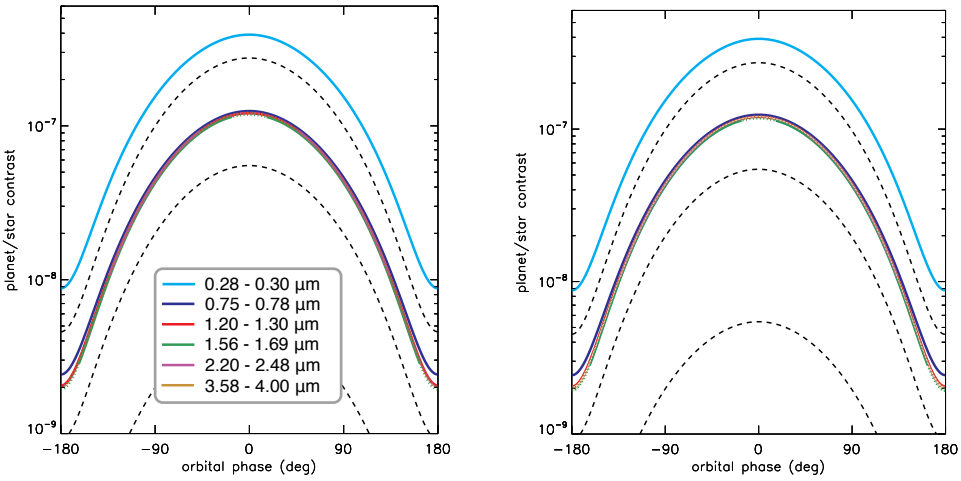

Figure 3.23: Reflection phase curves computed for a dry planet with an Earth-like atmosphere in synchronous rotation (left) and 3:2 spin-orbit resonance (right).

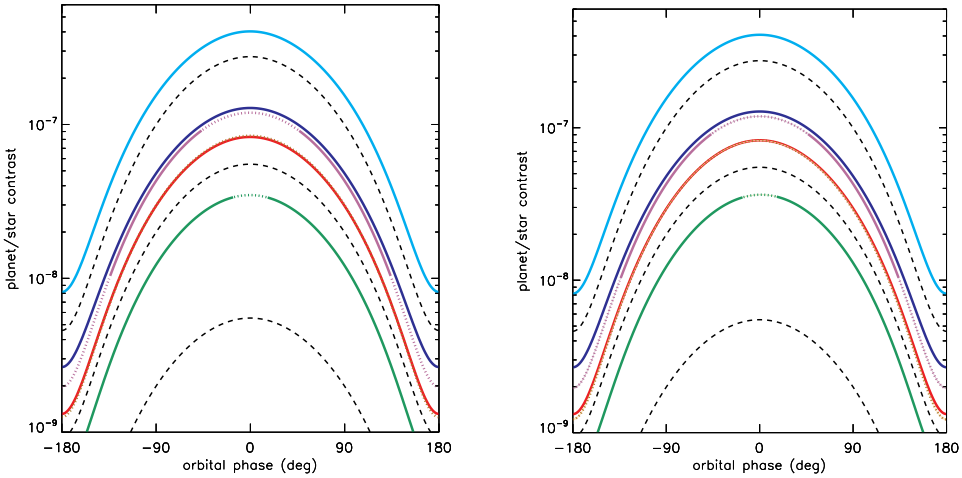

Figure 3.24: Reflection phase curves computed for a dry planet with a 1 bar CO_2-dominated atmosphere in synchronous rotation (left) and 3:2 spin-orbit resonance (right).

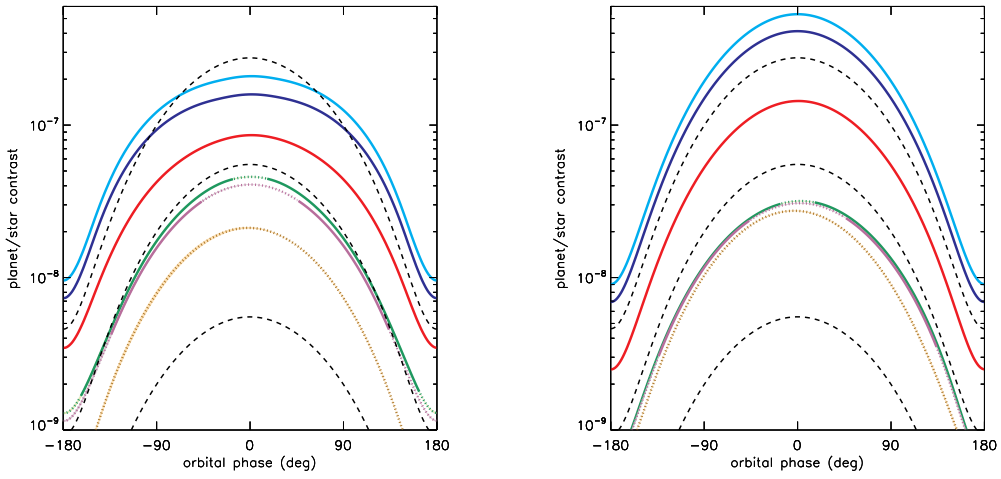

Figure 3.25: Reflection phase curves computed for an aquaplanet with a 10 mbar N_2-dominated (+ 376ppm of CO_2) atmosphere in synchronous rotation (left) and 3:2 spin-orbit resonance (right).

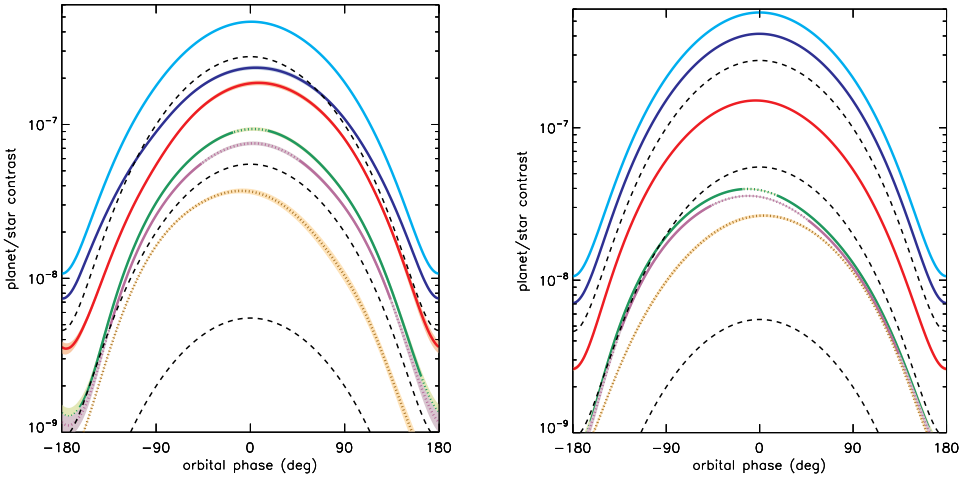

Figure 3.26: Reflection phase curves computed for an aquaplanet with an Earth-like atmosphere in synchronous rotation (left) and 3:2 spin-orbit resonance (right).

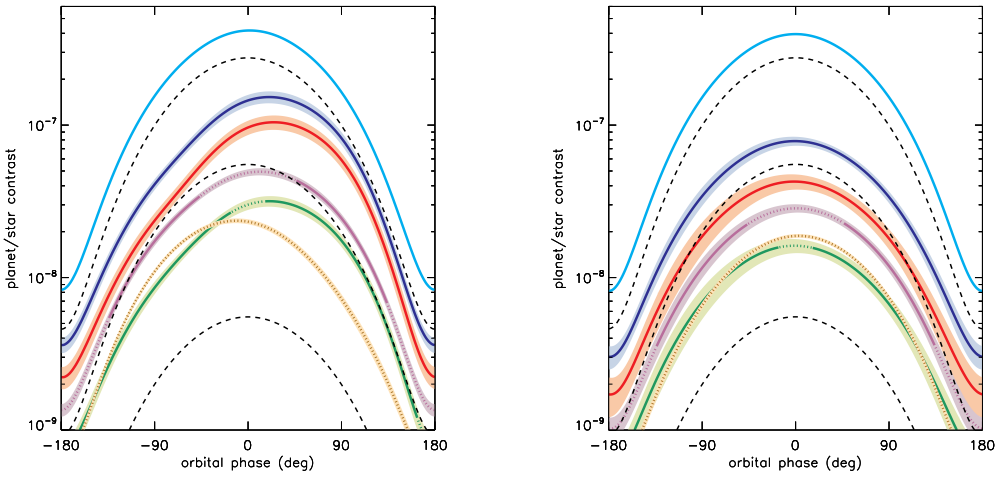

Figure 3.27: Reflection phase curves computed for an aquaplanet with a 1 bar CO_2-dominated atmosphere in synchronous rotation (left) and 3:2 spin-orbit resonance (right).

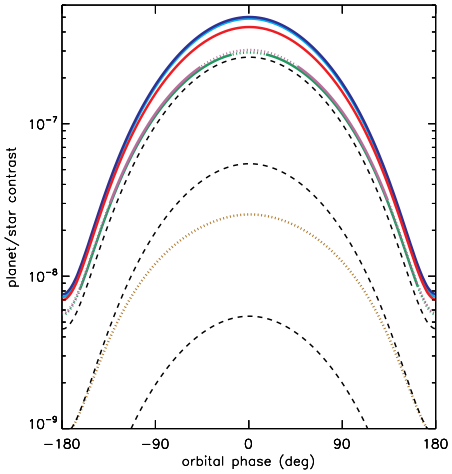

Figure 3.28: Reflection phase curves computed for a dry planet with a Venus-like atmosphere (including aerosols).

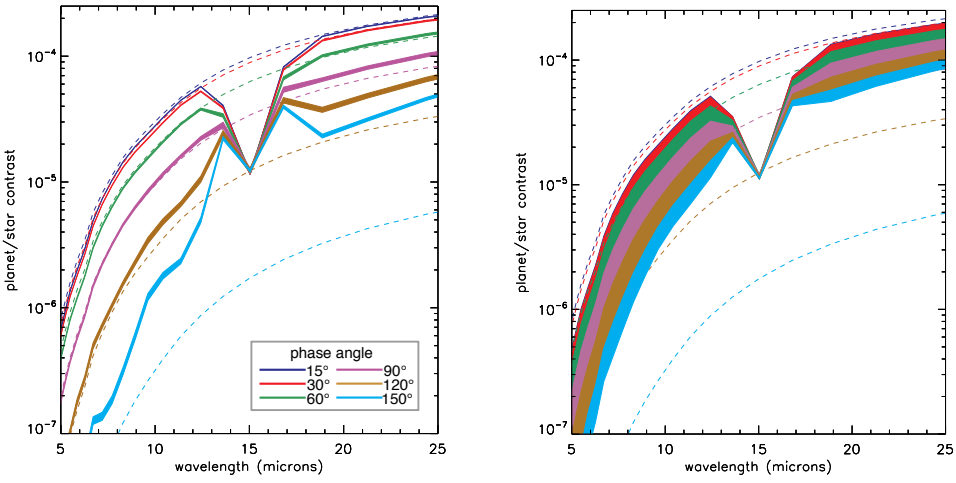

Figure 3.29: Emission spectra computed for a dry planet with an Earth-like atmosphere in synchronous rotation (left) and 3:2 spin-orbit resonance (right).

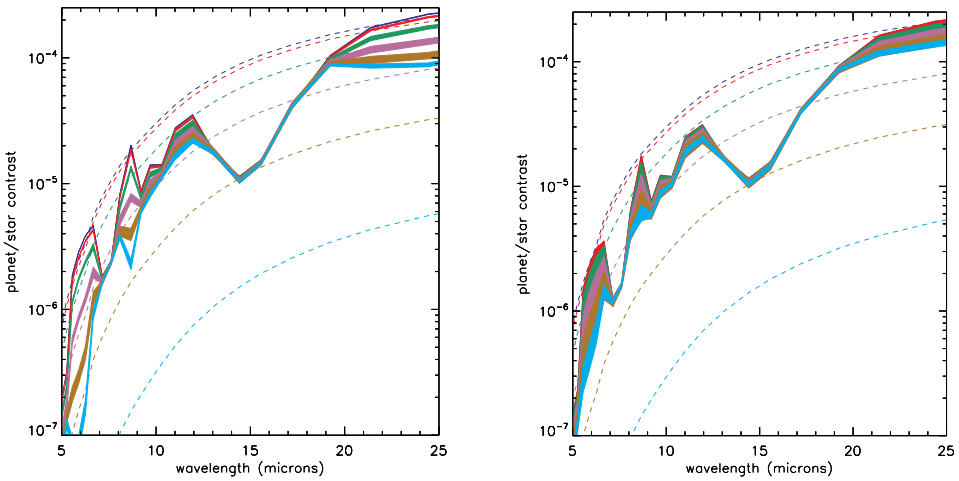

Figure 3.30: Emission spectra computed for a dry planet with a 1 bar CO_2-dominated atmosphere in synchronous rotation (left) and 3:2 spin-orbit resonance (right).

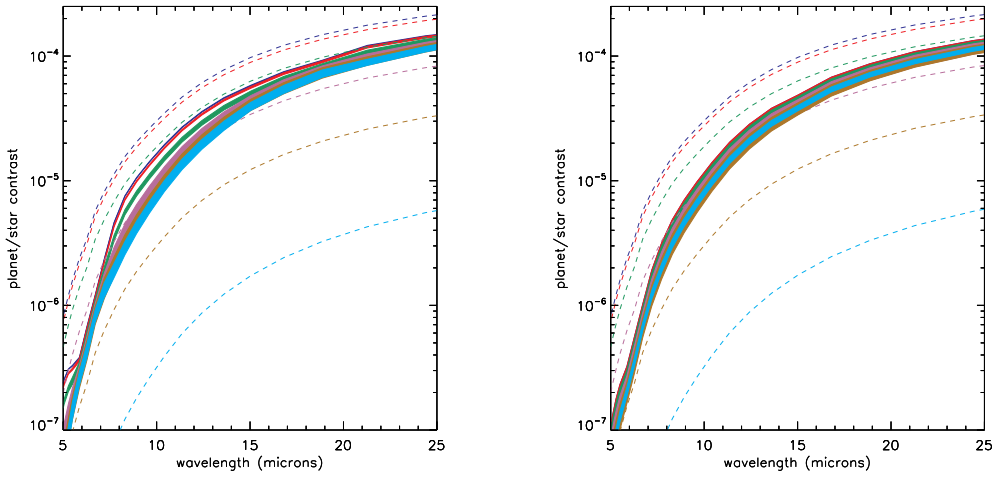

Figure 3.31: Emission spectra computed for an aquaplanet with a 10 mbar N_2-dominated (+ 376ppm of CO_2) atmosphere in synchronous rotation (left) and 3:2 spin-orbit resonance (right).

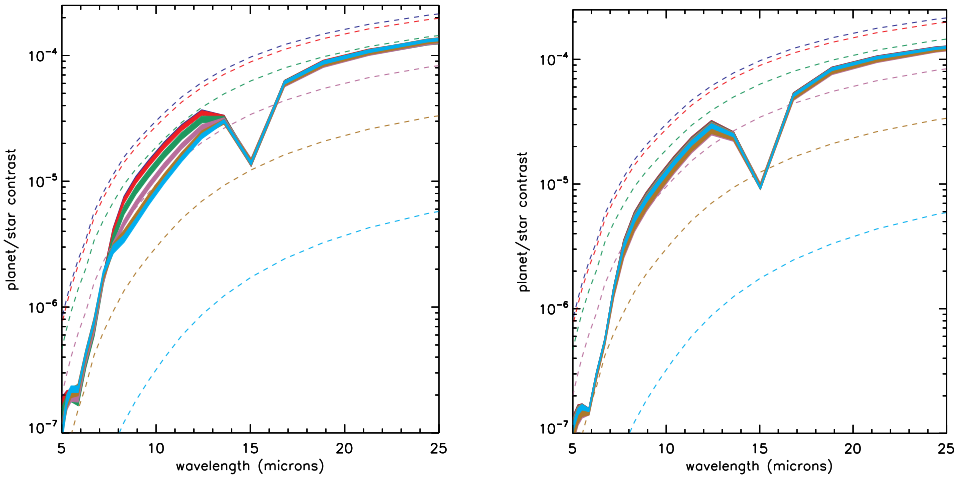

Figure 3.32: Emission spectra computed for an aquaplanet with an Earth-like atmosphere in synchronous rotation (left) and 3:2 spin-orbit resonance (right).

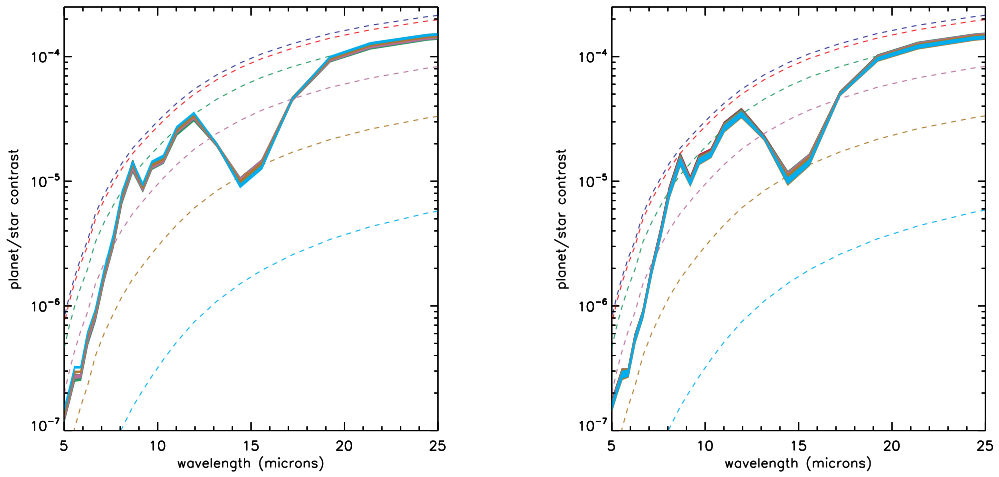

Figure 3.33: Emission spectra computed for an aquaplanet with a 1 bar CO_2-dominated atmosphere in synchronous rotation (left) and 3:2 spin-orbit resonance (right).

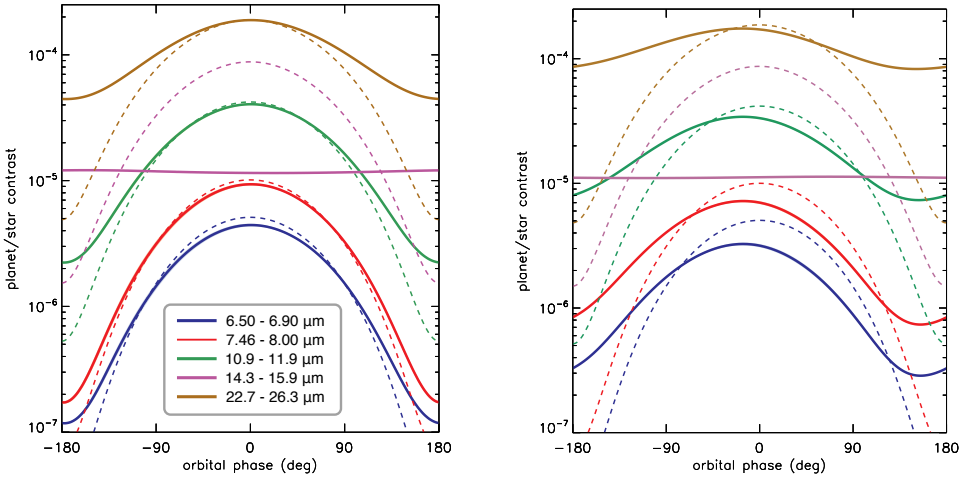

Figure 3.34: Emission phase curves computed for a dry planet with an Earth-like atmosphere in synchronous rotation (left) and 3:2 spin-orbit resonance (right).

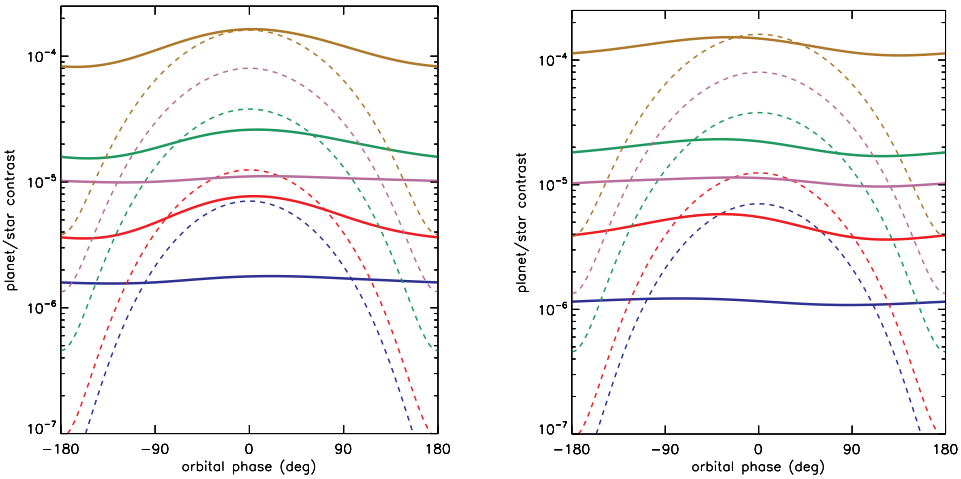

Figure 3.35: Emission phase curves computed for a dry planet with a 1 bar CO_2-dominated atmosphere in synchronous rotation (left) and 3:2 spin-orbit resonance (right).

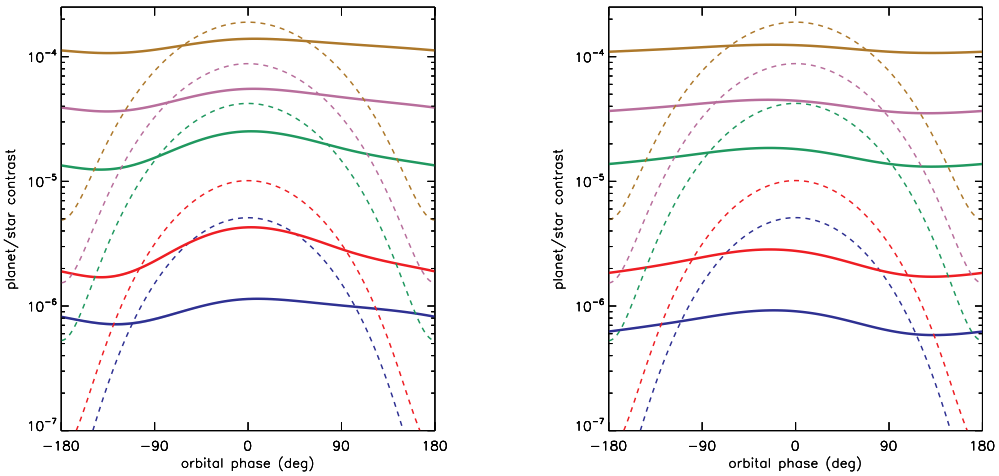

Figure 3.36: Emission phase curves computed for an aquaplanet with a 10 mbar N_2-dominated (+ 376ppm of CO_2) atmosphere in synchronous rotation (left) and 3:2 spin-orbit resonance (right).

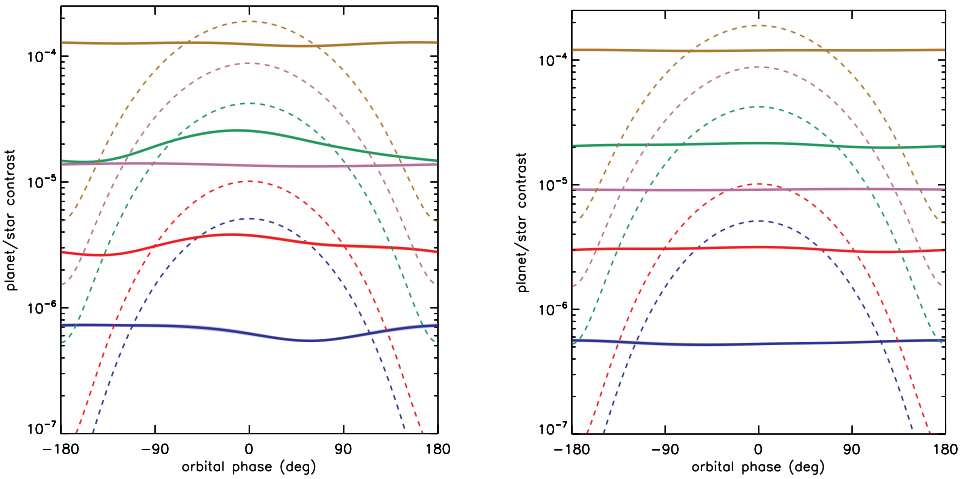

Figure 3.37: Emission phase curves computed for an aquaplanet with an Earth-like atmosphere in synchronous rotation (left) and 3:2 spin-orbit resonance (right).

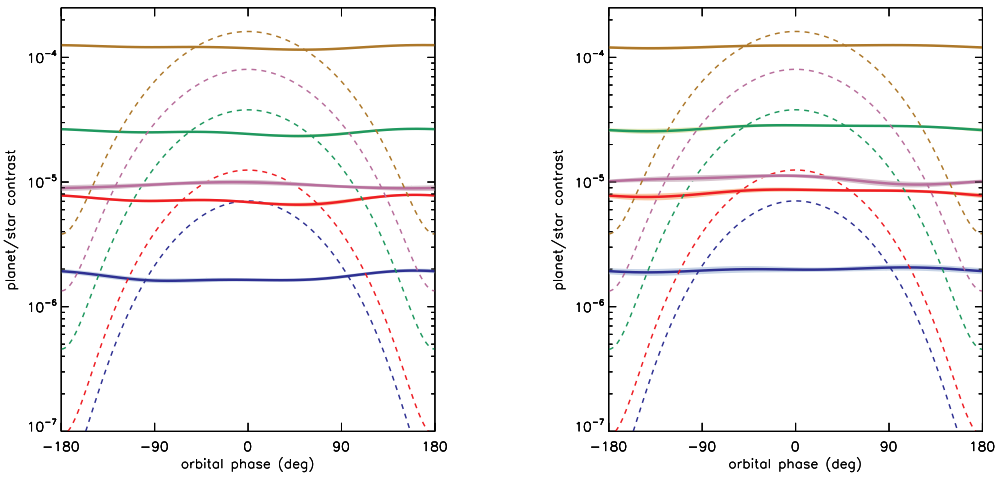

Figure 3.38: Emission phase curves computed for an aquaplanet with a 1 bar CO_2-dominated atmosphere in synchronous rotation (left) and 3:2 spin-orbit resonance (right).

Chapter 4

Possible climates of TRAPPIST-1 planets

Contents

4.1 Preamble

In May 2016, Michael Gillon and his colleagues announced the discovery of a planetary system called TRAPPIST-1 made of at least 3 temperate, Earth-sized planets (Gillon et al., 2016). This system is amazing because it provides us with the best "Earth-like" planets (i.e. both Earth-sized and temperate) to target with the forthcoming James Webb Space Telescope. To date, the innermost planet of the system TRAPPIST-1b is our best chance - through atmospheric characterization - to get some insight - directly and indirectly - on the fate, evolution and potentially habitability of Earth-sized planets orbiting M stars.

A few months later[1], I was included in the team and was in charge of assessing the possible climates and more specifically the potential habitability of newly discovered planets of the system. For this reason, I co-authored two papers (Gillon et al., 2017; Luger et al., 2017b) (e.g. the discovery papers of the five outer planets of the TRAPPIST-1 system) for which I performed the first 1-D numerical climate simulations of the TRAPPIST-1 planets. With TRAPPIST-1, the future is promising. TRAPPIST-1e, f and g are the first potentially habitable planets (e.g. located inside the Habitable Zone of their star) that can be amenable to atmospheric characterization using the method of transit spectroscopy, with the James Webb Space Telescope. This is truely a revolution!

Following these discovery papers, my contribution was twofold. First, using my 1-D climate simulations of the TRAPPIST-1 planets, I was able to derive constraints on the density of the TRAPPIST-1 planets (Grimm et al., 2018). This work is described in the next section. Then, using 3-D Global Climate simulations, I explored all the variety of climates that all the outermost planets of the TRAPPIST-1 system could potentially harbour. This work is described in the following sections and is based on a paper published in Astronomy & Astrophysics in Mai 2018. The full reference is: Martin Turbet, Emeline Bolmont, Jeremy Leconte, Francois Forget, Franck Selsis, Gabriel Tobie, Anthony Caldas, Joseph Naar, and Michael Gillon, **Modeling climate diversity, tidal dynamics and the fate of volatiles on TRAPPIST-1 planets**, A&A, 2018 (`http://adsabs.harvard.edu/abs/2018A%26A...612A..86T`).

4.2 Transit Timing Variations in the TRAPPIST-1 system and constraints on the planet densities

TRAPPIST-1 is a planetary system of at least 7 transiting planets. The transit method measures the radii of the planets, but not their masses. Yet, we can learn a lot from knowing simultaneously the radius and the mass of a planet. In particular, we can calculate the density of the planet and thus get insights on its bulk composition.

Fortunately, there is a way to collect information on the masses of TRAPPIST-1, through the method of Transit Timing Variations (TTV). The TRAPPIST-1 system is in fact so compact[2] that the seven planets strongly and mutually interact with each others through gravitational forces. These gravitational interactions produce tiny changes in the orbit of the planets. In particular, this translates

[1] To be exact, this was on Thursday November 10th 2016. I can remember it because this was the day of my birthday. I acknowledge that this was a pretty nice gift!

[2] As an illustration, the 7 TRAPPIST-1 planets are located within the orbit of Mercury, the innermost planet of the Solar System.

into variations of the orbital periods of the planets - compared to the standard Keplerian orbit[3] - that can be detected through precise timings of the transits of the planets. With a continuous monitoring of TRAPPIST-1 light curve with 10 different astronomical observatories (ground or space-based), we accumulated nearly 300 individual transits of the TRAPPIST-1 planets and were able to derive the Transit Timing Variations (TTV) for the 7 planets of the system. Based on Monte Carlo Markov Chain (MCMC) approach, Grimm et al. (2018) explores the range of parameters (mass, eccentricity, and all the other unconstrained orbital parameters) that match the best the TTV. The results are presented in the mass-radius diagram shown in Figure 4.1.

The results are striking. In average, the density of the TRAPPIST-1 planets appear significantly lower than that of the Earth. The most natural explanation for these low densities is that TRAPPIST-1 planets may be composed of large quantities of water (gaseous, solid or liquid), because water is the most dominant of the volatile, low density species. Yet, this is such an important discovery (the first Earth-sized planets in the Habitable Zone of their star that possess water in abundance!!!) that we must be extremely careful when interpreting the measured density of TRAPPIST-1 planets. First, the uncertainties on the derived masses are still large; but hopefully they will decrease in the future thanks to the accumulation of TTV data. Second, there might be some systematic errors in mass or radius measurements that could introduce biases in density estimates. For example, it has been reported that stellar contamination could be responsible for an overestimation of the planetary radii of TRAPPIST-1 planets (Rackham et al., 2018). Eventually, the low density of the planets could be due to the presence of extended, low density atmospheres. I evaluated this possibility in Grimm et al. (2018), following the procedure described below.

To estimate the thickness of the atmospheres of these planets allowed by their observed densities, I computed 1-D cloud-free numerical climate simulations with the LMD-Generic Model to simulate the vertical temperature profiles of the seven TRAPPIST-1 planets. For this, I assume atmospheric compositions that range from pure H_2, H_2-CH_4, H_2-H_2O to pure CO_2. CH_4 and H_2O volume molecular mixing ratios are arbitrarily fixed to 5×10^{-4} and 1×10^{-3}, respectively, to match solar abundances in C and O (Asplund et al., 2009). Figure 4.2 shows the temperature profiles calculated for TRAPPIST-1b for the various atmospheric compositions.

Then, with the help of my colleagues Anthony Caldas and Jeremy Leconte, we calculated the atmospheric thickness required to match the measured transit radii. For each planet, atmospheric composition, and a wide range of surface pressures (from 10 mbar to 10^3 bar), we decomposed the thermal structure of the atmosphere into 500 log-spaced layers in altitude coordinates. Surface radius and gravity are calculated assuming a core composition of Fe/Mg = 0.75 and Mg/Si= 1.028. We estimate the transit radii of the planets, as measured by Spitzer in the 4.5μm IRAC band, solving radiative transfer equations including molecular absorption, Rayleigh scattering, and various other sources of continuua, i.e. Collision Induced Absorptions (CIA) and/or far line wing broadening, when needed and available. Radiative transfer equations are solved through the 500 layers in spherical geometry - using the input from my 1-D numerical climate simulations - by my colleagues Anthony Caldas and Jeremy Leconte to determine the effective transit radius of a given configuration in the Spitzer band. A fit was found when the surface pressure resides at the nominal transit radius of the Spitzer observations, and thus corresponds to the maximum surface pressure. It is maximal in the

[3]The third law of Kepler dictates that an isolated planet rotates around its host star with a period $T^2 = \frac{4\pi^2}{GM_\star} a^3$, with a the semi major axis, G the gravitational constant and $M_\star$ the mass of the host star

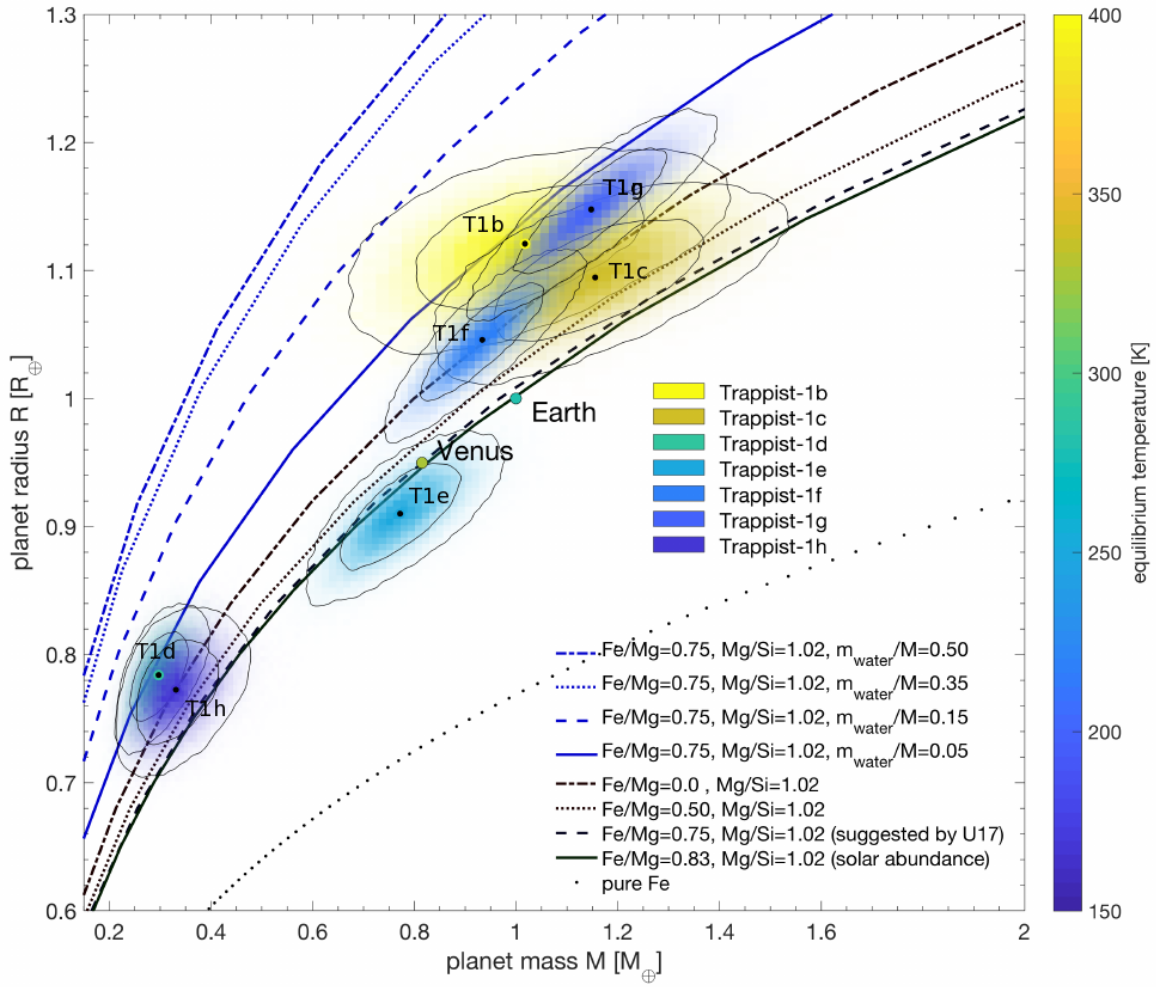

Figure 4.1: Mass-radius diagram for the TRAPPIST-1 planets, Earth, and Venus. Curves trace idealised compositions of rocky and water-rich interiors (surface temperature fixed to 200 K). Median values are highlighted by a black dot. Coloured contours correspond to significance levels of 68% and 95% for each planet. The interiors are calculated with model II of Dorn et al. (2017). Rocky interiors are composed of Fe, Si, Mg, and O, assuming different bulk ratios of Fe/Mg and Mg/Si. U17 refers to Unterborn et al. (2018). Equilibrium temperatures for each planet are indicated by the coloured contours. Adapted from Grimm et al. (2018).

sense that any reservoir of volatiles at the surface would yield a higher core radius, and reduce the mass of the atmosphere needed to match the observed radius.

Given the density constraints and a standard core composition (Unterborn et al., 2018), planets b, c, d, e, f and h cannot accommodate H_2-dominated atmospheres thicker than a few bar (see Table 4 in Grimm et al. 2018). Considering the expected intense atmospheric escape around TRAPPIST-1 (Bolmont et al., 2017), the lifetime of such atmospheres would be very limited, making this scenario rather unlikely. This is actually supported by transit spectroscopy with HST suggesting that TRAPPIST-1 planets should not have a cloud/haze free H_2-dominated atmosphere (De Wit et al., 2016; de Wit et al., 2018).

For atmospheres with a higher mean molecular weight, the inferred pressures are too large for a perfect gas approximation (i.e. a more detailed equation of state would be needed). Assuming that the mass of the atmosphere is much lower than the planetary core, the surface pressure P_{surf} can be estimated by integrating the hydrostatic equation, which yields:

$$P_{\rm surf} = P_{\rm transit}\ \exp\Big((1 - \frac{R_{\rm core}}{R_{\rm transit}})\ \frac{R_{\rm core}}{H}\Big) \tag{4.1}$$

where $H = \frac{kT}{\mu m_H g}$ is the mean atmospheric scale height, $P_{transit}$ the pressure at the transit radius, R_{core} the radius at the solid surface, T the surface temperature, μ the mean molecular weight, k is the Boltzmann constant, and m_H the mass of the hydrogen atom. This relation demonstrates that the surface pressure increases exponentially with T ; and is why, at the low temperatures expected for the planets beyond d, it is difficult to explain the observed radii with an enriched atmosphere above a bare core without unrealistically large quantities of gas. For the colder, low density planets (f, g, and h), explaining the radius with only a CO_2 atmosphere is difficult due to the small pressure scale height and the fact that CO_2 should inevitably collapse on the surface beyond the orbit of planet g (Turbet et al., 2018a).

Planet b however, is located beyond the runaway greenhouse limit for tidally locked planets (Kopparapu et al., 2016; Turbet et al., 2018a) and could potentially reach - with a thick water vapour atmosphere - a surface temperature up to 2000 K (Kopparapu et al., 2013). Assuming more realistic mean temperatures of 750-1500 K, the above estimate yields pressures on the order of 10^1-10^4 bar, which would explain its relatively low density (assuming $P_{transit}$ = 20 millibar).

Because outer planets of the TRAPPIST-1 system have in average a low density, and that this low density can hardly be explained by the presence of a light, extended atmosphere, the most likely scenario is that these planets could be enriched in various types of volatiles (H_2O, CO_2, CH_4, NH_3, etc.) in solid, liquid and/or gaseous form. This scenario is discussed extensively in the following sections.

4.3 Abstract of "Modeling climate diversity, tidal dynamics and the fate of volatiles on TRAPPIST-1 planets"

TRAPPIST-1 planets are invaluable for the study of comparative planetary science outside our Solar System and possibly habitability. Both Time Transit Variations (TTV) of the planets and the compact, resonant architecture of the system suggest that TRAPPIST-1 planets could be endowed with various volatiles today. First, we derive from N-body simulations possible planetary evolution scenarios, and

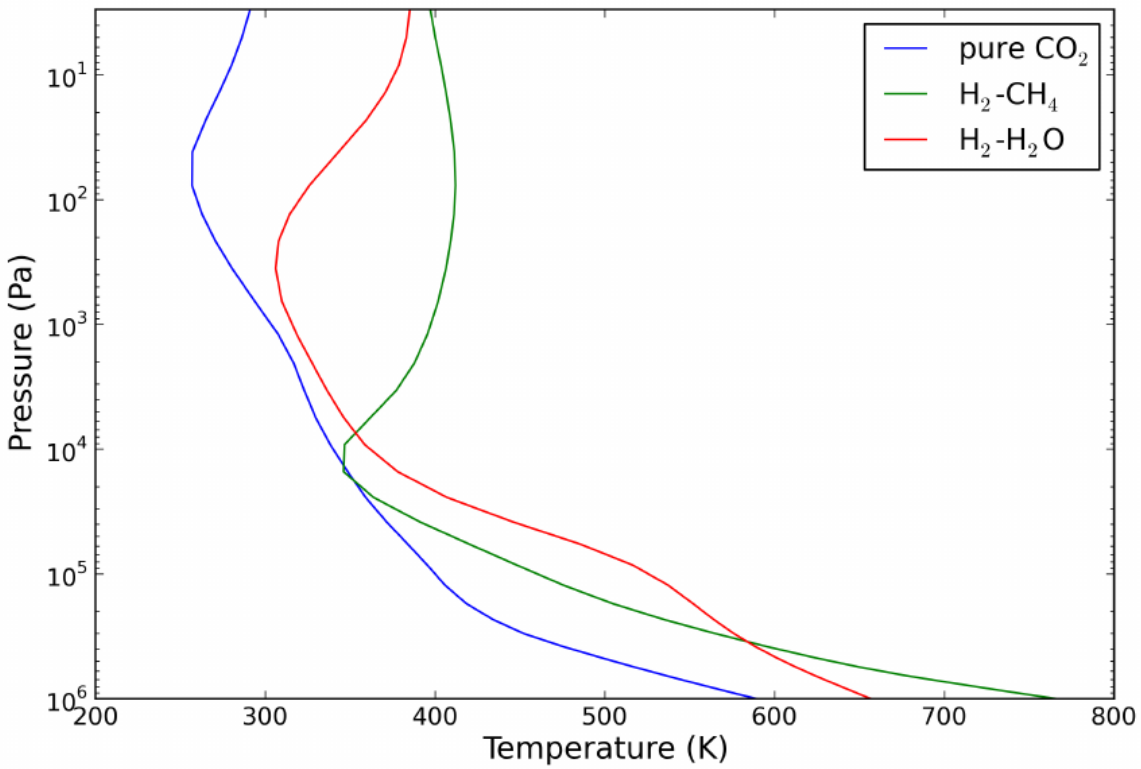

Figure 4.2: Temperature vertical profiles of TRAPPIST-1b calculated with the 1-D numerical climate model, for various atmospheric compositions: H_2-CH_4, H_2-H_2O and pure CO_2. The surface pressure is arbitrarily fixed here to 10 bar.

show that all the planets are likely in synchronous rotation. We then use a versatile 3-D Global Climate Model (GCM) to explore the possible climates of cool planets around cool stars, with a focus on the TRAPPIST-1 system. We look at the conditions required for cool planets to prevent possible volatile species to be lost permanently by surface condensation, irreversible burying or photochemical destruction. We also explore the resilience of the same volatiles (when in condensed phase) to a runaway greenhouse process. We find that background atmospheres made of N_2, CO or O_2 are rather resistant to atmospheric collapse. However, even if TRAPPIST-1 planets were able to sustain a thick background atmosphere by surviving early X/EUV radiation and stellar wind atmospheric erosion, it is difficult for them to accumulate significant greenhouse gases like CO_2, CH_4 or NH_3. CO_2 can easily condense on the permanent nightside, forming CO_2 ice glaciers that would flow toward the substellar region. A complete CO_2 ice surface cover is theoretically possible on TRAPPIST-1g and h only, but CO_2 ices should be gravitationally unstable and get buried beneath the water ice shell in geologically short timescales. Given TRAPPIST-1 planets large EUV irradiation (at least $\sim 10^3 \times$ Titan's flux), CH_4 and NH_3 are photodissociated rapidly and are thus hard to accumulate in the atmosphere. Photochemical hazes could then sedimentate and form a surface layer of tholins that would progressively thicken over the age of the TRAPPIST-1 system. Regarding habitability, we confirm that a few bar of CO_2 would suffice to warm the surface of TRAPPIST-1f and g above the melting point of water. We also show that TRAPPIST-1e is a remarkable candidate for surface habitability. If the planet is today synchronous and abundant in water, then it should very likely sustain surface liquid water at least in the substellar region, whatever the atmosphere considered.

4.4 Introduction

TRAPPIST-1 planets recently discovered by Gillon et al. (2016, 2017) are the closest known transiting temperate Earth-sized exoplanets. The TRAPPIST-1 system hosts at least seven planets that are similar in size (from ~ 0.72 to $\sim 1.13 R_\oplus$) and irradiation (from ~ 0.14 to $\sim 4.3 S_\oplus$) to Solar System rocky planets. Considering that the parent star TRAPPIST-1 is an ultra-cool ($T_{\rm eff}$ = 2550 K), low-mass ($M_\star$ = 0.09 $M_\odot$) star, the planets of the system should have potentially followed evolutionary pathways very different from what the Solar System planets experienced. They are therefore invaluable probes for comparative planetary science and habitability.

In a first approach, we can speculate on what TRAPPIST-1 planets might look like by comparing their size and irradiation with Solar System planets. TRAPPIST-1b (0.64 $S_{\rm Mercury}$) and TRAPPIST-1c (1.19 $S_{\rm Venus}$) might be airless planets like Mercury, or endowed with a thick atmosphere like Venus. TRAPPIST-1d (1.14 $S_\oplus$) is located near the inner edge of the Habitable Zone, traditionally defined as the range of orbital distances within which a planet can possibly maintain liquid water on its surface (Kasting et al., 1993; Kopparapu et al., 2013). Its capacity to host surface oceans, assuming an Earth-like atmosphere and water content, should depend on 1) its rotation mode and 2) subtle cloud albedo feedbacks (Yang et al., 2013; Kopparapu et al., 2016). TRAPPIST-1e (0.66 $S_\oplus$) lies at the right distance to maintain surface liquid water if enough water is available and the atmosphere suitable. TRAPPIST-1f (0.89 $S_{\rm Mars}$) and TRAPPIST-1g (0.60 $S_{\rm Mars}$), being slightly bigger than Mars, could have retained a thick CO_2 atmosphere and thus conditions potentially similar to Early Mars for a long period of time. Eventually, TRAPPIST-1h (0.30 $S_{\rm Mars}$, 12 $S_{\rm Titan\ /\ Enceladus}$) could look like a warm CH_4/N_2-rich Titan-like planet, or a Snowball icy-moon-like planet.

However, TRAPPIST-1 planets formed and evolved in a very different environment from our Solar System planets. At any rate, each of the seven planets may potentially all be airless today, as a result of the star extreme X/EUV irradiation (Wheatley et al., 2017; Bourrier et al., 2017) and stellar wind through history that could have blown away their atmosphere (Airapetian et al., 2017; Dong et al., 2017; Garcia-Sage et al., 2017; Dong et al., 2018a). Moreover, during the first hundreds of million years following their formation, while TRAPPIST-1 was a pre-main-sequence star and its luminosity significantly higher, each of the seven planets could have faced a runaway phase where the most condensable volatiles (e.g. water) would have been vaporized, and exposed to atmospheric escape. As much as several Earth ocean hydrogen content could have been lost in the process (Bolmont et al., 2017; Bourrier et al., 2017). The remaining oxygen could have therefore potentially built up in the atmosphere of the seven TRAPPIST-1 planets (Luger and Barnes, 2015).

Transit-timing variations (TTVs) measurements of TRAPPIST-1 planets (Gillon et al., 2017; Wang et al., 2017) suggest that planet bulk densities are compatible with terrestrial or volatile-rich composition. The latter possibility, and the fact that TRAPPIST-1 planets are in a near-resonant chain, suggest that the planets could have formed far from their star and migrated afterward to their current position. The planets may thus have been formed near or beyond the snowline and could have remained enriched in volatiles until now, despite a potentially massive early atmospheric escape (Bolmont et al., 2017). Uncertainties on the masses derived from TTVs are still affected by significant uncertainties but TTVs will eventually provide robust constraints on the density and volatile content.

Transit spectroscopy with the Hubble Space Telescope (HST) has been done on the two innermost planets, and suggest that they do not have a cloud/haze free H_2-dominated atmosphere (De Wit et al., 2016). This is somehow consistent with the fact that primordial H_2 enveloppes would have been exposed to efficient atmospheric escape on the small TRAPPIST-1 planets. At any rate, TRAPPIST-1 planets could still harbor a large variety of atmospheres, such as thick H_2O, CO_2, N_2, O_2 or CH_4 dominated atmospheres (see the review by Forget and Leconte 2014). In any case, each of these seven planets should be amenable to further characterization by the James Webb Space Telescope (JWST) as early as 2019 (Barstow and Irwin, 2016; Morley et al., 2017).

The goal of the present study is to explore in more details the possible climates of temperate-to-cold planets orbiting synchronously around cool stars in general, with a focus on the TRAPPIST-1 system (e,f,g,h). The constraints that we derive on their possible atmospheres could serve as a guideline to prepare future observations with JWST. We explore in this work the conditions required for the coldest TRAPPIST-1 planets to prevent possible volatile species from atmospheric collapse, escape, or photodissociation. TRAPPIST-1 is a particular system where even weakly irradiated planets should likely be tidally locked. On synchronously rotating planets, the surface temperature of the cold points can be extremely low, making the different volatile species (N_2, CH_4, CO_2, etc.) highly sensitive to nightside trapping and potentially atmospheric collapse.

Conversely, we explore the stability of the same volatile species in the condensed phase (either icy or liquid) and on the surface, either on the dayside or the nightside. This condition, widely known for water as the runaway greenhouse limit, is extended here to other molecular species.

Because these processes (runaway and collapse) are 3-D on a synchronous planet, the most suited tools to explore them are 3D Global Climate Models (GCM).

In Section 4.5, we describe our 3D Global Climate Model, and more generally the physical parameterizations adopted in this work. In Section 4.6 we discuss the effect of tides on the rotation of

Parameter	Tb	Tc	Td	Te	Tf	Tg	Th	Unit
R_p	1.09[a]	1.06[a]	0.77[a]	0.92[a]	1.05[a]	1.13[a]	0.75[b]	$R_\oplus$
M_p	0.85[a]	1.38[a]	0.41[a]	0.62[a]	0.68[a]	1.34[a]	0.38 (arb.)	$M_\oplus$
g_p	7.07	12.14	6.75	7.22	6.11	10.34	6.6 (arb.)	m s^{-2}
Semi-major axis	0.011[a]	0.015[a]	0.021[a]	0.028[a]	0.037[a]	0.045[a]	0.060[b]	au
S_p	4.25[a]	2.27[a]	1.143[a]	0.662[a]	0.382[a]	0.258[a]	0.165[b]	$S_\oplus$
S_p	5806	3101	1561	904	522	352	225	W m^{-2}
Spin-orbit resonance				1:1				
Period	1.51[a]	2.42[a]	4.05[a]	6.10[a]	9.21[a]	12.35[a]	18.76[b]	Earth days
Ω_p	4.82	3.00	1.80	1.19	0.790	0.589	0.388	10^{-5} rad s^{-1}
Obliquity				0				°
Eccentricity				0				

Table 4.1: Adopted planetary characteristics of TRAPPIST-1 planets for climate simulations. Most of the values derive from Gillon et al. (2017)[a] and Luger et al. (2017b)[b]. Note that mass estimates are all compatible (at less than 1 σ) with the TTV analysis of Wang et al. (2017) that included both Spitzer (Gillon et al., 2017) and K2 (Luger et al., 2017b) transits.

TRAPPIST-1 planets. In the next sections, we explore the possible climates that can be expected on the four outer TRAPPIST-1 planets assuming that they are tidally locked and endowed with various volatiles: We discuss in Section 4.7 the ability of the three outer TRAPPIST-1 planets to sustain an atmosphere of background gases (N_2, CO or O_2). Then, we explore whether we should expect oxidized CO_2-dominated atmosphere (in Section 4.8) or reduced CH_4-dominated atmosphere (in Section 4.9). Eventually, we derive in Section 4.10 all the implications for the habitability of TRAPPIST-1 planets.

4.5 Method - the LMD Generic Global Climate Model

The LMD Generic Model is a full 3-Dimensions Global Climate Model (GCM) that initially derives from the LMDz Earth (Hourdin et al., 2006) and Mars (Forget et al., 1999) GCMs. Since then, it has been extensively used to study a broad range of (exo)planetary atmospheres (Wordsworth et al., 2011; Forget et al., 2013; Wordsworth et al., 2013; Charnay et al., 2013; Leconte et al., 2013a,b; Wordsworth et al., 2015; Charnay et al., 2015a,b; Bolmont et al., 2016a; Turbet et al., 2016, 2017a,b).

Simulation input parameters include the observed characteristics of TRAPPIST-1 planets (Gillon et al., 2017; Luger et al., 2017b), as summarized in Table 4.1. All simulations were performed assuming a circular orbit, a choice motivated by the small value of the maximum eccentricities derived from the stability of the system (Gillon et al., 2017; Luger et al., 2017b). Even for a non circular orbit, the orbital period is sufficiently small that the eccentricity should probably be quite high to significantly impact the climate of synchronous planets (see Bolmont et al. 2016a for their 10^{-4} L_{sun} case). We assumed that each of the planets is in synchronous rotation with 0° obliquity, as supported by calculations presented in Section 4.6.

The numerical simulations presented in this paper were all carried out at a horizontal resolution of 64 × 48 (e.g., 5.6 ° × 3.8°) in longitude × latitude. In all the simulations, the dynamical time step is set to 90 s. The physical parameterizations and the radiative transfer are calculated every 15 min and 1 h,

respectively. Subgrid-scale dynamical processes (turbulent mixing and convection) were parameterized as in Forget et al. (2013) and Wordsworth et al. (2013). The planetary boundary layer was accounted for by the Mellor and Yamada (1982) and Galperin et al. (1988) time-dependent 2.5-level closure scheme, and complemented by a convective adjustment which rapidly mixes the atmosphere in the case of unstable temperature profiles. A filter is applied at high latitude to deal with the singularity in the grid at the pole (Forget et al., 1999). In the vertical direction, the model is composed of 26 distinct atmospheric layers that were built using hybrid σ coordinates and 18 soil layers. These 18 layers are designed to represent either a rocky ground (thermal inertia I_{rock} = 1000 J m^{-2} K^{-1} s$^{-\frac{1}{2}}$), an icy ground (I_{ice} = 2000 J m^{-2} K^{-1} s$^{-\frac{1}{2}}$) or an ocean (I_{ocean} = 20000 J m^{-2} K^{-1} s$^{-\frac{1}{2}}$ to take into account the efficient vertical mixing in the first tens of meter of the ocean, as previously done in Leconte et al. 2013a and Charnay et al. 2013) depending on the assumed surface. Since all the simulations were carried out for a synchronous rotation, thermal inertia should only affect the variability of the atmosphere. Oceanic heat transport is not included in this study.

The GCM includes an up-to-date generalized radiative transfer that takes into account the absorption and scattering by the atmosphere, the clouds and the surface from visible to far-infrared wavelengths, as described in Wordsworth et al. (2011). The radiative transfer is performed here for variable gaseous atmospheric compositions made of various cocktails of CO_2, CH_4, N_2 and H_2O, using the correlated-k method (Fu and Liou, 1992; Eymet et al., 2016). Molecular absorption lines were taken from HITRAN 2012 (Rothman et al., 2013). Sublorentzian profiles (Perrin and Hartmann, 1989; Campargue et al., 2012), Collision Induced Absorptions (Gruszka and Borysow, 1997; Baranov et al., 2004; Wordsworth et al., 2010a; Richard et al., 2012) and various other continua (Gruszka and Borysow, 1997; Clough et al., 2005; Richard et al., 2012) were properly included in the calculations when needed. For the computation, we used between 32 and 38 spectral bands in the thermal infrared and between 36 and 41 spectral bands in the visible domain, depending on the atmospheric composition considered. 16 non-regularly spaced grid points were used for the g-space integration, where g is the cumulative distribution function of the absorption data for each band. We used a two-stream scheme (Toon et al., 1989) to take into account the scattering effects of the atmosphere and the clouds, using the method of Hansen and Travis (1974).

The emission spectrum of TRAPPIST-1 was computed using the synthetic BT-Settl spectrum[4] (Rajpurohit et al., 2013) assuming a temperature of 2500 K, a surface gravity of 10^3 m s^{-2} and a metallicity of 0 dex.

The GCM directly computes the wavelength-dependent albedo of water ice / snow from a simplified albedo spectral law of ice / snow, calibrated to get ice / snow bolometric albedo of 0.55 around a Sun-like star, as in Turbet et al. (2016). Around TRAPPIST-1, we calculate that the average bolometric albedo for water ice / snow is $\sim$ 0.21. Around an ultra-cool star like TRAPPIST-1, the bolometric albedo of water ice / snow is drastically reduced (Joshi and Haberle, 2012; von Paris et al., 2013b; Shields et al., 2013) due to the shape of its reflectance spectrum (Warren and Wiscombe, 1980; Warren, 1984).

Melting, freezing, condensation, evaporation, sublimation, and precipitation of H_2O are included in the model. Water vapor is treated as a variable species in most of our simulations. This means that relative water vapor humidity is let free, but is always limited to 100% by our moist convective adjustment scheme. Similarly, we take into account the possible condensation/sublimation of CO_2

[4]Downloaded from https://phoenix.ens-lyon.fr

in the atmosphere (and on the surface) when needed but not the radiative effect of CO_2 ice clouds because their scattering greenhouse effect (Forget and Pierrehumbert, 1997) should be low around cool stars like TRAPPIST-1 (Kitzmann, 2017) and limited by partial cloud coverage (Forget et al., 2013). The effect of latent heat is properly taken into account when H_2O and/or CO_2 condense, evaporate or sublimate.

CO_2 and H_2O cloud particle sizes are determined from the amount of condensed material and the number density of cloud condensation nuclei [CCN]. The latter parameter was taken to be constant everywhere in the atmosphere, and equal to 10^6 kg^{-1} for liquid water clouds, 10^4 kg^{-1} for water ice clouds (Leconte et al., 2013a) and 10^5 kg^{-1} for CO_2 ice clouds (Forget et al., 2013). Ice particles and liquid droplets are sedimented following a Stokes law described in Rossow (1978). H_2O precipitation is computed with the scheme from Boucher et al. (1995), with precipitation evaporation also taken into account.

All the numerical climate simulations were run long enough (up to 30 Earth years) to reach equilibrium. Simulations that lead to unstable CO_2 surface collapse were stopped when the rate of CO_2 surface condensation reached a positive constant, as in Turbet et al. (2017b).

Note that more details on the LMD Generic model can be found in Forget et al. (1999); Wordsworth et al. (2011); Forget et al. (2013); Wordsworth et al. (2013); Charnay et al. (2013); Leconte et al. (2013a); Turbet et al. (2016) and Turbet et al. (2017a).

4.6 Effect of tides on TRAPPIST-1 planets

All observed TRAPPIST-1 planets are inside an orbital distance of 0.06 au. As a comparison, Mercury orbits at ~ 0.4 au from the Sun. For such close-in planets, tidal interactions are expected to be strong and influence the orbital and rotational dynamics of the system.

We use here a standard equilibrium tide model (Mignard, 1979; Hut, 1981; Eggleton et al., 1998; Bolmont et al., 2011) to estimate the tidal evolution of the system. We combine an approach based on evolution timescale calculations and N-body simulations of the system using Mercury-T (Bolmont et al., 2015).

Mercury-T is a N-body code, which computes the orbital and rotational evolution of multi-planet systems taking into account tidal forces and their resulting torques (in the equilibrium tide framework), the correction for general relativity and the rotational flattening forces and torques. From this code, the evolution of the orbital parameters can be calculated (such as semi-major axis, eccentricity and inclination) as well as the rotation of the different bodies (i.e., the rotation period and obliquity of the planets). This code has previously been used to study the orbital dynamics of close-in and/or compact and/or near-resonant systems such as 55-Cnc (Bolmont et al., 2013), Kepler-62 (Bolmont et al., 2015) and Kepler-186 (Bolmont et al., 2014), and is now used here for the TRAPPIST-1 system.

4.6.1 Tidal dissipation and orders of magnitude

Simple order of magnitude calculations allow us to determine that the tide raised by the planets in the star is a priori negligible for this system today. Even considering a relatively high dissipation for a purely convective body (i.e., the dissipation of a hot Jupiter as estimated by Hansen 2010), we find semi-major axis and eccentricity evolution timescales of 10^8 Myr and 5×10^7 Myr respectively. Note that the dissipation is a measure of how fast the system is tidally evolving: the higher the dissipation,

the faster the evolution. The age of TRAPPIST-1 has recently been estimated to be between 5 and 10 Gyr (Luger et al., 2017b; Burgasser and Mamajek, 2017). The evolution timescales for semi-major axis and eccentricity are thus consistent with Bolmont et al. (2011), which showed that the stellar-tide driven evolution around low mass stars and brown dwarfs was negligible for ages superior to ~ 100 Myr due to the decrease of the stellar radius.

The system therefore principally evolves due to the gravitational tide raised by the star in the planets (the planetary tide). The planetary tide mainly acts to decrease the obliquity of the planet, synchronize the rotation and on longer timescales decrease the eccentricity and semi-major axis. The dissipation in the planets depends on their internal structure and thermal state (Henning and Hurford, 2014), as well as on the extension of the external fluid envelop (presence of surficial liquids - water ocean, magma ocean - and of a massive atmosphere) (e.g. Dermott, 1979; Remus et al., 2015). On Earth, the dissipation is dominated by the dynamical response of the ocean and friction processes along the costline and to a lesser extent to interactions with seafloor topography in deep ocean (Egbert and Ray, 2000, 2003; Williams et al., 2014). Dissipation on the Earth is highly dependent on the continent configuration and is therefore expected to significantly change on geological timescale as a consequence of tectonic plate motion (e.g. Poliakow, 2005; Williams et al., 2014). The Earth's dissipation is close to its highest value right now, and could have varied by a factor of almost ten during the last 200 Myr (Poliakow, 2005).

In order to take into account the huge uncertainties in the dissipation factors of exoplanets (for which we do not know the internal structure), we consider various dissipation factors for the planets (from 0.1 to 10 times the dissipation of the Earth). The lowest value we consider here is roughly one order of magnitude larger than the dissipation estimated in Saturn (Lainey et al., 2017), representative of planets dominated by tidal response of a massive fluid envelop. The highest value is close to the maximal possible value and would be representative of very hot planets dominated by fluid-solid friction. There is no example in the Solar system of such a dissipative object. Even the highly dissipative Jupiter's moon Io (Lainey et al., 2009) has a dissipation function smaller than this extreme value, which is comparable to the Earth's value (even if the dissipation process is very different). However, we could envision that Earth-sized bodies with a dissipation process comparable to that of Io could reach such a highly dissipative state. The tidal dissipation is also sensitive to the forcing frequency (e.g. Sotin et al., 2009; Henning and Hurford, 2014), and therefore to the distance from the star. For simplicity, we ignore this effect here and consider constant dissipation functions, independently of the distance from the star and the size of the planet, which is sufficient at first order to provide some typical tendencies.

Considering the dissipation for the planets of the system to be a tenth of the dissipation of the Earth (Neron de Surgy and Laskar, 1997; Williams et al., 2014), comparable to the dissipation in Mars for instance (Yoder et al., 2003; Bills et al., 2005), we find evolution timescales for the rotation to range from 10^{-4} Myr for TRAPPIST-1b to 7 Myr for TRAPPIST-1h. For the obliquity, the evolution timescales range from 10^{-3} Myr for planet-b to 80 Myr for planet-h. Given the estimated age of the system, all planets are thus expected to have a small obliquity and to be near synchronization.

In the tidal framework we use here, the rotation of the planets tend to pseudo-synchronization if the orbit is not circular. However, Makarov and Efroimsky (2013) showed that considering a more physical rheology for the planet rather lead to a succession of spin-orbit resonance captures as the eccentricity of the planet decreases. We discuss the possibility of capture in spin-orbit resonant configuration in

Parameter	T1-b	T1-c	T1-d	T1-e	T1-f	T1-g	T1-h	Unit
				$\sigma_p = 0.1\sigma_\oplus$				
ecc mean ($\times 10^{-3}$)	0.70	0.50	1.8	2.5	3.2	1.5	1.3	
Φ_{tid}mean	0.73	0.020	5.3×10^{-3}	3.0×10^{-3}	$< 10^{-3}$	$< 10^{-5}$	$< 10^{-6}$	W m^{-2}
				$\sigma_p = 1\sigma_\oplus$				
ecc mean ($\times 10^{-3}$)	0.56	0.37	1.8	2.3	3.0	1.4	1.3	
Φ_{tid}mean	4.0	0.085	0.040	0.019	2.0×10^{-3}	$< 10^{-4}$	$< 10^{-5}$	W m^{-2}
				$\sigma_p = 10\sigma_\oplus$				
ecc mean ($\times 10^{-3}$)	0.56	0.37	1.7	2.3	3.0	1.4	1.2	
Φ_{tid}mean	40.	0.80	0.34	0.12	0.020	$< 10^{-3}$	$< 10^{-4}$	W m^{-2}

Table 4.2: Mean eccentricities and tidal heat fluxes for TRAPPIST-1 planets coming from dynamical simulations of the system, for different tidal dissipation factors: from 0.1 to 10 times the Earth's value (taken from Neron de Surgy and Laskar, 1997).

the following section.

4.6.2 Should we expect TRAPPIST-1 planets to be all tidally locked?

With such short period orbits, it is often assumed that bodily tides have spun-down the planets to the spin-orbit synchronous resonance in a relatively short time. However, it is now known that some other processes can sometimes act to avoid the synchronous state. We will thus briefly review these processes. However, it appears that around such a low mass star, none of them is strong enough to counteract bodily tides so that all TRAPPIST-1 planets are probably in a synchronous-rotation state.

Indeed, one of the possibility for planets on an eccentric orbit is the capture into a higher order spin-orbit resonance (Goldreich and Peale, 1966). However, as discussed by Ribas et al. (2016) for the case of Proxima Centauri b, around a low mass star, the question is whether the dissipative tidal torque exerted by the star on the planet is strong enough to avoid the capture into resonance (which is permited by the non-axisymetric deformation of the planet). We use the methods detailed in the section 4.6 of Ribas et al. (2016) to calculate the probability of spin-orbit resonance capture of the planets of TRAPPIST-1. This method relies on comparing the tidal torque and the triaxiality torque, which depend strongly on eccentricity. The lower the eccentricity, the lower the spin-orbit resonance capture probability. For the capture to be possible, the eccentricity of a given planet in the system would need to be roughly above 0.01. The capture probability becomes greater than 10% only for an eccentricity greater than 0.03. However, simulations of the dynamics of the system accounting for tides and planet-planet interactions (see below) seem to show that such eccentricities are on the very high end of the possible scenarios. The spin orbit capture is thus seen as rather improbable in such a compact system.

The other possibility is that thermal tides in the atmosphere can create a strong enough torque to balance the stellar tidal torque on the mantle, as is expected to be the case on Venus (Leconte et al., 2015; Auclair-Desrotour et al., 2017b). For this process to be efficient, the planet must be close enough from the star so that tides in general are able to affect the planetary spin, but far enough so that bodily tides are not strong enough to overpower atmospheric tides. In a system around such a

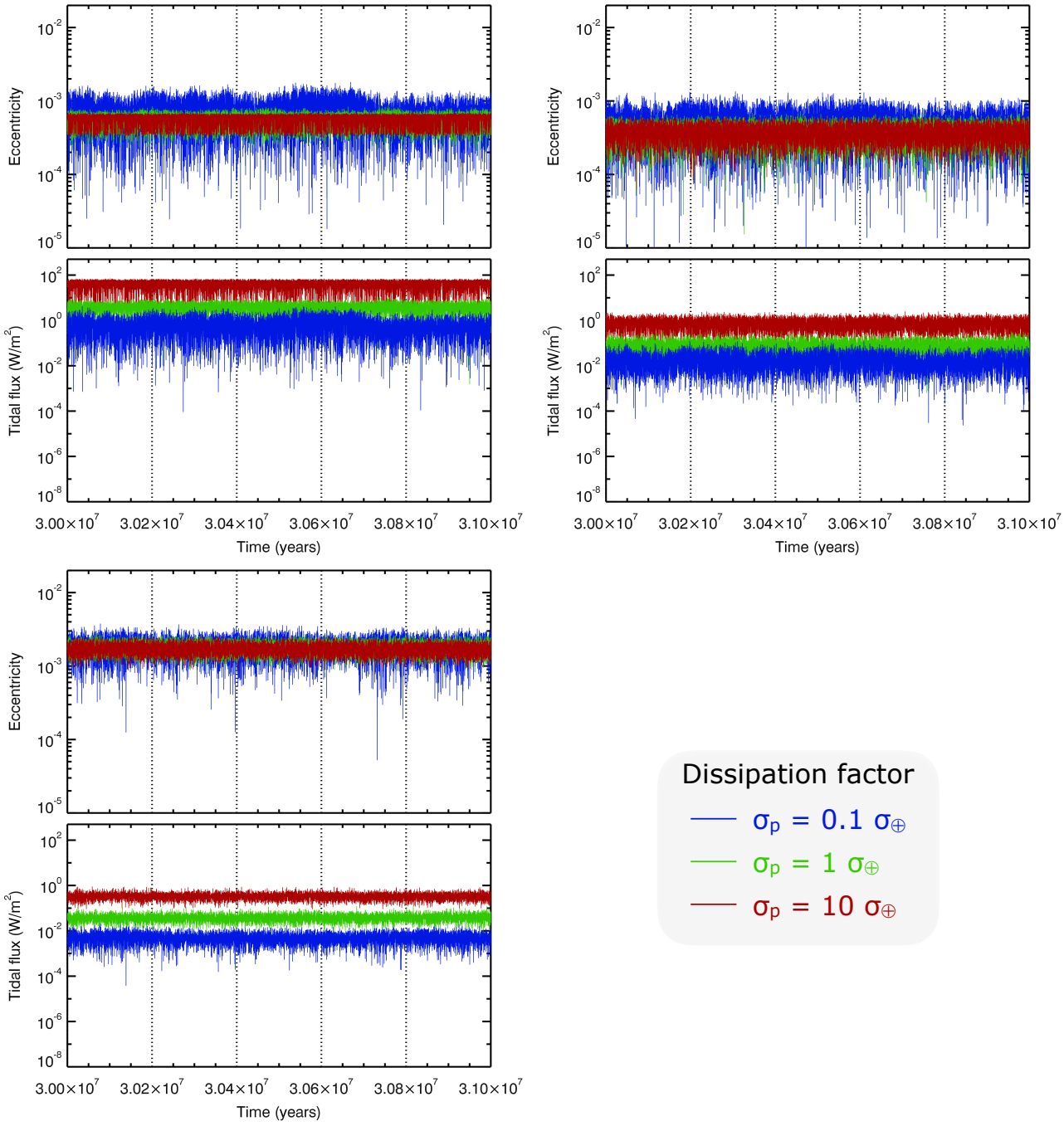

Figure 4.3: Eccentricity (top panels) and tidal heat flux (bottom panels) for the three inner planets of TRAPPIST-1 for different tidal dissipation factors (different colors): from 0.1 to 10 times the Earth's value (taken from Neron de Surgy and Laskar, 1997). Stars indicate the mean values.

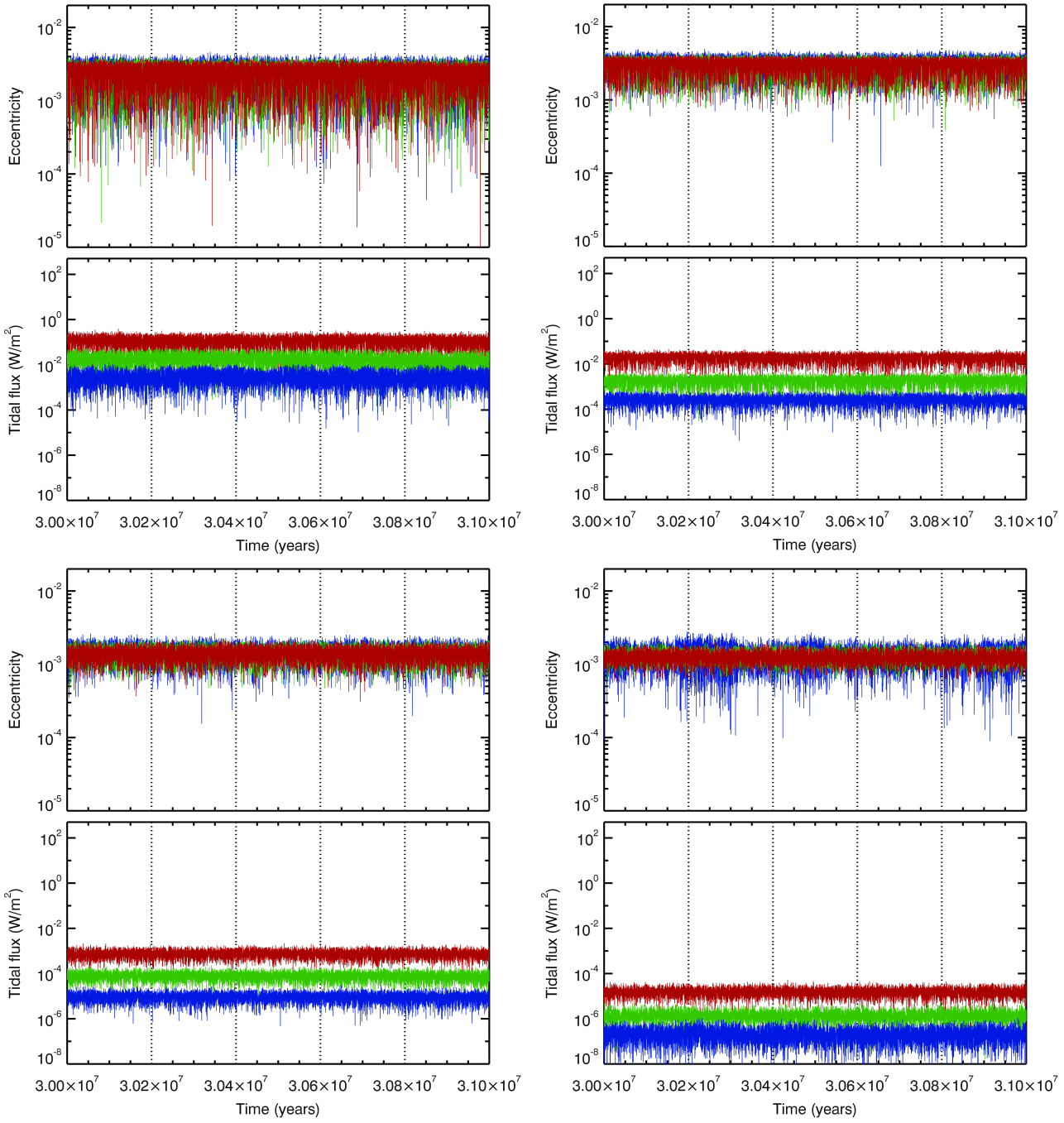

Figure 4.4: Same than Figure 4.3 but for the four outer planets.

low-mass star, this zone rests well beyond the position of the seven discovered planets (see Fig 3 of Leconte et al. 2015). Atmospheric tides are thus unable to affect the spin of the planet significantly.

4.6.3 Tidal N-body simulations

We then performed N-body simulations using Mercury-T (Bolmont et al., 2015) to compute the complete evolution of the system, taking into account tides, general relativity and the rotational flattening of the different rotating bodies. We explored the dissipation factors range discussed above (from 0.1 to 10 times the dissipation of the Earth). Figures 4.3 and 4.4 show the evolution of the eccentricity and resulting tidal heat flux for the different planets of TRAPPIST-1 and for the different dissipation factors. Table 4.2 summarizes the mean values of eccentricities and tidal heat fluxes for all the planets. Due to computation time considerations, simulations corresponding to a dissipation of 0.01 Earth dissipation and lower did not reach equilibrium. In the state of equilibrium, one should observe the following trend: the higher the tidal dissipation, the lower the equilibrium eccentricity, but the higher the tidal heat flux (see Bolmont et al. 2013 where this was discussed for 55 Cancri).

The initial state of our simulations corresponds to the orbital state of the system determined in Gillon et al. (2017) for planets b to g, and we used Luger et al. (2017b) for the orbital parameters of planet h. As the evolution timescales of rotation and obliquity are small compared to the estimated age of the system, we considered the planets to be initially in synchronization and with a very small obliquity. We considered two sets of initial eccentricities: all eccentricities at 10^{-6} and the eccentricities derived from TTVs of Gillon et al. (2017).

All simulations display the same behavior: after a short initial phase of eccentricity excitation, all excentricities decrease on a timescale depending on the dissipation factor, to reach a mean equilibrium value. This equilibrium value is the result of the competition between tidal damping and planet-planet excitations (e.g. Bolmont et al., 2013) and the eccentricity oscillates around it. The eccentricities corresponding to the equilibrium value are all relatively small as they are inferior to 10^{-3} for planets b and c, and inferior to 10^{-2} for planets d to h. The equilibrium value depends slightly on the dissipation factor of the planets: the higher the dissipation factor, the smaller the eccentricity. Note that such small eccentricities would have no effect on the climate (e.g., Bolmont et al. 2016a), that is why we assumed circular orbits for all planets in the climate simulations performed in this study.

The same kind of behavior can be seen for the obliquity of the planets: they assume an equilibrium value, result of the competition between tidal damping and planet-planet excitations. The equilibrium values are very small. For instance, the obliquities of the planets are smaller than 1°, which is why here we also assumed a zero obliquity for all planets.

Estimates of internal heat fluxes

Due to planet-planet interactions, the eccentricities and obliquities of the planets are not zero. This means that the planets are constantly submitted to a changing potential and constantly being deformed. This implies that the planets get tidally heated.

Our simulations with Mercury-T allow us to derive a possible state of the system and the corresponding tidal heat flux for all planets (see Fig 4.5). We find that the equilibrium eccentricity is enough to create a significant heat flux for the inner planets. For instance, assuming the tidal dissipation of the Earth for all the TRAPPIST-1 planets, we find that the eccentricity of planet b varies from

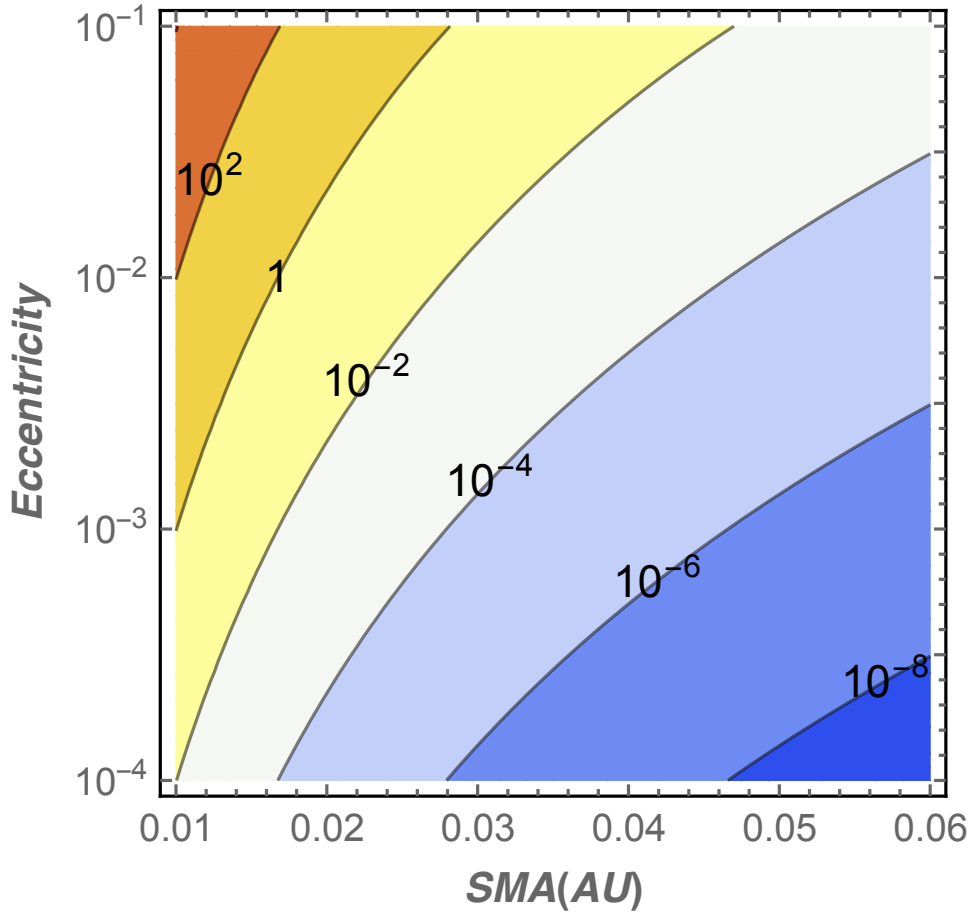

Figure 4.5: Tidal heat flux map (in W m^{-2}) as a function of semi-major axis (X axis) and eccentricity (Y axis) for planets with the Earth mass and radius. The dissipation efficiency is assumed to be one tenth of the Earth one to account for the dissipation in the mantle only. The tidal flux scales linearly with this parameter. But one has to keep in mind that this value can easily change by orders of magnitude with the internal structure of each planet. This map should thus serve as a rough guide only.

$\sim 8 \times 10^{-6}$ to 1.5×10^{-3}, with a mean value at 6×10^{-4}. These eccentricities lead to a tidal heat flux which varies from ~ 0.02 W m^{-2} to ~ 25 W m^{-2}, with a mean value at ~ 4 W m^{-2}. Table 4.2 shows mean values for the tidal heat flux for all the planets, for different scenarios of dissipation. Figures 4.3 and 4.4 show a snapshot of the evolution of the eccentricity and tidal heat flux over 1 Myr for each planet and for 3 different tidal dissipation factors.

We warn the readers that the mechanism of electromagnetic induction heating recently proposed by Kislyakova et al. (2017) should have a negligible contribution to the surface heat flux. We calculate from Kislyakova et al. (2017) (Table 1) that the induction heating should not produce more than 8, 19, 8, 0.6, 0.2, 0.08 and 0.03 mW m^{-2} for TRAPPIST-1b, c, d, e, f, g and h, respectively.

For the four outer planets of the TRAPPIST-1 system, the mean tidal heat fluxes derived from N-body calculations are lower than 0.09 W m^{-2}, which corresponds roughly to the Earth mean geothermal heat flux (Davies and Davies, 2010). Therefore, tidal heat flux is expected to play a minor role on the climate of these planets. It could nonetheless contribute significantly to:

1. the surface temperature of the cold traps, and hence to the atmospheric condensation of background gas (like N_2).
2. the maximum amount of the various sort of volatiles that could be trapped on the cold points of the planets.
3. the maximum depth of a subsurface liquid water ocean (Luger et al., 2017b).
4. more generally, the internal structure and the orbital dynamics of the planets.

The two first effects are explored in the next sections.

4.7 Could TRAPPIST-1 planets be airless planets?

Leaving aside the case of H_2/He-rich atmospheres, we focus here specifically on the case of the next three most volatile species: N_2, CO and O_2, because they are the best compromise between volatility (see Figure 4.6) and abundance. The cases of CO_2 and CH_4, which are significantly less volatile, are discussed later on in Sections 4.8 and 4.9, respectively. The main goal of this section is to assess the necessary conditions for the three outer TRAPPIST-1 planets to sustain a global, background atmosphere (i.e. a rather transparent atmosphere that can ensure the transport of heat and the pressure broadening of absorption lines of greenhouse gases). Background gases are essential because they can prevent the more volatile species such as CO_2 or NH_3 from collapsing on the nightside.

We assume for now that the surface is covered by water (liquid or icy) because it is expected to be the most abundant volatile, as well as the less dense (this is a key element for planetary differentiation) and most condensable (see Figure 4.6).

We refer the reader to the review by Forget and Leconte (2014) (and the references therein) for more information on possible sources and sinks of these volatile species.

4.7.1 Can a global atmosphere avoid atmospheric collapse?

To begin, we assume that the three outer TRAPPIST-1 planets initially start with an atmosphere. On synchronously rotating planets, the nightside surface temperature can be so low that the atmosphere

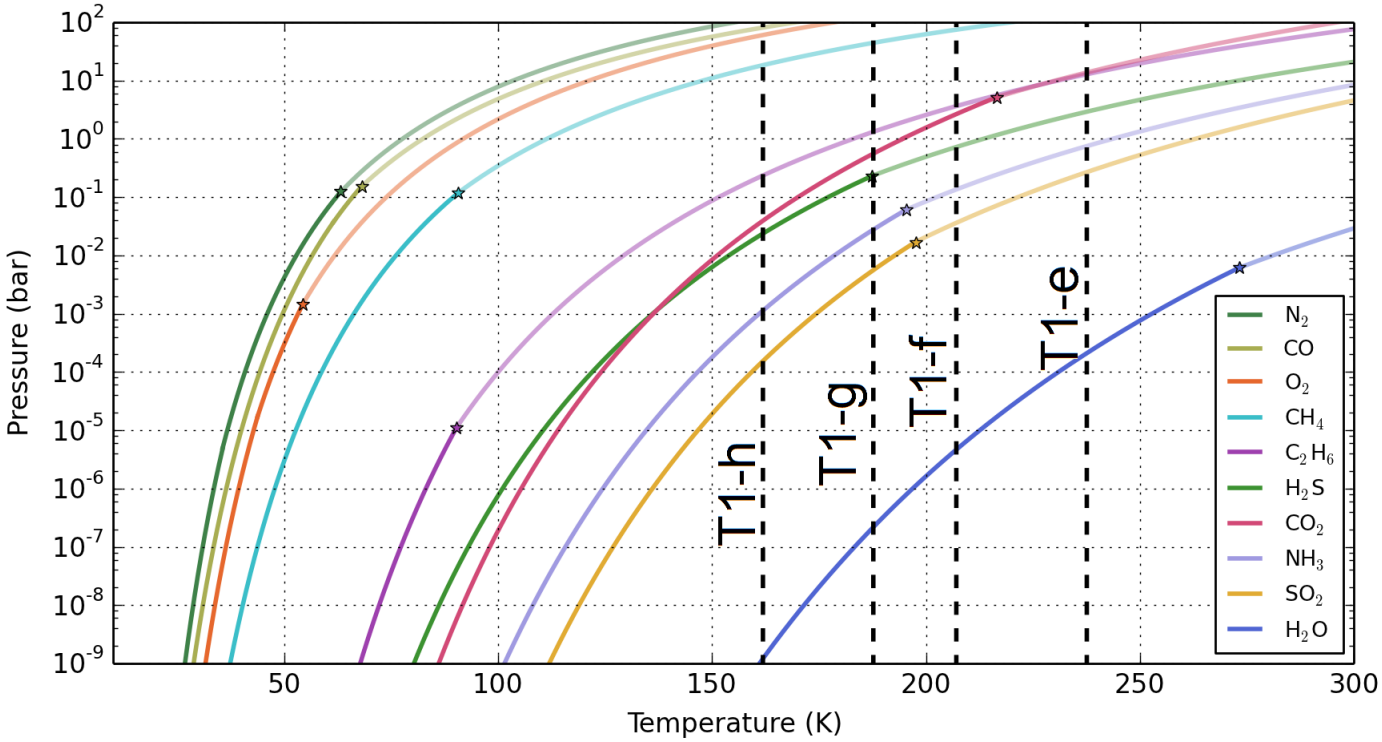

Figure 4.6: Equilibrium vapor pressures as a function of temperature for 9 different species (where experimental data are available) that could be abundant on TRAPPIST-1 planets. Solid black lines where superimposed to indicate the equilibrium temperatures of TRAPPIST-1e,f,g and h (assuming a surface albedo of 0.2). Stars indicate the positions of the triple points. These curves were adapted from Fray and Schmitt (2009).

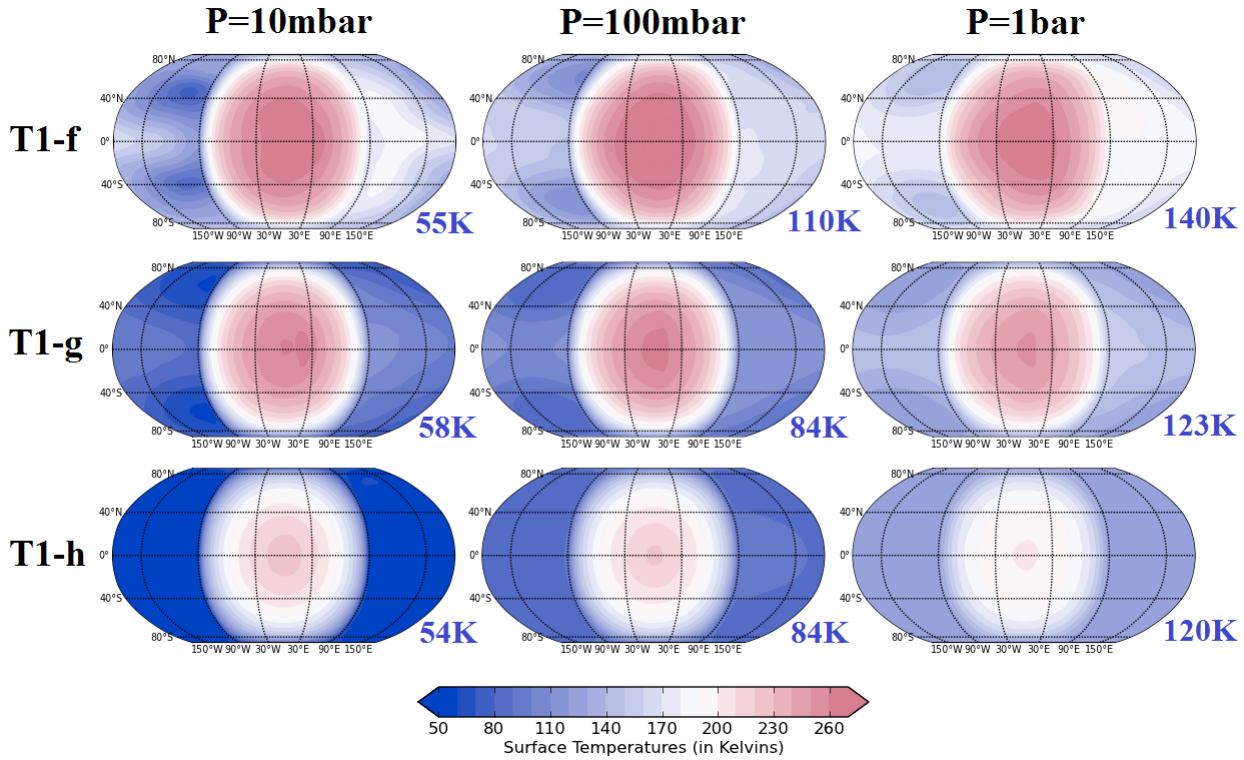

Figure 4.7: Maps of surface temperatures (averaged over 50 Earth days) for TRAPPIST-1f, g and h, assuming initially cold, water ice covered frozen planets, endowed with a pure N_2 atmosphere (with H_2O as a variable gas) at 3 different surface pressure (10 millibar, 100 millibar, 1 bar). Blue colored label indicates the mininum temperature reached by the coldest point of the planet throughout the entire simulation. As a reminder, for partial pressures of 10 millibar (resp. 100 millibar and 1bar), N_2 is expected to collapse at 53K (resp. 62K and 79K), CO at 56K (resp. 66K and 83K), and O_2 at 61K (resp. 72K and 87K). The geothermal heat flux is not taken into account, but the coldest temperatures found in these cases a posteriori show that it can be neglected.

itself starts to condense on the surface. We look for the minimal atmospheric pressure necessary to prevent them from atmospheric collapse, a configuration for which all the volatiles are permanently frozen on the nightside.

For this, we performed several simulations of TRAPPIST-1f, g and h planets (surface albedo fixed to 0.2 corresponding to a water ice surface around TRAPPIST-1, or coincidentally to a rocky surface) endowed with a pure N_2 atmosphere (with H_2O as a variable species) for various atmospheric pressures (from 1 bar down to 10 millibar). Surface temperature maps corresponding to these experiments are shown in Figure 4.7.

We find that a pure N_2 atmosphere (with H_2O as a variable gas) is quite resistant to atmospheric collapse for each of the three TRAPPIST-1 (fgh) outer planets. A collapse would be expected for N_2 partial pressure (pN_2) slightly lower than 10 millibar, and this value should hold for each of the 3 planets notwithstanding their various levels of irradiation. Our simulations indicate in fact (see Fig 4.7) that if TRAPPIST-1h is always globally colder than TRAPPIST-1g (which is globally colder

than planet f), it is not necessarily the case for the temperature of their cold points. TRAPPIST-1f, g and h planets have rotation periods $\sim 10^1$ Earth days and they lie thus near the transition between slow and fast rotating regimes (Edson et al., 2011; Carone et al., 2015, 2016). They should be in one of these two regimes and could potentially be in both, depending on the initial forcing (Edson et al., 2011). Since the temperature of the cold points is critically dependant on the circulation regime (see Carone et al. 2016, their Figure 1,2,3), it is difficult to assess which of these 3 TRAPPIST-1 planets should be more sensitive to atmospheric collapse.

In the same fashion than N_2, CO and O_2 are rather transparent in the infrared region of the surface thermal emission (between 10 and 100 microns, here) and have a similar molar mass than N_2 (between 28 and 32 g mol^{-1}). We can then safely extend our results for N_2 to CO and O_2-dominated atmospheres. These two gases are slightly more condensable gas and are thus expected to collapse for atmospheric pressure slightly higher than 10 millibar (see the legend of Figure 4.7). These results could be tested in future studies with models that would properly take into account the radiative properties of a CO or O_2-dominated atmosphere, and that would explore the sensitivity of these results to the assumption made on the surface composition (water, rock, etc).

More generally, note that as the dominant gas becomes less and less volatile, building up an atmosphere becomes more and more complicated due to atmospheric collapse. At any rate, such collapse would trigger a positive feedback, because as the atmosphere condenses, the heat redistribution would become less efficient, leading to even more condensation. This would drive the planets to a complete and irreversible atmospheric collapse.

4.7.2 How much volatile can be trapped on the nightside of an airless planet?

Conversely, we suppose now that the planets initially start without a global atmosphere, which could have been blown away during the early active phase of TRAPPIST-1. In this configuration, all the volatiles (accreted, outgassed, or residual from the initial collapse) are expected to accumulate on the cold side of the planet. We calculate here the maximum amount of volatiles that could be trapped in ice caps before a global atmosphere would be (re)formed.

The nightside surface temperature T_{night} on an airless tidally locked planet is determined by the geothermal heat flux F_{geo} of the planet:

$$T_{\text{night}} = \left(\frac{F_{\text{geo}}}{\sigma} \right)^{\frac{1}{4}}. \tag{4.2}$$

For geothermal heat flux of 500 mW m^{-2} (corresponding to planets with strong tidal dissipation in their interior) (resp. 50 mW m^{-2}), we get a nightside surface temperature of 50 K (resp. 30 K). The temperature at the base of the nightside ice cap (e.g. the temperature below the volatiles) depends on the geothermal heat flux F_{geo} and the nightside surface temperature T_{night}. When the ice cap is full (e.g. when ices start to convert into liquids), the temperature at the base of the nightside ice cap should be close (always higher, though) to that of the triple point. The triple point temperature is equal to 63K for N_2, 68K for CO, and 55K for O_2.

At these temperatures that are slightly warmer than those expected at the surface of Pluto (Forget et al., 2017), the viscosity of ices can be rather low. For instance, we estimate from Umurhan et al. (2017) (Equation 7) that the viscosity of N_2 ice at 45 K (resp. 52 and 60 K) should be roughly 1.6×10^{10} Pa s (resp. 8×10^{8} and 7×10^{7} Pa s). With this condition in mind, it is not clear whether the

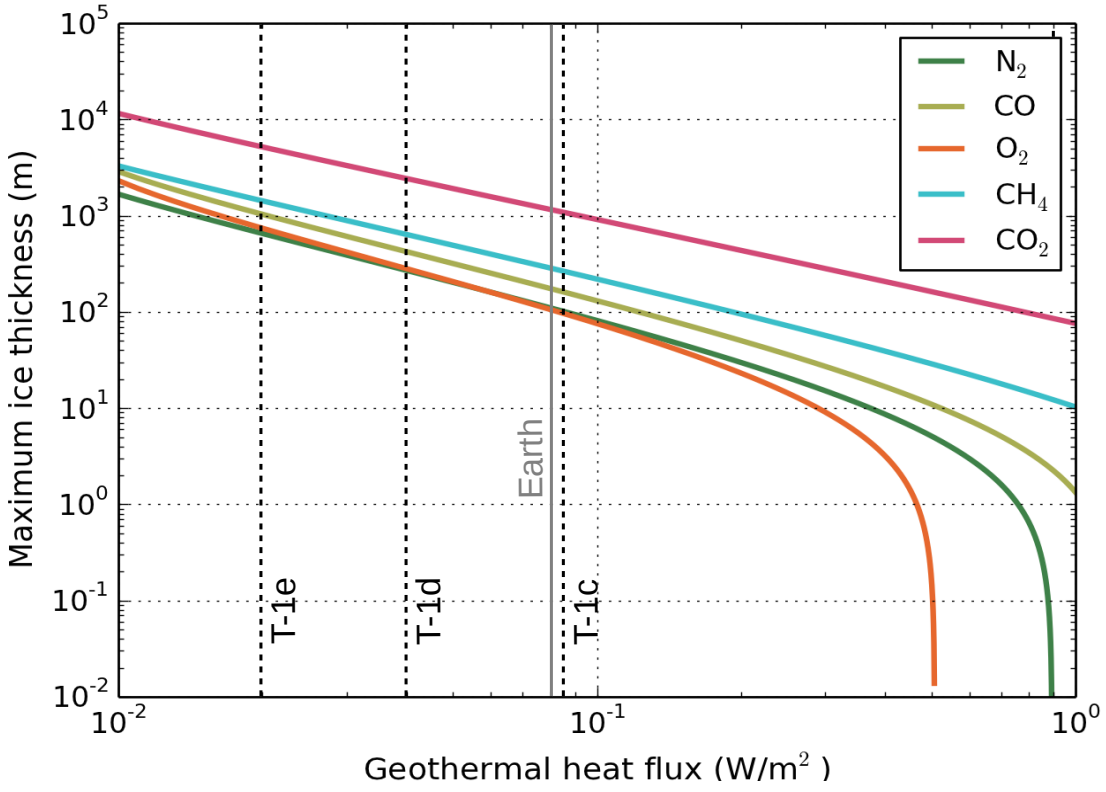

Figure 4.8: Maximum nightside thickness of various types of ice (N_2, CO, O_2, CH_4 and CO_2) - assuming that it is limited by basal melting - as a function of the geothermal heat flux. It is assumed here that the entire atmosphere has collapsed at the cold points of the planet and that the surface temperature at the top of the glacier is controlled by the geothermal heat flux. As a reference, vertical dashed lines indicate the average surface tidal heat flux on TRAPPIST-1 planets derived from Table 4.2, for a tidal dissipation equal to that of the Earth. We also added (vertical solid gray line) the average geothermal heat flux on Earth, to give the reader a rough sense of the amplitude of the radiogenic heating on TRAPPIST-1 planets. These quantities can be numerically converted in term of global equivalent surface pressure when multiplied by a factor $\frac{\rho g}{2}$. The thermodynamical and rheological properties of the ices were taken from `https://encyclopedia.airliquide.com`, `http://webbook.nist.gov`, Roder (1978); Schmitt et al. (1997); Fray and Schmitt (2009); Trowbridge et al. (2016), and Umurhan et al. (2017). Missing rheological data were mimicked on N_2.

maximum size of glaciers - formed by the accumulation of volatiles - should be controlled by the basal melting condition or by the glacial flow. Assessing this question properly would require to compare the efficiency of the glacial flow with the rate at which and the position where gaseous N_2 would condense on the nightside.

We assess below the case of the basal melting condition as it gives us an upper limit on the maximum amount of volatile possibly trapped on the nightside. When the nightside glaciers start to melt at their base, the ice flow should accelerate and expand significantly on the dayside of the planet. Not only basal melting is expected to be a very efficient process to transport ices (e.g. N_2, CO, O_2, etc.) from the nightside to the dayside, but the ices that reach the terminator should get sublimed and transport latent heat from the dayside to the nightside. This positive feedback would drive the planet into a runaway process, resulting in the formation of a new, global atmosphere.

For any species (we arbitrarily chose N_2 here), and for any of the seven TRAPPIST-1 planets, we derive from the basal melting condition the following set of 2 equations:

$$\begin{cases} T_{\rm base,liq} &= T_{\rm ref}\, e^{\frac{\left(\frac{1}{\rho_{\rm liq}}-\frac{1}{\rho_{\rm ice}}\right)}{L_{\rm fus}}\,(g\rho_{\rm ice}h_{\rm max}+P_{\rm N_2}-P_{\rm ref})} \\ h_{\rm max} &= \frac{\lambda_{\rm N_2}\,(T_{\rm base,liq}-T_{\rm night})}{F_{\rm geo}} \end{cases}, \tag{4.3}$$

with $T_{\rm base,liq}$ the temperature at the bottom of the glacier, $\lambda_{\rm N_2}$ the conductivity of N_2 ice, $\rho_{\rm liq}$ and $\rho_{\rm ice}$ the volumetric mass densities of liquid and icy N_2, $L_{\rm fus}$ the latent heat of N_2 ice melting, $P_{\rm ref}$ and $T_{\rm ref}$ the pressure and temperature of the triple point of N_2. P_{N_2} is the partial pressure of N_2 calculated at saturation from the Clausius-Clapeyron relationship (see Fig 4.6) at the surface nightside temperature $T_{\rm night}$.

This set of 2 equations corresponds respectively to:

1. the solid/liquid thermodynamical equilibrium at the base of the glacier. Note that the pressure at the bottom of the glacier is controlled by the weight of the glacier (and marginally, by the atmospheric pressure).

2. the geothermal gradient. It is assumed that the temperature inside the glacier rises linearly with depth, with a lapse rate fixed by the internal heat flux (conductive regime).

This set of equations can be solved explicitly after several variable changes and using the Lambert W function, defined as the solution of $X = e^X$, as done in Turbet et al. (2017b).

We calculated and plotted in Figure 4.8 the nightside maximum thickness as a function of geothermal heat flux for various ices. For geothermal heat flux ranging from 50 to 500 mW m^{-2}, the maximum thicknesses range:

1. from 200 to 5 meters (Global Equivalent Pressure - GEP - from 15 to 0.2 bar) for N_2

2. from 300 to 10 m (GEP from 15 to 0.5 bar) for CO

3. from 200 to 0 m (GEP from 10 to 0 bar) for O_2. O_2 has the lowest triple point temperature (see Fig 4.6).

Note that these values are of the same order of magnitude than in the atmosphere of Venus ($\sim$ 3 bar of N_2), Earth (0.78 bar of N_2; 0.21 bar of O_2) and Titan ($\sim$ 1.5 bar of N_2), the only Solar System rocky bodies that were able to sustain a thick, global atmosphere.

- For geothermal heat flux roughly lower than $\sim 5{\times}10^2$ mW m^{-2}, there is a strong hysteresis on the initial state (volatiles in the atmosphere; or volatiles condensed at the cold points). Planets that initially lost their atmosphere could stably accumulate quantities of $N_2/O_2/CO$ up to the equivalent of a few bar, in condensed form on the surface of their nightside. If somehow this scenario occured (through massive accretion or outgassing), the volatiles could not be retained on the nightside. The planet would suddenly sublime the entire volatile content of N_2, CO, O_2, CH_4, etc. forming a brand new, global atmosphere.

  Extreme events such as large meteoritic impact events could also have the potential to destabilize the volatiles that have been trapped in condensed form on the surface of the nightside. Only very eccentric bodies orbiting in the TRAPPIST-1 system could hit the planets near the anti-substellar point and potentially sublime the volatiles that should be preferentially trapped there. In the Solar System, it has for instance been proposed that the observed distribution of impact craters on Mercury could be explained by a large number of very eccentric bodies that would have hit Mercury near the substellar and anti-substellar regions, while the planet was in synchronous rotation (Wieczorek et al., 2012). Note that, there should be generally a large proportion of high-eccentricity bodies in the vicinity of the star, favoring subsequently impact events in the anti-substellar region.

- For geothermal heat flux roughly higher than $\sim 5{\times}10^2$ mW m^{-2}, we find that the planets could easily form an atmosphere even with very low amount of volatiles. In fact, we start to reach a regime here where the geothermal heat flux itself could significantly contribute to limit the atmospheric collapse as discussed in the previous section. Note that, at such high geothermal heat flux, heat could - and should - be transported by convection; this would significantly alter the calculations made here.

As shown in the previous section, eccentricities of TRAPPIST-1 planets are expected to vary with time, and tidal dissipation and surface heating with it, on timescales $\sim$ 1 Earth year (see Luger et al. 2017b - their Supplementary Figure 6). Peaks of tidal surface heating could trigger the destabilization of volatiles trapped on the nightside, although we would expect a delay and smoothing depending on where the tidal dissipation occurs. Actually, the heat itself could alter the internal structure. Detailed calculations of time-dependant tidal-induced surface heat flux (and implications) could be assessed in future studies.

As previously suggested in Turbet et al. (2016), the large-scale gravitational anomalies on tidally locked planets could be aligned with the star-planet axis. This means for instance that it is likely that a large basin (for example impact-induced) could be present at the anti-substellar point of TRAPPIST-1 planets. This could - in the same fashion than nitrogen ice is trapped on Pluto, in Sputnik Planum (Bertrand and Forget, 2016) - significantly increase the amount of volatiles possibly trapped at the cold point of the planets. Furthermore, the weight of the ices trapped on the nightside could cause the underlying water ice shell to slump, creating by itself (or amplifying the size of) an anti-substellar basin. Such process has recently been proposed as one of the possible scenarios to explain the formation of Sputnik Planitia on Pluto (Hamilton et al., 2016).

4.7.3 Residual atmospheres

Even though the atmosphere may have collapsed on the cold side of the planet, a residual, thin atmosphere could remain. The volatiles trapped on the nightside should be in fact in thermodynamical equilibrium with a residual atmosphere whose thickness depends on the surface temperature of the nightside, and on the type of volatiles trapped (assuming that the reservoir of volatiles is large enough).

For a geothermal heat flux of 100 mW m^{-2} (resp. 200 and 400 mW m^{-2}), the temperature of the cold side is $\sim$ 36K (resp. 42 and 50 K) and the remnant atmosphere could be as thick as $\sim$ 0.6 Pa of N_2 (resp. 18 and 400 Pa), 7×10^{-2} Pa of CO (resp. 3 and 110 Pa), and 7×10^{-3} Pa of O_2 (resp. 0.6 and 30 Pa). For the other volatiles (CH_4 and CO_2, for example), the thickness (or surface pressure) of a residual atmosphere would be several orders of magnitude lower.

Such residual atmospheres should not be thick enough to significantly increase the global heat redistribution (or possibly the greenhouse effect) and trigger subsequently a N_2, CO or O_2 runaway process. We remind (from Section 4.7.1) that the minimum atmospheric pressure required to sustain a global atmosphere is $\sim 10^3$ Pa.

Even though detecting a residual atmosphere of N_2, CO, O_2, etc. might be extremely challenging, as shown above such measurements could tell us a lot about 1) the temperature of the nightside and thus the internal heat flux of the planet and 2) the composition of the nightside reservoir of volatiles.

We also note that volatiles possibly trapped on the nightside of airless close-in planets would form a residual atmosphere that would be exposed to various processes of atmospheric escape (mainly stellar-wind sputtering and X/EUV-driven hydrodynamic escape). This indicates that volatiles trapped on the nightside of geothermally active tidally-locked planets might not be protected from atmospheric escape.

4.8 CO_2-dominated atmospheres

All the Solar System terrestrial planets are either airless bodies (e.g. Mercury) or worlds where CO_2 is - or was - abundant in the atmosphere (e.g. Venus, Mars) and/or in the subsurface (e.g. Earth). We assume in this section that the four TRAPPIST-1 outer planets possess today large quantities of CO_2 either in their atmosphere, on their surface or in their subsurface, and we explore the possible implications.

4.8.1 Stability of a CO_2-dominated atmosphere

CO_2 is much more condensable than any other species discussed in the previous section, as illustrated in Figure 4.6. On synchronously rotating planets, the nightside surface temperature can be extremely low, leading to the condensation of gaseous CO_2 on the surface. This could potentially prevent TRAPPIST-1 planets from building up thick CO_2 atmospheres.

To test this idea, we performed 130 3D climate numerical simulations of the four TRAPPIST-1 outer planets (surface albedo fixed to 0.2) for atmospheres made of various mixtures of N_2 and CO_2. In the same vein as Turbet et al. (2017b), we find that depending on the partial pressure of background gas (N_2, here) and on the partial pressure of CO_2, the gaseous CO_2 might condense or not, as shown on Figure 4.9. The shape of the diagrams is controlled by various physical processes:

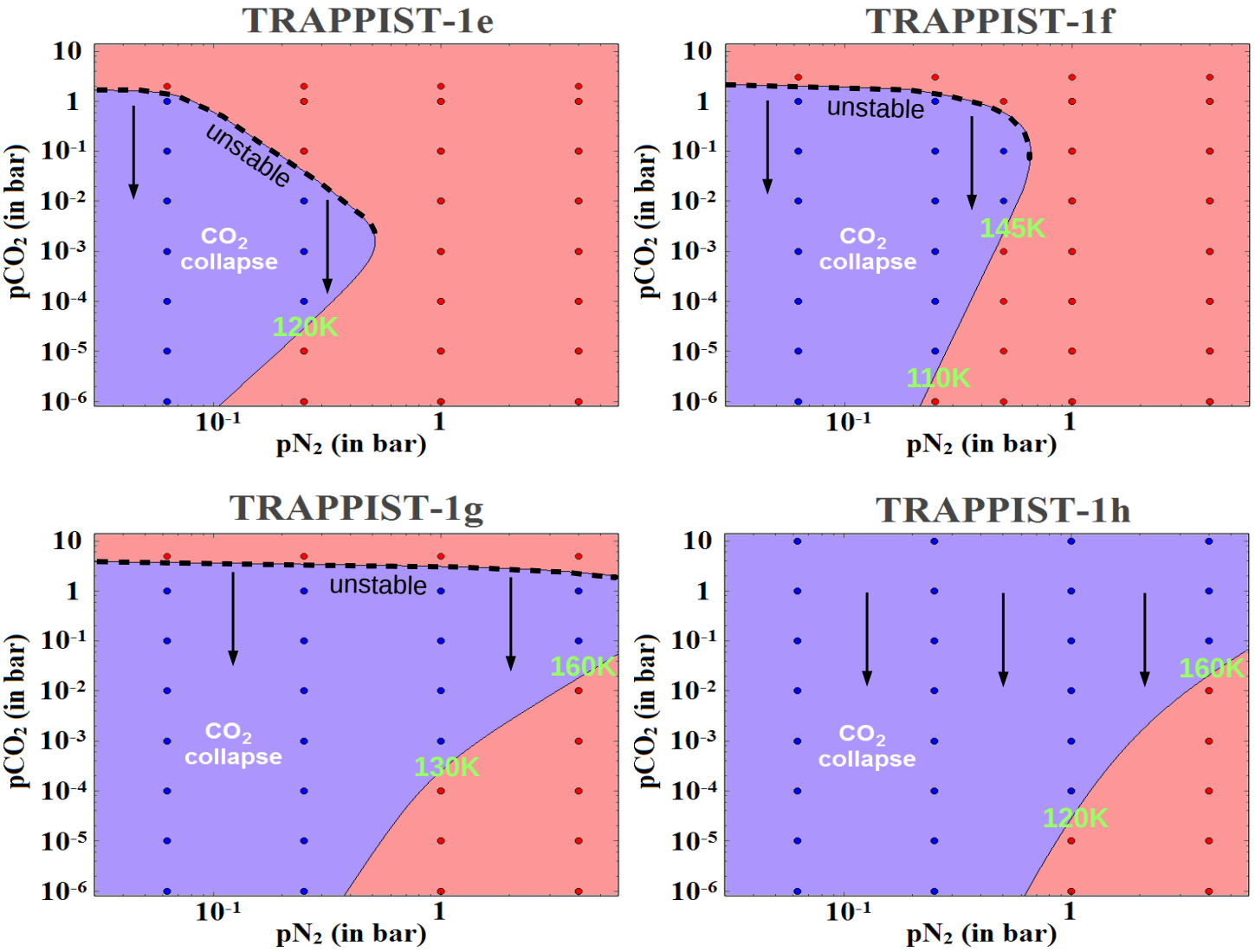

Figure 4.9: Climate regimes reached as a function of the partial pressures of N_2 and CO_2. For each set of (pN_2, pCO_2), it is indicated if the atmosphere is stable (red) or not (blue) to the atmospheric condensation/collapse of CO_2. The black arrows indicate how planets that have an unstable atmosphere would evolve on this diagram. Temperatures (in green) correspond to the rough estimate of the temperature of the cold point, at the stable lower boundary (blue is up; red is down). Simulations were performed assuming a surface albedo of 0.2 (corresponding both to a water ice surface around TRAPPIST-1, or a rocky surface). Water vapor is not included in these simulations. On TRAPPIST-1e, the inclusion of water vapor might substantially increase the temperature of the cold points through transport of latent heat from substellar to anti-substellar regions, and through the greenhouse effect of water vapor. On colder planets, the effect should be marginal.

1. The higher the background gas content is, the more efficient the heat redistribution is. This tends to increase the temperature of the cold points and limit the CO_2 condensation. High background gas content also favor the pressure broadening of CO_2 absorption lines, which increases the greenhouse effect of the atmosphere.

2. The higher the CO_2 content is, the higher its greenhouse effect is, but the higher its condensation temperature is. These two processes are competing each other, as illustrated in Soto et al. (2015) (in their Figure 1).

Figure 4.9 shows in fact a bistability in the CO_2 atmospheric content. If the planet initially starts with a thick CO_2 atmosphere (e.g. 10 bar), the greenhouse effect and the heat redistribution are efficient enough for such atmosphere to be stable (red color). Conversely, if the planet initially starts with a low CO_2 atmospheric content or no CO_2 at all and progressively accumulates somehow additional CO_2 in the atmosphere (e.g. by volcanic outgassing), all the extra CO_2 should keep condensing on the nightside (blue color). The planet would thus be permanently locked with a cold, thin CO_2 atmosphere.

We can for instance see in Figure 4.9 that a background atmosphere of $\sim$ 100 millibar of N_2 is not sufficient to build up a CO_2-rich atmosphere from scratch - on any of the four outer planets - due to the nightside surface condensation of CO_2. We can also see that TRAPPIST-1h is unable to sustain a dense CO_2 atmosphere ($>$ 100 mbar) even with several bar of N_2. For TRAPPIST-1e, f and g, if the initial CO_2 content is - for a given amount of background gas - below the "unstable" dotted line, then the planets are unable to build up CO_2-rich atmospheres (blue color). However, if the same planets start with an initial CO_2 content higher than this limit, CO_2 thick atmospheres are found stable (red color).

4.8.2 The fate of surface condensed CO_2

What happens when CO_2 starts to condense on the nightside? As shown in Turbet et al. (2017b), there should be two processes that control the maximum amount of CO_2 possibly trapped on the cold side of the planets: 1) CO_2 ice flow from the nightside to regions of sublimation; and 2) gravitational burial of CO_2 ice beneath water ice cover due to its higher density.

4.8.2.1 Glacial flow

There are in fact two distinct processes that could limit the growth of CO_2 ice glaciers:

1. The gravity pushes the glaciers to flow from the nightside to the dayside where CO_2 ice can be sublimated. This limit depends mostly on the gravity of the planet and the rheological properties of CO_2 ice (e.g., viscosity).

2. The internal heat flux of the planet causes the basal melting of the CO_2 ice glaciers. In such conditions, glaciers would slip and flow to the dayside where they would sublimate. This limit depends mostly on the geothermal heat flux of the planet and the thermodynamical properties of CO_2 ice (e.g., thermal conductivity).

It has in fact been shown in similar conditions (Turbet et al., 2017b), owing to the low conductivity of CO_2 ice ($\lambda_{CO_2} \sim 0.5$ W m^{-1} K^{-1}; Schmitt et al. 1997 – Part I, Thermal Conductivity of ices,

Figure 4), that it is mostly the basal melting that controls the maximum size of a CO_2 ice glacier. Using nightside temperatures from GCM simulations (roughly indicated in Figure 4.9, in green), we solve a set of 2 equations similar to Equations 4.3 (the only difference being the effect of the partial pressure of the background gas, N_2 here) to derive the maximum thickness of nightside CO_2 ice deposits. These equations are: 1) the solid/liquid thermodynamical equilibrium at the base of the glacier; and 2) the linear relationship between top and bottom glacier temperatures, assuming a fixed lapse rate (conductive regime) forced by the geothermal heat flux.

For 1 bar of background gas (N_2), TRAPPIST-1e and f should be protected from CO_2 atmospheric collapse. However, for TRAPPIST-1g (resp. h), CO_2 could collapse, and as much as 900 / 200 / 80 m of CO_2 (resp. 1000 / 250 / 100 m) could be trapped on the nightside for geothermal heat fluxes of 50 / 200 / 500 mW m^{-2}. This corresponds roughly to Global Equivalent Pressure of 45 / 10 / 4 bar (resp. 50 / 12 / 5 bar) of CO_2 that could be trapped.

We note that these quantities are of the same order of magnitude than the amount of CO_2 outgassed in the Venusian atmosphere ($\sim$ 90 bar), or the amount of CO_2 contained in the Earth's surface, mostly in the form of carbonate rocks on the continents ($\sim 10^2$ bar; Walker 1985).

4.8.2.2 When CO_2 ice caps are full

When the CO_2 nightside ice cap becomes "full" (e.g. when CO_2 ice starts to convert into liquid), all the extra CO_2 ice (or liquid) that reaches the irradiated side sublimates/vaporizes into the atmosphere. The extra (now gaseous) CO_2 increases the greenhouse effect of the atmosphere. It tends to warm the nightside and thus strengthens the CO_2 ice glacial flow, leading to even more CO_2 ice sublimation. Depending on the level of irradiation, the planet either finds an equilibrium (with stable CO_2 ice/liquid deposits) or enters into a CO_2 runaway greenhouse. This scenario has previously been explored for H_2O-covered planets (Leconte et al., 2013b) and is extended here to the case of CO_2.

It has in fact previously been shown (Turbet et al. 2017b; Appendix C) that CO_2 ice caps when full should be unstable on planets:

1. that have a low enough geothermal heat flux (typically lower than $\sim$ 1 W m^{-2} for the present study).

2. and that absorb irradiation fluxes equal or larger than TRAPPIST-1f.

CO_2 ice caps are expected to be entirely injected in the atmosphere.

To test this idea, we performed 3D GCM simulations of the four TRAPPIST-1 outer planets (efgh) endowed with a pure CO_2 atmosphere where we artificially entirely covered the surface of the planets with CO_2 ice (with a CO_2 ice cover that is large enough that CO_2 ice is always present everywhere on the surface). CO_2 ice albedo is arbitrarily fixed at 0.5. For TRAPPIST-1e and f, we find that no equilibrium is possible. The planets cannot maintain surface CO_2 ice on their dayside and should always end up in a CO_2 runaway greenhouse. No equilibrium is possible until 1) all the CO_2 ice/liquid content has been sublimed/vaporized, or 2) the CO_2 gas content becomes so large that CO_2 greenhouse effect starts to saturate (whereas the CO_2 condensation temperature increases), as discussed in von Paris et al. (2013a).

The scenario is however different for planets that are substantially less irradiated: TRAPPIST-1g and h. For these planets, 3D GCM simulations (see Figure 4.10) indicate that an equilibrium where

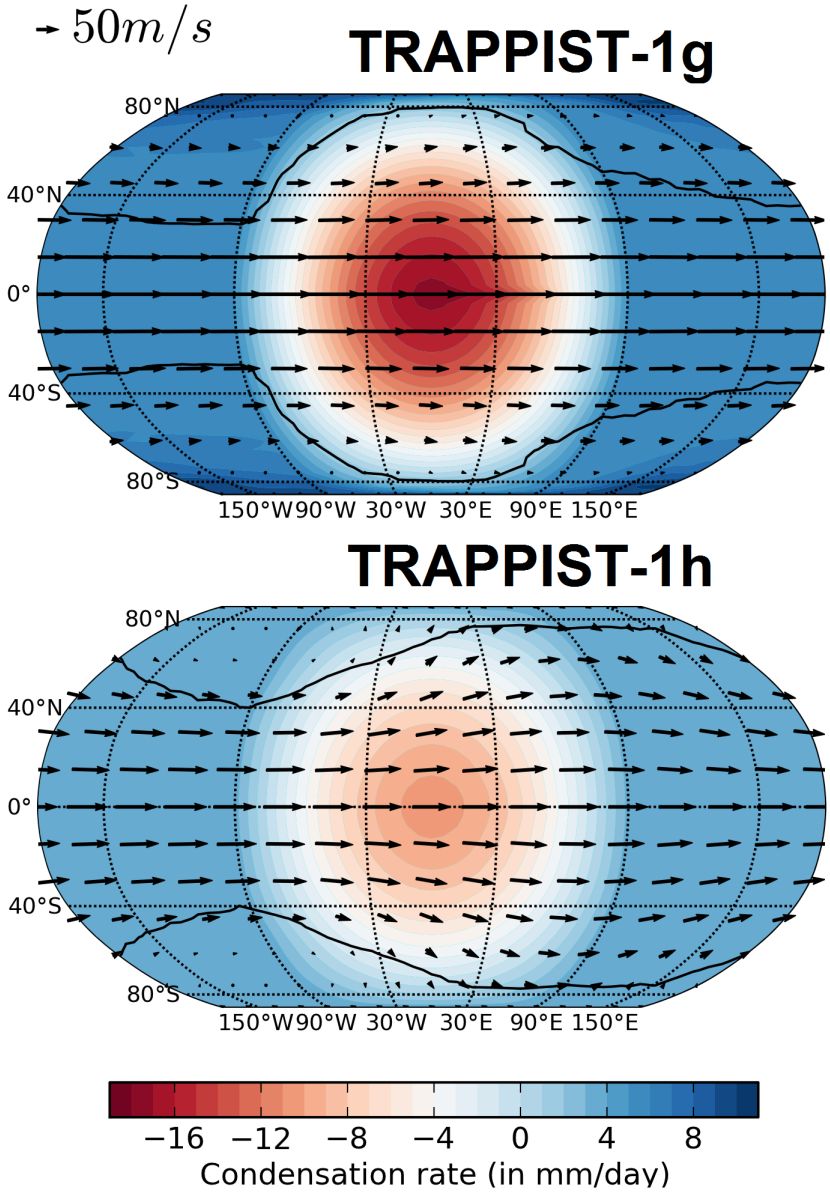

Figure 4.10: Maps of CO_2 ice condensation(+)/sublimation(-) mean day rates (averaged over 50 Earth days) for TRAPPIST-1g and h. Wind vectors at 5 km are presented as black arrows (see the 50 m s^{-1} arrow for the normalization). The black line contour indicates the horizontal extent of the CO_2 ice clouds (at the 1 g/m^{-2} level). It is assumed here that the planets are endowed with a pure CO_2 atmosphere and have with a surface that is entirely covered with CO_2 ice. CO_2 ice albedo is arbitrarily fixed at 0.5. We remind that the radiative effect of CO_2 ice clouds is not included here.

CO_2 ice and gaseous coexist is possible. In this configuration, the surface temperatures are roughly constant over the planet. For a pure CO_2 atmosphere, we find an equilibrium at 150±1 mbar and 174±0.1K for TRAPPIST-1g (resp. at 4±0.1 millibar and 145±0.1K for TRAPPIST-1h). The dayside intense CO_2 ice sublimation is offset by the nightside condensation, as illustrated in Figure 4.10. For TRAPPIST-1g, approximately 6 m of CO_2 per Earth year (resp. 4 m per Earth year for TRAPPIST-1h) is expected to get sublimed near the substellar point.

This tells us that if TRAPPIST-1g somehow progressively accumulates enough CO_2 on its nightside so that it starts to spill on its dayside and get sublimed, the planet should not be able to accumulate enough CO_2 in the atmosphere to reach the warm state depicted in Figure 4.9. Instead, the planet should be permanently trapped in a cold state, with CO_2 ice covering potentially as much as the entire surface of the planet.

Conversely, note that - for TRAPPIST-1g only - if the planet initially starts with a large content of gaseous CO_2 (so that it lies above the "unstable" lines, in Figure 4.9), then CO_2 ice/liquid deposits are unstable.

4.8.2.3 CO_2 ice gravitational stability

We assume here that some CO_2 has condensed on the nightside of TRAPPIST-1 outer planets, above the water ice shell. CO_2 ice is 1.6 times denser than water ice. This difference of density between the two types of ice (CO_2 above, H_2O below) should trigger an instability of Rayleigh-Taylor (Turbet et al., 2017b) that forces CO_2 ice to sink below the water ice cover. At first order, and assuming that both layers of CO_2 and H_2O ices are isoviscous (i.e. have a fixed viscosity), the density contrast should initiate Rayleigh-Taylor instabilities at a timescale $\tau_{\text{R-T}}$ given by (Turcotte and Schubert, 2001):

$$\tau_{\text{R-T}} = \frac{13\ \eta}{\Delta\rho g b}, \tag{4.4}$$

with η the viscosity of the more viscous layer, $\Delta\rho$ the density contrast between the two layers and b the characteristic size of the domain. We discuss in the following paragraph how we estimate the different terms of this equation.

Depending on whether CO_2 is liquid or solid at the interface with the H_2O layer, the density contrast $\Delta\rho$ would range between 240 and 570 kg m^{-3}. Depending on the planet and the background gas content, the surface temperature at the cold point is expected to range between 120 K and 160 K (see Figure 4.9). However, the basal temperature should rapidly increase with the glacier thickness, given the low conductivity of CO_2 (Schmitt et al., 1997). Assuming that the CO_2 glaciers are nearly full, they should have a thickness $\sim 10^2$ m and the basal temperature could be as high as $\sim$ 218K (temperature at the CO_2 liquid/solid equilibrium for a pressure of 1.5 MPa). For a stress at the interface between the two layers of the order of 1 MPa and a temperature $\sim$ 218 K, the viscosity of the CO_2 ice layer is estimated $\sim 10^{12}$ Pa s, based on available experimental data (Durham et al., 1999). At the same temperature and stress conditions, water ice has a viscosity $\leq 10^{16}$ Pa s, for grain size lower than 1 mm, based on experimental data (Durham et al., 2001; Durham and Stern, 2001; Goldsby and Kohlstedt, 2001). The water ice layer should thus be the layer controlling the Rayleigh-Taylor timescale. Assuming that a thickness of 10^2 m of CO_2 deposit is representative of the characteristics size of the domain, the R-T timescale $\tau_{\text{R-T}}$ is $\leq 10^4$ Earth years, which is geologically short.

Once gravitationally destabilized, the CO_2 ice deposit would sink at the base of the water ice shell at a rate that is determined mostly by the viscosity of water ice and the size of the CO_2 ice diapir (e.g.

the domed CO_2 ice formation piercing the overlying water ice shell). The time required for a CO_2 ice diapir to cross the water ice layer can be estimated using the Stokes velocity, the terminal velocity of a sphere falling through a constant viscosity medium (Ziethe and Spohn, 2007):

$$U_s = \frac{2}{9} \Delta\rho g \, (r^2/\eta) \tag{4.5}$$

For a diapir radius r of 100 m (comparable to the thickness of the CO_2 deposit) and a conservative value for water ice viscosity of 10^{15}-10^{16} Pa s, this leads to a velocity of 0.04-0.4 m per Earth year. As temperature increases as a function of depth (~ 2 F_{geo} K m^{-1}), the viscosity of water ice is expected to decrease with depth, resulting in an acceleration of the diapir fall. A 100-m diapir of CO_2 ice would thus not need more than $\sim 10^4$ Earth years to reach the bottom of a 1.5-km thick water ice layer, which is the expected depth of a subglacial ocean for a geothermal heat flux ~ 0.1 W m^{-2}.

These two calculations (Rayleigh-Taylor and diapir fall timescales) tell us that the lifetime of surface CO_2 ice on TRAPPIST-1 planets should be geologically short. In particular, it should be short compared to:

the volcanic CO_2 outgassing timescale:

The present-day Earth CO_2 volcanic outgassing rate is 60 bar/Gy (Brantley and Koepenick, 1995; Jarrard, 2003). It takes roughly 10^6 Earth years to outgass a $\sim$60 cm Global Equivalent Layer (GEL) of CO_2 ice (equivalent to a 10^2m-thick nightside CO_2 ice cap with a radius of 10^3 km).

the CO_2 ice flow and sublimation timescale:

We assume that a 10^2m-thick, 10^3km-radius nightside CO_2 ice cap is in dynamic equilibrium with the atmosphere. This means that the CO_2 ice flow - controlled here by the rheological properties of CO_2 ice - has reached a constant, positive rate. This also means that the integrated CO_2 ice sublimation rate at the edges of the glacier is equal to the total gaseous CO_2 condensation rate on the ice cap.

We model the steady state flow of the CO_2 ice cap using equations 1-4 from Menou (2013). We take the flow rate constants of CO_2 ice from Nye et al. (2000), derived from the measurements of Durham et al. (1999). We chose the rheological properties of CO_2 ice for a creep exponent n=2, and at 218K. This is the maximum temperature expected at the bottom of the CO_2 ice glacier, before basal melting occurs. These are conservative assumptions in the sense that these are the parameters (creep law and temperature) that maximize the velocity of the CO_2 ice flow. With these assumptions, we estimate that it takes at least 10^8 Earth years to recycle the entire CO_2 ice cap.

In summary, CO_2 that starts to collapse on the nightside of TRAPPIST-1 planets is expected to form permanent CO_2 ice caps. This condensed CO_2 can be entirely returned into the atmosphere if:

1. the CO_2 ice caps reach their maximum size, defined by the condition of basal melting. This can be achieved through CO_2 volcanic outgassing.

2. the CO_2 ice caps are removed efficiently from the nightside by the dry, rheological CO_2 ice flow, and then get sublimated.

However, these two processes operate on much longer timescales than the time required to burry the CO_2 ice caps below the water ice cover. Consequently, CO_2 that condense on the nightside of

TRAPPIST-1 planets (and by extent, any water-rich, synchronous planet) can very likely end up burried below the water ice shell.

4.8.2.4 The fate of buried CO_2

CO_2 ice is expected to completely melt and equilibrate thermally with the surrounding H_2O media when stabilized at the bottom of the water ice shell. The temperature and pressure conditions at the bottom of the water ice layer depend on its thickness and on the geothermal flow. For geothermal heat flux lower than $\sim$ 0.4 W m^{-2}, the melting of water ice would be reached for depth larger than $\sim 4{\times}10^2$ m, and pressure of $\sim$ 3.5 MPa, corresponding to the saturation vapor pressure of CO_2 at $\sim$ 273 K (Lide, 2004). Destabilizing the liquid CO_2 would therefore require a geothermal heat flux higher than 0.4 W m^{-2}. At such large geothermal heat flux, CO_2 ice (or liquid) should indeed get sublimed (or vaporized) within the water ice shell.

However, for geothermal heat flux lower than 0.4 W m^{-2}, CO_2 ices/liquids should be stable during their fall. Even if the density of liquid CO_2 decreases with increasing temperature as it equilibrates with the surrounding water ice media, it remains always denser than water ice (Span and Wagner, 1996), and therefore should always accumulate at the bottom of the ice shell. At T = 273 K and pressure between 3.5 and 28 MPa (subglacial pressures estimated for geothermal heat flux between 400 and 50 mW $^{-2}$), liquid CO_2 has a density very close to that of liquid water (928 and 1048 kg m^{-3}, respectively, using the equation of state of Span and Wagner 1996), so that CO_2 should coexist with H_2O at the ice-water interface.

From this point, two processes are expected to occur and compete with each other. Firstly, part of the CO_2 should dissolve in the liquid water. The total amount of CO_2 that could be dissolved in the water layer would depend on the volume (thickness) of the water layer.

Secondly, pressure and temperature conditions expected at the bottom of the ice layer are in the stability field of CO_2 clathrate hydrate (Sloan, 1998; Longhi, 2005), therefore CO_2 should rapidly interact with H_2O molecules to form clathrate hydrate. Clathrate hydrates are non-stoichiometric compounds consisting of hydrogen-bonded H_2O molecules forming cage-like structures in which guest gas molecules, such as CO_2, can be trapped (Sloan, 1998). Once formed, these clathrates are very stable and can be dissociated only if the temperature is raised about 5-10 K above the melting point of water ice. The storage of CO_2 in the form of clathrate should be particularly efficient as liquid CO_2 and liquid water coexist. As CO_2 clathrate hydrates have a density of about 1150 kg m^{-3} (assuming full cage occupancy, Sloan 1998), they would rapidly sink at the bottom of the water liquid layer, ensuring an almost complete clathration of CO_2. Note that we expect some of the CO_2 to get dissolved in the liquid water during the clathrate sinking. The relative proportion of CO_2 trapped in the form of clathrate hydrate or dissolved in the water layer would depend on the volume of CO_2 that is buried at the base of the ice shell and on the volume (thickness) of the water layer.

In summary, as long as the geothermal heat flux is lower than $\sim$ 0.4 W m^{-2}, the water ice shell should exceed several hundreds of meters, and CO_2 should remain sequestered either in the form of CO_2 clathrate hydrates or dissolved in the subglacial liquid water ocean. Release of gaseous CO_2 in the atmosphere may occur in particular following local increase of geothermal heat flux resulting in a significant thinning and breaking-up of the water ice shell. The total amount of CO_2 that can be stored in the H_2O layer (by any of the two processes discussed above) depends on the total abundance of H_2O of the planet as well as the CO_2/H_2O ratio. Evaluating the maximum amount of CO_2 that can

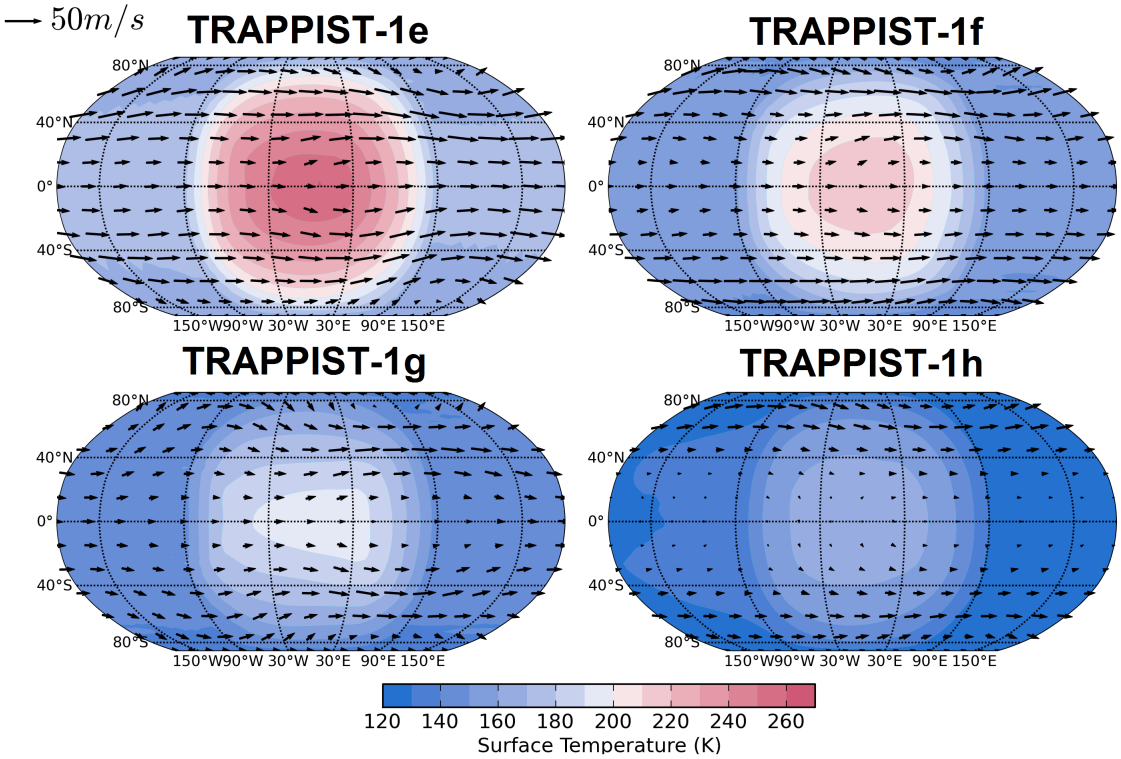

Figure 4.11: Maps of surface temperatures (averaged over 50 Earth days) for TRAPPIST-1e, f, g and h, assuming planets endowed with a 1 bar N_2-dominated atmosphere composed of 10% of CH_4. Wind vectors at 5 km are presented as black arrows (see the 50 m s^{-1} arrow for the normalization). Surface albedo is arbitrarily fixed at 0.2.

be trapped underneath the water ice cover require a detailed description of the H_2O layer structure as well as thermodynamic models predicting the partitionning of CO_2 between the different phases.

4.9 CH_4-dominated worlds

The only Solar System terrestrial-size object that possesses a thick atmosphere that deviates from the one discussed as far is Titan. Titan (0.012 $S_\oplus$, 0.4 $R_\oplus$) has a 1.5 bar thick N_2-dominated atmosphere, with as much as 5 % of methane near the surface (Niemann et al., 2005). We explore in this section the possibility that TRAPPIST-1 outer planets could be hydrocarbon-rich worlds, and the possible implications.

4.9.1 Warm Titans

What would happen if you suddenly place Titan at the location of each of the seven TRAPPIST-1 planets and how would the planet evolve? At the equilibrium temperatures of the four TRAPPIST-1 outer planets (e to h), the saturation vapor pressure of CH_4 ranges between 10 and 100 bar (resp. between 5×10^{-2} and 5 bar for C_2H_6). Unlike Titan, we should thus expect all the methane and/or

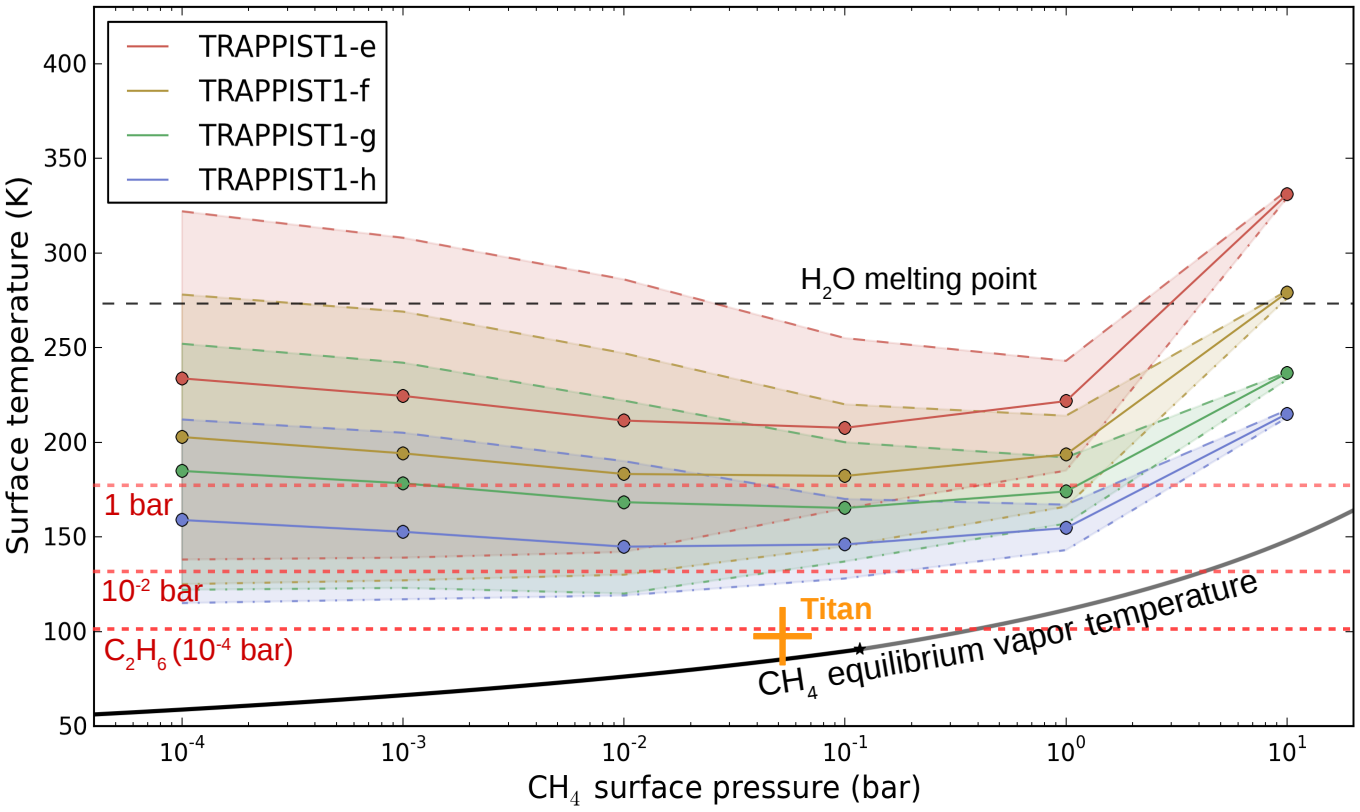

Figure 4.12: Mean surface temperatures of TRAPPIST-1 outer planets, assuming atmospheres made of N_2 and CH_4 only. Each simulation was performed with the 3D LMD Generic Global Climate Model, for 1 bar of N_2, and various CH_4 partial pressures (from 10 Pa to 10 bar). The four regions filled in colors show the range of surface temperatures reached by the four outer planets (red, yellow, green and blue for TRAPPIST-1e, f, g and h, respectively). Solid, dashed and dash-dotted lines depict the mean, maximum and minimum surface temperatures reached in the simulations, respectively. Note that the highest surface temperature for TRAPPIST-1f, g and h is almost always lower than 273 K (e.g. the melting point of water). The black line indicates the CH_4 equilibrium vapor pressure. Dashed red lines show the equilibrium vapor temperature of ethane (C_2H_6) for various partial pressures (10^{-2}, 10^{-4}; and 1 bar). The melting point of water is indicated by the black horizontal dashed line. As a reminder, equilibrium temperatures of TRAPPIST-1e, f, g and h planets are (for a Titan-like bond albedo of 0.3) respectively 230, 198, 182 and 157 K.

ethane content to be vaporized in the atmosphere.

To check this, we performed haze-free 3D numerical climate simulations of N_2/CH_4 atmospheres, for various CH_4 contents, and for the four TRAPPIST-1 outer planets. Some of these simulations (for a 1 bar N_2-dominated atmosphere with 0.1 bar of CH_4, similar to Titan) are presented in Figure 4.11.. Fig 4.12 shows the mean, maximum and minimum surface temperatures obtained for each of the TRAPPIST-1e, f, g and h outer planets. The calculated surface temperature of the planets results from a subtle balance between the radiative cooling of stratospheric CH_4 and the greenhouse effect of tropospheric CH_4. Around a star like TRAPPIST-1, absorption of stellar radiation by CH_4 is particularly efficient around 0.89, 1.15, 1.35, 1.65, 2.3 and marginally 3.3 μm bands. Consequently, CH_4 absorption warms the upper atmosphere and also reduces the short wave irradiation flux that reaches the surface and troposphere, contributing to a cooling of the planetary surface. For example, approximately 40% of the incoming stellar radiation is able to reach the surface in the simulations shown in Figure 4.11.

Despite the anti-greenhouse effect of CH_4 that tends to cool the surface temperature, it would be extremely hard for TRAPPIST-1 planets to sustain surface liquid/icy CH_4. This is illustrated in Fig 4.12 with the comparison between the saturation pressure curve of CH_4 and the calculated minimum surface temperatures (on the nightside). Additionally, a partial pressure of at least $\sim 10^{-2}$ bar of ethane (C_2H_6) would be required for the coldest planets to start forming nightside surface lakes or seas of ethane, similar to the ones observed on Titan.

EUV flux should lead to the formation of photochemical hazes in CH_4-rich planetary atmospheres, in the same fashion than on Titan. Such hazes could potentially have an additional powerful anti-greenhouse (i.e. radiative cooling) effect, by absorbing and reflecting a significant part of the incoming stellar flux (Lorenz et al., 1997). TRAPPIST-1 outer planets (e, f g and h) should receive a EUV flux ranging between 600 and 3000 times Titan's flux (Wheatley et al., 2017). Photochemical hazes could thus form efficiently and accumulate in the atmosphere. This could potentially cause a catastrophic cooling of the planetary surface (McKay et al., 1991), and change the aforementioned conclusions on the likeliness for TRAPPIST-1 outer planets to sustain surface condensed methane.

Nonetheless, using a 1D photochemical-climate model taking properly into account the microphysics and the radiative effect of photochemical hazes (Arney, 2016), it has been shown that the thickness (and thus the opacity) of organic hazes should be self-regulated (Arney et al., 2016). In fact, thick hazes should inhibit methane photolysis, which would in turn drastically limit haze production rates. In other words, the rate of methane photolysis should not scale linearly with the incoming EUV flux, but instead should at some point saturate. Moreover, organic hazes are much less opaque at the emission wavelengths of cool stars like TRAPPIST-1 than solar emission ones (Khare et al., 1984; Vinatier et al., 2012; Arney et al., 2017). This indicates that a large part of the incoming stellar flux would reach TRAPPIST-1 planetary surfaces and tropospheres and easily vaporize all the methane in the atmosphere. In other words, even when taking into account the radiative effect of hazes, all the TRAPPIST-1 planets should be well beyond the CH_4 runaway-greenhouse-like limit. Eventually, it is important to note that, at the high EUV fluxes expected on TRAPPIST-1 planets, CO_2 (if present) could be also photodissociated into oxygen radicals that should seriously limit the build up of the organic hazes (Arney et al., 2017). In particular, if the atmospheric CO_2/CH_4 ratio is high, and if the emission of TRAPPIST-1 is high in the spectral region $\sim$ [120-180] nm, where the UV cross section of CO_2 / O_2 is maximum (Arney et al. 2017, Figure 2c), then the formation of photochemical hazes could be severely halted.

We remind that a potentially thick O_2 atmosphere could have built up abiotically during the early runaway phase (Luger and Barnes, 2015; Bolmont et al., 2017) while TRAPPIST-1 was a pre-main-sequence star, playing potentially a strong role here on the haze formation. But above all, the combustion of CH_4 (and more generally, of any reduced compound such as NH_3 or H_2S), following $CH_4 + 2O_2 \rightarrow CO_2 + 2H_2O$, should prevent CH_4 to substantially build up in a thick O_2-rich atmosphere. If the build-up of O_2 during the early runaway phase exceeds the total reservoir of CH_4, there might not be enough room left for CH_4 to accumulate in the atmosphere.

4.9.2 Titan-like world lifetime

Through 1) CH_4 and hydrocarbons photodissociation, 2) organic hazes formation and 3) haze sedimentation, the atmospheric CH_4 and hydrocarbon content of TRAPPIST-1 planets should deplete rapidly. It is for example estimated that it should take roughly 10 My for Titan to remove all the methane (0.07 bar) from the atmosphere (Yung et al., 1984), and as much as $\sim$ 30 bar could have been destroyed since the beginning of the Solar System.

Therefore, as much as 600-3000 times more methane (averaged over the surface) could potentially be photolyzed on TRAPPIST-1 outer planets. Over the expected age of the TRAPPIST-1 system (between 5 and 10 Gyr, according to Luger et al. 2017b and Burgasser and Mamajek 2017), at least $\sim$ 120 bar of CH_4 (Titan's limit, including the gravity correction) and as much as 10^5 bar of CH_4 (when scaling linearly the CH_4 loss with the EUV flux) could have been destroyed by photolysis.

Sustaining continuously a CH_4-rich (and NH_3-rich, by analogy) atmosphere over TRAPPIST-1 lifetime would require an extremely large source of methane. It is in fact widely believed that the CH_4 current level on Titan might be somewhat anormal and produced by an episodic replenishment due to destabilization of methane clathrates in Titan's subsurface (Tobie et al., 2006).

Similarly, large quantities of N_2 could be photodissociated, forming HCN (Liang et al., 2007; Krasnopolsky, 2009; Tian et al., 2011; Krasnopolsky, 2014), and could be lost subsequently in longer carbonated chains that could sedimentate on the surface (see next subsection). This mechanism could remove efficiently N_2 from the atmosphere in the long term.

We acknowledge however that the arguments stated in the previous section (especially the haze negative feedback on CH_4 photolysis, as proposed by Arney et al. 2016) could drastically limit the CH_4 photolysis rate and relax the constraint on the methane production rate required to sustain a CH_4-rich atmosphere.

4.9.3 Surface conditions

Even for large CH_4/N_2 contents, and even when neglecting the radiative effect of photochemical hazes, TRAPPIST-1f, g and h should be cold enough (see Figure 4.12 and the associated legend) to be covered by a complete layer of water ice. In this case, photolysis of methane would produce organic hazes that should sedimentate and progressively accumulate at the surface in large quantities. On Titan, it is estimated that $\sim$ 1 m Global Equivalent Layer (GEL) of heavy hydrocarbons - or tholins - are covering the surface (Lorenz et al., 2008). This is in fact two orders of magnitude lower than what we would expect from the direct conversion of current CH_4 photolysis rate through the age of the Solar System (Lorenz and Lunine, 1996). Possible solutions to this discrepency are discussed in Lorenz et al. (2008).

Similarly, signatures of long carbonated chains have also been detected on many Kuiper Belt

Objects (Johnson et al. 2015; see Table 1 and references therein), including Pluto, Triton, Makemake, Sedna, etc. The New Horizon mission has even directly observed and mapped (during its flyby) dark tholins deposits on Pluto, in Cthulhu Regio (Stern et al., 2015).

TRAPPIST-1 planets could thus be covered by a thick surface layer of tholins today. Once the CH_4 atmospheric reservoir would be empty, only condensable hydrocarbons and long-carbonated chains (and potentially gaseous N_2, leftover from NH_3) would remain. In general, because sedimented organic hazes should be rather rich in hydrogen, they should have a density of the same order of magnitude than water ice, and should be in particular more stable than CO_2 to gravitational burial.

Assuming that photochemical hazes have a limited radiative effect in the near-infrared (Khare et al., 1984; Vinatier et al., 2012; Arney et al., 2017) where the emission of TRAPPIST-1 peaks, large quantities of CO_2 (added to CH_4/N_2 and other greenhouse gases) could be sufficient to raise the surface temperature of TRAPPIST-1 outer planets above the melting point of water, although this need to be tested with coupled photochemical / 3-D climate model in the future. In this case, sedimented organic carbonated chains should not accumulate at the surface but instead should get dissolved in the liquid water ocean. This, and the UV shield provided by the photochemical hazes (Wolf and Toon, 2010; Arney et al., 2017) could provide TRAPPIST-1 planets with surface conditions favorable for life - as we know it - to emerge and develop.

We discuss more generally in the next section the conditions required for TRAPPIST-1 planets to sustain surface habitability.

4.10 The habitability of TRAPPIST-1 planets

Most of our knowledge on habitability comes from the study of Venus, Mars, and Earth. The system of TRAPPIST-1 displays a fantastic zoology of planets to confront our theories with, and potentially revolutionize all what we know on this domain.

4.10.1 The habitability of the inner planets TRAPPIST-1bcd

The two inner planets of the system (TRAPPIST-1b and c) are likely too hot to sustain global oceans of liquid water (Kopparapu et al., 2013; Yang et al., 2013; Kopparapu et al., 2016). Nonetheless, they could still be desert worlds with limited surface water (Abe et al., 2011) trapped in nightside niches (e.g. land planets) or at the edge of large scale glaciers near the terminator (Leconte et al., 2013b).

TRAPPIST-1d ($S_{eff} \sim 1.14\ S_\oplus$) however is near the inner edge of the Habitable Zone of synchronously-rotating planets (Yang et al., 2013; Kopparapu et al., 2016). If TRAPPIST-1d is able somehow to sustain a thick, highly reflective water cloud cover near the substellar region, it could sustain surface liquid water global oceans. Detailed 3D modeling of clouds, and more generally of all the possible parameters that could affect the atmospheric circulation, would be required to assess this possibility.

4.10.2 The remarkable potential of TRAPPIST-1e for habitability

According to our simulations, TRAPPIST-1e is the only planet in its system with the ability to host surface liquid water without the need of greenhouse warming from another gas than H_2O. This requires a sufficient H_2O reservoir covering the whole surface (i.e. that cannot be fully trapped on the

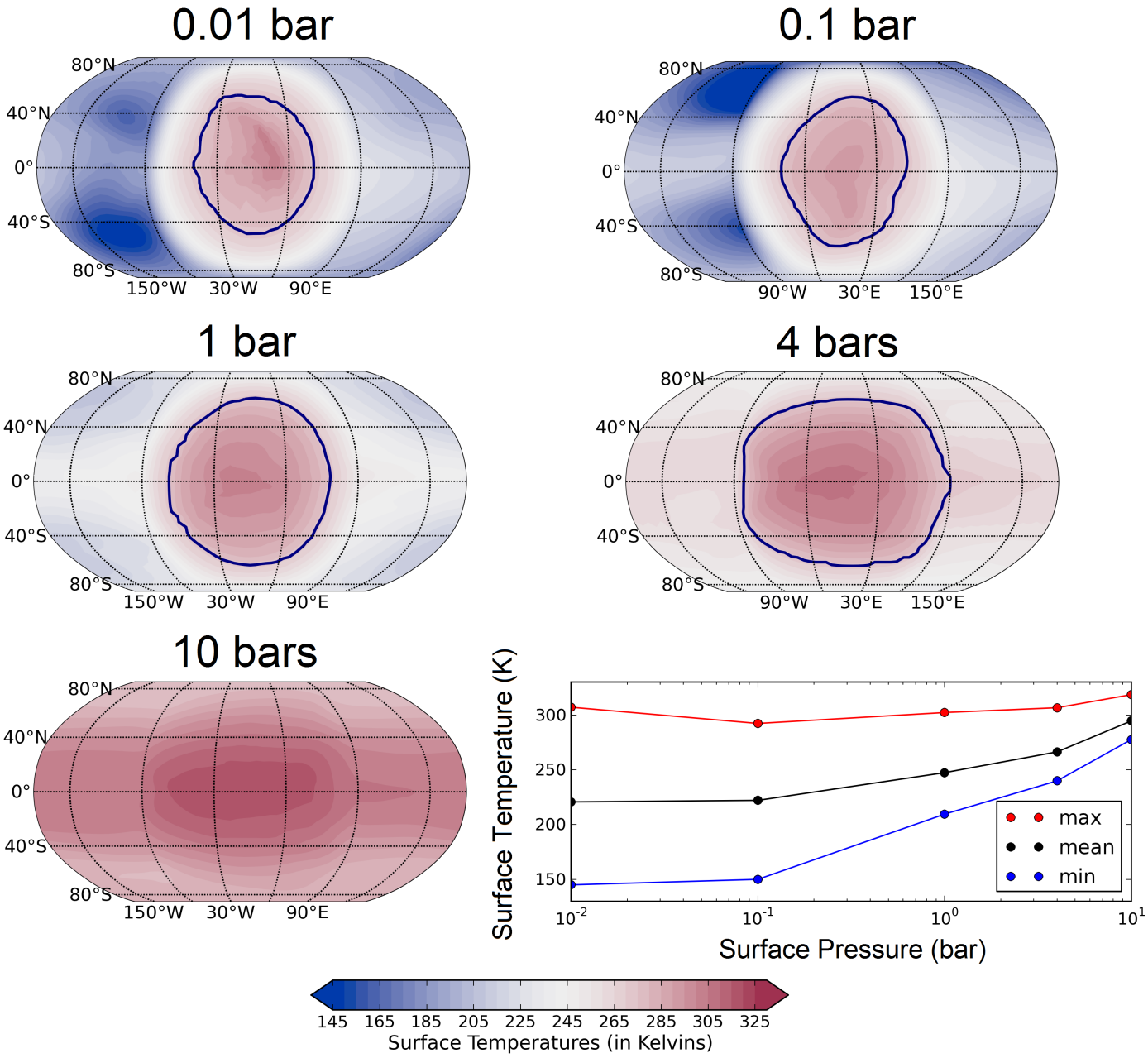

Figure 4.13: 4-years average surface temperature maps of TRAPPIST-1e endowed with atmospheres made of N_2 and 376 ppm of CO_2, and for various atmospheric pressures (10 mbar, 0.1 bar, 1 bar, 4 bar and 10 bar). Solid line contours correspond to the delimitation between surface liquid water and sea water ice. The Figure in the bottom right panel indicates in blue, black and red the minimum, mean, and maximum surface temperatures, respectively. Note that the planets were assumed to be initially cold (T = 210 K everywhere) and completely covered by water ice.

nightside). Thanks to the synchronous rotation, the received stellar flux (F∼904 W m^{-2}) is sufficient to maintain a least a patch of liquid water at the substellar point, even in the absence of a background atmosphere. This configuration is usually known as the eyeball regime (Pierrehumbert, 2011).

This situation is similar to that of Proxima Cen b (Anglada-Escudé et al., 2016). This potentially rocky (most probable mass of $1.4M_{\oplus}$) planet orbiting the closest star from our Sun receives within uncertainties nearly the same amount of stellar energy (F∼890 W m^{-2}) as TRAPPIST-1e. Two studies with two different GCMs (Turbet et al., 2016; Boutle et al., 2017) showed that a water-rich and synchronous scenario for Proxima b generates a substellar surface ocean. The reader is refered to Turbet et al. (2016) (in particular, their Figure 1) for a detailed discussion on the possible climate regimes on TRAPPIST-1e, analogous to Proxima Cen b.

We performed several 3D GCM simulations (see Fig 4.13), assuming a cold start (T = 210 K everywhere, full water ice coverage). We find that for any atmosphere, TRAPPIST-1e always ends up with surface liquid water, at least in the substellar region. This would hold even with no background atmosphere at all; in this case, the atmosphere would be composed of water vapor. Starting from this point, adding greenhouse gases to the atmosphere would increase the mean surface temperature and increase the size of the patch of liquid water. We not only confirm here that the case of TRAPPIST-1e is analogous to Proxima Cen b, but we also show that, due to the lowered albedo of water ice around TRAPPIST-1, these conclusions do not depend on the initial state.

In summary, if 1) TRAPPIST-1e is in synchronous rotation and 2) is water-rich, then the planet should have a patch of liquid water at its substellar point, whatever its atmosphere (as thin or thick as wanted) and whatever its initial state (fully glaciated or not). This result must hold for any arbitrary atmospheric composition, unless a tremendous anti-greenhouse effect occurs (e.g. absorption by stratospheric methane, or absorption and reflection by photochemical hazes), or unless a tremendous greenhouse effect (by a thick Venus-like atmosphere, for example) raises the mean surface temperature above the critical point of water (647K). These possibilities will be explored in details in future studies.

If low density estimates of TRAPPIST-1e (Gillon et al., 2017; Wang et al., 2017) were to be confirmed in the future, indicating that the planet could have retained large quantities of water, TRAPPIST-1e would thus become a fantastic candidate for habitability outside our Solar System. More generally, TRAPPIST-1e together with Proxima Cen b highlight a new type of planets that **are very likely to** sustain surface liquid water, and that are therefore extremely promising for habitability prospects.

4.10.3 The habitability of outer planets

Besides TRAPPIST-1e, the three outer planets of the system (TRAPPIST-1f, g and h) are interesting probes to study habitability outside our Solar System.

4.10.3.1 Surface habitability cannot be sustained with background gases only

From the set of simulations described in Section 4.7.1 and extended to atmospheric pressures as thick as 4 bar, we find that none of the 3 TRAPPIST-1 outer planets (f, g and h) are able to maintain surface liquid water, assuming a background atmosphere - not able to generate a significant greenhouse effect - that would only be made of N_2, CO or O_2 (with H_2O included as a variable species).

It tells us that TRAPPIST-1f, g and h need to build up greenhouse gases in their atmosphere

(e.g. CO_2, CH_4, NH_3, H_2, etc.) to sustain surface habitability. We explore this possibility in the next sections.

4.10.3.2 Minimum CO_2 content required for surface habitability

Using 3D and 1D (with our one-dimensional cloud-free climate model (Wordsworth et al., 2010b) that uses the same physical package than the 3-D LMD Generic GCM described in Section 4.5) simulations of planets endowed with thick CO_2-dominated atmospheres, we find that:

1. Planet f can maintain surface liquid water for CO_2-dominated atmosphere thicker than ~ 1 bar. Note that a warm solution is possible for lower CO_2 atmospheric pressures, although CO_2 would condense on the surface, leading to a complete atmospheric collapse.

2. Planet g can maintain surface liquid water for CO_2-dominated atmospheres thicker than ~ 5 bar.

3. Planet h is not suitable for surface liquid water, whatever the thickness of the CO_2 atmosphere is, and even when maximizing the radiative effect of CO_2 ice clouds (parameterized following Forget et al. 2013). In fact, Figure 4.9 also tells us that TRAPPIST-1h is unable to build up a CO_2 atmosphere, whatever the background gas content. For a 1 bar N_2 atmosphere, TRAPPIST-1h should not be able to build up more than a few tens of ppm of CO_2 in the atmosphere.

Our results are roughly in agreement with the reference papers by Kopparapu et al. (2013) and Kopparapu et al. (2014) on habitability. We note however that the recent paper by Wolf (2017), which finds that CO_2-dominated atmospheres as thick as 30 bar cannot warm the surface of TRAPPIST-1f and g above the melting point of water, is at odd with our results, and more generally, with the related literature. We believe that the discrepancy comes potentially from the fact that Wolf (2017) underestimated in his calculations the effect of the lowered albedo of ice / snow around cool stars (mean water ice albedo of 0.21 around TRAPPIST-1) due to the shape of its reflectance spectrum, as supported by experimental data (Warren and Wiscombe, 1980; Joshi and Haberle, 2012). This would suppress the runaway glaciation positive feedback invoked by Wolf (2017).

The discrepency could also come from differences in the radiative treatment of CO_2-rich atmospheres. We used here the parameterization of CO_2 absorption lines following Wordsworth et al. (2010a), using updated line intensities and positions, and half-width at half-maximum from HITRAN-2012 (Rothman et al., 2013), sublorentzian line shape of Perrin and Hartmann (1989) and Collision-Induced Absorptions (CIA) of Gruszka and Borysow (1997) and Baranov et al. (2004). Wolf (2017) used instead CO_2 cross sections from Wolf and Toon (2013), based on HITRAN-2004, and did not include the effect of Collision Induced Absorptions (CIA) and dimer absorptions despite their importance when modelling thick CO_2 atmospheres (Wordsworth et al., 2010a; Turbet and Tran, 2017).

More generally, using our 1D / 3D GCM simulations, we find that the outer edge of the classical Habitable Zone around TRAPPIST-1 (using the TRAPPIST-1 synthetic spectrum, and for an atmosphere of 70 bar of CO_2) lies around 306 W m^{-2} ($S_{eff} = 0.225$). This value is slightly higher than the one (302 W m^{-2}; $S_{eff} = 0.221$) given in Kopparapu et al. (2013).

We explored the effect of 1) gravity, 2) rotation mode, 3) changing the stellar spectrum (from synthetic to blackbody), and 4) including the radiative effect of CO_2 ice clouds, and found that their cumulative effect on the limit of the outer edge of the Habitable Zone should not exceed roughly 30 W m^{-2} in the context of the TRAPPIST-1 exoplanetary system.

4.10.3.3 The case of TRAPPIST-1h

TRAPPIST-1h is a poor candidate for surface habitability, and here are the following reasons why:

- As explained in Section 4.8.1, TRAPPIST-1h is unable to accumulate a dense CO_2 atmosphere (because of surface condensation) that could warm the surface and favor surface habitability.
- As shown in Section 4.9, even 1) when considering an unlikely scenario where a CH_4 thick atmosphere would have been built, and even 2) when neglecting the radiative cooling of photochemical hazes, we find that (see Fig 4.12) CH_4-dominated atmospheres are unable to raise the mean surface temperature of TRAPPIST-1h above $\sim$ 160 K for an atmosphere made of 1 bar of N_2 and CH_4 content lower than 1 bar. This result is mostly due to the anti-greenhouse effect of stratospheric methane.
- H_2, through Collision Induced Absorptions, is an extremely powerful greenhouse gas that could potentially warm the surface of TRAPPIST-1h well above the melting point of water (Stevenson, 1999; Pierrehumbert, 2011; Luger et al., 2017b). However, given the small size of the planet, and given the preliminary results of transit spectroscopy with HST (De Wit et al., 2016), the possibility of an H_2-rich atmosphere around TRAPPIST-1h seems unlikely.

4.11 Conclusions

In this paper we have used sophisticated numerical models (a N-body code and a Global Climate Model) to better constrain the nature of the TRAPPIST-1 planets. The main conclusions of our paper are summarized below:

Tidal dynamics constraints

We showed that, given the low eccentricities derived from our N-body numerical simulations, the seven planets of the TRAPPIST-1 system are very likely in synchronous rotation today, with one side permanently facing their ultra-cool host star TRAPPIST-1, and one side in the permanent darkness.

Using the same N-body simulations, we also showed that tidal heating is expected to be the dominant process of internal heating for the three inner planets of the system (TRAPPIST-1b, c and d). Tidal heating could play a significant role on TRAPPIST-1e (given that TRAPPIST-1 seems to be an old system and that radiogenic heating should have decreased), but should have a much less pronounced effect on the three outer planets (TRAPPIST-1f, g and h).

Climate diversity constraints

Assuming that the TRAPPIST-1 planets are all in synchronous rotation today, we detail below the main conclusions of our paper regarding the possible climates of TRAPPIST-1 planets:

• **Airless planets should remain airless.** TRAPPIST-1 planets are exposed to X/EUV radiation and stellar wind atmospheric erosion, and could have lost their atmosphere earlier in their history. We showed that planets that - at some point - completely lost their atmosphere are more likely to remain airless.

1. Planets that have a low internal heat flux (e.g. TRAPPIST-1e, f, g and h) have to accumulate very large quantities of volatiles on their nightside before a runaway greenhouse process re-forms a global atmosphere.

2. Planets that have a large internal heat flux (e.g. TRAPPIST-1b, c and d) would struggle to store and protect volatiles located on their nightside. The warmer temperature of the nightside should be responsible for the formation of a residual atmosphere that would be exposed to atmospheric escape.

However, both TTV analysis of the planets and the compact, resonant architecture of the system suggest that each of the TRAPPIST-1 planets could still be endowed with various volatiles today. Assuming that the four TRAPPIST-1 outer planets (e, f, g and h) were able to retain various volatiles in their atmosphere, surface or subsurface, we summarize the last part of our results below:

• **Background atmospheres are stable regarding atmospheric collapse.** TRAPPIST-1 planets are all highly resistant to complete atmospheric collapse of N_2 or any other background gas (CO, O_2). Around 10 millibar of N_2 or any other background gas should suffice to avoid surface condensation on the nightside of the TRAPPIST-1 planets. This is an essential property, because background gases can prevent the more volatile species (CO_2, NH_3, etc.) from collapsing on the nightside.

• **CO_2-dominated atmospheres are sensitive to atmospheric collapse and gravitational burial.** If TRAPPIST-1e, f, and g outer planets have a CO_2-dominated atmosphere, this atmosphere must be very thick.

1. Thin CO_2 atmospheres would collapse permanently on the nightside of the planets. For example, a Mars-like atmosphere would be unstable on TRAPPIST-1e, f, g and h.

2. Thick (multi-bar) CO_2 atmospheres are found stable, thanks to an efficient greenhouse warming and heat redistribution. For example, a Venus-like atmosphere would be stable on TRAPPIST-1e, f and g. Note however that TRAPPIST-1h is beyond the CO_2 condensation limit.

If CO_2 somehow starts to condense on the nightside of TRAPPIST-1 outer planets, it would form CO_2 ice glaciers that would flow toward the substellar region. A complete CO_2 ice cover is not possible for TRAPPIST-1f and the inner planets because they receive an insolation that is greater that the runaway greenhouse threshold for CO_2. A complete CO_2 ice cover is found possible on TRAPPIST-1g and h only, although the CO_2 ice glaciers should be gravitationally unstable and get buried beneath the water ice shell (if present) in geologically short timescales. CO_2 could be permanently sequestred underneath the water ice cover, in the form of CO_2 clathrate hydrates or dissolved in a subglacial water ocean. This makes the presence of surface CO_2 ice deposits rather unlikely on water-rich, synchronous planets.

• **Sustaining continuously a CH_4-rich atmosphere is challenged by photochemical destruction.** Given TRAPPIST-1 planets large EUV irradiation (at least $\sim 10^3 \times$ Titan's flux) and the large photodissociation rates that are associated, sustaining continuously a CH_4-rich (and NH_3-rich, by analogy) atmosphere over TRAPPIST-1 lifetime is difficult. Calculations of the surface temperatures of the three TRAPPIST-1 outer planets (f, g and h), under a CH_4-rich atmosphere, indicate that:

1. their surface (even on the nightside) should be too warm to sustain oceans of methane and/or ethane.

2. their surface should be to cold to sustain surface liquid water. This is mostly due to the anti-greenhouse effect of photochemical hazes and stratospheric methane. The planets could then more likely be covered by water ice.

Photochemical hazes when sedimenting could thus form a surface layer of tholins that would progressively thicken - over the age of the TRAPPIST-1 system - above the surface.

The habitability of the TRAPPIST-1 system.

Remarkably, provided a sufficient H_2O reservoir is present, TRAPPIST-1e **is very likely to** sustain surface liquid water, at least in the substellar region. This stems from the synchronous rotation coupled to an ideal insolation, and is independent of the atmospheric background content (from no atmosphere at all, to a thick atmosphere of hundreds of bar). The H_2O reservoir should be large enough to avoid trapping on the nightside.

Conversely, TRAPPIST-1f, g and h are unable to sustain surface habitability only with background gases (i.e. a rather transparent atmosphere that can ensure the transport of heat and the pressure broadening of absorption lines of greenhouse gases). $\sim$ 1 bar of CO_2 (respectively $\sim$ 5 bar) would be needed to raise the surface temperature above the melting point of water on TRAPPIST-1f (resp. g). A thick CH_4 atmosphere should be unable to sustain surface habitability on TRAPPIST-1f, g and h.

TRAPPIST-1h is unable to sustain surface habitability with N_2, CO_2, CH_4, etc. only. This could only be achieved with an unlikely, thick H_2-dominated atmosphere.

Future atmospheric exploration of the TRAPPIST-1 system with the James Webb Space Telescope and other forthcoming astronomical observatories is extremely promising. TRAPPIST-1 planets are about to become invaluable probes for comparative planetary science outside our Solar System and possibly habitability. The results of our paper could serve to prepare and then interpret the future observations of the TRAPPIST-1 system and analogous. The various numerical climate simulations presented in this paper will actually be used in follow-up papers to provide the community with synthetic observables (transit spectra, phase curves, and secondary eclipses), that should be directly comparable with future JWST observations. Eventually, we remind the reader that the results of this paper can be applied to any other cool Earth-sized planets orbiting in synchronous rotation around any cool to ultra-cool star.

Part II

Habitability of early Mars

Chapter 5

Environmental effect of outflow channel events on ancient Mars

Contents

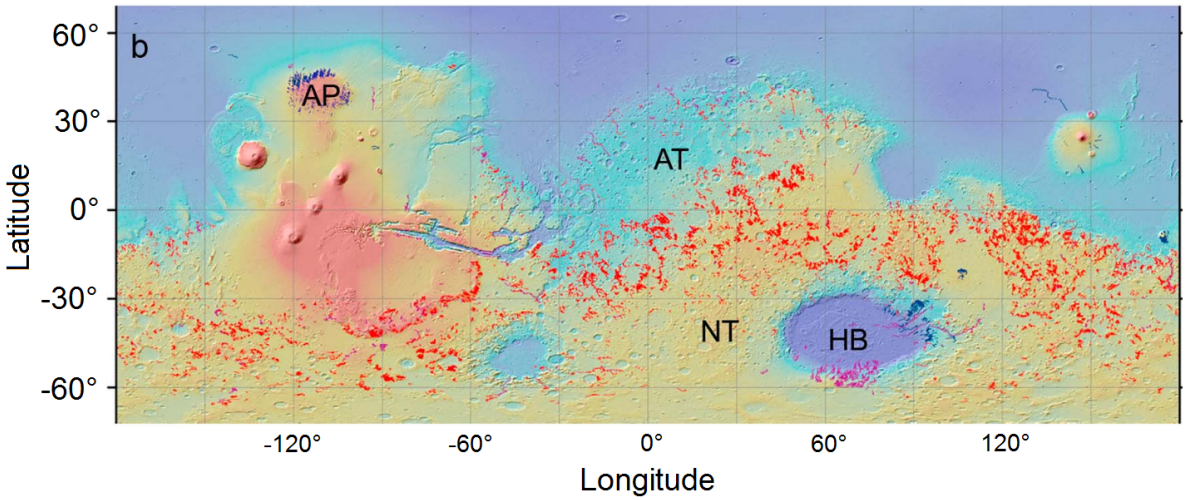

Figure 5.1: Map of valley networks identified by Hynek et al. (2010) using THEMIS data on top of a MOLA topography map from high (red) to low (blue) elevation. Line colors on represent inferred valley ages determined by the youngest terrain unit they incise (blue, Amazonian; purple, Hesperian; red, Noachian). AP stands for Alba Patera; AT, Arabia Terra; HB, Hellas Basin; NT, Noachis Terra. From Hynek et al. (2010).

5.1 Preamble

The most striking evidence that liquid water flowed on ancient Mars is the valley networks. Almost all the valley networks visible today on Mars are dated from the Late Noachian era (Hynek et al., 2010). Yet, a few of them formed much later. This is illustrated in Figure 5.1 where the position of all the known (as of 2010) valley networks is mapped (Hynek et al., 2010). Valley networks are separated in three categories, as a function of their age: Noachian (red), Hesperian (purple) and Amazonian (blue).

The detection of these late valley networks is intriguing because it demonstrates that liquid water flowed on Mars at multiple epochs (and for extended periods of time) during Mars history. More specifically, Mangold et al. (2004) reported the discovery of a dendritic, very mature valley network in the Valles Marineris area. Mangold et al. (2004) argued that this type of valley networks requires (1) atmospheric precipitation and (2) a lot of time to form. This indicates that the environment of Mars (atmosphere, surface temperatures, etc.) was favorable for liquid water to flow and remain stable relatively late in the Martian history.

Interestingly, more or less at the same epoch and in the same region of Mars, the large outflow channels of Mars were carved by flowing water coming most likely from subsurface aquifers (Clifford, 1993; Clifford and Parker, 2001). Many have speculated that these sudden discharge of possibly warm, liquid water could have induced a climate change on Mars, warming the surface and the atmosphere, and producing precipitation that could potentially have formed late-stage valley networks on Mars. This idea is illustrated schematically in Figure 5.2.

Using sophisticated 3-D numerical climate models, I explored how outflow channel formation events could have affected both qualitatively and quantitatively the climate of Mars to assess whether or not they could be responsible for the formation of some of the late valley networks. This chapter is based

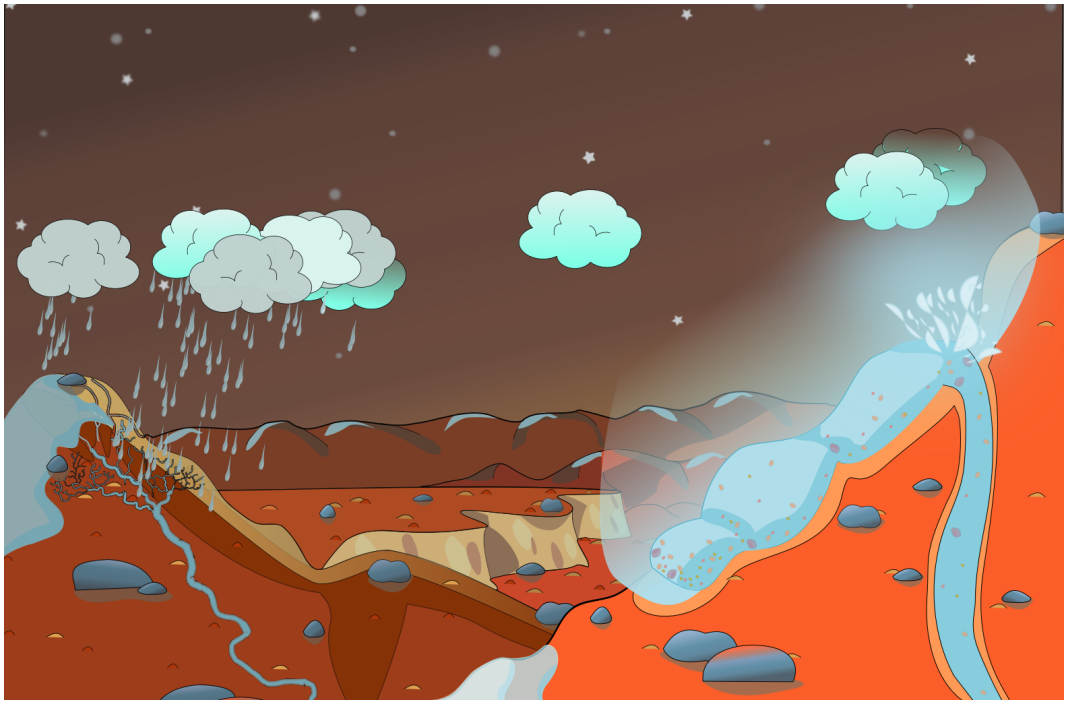

Figure 5.2: Schematic view of how outflow channel formation events could have induced precipitation on Mars. Warm liquid water is released from subsurface aquifers. The flow triggers a climate change by warming the surface, the atmosphere, and injecting water vapor in the atmosphere. This produces precipitation that could form some valley networks. Credit: N. Chaniaud.

on a paper published in Icarus in May 2017. The full reference is: Martin Turbet, Francois Forget, James W. Head & Robin Wordsworth, **3D modelling of the climatic impact of outflow channel formation events on early Mars**, Icarus, 2017 (http://adsabs.harvard.edu/abs/2017Icar..288...10T).

5.2 Abstract

Mars was characterized by cataclysmic groundwater-sourced surface flooding that formed large outflow channels and that may have altered the climate for extensive periods during the Hesperian era. In particular, it has been speculated that such events could have induced significant rainfall and caused the formation of late-stage valley networks. We present the results of 3-D Global Climate Model simulations reproducing the short and long term climatic impact of a wide range of outflow channel formation events under cold ancient Mars conditions. We find that the most intense of these events (volumes of water up to 10^7 km^3 and released at temperatures up to 320 Kelvins) cannot trigger long-term greenhouse global warming, regardless of how favorable are the external conditions (e.g. obliquity and seasons). Furthermore, the intensity of the response of the events is significantly affected by the atmospheric pressure, a parameter not well constrained for the Hesperian era. Thin atmospheres (P $<$ 80 mbar) can be heated efficiently because of their low volumetric heat capacity, triggering the formation of a convective plume that is very efficient in transporting water vapor and ice at the global scale. Thick atmospheres (P $>$ 0.5 bar) have difficulty in producing precipitation far from the water flow area, and are more efficient in generating snowmelt. In any case, outflow channel formation events at any atmospheric pressure are unable to produce rainfall or significant snowmelt at latitudes below 40°N. As an example, for an outflow channel event (under a 0.2 bar atmospheric pressure and 45° obliquity) releasing 10^6 km^3 of water heated at 300 Kelvins and at a discharge rate of 10^9 m^3 s^{-1}, the flow of water reaches the lowest point of the northern lowlands (around $\sim$ 70°N, 30°W) after $\sim$ 3 days and forms a 200m-deep lake of 4.2×10^6 km^2 after $\sim$ 20 days; the lake becomes entirely covered by an ice layer after $\sim$ 500 days. Over the short term, such an event leaves 6.5×10^3 km^3 of ice deposits by precipitation (0.65% of the initial outflow volume) and can be responsible for the melting of $\sim$ 80 km^3 (0.008% of the initial outflow volume; 1% of the deposited precipitation). Furthermore, these quantities decrease drastically (faster than linearly) for lower volumes of released water. Over the long term, we find that the presence of the ice-covered lake has a climatic impact similar to a simple body of water ice located in the Northern Plains.

For an obliquity of $\sim$ 45° and atmospheric pressures $>$ 80 mbar, we find that the lake ice is transported progressively southward through the mechanisms of sublimation and adiabatic cooling. At the same time, and as long as the initial water reservoir is not entirely sublimated (a lifetime of 10^5 martian years for the outflow channel event described above), ice deposits remain in the West Echus Chasma Plateau region where hints of hydrological activity contemporaneous with outflow channel formation events have been observed. However, because the high albedo of ice drives Mars to even colder temperatures, snowmelt produced by seasonal solar forcing is difficult to attain.

5.3 Introduction

During the Late Hesperian epoch of the history of Mars (about 3.1-3.6 Gyrs ago; Hartmann and Neukum 2001), the large outflow channels observed in the Chryse Planitia area are thought to have been carved by huge water floods caused by catastrophic and sudden release of groundwater (Baker, 1982; Carr, 1996). It has been speculated that such events could have warmed the climate and possibly explain the contemporaneous formation of dendritic valley networks observed in the nearby Valles Marineris area and on the flanks of Alba Patera, Hecates Tholus, and Ceraunius Tholus, and that have been interpreted to be precipitation-induced (Gulick and Baker, 1989, 1990; Baker et al., 1991; Gulick et al., 1997; Gulick, 1998, 2001; Mangold et al., 2004; Quantin et al., 2005; Weitz et al., 2008; Santiago et al., 2012). Although the Late Hesperian epoch is thought on the basis of geology and mineralogy to have been cold (Head et al., 2004; Bibring et al., 2006; Ehlmann et al., 2011), the characteristics of these dendritic valleys suggest that the valleys were formed under persistent warm conditions (.e.g, Mangold et al. 2004). First, their high degree of branching is interpreted to indicate formation by precipitation. Second, their high drainage densities - evidence of their high level of maturity - and the presence of inner channels favor the presence of stable liquid water for geologically long periods of time (Craddock and Howard, 2002). Third, sedimentary morphologies observed in the region of Valles Marineris (Quantin et al., 2005) suggest a fluvial and lacustrine environment. Under this hypothesis, the warm liquid water floods that formed the outflow channels would inject water vapor into the atmosphere, a powerful greenhouse gas that could trigger a significant warming period possibly leading to long lasting pluvial activity (rainfall).

In this paper, we use a 3-Dimensional Global Climate Model (LMD GCM) to explore the global climatic impact of outflow channel water discharge events on a Late Hesperian Mars over a range of temperatures and atmospheric pressures. These bursts of warm liquid groundwater outflows onto the surface can trigger strong evaporation, possibly leading to global climate change. How warm and how wet was the atmosphere of Late Hesperian Mars after such major outflow channel events? The climatic effect of relatively small and cool groundwater discharges has been studied on a regional scale (Kite et al., 2011a) and localized precipitation is indicated. In this contribution, we investigate the climatic impact at a global scale of a wide range of possible outflow channel events, including the case of the most intense outflow events ever recorded on Mars (Carr, 1996). Our work focuses on both (1) the direct short-term climate change due to the initial strong evaporation of water vapor and (2) the long-term change of the water cycle due to the presence of liquid water and ice at non-stable locations.

When a warm liquid water flow reaches the surface, strong evaporation occurs and the total evaporation rate increases with the temperature and the surface area of the flow. In term of energy budget, a 300K warm liquid water flow can potentially convert $\sim 5\%$ of its total mass into water vapor before freezing starts. The injected water vapor will have a major role on the radiative budget of the planet. First, water vapor is a greenhouse gas that can absorb ground thermal infrared emission efficiently. Second, water vapor can condense to form clouds. In the process, large amounts of latent heat can be released in the atmosphere. The clouds can reflect the incoming solar flux as well as contribute to an additional greenhouse effect, depending on their height and the opacity of the background atmosphere, which depends on the total atmospheric pressure.

To study the global climatic effect of localized outflow channel events, 3D Global Climate Models are particularly relevant because they not only model the physical processes described above, but also the 3D dynamical processes that play a major role in climatic evolution. In particular, we show in this

paper that 3D dynamical processes (horizontal advection, in particular) are key to understanding the relaxation timescale of the Late Hesperian martian atmosphere immediately following major outflow channel events.

5.4 Background

5.4.1 Outflow channels

5.4.1.1 Description

Outflow channels are long (up to $\sim$ 2000 km) and wide (up to $\sim$ 100 km) valleys that were sculpted by large-scale debris-laden water flows (Baker, 1982; Baker et al., 1992; Carr, 1996). The most prominent martian outflow channels are located in the circum-Chryse area and debouch in the Chryse Planitia itself (Carr, 1996; Ivanov and Head, 2001).

Several processes have been suggested to have caused such outburst floods (Kreslavsky and Head, 2002). It is likely that the water that was released during these events come from subsurface aquifers (Clifford, 1993; Clifford and Parker, 2001). In this scenario, the temperature of the extracted subsurface water is controlled by the geothermal gradient and thus would depend on its initial depth of origin. During the Late Hesperian, when outflow channel events largely occured, this gradient could have been locally higher (Baker, 2001), because the circum-Chryse area is close to the volcanically active Tharsis region (Cassanelli et al., 2015). Therefore, the discharged water could have reached the surface at a maximum temperature of tens of degrees above the freezing point (Kreslavsky and Head, 2002). We note that the run-away decomposition of CO_2 clathrate hydrate (Milton, 1974; Baker et al., 1991; Hoffman, 2000; Komatsu et al., 2000), proposed as a possible mechanism for the origin of the outflow water, cannot produce water temperature greater than 10K above the freezing point. To a first approximation, and from a climatic point of view, the only difference between these two processes of liquid water discharge is the temperature of the water. Thus, we considered in this paper various cases ranging from 280 Kelvins to 320 Kelvins (see section 5.8.1).

Whatever the physical process operating, large amounts of water released at very high rates are needed at the origin of the water flow in order to explain the erosion of the circum-Chryse outflow channels. The quantity of water estimated to erode all the Chryse basin channels is $\sim 6 \times 10^6$ km^3 assuming 40% by volume of sediment (Carr, 1996) but could possibly be much more if one assume lower sediment loads (Kleinhans, 2005; Andrews-Hanna and Phillips, 2007), which is, for example the case on Earth ($\sim$0.1% of sediment by volume).

The different estimates of outflow channel single-event volumes, discharge rates and durations lead to a wide range of results, but two endmember scenarios can be defined and explored. On the one hand, some researchers estimated that only a limited number of very intense (volume up to 3×10^6 km^3, discharge rates up to 10^9 m^3 s^{-1}) outflow channel formation events actually occured (Rotto and Tanaka, 1992; Baker et al., 1991; Komatsu and Baker, 1997).

On the other hand, more recently, other researchers argued that outflow channels were formed by numerous individual small events (Andrews-Hanna and Phillips, 2007; Harrison and Grimm, 2008). This latter work implies water volumes from hundreds to thousands of km^3, discharge rates of 10^6-10^7 m^3 s^{-1} for individual events and a minimum period between successive single events of $\sim$ 20 martian years. These endmember estimates differ by several orders of magnitude, but in this paper, we explored

the full range.

5.4.1.2 Fate of the outflow channel liquid water flow

In this section, we provide a description of the possible fate, and calculations of the possible velocities, of the outflow channel water; these will serve as input for the description of the liquid water runoff under various conditions in the GCM simulations.

The ejected liquid water flows from the circum-Chryse area all inevitably debouch into the basin of Chryse. However, Chryse Planitia is not a closed basin and if the total amount of water released in a single event is high enough, the water will spill into the Northern Plains (Ivanov and Head, 2001), flowing down on slopes inclined at ∼0.03° for more than 2000km. This is an important point because, as the wetted area of the flow increases, the total rate of evaporation rises. The fate of the outflow channel liquid water flow can be subdivided into two steps:

1. First, the ground-surface liquid water flows 'inside' the outflow channels. The Reynolds Number Re of such flows is given by

$$Re = \rho U_c R_c / \mu, \tag{5.1}$$

with U_c the mean water flow velocity in the channel, R_c the hydraulic radius (see below) of the channel, ρ the density and μ the viscosity of the flow. For most of the outfow channel events, this number must have been orders of magnitude higher than 500 (Wilson et al., 2004), meaning that the released ground water flows were turbulent.

The most accurate way (Bathurst, 1993; Wilson et al., 2004) to calculate the mean velocity of such flows is to use the Darcy-Weisbach equation:

$$U_c \;=\; (8 g R_c \sin\alpha / f_c)^{1/2}, \tag{5.2}$$

with $g = g_{\rm mars} = 3.71\ m\ s^{-2}$ the gravity on Mars, α the slope angle of the channel and f_c a dimensionless friction factor which mostly depends on the bed roughness z_c and the water depth h of the flow. This factor can be expressed as follows (Wilson et al., 2004):

$$(8/f_c)^{1/2} \;=\; a\ \log_{10}(R_c/z_c) + b, \tag{5.3}$$

with a and b two empirical coefficients, which are respectively equal to 5.657 and 6.6303 if the bed roughness z_c ($z_c = 10^{-2}$ m here) is fixed (Knudsen and Katz, 1958): This leads equation (5.2) to the following equation:

$$U_c \;=\; (g R_c \sin\alpha)^{1/2}\ (a\ log_{10}(R_c/z_c) + b). \tag{5.4}$$

The hydraulic radius R_c is defined as the cross-sectional area of the channel divided by its wetted perimeter:

$$R_c \sim (W_c\ h)/(W_c + 2h), \tag{5.5}$$

with W_c the channel width and h the flow depth. Because outflow channels are wider than deep ($W_c \sim$ 10-100 km wide but $h \leq 1$ km deep), the hydraulic radius R_c can be replaced by the depth of the water flow h.

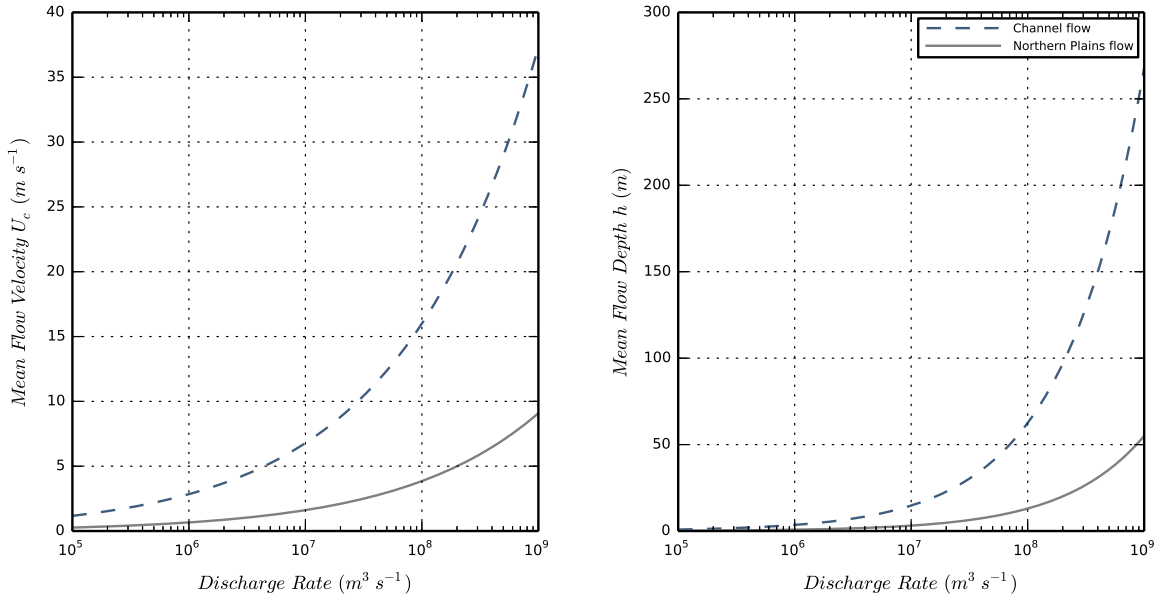

Figure 5.3: Estimates of mean flow velocity (left) and mean flow depth (right) for 1. (blue) the case of a 100 km-wide channel flow on an $\sim 0.1°$ slope angle and 2. (grey) the case for the same flow spilling onto the Northern Plains of Mars ($\sim$ 2000 km-wide and slope angle $\sim 0.03°$). These quantities were calculated for a wide range of water discharge rates, using the Darcy-Weisbach equation.

To estimate the velocity of the flow according to its discharge rate $Q = U_c W_c h$, we solve equation (5.4) using the Lambert special function W defined by $x = W(xe^x)$. We obtain:

$$h = \left(\frac{3\ \ln 10}{2a\ W_c (g \sin\alpha)^{\frac{1}{2}}} \frac{Q}{W\left(\frac{3\times 10^{\frac{3b}{2a}}\ \ln 10}{2a\ z_c^{\frac{3}{2}}\ W_c (g\sin\alpha)^{\frac{1}{2}}}\ Q \right)} \right)^{\frac{2}{3}} \tag{5.6}$$

and

$$U_c = \left(\frac{2a\ (g\sin\alpha)^{\frac{1}{2}} W\left(\frac{3\times 10^{\frac{3b}{2a}}\ \ln 10}{2a\ z_c^{\frac{3}{2}}\ W_c (g\sin\alpha)^{\frac{1}{2}}}\ Q \right)}{3\ \ln 10\ W_c^{\frac{1}{2}}} \right)^{\frac{2}{3}} Q^{\frac{1}{3}}. \tag{5.7}$$

The high concentrations of sediments in the flows (up to 40% of the volume) can increase the volumetric mass density ρ (initially of $\rho_{\text{water}} \sim 1000$ kg m^{-3}) by a factor of 2 and the viscosity μ (initially of $\mu_{\text{water,300K}} \sim 8\times10^{-4}$ Pa s) by a factor of 16 (Andrews-Hanna and Phillips, 2007), reducing by almost 10 the corresponding Reynolds Number. Nonetheless, since both the sediment load (from 0.1 to 40 %) and the dependence of the friction factor f_c on the Reynolds Number Re, are poorly known (Andrews-Hanna and Phillips, 2007), their effects were not taken into account in the flow depth/velocity calculations.

2. As soon as the water flow leaves its channel and reaches Chryse Planitia, the width of the flow strongly increases (up to 2000 km) and the slope angle decreases down to 0.03°. The mean flow

velocity and height both decrease (Figure 5.3) whereas the wetted area increases significantly, leading to even more evaporation. The water will eventually end up in the main topographic depression of Vastitas Borealis (around -30°/70° in longitude/latitude) building up with time. If the volume of water released by the outflow channel event is higher than $\sim 2.6\times10^6$ km^3, the water will spill from the North Polar basin to the Utopia Basin, filling it potentially up to 1.1×10^6 km^3 (Ivanov and Head, 2001). If the volume of water exceeds 3.7×10^6 km^3, the two basins become connected. They can be filled up to a few tens of millions of km^3.

Once the flow stops, some water will possibly remain in local topographic depressions such as impact craters or tectonic basins, thereby contributing to extended evaporation.

If the volume of water or the temperature of the flow are too low, the liquid water flow can potentially freeze before reaching the lowest points of the northern lowlands. This would likely occur only for the weakest outflow channel events (low volumes/discharge rates/temperatures), and we do not discuss this possibility further in this work.

5.4.2 Late Hesperian Climate

Late Hesperian Mars was likely to have been cold and dry globally, as suggested by the weak occurence of well-developed valley networks (Carr, 1996; Fassett and Head, 2008a; Harrison and Grimm, 2005), the absence of observed phyllosilicates within layered deposits (Bibring et al., 2006; Chevrier et al., 2007; Carter et al., 2013), and the low erosion rates inferred from impact craters morphologies (Craddock and Maxwell, 1993; Golombek et al., 2006; Quantin et al., 2015).

As suggested by the stability of liquid water, and as supported by using the size distribution of ancient craters (Kite et al., 2014), the atmosphere of Mars at the end of the Noachian epoch was likely to have been thicker than the ~ 8 mbar present day atmosphere. From the Noachian-Hesperian transition to the Late Hesperian era, magmatism may have been responsible for the build up of up to 400 mbar of CO_2 in the atmosphere (Grott et al., 2011, Figure 4). In fact, it is during the period of formation of the outflow channels that the release of gaseous CO_2 could have been at its maximum (Baker et al., 1991; Gulick et al., 1997): 1. Up to 100 mbar of CO_2 could have been released by the contemporaneous Tharsis volcanism; 2. up to 60 mbar of CO_2 per volume of 10^6 km^3 of outflow waters if produced by clathrate destabilization; and 3. up to 20 mbar of CO_2 per volume of 10^6 km^3 of outflow waters if coming from highly pressurized groundwater reservoirs saturated in CO_2. However, most recent estimates of the several CO_2 loss processes (photochemical escape, effect of solar wind, sputtering, impact erosion, loss to carbonates, etc.; summarized in Forget et al. 2013, section 3) suggest that, in spite of the previously mentioned high estimates of CO_2 outgassing amounts, it is very unlikely that the atmosphere of Late Hesperian Mars was thicker than 1 bar (Lillis et al., 2017; Dong et al., 2018b). In other words, there are currently no known physical/chemical processes that could accommodate the loss of an atmosphere at pressures of more than 1 bar.

To summarize, the Late Hesperian atmosphere was probably thicker than 8 mbar and thinner than 1 bar, but the actual surface pressure is still a matter of debate. In this paper, we find that the thickness of Late Hesperian Mars atmosphere plays an important role in relation to the climatic impact of outflow channel formation events. We chose to explore a wide possibility of atmospheric surface pressures, ranging from 40 mbar to 1 bar.

5.5 Model description

5.5.1 The Late Hesperian Global Climate Model

In this paper we use the 3-Dimensions LMD Generic Global Climate Model, specifically developed for the study of the climate of ancient Mars (Forget et al., 2013; Wordsworth et al., 2013), and adapted here for the study of the influence of outflow channel events on Mars climate during the Late Hesperian.

This model is originally derived from the LMDz 3-dimensional Earth Global Climate Model (Hourdin et al., 2006), which solves the basic equations of geophysical fluid dynamics using a finite difference dynamical core on an Arakawa C grid.

The same model has been used to study many different planetary atmospheres including Archean Earth (Charnay et al., 2013), a highly irradiated 'future' Earth (Leconte et al., 2013a), Pluto (Forget et al., 2017), Saturn (Guerlet et al., 2014; Spiga et al., 2015) and exoplanets (Wordsworth et al., 2011; Leconte et al., 2013b; Forget and Leconte, 2014; Bolmont et al., 2016a; Turbet et al., 2016, 2017b).

Most of the simulations presented in this paper were performed at a spatial resolution of 96 × 48 (e.g. 3.75° × 3.75°; at the equator, this gives in average 220 km × 220 km) in longitude / latitude. This corresponds approximately to twice the horizontal resolution used and eight times the calculation time needed in the work done by Forget et al. (2013) and Wordsworth et al. (2013). For this reason, a parallelized version of the GCM was used to deal with the long computation times. We explored the influence of the horizontal resolution (up to 1° x 1° / 360 × 180 grid in longitude / latitude) and did not find any significant discrepency compared with the 96 × 48 lower resolution simulations.

In the vertical direction, the model is composed of 15 distinct atmospheric layers, generally covering altitudes from the surface to ∼ 50 km. Hybrid σ coordinates (where σ is the ratio between pressure and surface pressure) and fixed pressure levels were used in the lower and the upper atmosphere, respectively. The lowest atmospheric mid-layers are located around [18, 40, 100, 230, ..] meters and the highest at about [.., 20, 25, 35, 45] kilometers.

We used the present-day MOLA (Mars Orbiter Laser Altimeter) Mars surface topography (Smith et al., 1999; Smith et al., 2001), and we considered that most of the Tharsis volcanic load was largely in place by the end of the Hesperian epoch (Phillips et al., 2001).

We set the obliquity of Mars at 45° to be consistent with both the most likely obliquity (41.8°) for ancient Mars calculated by Laskar et al. (2004) and one of the reference obliquities (45°) used in Wordsworth et al. (2013). The sensitivity of obliquity (and more generally of the seasonal effects) is discussed in section 5.6.

To account for the thermal conduction in the subsurface, we use an 18-layer thermal diffusion soil model that originally derives from Hourdin et al. (1993) and has been modified to take into account soil layers with various conductivities. The mid-layer depths range from $d_0 \sim 0.1$ mm to $d_{17} \sim 18$ m, following the power law $d_n = d_0 \times 2^n$ with n being the corresponding soil level, chosen to take into account both the diurnal and seasonal thermal waves. We assumed the thermal inertia of the Late Hesperian martian regolith to be constant over the entire planet and equal to 250 J m^{-2} s$^{-1/2}$ K^{-1}. This is slightly higher than the current Mars global mean thermal inertia in order to account for the higher atmospheric pressure.

Subgrid-scale dynamical processes (turbulent mixing and convection) were parameterized as in Forget et al. (2013) and Wordsworth et al. (2013). The planetary boundary layer was accounted for by the Mellor and Yamada (1982) and Galperin et al. (1988) time-dependent 2.5-level closure scheme,

Physical parameters	Values
Mean Solar Flux	465 W m^{-2} (79% of present-day)
Obliquity	45°
Bare ground Albedo	0.2
Liquid water Albedo	0.07
H_2O and CO_2 ice Albedos	0.5
Surface Topography	Present-day
Surface Pressure	0.2 bar
Surface roughness coefficient	0.01 m
Ground thermal inertia	250 J m^{-2} $s^{-1/2}$ K^{-1}

Table 5.1: Physical Parameterization of the GCM.

and complemented by a convective adjustment which rapidly mixes the atmosphere in the case of unstable temperature profiles (see section 5.5.1.3 for more details).

In the simulations that include outflow channel events, the dynamical time step is $\sim$ 45 seconds (respectively $\sim$ 184 s for the control simulations). The radiative transfer and the physical parameterizations are calculated every $\sim$ 15 minutes and $\sim$ 4 minutes (respectively every $\sim$ 1 hour and $\sim$ 15 minutes for the control simulations).

5.5.1.1 Radiative Transfer in a CO_2/H_2O mixed atmosphere.

The GCM includes a generalized radiative transfer for a variable gaseous atmospheric composition made of a mix of CO_2 and H_2O (HITRAN 2012 database, Rothman et al. 2013) using the 'correlated-k' method (Fu and Liou, 1992)) suited for fast calculation. For this, we decomposed the atmospheric Temperatures / Pressures / Water Vapor Mixing Ratio into the following respective 7 x 8 x 8 grid: Temperatures = {100,150, .. ,350,400} K; Pressures = {10^{-6},10^{-5}, .. ,1,10} bar; H_2O Mixing Ratio = {10^{-7},10^{-6}, .. ,10^{-2},10^{-1},1 } mol of H_2O / mol of air (H_2O+CO_2 here).

CO_2 collision-induced absorptions (Gruszka and Borysow, 1997; Baranov et al., 2004; Wordsworth et al., 2010a)) were included in our calculations as in Wordsworth et al. (2013), as well as the H_2O continuums. For this, we used the CKD model (Clough et al., 2005) with H_2O lines truncated at 25 cm^{-1}.

For the computation, we used 32 spectral bands in the thermal infrared and 35 in the visible domain. 16 non-regularly spaced grid points were used for the g-space integration, where g is the cumulative distribution function of the absorption data for each band. We used a two-stream scheme (Toon et al., 1989) to take into account the radiative effects of aerosols (CO_2 ice and H_2O clouds) and the Rayleigh scattering (mostly by CO_2 molecules), using the method of Hansen and Travis (1974).

In summary, compared to the radiative transfer calculation used in Wordsworth et al. (2013), we utilized here a more recent spectroscopic database (HITRAN2012 instead of HITRAN2008) and built new correlated-k coefficients suited for wet atmospheres (water vapor VMR up to 100%). In practice,

the maximum water vapor Mass Mixing Ratio that was reached in our simulations (in the case of low surface pressure simulations) was $\sim 20\%$.

In addition, we chose a mean solar flux of 465 W.m^{-2} (79% of the present-day value of Mars; 35% of Earth's present-day value; and 105% of the flux used in the Wordsworth et al. (2013) work), corresponding to the reduced luminosity from standard solar evolution models (Gough, 1981) 3.0 Byrs ago, during the Late Hesperian era. During this epoch, the Sun was also 1.5 % cooler (Bahcall et al., 2001); we did not, however, include in our model the resulting shift in the solar spectrum.

It is worth nothing anyway that absolute ages are based here on crater counting and are therefore not well constrained. For instance, the valley networks observed in West Echus Chasma Plateau are 2.9 to 3.4 billion years old (Mangold et al., 2004).

5.5.1.2 CO_2 and Water cycles

Both CO_2 and H_2O cycles are included in the GCM used in this work.

1. Carbon Dioxide is here the dominant gaseous species. In our model, CO_2 can condense to form CO_2 ice clouds and surface frost if the temperature drops below the saturation temperature. Atmospheric CO_2 ice particles are sedimented and thus can accumulate at the surface. The CO_2 ice layer formed at the surface can sublimate and recycle the CO_2 in the atmosphere. The CO_2 ice on the surface contributes to the surface albedo calculation: if the CO_2 ice layer overpasses a threshold value of 1 mm thickness, then the local surface albedo is set immediately to the albedo of CO_2 ice (0.5 in this work).

2. A self-consistent H_2O water cycle is also included in the GCM. In the atmosphere, water vapor can condense into liquid water droplets or water ice particles, depending on the atmospheric temperature and pressure, forming clouds. At the surface, because the range of surface pressures modeled in this work are well above the triple point 6 mbar pressure, liquid water and water ice can coexist. Their contributions are both taken into account in the albedo calculation as in Wordsworth et al. (2013).

The stability of liquid water / ice / CO_2 ice at the surface is governed by the balance between radiative and sensible heat fluxes (direct solar insolation, thermal radiation from the surface and the atmosphere, turbulent fluxes) and thermal conduction in the soil. Melting, freezing, condensation, evaporation, sublimation and precipitation physical processes are all included in the model.

5.5.1.3 Convective Adjustment

Outflow channel events result in the emplacement of warm liquid water, which leads to the sudden and intense warming of the atmosphere. Global Climate Models ($\sim$ 200 km grid size for our simulations) are not suited to resolve the convection processes as is done in the case of mesoscale models, which have a typical km-size resolution (Kite et al., 2011a,b).

Moist convection was taken into account following a moist convective adjustment that originally derives from the 'Manabe scheme' (Manabe and Wetherald, 1967; Wordsworth et al., 2013). In our scheme, relative humidity is let free and limited to 100%, since it is inappropriate here to use an empirical value for relative humidity (versus altitude) that comes from Earth observations, as proposed in the original scheme.

This scheme has been chosen instead of more refined ones because it is: 1. robust for a wide range of pressures; 2. energy-conservative; and 3. it is the most physically consistent scheme for exotic

(non Earth-like) situations such as the ones induced by outflow channel events. In practice, when an atmospheric grid cell reaches 100% saturation and the corresponding atmospheric column has an unstable temperature vertical profile, the moist convective adjustment scheme is performed to get a stable moist-adiabatic lapse rate.

In our simulations, after major outflow channel events, large amounts of water vapor can be released into the atmosphere and the water vapor can easily become a dominant atmospheric species. In fact we recorded up to 20% water vapor Mass Mixing Ratios following intense outflow channels (in the case of low surface pressure). Thus, we used a generalized formulation of the moist-adiabiat lapse rate developed by Leconte et al. (2013a) (Supplementary Materials) to account for the fact that water vapor can become a main species in our simulations.

In our model we also used the numerical scheme proposed by Leconte et al. (2013a) to account for atmospheric mass change after the condensation or the evaporation of gases (water vapor in our case); this calculation is usually neglected in most of the well-known Global Climate Models. More details on the scheme can be found in Leconte et al. (2013a) (Supplementary Materials). This scheme comes from previous work for the CO_2 cycle on present-day Mars (Forget et al., 1998), where there is some observational validation.

5.5.1.4 Parameterization of the precipitation events

H_2O precipitation events were parameterized using a simple cloud water content threshold scheme (Emanuel and Ivkovi-Rothman, 1999) as in Wordsworth et al. (2013). If the cloud water content overpasses a threshold l_0 in a given atmospheric grid cell, precipitation occurs. We chose l_0 to be constant and equal to 0.001 kg/kg as in Wordsworth et al. (2013). Wordsworth et al. (2013) examined the influence of l_0 and found it to be very low (1K difference between l_0=0.001 and 0.01 kg/kg).

We note that the reevaporation of the precipitation is also taken into account in our numerical scheme.

5.5.2 Control Simulations without outflow events

We performed control simulations in the conditions described above for 5 different surface pressures (40 mbar, 80 mbar, 0.2 bar, 0.5 bar, 1 bar) and we obtained results which are consistent with Wordsworth et al. (2013) and Forget et al. (2013). For these control runs, the three main differences between our work and Wordsworth et al. (2013) were: 1. the updated absorption coefficients (now HITRAN 2012); 2. an increase of the solar luminosity (now 79% of Mars present-day value); and 3. the increase of the horizontal model resolution (from 32 x 32 to 96 x 48 in longitude x latitude).

Figure 5.4 shows the mean annual surface temperatures and the position of the stable ice deposits for the reference case (0.2 bar) and the two surface pressure endmembers (40 mbar and 1 bar). The mean annual surface temperatures are slightly lower than in Figure 3 in Wordsworth et al. (2013) which were obtained for a fixed 100% relative humidity. It is also perhaps due to a slightly reduced CO_2 ice cloud warming effect at high spatial resolution. The stable surface ice deposit locations were calculated using the ice equilibration algorithm of Wordsworth et al. (2013). Starting from a random initial surface ice distribution, (1) we run the GCM for two martian years then (2) we extrapolate the ice layer field h_{ice} evolution calculation using:

$$h_{\mathrm{ice}}(t + n_{\mathrm{years}}) = h_{\mathrm{ice}}(t) + n_{\mathrm{years}} \times \Delta h_{\mathrm{ice}}, \tag{5.8}$$

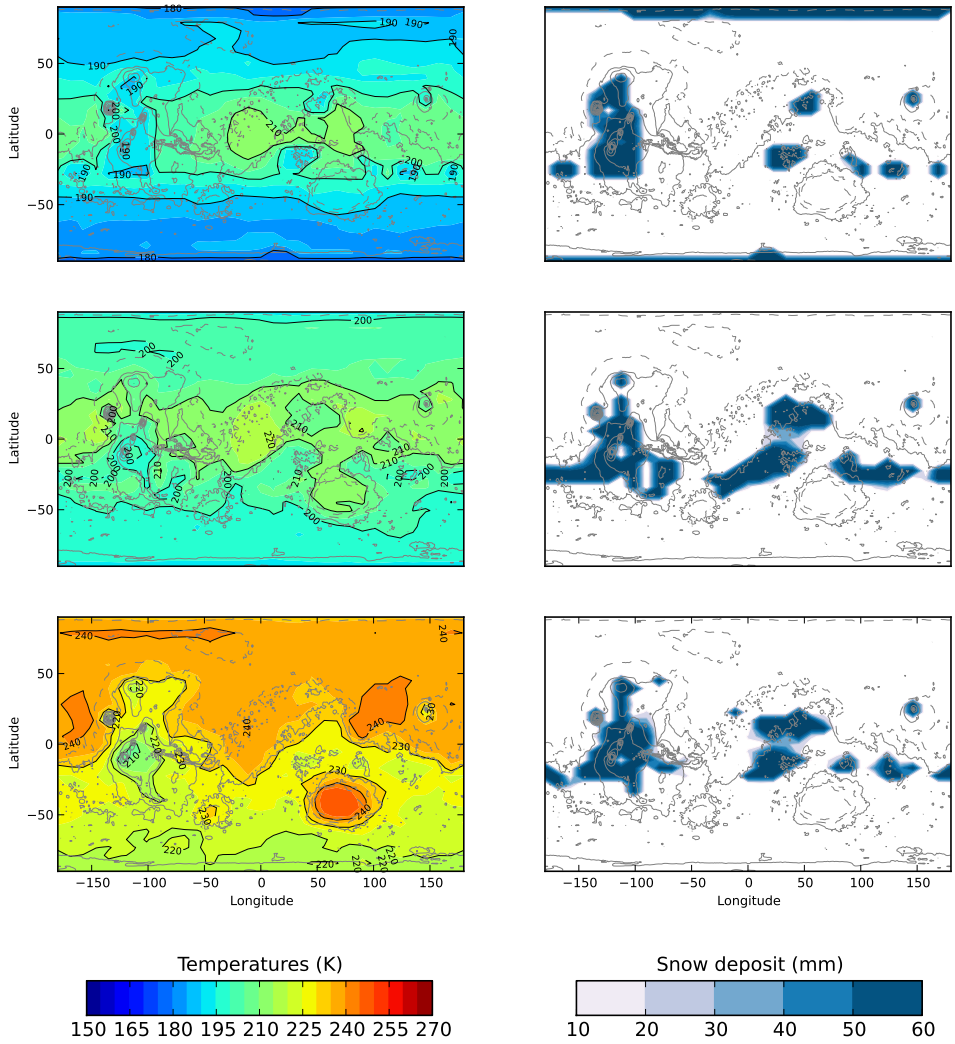

Figure 5.4: Surface Temperatures (left) and H_2O ice deposit (right) annual means for the control simulations (at a 96 x 48 horizontal resolution) after $\sim$ 800 martian years (or 30 loops of the ice iteration scheme). Top, middle and bottom plots correspond respectively to control simulations performed at 40 mbar, 0.2 bar and 1 bar. Grey contours show the topography used in the simulation. Ice iteration was performed every 2 years, with a 100-year timestep used for the first five iterations and 10-year timesteps used thereafter.

with $\Delta h_{\rm ice}$ the annual mean ice field change of the one-martian-year previous simulation and $n_{\rm years}$ the number of years requested for the extrapolation. Then, (3) we eliminate of seasonal ice deposit and (4) we normalize the extrapolated ice field by the initial ice inventory to conserve the total ice mass. Eventually, (5) we repeat the process.

This algorithm has been shown (Wordsworth et al., 2013) to be insensitive to the proposed initial ice field location at the beginning of the simulation, at least assuming that the scheme has been repeated a sufficient number of times.

In total, for our control simulations, we performed the scheme 30 times, with $n_{\rm years}$=100 for the first 5 loops and $n_{\rm years}$=10 for 20 more loops for a resolution of 32 x 32. Then, we ran the algorithm 5 more times at the increased resolution of 96 x 48 to obtain a stable initial state necessary for the implementation of outflow channel events.

We note that 3D climate modeling under conditions similar to those described above (Forget et al., 2013; Wordsworth et al., 2013) have not yet been able to produce liquid water or at least significant precipitation by climatic processes anywhere on the planet, even when maximizing the greenhouse effect of CO_2 ice clouds.

5.5.3 Experiment - Modeling of Outflow Channel Events

5.5.3.1 Description of the parameterization

Outflow channel events can be modeled to a first approximation by the sudden release, and then the spread of warm liquid water over the surface of Mars. In our simulations, this was accomplished by the emplacement of a fully mixed layer of warm liquid water at the surface. The fate of this water depends on the following processes (summarized in Figure 5.5).:

1. The liquid water layer loses some energy by thermal conduction to the initially cold ground. For this, we fix the uppermost of the 18th martian regolith layers at the temperature of the water, and calculate the heat flux lost (or gained) by the warm water to the downward layers.

2. The warm liquid water layer cools by emitting thermal infrared radiation at σ $T^4_{\rm surf}$. This emission contributes to the radiative transfer budget.

3. The liquid water evaporates and looses some latent heat. The evaporation E at the location of the warm water was computed within the boundary-layer scheme, using the following bulk aerodynamic formula:

$$E = \rho_1 C_d V_1 [q_{\rm sat}(T_{\rm surf}) - q_1], \tag{5.9}$$

where ρ_1 and V_1 are the volumetric mass of air and the wind velocity at the first atmospheric level, $q_{\rm sat}(T_{\rm surf})$ is the water vapor mass mixing ratio at saturation at the surface, and q_1 is the mixing ratio in the first atmospheric layer. The aerodynamic coefficient is given by: $C_d = (\kappa/ln(1+z_1/z_0))^2 \sim 2.5\times10^{-3}$, where $\kappa = 0.4$ is the Von Karman constant, z_0 is the roughness coefficient and z_1 is the altitude of the first level ($\sim$ 18 meters).

We modeled the sensible heat exchanged between the surface and the first atmospheric layer using a similar formula:

$$F_{\rm sensible} = \rho_1 C_p C_d V_1 [T_{\rm surf} - T_1], \tag{5.10}$$

with T_1 the temperature of the first atmospheric level and C_p the mass heat capacity assumed equal to 850 J K^{-1} kg^{-1} in case of a CO_2-only atmospheric composition.

4. Depending on the volume of water modeled, liquid water will flow from the Circum-Chryse outflow channel sources to Chryse Planitia, then to Acidalia Planitia, and eventually to the Northern Plains. First, we modeled the displacement of the flow calculated from its height and its velocity. The velocity of the flow mostly depends on its width but also on the slope of the terrain. For each grid, we used the subgrid mean slope and the subgrid mean orientation of the slope to evaluate (using equations (5.4) and (5.7)) the velocity and the direction of the flow. Second, we used a simple bucket scheme to model the progressive filling of the topographic depressions.

Warm waters flowing on the Northern Plain slopes can also encounter H_2O ice (it can be either stable at a particular latitude, or related to previous outflow channel events, but from the point of view of latent heat exchange and climate, it does not change anything) or seasonal CO_2 ice (typically present for atmospheres thinner than 1 bar). We modeled the interaction of H_2O and CO_2 ices with warm liquid water using energy conservation. If the liquid water is warm and in a sufficient amount, all the CO_2 ice sublimates and is added to the atmosphere. Similarly, all the water ice encountered by the warm flow is melted and converted at the resulting equilibrium temperature.

Once the flow has reached a stable position (e.g. forming a lake), in reality some water may be trapped in local topographic depressions (impact craters, tectonic basins, ...); it is difficult, however, to estimate adequately how much water might be sequestered in this manner. First, the detailed topography of the terrains is unknown prior to resurfacing by the outflow channel events. Second, the water outflows themselves modified (and probably smoothed) the topography. Thus, to take into account not only the effect of the trapped water but also the role of the wet ground, we arbitrarily placed a minimum 20 cm layer of liquid water in all the locations where the liquid water flow passed through. This assumption may also be representative of the fact that in reality the discharge rate does not have a rectangular shape (in time) as we assumed in our parameterizations.

5. As time goes on, the liquid water flow cools. If its temperature reaches the 273.15 K freezing temperature (assuming no salts), the water starts to freeze. On Earth, salinity drives the freezing point of oceans to $\sim$ 271K and assuming similar salt rates in outflow waters would not change much our results. To account for this process, we developed a multiple layer modified version of the soil thermal conduction model already included in the GCM. We have in total 100+ layers, with mid-layer depths ranging from $d_0 \sim 0.1$ mm to $d_{14} \sim 2$ m, following the power law $d_{n,n\leq 14} = d_0 \times 2^n$ with n being the corresponding soil level and the linear law $d_{n,n>14}=d_{14} \times (n-13)$ for the deepest layers. The layers are separated into two parts: the ice cover above and the liquid water below. For the water ice layers, we use a thermal conductivity of 2.5 W m^{-1} K^{-1} and a volumetric heat capacity of 2×10^6 J m^{-3} K^{-1}. For the liquid water, we use, respectively, a thermal inertia of 20000 J m^{-2} K^{-1} s$^{-1/2}$ (artificially high to account for convection) and a volumetric heat capacity of 4×10^6 J m^{-3} K^{-1}. At each physical timestep, we estimate the thermal diffusion flux lost by the liquid water layer to the water ice layer and calculate (using the conservation of energy) the amount of liquid water to freeze. If the depth of the ice - initially going down to $d=d_n$ - overpasses the layer d_{n+1}, we convert the $n+1$ layer into ice.

We note that the use of a multi-layer soil model is important to describe the sea-ice formation, evolution and its impact on possible cold early martian climates. Such refined models are better suited to represent the temperature profile evolution within the ice layer (that may evolve with seasonal forcing or as the ice layer thickens) and thus the surface temperature that controls the sublimation rate. In particular, our simulations show that up to 95% of the annual sublimation rate can be produced during the summer seasons. This requires a good estimate of the seasonal variations of the surface temperature above the ice.

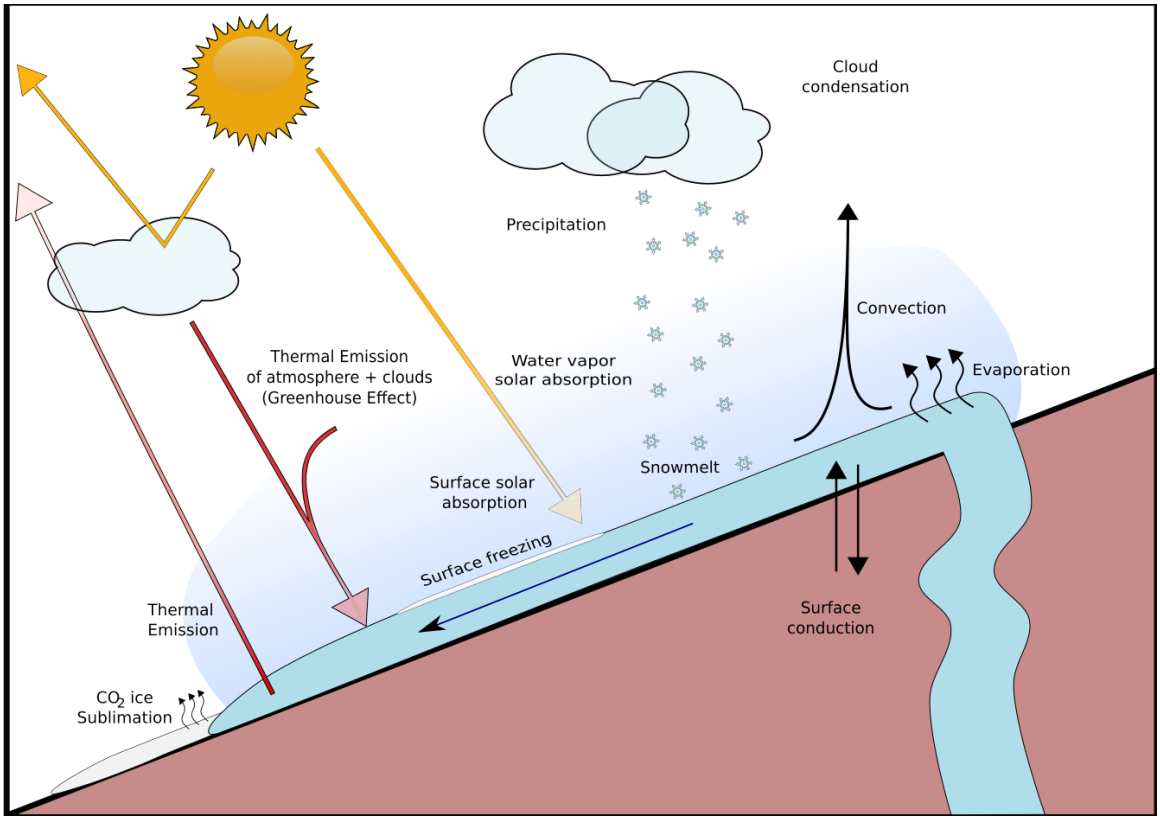

Figure 5.5: Schematic drawing of the physical processes taken into account during outflow channel events in our GCM simulations. Credit: N. Chaniaud.

Simultaneously, as the ice layer forms, we also linearly increase the surface albedo from $A_{liq} = 0.07$ (if no ice) to $A_{ice} = 0.5$ (if the ice layer thickness h overpasses the threshold value of $h_* = 3.5$ cm; Le Treut and Li 1991) as follows:

$$A = A_{liq} + (A_{ice} - A_{liq}) \frac{h}{h_*}. \tag{5.11}$$

6. The amount of water delivered by outflow events can be very large and thus lead to the accumulation of large quantities of liquid water. The timing expected for this water to freeze can be evaluated using a combination of the thermal conduction flux in the ice layer $F = \lambda_{ice} \frac{(T_{surf} - T_{bottom})}{h}$ and the conservation of energy. Assuming that the temperature in the frozen layer varies linearly between $T_{bottom} = 273.15$ K and T_{surf} (assumed constant) as hypothesized in classical 2-layers thermodynamical models (Codron, 2012), we have:

$$\rho_{ice} \left(L_m - C_{ice} \frac{(T_{bottom} - T_{surf})}{2}\right) \frac{\partial h}{\partial t} = \lambda_{ice} \frac{(T_{bottom} - T_{surf})}{h}, \tag{5.12}$$

where ρ_{ice} is the volumetric mass of the ice (9.2×10^2 kg m^{-3}), C_{ice} is the specific heat capacity of the ice (2.1×10^3 J kg^{-1} K^{-1}), λ_{ice} is the conductivity of the ice (2.5 W m^{-1} K^{-1}) and $L_m \sim 3.34 \times 10^5$ J kg^{-1} is the latent heat of fusion of water ice.

This leads after integration over time to an expression of t(h), the timing required to freeze a layer of depth h:

$$t(h) = \frac{\rho_{ice}}{2\ \lambda_{ice}} \left(\frac{L_m}{(T_{bottom} - T_{surf})} - \frac{C_{ice}}{2}\right) h^2. \tag{5.13}$$

For example, the outflow event presented in section 5.6 leads to the accumulation of up to 600 meters of liquid water. A typical timescale (for $T_{surf} \sim 200$ K) for this water to freeze, according to equation 5.13, is $\sim 4 \times 10^3$ martian years.

To account for such long timescales, we developed a modified version of the ice iteration scheme presented above. (1) First, we run the GCM for a few years then (2) every 2 years, we extrapolate the amount of ice that has locally condensed and sublimed in the simulations by an arbitrary factor n_{years}. Simultaneously, (3) we proceed to a linear extrapolation of the amount of frozen water/of the growth of the ice layer thickness by the same factor n_{years}, using the conservation of energy. We actually fit the t = f(h) function by straight lines of sizes multiple of n_{years}. In the reference simulation presented in section 5.6, we performed first 5 martian years, then we extrapolated every 2 years using n_{years}=[5,5,20,20,50,50,100,100,500,500]. After the extrapolation of the ice field/the ice layer depth is completed, (4) we arbitrarily set the ground temperature profile (where liquid water remains) to be linear, between $T_{bottom} = 273.15$ K and T_{surf} calculated using the conservation of energy. This is a way to take into account (at first order) the evolution of the deepest ground layers that require very long timescales to stabilize their temperature profiles. The year following the extrapolation is thus also useful to get back a consistent temperature profile in the first layers (up to 15 meters typically).

7. Once the outflow water is completely frozen, we use again the ice iteration scheme (see section 5.5.2) to get estimates of the timing required for the ice to reach its stable positions.

5.6 Results - the reference simulation

We present in this section the results of simulations of outflow channel formation events occuring in the largest of the Circum Chryse channels: Kasei Vallis. We chose this particular location because 1. The Kasei Vallis outflow channel begins in Echus Chasma, which is close to the West Echus Chasma Plateau valley networks; and 2. Kasei Vallis is one of the largest outflow channels on Mars (Carr, 1996).

We focus first on a discharge of 10^6 km^3 (6.9 meters of GEL - Global Equivalent Layer) of liquid water heated at 300 Kelvins. Water is released at a constant rate of 10^9 m^3 s^{-1} in the region of Echus Chasma (see Figure 5.6 for the associated flow). This event is an upper estimate (in volume, discharge rate and temperatures) of the characteristics of outflow channel formation events (see section 5.4.1.1 for references).

As explained in section 5.4.2, surface atmospheric pressure in the Late Hesperian epoch is poorly constrained. Thus, we focus first on the case of a surface pressure of 0.2 bar.

5.6.1 Description of the flow

A volume of 10^6 km^3 of liquid water is released at the discharge rate of 1 km^3 s^{-1}. It takes approximately 1.1 martian days for the liquid water to travel from the source of the flow (in Echus Chasma, at $\sim$ 4°N,-79°E) to the end of Kasei Vallis (at $\sim$ 30°N,-45°E), and 1.5 more days for the same flow to reach the main topographic depression of the northern plains (at $\sim$ 70°N,-30°E). This corresponds, respectively, to mean flow speeds of $\sim$ 30 m s^{-1} and $\sim$ 16 m s^{-1}, which are consistent with the two endmembers values shown in Figure 5.3.

After $\sim$ 11 days, the source of ground water (located in Echus Chasma) becomes inactive. Eventually, it takes approximately 20 martian days in this scenario for the liquid water that has erupted in Echus Chasma to form a stable lake in the lowest part of the Northern Plains. This lake extends over an area of 4.2 millions of km^2 ($\sim$ 2.9% of the global surface area of Mars), has a mean depth of $\sim$ 240 meters and a peak depth of $\sim$ 600 meters. Some water ($\sim$ 20 centimeters) is left at locations with latitude < 50°N to account for the wet ground and the water possibly trapped in the topographic depressions.

The fate of the outflow channel formation event can be divided into two main parts:

1. During the first $\sim$ 500 days following the event, the 'Warm Phase', an intense hydrological cycle takes place. The end of this phase approximately coincides with the time when the Northern Plains lake becomes fully covered by an ice layer.

2. During the following $\sim 10^5$ martian years, the martian climate is controlled by a weak and cold water cycle. It takes approximately the first 4×10^3 years (as predicted by simple energy-balanced models; Kreslavsky and Head 2002) for the lake to be entirely frozen, and the rest to sublimate the lake completely and move the ice to its positions of equilibrium, assuming no ice gets buried below a lag deposit or gets transported through glacier flows.

5.6.2 The Warm Phase

As soon as the simulation starts, the warm 300 K liquid water released in Echus Chasma evaporates efficiently following equation 5.9, while flowing over the Northern Plains slopes. At the locations reached by the flow, which represent $\sim$ 11 million km^2 ($\sim$ 7.5% of the global surface area of Mars),

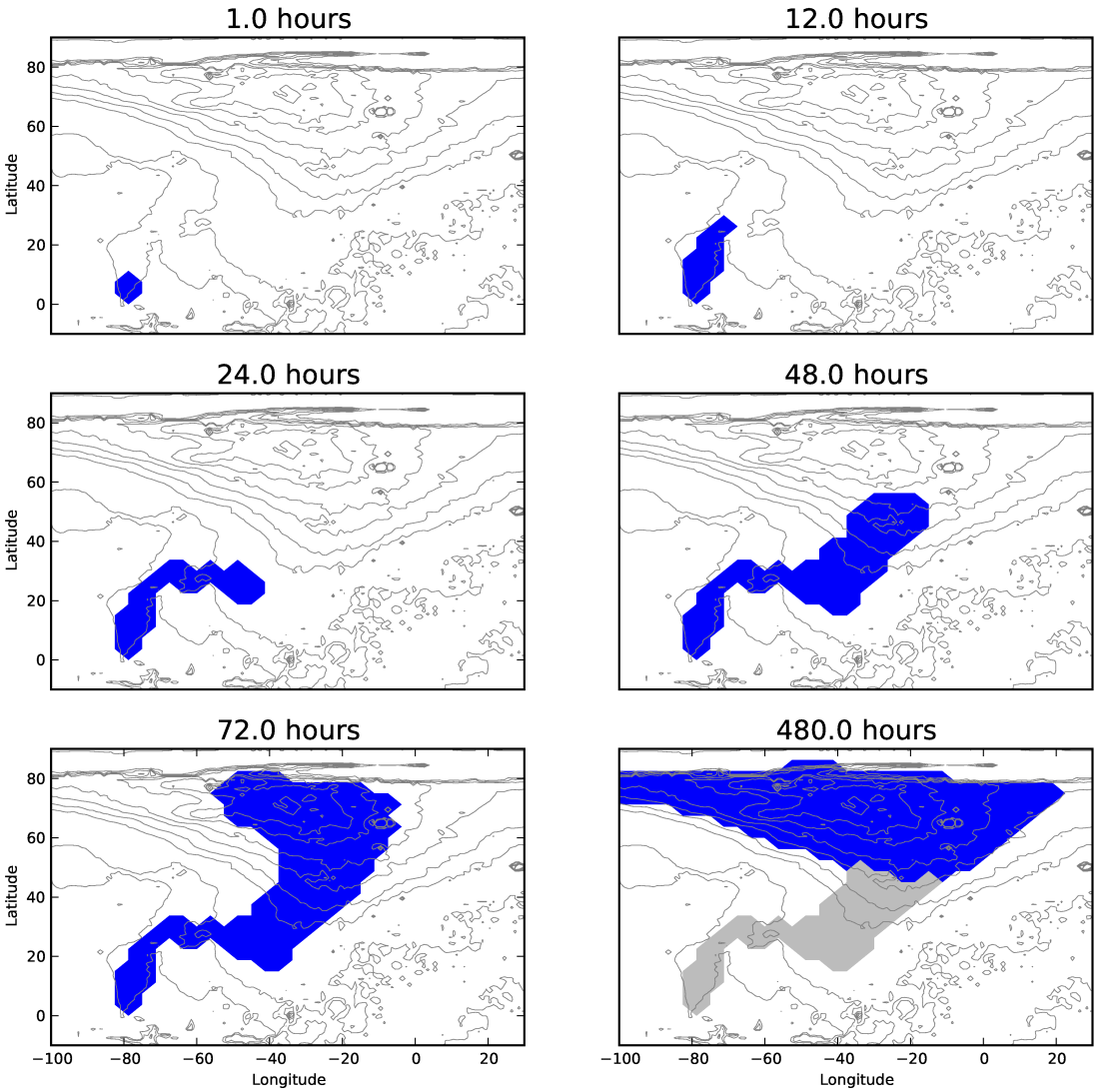

Figure 5.6: Time lapse of the runoff of the outflow channel event occuring in Echus Chasma, and flowing from Kasei Vallis down to the Northern Plains main topographic depression. The blue area corresponds to the position of the flow. The grey color was used to represent the 'wet' regions where the flow passed through but did not accumulate.

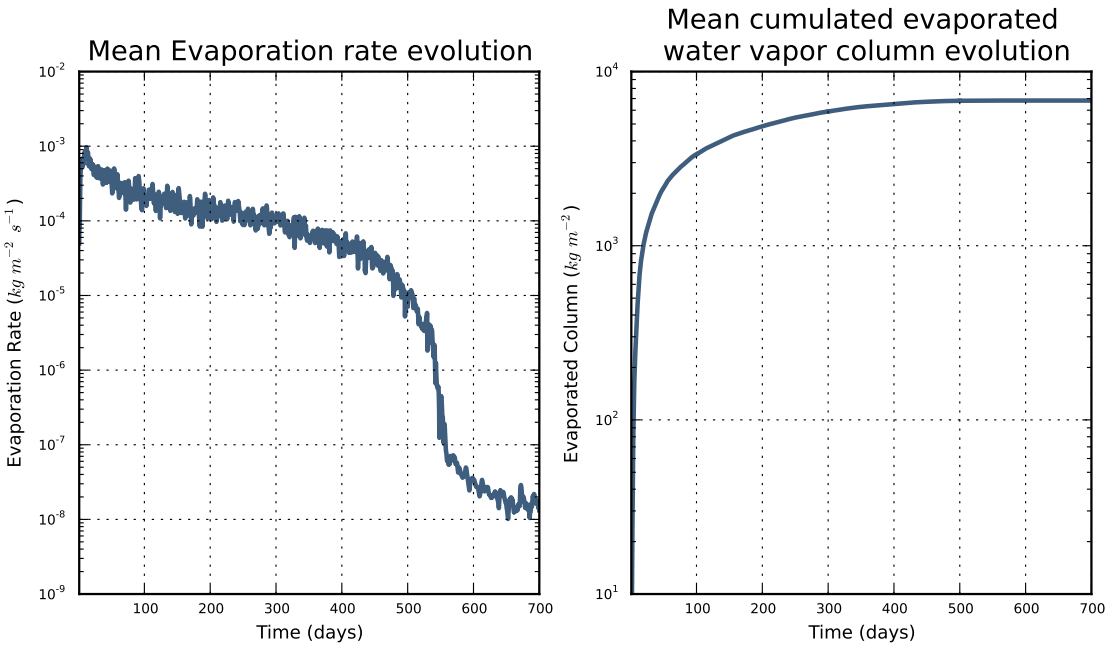

Figure 5.7: Mean lake evaporation rate evolution (left) and mean cumulative evaporated liquid water from the lake (right). The right curve is the cumulative integral over time of the left curve.

the evaporation rate can reach $\sim 10^{-3}$ kg m^2 s^{-1} for tens of days. Figure 5.7 (left) shows the mean evaporation rate for the $4.2{\times}10^6$ km^2 Northern Plains stable lake formed by the outflow channel flood accumulation.

During the 500 days following the event, a global precipitable water amount of $\sim$ 23 centimers is evaporated by the liquid water flow. Evaporation of the lake accounts for 96 % of this amount (blue region in Figure 5.6, after 480 hours) and 4 % by the evaporation of the transient flow (grey region in Figure 5.6, after 480 hours). This amount of cumulative evaporation corresponds to $\sim$ 3.4 % of the initial volume of water ejected by the ouflow event, which is approximately 0.7 times the amount of evaporated water that would be expected if the extra thermal heat (compared to 273 K) of the 300 K flow was simply converted into latent heat.

5.6.2.1 Mechanisms warming the atmosphere

As the water vapor starts to accumulate above the flow, the initially cold martian lower atmosphere soon reaches the water vapor saturation pressure. For instance, at 210 Kelvins, which is typically the mean surface temperature expected for a 0.2 bar atmosphere (Figure 5.4), the water vapor saturation pressure is $\sim$ 1.4 Pascals and the mass mixing ratio at saturation in a 0.2 bar atmosphere is thereby $\sim$ $7{\times}10^{-5}$ kg/kg^{-1}. This situation leads to the early condensation of the water vapor, latent heat release and thus to the warming of the atmosphere. We identified this process as the dominant mechanism responsible for the warming of the atmosphere after an outflow event.

As the atmospheric temperatures increase, the capability of the atmosphere to retain water vapor

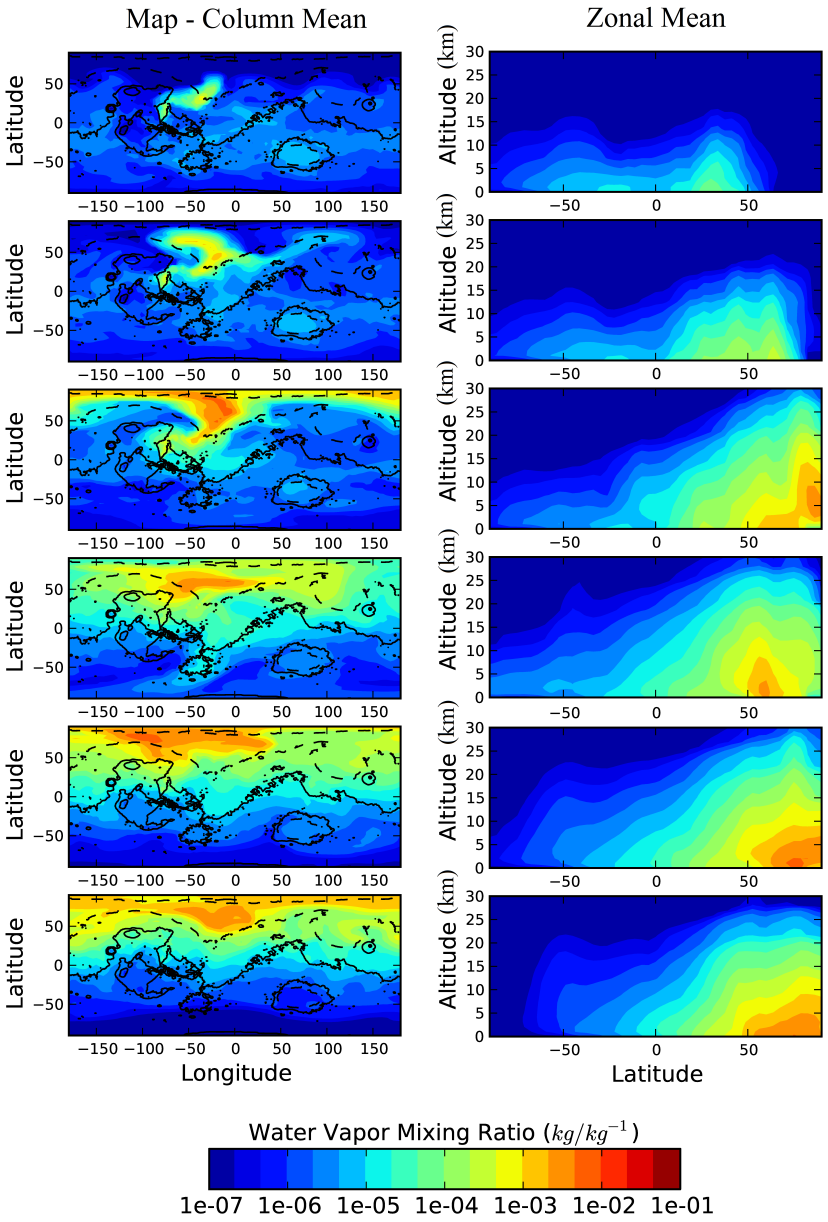

Figure 5.8: Time-lapse of the water vapor mixing ratio after (from the top to the bottom) 2.5/5/10/20/40/80 days. The left panels show the map of the water vapor distribution (column mean mixing ratio); the right panels show the corresponding zonal mean distribution (water vapor mixing ratio) as a function of latitude (°N) and altitude (km).

also increases. The mass mixing ratio at saturation, namely $Q_{\rm sat}$, can be written as follows:

$$Q_{{\rm sat},H_2O} = \frac{P_{{\rm sat},H_2O}}{P_{CO_2} + P_{{\rm sat},H_2O}},\ with\ P_{{\rm sat},H_2O}(T) = P_{\rm ref}\ e^{\frac{L_v M_{,H_2O}}{R}(\frac{1}{T_{\rm ref}} - \frac{1}{T})}, \tag{5.14}$$

with $P_{{\rm sat},H_2O}$ the water vapor saturation pressure and P_{CO_2} the CO_2 partial pressure, with $P_{\rm ref}$ and $T_{\rm ref}$ the pression/temperature of the triple point of water, respectively equal to 612 Pascals/273.16 Kelvins, $M_{,H_2O} \sim 1.8{\times}10^{-2}$ kg mol^{-1} the molar mass of water, and $L_v \sim 2.26{\times}10^6$ J kg^{-1} the latent heat of vaporization of liquid water. For low amounts of water, this relation simply becomes:

$$Q_{{\rm sat},H_2O}(T) \sim \frac{P_{\rm ref}}{P_{CO_2}}\ e^{\frac{L_v M_{H_2O}}{R}(\frac{1}{T_{\rm ref}} - \frac{1}{T})}. \tag{5.15}$$

Therefore, as the atmospheric temperatures increase, the atmosphere is also able to transport more and more water upwards. Thus, as time goes on, the atmosphere becomes more and more warm and wet. As the atmospheric water vapor content increases, the absorption of the atmosphere in the infrared wavelength range (essentially due to the thermal emission of the warm outflow waters) increases and thus contributes to an additional warming of the atmosphere.

In total, during the warm phase (the first 500 days), the atmosphere (above the flow/lake) is directly warmed by the following processes (in decreasing order of importance): 1. the condensation of the water vapor produced by the warm flow ($\sim$ 56 %); 2. the sensible heat exchanged between the flow/lake and the lowest atmospheric layer ($\sim$ 22 %); 3. the thermal infrared emission of the flow absorbed by the mixture of gaseous CO_2/H_2O ($\sim$ 13 %); and 4. the extra solar absorption resulting from the presence of water vapor excess, which has strong absorption lines in the solar domain ($\sim$ 9 %);. The atmospheric solar absorption is particularly important in this scenario, because we chose the outflow channel event to start at Ls = 5° and thus to occur during the northern hemisphere spring and summer. Of course, all these processes reinforce and strengthen each other.

Figure 5.8 shows the spatial evolution of the water vapor atmospheric content. Initially, water vapor accumulates at low altitudes, in the regions where the liquid water flow is located. After a few days, the water vapor has reached much higher altitudes (up to $\sim$ 30 km) through the aforementioned warming mechanisms and the convective adjustment scheme. Eventually, once the upper part of the atmosphere has become wet enough (typically after $\sim$ 10 days in this scenario), the high altitude horizontal winds (around $\sim$ 15 km) advect the water vapor into the neighbouring regions. After $\sim$ 50 days, all the martian regions located above $\sim 50°N$ have become more or less wet, with a typical water vapor mean mass mixing ratio of 0.3%.

Similarly, the impact of H_2O condensation (and other additional warming sources) on atmospheric temperatures is shown in Figure 5.9. After $\sim$ 100 days, at the peak of the outflow channel event, the atmospheric temperatures in the lower atmosphere (0-5 km) almost reach 280 K, +90 Kelvins above the regular temperature (peak above the lake) as calculated in the control simulation; the atmospheric temperatures in the higher parts of the atmosphere typically extend up to 230 Kelvins (at 10 km) and to 170 Kelvins (at 25 km), which are respectively +50 K and +25 K above the temperatures prescribed by the control simulation.

5.6.2.2 The mechanisms cooling the flow

After $\sim$ 500 days, which corresponds to the complete surface freezing of the outflow channel event water, the evaporation E produced by the stable lake (see Figure 5.7) suddenly reduces (by almost 3

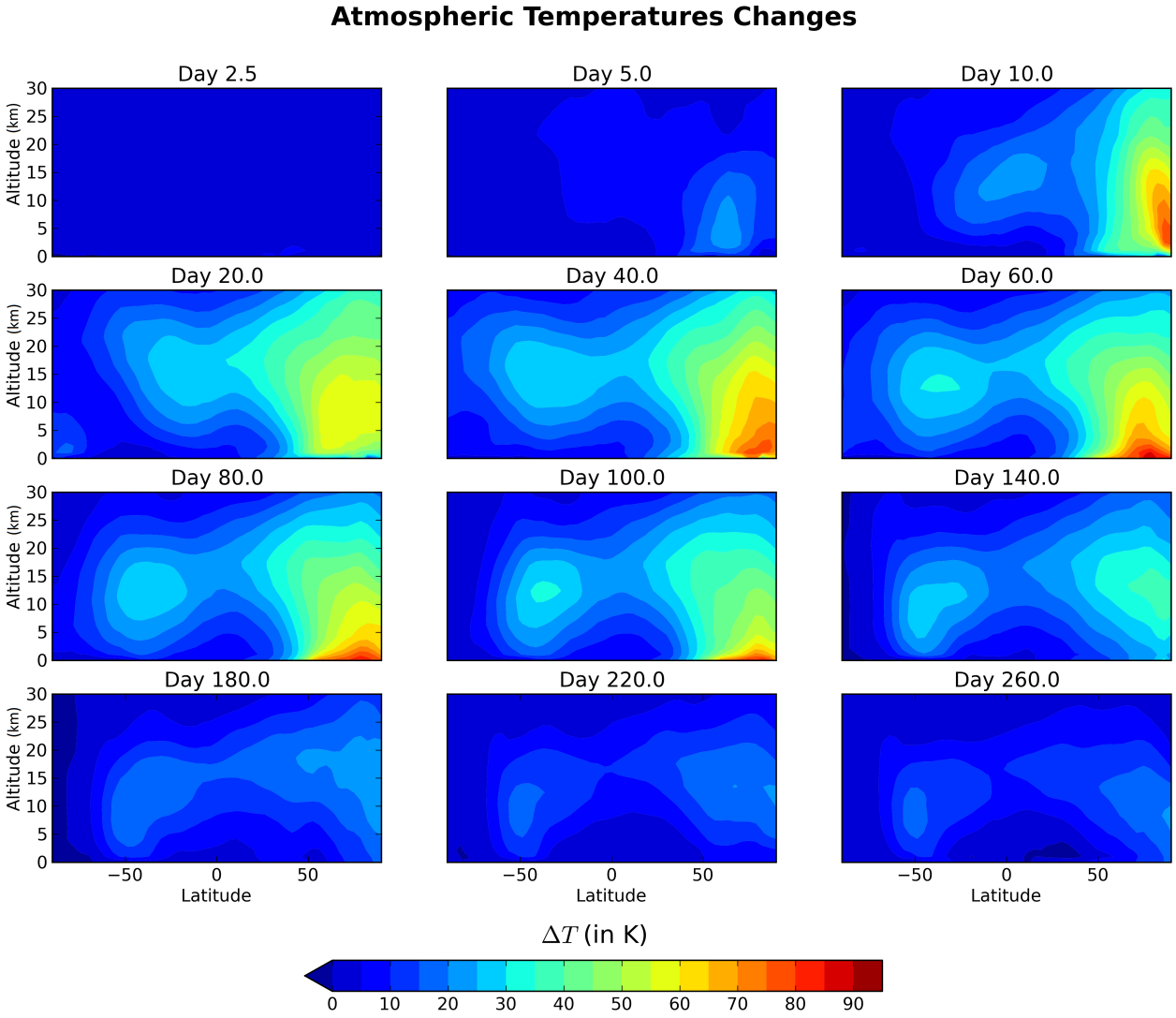

Figure 5.9: Time-lapse of the zonal mean cross-section atmospheric temperature difference between the reference simulation (with outflow) and the control simulation (without outflow) for the same surface pressure of 0.2 bar.

orders of magnitude). To a first order, we have in fact:

$$E \propto Q_{\text{sat}}(T) \propto e^{-\frac{\alpha}{T}}, \tag{5.16}$$

with $\alpha = \frac{L_{\text{sub}} M_{H_2O}}{R}$ and L_{sub} the latent heat of sublimation of water ice. The evaporation rate E has thereby a strong dependence on temperature. This is why the drop in temperature associated with the surface freezing of the Northern Plains lake is responsible for the sudden decrease of evaporation visible in Figure 5.7 (also seen through the latent heat surface flux in Figure 5.10). This drop in evaporation defines the end of the 'warm phase', which includes the decrease of the water vapor content, the atmospheric temperatures and the precipitation events (see Figure 5.14).

There are several physical processes that are responsible for the cooling of the flow, leading to its solidification as ice. Figure 5.10 shows the relative importance of the different thermal heat losses by the Northern Plains lake, from the beginning of the event to one martian year later. For the first 500 days, the main cooling surface fluxes are the latent heat loss (420 W m^{-2}, 43.3 %), the sensible heat loss (190 W m^{-2}, 19.6 %), the radiative thermal emission loss (280 W m^{-2}, 28.8 %) and the ground conduction loss (8 W m^{-2}, 0.8 %). Some other surface fluxes related to the CO_2 ice sublimation by the warm flow (13 W m^{-2}, 1.3 %) and the cooling of the lake by the melting of the falling snow (60 W m^{-2}, 6.2 %) also contribute to the cooling of the outflow waters. In total, the average cooling flux of the outflow waters for the warm phase (first 500 days) is $\sim$ 970 W m^{-2}.

For large outflow channel formation events like the one described in this section, the sublimation of the seasonal carbon dioxide ice deposit represents a small fraction of the heat loss. Nonetheless, smaller outflow channel events (5×10^3 km^3 for example (Andrews-Hanna and Phillips, 2007)) flowing on the Northern Plains slopes may be deeply affected by the energy gap required to sublimate the CO_2 ice seasonal deposit. For a 0.2 bar atmosphere, the control simulations show, for example, that the CO_2 ice seasonal deposit reaches a yearly average of $\sim$ 300 kg m^{-2} from the North Pole down to 30°N latitudes.

Two radiative processes may counteract the cooling of the flow: 1) the absorption of solar radiation and 2) the greenhouse effects (of the atmosphere and of the clouds).

1. We chose in this scenario to start the outflow channel event at Ls = 5° in order to maximize the role of solar absorption. The peak of the event (between ~0-300 days, Ls ~ 5-165°) was therefore chosen to overlap with the peak of insolation in the Northern hemisphere, which is a maximum of $\sim$ 170 days after the event (Ls = 90°). There are three factors that need to be taken into account in the solar absorption processes: absorption by water vapor, albedo changes and clouds. For this reference simulation, compared to the control simulation, these three effects more or less compensate at the location of the flow. The increase of the solar absorption due to the low albedo of liquid water (0.07 compared to 0.2 for the bare ground and 0.5 for the remaining CO_2 ice seasonal cover) and due to the absorption by water vapor are more or less balanced by the reflection of the cloud cover, which can reach on average a coverage of 80 % during the first 500 days above the lake (Figure 5.13). Most of these water clouds are located at low altitude (Figure 5.13). During the warm phase, the lake absorbs a solar flux of $\sim$ 67 W m^{-2} ($\sim$ 16 W m^{-2} less than the control run, see Figure 5.11) and the atmosphere (essentially the troposphere) $\sim$ 20 W m^{-2} ($\sim$ 12 W m^{-2} more than the control run). This corresponds to an average absorption of 65 % of the available incoming solar flux ($\sim$ 135.6 W m^{-2} for the first 500 days).

2. The downward thermal infrared emission from the atmosphere and the clouds is the dominant warming flux (see Figure 5.11). On average, during the warm phase, this greenhouse effect brings

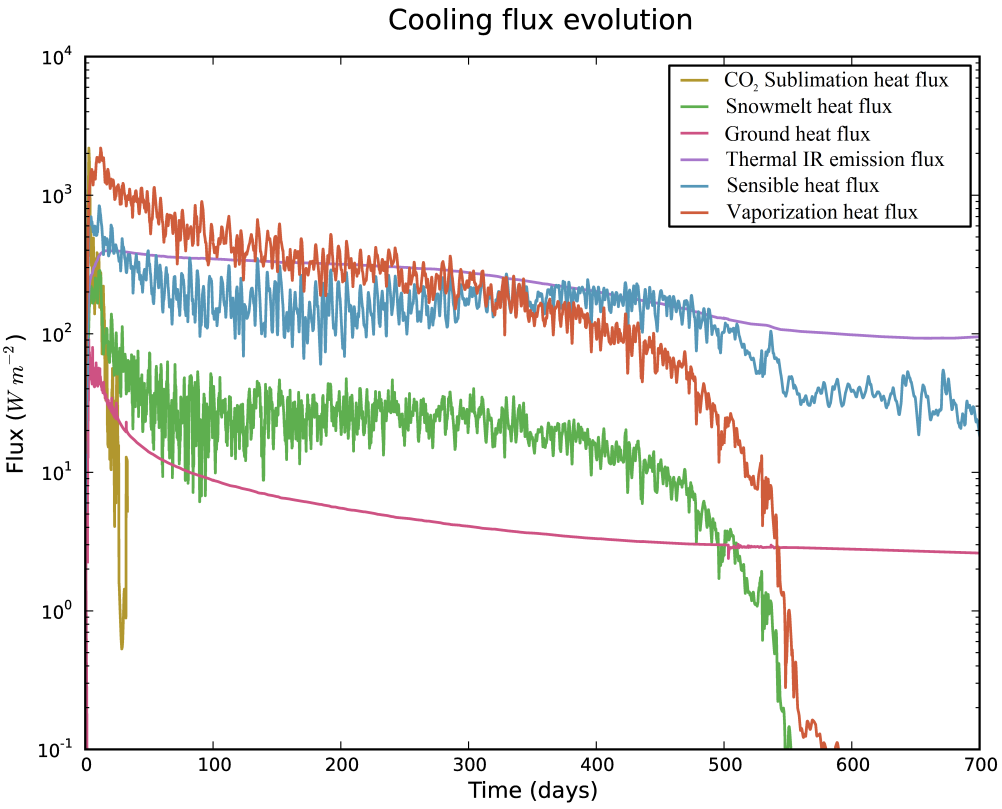

Figure 5.10: Surface cooling heat fluxes evolution averaged over all the Northern Plains lake grid cells in the P_{surf} = 0.2 bar reference simulation. We note here that, depending on the nature and the intensity of a given outflow channel formation event, each of these fluxes can potentially become dominant.

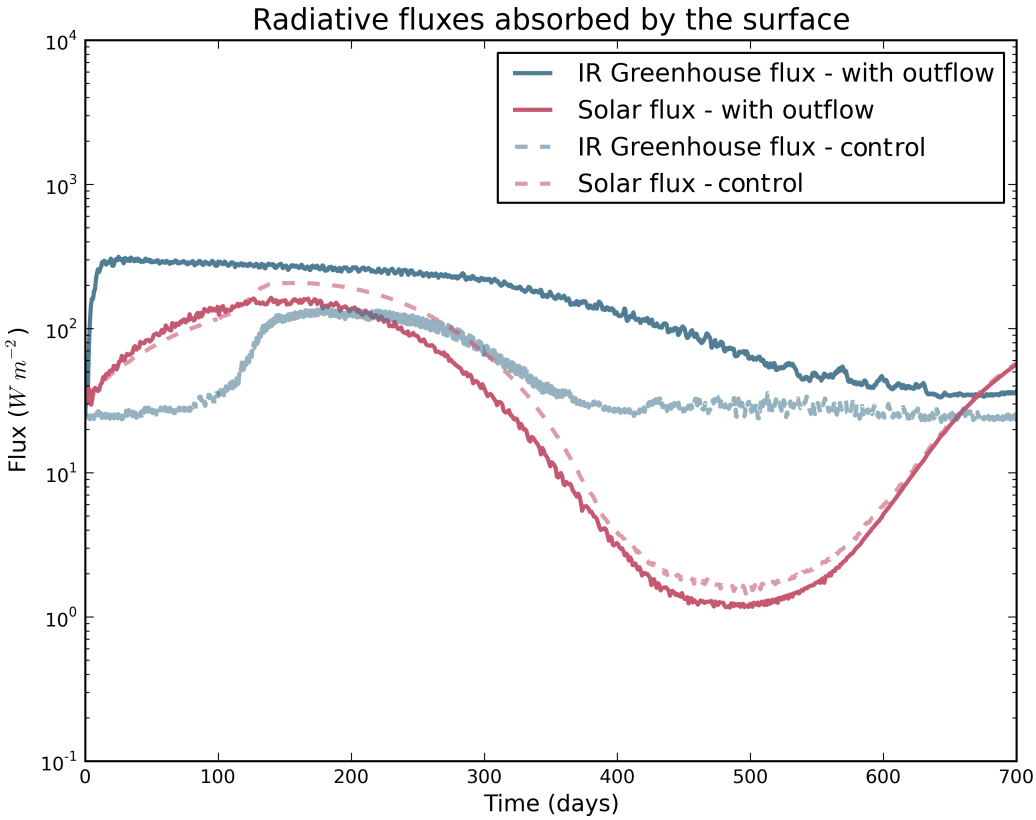

Figure 5.11: Evolution of the radiative fluxes absorbed by the surface and averaged over all the Northern Plains lake grid cells. Solid lines refer to the solar flux (in red) and the thermal infrared (in blue) for the reference simulation. Dashed lines correspond to the control simulations. For better visibility, we filtered diurnal waves from the absorbed solar fluxes using a 1 day running average.

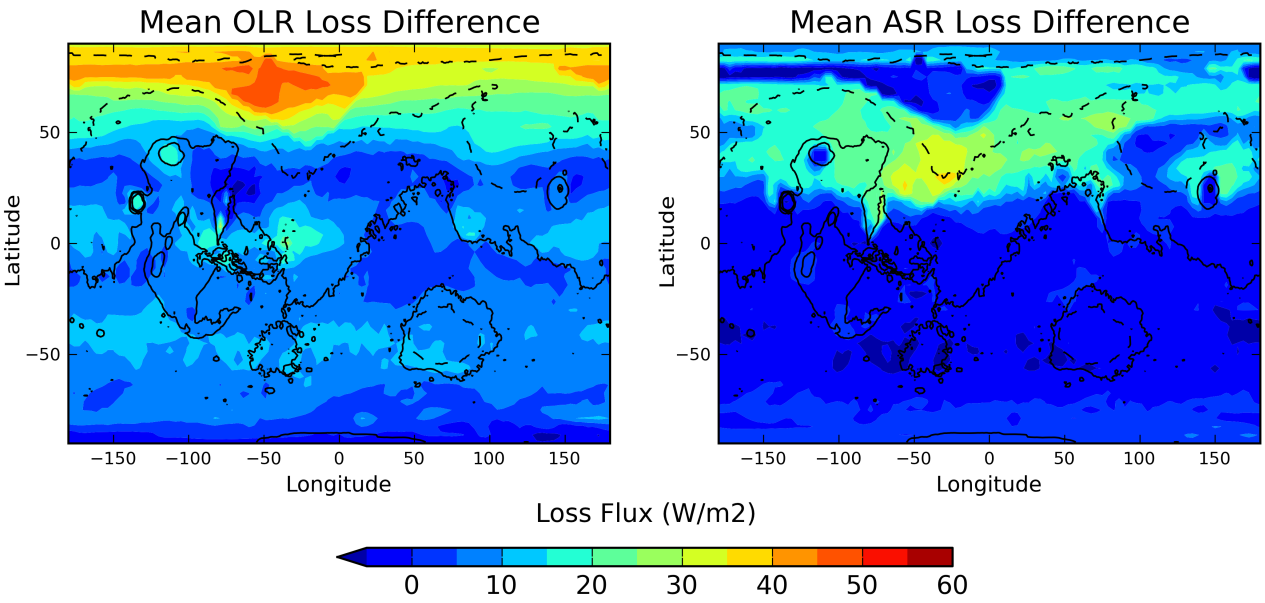

Figure 5.12: Mean Outgoing Longwave Radiation (OLR, left) and Absorbed Solar Radiation (ASR, right) loss during the warm phase, for the reference simulation, and relative to the control simulation performed for the same surface pressure.

$\sim$ 210 W m^{-2} to the lake (+ 150 W m^{-2} more than the control run). The main source of thermal infrared emission surface heating comes from the gaseous atmosphere itself, which can reach up to $\sim$ 280 K (above the lake) for the first 5 km, at the peak of the event.

In total, both solar and infrared heating counterbalance only $\sim$ 30% of the cooling of the flow, and are thus unable to sustain the perturbation generated by the ouflow channel. We note here that the radiative effect of H_2O clouds during the warm phase is approximately neutral or at least very limited (only +7 W m^{-2}) above the Northern Plains lake, with +23 W m^{-2} of greenhouse warming and -17 W m^{-2} due to the reflection of the sunlight.

5.6.2.3 The mechanisms cooling the atmosphere

One of the main results of our work is that outflow channel events are not able to sustain warm conditions. We present here the two processes that act efficiently together to cool down the atmosphere after outflow events.

1. In the time following catastrophic outflow channel events like the one described in this section, the atmosphere above the flow warms very quickly. In our reference simulation, 10 days after the beginning of the event, the temperature in the lower atmosphere (0-5 km) above the lake increases by almost 90 Kelvins. During the first 500 days after the event, because of this significant warming, the flow and the atmosphere just above it contribute to an extra thermal infrared emission loss to space of 38 W m^{-2} compared to the control simulation. Yet the amount of energy lost by the lake and the atmosphere above represent only $\sim$ 11% of the extra total cooling to space. Figure 5.9 shows that, as

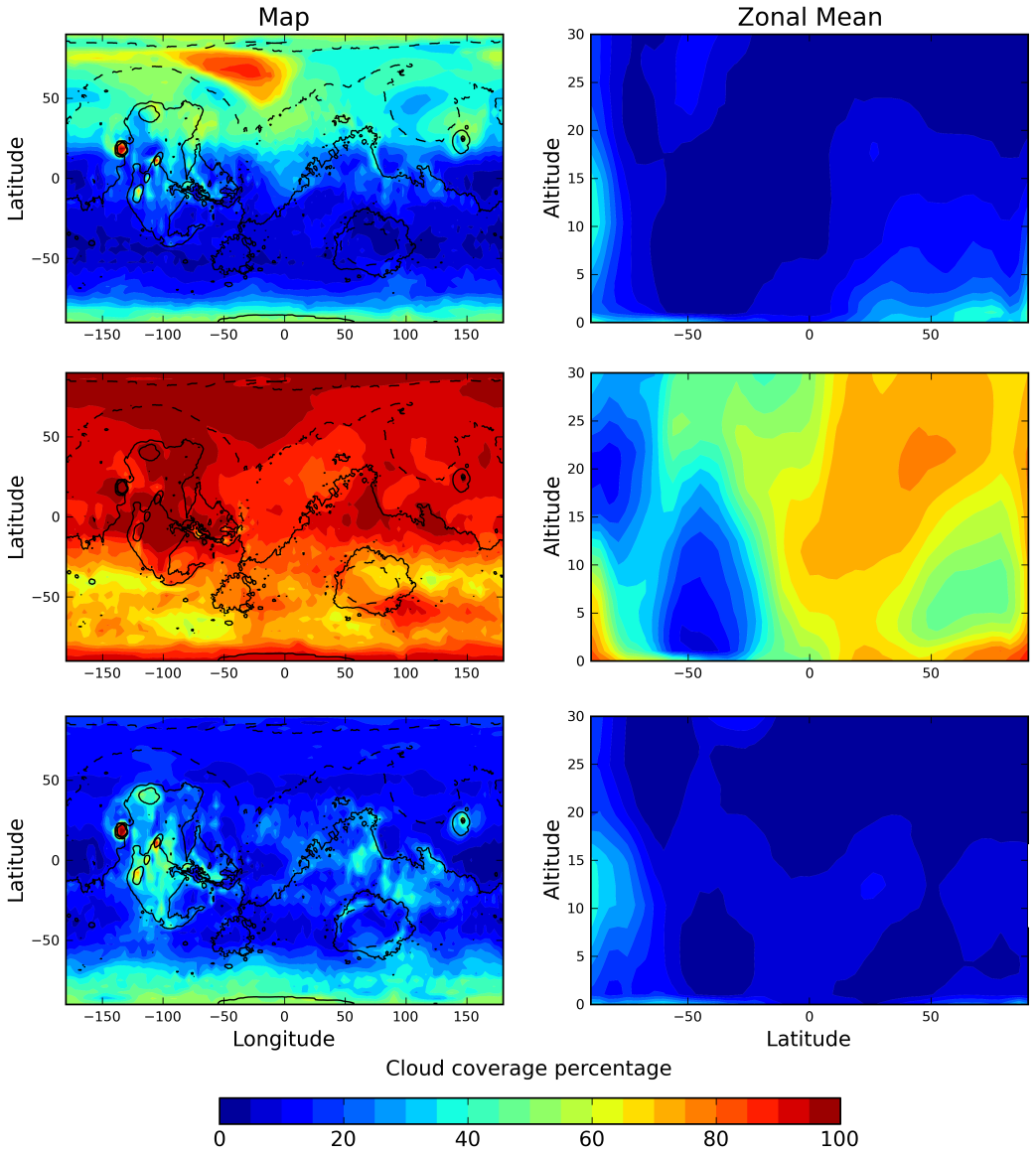

Figure 5.13: One year average of the cloud coverage following the outflow event. The first row corresponds to the map and the zonal mean cross-section of the reference simulation. In the second row, precipitation was removed (see section 5.9.2). The third row is for the control simulation.

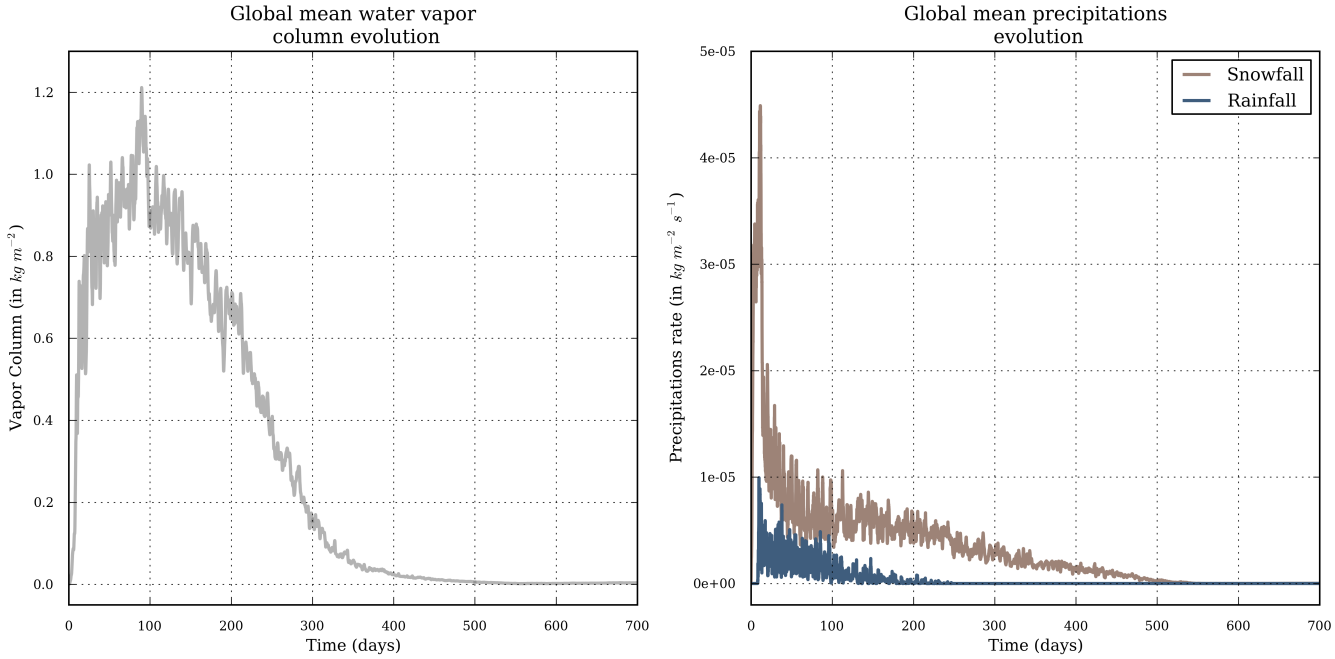

Figure 5.14: Evolution of the global mean water vapor column (left) and the precipitation (right), during the year following the outflow channel reference event.

the atmosphere gets warmer in the regions of the flow, high altitude winds around $\sim$ 15 km advect the heat to the neighbouring areas (in particular into the Northern Plains). This increases the surface of the emissions and therefore strengthens the cooling.

Figure 5.12 (left) shows the regions of the planet responsible for the extra thermal emission to space. Globally, during the warm phase (the first 500 days), the planet loses $\sim$ 10 W m^{-2}. One third of the emissions are due to the regions of latitude > 50°N. During the warm phase, the most important mechanism of cooling is the thermal infrared emission, enhanced by the advection processes.

2. Interestingly, another important cooling mechanism is the decrease of solar absorption due to the increase of surface albedo that follows the outflow channel event. In fact, the precipitation caused by the event, essentially in the form of snowfall (see Figure 5.14), leaves ice (see Figures 5.15 and 5.12) over an area of $\sim 30 \times 10^6$ km^2 that reflect an important part of the sunlight ($\sim$ 21.5 W m^{-2}). In total, during the warm phase and compared to the control simulation, the decrease of solar absorption contributes to a global equivalent extra cooling of $\sim$ 4.5 W m^{-2}, which represents half of the infrared emission loss to space.

The large amount of water vapor released after the outflow channel event condenses very quickly in the atmosphere, forming clouds that are mostly located in the area of the flow and of the resulting lake (see Figure 5.13). In total, for the reference simulation, the clouds have a slight positive effect of +1.3 W m^{-2} (+ 2.3 W m^{-2} of greenhouse effect and - 1.0 W m^{-2} of solar reflection).

5.6.2.4 Consequences on the water cycle and the precipitation

The maximum total amount of water vapor that is carried by the atmosphere during the event (GEL of 1.2 mm at the peak) remains limited by comparison to the cumulative total amount of precipitable water generated (GEL of 230 mm). It represents only $\sim$ 0.5% of the cumulative evaporated water vapor produced by the entire ouflow channel event during the first 500 days. Figure 5.14 (left) shows the global mean atmospheric water vapor content (column mass in kg m^{-2}, and also GEL in mm). It peaks at $\sim$ 100 days and considerably decreases from $\sim$ 200 days to $\sim$500 days.

The fact that the atmosphere is not able to accumulate more than $\sim$ 1.2 kg m^{-2} (globally) and $\sim$ 50 kg m^{-2} (locally, just above the warm lake) has one main consequence: the atmosphere does not manage to carry enough water vapor far enough from the lake to create precipitation in regions of interest (West Echus Chasma Plateau in particular). The typical lifetime of the atmospheric water vapor is in fact $\sim$ 0.5 days.

Rainfall, which represents a very small fraction ($\sim$ 10 %) of the precipitation (Figure 5.14), occurs only above the Northern Plain lake, because this is the only location of Mars where atmospheric temperatures exceed (up to 10 km) the temperature of the triple point. Outside the lake, the only mechanism of precipitation is snowfall. Approximately 50 % of the snow falls back directly on the flow/lake. The rest of the precipitation (the 50 % remaining) is essentially confined in the northern regions. Figure 5.15 shows the map of the deposited ice field (generated by precipitation) after a simulation of one martian year. The fraction of this ice that is melted after an outflow event is very limited (see Figure 5.19), because 1) most of the thermal perturbation has been dissipated by advection/cooling to space processes after $\sim$ 200 days, 2) the remaining water vapour abundance after these 200 days is too low to trigger a significant greenhouse warming (as found by Kite et al. 2011a) and 3) the ice field itself raises the albedo of the surface and thus acts as a very efficient climatic cooling agent.

In summary, the short-term climatic impact of outflow channel formation events seems very limited. For a 0.2 bar atmosphere, an outflow channel event of 10^6 km^3/300 K leads to the formation of a lake (located in the Northern Plains main topographic depression) that triggers a warm period that lasts for $\sim$ 500 days, which coincides approximately with the complete surface freezing of the water in the lake. Such events leave globally $\sim 6.5 \times 10^3$ km^3 of water ice/snow (0.65% of the initial outflow reservoir) and are able to melt $\sim$ 80 km^3 (0.008% of the initial reservoir; 1% of the deposited precipitation). Because the outflow events do not manage to warm the atmosphere enough, water vapour stays confined to the regions neighbouring the lake (essentially in the Northern Plains) and therefore precipitation (mostly snowfall) and melting only occur in the lowland regions.

The long-term climatic impact of the ice-covered lake is discussed in the next section.

5.6.3 The Cold Phase

After 500 martian days, the surface of the Northern Plains lake is completely covered by ice. Temperatures, water vapor content and precipitation all decrease. Because the area of high albedo ice deposits is larger than in the control simulations, the mean surface temperatures extend even lower than before the ouflow event (-2 K for the global annual surface temperatures of the 0.2 bar reference simulation, and compared to the control simulation).

Using the extrapolation scheme presented in section 5.5.3.1, we estimated that the released water

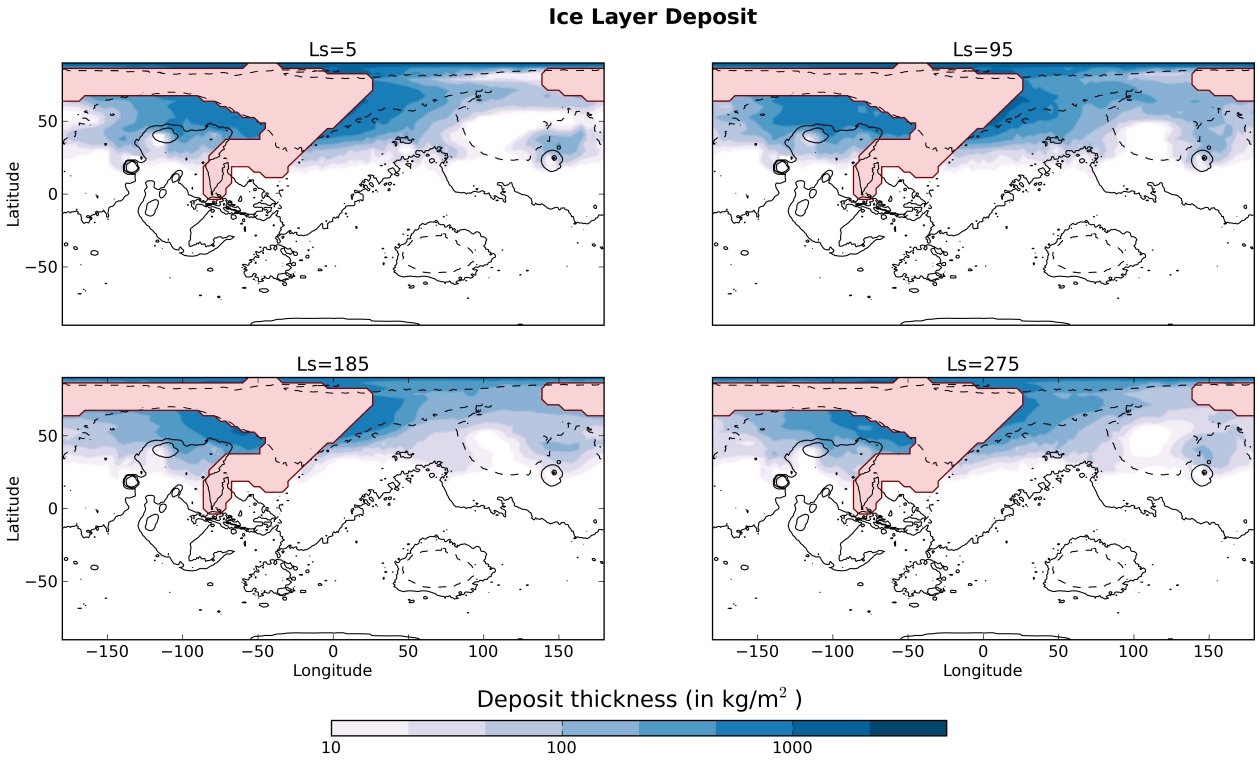

Figure 5.15: Ice deposit field obtained 1 martian year after the beginning of the event, for four different start dates (Ls = 5°, 95°, 185°, 275°). The first figure (on the top left corner) corresponds to the reference simulation and starts at Ls = 5°. We use the pink color for the regions where the flow passed through on its way to the lake.

was completely frozen after $\sim 4 \times 10^3$ martian years. This corresponds to the full solidification of the water to ice at the location of the main Northern Plains topographic depression (which is the deepest point of the lake). After $\sim$ 500 years, more than 70 % of the lake (in area) is frozen, from the surface to the top of the regolith. We note that the ground thermal flux (Clifford and Parker, 2001) during the Late Hesperian era was one order of magnitude too low (at best) to be able to increase the lifetime of the $\sim$ 500 m deep lake.

In our simulations, $\sim$ 10 years after the beginning of the lake-forming event, the mean ice thickness over the lake is $\sim$ 25 meters. The annual mean conduction heat flux for this ice thickness is $\sim$ 10 W m^{-2}. The annual mean solar/IR fluxes absorbed by the ice are $\sim$ 53/57 W m^{-2} by comparison, 110 W m^{-2} in total. Under these conditions, the thermal conduction flux represents less than 10 % of the total heat flux received by the surface at the location of the lake. Moreover, because the temperature profile oscillates annually, in the first 5 meters (typically) of the ice cover, from positive values (summer season) to negative values (winter season), the heat conduction from the liquid water to the surface is mainly returned during the winter seasons. Yet, the water cycle in this cold phase is essentially controlled by the summer seasons, because sublimation rates are several orders of magnitude higher

than during the winter seasons (see section 5.5.3.1 for discussion). Thus, after a few years (typically around 10), the climatic effect of the lake becomes, to a first order, the same as simply placing a comparable-sized body of ice in the Northern Plains. During these 10 years, ice transportation/water vapor cycle/precipitation is very limited by comparison to the warm phase and do not play any significant role in the ice field position.

Within the lifetime of the liquid water lake, the ice field position evolution is completely controlled by the $\sim 4 \times 10^3$ (-10) years of the water cycle forced by the sublimation of the large body of non-stable ice.

Each year, during Northern summer, ~ 20 mm year^{-1} of lake ice sublimes to condense elsewhere and approximately 30 % of it is transported away from the lake. Progressively, the water vapor produced during the summers migrates southward and - through the mechanism of adiabatic cooling - condenses on the regions of high altitudes and low latitudes. The lifetime of the frozen lake predicted by our simulations is $\sim 7 \times 10^4$ martian years.

The evolution of the ice field through the phases that follow the outflow channel reference event are shown in Figure 5.16. After $\sim 10^5$ martian years, the outflow channel water is located more or less exclusively in the highland regions. During this cold phase ($\sim 10^5$ martian years), some ice appears stable in the region of West Echus Chasma Plateau, due to the uninterrupted supply of ice coming from the northern parts of the planet. This snow deposit is produced by the adiabatic cooling of the ascending air masses that provoke the condensation of the water vapor initially generated by the sublimation of the Northern Plains ice field.

Some water ice is also transported to the drainage regions of Alba Patera, Hecates Tholus and Ceraunius Tholus but this might not be a critical factor since our model already predicts that ice deposits should be stable in these regions (Wordsworth et al. 2013, Figure 2; this work) and therefore available for either seasonal snowmelt or ground melting.

In spite of this, because the global surface albedo is increased during that period, global temperatures are much lower than before the outflow event, making snowmelt difficult.

We note here that we did not take into account the flow of the ice on the Northern Plains slopes. This could significantly increase the lifetime of the lake located in the main topographical depression and thus the lifespan of the snow deposited in non-stable locations (in particular in West Echus Chasma Plateau area). However, at these temperatures and over these timescales, ice is unlikely to flow significantly (Fastook et al., 2012; Fastook and Head, 2014, 2015). In addition, we did not take into account the formation of a possible lag deposit (Kreslavsky and Head, 2002; Mouginot et al., 2012) which could have decreased the sublimation rate of the ice. Both of these factors, however, appear to have minimal effects on the general processes.

5.6.3.1 Influence of obliquity

Orbital spin-axis obliquity is a very important factor in the duration and the characteristics of the cold phase, because it controls the latitudinal distribution of the solar flux and thus the sublimation processes. We performed two simulations of the reference outflow channel event, at obliquities of 25 ° and 65 °, to complement the 45 ° obliquity case presented initially.

In the low obliquity simulation, the sublimated ice migrates slowly toward the coldest points of the planet: the South pole and the North pole (in agreement with Wordsworth et al. (2013), Figure 4). The water present in the northern part of the lake is stable in the long term. In this situation, ice

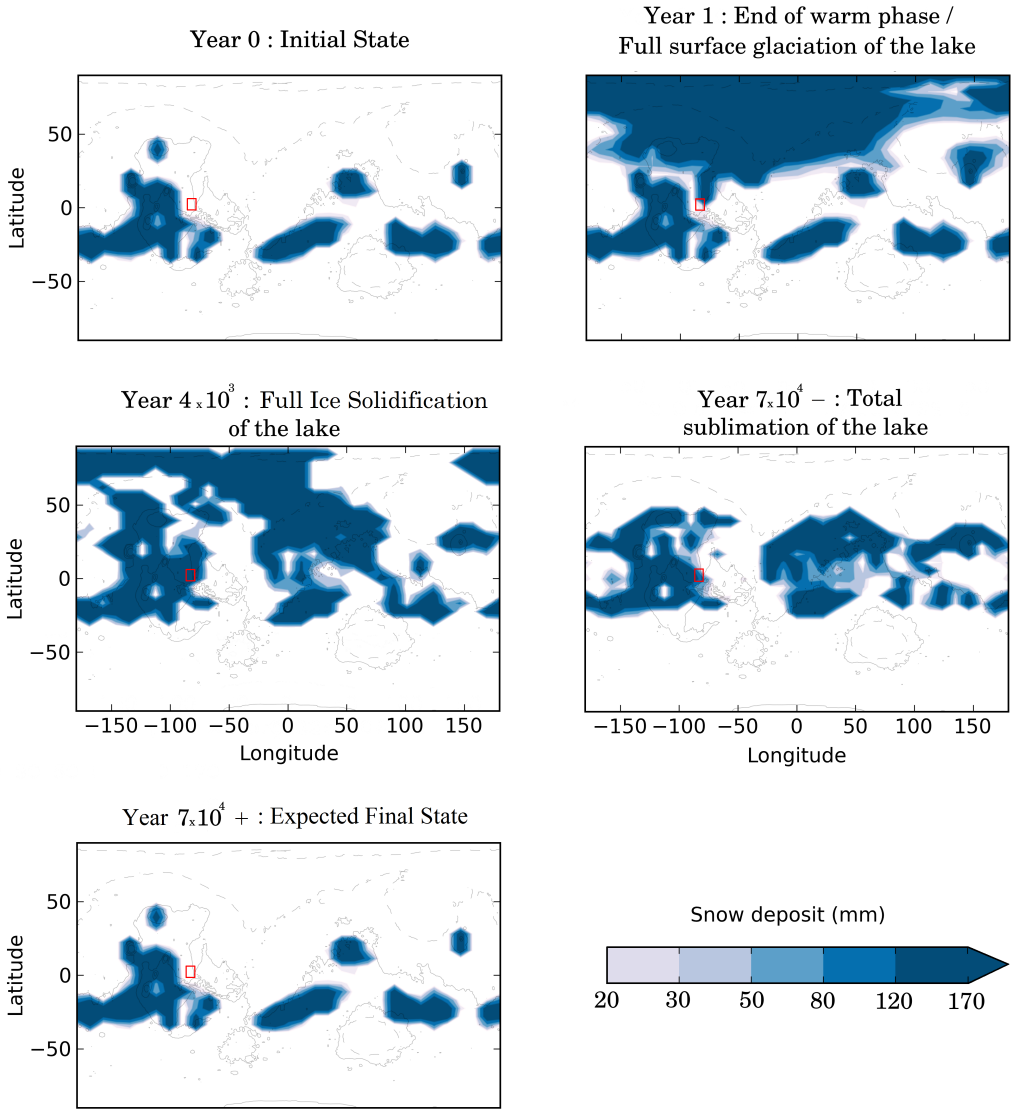

Figure 5.16: Ice deposit field after 0 / 1 / 4 × 10^3 / 7 × 10^4 martian years, corresponding to the main phases following the outflow channel reference event. The red rectangle corresponds to the West Echus Chasma Plateau area.

never accumulates in the region of West Echus Chasma.

In the high obliquity simulation, the water cycle is much more intense because the peak of insolation at high latitudes is higher. Approximately $\sim$ 55 mm of the sublimated northern lake ice migrates southward each year. The lifetime of the lake is thereby lowered to $\sim 9 \times 10^3$ martian years. For the same reasons as that in the reference simulation, a thick ice deposit is present in the region of West Echus Chasma Plateau. Yet, its duration, $\sim 10^4$ years, is almost 10 times less than in the reference simulation, more or less coincident with the lifetime of its supply (the frozen lake).

As a result, the lifetime of the ice located in West Echus Chasma area seems to be favored at obliquity $\sim$ 45 °.

5.7 The effect of surface pressure

For many reasons (see discussion in section 5.4.2), the atmospheric pressure during the Late Hesperian epoch is not well constrained. We explore in this section the role of surface pressure on the climatic impact of outflow channels.

For this, we performed five different simulations of the same outflow channel event (10^6 km^3, 300 K water released at 1 km^3 s^{-1} in Echus Chasma) for five different surface pressures (40 mbar, 80 mbar, 0.2 bar (the reference simulation), 0.5 bar and 1 bar).

5.7.1 Warm Phase

Atmospheric pressure is one of the key factors that control the efficiency at which the warming of the atmosphere and the transport of water occur during the warm phase, as pointed out by Kite et al. (2011a).

1. The evaporation rate: Combining equations 5.9 and 5.15 for low amounts of water vapor, the evaporation rate E can be written:

$$E = \frac{C_d V_1 P_{\rm ref} M_{\rm CO_2}}{R\, T_1}\, e^{\frac{L_{\rm v} M_{\rm H_2O}}{R}(\frac{1}{T_{\rm ref}}-\frac{1}{T_{\rm surf}})}. \tag{5.17}$$

Hence, the evaporation rate does not (directly) depend on the surface pressure and is mostly controlled by the temperature T_{surf} of the flow/lake. To first order (and this is confirmed by our simulations), the wind velocity V_1 and the atmospheric temperatures T_1 do not differ sufficiently from one atmospheric pressure to another to play a major role on the rate of evaporation.

2. The warming rate: The volumetric heat capacity of the atmosphere increases linearly with the volumetric mass density and thus the atmospheric pressure. For example, it takes approximately $\frac{1.0}{0.040} = 25 \times$ more energy to warm a 1 bar atmosphere than a 40 mbar one.

When the outflow channel event occurs, the rate of warming of the atmosphere (in K/s) is roughly proportional to the evaporation rate (which is the main source of heating) and inversely proportional to the volumetric heat capacity of the atmosphere. In our simulations, it takes $\sim$ 10/40 martian days - respectively for the 40 mbar/1 bar case - for the atmospheric temperatures at 10 km to reach a plateau at 250 K/220 K, which correspond to a +80 K/+30 K temperature increase (for initial temperatures equal to 170 K/190 K). This corresponds approximately to a factor of 10 in heating efficiency for these two endmember situations. The difference between the factor of 25 predicted and the factor of 10 obtained in our simulations is mostly due to two processes: advection and thermal emission to space.

The same two processes limit the growth of atmospheric temperatures. First, the advection tends to dilute the heat perturbation horizontally. In the 1 bar case, this is the dominant process for example. Second, the thermal emission to space acts as a very efficient negative feedback. This is, in fact, the first limiting process in the 40 mbar case.

The capability of an atmosphere to maintain high temperatures from the surface (where evaporation occurs) to the altitude where advection occurs is in fact the most important factor in the ability to transport water vapor globally and produce precipitation far from the region of evaporation. The warmer the atmospheric column above the lake is, the more water vapor will be possibly lifted and then transported globally by the high altitude winds.

Thin atmospheres (such as the 40 mbar) warm efficiently above the region of the flow, allowing the formation of a persistent water vapor plume that can transport (through advection) water vapor far from the flow/lake. In contrast, thick atmospheres (such as the 1 bar case) ironically do not manage to transport water efficiently because of the advection itself. The advection prevents the atmospheric temperatures above the lake from building up and thus the water vapor from accumulating. This limits the transport of water vapor and favors local precipitation. This is summarized by Figure 5.17 that shows the radial mean distribution (centered above the Northern Plains lake) of precipitation for the entire warm phase (first 500 days). Our experiments show that thin atmospheres are able to transport much more water and for much longer distances than thick ones.

We compare in Figure 5.18 the spatial distribution of the precipitation (only snowfall, because rainfall occurs only above the lake) for the different atmospheric pressures. Whatever the surface pressure considered, the precipitation stays confined to the Northern Plains.

Another important aspect concerns the role of atmospheric pressure on the ability to melt the ice initially present / transported by the outflow event itself. Thin atmospheres, while able to reach temperatures in excess of 273 K above the flow, are not able to raise global temperatures significantly. First, the relaxation timescale of the temperature field is very low in such atmospheres because of the weak infrared absorption of the atmosphere. Second, outflow channel events under thin atmospheres generate a very large ice cover that reflects sunlight efficiently. As a result, an outflow channel of 10^6 km^3 that occurs under a 40 mbar atmosphere, leaves globally $\sim 1.5 \times 10^4$ km^3 of water ice/snow (1.5%) and is able to melt only ~ 50 km^3 (0.005%).

Thick atmospheres are initially warmer than thin atmospheres (+ 30 K between the 1 bar and 40 mbar atmospheres). They also have a much more efficient infrared absorption and thus are better candidates to melt the deposited ice field. For example, an outflow channel of 10^6 km^3 that occurs under a 1 bar atmosphere, leaves globally $\sim 4 \times 10^3$ km^3 of water ice/snow (0.4%) and is able to melt ~ 110 km^3 (0.011%).

Nonetheless, this melting occurs only in the Northern Plains, in the close vicinity of the lake, because such thick atmospheres do not transport much ice anywhere on the planet in any case. In addition, ice albedo feedback (which is yet lower for thicker atmospheres) and the high volumetric heat capacity (lower heat perturbation) of such atmospheres contribute to lower the possibility of reaching melting temperatures.

Whatever the value of the surface pressure, the ability of the atmosphere to produce liquid water from melting is very limited.

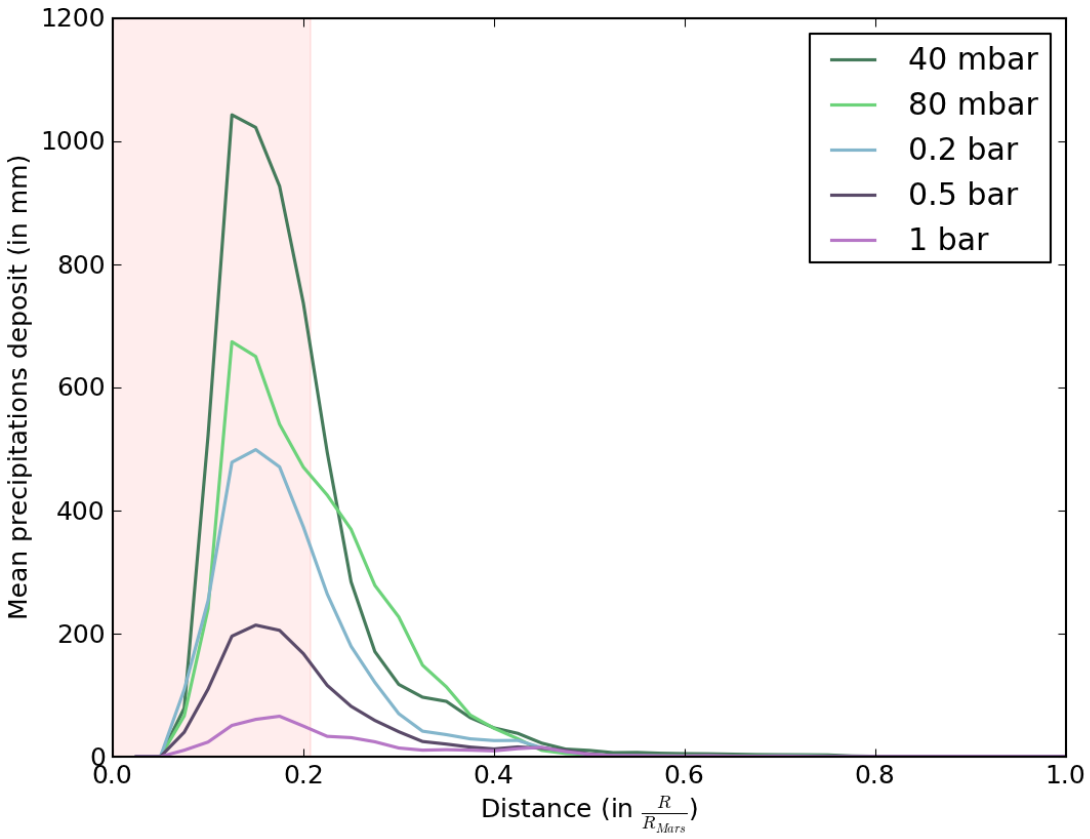

Figure 5.17: Radial precipitation distribution around the center of the lake (70°N,-30°E), averaged for the first 500 days following the outflow channel event, and for 5 different atmospheric pressures. The precipitation falling back on the lake/flow was removed from the plot. Because the lake is not circular, we used the pink color to represent the maximum radial extent of the lake.

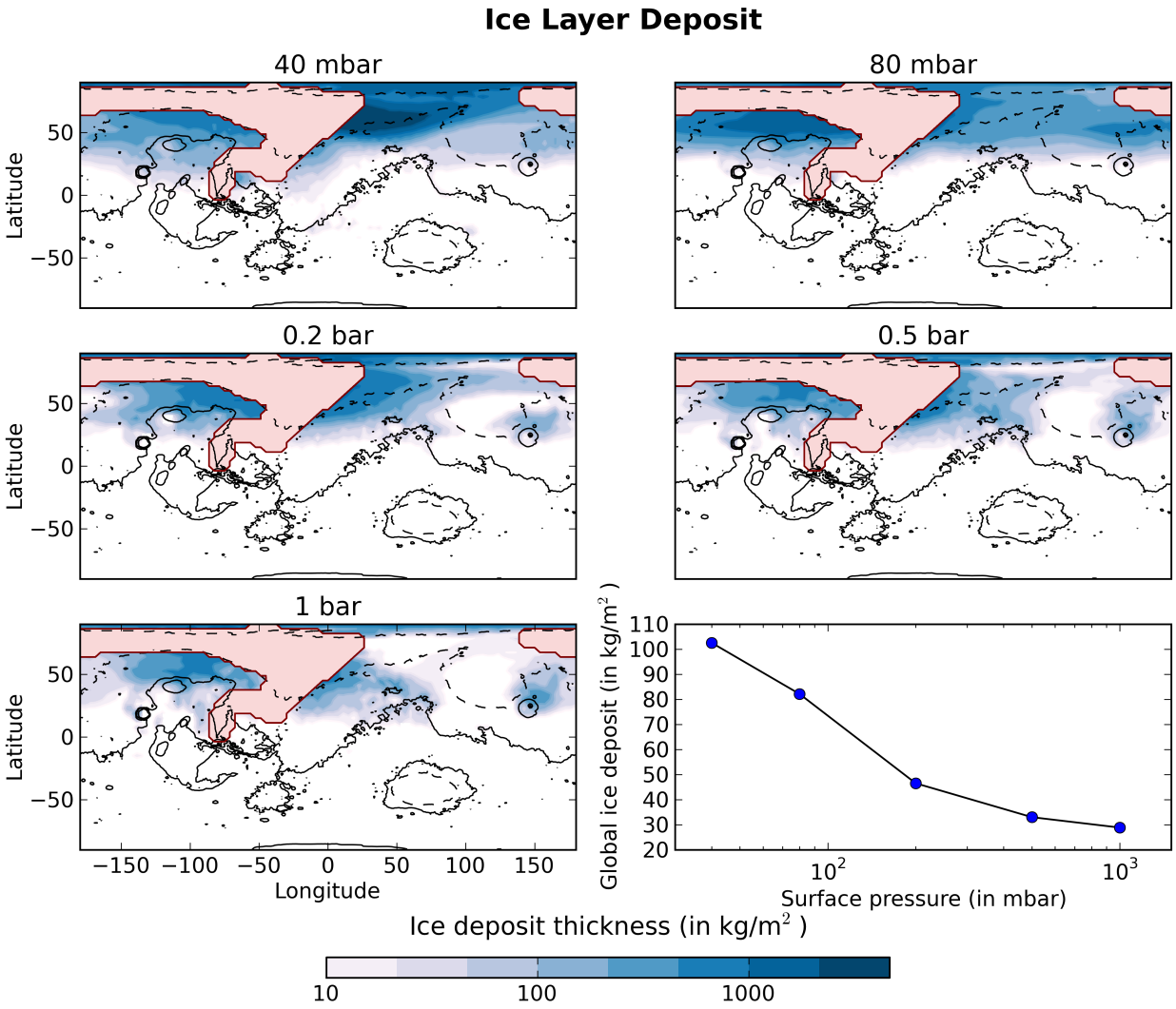

Figure 5.18: Final Ice layer deposit map (in kg m^{-2}) after 1 martian year of simulations, for five different surface pressures (40 mbar, 80 mbar, 0.2 bar, 0.5 bar and 1 bar). The pink color denotes the regions where the flow passed through on the way to the lake.

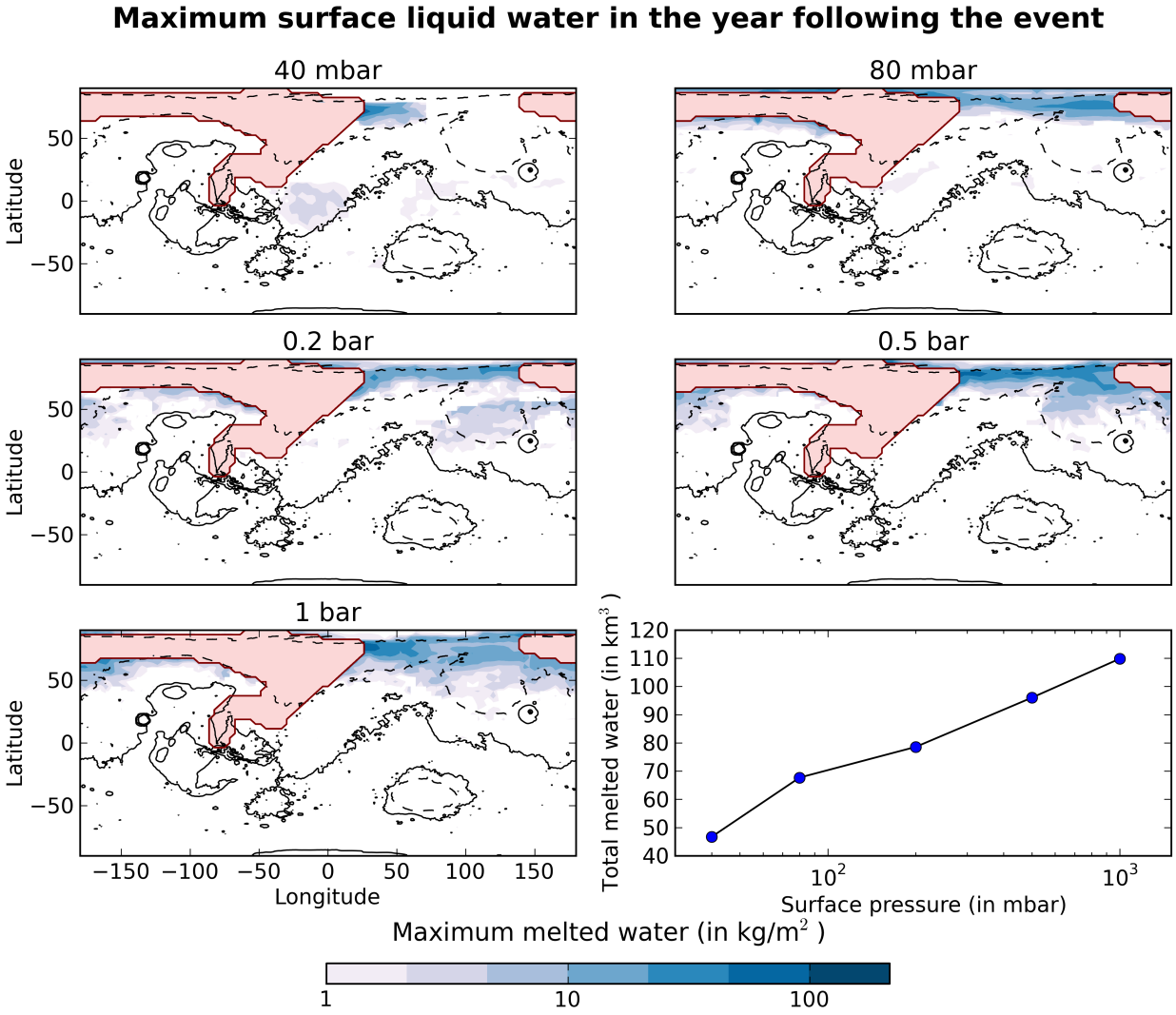

Figure 5.19: Maximum surface liquid water after 1 year of simulation and for five different surface pressures (40 mbar, 80 mbar, 0.2 bar, 0.5 bar and 1 bar). The pink color denotes the regions where the flow passed through on the way to the lake.

5.7.2 Cold Phase

The water cycle during the cold phase is, in contrast, more intense for thick atmospheres than for thin ones. The sublimations rates are higher because global temperatures (and also summer temperatures) are also higher. At the end of the warm phase, the mean global temperatures for the 40 mbar/1 bar simulations are respectively $\sim$ 193 K (3.5 K lower than the control simulation) and $\sim$ 226 K (1 K lower than the control simulation). This difference is due to the increased ice cover following the outflow event.

In the 1 bar simulation (thick case), the lifetime of the frozen lake is $\sim 5 \times 10^4$ martian years, slightly lower than in the reference simulation. The climatic response during the cold phase behaves more or less in the same manner as in the reference 0.2 bar simulation.

In the 40 mbar simulation (thin case) however, because the water cycle is too weak (sublimation rate of the lake of 2mm/year; lifetime of the frozen lake $\sim 2 \times 10^5$ years), the southward flux of the atmospheric water ice is not high enough to allow the presence of stable ice in the area of the West Echus Chasma Plateau.

More generally, atmospheres with pressure higher than 80 mbar seem necessary to produce ice deposits in the region of West Echus Chasma Plateau.

5.8 The intensity of the event

Because outflow channel formation events such as the one presented in Section 5.6 fail to produce rainfall/transient warming, it is tempting to explore even more extreme parameterizations of the outflow events. In this section, we study how the intensity of outflow channel formation events would affect their environmental effect.

5.8.1 Temperature of the flow

The temperature of the groundwater released during outflow events is not well constrained (see section 5.4.1.1). Hence, we used the temperature of the flow as a tuning parameter to explore the sensitivity of our results to the intensity of the outflow event. We performed three simulations of the same outflow event (10^6 km^3, released in Echus Chasma) for three different groundwater temperatures: 280 K, 300 K (reference simulation) and 320 K.

As expected, the warmer the water, the more intense the climatic effect becomes. For example, at the peak of the warm phase, the 320 K event is able to carry approximately 8 $\times$ more water vapor than in the reference simulation because atmospheric warming processes are amplified by the temperature (evaporation/condensation cycle, IR emission of the flow, ...). Consequently, 25 % of the precipitation following the 320 K event is rainfall (respectively 10 %/ 0 % for the reference/280 K simulations). Yet, rainfall still occurs exclusively above the lake (70 %) or in the northern lowlands of Mars (30 %). Snow precipitation also remains confined to the Northern Plains down to 15 °N (25/40 °N for the 300 K/280 K simulations).

The amount of water ice transported (Figure 5.20) and melted (Figure 5.21) after outflow channel events with 280 K/300 K/320 K water shows that in all cases, the mechanism of advection/cooling to space is very efficient, and as a result, the duration of the warm phase is approximately the same ($\sim$ 500 days) between the reference and the 320 K simulations.

We note that, at the end of the warm phase, because the amount of ice transported (and the area of the deposit with it) increases with the initial temperature of the flow, the average surface albedo raises and the mean temperatures decrease: Warmer flows lead to colder states.

5.8.2 Magnitude of the event: from small outflows to oceans.

Recent work (Andrews-Hanna and Phillips, 2007; Harrison and Grimm, 2008) has suggested that outflow channels were preferentially carved by multiple events of reduced sizes ($\sim 10^3$ km^3) rather than by large ($> 10^5$ km^3) single outflows. We performed simulations for different volumes of water at 300 K and released in Echus Chasma at a rate of 1 km^3 s^{-1}, from 10^3 km^3 (consistent with the most recent estimations of outflow volumes) to 10^7 km^3 (ocean case). Figure 5.22 shows the final position of the lake as a function of the initial volume of water. The 10^6 km^3 case is the reference simulation.

Our results show that the large outflows, during the warm phase, transport much more water than the small ones (cumulative). Small outflows (typically $\sim 10^3$-10^4 km^3) have a small wetted area (typically 0.15-0.41 $\times$ 10^6 km^3) and a small initial heat reservoir, so that they cannot warm the atmospheric column above the flow/lake sufficiently to transport water vapor into the neighbouring regions. Small outflow events inject more or less the same amount of water vapor (in proportion) than large ones, but they are not able to transport it far from the flow/lake. For example, 2 $\times$ 10^2 events of 5 $\times$ 10^3 km^3 transport 2 orders of magnitude less ice outside the flow/lake than a large 10^6 km^3 one (reference simulation). Moreover, large outflows are able to generate precipitation up to $\sim$ 5000 km from the edge of the flow/lake whereas small ones cannot produce any precipitation at a distance greater than $\sim$ 400 km (typically the size of 2 GCM grids).

We did not explore in detail the effect of the discharge rate, which has a net impact on the size and duration of the wetted area (and thus on the evaporation and the albedo), but also on the intensity of the event. Nonetheless, the climatic response to lower discharge rate events ($< 10^9$ m^3 s^{-1}) was found to be lower, because in such cases the temperatures and the amount of water vapor struggle to build up above the flow/lake.

Because large outflows seem to be much better candidates for generating precipitation globally, we examined the extreme case of a catastrophic outflow event of 10^7 km ^{3} released simultaneously by all of the circum-Chryse outflow channels (Kasei, Ares, Tiu, Simu Vallis, etc.). This possibility, sometimes called the MEGAOUTFLO (Mars Episodic Glacial Atmospheric Oceanic Upwelling by Thermotectonic Flood Outburst) hypothesis (Baker et al., 1999), speculates that such events could warm Mars during periods of 10^4-10^5 years through a transient greenhouse effect provoked in part by the injection of large amounts of water vapor.

Our experiments show that such events cannot sustain long-term greenhouse effects, whatever the size and the temperatures considered for the northern lake/see/ocean. After 3.5 martian years, for the outflow event described above, the surface of the lake/see/ocean becomes totally frozen. The thermal infrared emission to space (enhanced by the heat horizontal advection and by the water vapor advection that release latent heat because of adiabatic cooling; see Figure 5.23 for the detailed mechanism) acts very efficiently to cool the planet. The ice deposited on the Northern Plains slopes (Figure 5.20) also enhances the cooling through a depletion of surface solar absorption. As a result, in such a scenario, rainfall/snowmelt still only occurs in the lowest northern lowlands (see Figure 5.21) of the planet (far from the region of interests).

In summary, the most intense outflow channel events possible are not able to sustain a global

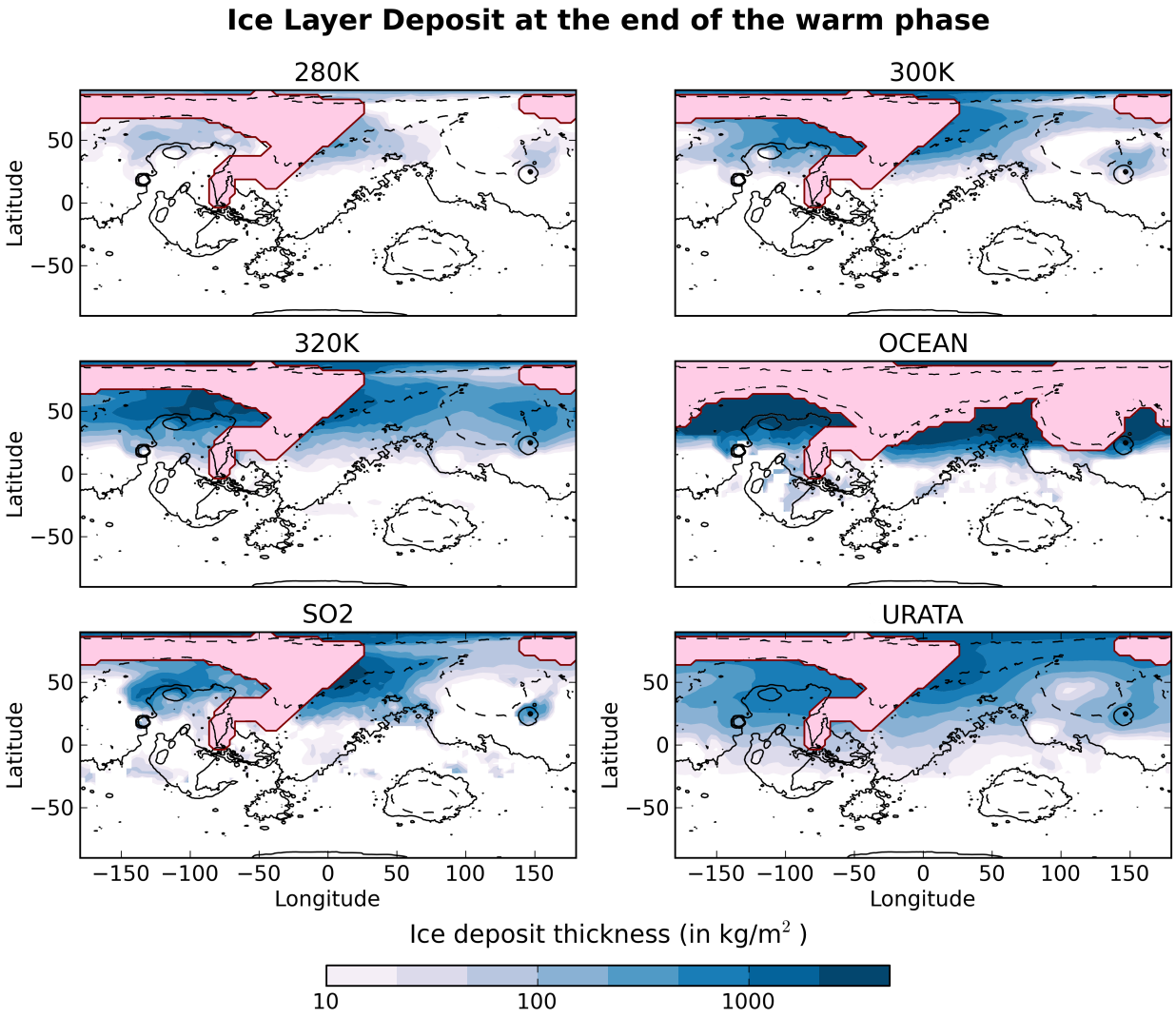

Figure 5.20: Final Ice layer deposit map (in kg m^{-2}) after 1 martian year of simulations (4 martian years for the ocean case), for six different simulations: 1. 280 K outflow, 2. 300 K outflow (reference case), 3. 320 K outflow, 4. 10^7 km^3 ocean case, 5. 1 % SO_2 case and 6. l_0=∞ (no precipitation case). The pink color denotes the regions where the flow passed through on the way to the lake.

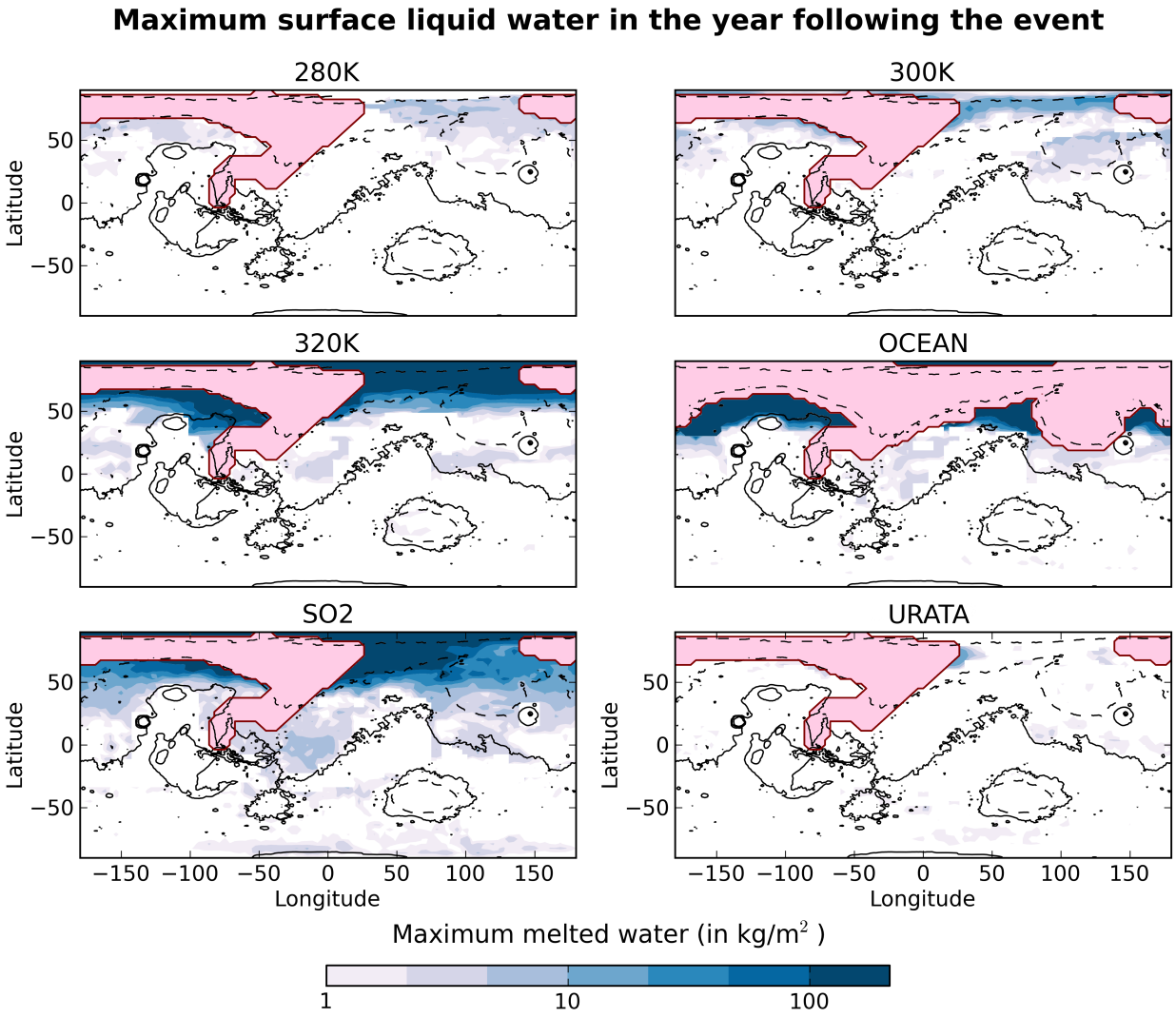

Figure 5.21: Maximum surface melted liquid water after 1 year of simulation (4 martian years for the ocean case) and for 6 different simulations: 1. 280 K outflow, 2. 300 K outflow (reference case), 3. 320 K outflow, 4. 10^7 km^3 ocean case, 5. 1 % SO_2 case and 6. $l_0=\infty$ (no precipitation case). The pink color denotes the regions where the flow passed through on the way to the lake.

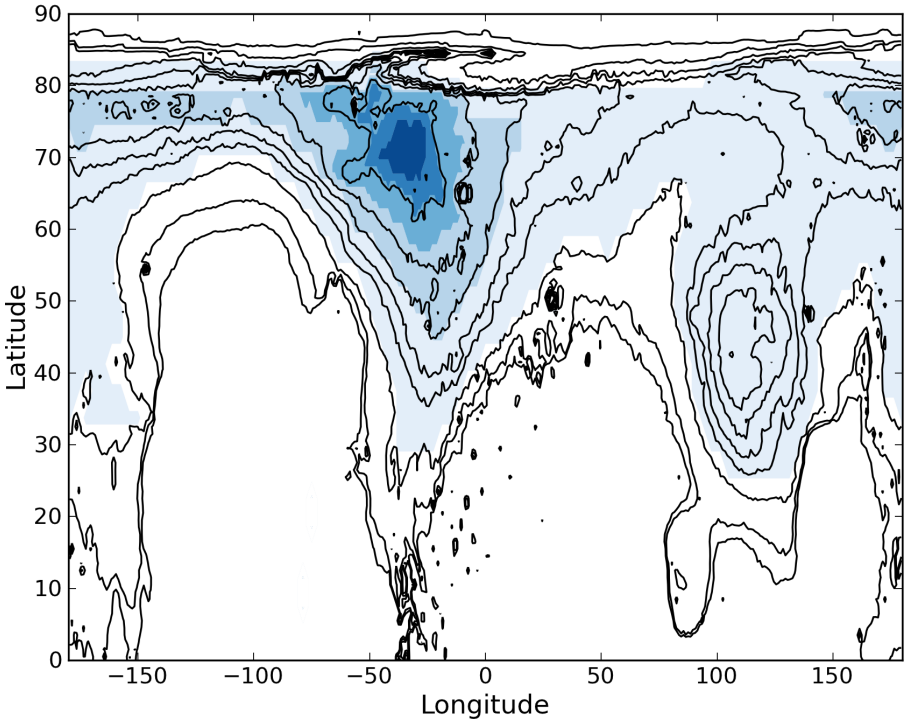

Figure 5.22: Stable water lake size obtained in our simulations depending on the volume of water released. Contour fills are for volumes of 10^3,10^4,10^5,10^6 (reference case) and 10^7 km^3 (ocean case). These correspond respectively to wetted areas of 0.15,0.41,1.19,4.15 and 20.4 millions of km^2.

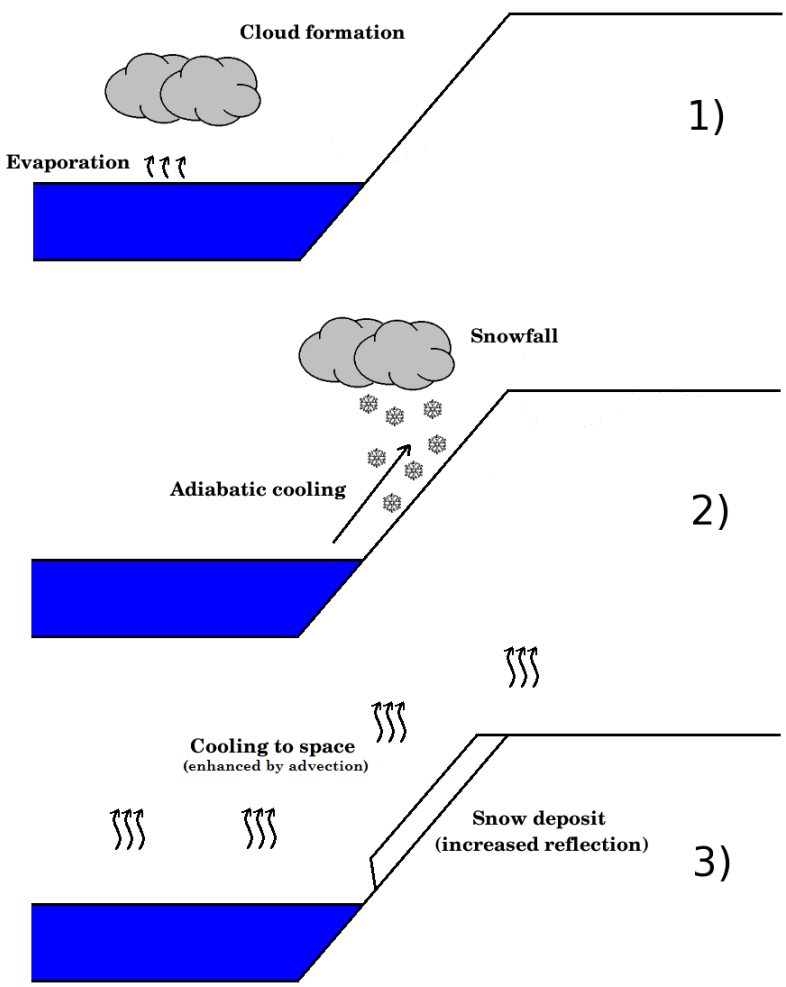

Figure 5.23: Why is a martian Northern ocean short-lived and unable to induce rain? The water vapor and the clouds that build up above the ocean (1) are advected southward (2). Because of adiabatic cooling, snowfall occurs from the edges of the ocean (starting from 70 °N, see Figure 5.22) to the highest parts of the planet (the 'Icy Highlands'). The advection of heat (increasing the surface of thermal infrared emission) and the increase of reflection (because of the snow deposit) both contribute to an intense cooling of the ocean and to reduced precipitation.

greenhouse warming. Such events only manage to warm up the atmosphere regionally, in the Northern Plains, and only for a few years at best. Consequently, rainfall (and snowmelt) occur only in the neighbourhood regions of the final stable lake. After complete surface freezing of the lake, the climate becomes much colder than initially (due to the increase of the surface albedo), making the snowmelt even more difficult.

We note that we did not take into account the modification of the topography by the presence of a lake/see/ocean, which might be a concern for very high volumes of water ($\geq 10^7$ km^3). It could reduce significantly the role of adiabatic cooling and thus favor the transport/deposit of water further south.

5.9 Discussion

5.9.1 Role of the atmospheric composition.

In this analysis, we made the assumption that the Late Hesperian martian atmosphere was made of 100% CO_2 (and some water vapor). Outflow channel events under a CO_2 dominated atmosphere seem not to be able to provoke long-term warming or precipitation at the global scale.

Ouflow channel formation events are very likely related to intense volcanic episodes during martian history (Baker et al., 1991; Head et al., 2002). During these periods, it is believed that volcanic gases like SO_2 may have been massively released [see section 1. of Kerber et al. (2015) for more details].

We performed a simulation of an outflow channel event under the same conditions as in section 5.6, but this time with 1 % of SO_2. Figures 5.20 and 5.21 show the corresponding amount of water ice transported/melted after the event. Small amounts of SO_2 (2 mbar here) are sufficient to raise the global atmospheric temperatures by several tens of Kelvins and thus to favor the transport of water vapor/water ice globally and create precipitation far from the Northern Plains stable lake.

However, using the same GCM, Kerber et al. (2015) (and earlier, Tian et al. 2010) have shown that massive volcanic SO_2 outgassing cannot lead to a global and substantial warming, because sulfur aerosols that would form at the same time have a very strong cooling effect, even in small amounts.

We also believe that, under more realistic parameterizations that would take into account sulfur aerosols (e.g. Halevy and Head 2014), the outflow channel climatic impact would be also very limited.

5.9.2 The role of clouds and precipitation.

The radiative effect of clouds is one of the main sources of uncertainty in GCMs and thus also on the consistency of our results.

In particular, it has been suggested (Urata and Toon, 2013) that high altitude ('cirrus-like') water ice clouds may trigger warm climates on Mars even under a faint young sun. This scenario requires four assumptions: 1) Water ice particles that have sizes > 10 microns; 2) that the rate of precipitation is very low (in order to extend the lifetime of the clouds); 3) When present, clouds need to completely cover a grid cell (no partial cloud cover); 4) Lastly, it also requires an initial 'warm' state, for example an outflow channel event.

To explore in a basic manner the role of clouds and precipitation on the climatic impact of outflow channels, we performed a simulation of the reference outflow channel event in which we eliminated the precipitation resulting from coalescence ($l_0=\infty$). For this case, the vertical motion of the ice particles

is governed only by gravitational sedimentation. Figure 5.13 shows that the total cloud cover is near 100% over all the planet during the first year following the event, because of the intense evaporation coupled with the increased lifetime of clouds.

We found that neglecting coalescence and the subsequent precipitation led to ice deposits that extend much more areally than in the reference case (Figure 5.20), because the lifetime of ice particles increases substantially. In such a situation, the global cloud cover (during the year following the event) has a net positive radiative impact on the global energy balance of + 12 W m^{-2} (+ 21.3 W m^{-2} of IR warming; - 9.2 W m^{-2} of solar absorption). This is ∼+ 11 W m^{-2} higher than in the reference simulation.

However, because the ice field produced by the event extends to a much larger area, the global albedo increases and contributes approximately 6 W m^{-2} of cooling. Moreover, because of advection processes, this also increases the horizontal extent of the heat perturbation and thereby the global infrared emission to space. Under clear sky conditions, this would lead to an extra cooling of ∼ 5 W m^{-2} compared to the reference simulation.

As a consequence, the total rate of cooling is more or less the same (∼ 15 W m^{-2}) as that in the reference simulation (l_0=0.001). The duration of the warm phase is also more or less the same than in the reference simulation (∼ 500 days).

We also note that the seasonal melting of the deposited ice (see Figure 5.21) would be very limited in such scenarios, because of the increased solar reflection by the clouds. In addition, because the ice field produced by the event extends over a large region (Figure 5.20), the planet becomes much colder one year after the event than initially.

Nonetheless, we highly encourage further studies to explore in more detail the possibility of warming early Mars through water ice clouds (as recently done by Ramirez and Kasting (2017)).

5.9.3 Conclusions

In this analysis, we explored the climatic impact of a wide range of outflow channel events under many possible conditions.

We find that even considering outflow events with intensity (in volumes and temperatures of water released) that exceed by far the most recent estimates, the short term climatic response is still very limited. The duration of the 'warm' phase that follows the outflow events is completely controlled by the total depth and temperature of the lake that is formed and is, in practice, no more than a few years for the most extreme cases (10^7 km^3 of water warmed at 300 K, e.g. ocean case). In other words, outflow events fail to trigger greenhouse-sustained warm episodes. Moreover, the precipitation (almost exclusively snowfall) produced by the events during their warm phase is limited and confined to the Northern Plains, in the area neighbouring the water outflow. These results are robust over a wide range of atmospheric pressures and external conditions (e.g. obliquity and season).

We also find that the intensity of outflow channel event effects can be significantly influenced by the atmospheric pressure which is not well constrained for the Hesperian era. Thin atmospheres (P < 80 mbar), because of their low volumetric heat capacity, can be warmed efficiently. This can trigger the formation of a convective plume, a very efficient mechanism to transport water vapor and ice to the global scale. Thick atmospheres (P > 0.5 bar) have difficulty in producing precipitation far from the outflow water locations but they are more suited to generate snowmelt. Nonetheless, outflow channel formation events are unable, whatever the atmospheric pressure, to produce rainfall

or significant snowmelt at latitudes below 40°N.

During the 'cold phase' that follows the solidification to ice of the outflow water, the body of water ice emplaced in the Northern Plains has a major contribution to the water cycle. The ice is sublimated seasonally and transported progressively southward toward the 'Icy Highlands' regions by the processus of adiabatic cooling. We find that under favorable conditions (obliquity $\sim 45°$, atmospheric pressure $\geqslant 80$ mbar), ice deposits can be stabilized in the West Echus Chasma Plateau area. For an initial 10^6 km^3 body of water (0.2 bar atmospheric pressure, 45° obliquity), they can be present during 10^5 martian years. However, seasonal melting related to solar forcing seems difficult because 1) the West Echus Chasma Plateau is not ideally located, and 2) the presence of (high albedo) snow at the surface has a significant cooling effect. The global temperatures after outflow events can thus easily be lowered by a few Kelvins making the solar melting possibility even more difficult. Therefore, in this scenario, localized warming such as geothermal activity or meteoritic impacts would be required to explain the formation of valley networks dated to the Late Hesperian era and yet observed at this specific location.

Chapter 6

The paradoxes of the Late Hesperian Mars ocean

Contents

6.1 Preamble

Despite the apparent difficulty of keeping an ocean of liquid water on Mars, there are a number of intriguing elements that suggest that there could have been oceans on Mars at several distinct epochs.

In 2016, Alexis Rodriguez and his colleagues published a paper in which they reported various pieces of evidence for tsunami events on Mars (Rodriguez et al., 2016). These tsunami events date from the Late Hesperian era, and are thought to be contemporaneous to the outflow channel formation events discussed in the previous Chapter. Rodriguez et al. (2016) and Costard et al. (2017) advocated that these tsunamis were produced by impacts of large meteorites on an ice-free ocean present in the northern lowlands of Mars. Their conclusion is important because it suggests that Mars would have hosted a large body of liquid water hundreds of millions of years later than the formation of most of the valley networks.

This topic has been the subject of a lot of excitement and intense discussions during the 4th Conference on early Mars (held on October 2-6 2017) that I attended.

The present Chapter presents a list of arguments that undermine the existence of a Late Hesperian ocean, partly based on the results of the previous Chapter, and partly based on the results of new numerical climate simulations incorporating the effect of additional strong greenhouse gases.

This chapter is based on a paper submitted to Nature Geoscience Perspectives in June 2017. The full reference is: Martin Turbet & Francois Forget, **The paradoxes of the Late Hesperian Mars ocean**, submitted to Nature Geoscience Perspectives, 2018.

6.2 Introduction

The long-standing debate on the existence of ancient oceans on Mars (Parker et al., 1989; Baker et al., 1991; Malin and Edgett, 1999; Carr and Head, 2003; Perron et al., 2007; Head et al., 2018) has been recently revived by evidence for tsunami resurfacing events that date from the Late Hesperian geological era (Rodriguez et al., 2016; Costard et al., 2017). It has been argued that these tsunami events originated from the impact of large meteorites on a deglaciated or nearly deglaciated ocean present in the northern hemisphere of Mars (Rodriguez et al., 2016; Costard et al., 2017). Here we show that the presence of such an ocean would imply an extreme Hesperian Mars climate and that it should have produced extensive erosion that is not observed on Hesperian Mars terrains. We suggest that these tsunami events could have been produced instead by the formation of catastrophic outflow channels that occured in the same region and at the same epoch, by a series of meteoritical impacts, or in response to impact-triggered waves in a thin ocean covered by a km-thick ice layer.

The existence of liquid water oceans on ancient Mars has long been a topic of debate (Parker et al., 1989; Baker et al., 1991; Malin and Edgett, 1999; Carr and Head, 2003; Perron et al., 2007; Head et al., 2018) and has strong implications for the search for life in the solar system. Backwash channels and water-ice-rich and bouldery lobes observed on the circum-Chryse and northwestern Arabia Terra regions of the northern plains have been interpreted as evidence for tsunami events that date from the Late Hesperian era (Rodriguez et al., 2016; Costard et al., 2017). It has been reported that these events were likely caused by the collision of large meteorites (3-6 km in diameter) on an ice-free or sea-ice covered ocean located in the northern lowlands of Mars (Rodriguez et al., 2016; Costard et al., 2017). Therefore, Mars could have hosted a large body of liquid water hundreds of millions of years later than the formation of the valley networks. Below we discuss the implications of the presence of a deglaciated (or nearly deglaciated) ocean on both the atmosphere and the geology of Late Hesperian Mars.

6.3 The paradoxes of a cold ocean

Sustaining a liquid-water ocean, even ice-covered, would require a very strong greenhouse effect involving a mixture of greenhouse gases. 3-D climate modeling of early Mars under an atmosphere composition of only CO_2 and H_2O, performed with a water cycle that includes water vapor and clouds, is unable to maintain significant amount of liquid water anywhere on the red planet, even when maximizing the greenhouse effect of H_2O and CO_2 ice clouds (Forget et al., 2013; Wordsworth et al., 2013). This major result holds independently of the specific CO_2 atmospheric content, water content and obliquity. More specifically, an initially warm northern ocean possibly fed by outflow channel formation events should freeze extremely rapidly under a Late Hesperian Mars CO_2 atmosphere (Kreslavsky and Head, 2002; Turbet et al., 2017a). For instance, a 30°C, 200m deep ocean (under a 0.2 bar CO_2 atmosphere, at 45° obliquity) would become entirely ice-covered after $\sim$ 1 martian year, and frozen solid after $\sim 4\times10^3$ martian years (Turbet et al., 2017a). More generally, a northern plains ocean would completely freeze within 10^4 years, whatever the obliquity, surface pressure of CO_2, and whatever the initial size and temperature of the ocean assumed (Turbet et al., 2017a). The freezing process is particularly efficient at low obliquity (because of the low insolation at the North Pole) and low CO_2 atmospheric pressure (because of the small greenhouse effect of CO_2). At high obliquity and high CO_2 surface pressures, the poles are warmer, but still too cold to sustain a liquid water ocean

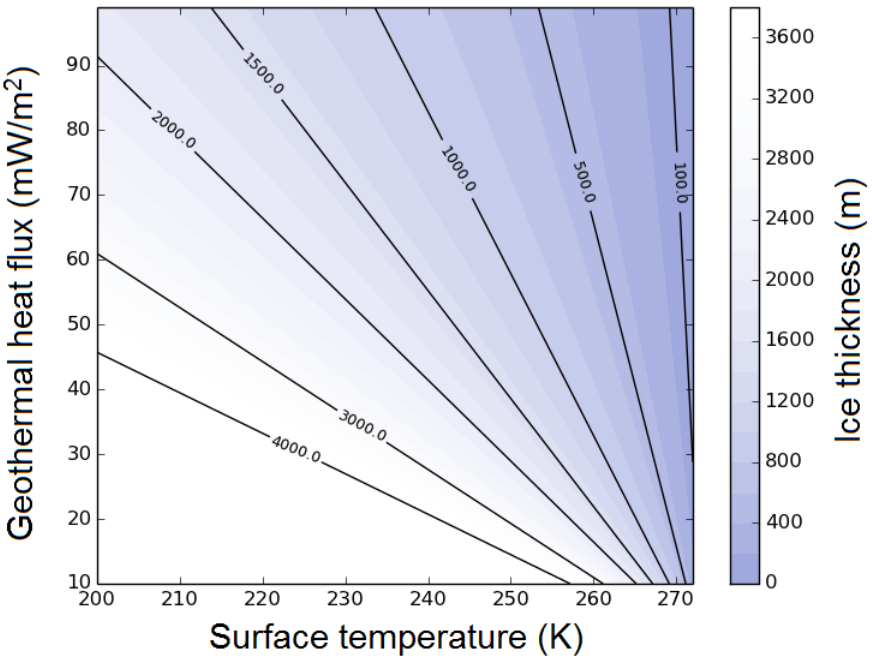

Figure 6.1: Minimum ice thickness covering the ocean calculated as a function of the temperature at the top of the sea ice cover and of the geothermal heat flux.

(even with ice cover) (Turbet et al., 2017a).

To avoid the need of additional hypothetical greenhouse gases (see below), it is tempting to speculate that the ocean could have remained liquid below a protective ice layer, thanks to a strong geothermal heat flux. We calculated the minimum ice thickness (see Methods) required to sustain subsurface liquid water, as shown in Fig. 6.1. Even for a geothermal heat flux of 80 mW m^{-2} (which is an upper limit on the geothermal heat flux expected during the Late Hesperian era, and for volcanically active regions (Ruiz et al., 2011)), we found that the ice thickness grows very rapidly as the surface temperature drops below freezing. The range of conditions that would have allowed a long-term ice-covered ocean is very narrow: for instance, to limit the growth of the ice thickness to 100 m or less, the annual mean surface temperature must range between 270 and 273 K. As a comparison, the minimum ice thickness is $\sim$ 1 km for an annual mean surface temperature of 240 K (see Fig. 6.1) which corresponds to the maximum annual mean temperature predicted in the northern lowlands by 3-D numerical climate models (Wordsworth et al., 2013; Turbet et al., 2017a).

Even with a frozen surface, a Northern ocean on Mars would have been unstable on geological timescales. If one assumes that a water ocean is formed during a short period of time (e.g. by catastrophic outflows) and then left on its own, calculations show that it would have eventually disappeared after $\sim 10^5$ martian years because the water would have been progressively transported toward the elevated regions of Mars through sublimation and subsequent adiabatic cooling and condensation (Wordsworth et al., 2013; Turbet et al., 2017a). Only a thick lag deposit of silicate material (Carr, 1990) formed on a permanently frozen surface could have prevented the water from getting sublimated

and migrating away to the elevated terrains of Mars. However, even then, it seems almost unavoidable that the ocean would have frozen down to its bottom.

6.4 The paradoxes of a warm ocean

Alternatively, we could imagine that for some time the Late Hesperian Martian climate was sufficiently warmed by additional strong greenhouse gases, and thus keeping the ocean at least partly liquid. For instance, reducing gases (e.g. CH_4 and H_2) offer a way to warm the surface of ancient Mars above the melting point of water (Ramirez et al., 2014a; Wordsworth et al., 2017; Kite et al., 2017a,b; Ramirez and Kasting, 2017). This effect results in part from the strong collision-induced absorptions of CO_2-CH_4, CO_2-H_2 and H_2-H_2 pairs (Ramirez et al., 2014a; Wordsworth et al., 2017; Turbet et al., 2018b).

However, the persistence of a deglaciated ocean during the Late Hesperian on Mars would raise several issues. New 3-D Global Climate simulations (see Methods) confirm that a deglaciated northern ocean could be sustained with the assumption of enough greenhouse gases (CO_2 and H_2 here). However, the water would migrate rapidly toward the elevated Martian terrains through the mechanism of adiabatic cooling mentioned above for the case of a frozen ocean. This process is rapid because evaporation and sublimation rates increase exponentially with temperature. In the simulations, a part of the atmospheric water returns to the surface as rain, near the ocean shoreline (see Fig. 6.2a). Such precipitation would produce extensive coastal erosion, in particular in the regions where evidence for tsunami events have been reported (Rodriguez et al., 2016; Costard et al., 2017). The remainder is sequestered as ice on the elevated terrains. In any case, for the northern ocean to survive, an intense hydrological cycle had to occur in order to replenish the water that was transported to the elevated terrains. This is problematic because we do not see any clear indication of such a strong hydrological cycle during the Hesperian geological record.

To solve this paradox, one hypothesis could be for the ocean to be replenished by groundwater. In this scenario, water that condensed on the elevated Martian volcanic regions would have formed thick glaciers that would undergo melting at their base, possibly introducing the meltwater into subsurface aquifers (Clifford and Parker, 2001). These subsurface liquid water reservoirs could then have provided the water that carved the outflow channels, thus replenishing the northern ocean. Such an hypothesis would be consistent with our 3-D Global Climate simulations (see Fig. 6.2b) in which water tends to condense preferentially close to the regions that sourced the outflow channels. However it is difficult to reconcile this hypothesis with the estimated lifetime of the ocean. It has been reported that at least two large tsunami events were produced by bolide impacts, resulting in craters 30-50 km in diameter (Rodriguez et al., 2016; Costard et al., 2017). Based on the crater frequency rates of Rodriguez (Rodriguez et al., 2016) and the suspected location of the ancient Late Hesperian ocean of Costard (Costard et al., 2017), we estimate that the rate of Late Hesperian marine impacts producing craters ~30 km in diameter is one every 4 million years. Unless the tsunami was the result of very unlikely occurences, the ancient ocean would have to survive for a period of at least a few million years to produce the reported tsunami events (Rodriguez et al., 2016; Costard et al., 2017). We estimate from our 3-D Global Climate simulations (see Fig. 6.2b) that the net evaporation rate of the ocean is at least 0.6 m per martian year, and that least 10^4 km^3 of water would be required for replenishment per martian year in order for the ocean to remain stable. Thus, as much as 2×10^{10} km^3 (e.g. $\sim$ 100 km

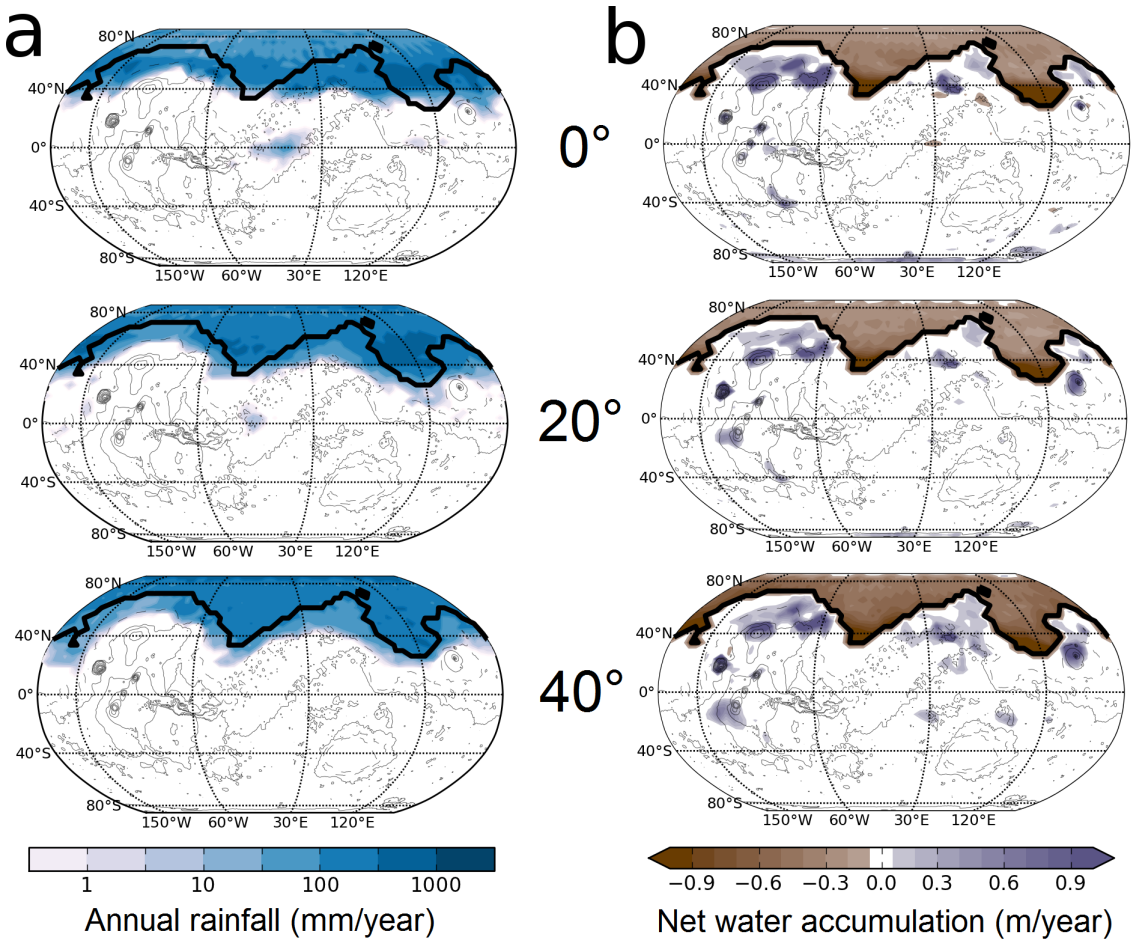

Figure 6.2: Annual cumulated rainfall (left pannel) and annual net surface accumulation of water (right pannel). These figures are based on the results of 3-D Global Climate simulations with a thick CO_2 atmosphere and H_2, with a permanent deglaciated ocean (indicated by the black line ; the location of the ocean is consistent with previous estimate (Costard et al., 2017)), and at three different obliquities (0, 20 and 40°). We used the present-day Mars MOLA topography, indicated by grey contour lines.

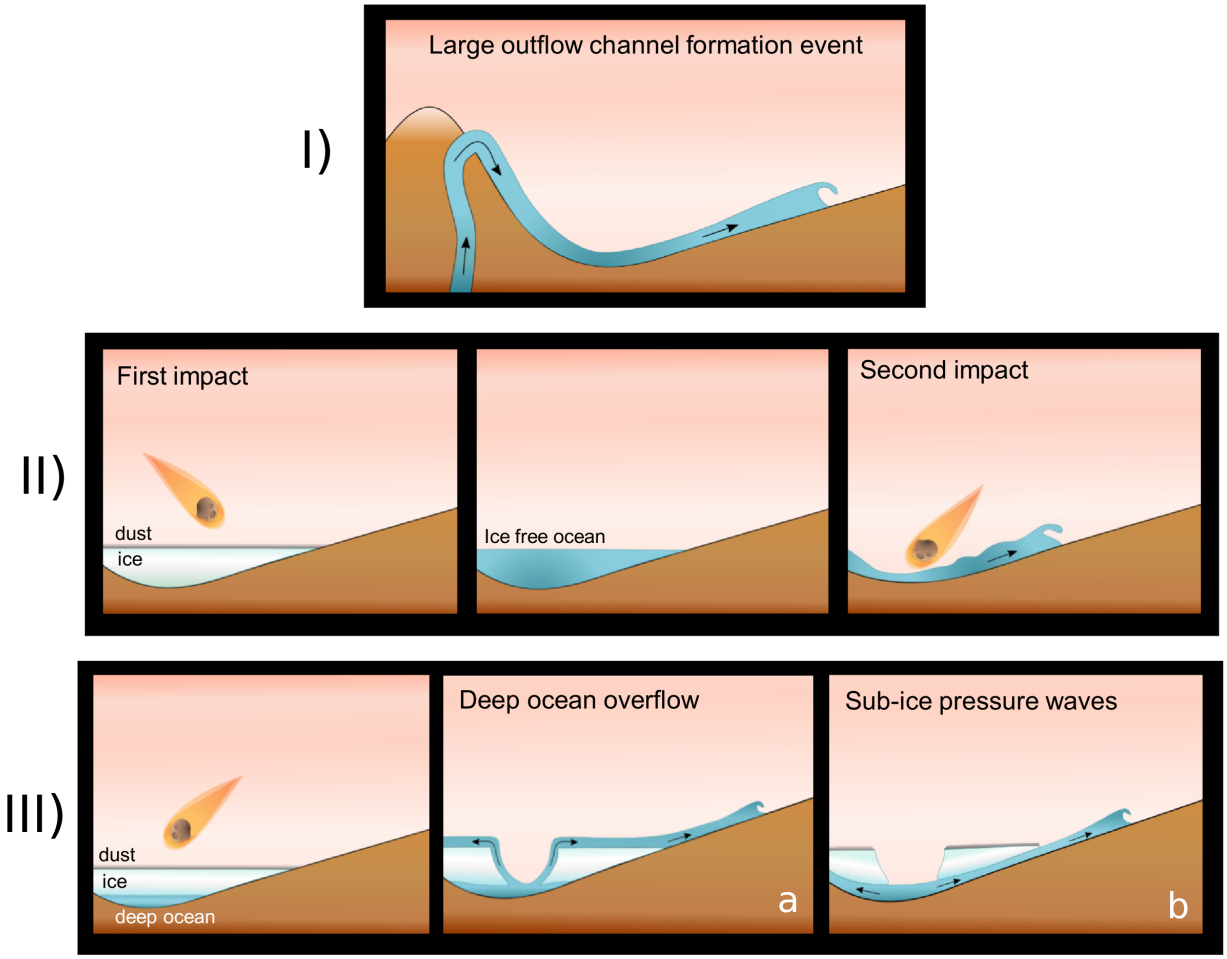

Figure 6.3: Schematic views of the proposed tsunami event scenarios. Credit: N. Chaniaud.

GEL) of water would need to have flown through the outflow channels for a deglaciated northern ocean to survive for 4 million years. This amount is several orders of magnitude larger than previous estimates of the total amount of water required to erode all the Martian outflow channels (Carr and Head, 2015).

6.5 Alternative solutions

Several scenarios could potentially reconcile the tsunami evidence (Rodriguez et al., 2016; Costard et al., 2017) with the geological records and our understanding of the Martian climate.

In one class of scenarios, the ocean existed but it was fully (or almost fully) glaciated, and potentially protected by a lag deposit. Tsunami events could have been produced in response to consecutive meteoritic impacts, for instance resulting from a collision with the different pieces of a broken body like the Shoemaker-Levy 9 comet which hitted Jupiter in July 1994 (Asphaug and Benz, 1996). The first impact would deglaciate the ocean, and the following impacts could then produce the tsunami

(Fig. 6.3, scenario II).

Tsunami events could also be produced in response to impact-triggered pressure waves propagating in a thin, deep subsurface ocean located below a km-thick cover of ice (Alexis Rodriguez, personal communication ; Fig. 6.3, scenario IIIb). The same impact could also expel liquid water from the deep ocean, that would then form a huge flow on top of the ice cover (Fig. 6.3, scenario IIIa). In principle, this scenario is compatible with the minimum ice cover thickness of $\sim$ 1 km (calculated above for the maximum annual mean temperature predicted in the northern lowlands by 3-D Global Climate models (Wordsworth et al., 2013; Turbet et al., 2017a)) and the maximum depth of the hypothetic ocean (Costard et al., 2017) estimated at $\sim$1.4 km.

In a second class of scenarios, there is no perennial ocean. Instead, the tsunami events could have been produced by the catastrophic outflow channel formation events that occurred in the same region and at the same epoch. The sudden release of extremely large amounts of water (potentially guided in various directions by remnant ice deposits) could then produce large waves across the northern lowlands terrains (Fig. 6.3, scenario I), and potentially resurfacing them.

The alternative solutions proposed here should be explored in greater detail with appropriate numerical models in the future.

6.6 Methods

6.6.1 Ice thickness calculation

The ice thickness can be estimated using the assumption that the transport of energy inside the water ice layer is controlled by conduction. The thermal conduction heat flux F can be written as follows:

$$F = \lambda_{\text{ice}} \frac{(T_{\text{bottom}} - T_{\text{surf}})}{h_{\text{ice}}} \tag{6.1}$$

with λ_{ice} the thermal conductivity of ice, h_{ice} the thickness of the water ice layer, T_{surf} the temperature at the top of the water ice layer and T_{bottom} the temperature at the bottom. At the interface between ice and liquid water, T_{bottom} is equal to 273,15 K. At equilibrium, the annual mean thermal conduction heat flux F is dominated by the geothermal heat flux F_{geo}. This results in the expression:

$$h_{\text{ice}} = \lambda_{\text{ice}} \frac{(273,15 - T_{\text{surf}})}{F_{\text{geo}}} \tag{6.2}$$

Figure 6.1 presents the minimum ice thickness of the ocean calculated as a function of the temperature at the top of the sea ice cover and of the geothermal heat flux.

6.6.2 Global Climate Model simulations

We use the LMD Early Mars 3-D Global CLimate Model (Forget et al., 2013; Wordsworth et al., 2013, 2015; Turbet et al., 2017a). The model includes both the water and CO_2 cycle (condensation and sublimation on the surface and in the atmosphere ; formation and transport of clouds ; precipitation and evaporation). It also includes a detailed radiative transfer module adapted to a thick CO_2-dominated atmosphere complemented with H_2O and H_2. We performed three numerical climate simulations at the obliquities 0°, 20° and 40°. Simulations were performed with a spatial resolution

of 64x48x26 (in longitude x latitude x altitude), using the present-day Mars MOLA topography. An ocean was placed in the northern lowlands of Mars, at elevations lower than -3.9 km. This value was chosen to match the best case of the tsunami propagation scenarios of Costard (Costard et al., 2017). We use a two layers slab-ocean model to treat the oceanic region (Codron, 2012). The transport of heat by the ocean circulation is not taken into account here. We fixed the total atmospheric pressure to 1 bar, and varied the concentration of H_2 (from 5 to 20%) in order to sustain a deglaciated ocean (annual mean temperature is around 3°C). This was achieved with concentrations of H_2 equal to 7, 6 and 5 % for the simulations at 0, 20 and 40° obliquities, respectively.

Figure 6.2 presents the annual cumulated rainfall and the annual net surface accumulation of water for various 3-D Global Climate simulations.

Chapter 7

The environmental effect of large meteoritic impacts on Early Mars

Contents

7.1 Preamble

Was the climate of Noachian Mars warm and wet for extended periods of time, or cold and transiently warmed? The outcome of this debate has important consequences for our general understanding of planetary habitability, and more specifically for the search of life on the red planet. It has been argued that large meteoritic impacts may have warmed and moistened the surface and atmosphere of early Mars for long periods of time (Segura et al., 2002, 2008; Toon et al., 2010; Segura et al., 2012; Urata and Toon, 2013). Here we explore the environmental effect of the largest impact events recorded on Mars using a hierarchy of climate models, ranging from a 1-D radiative-convective reverse model to a full 3-D Global Climate Model. The models were adapted to properly account for thick CO_2-H_2O atmospheres expected after the collision of large impactors on Mars. In particular, I put a lot of effort - through laboratory experiments and theoretical calculations - to accurately model the spectroscopy of dense CO_2+H_2O atmospheres, where any of the two gases can become dominant.

The work presented in this chapter will be submitted soon for publication. The full reference is: Martin Turbet, Baptiste Baudin, Cedric Gillmann, & Francois Forget, **"The environmental effect of very large meteoritic impacts on early Mars explored with a hierarchy of climate models"**, to be submitted, 2018.

7.2 Introduction

There are now numerous pieces of evidence that liquid water flowed on ancient Mars: high erosion rates (Craddock and Howard, 2002; Mangold et al., 2012), sedimentary deposits (Williams et al., 2013; Grotzinger et al., 2015), hydrated minerals (Poulet et al., 2005; Bibring et al., 2006; Mustard et al., 2008; Ehlmann et al., 2011; Carter et al., 2013, 2015) and dry river beds and lakes (Carr, 1995; Cabrol and Grin, 1999; Malin and Edgett, 2003; Moore et al., 2003; Mangold and Ansan, 2006; Hynek et al., 2010). Sophisticated climate modelling under ancient Mars conditions assuming a faint young Sun and $CO_2/N_2/H_2O$ atmospheres have not yet been able to produce liquid water or significant precipitation anywhere on the red planet (Forget et al., 2013; Wordsworth et al., 2013), unless additional hypothetic greenhouse gases were incorporated, such as reducing gases CH_4 or H_2 (Ramirez et al., 2014a; Wordsworth et al., 2017; Kite et al., 2017a; Ramirez and Kasting, 2017).

Meanwhile, it has been suggested that the warmer and wetter conditions required to explain the formation of the aforementioned geological and mineralogical evidence could have been produced in response to meteoritic impacts (Segura et al., 2002, 2008; Toon et al., 2010; Wordsworth et al., 2013; Wordsworth, 2016; Haberle et al., 2017). A large impact event could warm the surface and the atmosphere of Mars. Significant amount of water could get vaporized in the atmosphere, from the impactor, from the target materials (wet regolith) and from surface or near-surface water ice reservoirs exposed to the hot post-impact ejecta raining out from the atmosphere (Segura et al., 2002).

The impact scenario is seducing for two main reasons. First, the Late Noachian valley networks formed 3.5-3.8 billion years ago, during an epoch characterized by an impactor flux much higher than today (Segura et al., 2002; Toon et al., 2010). Secondly, amongst all the hypothetical scenarios that have been proposed to warm the surface of early Mars (Wordsworth, 2016; Haberle et al., 2017), the impact scenario is the only one that occured for sure, based on the geological record.

The environmental effect of such meteoritic impact events has already been studied with unidimensional radiative-convective models (Segura et al., 2002, 2008, 2012). Here we explore the climatic impact of large meteoritic impact events using a hierarchy of climate models, ranging from a 1-D radiative-convective model to a 3-D Global Climate Model. The 3-D Global Climate Model (GCM) simulations are useful to accurately simulate all the processes (cloud microphysics, large scale circulation, etc.) at play in the post-impact early Martian atmosphere. 1-D radiative-convective models are useful to simulate a wide range of possible post-impact conditions (initial atmosphere, size of impactor, etc.) and explore the sensitivity to parameterizations (e.g. microphysics of clouds), thanks to their low computational cost.

Here we focus on the environmental effect of the largest impact events ever recorded on Mars, those that are large enough (impactor diameter typically larger than 100 km) to vaporize the equivalent of the present-day Mars water content (around 30 m Global Equivalent Layer [GEL]) in the atmosphere, as estimated from energy conservation calculations.

Two main topics are explored in the present manuscript:

1. How long can the surface of Mars be kept above the melting point of water following large meteoritic impact events? In particular, can impact-induced, stable runaway climate exist on early Mars, as previously reported by Segura et al. (2012)? Can impact-induced, high altitude water ice clouds keep the surface of Mars above the melting point of water for extended periods of time, as previously reported by Urata and Toon (2013) and Segura et al. (2008)?

2. How much precipitation is generated after large meteoritic impacts events, and how is it distributed across the surface of Mars?

A major aspect of our work is to explore how 3-dimensional processes (atmospheric circulation and cloud formation) affect the environmental effect of meteoritic impact events.

We will first describe the various climate models used in this work in Section 7.3, with a particular focus on the recent improvements made on the spectroscopy of dense atmospheres of CO_2 and H_2O (where both gases can become dominant), typical of extreme post-impact atmospheric conditions. We will then present in Section 7.4 the results of the first 3-D simulations of the environmental effect of large meteoritic impact events on the atmosphere of early Mars. Because in some conditions 3-D post-impact atmospheres can be remarkably well described by 1-D simulations, we then use 1-D simulations in Section 7.5 to explore a wide range of possible impact conditions. We revisit throughout the manuscript the results of Segura et al. (2002, 2008, 2012); Urata and Toon (2013) and Ramirez and Kasting (2017).

7.3 Method

We used in this paper two different versions - 3D and 1D - of the LMD Generic climate model, designed here to reproduce the post-impact conditions following a very large impact hitting the surface of early Mars. We assume that the planet - initially endowed with a CO_2-dominated atmosphere - is suddenly warmed and moistened by the heat of the impact (and the subsequent hot ejecta) and the subsequent sublimation/vaporization of water into the atmosphere. In this section, we first describe our 3-D climate model and our 1-D climate model. We then present the radiative transfer scheme (common for the two models), with a particular focus on the recent improvements made on the spectroscopy of dense CO_2+H_2O atmospheres (typical of post-impact atmospheres) that are taken into account in the radiative transfer calculations.

7.3.1 3-D Global Climate Model simulations

The model described in this subsection was used to produce the results described in Section 7.4.

Our 3-D model is a full 3-Dimensions Global Climate Model (GCM) that has previously been developed and used for the study of the climate of ancient Mars (Forget et al., 2013; Wordsworth et al., 2013, 2015; Turbet et al., 2017a; Palumbo et al., 2018).

The simulations presented in this paper were performed at a spatial resolution of 96 x 64 in longitude x latitude (e.g. 3.8° × 2.8°; 220 km x 165 km at the equator). In the vertical direction, the model is composed of 45 distinct atmospheric layers, ranging from the surface up to a few Pascals. Hybrid σ coordinates (where σ is the ratio between pressure and surface pressure) and fixed pressure levels were used in the lower and the upper atmosphere, respectively.

The dynamical time step of the simulations ranged between 9 s (at the beginning of the large impact events) and 90 s. The radiative transfer and the physical parameterizations (such as condensation, convection, etc.) are calculated every 10 and 40 dynamical time steps, respectively.

We used the pre-True Polar Wander (pre-TPW) topography from Bouley et al. (2016). Bouley et al. (2016) showed that the formation of the late Noachian valley networks should have precluded the major part of the loading of the Tharsis volcanic bulge. The pre-TPW topography is based on the present-day MOLA (Mars Orbiter Laser Altimeter) Mars surface topography (Smith et al., 1999; Smith et al., 2001), but without Tharsis and all the younger volcanic features. Moreover, the formation of Tharsis should have produced a large True Polar Wander (TPW) event of 20°-25°, which is also taken into account in the pre-TPW topography.

We set the obliquity of Mars at 40° to be roughly consistent with the most likely obliquity (41.8°) for ancient Mars (Laskar et al., 2004).

The thermal conduction in the subsurface is taken into account using a 19-layers thermal diffusion soil model, with a ground thermal inertia varying from 250 to 1500 J $m^{-1/2}$ $s^{-1/2}$ K^{-1}, depending on the ground water content (see Chapter 9, Fig. 9.1).

Subgrid-scale dynamical processes (turbulent mixing and convection) were parameterized as in Forget et al. (2013) and Wordsworth et al. (2013). The planetary boundary layer was accounted for by the Mellor and Yamada (1982) and Galperin et al. (1988) time-dependent 2.5-level closure scheme, and complemented by a convective adjustment which rapidly mixes the atmosphere in the case of unstable temperature profiles. Moist convection was taken into account following a moist convective adjustment that originally derives from the "Manabe scheme" (Manabe and Wetherald, 1967; Wordsworth et al., 2013). In the version of our scheme, relative humidity is let free and limited to 100% (supersaturation is not permitted). This scheme was chosen instead of more refined ones because it is: 1. robust for a wide range of pressures; 2. energy-conservative; and 3. it is a physically consistent scheme for exotic (non Earth-like) situations such as the ones induced by large meteoritic impact events. In practice, when an atmospheric grid cell reaches 100 % saturation and the corresponding atmospheric column has an unstable temperature vertical profile, the moist convective adjustment scheme is performed to get a stable moist adiabatic lapse rate. In our simulations of large impact events, water vapor can become the dominant atmospheric species. Thus, we used a generalized formulation of the moist-adiabiat lapse rate developed by Leconte et al. (2013a) (Supplementary Materials) to account for the fact that water vapor can become a main species in our simulations. In our model we also used the numerical scheme proposed by Leconte et al. (2013a) (Supplementary Materials) to account for atmospheric mass change after the condensation or the evaporation of gases (water vapor in our case); this numerical scheme is crucial in our simulations of impact events to model accurately the evolution of the surface pressure and the relative content of CO_2 and H_2O. More details on the scheme can be found in Leconte et al. (2013a) (Supplementary Materials).

Both CO_2 and H_2O cycles are included in the GCM used in this work. In our model, CO_2 can condense to form CO_2 ice clouds and surface frost if the temperature drops below the saturation temperature of CO_2 (at a given CO_2 partial pressure). A self-consistent water cycle is also included in the GCM. In the atmosphere, water vapor can condense into liquid water droplets or water ice particles, depending on the atmospheric temperature and pressure, forming clouds.

The fraction of cloud particles $\alpha_{c,liquid}$ (in %) in liquid phase is given by (Charnay, 2014):

$$\alpha_{c,liquid} = \frac{T - (273.15 - 18)}{18} \tag{7.1}$$

where T is the atmospheric temperature of the corresponding GCM air cell. Above 0°C, particles are fully liquid and below -18°C they are assumed to be fully solid.

We use a fixed number of activated cloud condensation nuclei (CCNs) per unit mass of air N_c to determine the local H_2O cloud particle sizes, based on the amount of condensed material. Following Leconte et al. (2013a), we used $N_c = 10^4$ kg^{-1} for water ice clouds and 10^6 kg^{-1} for liquid water clouds. These numbers - that give satisfactory results to reproduce the present-day Earth climate (Leconte et al., 2013a) - are highly uncertain for post-impact conditions on Mars. On the one hand, impact events would inject a huge number of silicated particles in the atmosphere, potentially serving as CCNs. On the other hand, the huge rate of precipitation recorded in our 3-D simulations would remove efficiently these silicated particles. Eventually, we used $N_c = 10^5$ kg^{-1} for CO_2 ice clouds following Forget et al. (2013).

The effective radius r_{eff} of the cloud particles is then given by:

$$r_{\text{eff}} = \left(\frac{3\ q_c}{4\pi\rho_c N_c}\right)^{1/3} \tag{7.2}$$

where ρ_c is the density of the cloud particles (1000 kg m^{-3} for liquid and 920 kg m^{-3} for ice) and q_c is the mass mixing ratio of cloud particles (in kg per kg of air). The effective radius of the cloud particles is then used to compute both (1) their sedimentation velocity and (2) their radiative properties calculated by Mie scattering (see Madeleine 2011 for more details).

Water precipitation is divided into rainfall and snowfall, depending on the nature (and thus the temperature) of the cloud particles. Rainfall is parameterized using the scheme from Boucher et al. (1995), accounting for the conversion of cloud liquid droplets to raindrops by coalescence with other droplets. Rainfall is considered to be "instantaneous" (i.e. it goes directly to the surface) but can evaporate while falling through sub-saturated layers. The re-evaporation rate of precipitation E_{precip} (in kg/m^3/s) is determined by (Gregory, 1995):

$$E_{\text{precip}} = 2 \times 10^{-5}\left(1 - \frac{q_v}{q_{s,v}}\right)\sqrt{P} \tag{7.3}$$

where q_v and $q_{s,v}$ are the water vapour mixing ratios in the air cell and at saturation, respectively. P is the precipitation flux (in kg/m^2/s).

Snowfall rate is calculated based on the sedimentation rate of cloud particles in the atmospheric layer. The sedimentation velocity of particles V_{sedim} (in m/s) is assumed to be equal to the terminal velocity that we approximate by a Stokes law:

$$V_{\text{sedim}} = \frac{2\rho_c g {r_{\text{eff}}}^2}{9\eta}\ (1 + \beta K_n) \tag{7.4}$$

where η is the viscosity of atmospheric CO_2 (10^5 N s m^{-2}) and g the gravity of Mars (3.72 m s^{-2}). $(1+\beta K_n)$ is a "slip-flow" correction factor (Rossow, 1978), with β a constant equal to $\frac{4}{3}$ and K_n the Knudsen number that increases with decreasing atmospheric pressure.

At the surface, liquid water and water ice can co-exist. Their contributions are both taken into account in the albedo calculation as in Wordsworth et al. (2013). The stability of liquid water/ice/CO_2 ice at the surface is governed by the balance between radiative, latent and sensible heat fluxes (direct solar insolation, thermal radiation from the surface and the atmosphere, turbulent fluxes) and thermal conduction in the soil. Melting, freezing, condensation, evaporation, and sublimation physical processes are all included in the model as in Wordsworth et al. (2013) and Turbet et al. (2017a).

7.3.2 1-D reverse climate model simulations

The model described in this subsection was used to produce the results described in Section 7.5.

Our 1D reverse model is a single-column reverse radiative-convective climate model following the same approach ('reverse modeling') than Kasting et al. (1984), and using the same parameterizations than Ramirez and Kasting (2017). The atmosphere is decomposed into 200 logarithmically-spaced layers that extend from the ground to the top of the atmosphere arbitrarily fixed at 1 Pascal. The atmosphere is separated in three (at most) physical layers constructed as follows. First, we fix the surface temperature to the desired value. The first layer is constructed by integrating a moist (H_2O) adiabat upwards until CO_2 starts to condense. This first layer defines a convective troposphere assumed to be fully saturated. From the altitude where CO_2 starts to condense, we construct the second layer by integrating a moist (CO_2) adiabat upwards until the atmospheric temperature reaches the stratospheric temperature, arbitrarily fixed at 155 K as in Ramirez and Kasting (2017).

Once the thermal profile of the atmosphere is constructed, we compute the radiative transfer (described in subsection 7.3.3) in the 200 atmospheric layers. From this, we derive (1) the Outgoing Longwave Radiation (OLR) and (2) the fraction of the solar flux absorbed by the atmosphere. The radiative transfer calculations are described in details in subsection 7.3.3.

Following Ramirez and Kasting (2017), we assumed that the planet is flat and the Sun remains fixed at a zenith angle of 60°. The surface albedo is fixed to 0.216.

Our model can also take into account the radiative effect of clouds following the same approach than in Ramirez and Kasting (2017). A cloud layer can be placed at any arbitrary height (in any of the 200 atmospheric layers, and in any of the three physical layers previously described). We assume 1 km thick cloud decks. Following Ramirez and Kasting (2017), we compute the optical depth τ_{ice} of the water ice clouds as follows:

$$\tau_{\text{ice}} = \frac{3\ Q_{\text{eff}}\ IWC\ \Delta z}{4\ r_{\text{ice}}\ \rho_{\text{ice}}}, \tag{7.5}$$

with Q_{eff} the extinction coefficient, IWC the ice water content (in g/m^3), Δz the vertical path length of the cloud layer, arbitrarily fixed to 10^3 m, r_{ice} the effective radius of water ice particles, and ρ_{ice} the volumetric mass of water ice, We used the same Mie optical properties (tabulated values of Q_{eff}) for the cloud particles than in the 3-D Global Climate Model (same radiative properties than used in Wordsworth et al. 2013). We assumed that the IWC scales following Ramirez and Kasting (2017):

$$IWC\ =\ 0.88\ P, \tag{7.6}$$

with P the atmospheric pressure at the cloud deck level. To explore the sensitivity of the results to the cloud content, we used the "Relative Ice Water Content" which is a multiplicative factor applied to the IWC (Ramirez and Kasting, 2017). It is equal to 1 unless specified.

7.3.3 Radiative Transfer

Our climate models include a generalized radiative transfer code adapted to any mixture of CO_2 and H_2O gases. Our radiative transfer calculations are performed on 38 spectral bands in the thermal infrared and 36 in the visible domain, using the "correlated-k" approach (Fu and Liou, 1992) suited for fast calculations. 16 non-regularly spaced grid points were used for the g-space integration, where g is the cumulative distribution function of the absorption for each band.

Absorption caused by the absorption of H_2O and CO_2 in the atmosphere was computed using *kspectrum* (Eymet et al., 2016) to yield high-resolution line-by-line spectra. We used the HITRAN2012 database for the H_2O and CO_2 line intensities and parameters (Rothman et al., 2013). In addition, we incorporated the half-width at half maximum of H_2O lines broadened by CO_2 ($\gamma^{H_2O-CO_2}$) and CO_2 lines broadened by H_2O ($\gamma^{CO_2-H_2O}$), as well as the corresponding temperature dependence exponents ($n^{H_2O-CO_2}$ and $n^{CO_2-H_2O}$), based on Brown et al. (2007); Sung et al. (2009); Gamache et al. (2016) and Delahaye et al. (2016). More details can be found in Turbet et al. (2017c) and Tran et al. (2018).

Collision-induced absorptions, dimer absorptions and far wing absorptions were also taken into account, whenever possible and data was available. Far wings of CO_2 band lines (both CO_2-CO_2 and CO_2-H_2O) were computed using the χ-factor approach, using experimental data from Perrin and Hartmann (1989), Tran et al. (2011) and Tran et al. (2018). The χ-factor is an empirical correction of the Lorentzian line shape adjusted to laboratory measurements. CO_2-CO_2 collision-induced and dimer absorptions were computed based on Gruszka and Borysow (1997); Baranov et al. (2004); Stefani et al. (2013).

H_2O-H_2O continuum was taken into account using the MT_CKD 3.0 database (Mlawer et al., 2012), from 0 to 20,000 cm^{-1}. MT_CKD databases are available on `http://rtweb.aer.com/`. H_2O-CO_2 continuum was calculated with the line shape correction functions digitized from Ma and Tipping (1992) using line positions and intensities from the HITRAN2012 database (Rothman et al., 2013), with a cut-off distance at 25 cm^{-1}, and from 0 to 20,000 cm^{-1}. The temperature dependence of the continuum was empirically derived using data digitized from Pollack et al. (1993). More details can be found in Turbet et al. (2017c) and Tran et al. (2018).

7.4 Exploration of the environmental effect of a very large impactor with a full 3-D Global Climate Model

Here we study the environmental effect of very large impact events on the atmosphere and surface of early Mars, using the 3-D Global Climate Model presented in Section 7.3.1. Because Global Climate Model simulations can be computationally very expensive[1], I focus in this section on one reference post-impact simulation of a very large impactor hitting the surface of Mars, initially assumed to be endowed with a 1 bar pure CO_2 atmosphere. The impactor is assumed to be large enough to trigger the vaporization of $\sim$ 2 bar (i.e. 54 m GEL) of water into the atmosphere. The atmosphere, surface, and subsurface are assumed to be suddenly and uniformly heated up to 500 K. Such extreme post-impact conditions are likely typical of the few most extreme impact events ever recorded on Mars (Segura et al., 2002; Toon et al., 2010).

7.4.1 Chronology of the event

Our 3-D simulations indicate that the sequence of events following the very large impact event previously described can be decomposed into four main phases:

Phase I: very hot atmosphere, no precipitation. In this first phase, the atmosphere is too warm for water to condense on the surface. Precipitation (produced in the cooler, upper atmosphere)

[1]It actually took me three months (using 24 processors of the french supercomputer OCCIGEN) to perform the reference simulation described in this work.

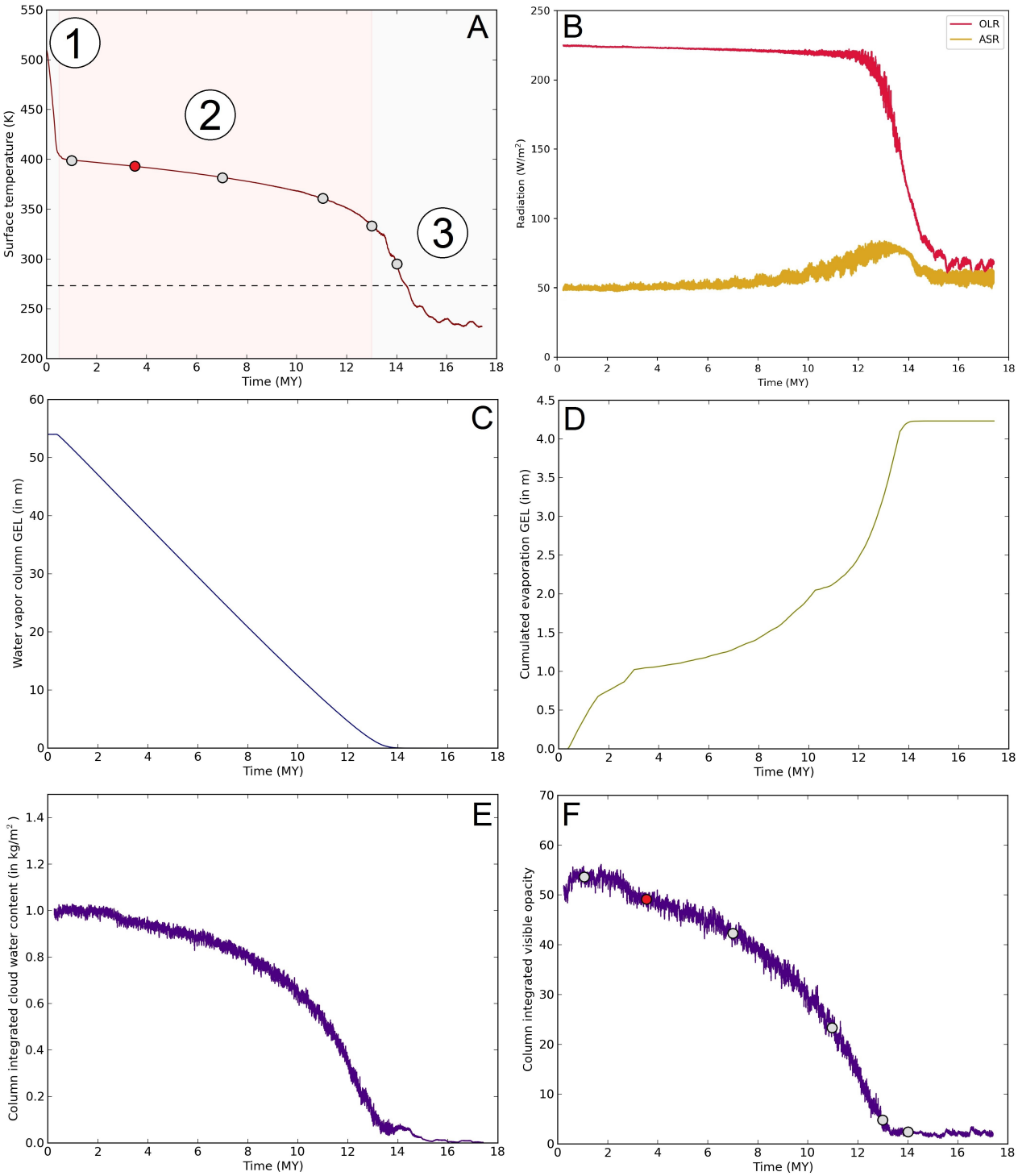

Figure 7.1: Globally averaged temporal evolution of the (A) surface temperature (in K), (B) top of atmosphere radiative fluxes (in W/m^2), (C) integrated column of water vapour (in m GEL), (D) cumulated surface evaporation of water (in m GEL), (E) column integrated cloud water content (in kg/m^2) and (F) column integrated cloud visible opacity. All these quantities were computed for the reference simulation described extensively in Section 7.4 of this paper. The grey/pink zones (and numbers 1,2,3) in panel A indicate the three first post-impact phases described in the manuscript. MY is for Martian Years.

is re-evaporated (in the lower atmospheric layers). This phase ends when the first droplet of water reaches the ground. The atmosphere is then almost entirely saturated in water vapour, and the atmospheric thermal profile follows a moist adiabat as shown in Fig. 7.4A. Therefore, the atmospheric state at the end of this first phase (when the first droplet of water reaches the ground) does only depend on the amount of CO_2 and H_2O in the atmosphere, but does not depend on the initial post-impact temperature assumed. This means that, for the impact event described here (1 bar CO_2 atmosphere + 2 bar of water vaporized), the initial temperature (here, 500 K) does not have any major effect on the nature of the environmental effect (on the atmosphere and the surface, but not the subsurface) of the impact during the following phases (described below). The duration of this first phase is roughly controlled by (i) the net top of atmosphere (TOA) radiative budget and (ii) the amount of extra thermal energy of the atmosphere (the difference of thermal energy between a 500 K isotherm thermal profile and a moist adiabat thermal profile.). The duration of this phase is usually short because the initially hot atmosphere quickly cools by emitting thermal radiation to space. For our reference simulation, it takes $\sim$ 0.5 Martian year (MY)[2] for the first droplet of water to reach the surface, which sets the end of this first phase (see Fig. 7.1A). This phase is not interesting from the point of view of surface erosion because no water is present at the surface.

Phase II: hot atmosphere, intense precipitation. At the beginning of the second phase the lower atmosphere is now saturated in water vapour, and water can start to condense on the surface and accumulate. This is the most interesting phase because it coincides with the main bulk of precipitation (rainfall). During this phase, our 3-D Global Climate simulations indicate that (1) a thick, reflective and quasi-uniform cloud cover is present and (2) the net radiative budget at the top of the atmosphere (TOA) is roughly constant, because both the outgoing longwave radiation (OLR) and the planetary albedo are constant (see Fig. 7.1B). For our reference simulation, the net top of atmosphere (TOA) radiative budget is -180 W/m^2. As a result, the water vapour atmospheric content gets progressively depleted (see Fig. 7.1C). The duration of this second phase is roughly controlled by (i) the net TOA radiative budget and (ii) the total amount of latent heat that can be extracted from the condensation of the entire water vapour atmospheric column. For our reference simulation, the duration of the phase is $\sim$ 12 Martian years (MY). This duration can be empirically approximated by $q_{\mathrm{col},H_2O}(m)/4.5$, where q_{col,H_2O} is the initial global mean integrated column of water vapour in GEL (m). Approximately 2.6 m of water condenses on the surface per Earth year, which is very similar to the result obtained by Segura et al. (2002) with a 1-D cloud-free numerical climate model. Note that the surface evaporation of water is very limited during this phase. In our reference simulation, approximately 8% of the precipitation gets re-evaporated from the surface (see Fig. 7.1D). We investigate this phase in more details below.

Phase III: conversion of surface liquid water into ice. When the third phase starts, most water vapour has already condensed on the surface. Surface water rapidly freezes and the planet get cold (see Fig. 7.1A), even colder than before the impact event because the planet is now covered by a thick, reflective ice cover. Based on the results of Turbet et al. (2017a), water - that should accumulate in the topographic depressions of the planet - would freeze (down to the bottom) in 10^4 years maximum.

Phase IV: migration of water ice to the cold traps. In the fourth phase, water progressively migrates in the cold traps of the planet. For our reference simulation (thick CO_2 atmospheric pressure, high obliquity), water should migrate to the southern highlands (Wordsworth et al., 2013; Bouley et al.,

[2]One martian year lasts approximately 687 Earth days, i.e. 1.88 Earth year.

2016; Turbet et al., 2017a). We do not explicitly simulate this phase here. However, based on the results of Turbet et al. (2017a), water should migrate to the cold traps of the planet within 10^5 years.

In total, it takes ∼15 Martian years (MY) for the surface temperature to drop below the freezing temperature of water (273 K). Note that subsurface temperatures could remain above 273 K for much longer periods of time, as reported in Segura et al. (2002). At the end of our simulations (after ∼ 18 Martian years), the mean (regolith) subsurface temperatures at 5 and 50 m are respectively 320 and 470 K.

Below we investigate in much more details the second phase, because this is during this phase that most of precipitation (rainfall) occurs.

7.4.2 Clouds and radiative budget

The second phase starts when the first droplet of (liquid) water reaches the surface of Mars. At this stage, the atmosphere is almost entirely saturated in water vapour. The outgoing longwave radiation (OLR) is roughly constant through time (see Fig. 7.1B) and across the planet. The OLR is dominated by the infrared thermal emission of the moist, upper atmosphere (see Fig. 7.3D). This result is similar in nature with the asymptotic behaviour of the OLR predicted by 1-D radiative convective models assuming a thermal profile following the water vapor saturation curve (Nakajima et al., 1992; Kasting et al., 1993; Kopparapu et al., 2013). This is the typical state reached by planets entering in runaway greenhouse. For a Mars-size planet, Kopparapu et al. (2014) estimates that the asymptotic outgoing longwave radiation (for a pure water vapour atmosphere) is 250 W/m^2, i.e. 20 W/m^2 higher than our result. This small difference is likely due to (i) a different CO_2 atmospheric content (discussed in the next section ; see also Goldblatt and Watson 2012; Ramirez et al. 2014b and Marcq et al. 2017), (ii) different treatments of water vapour absorption (Kopparapu et al., 2013), (iii) the radiative effect of clouds in the infrared.

Thermal radiation cooling occurs mainly in the upper atmospheric layers (see Fig. 7.3D). This triggers moist convection and thus water vapour condensation, forming clouds in the upper atmosphere (see Fig. 7.3ABC). Because this radiative cooling occurs everywhere (at each latitude and longitude of the planet), clouds form everywhere on the planet(see Fig. 7.2 and 7.3A). This result is qualitatively in agreement with Segura et al. (2008). Moreover, simple energy conservation consideration (supported by our 3-D Global Climate simulations) show that approximately 1kg/m^2 of cloud particles are produced every 3 hours. The production rate of cloud particles is so high that cloud particles accumulate, growing to large sizes up to several hundreds of microns for icy particles in the upper cloud layer (see Fig. 7.3C). The accumulation of cloud particles is limited by (i) coagulation of cloud liquid droplets into raindrops (following the numerical scheme of Boucher et al. 1995) and (ii) sedimentation of large ice particles (parameterized following a Stokes law (Rossow, 1978)). As a result, our 3-D Global Climate simulations show that a thick, uniform cloud cover is produced in the upper layers of the planet (see Fig. 7.3ABC).

This thick, uniform cloud cover (mostly located in the upper atmosphere, as illustrated in Fig. 7.3AB) reflects incoming solar radiation efficiently. In average, the planetary albedo reaches ∼ 0.55 (see Fig. 7.1B). Moreover, a large fraction of the incoming solar radiation is absorbed in the upper atmospheric layers, mostly by water vapour and clouds. As a result, the strong deficit of absorbed stellar radiation versus outgoing longwave radiation (see Fig 1D) cools down the planet very

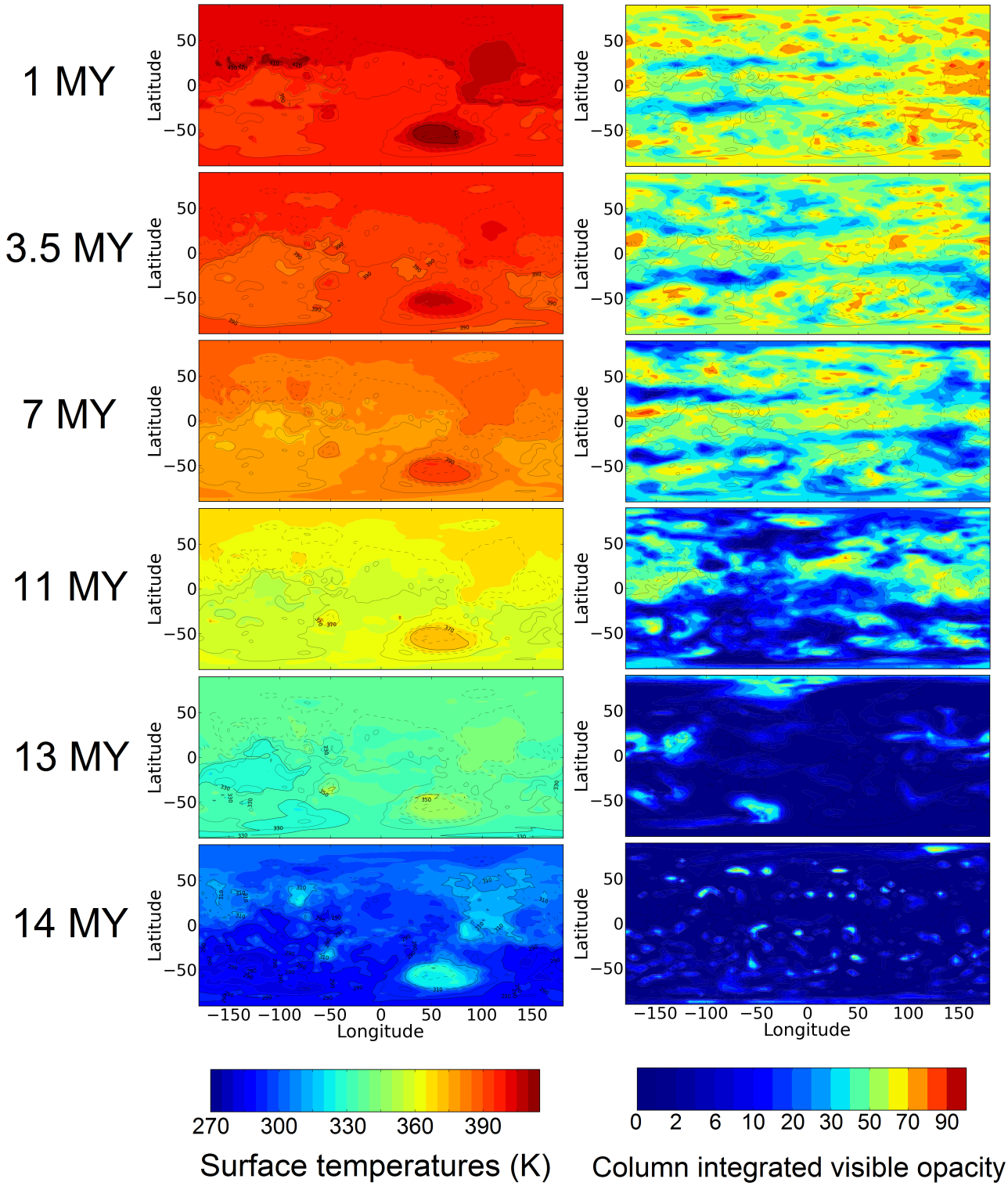

Figure 7.2: Snapshots of post-impact surface temperature (in K) and visible opacity maps at six distinct timings (1, 3.5, 7, 11, 13 and 14 Martian years [MY]). These six timings are also highlighted in Fig. 7.1 with dots.

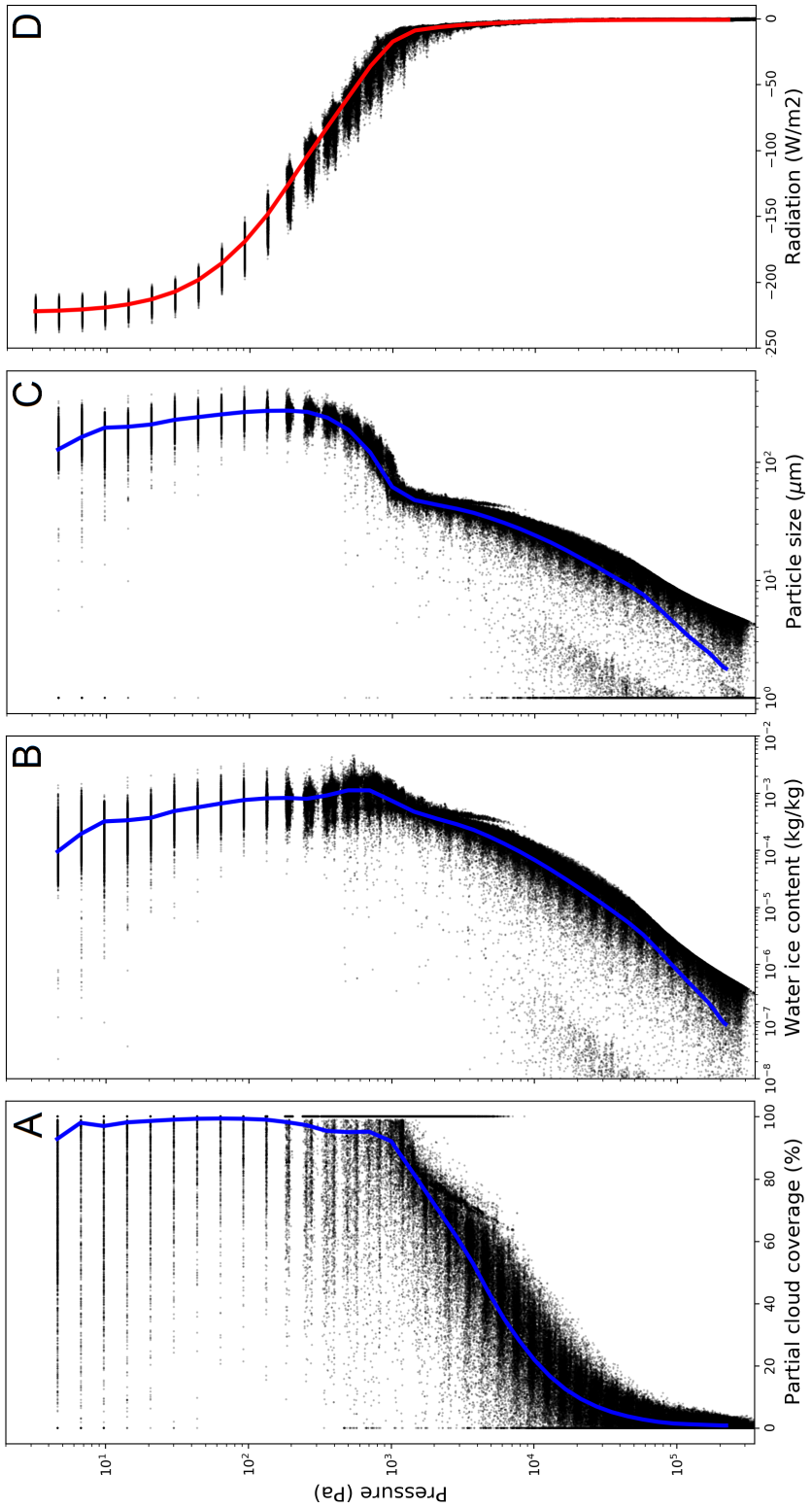

Figure 7.3: Vertical profiles of (A) the partial cloud coverage (in %), (B) the water ice content (in kg/kg), (C) the effective radius of cloud particles (in μm) and (D) the net thermal infrared flux passing through each of the atmospheric layer (negative means upward). These profiles are snapshots calculated 3.5 MY after the impact event. This timing is highlighted in Fig. 7.1 with a red dot. The colored thick lines vertical profiles are globally averaged snapshots. Small black dots are snapshots of all possible values reached by GCM air cells. In total, there are 276480 (i.e. the number of GCM air cells) black dots in each subfigure.

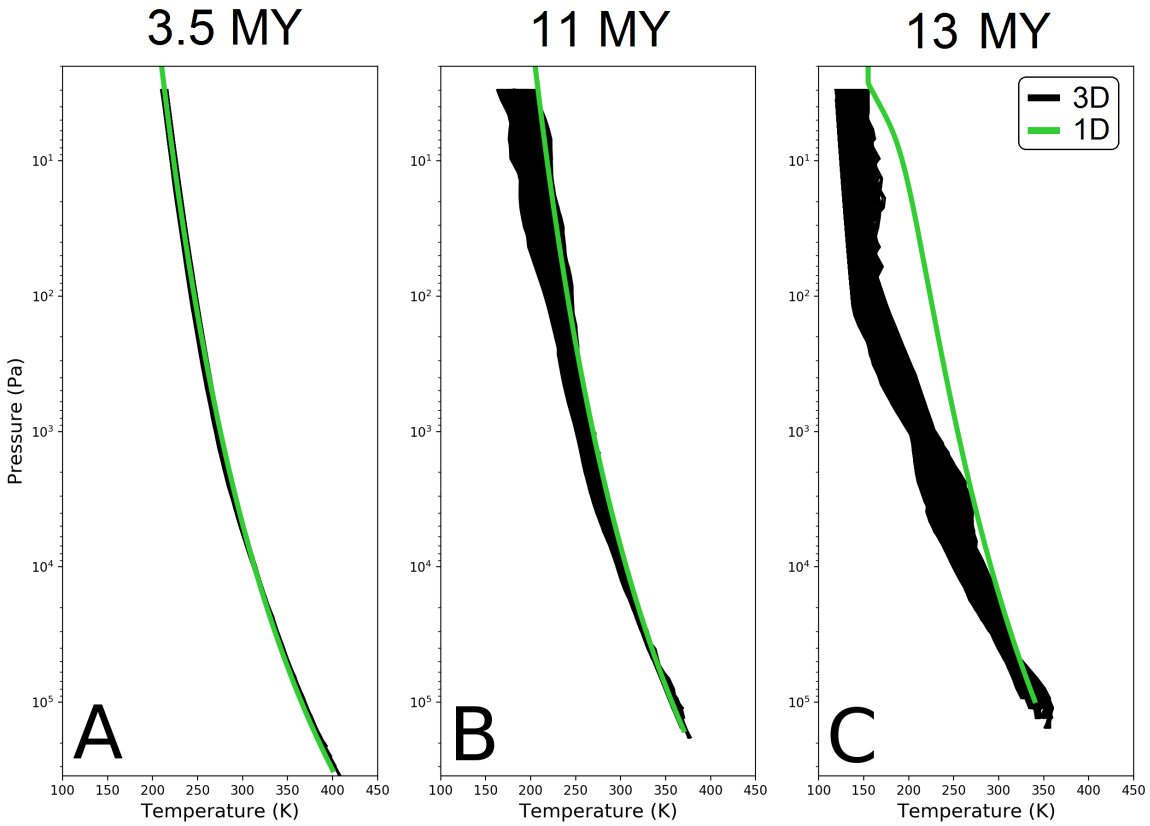

Figure 7.4: Snapshots of the vertical thermal profiles after 3.5 (left panel), 11 (middle panel) and 13 Martian years (right panel). The black region indicates all the pressure,temperature reached in the 3-D Global Climate simulation. The green solid line indicates the thermal profile calculated in our 1-D reverse climate model (see description in Section 7.3.2) for the same surface temperature and CO_2 partial pressure than assumed in the GCM reference simulation.

rapidly. During most of this phase, the radiative disequilibrium at the top of the atmosphere is $\sim$ -180W/m^2. As a result, the atmosphere and the planet progressively cool down (see Fig. 7.1A and 7.2).

As the planet cools down, the globally averaged cloud water content and visible opacity slowly decrease (see Fig. 7.1EF). While water is progressively raining out from the atmosphere, the atmosphere is progressively drying out. The upper atmosphere become slowly drier through time, producing more and more unsaturated regions. Progressively, we enter in a regime of radiative fins as predicted by Pierrehumbert (1995) and simulated with a 3-D Global Climate Model in Leconte et al. (2013a) in the context of the runaway greenhouse. This can be observed in Fig. 7.2 (right panel) where the clouds become more and more patchy through time. Regions where clouds are absent coincide (i) with sub-saturated regions and (ii) with regions where the thermal emission to space exceeds the maximum emission ($\sim$ 230W/m^2, here) calculated for a quasi-saturated atmosphere.

While the planet cools down, not only the globally averaged surface temperature decreases, but

also the variability of the surface temperature and more generally of the atmospheric temperature progressively increases (see Fig.7.4ABC). During most of the second phase, the 1D thermal profiles calculated at each location of the planet in the GCM follow remarkably well the thermal profile predicted by 1D climate calculations (see Fig. 7.4A) assuming a fully saturated profile. But as the planet cools down, subsaturated regions appear and discrepancies with the 1-D calculations start to emerge (see Fig. 7.4BC). The fact that the thermal profile matches very well 1-D calculations during most of the second phase is important, because it indicates that we can use a 1-D model (much faster than 3-D simulations) to explore the nature of the post-impact main phase of precipitation, depending on many different parameters (e.g. CO_2 and H_2 total atmospheric contents). This exploration is the topic of Section 7.5.

7.4.3 Localization of precipitation

Precipitation is produced uniformly in the upper cloud layer. Yet, most of the precipitation (if not all) of the main, upper cloud layer is re-evaporated while falling through some sub-saturated lower layers (following the numerical scheme of Gregory 1995). This is illustrated in Figure 7.5 that presents a snapshot of the zonal mean budget of precipitation/re-evaporation. In fact, 3-D GCM simulations indicate that none (or almost none) of the precipitation produced in the upper cloud layer actually reach the surface (see Fig. 7.5). Instead, this is the condensation produced by the large scale air movements in the lower atmosphere that is the primary source of precipitation reaching the ground of the planet.

The equatorial regions receives (in our 3-D simulations) in average a few tens of W/m^2 of solar radiation in excess compared to the pole. This is likely enough to trigger large scale movements in the lower atmosphere, in particular to transport energy from the equator to the tropics, following a Hadley cell-like structure. Near the equator, ascending air produces condensation and thus precipitation (see Fig. 7.5D). Near 30°S/30°N latitudes, this is the descending branch of the Hadley cell. These regions of air subsidence are highly subsaturated, and (almost) no precipitation reaches the ground (see Fig. 7.5D).

Figure 7.6 illustrates the fact that the precipitation (rainfall) patterns mostly produced in response to the large scale circulation in the lower atmosphere. We note a peak of precipitation near the equator (ascending branch of Hadley cell) and a lack of precipitation near 30°S/30°N (descending branch of Hadley cell). Significant precipitation is also recorded at higher latitudes, likely produced by large scale atmospheric circulation. In addition, we also note some localized sources of precipitation (e.g. east of Hellas crater) likely due to coupling between low atmospheric circulation and topography.

In average, $\sim$ 58 m of precipitation (54 m from the initial water vapor reservoir, 4 m from surface re-evaporation) is recorded throughout the 3-D simulations. Note that, although there are some latitudinal differences in the surface distribution of precipitation, cumulated precipitation is high everywhere on the planet (at least 20 m of cumulated precipitation). Precipitation is deluge-like with an average of 2.6 m of precipitation per Earth year. Moreover, because most of the precipitation that reaches the ground does not get re-evaporated, the impact-induced hydrological cycle is a "one-shot" cycle. The total amount of precipitation produced in response to the impact event can be well predicted by the total amount of water vapor initially vaporized/sublimed in the atmosphere.

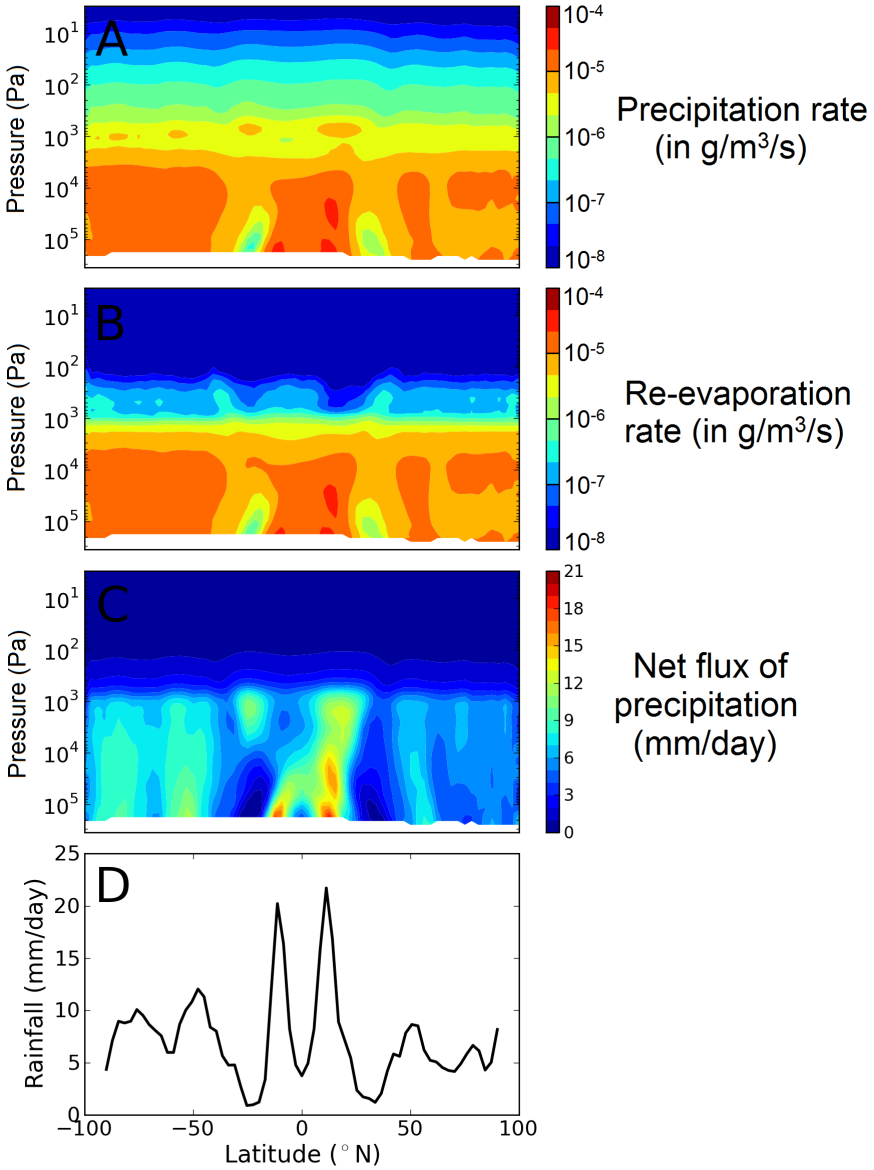

Figure 7.5: Snapshot of the zonal means of (A) the cloud particle rate of precipitation (in g/m^3/s), (B) the rate of re-evaporation of precipitation (in g/m^3/s), (C) the downward flux of precipitation (accounting for re-evaporation) in kg/m^2/day (or mm/day) and (D) the surface accumulation of precipitation (in mm/day). This is a snapshot 3.5 Martian years (MY) after the reference impact event.

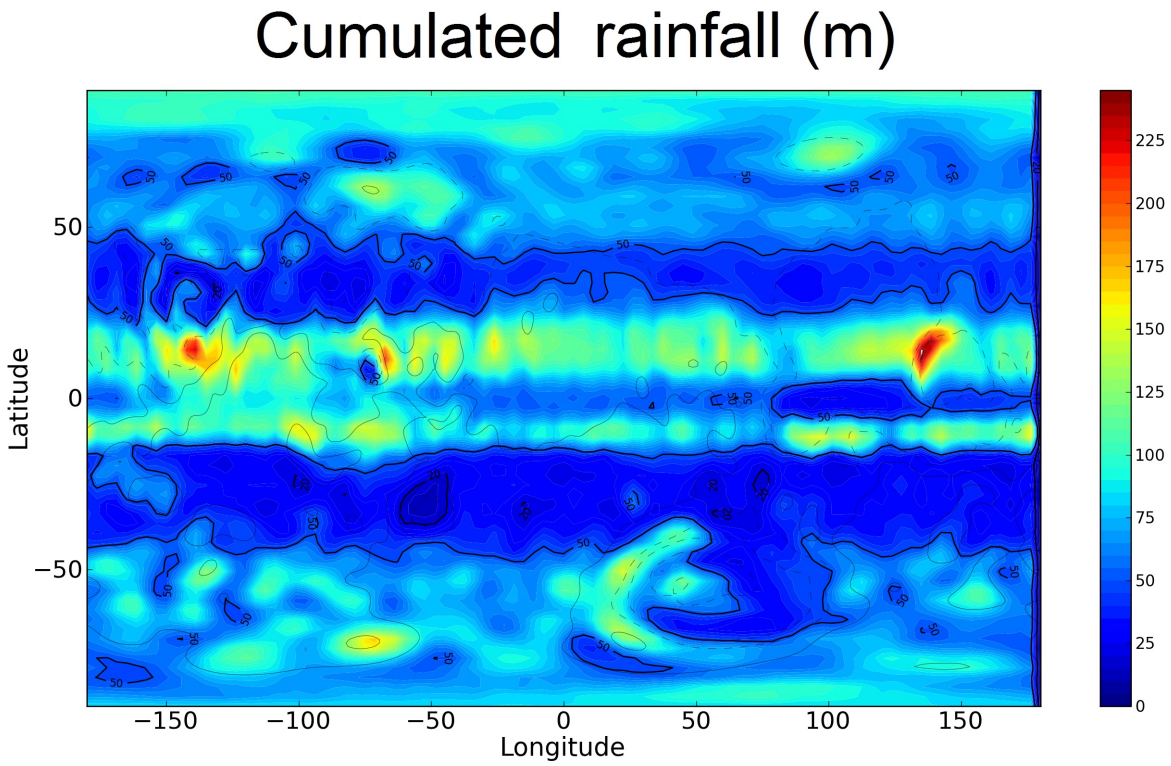

Figure 7.6: Cumulated rainfall map (in m) 15 martian years (MY) after the meteoritic impact event.

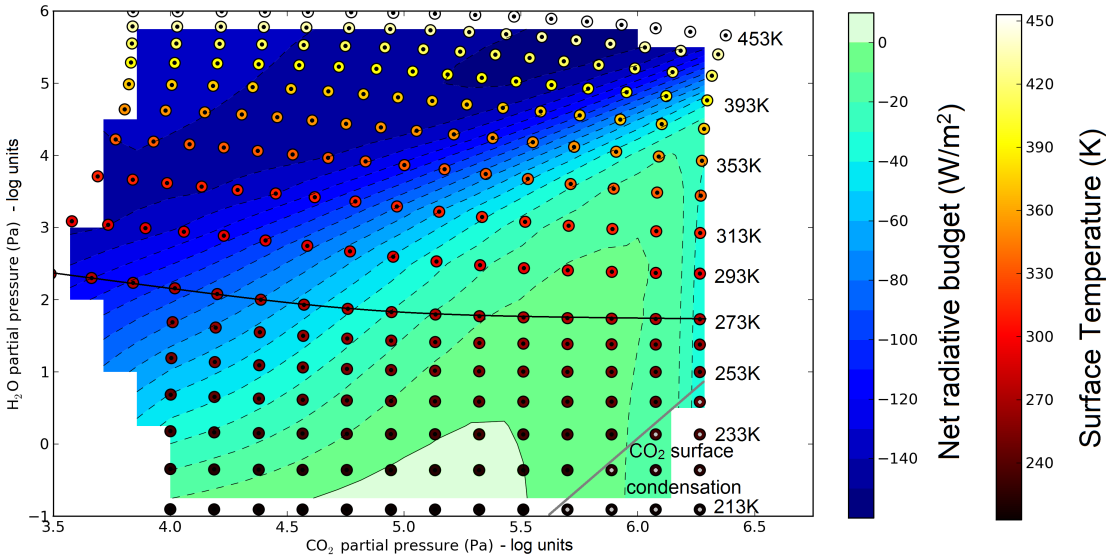

Figure 7.7: Contour plot of the net radiative budget at the TOA (top of atmosphere) of the post-impact early Mars atmosphere, as a function of CO_2 and H_2O partial pressure in the atmosphere. The contour plot was calculated by interpolating the data points of the scatter plot. The color of the data points corresponds to the surface temperature of the simulation. Note that the planet is at equilibrium if the radiative budget is equal to 0, which is never the case for any of the post-impact simulations. Note that, for a given CO_2 atmospheric content, increasing the H_2O content increases the OLR (despite the greenhouse effect of water vapour) because the surface temperature also increases. This dependency stops when the OLR reaches its asymptotic value.

7.5 Exploration of the diversity of post-impact atmospheres with a 1-D reverse climate model

3-D simulations are great to explore in details the post-impact atmospheric evolution due to atmospheric circulation, formation and evolution of clouds, etc. but are not suited (due to their high computational cost) to explore the sensitivity of the results to a wide range of parameters. We demonstrated in the previous section that the thermal profiles of the atmosphere in the GCM are well reproduced by 1D radiative-convective calculations during the main post-impact phase of precipitation (see Fig 7.4AB). Here we use a 1-D radiative-convective reverse climate model presented in Section 7.3.2 to explore the sensitivity of the results obtained with 3-D Global Climate Model. In particular, we want to explore how (i) the total CO_2 and H_2O initial inventories and (ii) the microphysics of clouds can affect the TOA (Top of Atmosphere) radiative budget and thus the duration of the post-impact climate change.

7.5.1 Results from cloud-free numerical climate simulations

We first explore cloud-free numerical climate simulations to investigate the role of the initial, post-impact CO_2 and H_2O atmospheric inventories. Here we vary two parameters: the initial surface

temperature (from 213 to 453 K) and the initial atmospheric pressure (from 3 mbar to 30 bar). Cold temperatures (< 240 K) are typical of global mean pre-impact surface temperatures calculated for CO_2-dominated atmospheres (Forget et al., 2013; Wordsworth et al., 2013). Warm temperatures (> 240 K) are typical of post-impact surface temperatures expected during the main phase of precipitation (corresponding to the second phase depicted in Section 7.4.1). As a comparison, we recall that the maximum post-impact temperature recorded in our 3-D reference simulation (discussed in the previous section) during the precipitation phase is ~ 400 K. Because we assume that water vapor is saturated everywhere in the atmosphere (except in the isothermal [155 K] stratosphere, whenever a stratosphere exists), the total water vapour content and thus the atmospheric CO_2 content can be calculated a posteriori. In our 1-D simulations, the total water vapor partial pressure ranges approximately between 0.1 Pa to 10 bar, and the CO_2 partial pressure between 3 mbar to 25 bar.

From these simulations, we calculated the radiative disequilibrium at the top of the atmosphere (TOA) for various combinations of CO_2 and H_2O atmospheric contents, summarized in Figure 7.7. Our results are unequivocal. Whatever the amount of water vapor, CO_2 in the atmosphere, and whatever the initial post-impact temperature assumed, the atmosphere is always out of equilibrium, and there is no long-term self-maintained greenhouse effect warm climate induced by the impact.

The only balanced solutions are found for very low surface temperatures (below 230 K), for CO_2 partial pressures on the order of a few bar, recovering the cold surface temperatures predicted by 1-D simulations of early Mars assuming CO_2/H_2O atmospheres (Wordsworth et al., 2010a; Ramirez et al., 2014a; Turbet and Tran, 2017). These solutions result from a subtle balance between the greenhouse effect of CO_2, the CO_2 atmospheric condensation and the CO_2 Rayleigh scattering.

In the upper part of the diagram, the outgoing longwave radiation (OLR) has an asymptotic behaviour whatever the CO_2 atmospheric pressure, whenever water vapour is a dominant species. At 1 bar of CO_2 and 2 bar of H_2O, we match the reference case described with the 3-D Global Climate Model in the previous section. The OLR and absorbed stellar radiation (ASR) are 235 and 85 W/m^2, respectively, which gives a TOA radiative disequilibrium of -150W/m^2. The radiative disequilibrium is 30W/m^2 less than calculated in the 3-D simulation (see Fig.7.1B). Although we recover a very similar OLR, the ASR is much higher (+ 30 W/m^2) in the 1-D simulation. The difference is likely due to the fact that the 3-D simulation accounts for the albedo of the thick cloud cover forming in the upper atmosphere, whereas clouds are not taken into account in the 1-D simulations presented here.

We confirm the result obtained in the previous section (with the 3-D GCM) that whenever water vapour becomes a dominant species, the outgoing longwave radiation reaches asymptotic values that are very similar to those calculated by 1-D climate models for moist atmospheres in or near the runaway greenhouse (Kopparapu et al., 2013, 2014). This demonstrates that the result of Segura et al. (2012) that stable, runaway greenhouse states are stable on early Mars, is inaccurate. Although two stable solutions (one cold, one warm) are indeed predicted by calculations assuming purely radiative H_2O-dominated atmospheres, the warm solution is physically implausible (Ingersoll, 1969; Nakajima et al., 1992; Goldblatt and Watson, 2012). First, this warm solution requires water vapour supersaturation levels that are extremely high (see Goldblatt and Watson 2012, Fig. 2), so high that they lie well above the maximum supersaturation limits (even imposed by homogeneous nucleation) of water vapour (Pruppacher and Klett, 1996). Secondly, these purely radiative calculations neglect convective processes that control the thermal structure of the atmosphere. Whenever (i) convection processes are included and (ii) water vapour is limited by saturation, the bistability disappears and we recover the Nakajima limit (Nakajima et al., 1992; Goldblatt and Watson, 2012), i.e. the asymptotic behaviour

of the OLR at the runaway greenhouse.

Whatever the initial reservoir of CO_2 and the amount of H_2O produced in response to the impact event, the duration of the warm period (i.e. for surface temperatures above the freezing point of water) is short. Figure 7.7 provides estimates of the radiative disequilibrium at the TOA for many different combinations of CO_2 and H_2O reservoirs. These TOA radiative disequilibriums can be used to estimate the lifetime of the post-impact warm periods. For instance, for a 1bar CO_2 atmosphere (similar to the 3-D reference simulation), the lifetime of the warm period (around 10-20 Martian years [MY]) is very similar to that calculated with a 3D Global Climate Model. More generally, our calculations are in rather good agreement with the 1-D cloud-free climate calculations of Segura et al. (2002) and Segura et al. (2008).

The duration of the impact-induced warm period increases with increasing CO_2 atmospheric content (see Fig. 7.7) because as CO_2 atmospheric levels increase, the temperature - at a given atmospheric pressure - decreases. This results from the fact that the atmospheric temperature - at saturation - is governed by the partial pressure of water vapour (and not the total pressure). As a result, adding CO_2 cools the upper atmosphere, which drastically reduces the OLR. Fig. 7.7 indicates that, for atmospheres made of 10+ bar of CO_2, the net TOA radiative budget could be reduced by a factor of ten and the duration of the impact-induced warm period could thus increase by a factor of ten, compared to the reference simulation presented in the last section. However, such high CO_2 atmospheric contents are unlikely.

7.5.2 Results from cloudy numerical climate simulations

We now include in our 1-D simulations the radiative effect of a cloud cover (as described in Section 7.3.2). We use these simulations to explore how cloud microphysics (that depends in our 3-D Global Climate Model on the assumed number of cloud condensation nucleis [CCNs], and on the efficiency of the coagulation and sedimentation processes) could affect the results presented in the previous section.

7.5.2.1 The radiative effect of water ice clouds: comparison with Ramirez and Kasting (2017)

We first compare the results of our 1-D reverse cloudy climate model in "temperate" (surface temperature fixed to 273 K) conditions with the results of Ramirez and Kasting (2017). Ramirez and Kasting (2017) used a very similar model to explore if cirrus clouds could have warmed the surface of early Mars above the melting point of water. Figure 7.8 shows a comparison of the results of our model with theirs using similar assumptions. Whenever data points are available, the agreement between the two models is really good. We note a slight difference for the bond albedo of low altitude clouds (affecting subsequently the calculation of the effective flux S_{eff} ; see Fig. 7.8BD) that is likely due to slight differences in the (visible) radiative properties of water ice particles.

Ramirez and Kasting (2017) intentionally limited the maximum altitude of clouds explored in their simulations to the top of the (H_2O) moist convective region. Above, they claimed that production of water ice clouds should be unfeasible. This is why they did not provide any data point for pressures below 0.15 bar. As a result, Ramirez and Kasting (2017) did not capture the radiative effects of water ice clouds above the hygropause, although injections of water ice particles could be produced

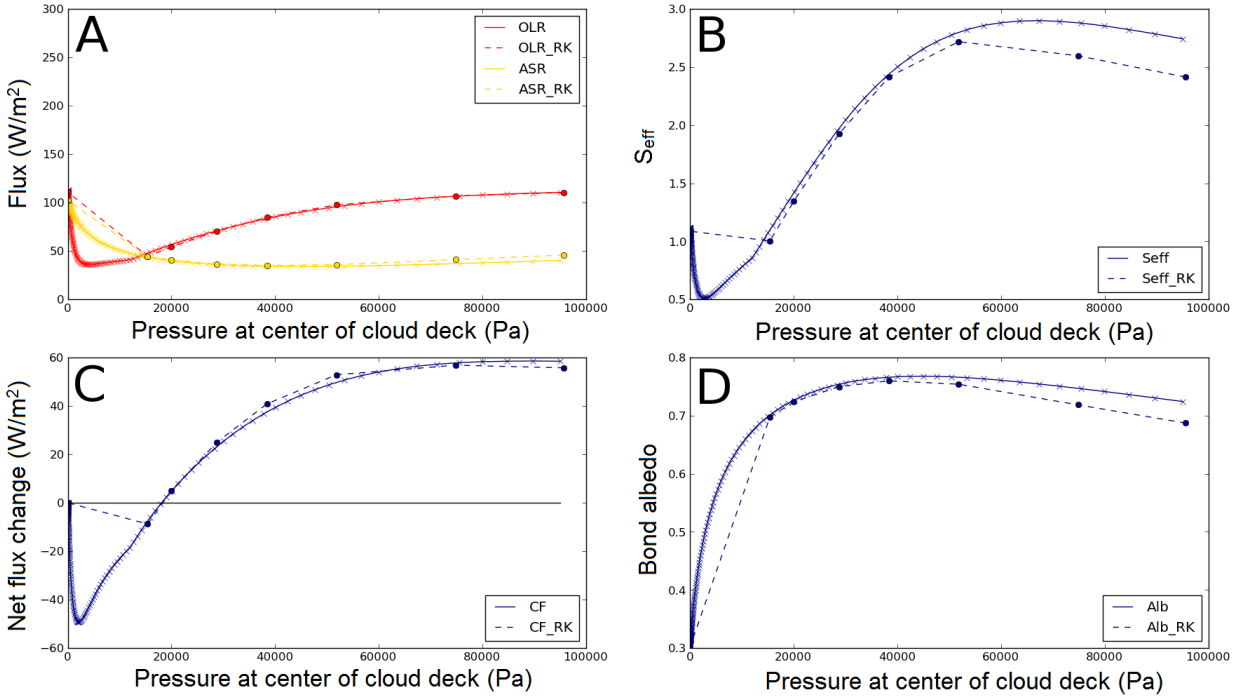

Figure 7.8: Effect of a single cloud layer on the radiative budget of early Mars, as a function of the pressure at the center of the cloud deck. (A) Outgoing longwave radiation (OLR) and absorbed stellar radiation (ASR) ; (B) Effective solar flux S_{eff} ; (C) Net flux change between cloudy and non-cloudy cases ; (D) Bond albedo. The dashed lines correspond to the results of Ramirez and Kasting (2017) (presented in their Figure 2 and Table 1b). The solid lines correspond to the results obtained with our 1-D reverse climate model. We assumed here a 1 bar CO_2 dominated atmosphere (fully saturated in H_2O, except in the stratosphere [if present]). The cloud layer is assumed to be composed only of 10μm cloud particles. The surface temperature is assumed to be that of the freezing point of water, i.e. 273K. The solar flux is assumed to be that of present-day Mars. Note that the effective solar flux corresponds to the value of the solar flux (with respect to the Solar constant on Earth) required for the planet to be at the TOA radiative balance.

for example in response to extreme events such as meteoritic impact events as discussed in Urata and Toon (2013). Interestingly, this corresponds exactly to the altitude where the radiative effect of clouds is maximum (see Fig. 7.8C). This is not surprising because this is where the cloud temperature is minimal. For this reason, the linear interpolations proposed in Figures 2,5,8,9 and 11 of Ramirez and Kasting (2017) should be interpreted with great care by the readers.

Assuming that water ice clouds can exist above the hygropause, our model predicts that only a few tens of % of global cloud coverage should be sufficient to raise the surface of Mars above 273 K. This is illustrated in Figure 7.9A that shows the minimum cloud coverage needed to reach a surface temperature of 273 K in the simulation (assuming a 1 km-thick cloud cover) depending on the surface pressure, cloud particle sizes and relative ice cloud water content (compared to the IWC [Ice Water Content]) defined in Section 7.3.2. In theory, water ice cloud particles above the hygropause could thus warm early Mars above the melting point of water easily, even for relatively low (and thus reasonable) cloud coverage.

However, we do not want to give the reader the impression that this provides a satisfactory scenario to warm early Mars. For clouds to be stable at such high altitudes, a strong mechanism must be at play to replenish the upper atmosphere in cloud particles that are expected to sedimentate rapidly (Ramirez and Kasting, 2017). The strong greenhouse warming of water ice clouds reported by Segura et al. (2008) and Urata and Toon (2013) is likely due to the fact that they neglected the sedimentation of ice particles. This hypothesis is supported by back of the envelope calculations of sedimentation rates of icy particles (Ramirez and Kasting, 2017), and confirmed by our 3-D Global Climate model simulations. As soon as the initial impact-induced water vapour reservoir is depleted, the production rate of cloud particles drops and upper atmosphere water ice clouds rapidly disappear because of gravitational sedimentation. Therefore, the lack of sedimentation is the most reasonable hypothesis to explain the difference between Segura et al. (2008); Urata and Toon (2013) and our results. Until a plausible, long lasting source of upper atmospheric water ice clouds is evidenced, the water ice cloud greenhouse warming reported by Segura et al. (2008) and Urata and Toon (2013) is unlikely.

7.5.2.2 Post-impact 1-D cloudy simulations

We showed in Section 7.4.2 (using our 3-D climate simulations) that a thick, complete impact-induced cloud cover can be sustained in the upper atmosphere of early Mars for most of the duration of the main phase of precipitation following a large impact event. During this phase, surface temperatures are significantly higher than the value of 273 K explored above. Here we investigate how the cloud properties (size of particles, cloud thickness, etc.) can change the radiative effect of the impact-induced cloud cover and thus the net TOA radiative budget, during the post-impact main phase of precipitation.

Because we showed in the previous sections that (1) the thermal profiles calculated with our 1-D reverse climate model match very well those derived from 3-D Global Climate Model simulations during the main phase of precipitation, and that (2) the inclusion of a cloud layer in our 1-D model gives satisfactory results with regards to the existing literature (Ramirez and Kasting, 2017) for a surface temperature of 273 K, we can now safely apply our 1-D cloudy numerical climate simulations to higher post-impact surface temperatures (T$>$ 273 K). We use these simulations to investigate the radiative effect of the thick, complete cloud cover predicted by 3-D simulations.

Our findings are summarized in Figure 7.9, that presents the minimal cloud coverage required to

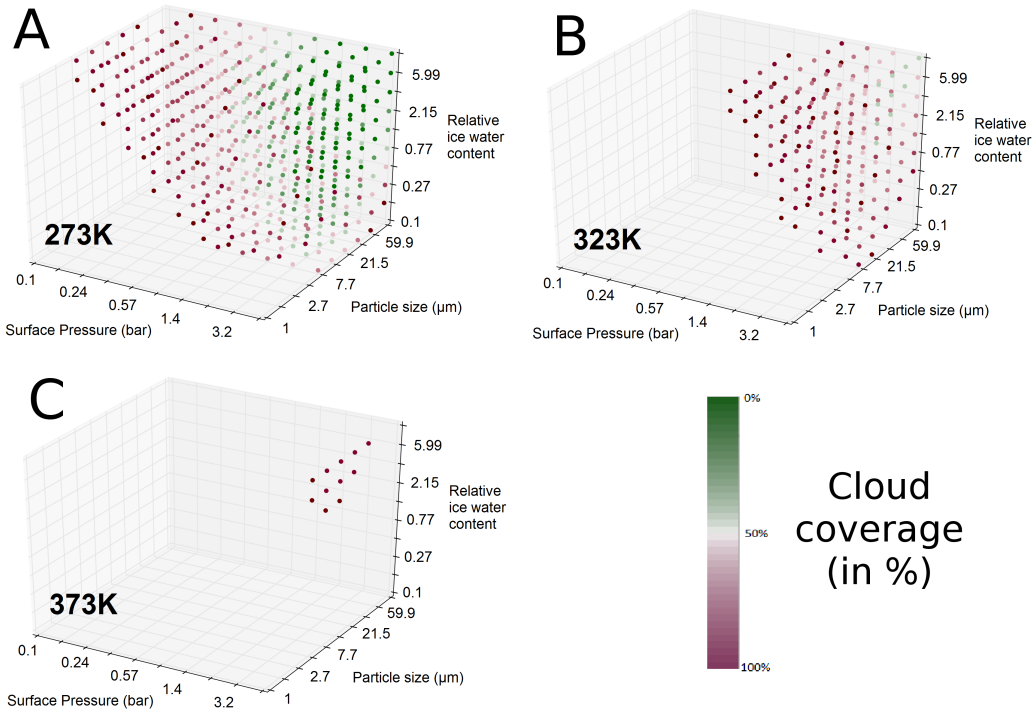

Figure 7.9: 3-D scatter plots of the minimal cloud coverage required to warm early Mars above the indicated post-impact surface temperatures (273, 323 and 373 K), for various CO_2 atmospheric pressure, relative ice water content (i.e. cloud thickness) and cloud particle size. Fractional cloud cover is modeled by averaging the radiative fluxes from cloudy and cloud-free 1-D simulations. No dot was plotted for sets of parameters unable to warm the planet above the indicated surface temperature even with a 100% cloud coverage.

warm the surface of early Mars above the indicated surface temperatures (323 and 373 K). For the two surface temperatures considered, there is at least one combination of parameters (cloud altitude, cloud particles, cloud content and surface pressure) that can stably keep the surface temperature of early Mars above the indicated post-impact temperatures (323 and 373 K). However, although the constraints on (i) the possible total cloud coverage and (ii) the maximum altitude of the cloud layer are relaxed during the main post-impact phase of precipitation (as demonstrated with 3-D simulations in Section 7.4.2), the range of parameters that provide a positive radiative balance gets narrower as the surface temperature increases. In fact, the solutions that work - at high post-impact surface temperatures - are limited to very thick multi-bar CO_2-dominated atmospheres[3] endowed with a very thick cloud cover located very high in the atmosphere, for cloud particles around 10μm in size. This very restrictive set of conditions - although it could theoretically lead to a self-sustained impact-induced warm atmosphere - seems very difficult to attain.

7.6 Conclusions and Discussions

We explored in this Chapter the environmental effect of the largest impact events recorded on Mars using a hierarchy of climate models, ranging from a 1-D radiative-convective reverse model to a full 3-D Global Climate Model. The models were adapted to properly account for thick CO_2-H_2O atmospheres expected after the collision of large impactors on Mars.

Our results indicate that the lifetime of the impact-induced warm period is usually very short, because the radiative budget at the top of the atmosphere (TOA) is in strong deficit. Whatever the initial CO_2 atmospheric content and whatever the size of the impactor, we show that the impact-induced stable runaway greenhouse state predicted by Segura et al. (2012) is physically inconsistent.

For an early Martian atmosphere made of 1 bar of CO_2, a large impact would produce ~2.6 m of surface precipitation per Earth year, until the reservoir of water vapour gets completely depleted. This is quantitatively similar to the results of Segura et al. (2002), obtained using a 1-D cloud free climate model. Surface evaporation of precipitation is weak. The total amount of precipitation produced in response to the impact event can thus be well predicted by the total amount of water vapor initially vaporized/sublimed in the atmosphere (from the impactor, the impacted terrain and from the sublimation of permanent ice reservoirs heated by the hot ejecta layer).

3-D simulations show that an optically thick, upper atmospheric cloud cover forms uniformly on the planet. Our 3-D simulations - taking into account the microphysics of clouds - indicate that this cloud cover contributes to an enhanced cooling of the surface of Mars, compared to cloud-free calculations. Although strong precipitation is generated in this cloud cover, most of it is re-evaporated in the atmosphere while falling. Instead, surface precipitation patterns are governed by lower atmospheric large scale circulation. In our 3-D simulations, precipitation (rainfall) is maximum near the equator, at the ascending branch of the Hadley cell, and are minimum near the tropics, at the descending branch. Although the cumulated amount of precipitation is rather high everywhere on the planet (at least 20 m of cumulated precipitation), we find that the main region of valley networks formation on Mars (located around -30°S in the pre-TPW topography, see Fig 1 in Bouley et al. 2016) coincides with a

[3]This behaviour can be understood by looking back at Figure 7.7 that shows that for post-impact cloud-free atmospheres, and for a fix water content/surface temperature, increasing the initial CO_2 atmospheric content decreases the TOA radiative disequilibrium. For example, for a surface temperature of 373K, and a CO_2 initial surface pressure of 10 bar, the net TOA radiative disequilibrium is ~ -40 W/m^2.

minimum of cumulated precipitation in our 3-D simulations (see Fig 7.6). We confirm the results of Segura et al. (2008) and Urata and Toon (2013) that - in theory - water ice clouds could significantly extend the duration of the post-impact warm period. However, as soon as the main bulk of the water vapour reservoir has condensed on the surface, the production rate of upper atmospheric cloud particles drops, and high altitude water ice clouds disappear because of gravitational sedimentation. This prevents the water ice cloud greenhouse warming mechanism from working.

We also find that the duration of the impact-induced warm period increases with increasing CO_2 atmospheric content. For instance, the duration can be increased by a factor 10 for a 10 bar CO_2 atmosphere (with respect to a 1 bar CO_2 atmosphere). However, such high CO_2 contents are unlikely.

In summary, the environmental effect of the largest impact events recorded on Mars are characterized by (i) a short impact-induced warm period, (ii) a "low" amount of precipitation (because there is almost no surface re-evaporation of precipitation), (iii) precipitation patterns that are uncorrelated with the observed regions of valley networks formation, and (iv) deluge-style precipitation. All these arguments put together indicate that the largest impact events[4] are unlikely to be the cause of formation of the Late Noachian valley networks.

[4] even though they may have contributed to the resurfacing of the martian surface through (i) deposition of a hot, globally distributed ejecta layer and (ii) by intense precipitation across the entire Martian surface; and even though they may have contributed to the mineralogic activity.

Chapter 8

The impact of mid-size meteoritic impacts on Early Mars

Contents

8.1 Preamble

I showed in Chapter 7 that the largest meteoritic impact events (diameter of impactor > 100km ; number of events $\sim 10^1$) recorded on Mars could have warmed the surface and the atmosphere of Mars globally well above the freezing point of water, and for periods up to tens of Martian years. However, the nature of the precipitation associated with such events (short, intense deluge-style precipitation ; total duration of precipitation is short ; total amount of cumulated runoff is small ; precipitation patterns do not match the position of the valley networks) is not compatible with our current understanding of the formation of valley networks and lakes on early Mars (Barnhart et al., 2009; Luo et al., 2017).

Some authors have argued that the smaller impactors (5 km < diameter of impactor < 50 km ; number of events $\sim 10^3$) - much more numerous than the very large impactors discussed in Chapter 7 - could have induced a regional climate change, and more importantly could have melted locally permanent water ice reservoirs (Wordsworth et al., 2013; Wordsworth, 2016). The melted water could have subsequently carved the valley networks. The full scenario is detailed in Figure 8.1. This scenario is particularly seducing because the position of the permanent ice reservoirs (in a cold, ancient Mars scenario) coincides with the regions of Mars where most of the late Noachian valley networks have been observed (Hynek et al., 2010; Wordsworth et al., 2013; Bouley et al., 2016). Moreover, atmospheric processes (sublimation, adiabatic cooling, precipitation) would slowly replenish water (after an impact

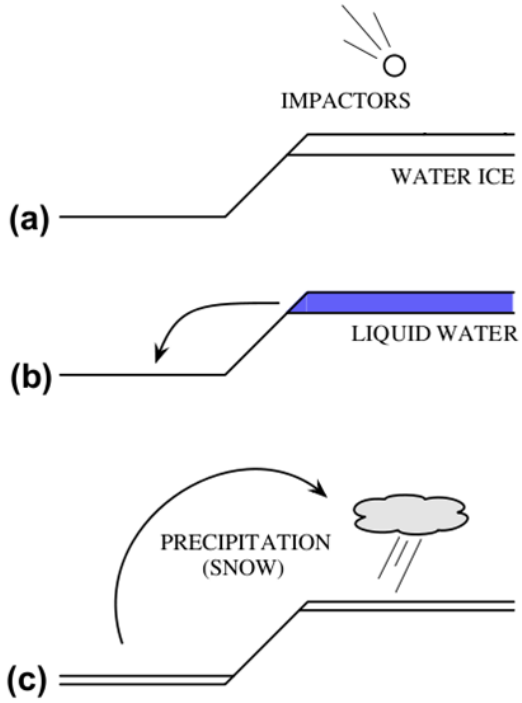

Figure 8.1: Schematic of the proposed scenario of formation of valley networks by regional impact events. (a) In a cold ancient Mars scenario, permanent ice deposits are mainly located in the colder highland regions of the planet. (b) An impactor hits the permanent ice deposits, causing transient ice melting and flow to regions of lower altitude. This step (b) is expected to occur on a relatively short timescale. (c) On much longer timescales, ice is transported back to the original location (i.e. the highland regions) via sublimation and subsequent adiabatic cooling and precipitation. Adapted from Wordsworth et al. (2013).

event) on the southern highlands of Mars. This would be a very efficient mechanism to recharge the valley network water sources between two impact-induced melting events.

Here we use sophisticated numerical tools to explore this scenario in details. First, in collaboration with Vladimir Svetsov (from the Institute for Dynamics of Geospheres, Russian Academy of Sciences), I used the 2-D version of the SOVA hydrocode (Shuvalov, 1999) to model short-term impact cratering processes. The hydrocode is designed to simulate the effect of meteoritic impact events from the very beginning of the collision with the planetary atmosphere, up to a few hours later, using minimum timesteps of the order of 10^{-2} seconds. The SOVA hydrocode provides estimates of the post-impact temperature field as well as estimates of the injection and trajectory of both water and stony particles emerging from the impact event, from which it is possible to calculate the temperature and thickness of the ejecta layer that is rapidly deposited on the surface. These post-impact conditions were then used as input in a 3-dimensions Global Climate Model to explore the environmental effect (precipitation, greenhouse warming, etc.) of impact events of moderate intensity. Eventually, the goal of the work presented in this Chapter is to derive from these simulations estimates of the amount of rainfall and/or snowmelt that could be expected after impact events of moderate size.

The work presented in this chapter is in preparation for a future publication. The full reference is: Martin Turbet, Vladimir Svetsov & Francois Forget, **"Exploring the environmental effect of medium-size meteoritic impacts on Early Mars combining hydrocode and global climate model simulations"**, in preparation, 2018.

8.2 Results from hydrocode simulations

8.2.1 The SOVA hydrocode and the simulation setup

Here we used a 2-dimensional version of the hydrodynamic computer code SOVA (Shuvalov, 1999) to model the interaction of an impactor with the atmosphere and the surface of early Mars. The SOVA hydrodynamical code (or "hydrocode") is a multi-material Lagrangian-based model designed to investigate a wide range of gas dynamical and geophysical problems. It has been used for a broad range of applications, in particular to model impact cratering processes (Shuvalov and Artemieva, 2002; Shuvalov, 2009; Svetsov, 2007, 2011; Svetsov and Shuvalov, 2016).

Here we consider the impact of a comet 16 km in diameter (this is the geometric average between 5 and 50 km) hitting the surface of Mars at a velocity of 10 km/s, and with a vertical angle (90°) with respect to the surface. A time-lapse of the event is shown in Fig. 8.2. The comet consists of pure water with density of 1g cm^{-3}. In the hydrocode simulations, the atmosphere of Mars is assumed to be isothermal, with a temperature fixed to 210 K. The atmospheric pressure is fixed to 0.15 bar. We adopted a fixed (temperature-independent) heat capacity for the atmosphere, equal to 650 J kg^{-1} K^{-1}.

We used here the 2-D version of the SOVA hydrocode, which is based on a system of polar coordinates r (distance from the core of Mars) and θ (the polar angle ; equal to 0 at the location of the impact and equal to π at the antipodal point). Both r and θ are decomposed into 300 grid points. Values of r starts from the core of Mars up to $\sim 10^4$ km above the surface and are tightened near the surface, with a minimum vertical resolution of 200 m. Values of θ (in radians) starts from 1.1801×10^{-4} up to π, corresponding to a minimum horizontal resolution of 400 m near the impact location. The minimum resolutions adopted in the vertical and horizontal resolutions correspond to 1/40th and 1/80th of the diameter of the impactor, respectively.

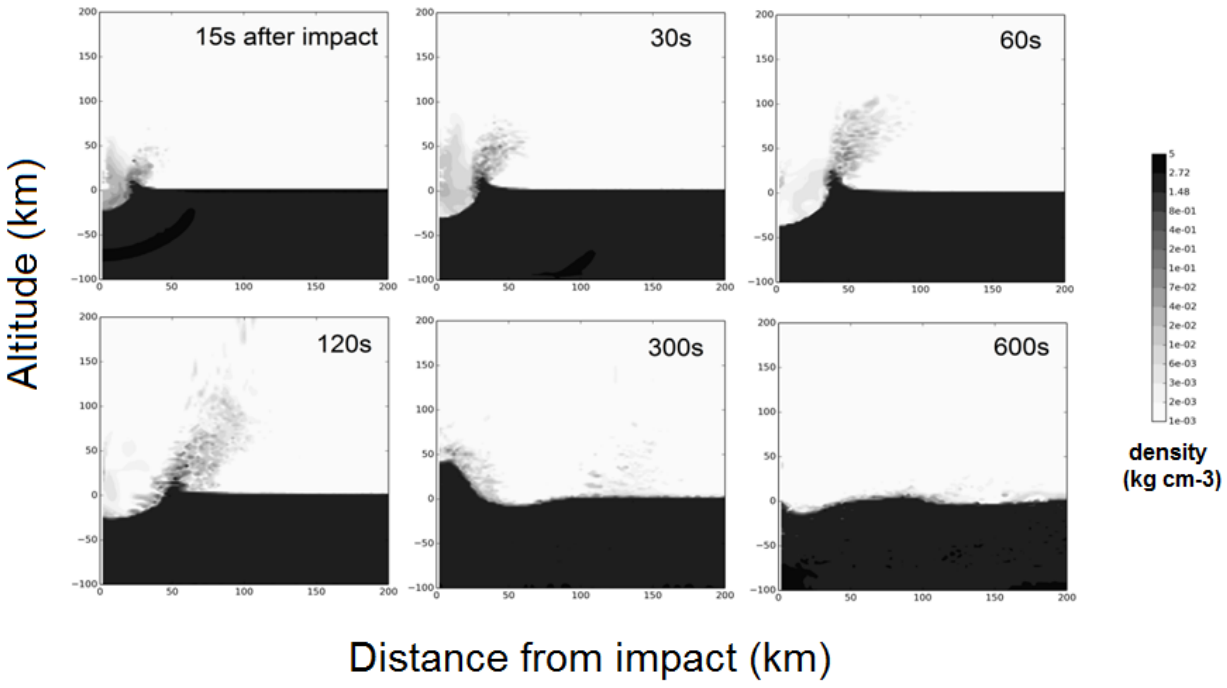

Figure 8.2: Time lapse of a SOVA hydrocode numerical simulation showing the volumetric density of materials following the impact of a 16 km-diameter comet hitting vertically the surface of early Mars at 10 km/s.

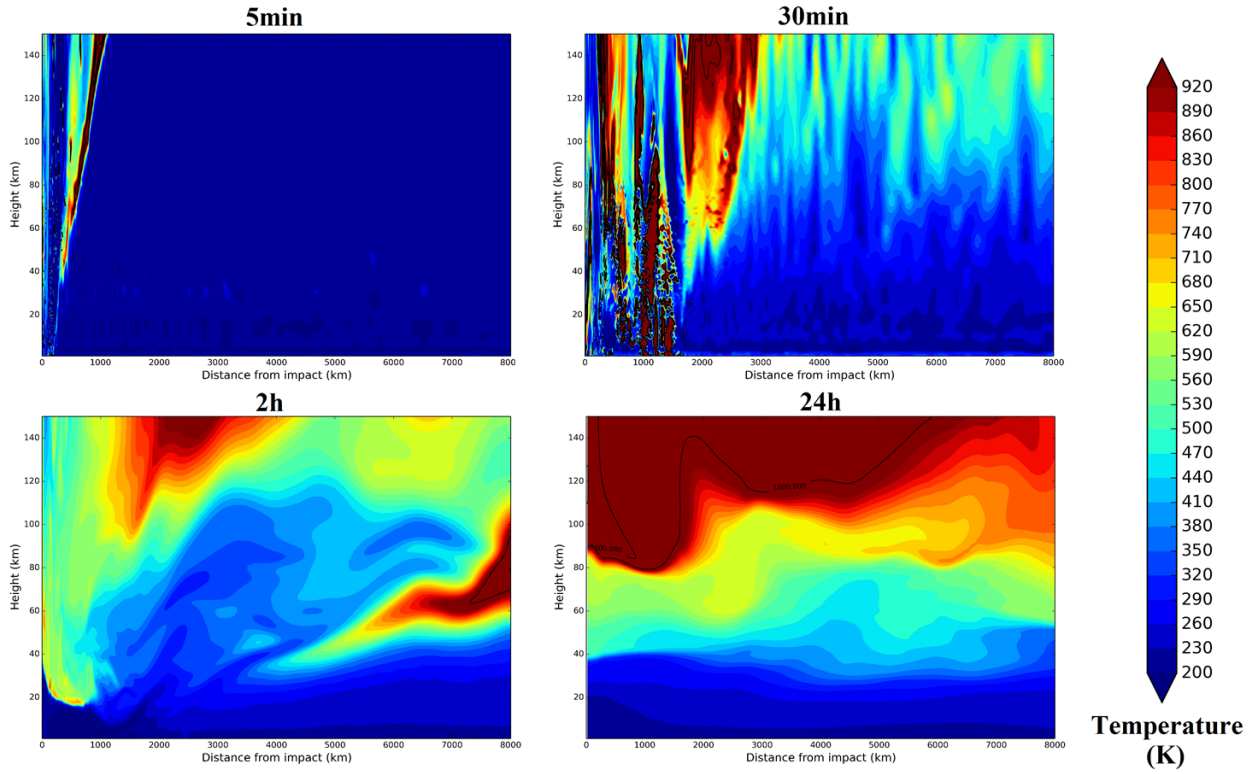

Figure 8.3: SOVA post-impact temperature field (in K) as a function of the height from the surface (in km) and the distance from the impact event along the surface (in km), at four different times after the impact event (5 min, 30 min, 2 h and 24 h). Note that the warming recorded in the upper atmosphere is artificial. This is a consequence of the radiative cooling of the atmosphere not being taken into account in the SOVA hydrocode simulations.

Particles of rock and water that are produced by the impact event are treated into six different categories according to their size: particles from 1 to 0.1 cm ; from 0.1 to 0.01 cm ; from 0.01 to 10^{-3} cm ; from 10^{-3} to 10^{-4} cm ; from 10^{-4} to 10^{-5} cm ; and from 10^{-5} to 10^{-6} cm. Particles can then be heated, transported, etc.

8.2.2 Post-impact temperature field and ejecta layer distribution

When the impactor (here a comet) hits the surface of Mars, stony particles from the ground and water particles from the comet are formed and ejected in all possible directions. While flying through the atmosphere, the particles warm the various layers of the (initially cold) atmosphere. A post-impact temperature field is described in Fig. 8.3. Particles that are ejected in all directions produce a warming that propagates from the location of the impact toward distant locations of Mars. Note that these temperature maps can actually be considered as upper estimates of the post-impact temperature field because the radiative cooling of the atmosphere is not taken into account in the hydrocode simulations

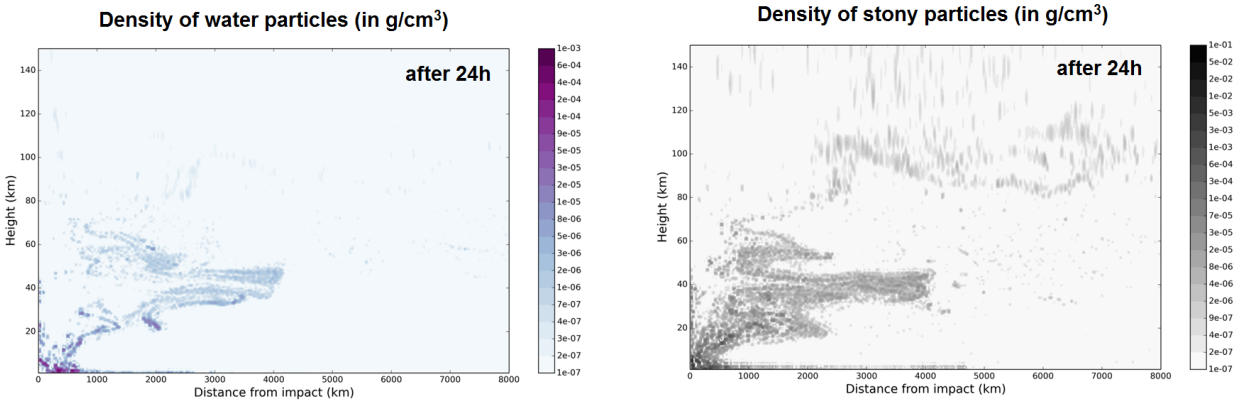

Figure 8.4: Post-impact water particles (in g cm^{-3}) and stony (in g cm^{-3}) particles fields, 24 hours after the impact event in the SOVA hydrocode simulation.

presented here. Therefore, the high temperatures recorded in the upper atmospheric layers (1000+K) are completely artificial. Nevertheless, hydrocode simulations show that the temperature perturbation in the lower atmosphere is almost entirely dissipated after $\sim$ 24 h (see Fig. 8.3). The mean temperature increase in the troposphere is actually limited to a few tens of Kelvins. This demonstrates that the direct warming of the lower atmosphere by moderate impact events is rather limited in the long-term.

Another important aspect is the environmental effect of the hot, ejecta layer deposited on the surface. It is possible to track the trajectory and position of stony particles (see Fig. 8.4), and record whenever they reach the surface of Mars. From this calculation, we can derive the thickness of the warm ejecta layer that get deposited on the surface, and that might subsequently produce melting of the permanent southern highlands ice deposits. Our findings are summarized in Fig. 8.5. The thickness of the ejecta layer can be as thick as 1 km near the location of the impact and decreases rapidly with increasing distance from the impact crater. At 100 km from the impact crater, the ejecta thickness is $\sim$ 300 m ; at 1000 km, the ejecta thickness is $\sim$ 30 cm. At the antipodal point of the impact crater, the ejecta layer thickness is on the order of 0.1-1 mm. The 10^{-3} slope actually provides a very good fit of the ejecta layer thickness obtained from the hydrocode numerical simulations. This distribution law agrees remarkably well with empirical observations of near-field ejecta on the Moon (Lorenz, 2000). It also gives satisfactory results with respect to reference scaling laws of crater ejecta distributions (Housen et al., 1983) and previous estimates of the impact ejecta thickness on Mars (Weiss and Head, 2016). The total mass of the ejecta layer is $\sim 7{\times}10^{16}$ kg, i.e. nearly 30 times the mass of the 16 km diameter comet that hit the surface of Mars.

The temperature of the hot ejecta layer is difficult to calculate. It requires to perform detailed radiative transfer calculations in a hot, dusty atmosphere for many particles, depending on their size. For this reason, we decided to calculate the temperature of the ejecta layer based on conservative, energy conservation arguments. We fix arbitrarily the temperature of the ejecta to 1000 K, which corresponds to $\sim$ 30% of the total kinetic energy of the impactor. This is an upper limit on the fraction of total kinetic energy used (Sleep and Zahnle, 1998), and thus also an upper limit on the temperature of the ejecta layer.

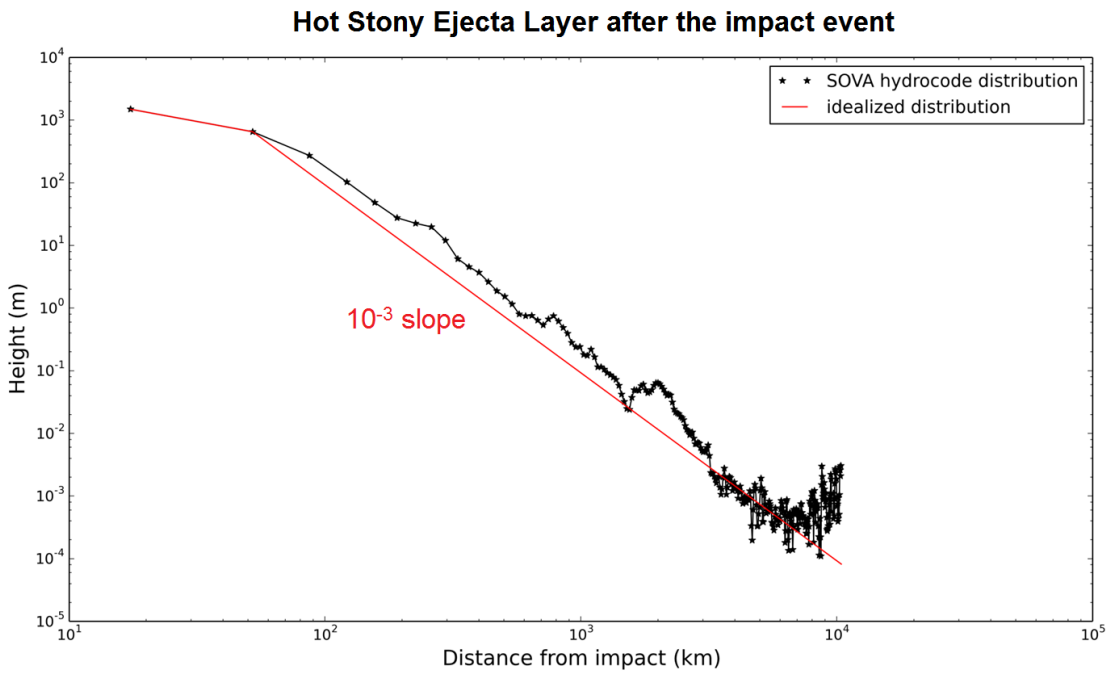

Figure 8.5: Hot stony ejecta layer thickness (in m) as a function of the distance from the impact crater along the surface (in km). The black line corresponds to the results obtained from the hydrocode simulations. The red line is a simple fit based on a 10^{-3} power law.

8.3 Results from 3-D Global climate simulations

8.3.1 The LMD Generic Global Climate Model and initial simulation setup

We use now the LMD Generic 3-D Global Climate model to simulate the environmental effect of moderate-size impact events, based on the results of the hydrocode simulations. We assume that Mars is initially endowed with a 1 bar CO_2-dominated atmosphere. The obliquity is fixed to 45°. The initial state (cold and dry) is very similar to the 1 bar CO_2 simulation described in Wordsworth et al. (2013), except that we used here the pre-True Polar Wander (pre-TPW) topography of Bouley et al. (2016). Water is initially trapped as ice in permanent reservoirs mainly located in the southern highlands (see Fig 8.9, row 1).

We suddenly add the effect of the cometary impact (described in the previous section) in the Global Climate Model. Our strategy is to maximize the environmental effect of the impact event. For this, we proceed with the following inputs:

- First, we take into account the effect of the 1000 K ejecta layer (with a thickness distribution calculated using the 10^{-3} slope, based on the results of the hydrocode simulations ; see previous section). This is done by adjusting the temperature of the different subsurface layers in the model, as a function of the distance to the impact crater (here, at 15°S 30°E ; i.e. right on a permanent ice deposit) up to 500 km away from the impact crater (because this is where most of the warming [90+%] by the hot ejecta layer is produced). In total, the thermal energy of the ejecta corresponds to 30% of the kinetic energy of the impact.

- Then, we take into account the warming of the atmosphere. Hydrocode simulations indicate that tropospheric warming should be limited to a few tens of Kelvins. To be conservative, we artificially warm the entire atmospheric column up to 350 K, at locations that are within 500 km from the impact crater (i.e., where the ejecta layer is thicker than 1 m). This warming corresponds to 1% of the kinetic energy of the impact.

- Eventually, we account for the sublimation of the water (1) from the impactor (a comet, here), (2) from the water initially present in the impacted terrain, and (3) from the permanent ice reservoirs that are suddenly heated by the hot ejecta layer. For this, we arbitrarily assume that 2 m of water is initially sublimed into the atmosphere (with a constant H_2O vapour mass mixing ratio equal to 0.1 from the surface to the top of the atmosphere) at locations that are within 500 km from the impact crater (i.e., where the ejecta layer is thicker than 1 m). The production of water vapor corresponds to 10% of the kinetic energy of the impact (through consumption of latent heat of sublimation), and more than 3 times the mass of water initially brought by the comet.

I believe that this is a conservative procedure to describe the maximum environmental effect of the cometary impact discussed in the previous section.

8.3.2 The sequence of events

We track in Fig. 8.6 the temporal evolution of the surface temperature, water vapor and water ice atmospheric columns, following the initial perturbation described in the previous subsection.

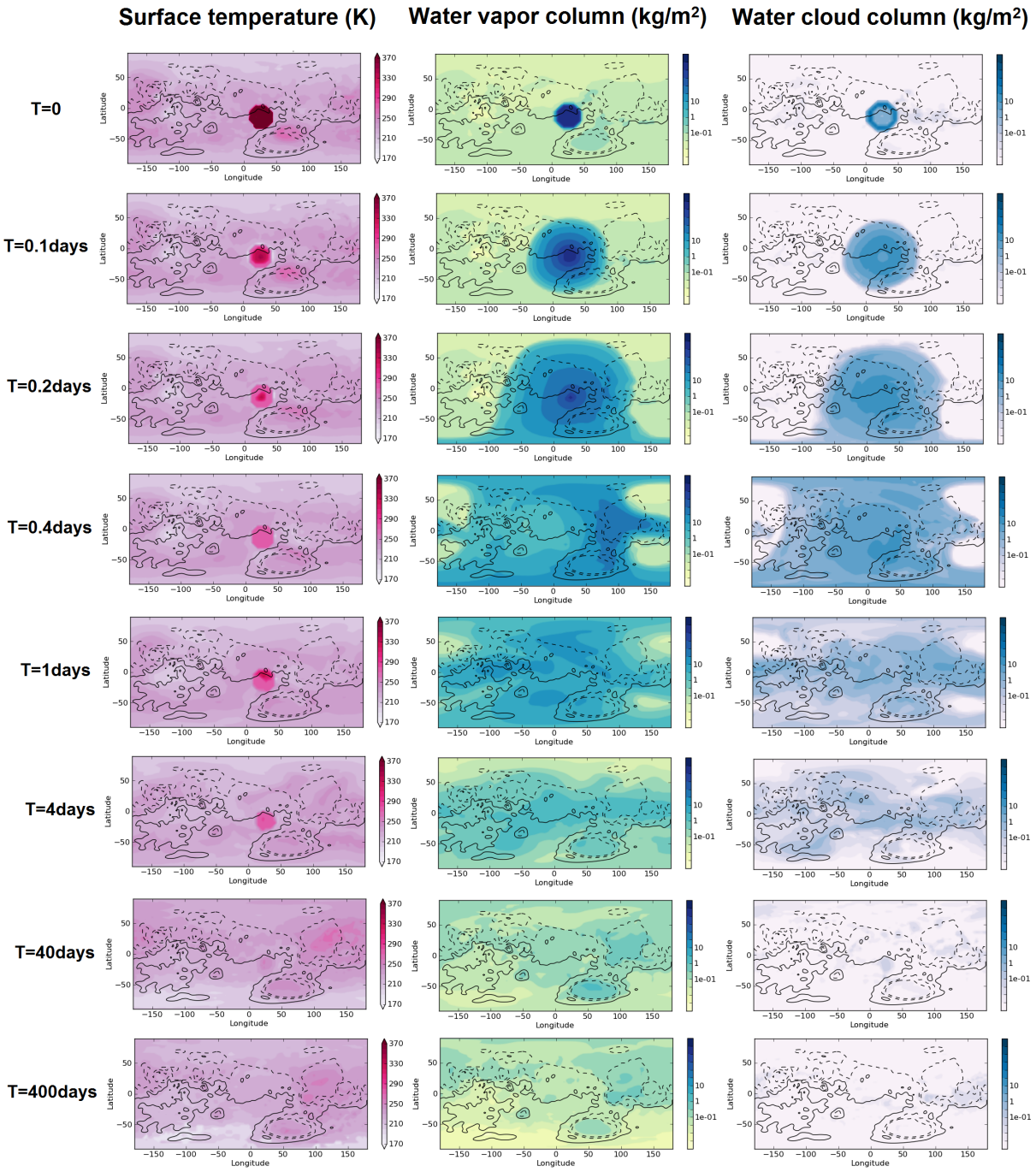

Figure 8.6: Temporal evolution of the surface temperature (in K), water vapour mass column (in kg/m^2) and water cloud mass column (in kg/m^2) maps simulated by the GCM, following the collision of a 16 km diameter comet hitting a cold, early Mars planet in the region of permanent ice deposits.

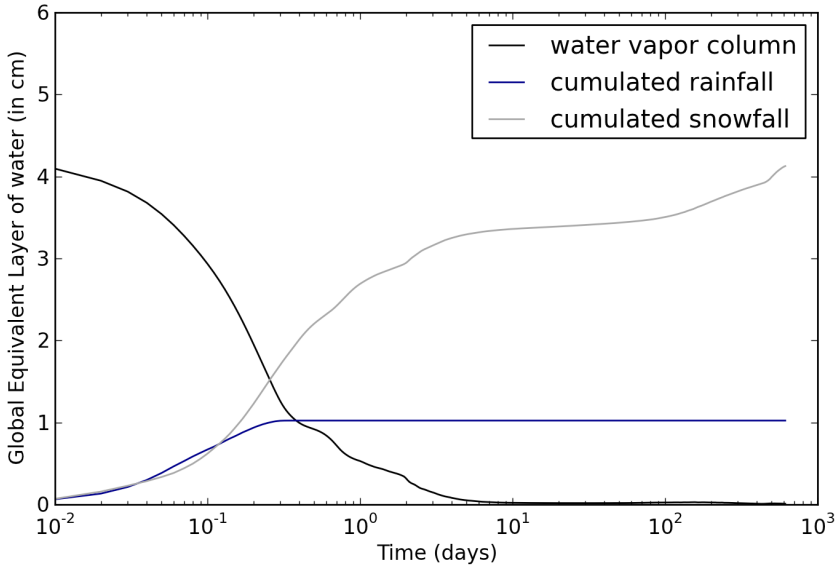

Figure 8.7: Globally-averaged temporal evolution of the total water vapor content (in black), cumulated rainfall (in blue) and cumulated snowfall (in grey) simulated by the GCM. All quantities are Global Equivalent Layer (GEL) expressed in cm.

The propagation of the initial atmospheric perturbation during the first day - although rather impressive - is unrealistic. The atmospheric perturbation propagates in the Global Climate simulations at the maximum possible speed in a GCM (i.e. speed of sound) of $\sim$ 200 m/s (see Fig.8.6), whereas hydrocode simulations show that stony particles can propagate much faster (see Fig.8.3).

We note that after $\sim$ 1 day, the surface temperatures (not the subsurface temperatures, that remain hot for much longer periods of time) have dropped below 0°C everywhere on the planet, because the radiative cooling of the surficial part of the ejecta layer is very efficient. Meanwhile, most of the initial atmospheric water vapour content has condensed on the surface, mostly as rain during the first few hours following the impact, mostly as snow during the following few days (see Fig. 8.7). Precipitation is distributed in a concentric circle centered around the impact crater, and the amount of precipitation decreases with the distance to the impact crater (about 1 m of precipitation near the impact crater ; about 1-10 mm at the antipodal point). Re-evaporation of precipitation is extremely limited (less than 1%). These results are not surprising, since the nature of the forcing is similar to the type of extreme events discussed in Chapter 5.

In summary, after a few days only, the initial perturbation (atmospheric and surface temperatures, water vapour content) has been almost entirely dissipated and the planet is almost back to initial conditions[1], with three exceptions: (1) the subsurface temperatures in the region of the impact crater are still hot, (2) the surface of Mars is temporarily covered by a thin layer of reflective snow and (3) significant amounts of water vapour have been injected into the upper atmosphere.

[1]Note that we assumed here that the impact was produced by a (water-rich) comet hitting a permanent ice reservoir. For dry impactors (e.g. meteorites) hitting dry regions of Mars, 3-D numerical climate simulations (not shown) indicate that the environmental effect of the impact event is even more limited.

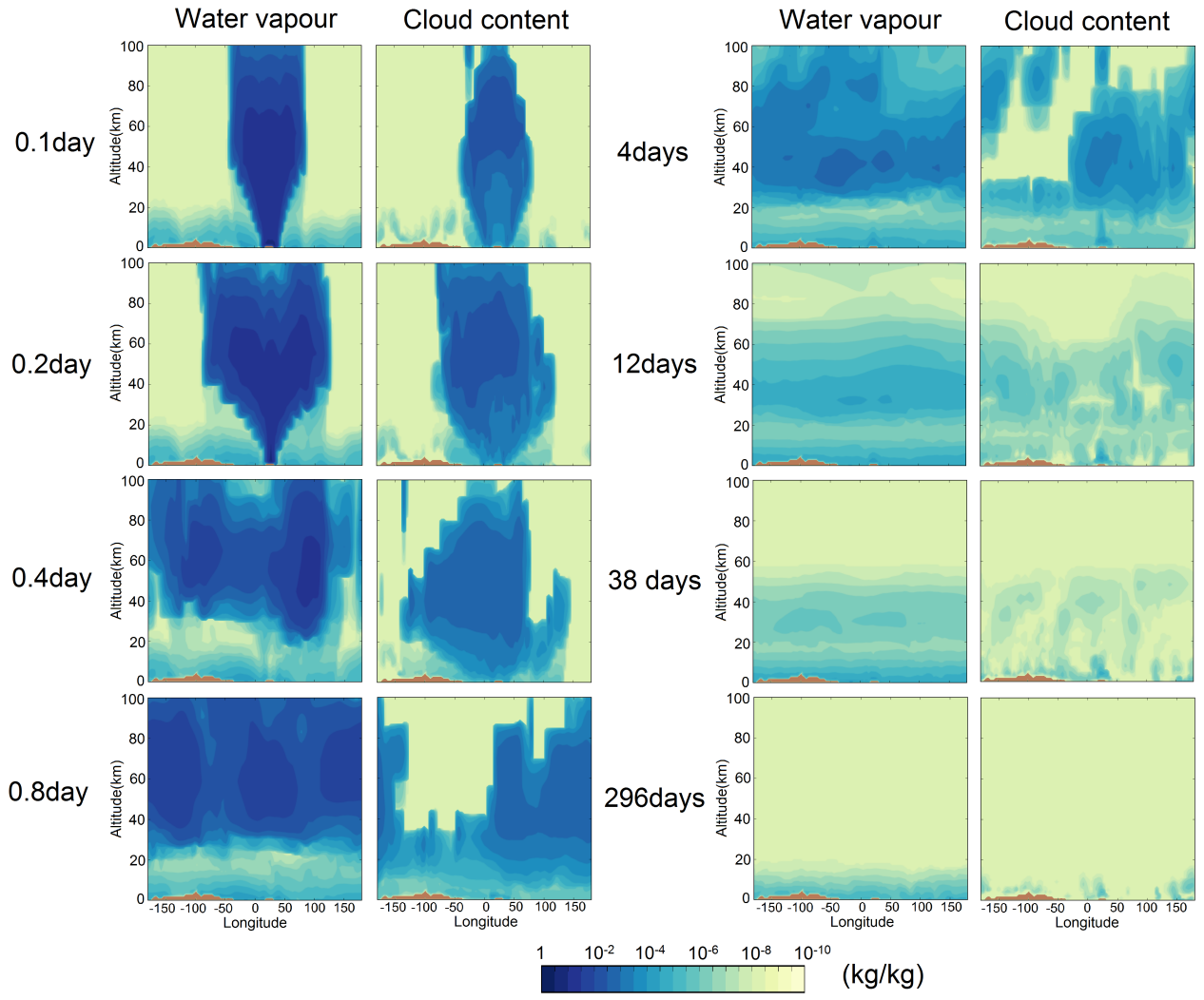

Figure 8.8: Temporal evolution of water vapour and water cloud content fields in the GCM simulations (in kg/kg of air) as a function of longitude and altitude, along latitude -15°N (corresponding to the latitude of the impact crater). The field is drawn at 8 different times after the impact event: 0.1, 0.2, 0.4, 0.8, 4, 12, 38 and 296 days.

Fig. 8.8 shows the evolution of the amount of water vapour and clouds in the atmosphere at the latitude of the impact crater. The strong updraft triggered by the impact injects - within a few hours - large amounts of water vapour in the upper atmosphere. After a few days, the water vapour is horizontally mixed in the upper layers, and peaks at 10^{-2} kg/kg of air levels between 40 and 80 km (or 1000 and 10 Pa). The injection of water vapour also heats the upper layers through radiation absorption and latent heat release. This warming is actually sufficient to dissipate all the CO_2 ice clouds.

Meanwhile, water ice clouds are produced to rather large quantities, up to 10^{-3} kg/kg of air between 40 and 80 km. We thus confirm the hypothesis of Urata and Toon (2013) that impact events can trigger the formation of significant amount of water ice clouds at high altitudes. However, our simulations do not produce the long-term warming predicted by Urata and Toon (2013), mostly because the residence time of upper atmospheric water ice clouds is short. After $\sim 10^2$ days, water ice clouds have entirely sedimented to the lower atmospheric layers and the surface (see Fig. 8.8). In fact, once the initial upper atmospheric water vapour content has been entirely depleted (through conversion into water ice clouds), the production of water ice clouds stops and the upper atmospheric water ice cloud content drops. Therefore, the long-term radiative effect of water ice clouds is very limited[2] and has almost no impact on the environmental effect of moderate-size impact events in our model.

8.4 Estimates of the maximum impact melt volume

We showed in the previous section that even when maximizing the environmental effect of the modeled impact event, the duration of the warm period and associated hydrological cycle is extremely short, on the order of a few days. The impact has somehow a "one-shot" effect on the climate. There is no re-evaporation of precipitation, and because the greenhouse warming is very limited, water ice heated by the hot ejecta should similarly melt only once, no more.

Based on this argument, we can estimate the maximum amount of water ice melt by making the conservative assumption that 100% of the thermal energy of the hot impact-induced ejecta layer is used to melt ice from permanent reservoirs (only if present). For the event described in the previous section, we calculated the maximum amount of melt based on (1) the ejecta layer distribution calculated from the hydrocode simulations (and assuming a uniform temperature of ejecta of 1000 K) and (2) the position of the permanent ice reservoirs calculated from GCM simulations. This is illustrated in Fig. 8.9, rows 1 and 2.

For the simulation described in details in this Chapter, we derive a maximum melt production of 85 cm Global Equivalent Layer (GEL). 80% of this melting is produced in regions located within 100 km of the impact crater (see Fig. 8.9, row 3).

We can roughly extrapolate this number to estimate the maximum cumulated melt production caused by all the impactors between 5 and 50 km in diameter[3], assuming (1) that impact events are randomly distributed over the surface (some bolides hit right in the permanent ice deposits, some don't) and (2) that the total number of impact events is equal to 10^3, based on Martian isochrons (Hartmann, 2005). In total, the maximum cumulated melt production is 150 m GEL (Global Equivalent Layer).

[2] In fact, our numerical simulations indicate that the radiative warming of water ice clouds is anyway offset by the thermal emission to space of the upper atmospheric layers that get heated by the release of latent heat and absorption of radiation by water vapour.

[3] This corresponds roughly to impact craters of 50 to 300 km in diameter

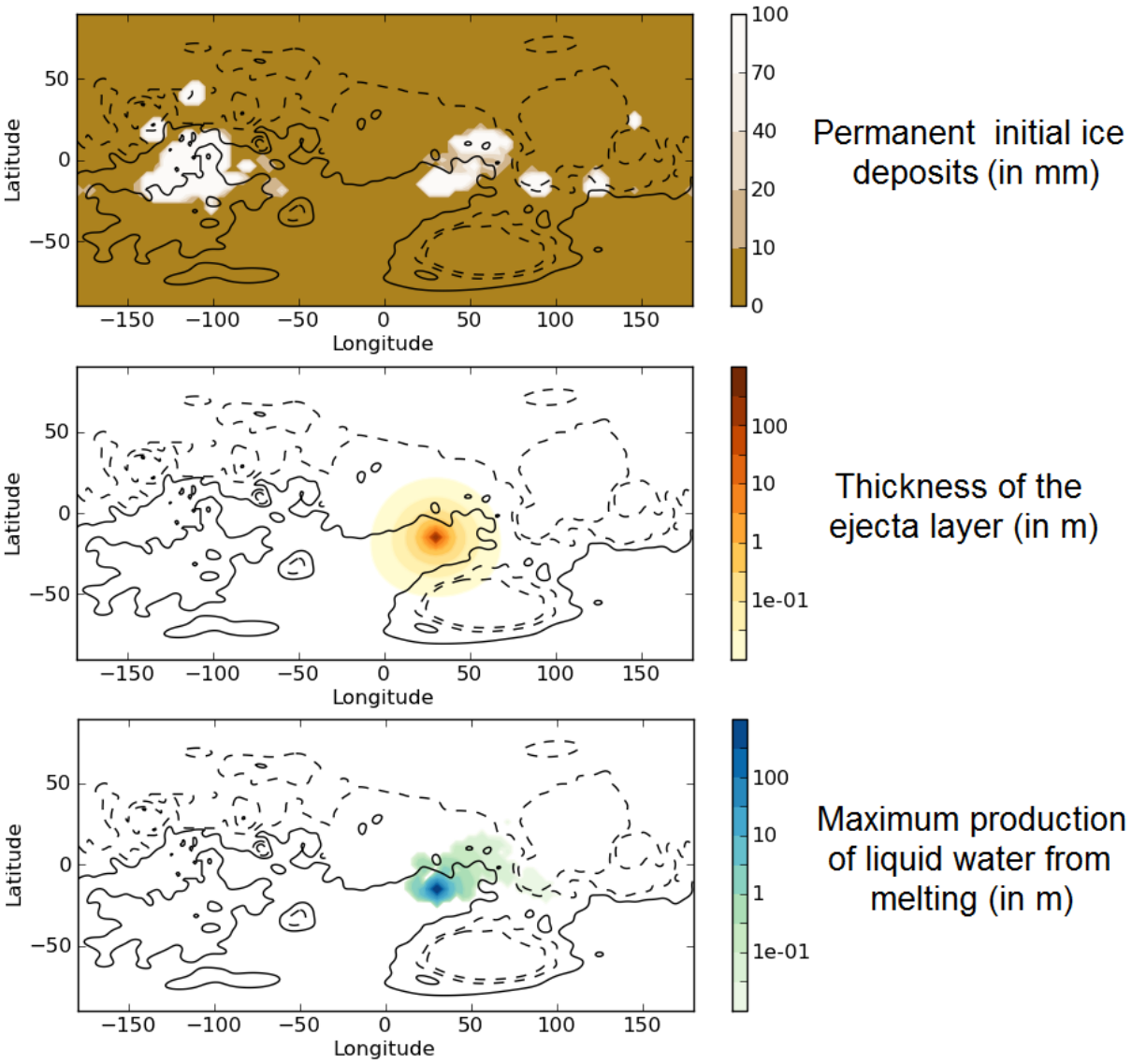

Figure 8.9: Initial permanent ice deposits before the impact event (top pannel), thickness of the ejecta deposit (mid pannel) and maximum melt production of ice reservoir by the hot ejecta deposit. It is assumed here that the impact hit directly the permanent ice reservoirs, which maximizes the total melt production.

We use the same strategy to account for the total melt production from impactors with a diameter lower than 5 km. Making the conservative assumption that $\sim$ 30% of the impact energy is converted into heating of the ejecta layer, we calculate that the maximum cumulated melt production for impactors with a diameter lower than 5 km is roughly 70 m GEL.

In summary, the maximum cumulated melt production for impactors of diameter lower than 50 km is roughly $2{\times}10^2$ m GEL.

8.5 Discussion and conclusions

Here we demonstrated, using a combination of numerical models designed to explore the effect of impact events from very short to long timescales, that the environmental effect of small and mid-size impact events (diameter of impactor roughly lower than 50 km) is really limited. The most significant environmental effect of the impact is the production of a thick ejecta layer deposited all over the planet, and that can potentially melt permanent water ice deposits.

We calculated that the **maximum** melt production for impactors of diameter lower than 50 km is $\sim$200 m GEL. This number is more than one order of magnitude lower than the most recent estimate of the **minimum** total amount of liquid water (5 km GEL) required to carve all the valley networks (Luo et al., 2017)[4].

Unless the atmosphere was very different from the one assumed in this Chapter (e.g. with much more greenhouse warming), or unless an important mechanism is missing here, the total melt production of $\sim$200 m GEL - calculated for all the impact events producing craters lower than $\sim$ 300 km in diameter - is a very conservative upper estimate. Detailed modeling of the interplay between the ejecta layer and ice permanent deposits (contact melting) combined with an accurate estimate of the initial temperature of the ejecta, combined with a detailed modeling of the climate feedbacks is necessary to better constrain the estimates of the total melt production.

However, unless the most recent estimate of the minimum total amount of liquid water (5 km GEL) - required to carve the valley networks - calculated by Luo et al. (2017) is wrong (i.e. too high) by several orders of magnitude, our calculations demonstrate here that the small and moderate-size meteoritic impacts cannot be the primary cause of valley networks formation.

In conclusion, and based on the results presented in Chapter 7 and the present one, I believe that impact events are poor candidates to explain the formation of the Late Noachian valley networks. An alternative, seducing solution is explored in the next Chapter.

[4] The actual amount of runoff needed to carve the Martian valley networks could have been several orders of magnitude higher though (Hoke et al., 2011).

Chapter 9

Greenhouse warming by reducing gases on early Mars

Contents

9.1 Preamble

I showed in the previous chapters that extreme events (e.g. meteoritic impacts, outflow channel formation events) are poor candidates to explain the formation of the Martian valley networks. I explore in this Chapter another mechanism to warm early Mars: the greenhouse warming produced by reducing gases, such as H_2, CH_4, NH_3, etc.

Reducing gases have been historically proposed by Sagan (1977) as a possible source of greenhouse warming in the atmosphere of early Earth and early Mars. More than 35 years later, Ramirez et al. (2014a) used a simplified 1D climate model to demonstrate that the atmosphere of early Mars could indeed have been warmed by reducing gases - in particular H_2 - that produce as strong greenhouse effect whenever combined in large quantities with CO_2. Yet, as of 2016, there were two main reasons why this scenario was not very convincing:

- The calculated levels of di-hydrogen (H_2) required to warm the surface of early Mars in a CO_2-dominated atmosphere were so high that a very strong source of production of H_2 was required to offset the efficient H_2 atmospheric escape to space (Ramirez et al., 2014a).

- The calculated levels of methane (CH_4) required to warm the surface of early Mars in a CO_2-dominated atmosphere were so high that CH_4 should have been photodissociated by XUV solar photons, forming highly reflective (and thus radiatively cooling) photochemical hazes. Moreover, stratospheric CH_4 can absorb a significant fraction of the incoming solar radiation and thus can produce an anti-greenhouse effect (Haqq-Misra et al., 2008; Wordsworth et al., 2017).

- Ammonia (NH_3) should have been photodissociated efficiently by XUV solar photons. H_2 would have escaped to space and the remaining N_2 should have built up in the atmosphere. Yet, we do not see any evidence for that scenario in present-day Mars atmosphere.

Wordsworth et al. (2017) recently calculated that the collision-induced absorptions (CIAs) produced by CO_2-H_2 and CO_2-CH_4 pairs were likely underestimated in Ramirez et al. (2014a) [1]. The remarkable implication of this result is that the levels of H_2 and CH_4 required to warm the surface of early Mars are much lower than calculated by Ramirez et al. (2014a), by a factor up to 6 (Ramirez, 2017). In this condition, the H_2 source and CH_4 anti-greenhouse effects become much less of an issue, and the scenario in which early Mars may have been warmed by the greenhouse effect of reducing gases becomes much more plausible.

My contribution to the exploration of this scenario is twofold:

- First, through experimental measurements of the ab initio calculations of Wordsworth et al. (2017) of the CO_2-H_2 and CO_2-CH_4 collision-induced absorptions. This is the main topic of Chapter 11.

- Then, through 3-D Global Climate simulations of early Mars taking into account the strong greenhouse warming of reducing atmospheres. This is the topic of the present chapter.

The work presented in this Chapter is somehow an extension of Wordsworth et al. (2015) that looked at the effect of large greenhouse warming on the surface and atmosphere of early Mars. Wordsworth et al. (2015) focused only on the case of large water content scenarios (large enough that a significant fraction of Mars was covered by open water oceans). Here I explore how the climate of early Mars would look like depending on (1) how much greenhouse gas is present and (2) how much surface water is available.

For this, I designed various 3-D numerical climate simulations of CO_2 dominated atmosphere (based on the work of Forget et al. 2013; Wordsworth et al. 2013), in which I added various quantities of H_2, producing an efficient greenhouse warming through strong collision-induced absorptions produced by the CO_2-H_2 and H_2-H_2 pairs. These simulations include various total water inventories, depicting various possible regimes ranging from a water-poor early Mars (total inventory of water on the order of 7 m GEL[2], 3 times less than the present-day Mars reservoir) to a water-rich early Mars (>500 m GEL, corresponding to the presence of a large ocean). Eventually, I adapted the 3-D Global Climate Model simulations to account for the effect of oceans as well as the effect of impact crater lakes that would form in a warm climate.

In Section 9.2, we present the LMD 3-D Global Climate Model, with a focus on all the improvements made (1) to account for the greenhouse warming produced by reducing gases and (2) to account

[1] Given the lack of available data, Ramirez et al. (2014a) used the CIA of N_2-H_2 pair instead of CO_2-H_2.

[2] The total water inventory is expressed here in global equivalent layer (GEL), which is the globally averaged depth of the layer that would result from putting all the available water in the system at the surface in a liquid phase.

for hydrologic feedbacks (oceans, lakes and glaciers). In Section 9.3, we reassess the amount of hydrogen required to produce fluvial activity on Mars, based on the results of 3-D climate simulations. Eventually, we explore in Section 9.4 the nature(s) of the early Mars climate and hydrology for strong greenhouse warming scenarios, and for a wide range of possible total water inventories.

The work presented in this chapter is in preparation for a future publication. The full reference is: Martin Turbet & Francois Forget, **"Influence of reducing greenhouse warming and water inventory on the climate of early Mars"**, in preparation, 2018.

9.2 Method

We used the LMD Generic Model, a full 3-Dimensions Global Climate Model (GCM) that initially derives from the LMDz Earth (Hourdin et al., 2006) and Mars (Forget et al., 1999) GCMs. This GCM has previously been developed and used for the study of the climate of ancient Mars (Forget et al., 2013; Wordsworth et al., 2013, 2015; Turbet et al., 2017a).

9.2.1 General description of the model

Simulations presented in this paper were performed at a horizontal resolution of 64 × 48 (e.g. 5.6° × 3.75°; at the equator, this gives in average 330 km × 220 km) in longitude × latitude. In the vertical direction, the model is composed of 26 distinct atmospheric layers, covering altitudes from the surface up to 10 Pascals. Hybrid σ coordinates (where σ is the ratio between pressure and surface pressure) and fixed pressure levels were used in the lower and the upper atmosphere, respectively. The dynamical time step of the simulations is $\sim$ 3 minutes. The radiative transfer and the physical parameterizations are calculated every $\sim$ 2 hours and $\sim$ 30 minutes, respectively.

Parameterizations of turbulence and convection, full CO_2 and H_2O cycles (condensation, evaporation, sublimation, cloud formation, precipitation, etc.), were all parameterized as in Wordsworth et al. (2013) and Turbet et al. (2017a) (see Chapter 5 for more details). I focus below on the new parameterizations developed specifically for the present study.

9.2.1.1 Radiative Transfer

The GCM includes a generalized radiative transfer code able to account for a variable gaseous atmospheric composition made of a mixture of CO_2, H_2, and H_2O (line list and parameters were taken from HITRAN 2008 database (Rothman et al., 2009)) using the 'correlated-k' approach (Fu and Liou, 1992) suited for fast calculation. Our correlated-k absorption coefficients directly derive from Wordsworth et al. (2013). They take into account the CO_2 Collision-Induced Absorptions (Gruszka and Borysow, 1998; Baranov et al., 2004; Wordsworth et al., 2010a), as well as the H_2O MT_CKD continua (Clough et al., 2005). Compared to Wordsworth et al. (2013), we added the radiative effect of H_2 through self H_2-H_2 and foreign CO_2-H_2 collision-induced absorptions (CIA). H_2-H_2 CIA were taken from Ramirez et al. (2014a) (Supplementary Materials). CO_2-H_2 CIA were taken from Wordsworth et al. (2017).

We adopted here a mean solar flux of 111 W.m^{-2} (75% of the present-day value of Mars; 32% of Earth's present-day value; as in Wordsworth et al. 2013), corresponding to the reduced luminosity derived from standard solar evolution models (Gough, 1981) 3.7 Gya, during the Late Noachian era.

Physical parameters	Values
Mean Solar Flux	111 W m^{-2} (75% of present-day Mars)
Bare ground albedo	0.2
Liquid water albedo	0.07
H_2O ice albedo	0.55
CO_2 ice albedo	0.5
Obliquity	40°
Surface Topography	Pre-True Polar Wander (modified if oceans are present)
Surface roughness coefficient	0.01 m
Ice thermal inertia	1500 J m^{-2} $s^{-1/2}$ K^{-1}
Ground thermal inertia	250+7 x_{H_2O}. J m^{-2} $s^{-1/2}$ K^{-1}, where x_{H_2O} is the soil moisture (in kg m^{-3})

Table 9.1: Physical Parameterization of the GCM.

9.2.1.2 Soil Model

To account for the thermal conduction in the subsurface, we use a 20-layers thermal diffusion soil model. The mid-layer depths range from $d_0 \sim 0.15$ mm to $d_{19} \sim 80$ m, following the power law $d_n = d_0 \times 2^n$ with n being the corresponding soil level, chosen to take into account both the diurnal and seasonal thermal waves.

We assumed the thermal inertia of the regolith I_{ground} to be equal to:

$$I_{\text{ground}} = I_{\text{dry}} + 7\ x_{H_2O}, \tag{9.1}$$

where $I_{dry} = 250$ J m^{-2} $s^{-1/2}$ K^{-1} and x_{H_2O} is the soil moisture (in kg m^{-3}). The dry regolith thermal inertia is slightly higher than the present-day Mars global mean thermal inertia in order to account for the higher atmospheric pressure (Piqueux and Christensen, 2009). This expression (plotted in Fig. 9.1) has been derived from the standard parameterization of the ORCHIDEE (Organising Carbon and Hydrology In Dynamic Ecosystems) Earth land model (Wang et al., 2016). Moreover, we arbitrarily fix the thermal inertia of the ground to a value of 1500 J m^{-2} $s^{-1/2}$ K^{-1}, whenever the snow/ice cover exceeds a threshold of 1000 kg m^{-2} (e.g. 1m).

We assume that the martian regolith has a maximum water capacity of 150 kg m^{-2}, based on a simple bucket model widely used in the Earth land community (Manabe, 1969; Wood et al., 1992; Schaake et al., 1996)[3]. When the water quantity exceeds this limit, the overage is treated as runoff. Similarly, we limit the maximum amount of snow/ice surface deposits to 3000 kg m^{-2} (i.e. 3 m).

9.2.1.3 Topography

We used the pre-True Polar Wander (pre-TPW) topography (see Fig 9.2, second row) from Bouley et al. (2016). Bouley et al. (2016) showed that the formation of the late Noachian valley networks

[3]This is actually known as the "Manabe" bucket model.

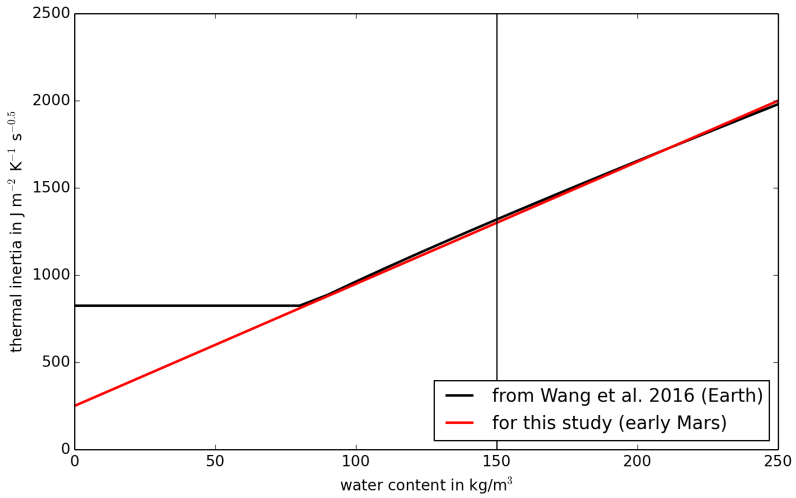

Figure 9.1: Thermal inertia of the soil as a function of the liquid water loading (in kg/m^3). The black line corresponds to the standard parameterization used in the ORCHIDEE Earth land model (Wang et al., 2016). The red curve corresponds to the parameterization that we used in the present study to account for the thermal inertia of the martian ground in early Mars conditions. Our parameterization is compatible with both (1) a standard dry ground thermal inertia of 250 J m^{-2} s$^{-1/2}$ K^{-1} and (2) the water-loading-dependency of the thermal inertia used in the ORCHIDEE Earth land model.

should have precluded the formation of most of the Tharsis volcanic bulge. The pre-TPW topography is based on the present-day MOLA (Mars Orbiter Laser Altimeter) Mars surface topography shown in Figure 9.2, first row (Smith et al., 1999; Smith et al., 2001), but without Tharsis and all the younger volcanic features. Moreover, the formation of Tharsis should have produced a large True Polar Wander (TPW) event of 20°-25°, which is also taken into account in the pre-TPW topography. This topography was adopted for numerical climate simulations assuming low water contents (GEL<10 m).

In the simulations that account for an ancient ocean, the pre-TPW topography was adjusted (see Fig 9.2, third and fourth rows) so that the minimum altitude were -4.26 and -2.54 km[4]:

- The -4.26 km shoreline case (third row) was calculated assuming a total surface water inventory of $\sim$ 100 m GEL.

- The -2.54 km shoreline case (fourth row) corresponds to the putative northern ocean shoreline based on delta deposit locations from Di Achille and Hynek (2010). $\sim$ 550 m GEL is needed to reach this shoreline. The same assumption has been adopted in Wordsworth et al. (2015).

All regions matching these elevations were then treated as 'oceanic regions'.

[4]These negative altitudes are defined according to the reference MOLA topography map (Smith et al., 1999; Smith et al., 2001).

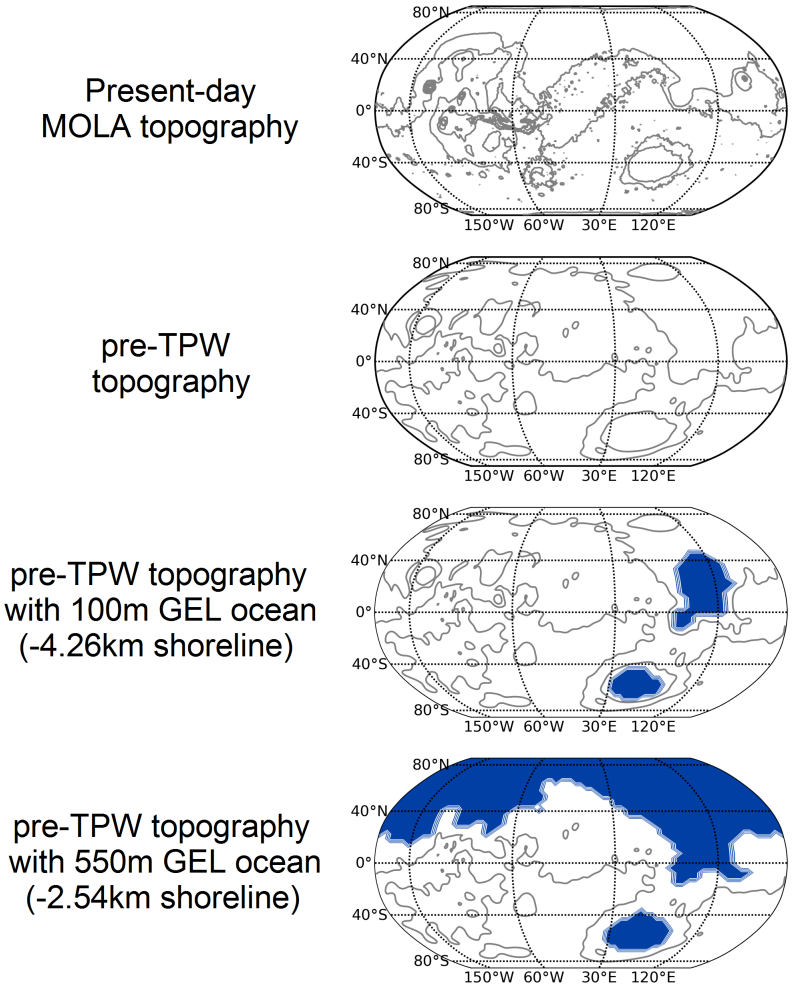

Figure 9.2: Various topography maps discussed and used in this work. The topography map on top is the classical present-day Mars MOLA topography (Smith et al., 1999; Smith et al., 2001). The second corresponds to the pre-TPW topography map (Bouley et al., 2016). The third and fourth rows correspond to the pre-TPW topography maps with the inclusion of ancient oceans (at -4.26 and -2.54 km shoreline, respectively).

9.2.1.4 Parameterization of oceanic regions

We use the simplified ocean model from Codron (2012) to treat oceanic regions. This model has been previously used to explore the past climate(s) of the Earth (Charnay et al., 2013). The modeled ocean is composed of two layers. The first upper layer (50 m deep) represents the surface mixed layer, where the exchanges with the atmosphere take place. The second lower layer (150 m deep) represents the deep ocean.

The oceanic model computes the formation of sea ice. Sea ice forms when the ocean temperature falls below 273 K and melts when its temperature rises above 273 K. The changes in ice extent and thickness are computed based on energy conservation, keeping the ocean temperature at 273 K as long as ice is present. A layer of snow can be present above the ice, and the surface albedo is calculated accordingly (Codron, 2012; Charnay et al., 2013).

The transport of heat by the ocean circulation is not taken into account here. The transport of sea ice is not either taken into account.

9.2.1.5 Parameterization of ancient lakes

The unsubmerged regions of the planet are covered by a large number of craters that can potentially host lakes. It is important to include these lakes in early Mars climate models because the presence of lakes controls whether the different regions of Mars are desertic or not (without lakes, the modeled precipitation would be erroneous). For each unsubmerged region (i.e. non-oceanic region, or region with an altitude higher than the assumed shoreline), we allow a fraction of up to 50% of the surface to be covered by lakes (we name this fraction α_{lake}). This is the maximum possible fraction of submerged regions in a highly craterized terrain, before all the lakes overflow (Matsubara et al., 2011).

In our parameterization, the contribution of lakes is twofold:

- First, we consider them as a source of water vapor, and we calculate their rate of evaporation E (or sublimation, if the temperature is below 273 K) as follows:

$$E = \alpha_{\text{lake}} \, \rho_1 C_d V_1 [q_{\text{sat}}(T_{\text{surf}}) - q_1], \tag{9.2}$$

  where ρ_1 and V_1 are the volumetric mass of air and the wind velocity at the first atmospheric level, $q_{\text{sat}}(T_{\text{surf}})$ is the water vapor mass mixing ratio at saturation at the surface, and q_1 is the mixing ratio in the first atmospheric layer. The aerodynamic coefficient is given by $C_d = (\kappa / ln(1 + z_1/z_0))^2 \sim 2.5 \times 10^{-3}$, where $\kappa = 0.4$ is the Von Karman constant, z_0 is the roughness coefficient and z_1 is the altitude of the first level ($\sim$ 18 meters). Simultaneously, evaporation from the solid ground is then multiplied by a factor (1-α_{lake}).

- Secondly, we take into account the effect of lakes on the surface albedo. If the surface temperature is below or equal to 273 K, the albedo of the lakes is 0.55; otherwise it is 0.07.

The formation and evolution of the impact crater lakes are discussed in the next subsection.

9.2.2 Convergence of the simulations

All the numerical climate simulations were first run 10 martian years (as in Forget et al. 2013) to reach a first atmospheric equilibrium, with surface and atmospheric temperatures roughly equilibrated. Yet,

it would take several orders of magnitude longer for the water cycle to reach an equilibrium. The reason is twofold:

- First, in the regions that are cold enough for permanent ice deposits to exist, sublimation and light snowfall are the dominant forms of water transport. Water ice distribution can then take thousands of years and even much more to reach a steady state (Wordsworth et al., 2013).
- Secondly, the evolution of impact crater lakes to their final size and location can also take a very long timescale, because this evolutions results from a subtle combination of evaporation of the lake, precipitation on the lake, and runoff from surrounding terrains.

9.2.2.1 Ice deposits and convergence algorithm

The locations of stable surface ice deposits were calculated using the ice equilibration algorithm of Wordsworth et al. (2013), later used in Turbet et al. (2017a). After the first ten martian years of evolution, we proceed to the following steps: (1) we run the GCM for two martian years then (2) we extrapolate the ice layer field h_{ice} evolution calculation using:

$$h_{\mathrm{ice}}(t + n_{\mathrm{years}}) = h_{\mathrm{ice}}(t) + n_{\mathrm{years}} \times \Delta h_{\mathrm{ice}}, \tag{9.3}$$

with Δh_{ice} the annual mean ice field change of the one-martian-year previous simulation and n_{years} the number of years requested for the extrapolation. Then, (3) we eliminate the seasonal ice deposits and (4) we limit the extrapolated ice field to a maximum value of 3000 kg m^{-2} (i.e. 3 m). Eventually, (5) we repeat the process.

This algorithm was shown (Wordsworth et al., 2013) to be insensitive to the proposed initial ice field location at the beginning of the simulation, assuming that the scheme was repeated a sufficient number of times.

In total, for our control simulations, we looped the algorithm 20 times, with n_{years}=50 years for the first 10 loops and n_{years}=20 for 10 more loops. Because our simulations are much warmer than those of Wordsworth et al. (2013), the water transport is much more efficient, and the convergence of the algorithm is more rapid.

Note that, for the cases of "dry" simulations (those that do not include oceans), we arbitrarily normalize the total amount of permanent water ice deposits to 1 m GEL after each iteration of the ice equilibrium algorithm.

9.2.2.2 Formation and evolution of ancient lakes

To calculate the formation and evolution of impact crater lakes, we based our algorithm on the works of Howard (2007) and Matsubara et al. (2011). Our algorithm relies on the X-ratio, defined as:

$$X = \frac{E - P}{P R_{\mathrm{b}}}, \tag{9.4}$$

with P the annual mean rate of precipitation (mm/year), E the annual mean rate of evaporation above the lakes only (mm/year), R_{b} is the fraction of precipitation above the unsubmerged land and that ends up in runoff, in the lake. These three quantities can be recorded at each grid point in our Global Climate Model simulations.

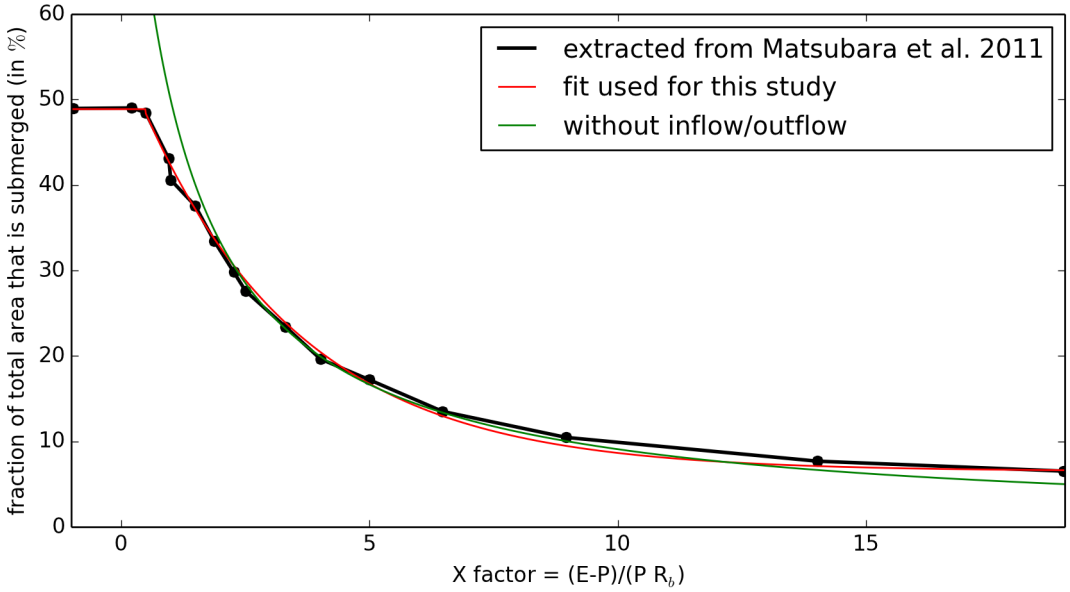

Figure 9.3: Fraction of lakes area (black line) covering a craterized terrain as a function of the X-ratio, derived from the results of Matsubara et al. (2011). The red line is the fit that we used for the lake evolution algorithm. Without inflow/outflow, $\alpha_{\text{lake}} = \frac{1}{X+1}$, corresponding to the green line.

Matsubara et al. (2011) provide a useful relationship between the fraction of unsubmerged lands (equal to 1-$\alpha_{\rm lake}$) as a function of this X-ratio, for a highly craterized terrain typical of Late Noachian terrains. This relationship is plotted in Fig. 9.3 (black line). We then fit this relationship (red line) as follows:

$$\begin{cases} \alpha_{\rm lake} &= 49 \text{ for } X < 0.5 \\ \alpha_{\rm lake} &= 6.5 + 42.5\ e^{\frac{X-0.5}{3.2}} \text{ for } 0.5 < X < 19 \\ \alpha_{\rm lake} &= 0 \text{ for } X > 19 \end{cases} \tag{9.5}$$

where $\alpha_{\rm lake}(X)$ is expressed in %.

Our lake evolution algorithm is performed as follows. After the first ten martian years of evolution[5], we proceed to the following steps: (1) we run the GCM for two martian years and we record at each timestep of the simulation of the second year (i) the precipitation over each grid, (ii) the evaporation of the lakes over each grid (= 0 if no lakes) and (iii) the runoff from unsubmerged lands to lakes. We assume that - for each GCM grid - 100% of the water that runoff (when the water content exceeds 150 kg m^{-2}) end up in the lakes of the same grid. (2) We calculate the X-ratio for each GCM grid. (3) We estimate $\alpha_{\rm lake}(X)$ based on the fit described above. We limit the variation of the size of the lakes to 10 % from one year to another, in order to kill numerical unstabilities.

Note that this algorithm does not conserve water. This is an issue only for the dry simulations (those for which the entire water inventory can be trapped in impact crater lakes). Therefore, for the cases of "dry" (those that do not include oceans) and warm (warm enough that water is not fully trapped as ice) simulations, we arbitrarily normalize the total amount of water stored in impact crater lakes to the initial total water content (e.g. 1 or 7 m here) after each iteration of the lake evolution algorithm.

9.2.3 Initial simulation setups

We describe in this section the initial simulation setups, summarized in Table 9.2. Initially, the surface/subsurface/atmosphere temperatures are arbitrarily fixed to 300 K everywhere on the planet.

We distinguish two main categories of initial states, depending on the total water content:

- **For cases where early Mars is water-rich (i.e. oceans are present)**. In this scenario, we initialize non-oceanic regions with completely dry conditions. Oceanic regions are assumed to be initially fully deglaciated, with a uniform temperature of 300 K.
- **For cases where early Mars is water-poor (i.e. no oceans are present)**. In this scenario, we assume that all the water is initially trapped as liquid water in impact crater lakes uniformly distributed on the surface. Unless specified, we assume that the initial total water content is equal to 1 m GEL. Based on the results of Matsubara et al. (2011), we start with a uniform lake coverage of 7 % (corresponding to a uniform X-ratio of 19).

The total amount of water h_{H_2O} (in GEL) trapped in impact crater lakes can be calculated using Figs. 9.3 and 9.4, based on Matsubara et al. (2011). We then fit the result with the following empirical relationship (that excludes the contribution of the largest Martian craters):

$$h_{\rm H_2O} = 21.7 - \frac{26}{(1+\alpha_{\rm lake}/100)^4} \tag{9.6}$$

[5]Note that the lake evolution algorithm is run in parallel with the ice equilibrium algorithm.

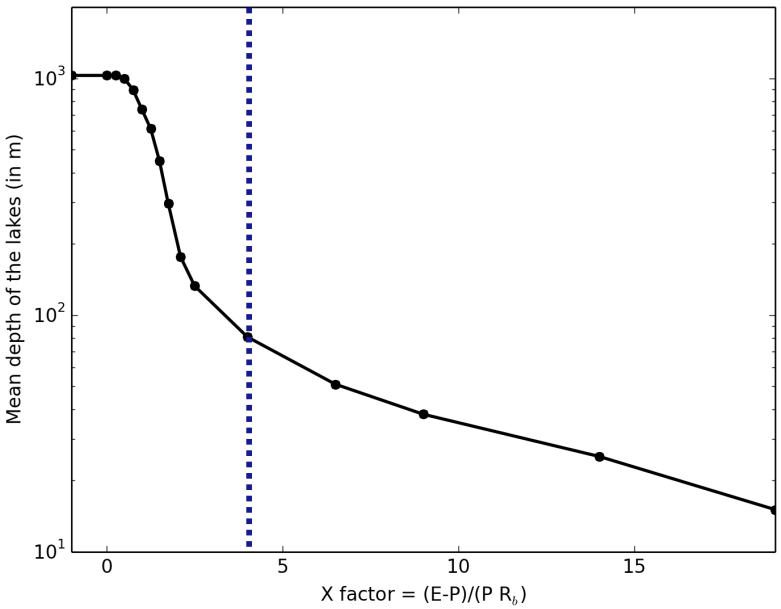

Figure 9.4: Mean lake depth (in m) versus X-ratio, derived from the results of Matsubara et al. (2011). Note that the mean lake depth at low X-ratio (typically lower than 4, denoted by the position of the dotted, vertical line) is biased by the contribution of the largest impact craters (Hellas, Argyre, etc.).

with h_{H_2O} the total amount of water is given in m and α_{lake} in %. For reference, the total amount of water that can be trapped in impact craters before all lakes overflow is $\sim$ 60 m and 500 m GEL, without and with the contribution of the largest Martian craters (mainly Hellas and Argyre), respectively.

The list of simulations performed and discussed in this work is summarized in Table 9.2.

9.3 How much hydrogen is required to warm early Mars?

As stated in the introduction, an important aspect of the plausibility of the H_2 greenhouse warming scenario is to assess whether or not the amount of H_2 required to warm early Mars is compatible with the possible H_2 production rates (Ramirez et al., 2014a; Wordsworth et al., 2017). Below we discuss how much hydrogen is required to produce fluvial activity on early Mars.

9.3.1 Results from 1-D calculations and comparison with previous 1-D studies

We used here the 1-D radiative-convective version of the LMD Generic climate model[6] to assess how much hydrogen is needed to warm early Mars above the melting point of water. Using our 1-D model, we selected two solutions with a mean surface temperature above 273 K:

[6]The model is a simple time-marching, radiative-convective climate model that uses the same radiative transfer than our 3-D Global Climate Model.

Table 9.2: List of simulations discussed in this work. The obliquity is fixed to 40° for all the simulations.

Simulation	Surface pressure	Amount of H_2	Ocean
1	0.75 bar	20%	yes (550m GEL)
2	0.75 bar	20%	no
3	2.3 bar	1%	yes (550m GEL)
4	2.3 bar	1%	yes (100m GEL)
5	2.3 bar	1%	no
6	2.3 bar	5%	yes (550m GEL)
7	2.3 bar	5%	yes (100m GEL)
8	2.3 bar	5%	no (7m GEL)
9	2.3 bar	5%	no (1m GEL)

1. a 0.75 bar CO_2-dominated atmosphere (with 20%H_2)

2. a 2.3 bar CO_2-dominated atmosphere (with 1%H_2)

The resulting vertical temperature profiles obtained in our simulations are shown in Fig. 9.5. As a comparison, Ramirez (2017) finds with another 1-D model[7] a surface temperature of 0°C with a 0.7 bar CO_2-dominated atmosphere with 20% H_2 and a 3 bar CO_2-dominated atmosphere with 1% H_2. Therefore, our 1-D results are in rather good agreement with Ramirez (2017).

We use then these two solutions as baseline compositions for our 3-D Global Climate Model simulations.

9.3.2 Differences between 1-D and 3-D calculations

3-D simulations using the same atmospheric compositions give rather different results.

We focus first on the 0.75 bar solution, which is the most plausible solution given constraints on the past atmospheric pressure of Mars based on crater counting (Kite et al., 2014) and estimates of atmospheric escape rates (Lillis et al., 2017; Dong et al., 2018b). For the 0.75 bar CO_2-dominated atmosphere (with 20%H_2), 3-D simulations indicate that globally-averaged surface temperatures are generally colder than calculated with 1-D model with the same atmospheric composition. More importantly, there is no perennial surface liquid water reservoir in our 3-D simulations. The production of liquid water is actually limited to seasonal melting (see Fig. 9.6). The source of discrepancies between 1-D and 3-D models is actually twofold:

- **For scenarios with a large water content**. Our 3-D simulations indicate that water that evaporates from the ocean is initially deposited almost everywhere on the planet. As the planet cools down, water freezes on the elevated terrains, which increases the albedo, which decreases the mean temperature, and induces even more freezing (e.g. the freezing of the ocean). This is the ice albedo positive feedback. The planet is rapidly covered by ice (i.e. becomes a "Snowball Mars") and the mean temperature drops to 250±5 K. Note that this effect could be taken into account in 1-D climate models by adjusting the surface albedo (Ramirez and Craddock, 2018).

[7] Calculations in Ramirez (2017) were performed using a 1-D reverse climate model.

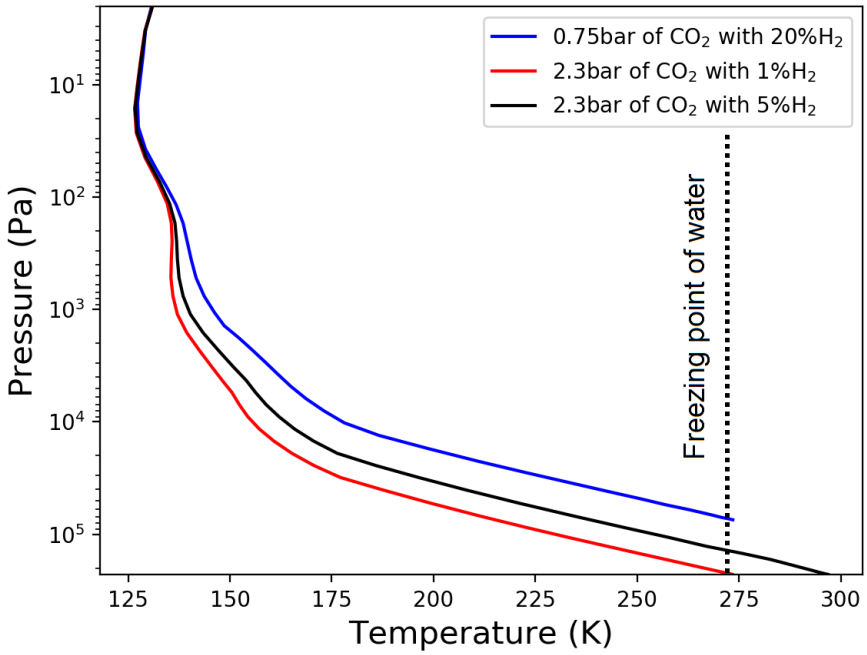

Figure 9.5: Thermal profiles calculated with our 1-D time-marching radiative-convective model for three different atmospheric compositions: 0.75 bar CO_2-dominated atmosphere (with 20%H_2); 2.3 bar CO_2-dominated atmosphere (with 1%H_2); and 2.3 bar CO_2-dominated atmosphere (with 5%H_2). The vertical dotted line corresponds to the melting temperature of water.

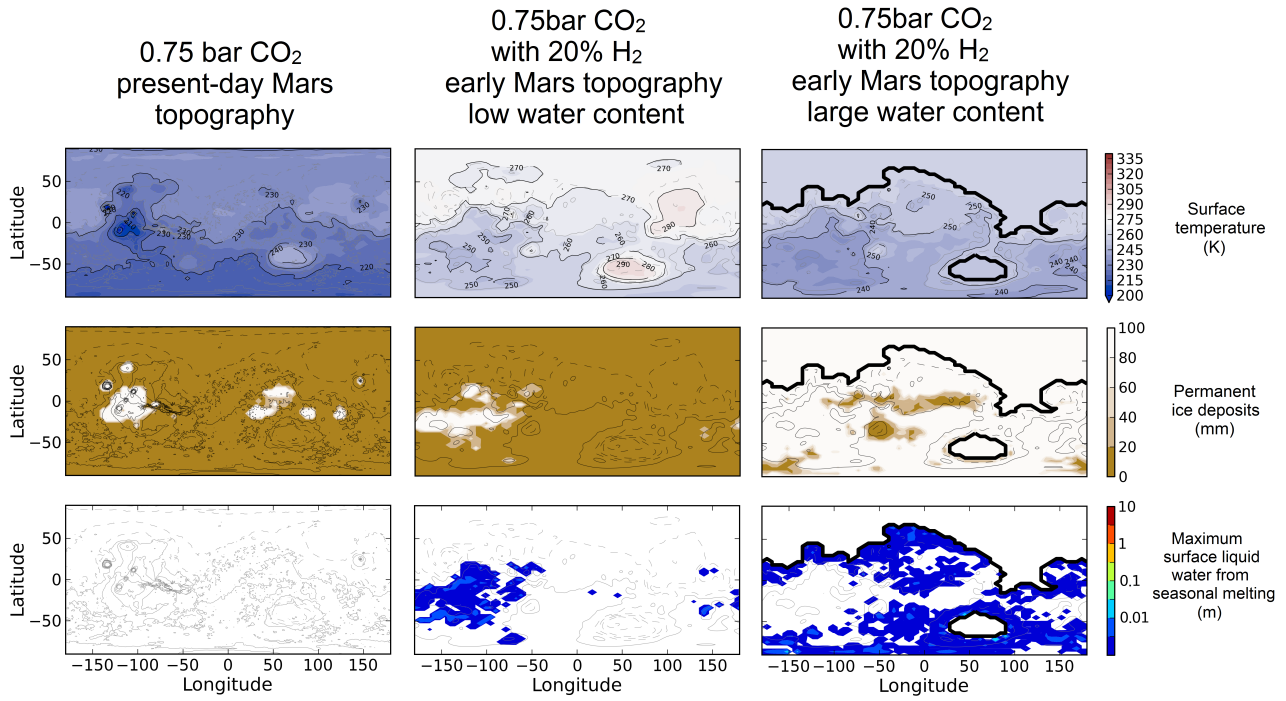

Figure 9.6: Annual mean surface temperatures (top row), permanent ice deposits (mid row) and maximum surface liquid water produced by seasonal melting (bottom row) maps. Maps were calculated for three different configurations shown on top of each of the columns. The 0.75 bar CO_2 atmosphere (left column) corresponds to the reference case shown in Turbet et al. (2017a). The maximum amount of water than can be trapped in water ice glaciers is $\sim$ 250 and 90 m, for the cold simulation with a pure 0.75 bar CO_2 atmosphere (column 1) and the warmer simulation with a low water content (column 2), respectively. This maximum amount was calculated based on the basal melting condition.

- **For scenarios with a small water content**. In this scenario, water migrates to the cold regions of the planet. There are regions of the planet where surface temperatures are high enough for liquid water to exist, but there is no liquid water available. This effect can only be explored with 3-D global climate models accounting for the topography of the planet. In that scenario, the mean surface temperature is 267±5 K. This is slightly lower than the temperature derived from 1-D calculations (273 K) because permanent ice deposits raise the fraction of reflected solar radiation.

With higher surface pressures, the ice albedo positive feedback is much less pronounced. Because the atmospheric transport is more efficient and the thermal inertia of the atmosphere higher, the planet is more resilient to seasonal excursions of temperature and seasonal glaciation, and thus to ice albedo positive feedbacks[8]. This is why in the 2.3 bar CO_2-dominated atmosphere (with 1%H_2) the oceans are deglaciated (see Fig. 9.7, columns 2 and 3.). In addition to that, the low albedo of oceans (equal to 0.07, compared to the Martian regolith albedo of 0.2) has a stabilizing effect.

The globally-averaged annual mean surface temperature of simulations shown in Figure 9.7 is 280±2 K for the dry case (left column) ; 274±2 K for the 100 m GEL ocean case (mid column); and 280±2 K for the 550 m GEL ocean case (right column). Small differences in the mean surface temperature come from differences in surface albedo, due to differences in oceanic and permanent ice deposits coverages (see Figure 9.7, rows 1 and 2).

However, for the low water content scenario, there is still no permanent surface liquid water reservoirs. The explanation is the same than for the 0.75 bar case. Although the globally-averaged mean annual temperature is 7 K above the melting point of water, water still migrates to the coldest regions of the planet. Places where surface temperatures are high enough for liquid water to exist are widespread over the planet, but there is no liquid water available in any of them. In this case, water is trapped as ice in the coldest regions of the planet (see Figure 9.7, 1st column, 1st and 2nd rows).

9.3.3 Constraints from the equatorial periglacial paradox

It has been argued that the presence of water ice glaciers in the Martian highlands is an issue, because there is no clear evidence of glacial erosion on these terrains (Ramirez and Craddock, 2018). This issue is usually known as the "equatorial periglacial paradox" (Wordsworth, 2016). Ramirez and Craddock (2018) advocated that that this so-called "equatorial periglacial paradox" is a piece of evidence against the "icy highland" scenario (Wordsworth et al., 2013; Bouley et al., 2016).

All the simulations already discussed above have permanent ice reservoirs located in the highlands. There, the annual mean surface temperatures are 230-245 K (for the 0.75 bar simulations) and 250-255 K (for the 2.3 bar simulations). This is illustrated in Figs. 9.6 and 9.7, rows 1 and 2. Not only a warmer climate does not prevent ice to accumulate in the cold traps (the southern highlands, here), but the glacial activity and thus erosion would be strongly enhanced in the highlands because the temperature at the cold traps - where ice accumulates - is higher than in a pure CO_2 atmosphere scenario.

A possibility to consider is that there were enough hydrogen or similar strong greenhouse gases to warm the coldest points of the planet roughly above 0°C, in order to remove all the glaciers. In

[8] To a lesser extent, this is also due to the fact that the planetary albedo of thick CO_2 atmospheres is already high (due to Rayleigh scattering); see Kopparapu et al. (2013), Fig. 5b.

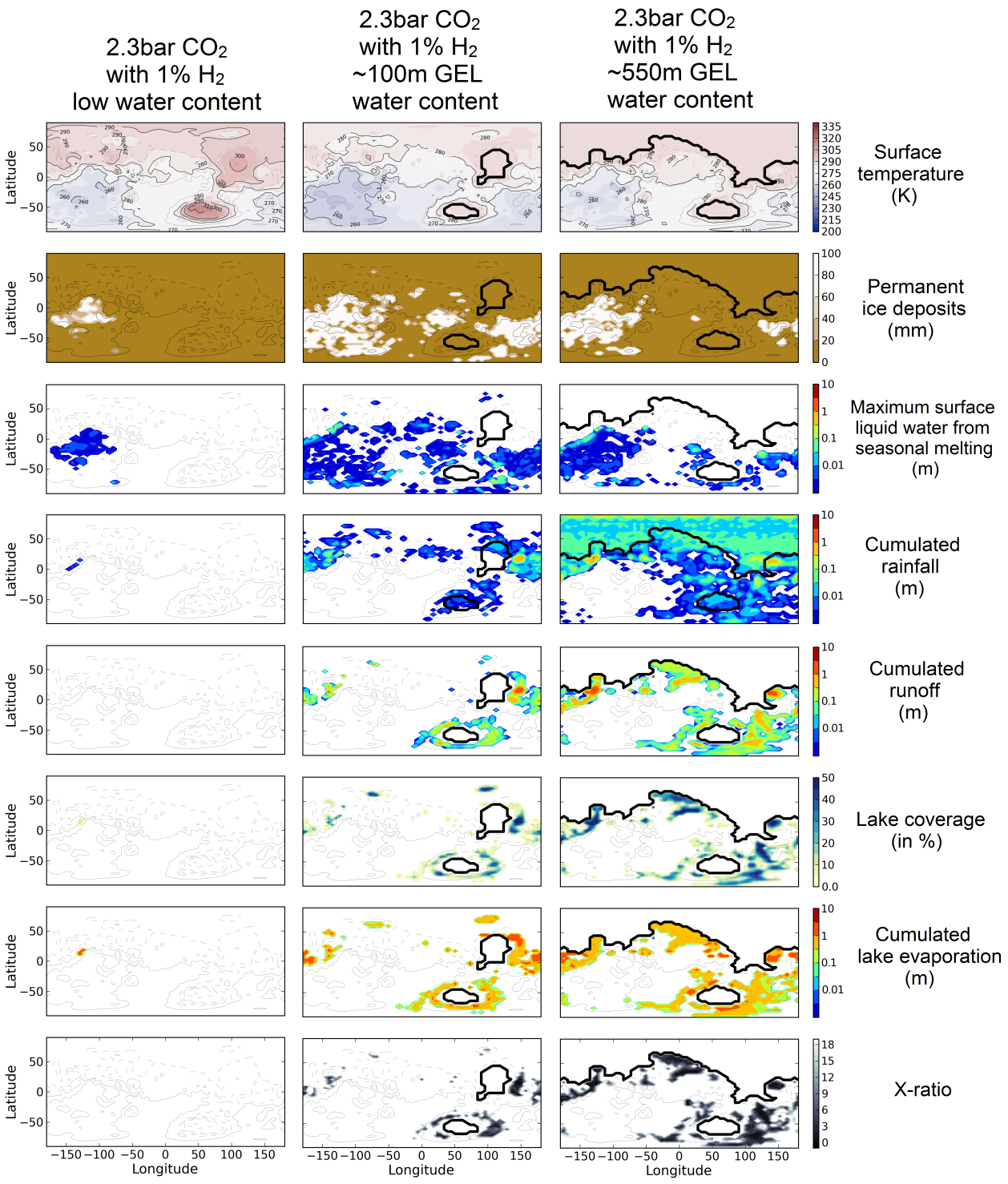

Figure 9.7: Annual-mean average quantities (surface temperatures, permanent ice deposits, maximum surface liquid water produced by seasonal melting, cumulated rainfall, cumulated runoff, lake coverage, cumulated lake evaporation and X-ratio) for atmospheres made of 2.3 bar of CO_2 and 1% of H_2, for various total water inventories. The maximum amount of water than can be trapped in water ice glaciers is $\sim$ 25 m for the low water content simulation (column 1). This maximum amount was calculated based on the basal melting condition. Note that the cumulated lake evaporation must be multiplied by the lake coverage α_{lake} to obtain the cumulated evaporation for the GCM grid.

practice, this was only achieved in our 3-D numerical climate simulations for hydrogen contents up to ~ 5 times higher than what is required to raise the globally-averaged annual mean surface temperature (in the 2.3 bar simulation), thus up to ~ 5 times the hydrogen level calculated in Ramirez (2017). The results are shown in Fig. 9.8 (rows 1 and 2), for atmospheres made of 2.3 bar of CO_2 and 5% H_2. For this extreme atmospheric composition, permanent ice reservoirs disappear whatever the assumed total water content. However, getting the same results for a 0.75 bar atmosphere seems out of reach. In any case, even if the climate was warm enough to avoid the formation of glaciers for some time, it seems difficult to avoid glaciation during climate transitions.

9.4 Rainfall and lakes in warm simulations

The total surface/near-surface water content available during the Late Noachian is still debated (Wordsworth, 2016). Carr and Head (2015) estimated that the total reservoir could have been as low as ~ 24 m GEL, based on water loss/gain budget during the subsequent Hesperian and Amazonian epochs. Villanueva et al. (2015) calculated that the late Noachian water content was ~ 60 m GEL, based on present-day Mars isotopic D/H ratio. Eventually, Di Achille and Hynek (2010) argued that the total water inventory was ~ 550m GEL, based on possible ancient ocean shorelines determined by the position of deltas.

We explore here the nature of the early Mars hydrologic cycle assuming a strong greenhouse warming (strong enough that glaciers are not present, strong enough that rain is produced and lakes are formed), and for various total water inventories. For this we designed 3-D numerical climate simulations to explore possibles climates ranging from warm & arid to warm & wet conditions.

9.4.1 Warm and arid scenarios

Warm & arid scenarios are cases where the total water content on Mars was low enough so that no oceans formed, as depicted in Fig 9.7 (column 1) and Fig 9.8 (columns 1 and 2).

Wordsworth et al. (2013) demonstrated using 3-D Global climate simulations that - in cold and arid scenarios - water should migrate to the cold traps of the planet (e.g. the southern highlands) and accumulate there as ice, through the mechanism of adiabatic cooling and subsequent condensation. We find the same behaviour in our simulations with low water inventory and moderate greenhouse warming (see Fig 9.6-column 2, and Fig 9.7-column 1). However, in our simulations, the size of the permanent ice reservoirs is much more limited, for two reasons:

- The number of locations on Mars where the annual mean surface temperature is above 0°C is reduced. Therefore, the number of possible locations where water can accumulate as ice is also reduced.
- The maximum thickness of the permanent ice reservoirs is also reduced, because the basal melting condition[9] is more restrictive at higher surface temperatures.

We actually find a similar behavior in simulations with a larger greenhouse warming (shown in Fig 9.8, columns 1 and 2). In our dry simulations (at 1 and 7m GEL), water was initially uniformly distributed in lakes all over the planet (with a mean lake surface coverage of 6.5 and 20%, respectively).

[9] The basal melting condition defines the maximum thickness of ice deposits, before they start to melt at their base.

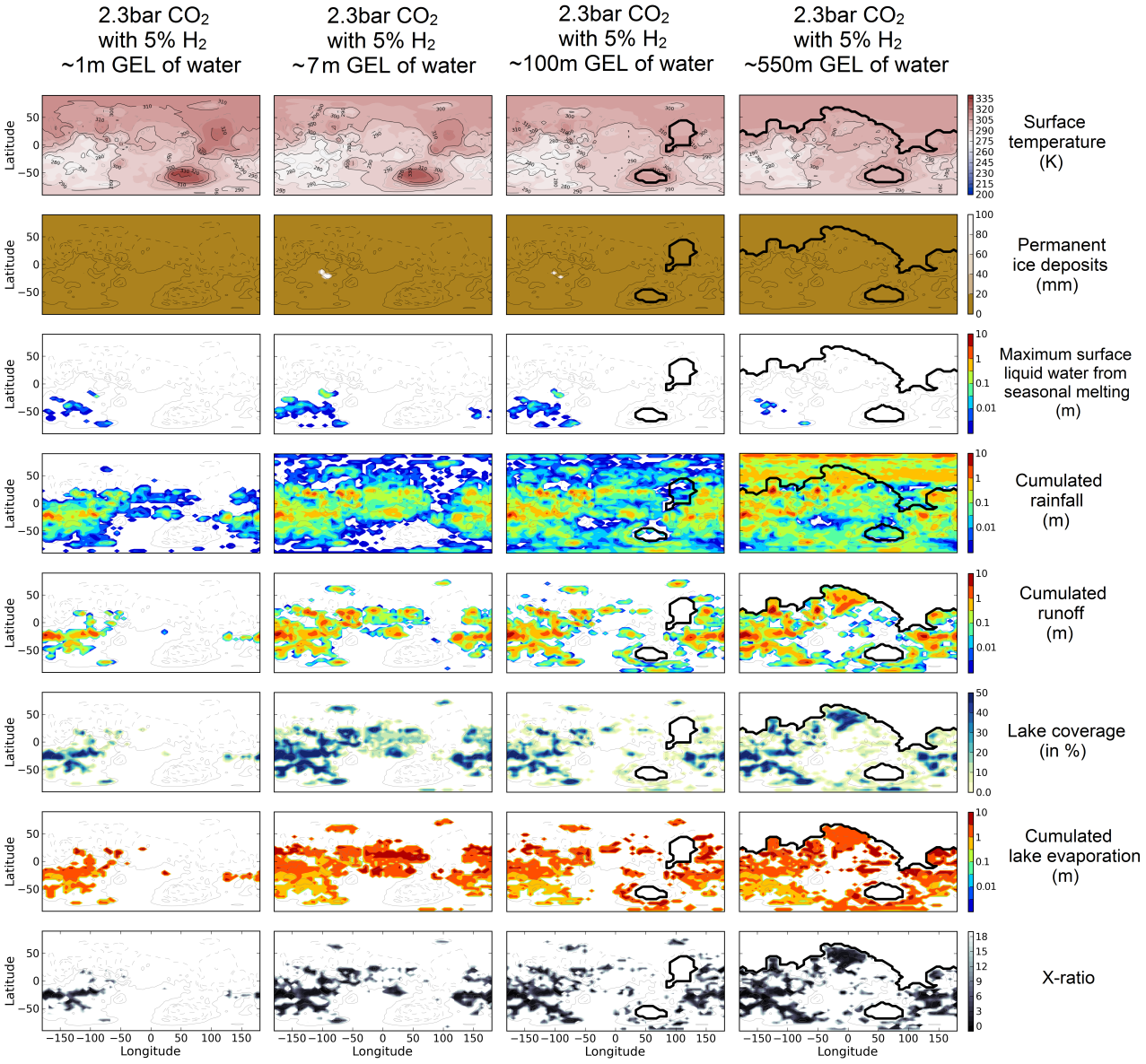

Figure 9.8: Annual-mean average quantities (surface temperatures, permanent ice deposits, maximum surface liquid water produced by seasonal melting, cumulated rainfall, cumulated runoff, lake coverage, cumulated lake evaporation and X-ratio) for atmospheres made of 2.3 bar of CO_2 and 5% of H_2, for various total water inventories. Note that the cumulated lake evaporation must be multiplied by the lake coverage α_{lake} to obtain the cumulated evaporation for the GCM grid.

Water progressively migrates in regions where the precipitation - evaporation budget is favorable, i.e. in the cold traps. Because of the adiabatic cooling process, the cold traps in our warm simulations are also located in the southern highlands, as calculated by Wordsworth et al. (2013) in much colder configurations. As a result, water rapidly migrates to the southern highlands where it accumulates - in liquid form - in impact crater lakes (see Fig 9.8, columns 1 and 2, row 6).

Once water is stabilized in southern highlands impact crater lakes, precipitation (rainfall) occurs close to the reservoirs of water (lakes), i.e. also in the southern highlands (see Fig 9.8, columns 1 and 2, row 4). A good predictor of the regions of valley networks formation is the annual mean cumulated runoff (see Fig 9.8, columns 1 and 2, row 5) that shows that valley networks - in this scenario - would also form in the southern highlands.

Depending on the total amount of water assumed to be trapped in impact crater lakes (1 and 7 m GEL in our simulations[10]), the lake coverage obviously varies. In the 1m GEL simulation (see Fig 9.8, column 1), lakes only exist on the coldest regions of Mars, whereas in the 7 m GEL simulation (see Fig 9.8, column 2), lakes expend to a broader region and almost entirely cover the southern highlands.

The simulation at 7m GEL is promising, because both lake formation and runoff (initiated by rainfall) are widespread on (but limited to) the southern highlands, were both impact crater lakes and valley networks have been observed (Fassett and Head, 2008b; Hynek et al., 2010).

However, there are two major issues in this scenario. First, the simulations explored here correspond to very low surface water total inventories when compared to the available estimates (Di Achille and Hynek, 2010; Villanueva et al., 2015; Carr and Head, 2015). Secondly, a large fraction of the lakes that form in our simulations are overflowing. Most of the lake forming regions are associated to very low X-ratios (see Fig 9.8, row 8). For a X-ratio lower than ~ 2, lakes are expected to overflow (Howard, 2007; Matsubara et al., 2011). Some lakes that reached their maximal size can even have a positive precipitation - evaporation positive budget. Therefore, in our simulations, a large number of lakes should be open-basin lakes. This seems in contradiction with the observational evidence that closed-basin lakes greatly outnumber open-basin lakes (Wordsworth, 2016).

9.4.2 Warm and wet scenarios

Warm & wet scenarios are cases where the total water content on Mars was high enough for large oceans to form, as depicted in Fig 9.8 (columns 3 and 4).

In the warm and wet simulations, the total amount of water possibly trapped in impact crater lakes is let free. Water evaporates from the oceans, precipitates on "continental" regions where it can accumulate and form impact crater lakes.

In these scenarios, a fraction of the available water migrates again toward the cold traps of the planet, where it accumulates because the evaporation/condensation budget is favorable there. For this reason, our simulations also indicate that impact crater lakes (and thus rainfall) are widespread in the southern highlands (see Fig 9.8, columns 3 and 4, row 6). This result actually differs from the prediction of Wordsworth et al. (2015), despite the fact that our simulations with ocean (at 550 m GEL) have a very similar setup. In fact, our simulations have three main differences with that of Wordsworth et al. (2015):

[10] Note that the total amount of water trapped in the atmosphere as water vapour/clouds and in the soils is at least one order of magnitude below the amount of water trapped in lakes. Moreover, mean annual temperatures are high enough everywhere on the planet that no permanent ice deposits form.

1. We use a different precipitation scheme. However, Wordsworth et al. (2015) demonstrated that the different precipitation schemes should produce similar results.

2. We use a more realistic atmospheric composition based on CO_2 and H_2 radiative properties, whereas Wordsworth et al. (2015) used artificial grey opacities.

3. We use a different topography.

We believe that the third difference between the setup of Wordsworth et al. (2015) and ours is the one that drives major differences in precipitation patterns. Here we used the pre-True Polar Wander (pre-TPW) topography (see Fig 9.2, second row) from Bouley et al. (2016). Bouley et al. (2016) showed that the formation of the late Noachian valley networks should have precluded the formation of most of the Tharsis volcanic bulge. The pre-TPW topography is based on the present-day MOLA (Mars Orbiter Laser Altimeter) Mars surface topography shown in Figure 9.2, first row (Smith et al., 1999; Smith et al., 2001) and used by Wordsworth et al. (2015), but without Tharsis and all the younger volcanic features. Moreover, the formation of Tharsis should have produced a large True Polar Wander (TPW) event of 20°-25°, which is also taken into account in the pre-TPW topography.

Wordsworth et al. (2015) reported a lack of precipitation in the Margaritifer Sinus region (east of Tharsis) and demonstrated that this absence of precipitation was due to a rain shadow effect. Westerly winds over Tharsis produce adiabatic cooling and thus precipitation on the western flank of Tharsis, which dries out the air and thus reduces precipitation on the east of Tharsis (Wordsworth et al., 2015). Because the Tharsis volcanic province has been removed from the topography in our simulations, this effect disappears and we record rainfall in the Margaritifer Sinus region in our simulations.

In addition, orographic precipitation (rainfall) is produced near the shorelines of the oceanic reservoirs of water. Subsequently, impact crater lakes are formed in these regions. For instance, a large northern lowland ocean (as illustrated in the 550 m GEL case; see Fig 9.8, column 4, rows 4-6) produces precipitation in Arabia Terra (a region with low valley networks drainage density). The same result is obtained by Wordsworth et al. (2015). However, in scenarios with a smaller ocean (or no ocean at all), precipitation and lakes are absent from Arabia Terra. Similarly, we find that the presence (and coverage) of a liquid water reservoir in Hellas crater dictates whether or not precipitation occurs in the nearby areas. With a low water reservoir in Hellas (or no reservoir at all), precipitation around Hellas and especially in Noachis Terra is suppressed. In summary, the position of lakes and rainfall events is tightly linked to the position of the oceanic reservoirs.

More generally, for warm scenarios, precipitation and lake formation patterns can be understood as the sum of two contributions:

1. A contribution due to the presence of cold traps on the planet. The precipitation/condensation budget will always favor the formation of lakes (and subsequently of precipitation) in the cold traps. This is a very generic process that explains why water accumulates in the cold traps in both cold regimes (Wordsworth et al., 2013) and warm regimes (this work). At high enough obliquity and high enough pressure, because of the adiabatic cooling effect, the cold traps are located in the southern highlands.

2. A contribution due to local sources of water (e.g. oceanic regions). Depending on the location and the area of the oceanic reservoirs, the precipitation patterns (and thus the lake formation patterns) are affected.

This result is promising because it indicates that 1) not only the presence of precipitation and impact crater lakes in the highlands is robust in 3-D global climate simulations, but also 2) the other geographic patterns of precipitation and impact crater lakes formation can be "tuned" in a warm scenario by using an adapted topography (typical of early Mars) and by adjusting the amount and locations of surface water reservoirs[11].

9.5 Conclusions and Discussions

In conclusion, arid and semi-arid climates are promising solutions to the early Mars enigma. Using a 3-D numerical climate model adapted to account for the hydrology of impact crater lakes, we demonstrated that precipitation and lake formation patterns deduced from geology can be roughly reproduced by climate models - in warm and arid/semi-arid climates - with two important conditions: (1) using a topography adapted for Late Noachian Mars conditions and (2) adjusting the amount of available surface water in the system.

In particular, the presence of valley networks around Margaritifer Sinus can be reconciled with climate models assuming that the main bulk of Tharsis was emplaced after the formation of valley networks, as predicted by Bouley et al. (2016). Moreover, the absence of valley networks around Noachis Terra and Arabia Terra can be reconciled with climate models assuming that the total reservoir of surface water is lower than the 550 m GEL assumed in Wordsworth et al. (2015).

However, there are some significant remaining caveats associated with this scenario. First, the total amount of reducing gas (here H_2) required to produce the aforementioned fluvial features is likely much higher than predicted in Ramirez (2017) because - by increasing order of importance - (1) of the ice albedo feedback, (2) of the (non-)availability of water in regions of higher temperatures, and (3) of the equatorial periglacial paradox. Levels of H_2 required (i) to produce rainfall on the southern highland (Noachian) terrains and (ii) to overcome the equatorial periglacial paradox are 5 times higher than predicted in Ramirez (2017) (based on 1-D climate model calculations). This is tremendous.

Secondly, in our warm simulations (either "dry" or "wet"), precipitation rates are high on the highlands. As a result, most of the impact crater lakes that form on the highlands are overflowing, which seems at odd with the observational evidence that closed-basin lakes outnumber open-basin lakes.

[11] The amount and locations of surface water reservoirs are anyway highly uncertain, not only because the total water content is unknown, but also because it depends on subsurface mechanisms of recharge.

Part III

Spectroscopy for habitability

Chapter 10

Effect of line mixing on dense CO_2 atmospheres

Contents

10.1 Preamble

Mars had very likely a thick CO_2-dominated atmosphere in the past. In such atmosphere, and at the surface temperature roughly expected on early Mars, longwave radiation losses essentially occur in the 200-600 cm^{-1} (e.g. 17-50 μm) region (Wordsworth et al., 2010a) where absorption and emission are dominated by the CO_2 roto-translational Collision Induced Absorptions (CIA) and the high wavelength far wing of the intense 15 μm-band lines.

While I was working on a comprehensive review of the CO_2 spectroscopy to design state-of-the-art numerical climate simulations of early Mars, Ozak et al. (2016) published a paper demonstrating that, using a line mixing model to calculate high resolution CO_2 spectra instead of the widely used χ-factor approach, surface temperatures on early Mars calculated by climate models could be 15 Kelvins lower than that of previous estimates (Wordsworth et al., 2010a). Their main finding was that the line mixing approach produces weaker absorptions in the high wavelength far wing of the 15 μm-band lines.

With the help of my colleague Ha Tran, we figured out soon that there were two issues with the calculations made in Ozak et al. (2016). First, line mixing models are suited for calculations of absorption lines near the center, but not in the far wings, where the effect of finite duration of collisions (not taken into account in the line mixing models) can become dominant. Secondly, and more importantly, Ozak et al. (2016) used a line mixing model designed for Earth applications, i.e. calibrated for CO_2 lines broadened by air, instead of CO_2. We demonstrated through calculations using a pure CO_2 line mixing model that the 15 K cooling reported by Ozak et al. (2016) is in fact mainly due to this mistake.

This chapter is based on a paper (comment) published in the Journal of Geophysical Research Planet in November 2017. The full reference is: Martin Turbet & Ha Tran, **Comment on "Radiative Transfer in CO_2-Rich Atmospheres: 1. Collisional Line Mixing Implies a Colder Early Mars"**, JGR Planet, 2017 (`http://adsabs.harvard.edu/abs/2017JGRE..122.2362T`).

10.2 Abstract

Ozak et al. (2016) claimed that explicitly including the effect of CO_2 collisional line mixing (LM) in their radiative transfer calculations yield CO_2 atmospheres that are more transparent to infrared radiation than when spectra calculations are made using sub-Lorentzian line shapes. This would in particular imply significantly colder surface temperatures (up to 15 K) for early Mars than estimated in previous studies. Here we show that the relative cooling that Ozak et al. (2016) associated to the effect of collisional line mixing is in fact due to a wrong choice of broadening species (air instead of CO_2). We then calculated Line-by-Line spectra of pure CO_2 atmospheres using a line-mixing model developed for self-broadened CO_2. Using the LMD Generic model (in 1D radiative-convective mode), we find that calculations made with the proper collisional line mixing model and with sub-Lorentzian line shapes lead to differences between early Mars surface temperatures smaller than 2 Kelvins only.

10.3 Comment on CO_2 line mixing

We first introduce here the various spectroscopic terms needed for the reader to understand the content of this comment. Modeling the entire CO_2 'allowed' spectrum (i.e. due to the molecule dipole and not to collision induced absorption), including both the regions near the lines centers and the far wings, is an extremely difficult task for which no rigorous model is available so far. The measured spectrum can be significantly different from that calculated with the usual Lorentz (or Voigt) profile, due to two effects that are neglected by this profile. The first one, called line mixing, is associated with the collisional transfers of rotational populations between absorption lines. It modifies the shape of clusters of closely spaced lines and results in transfers of absorption from the band wing region to the band center (Hartmann et al., 2008) leading to the strongly sub-Lorentzian behavior observed in CO_2 band wings. The second effect, related to the finite duration of collisions, affects the absorption in the far wings of the lines only (Hartmann et al., 2008). To model CO_2 absorption spectral shape, two approaches are commonly used. In the first, called the χ-factor approach, an empirical correction of the Lorentzian shape is adjusted to laboratory measurements of the absorption in some band wings (e.g., at 4.3 microns in Perrin and Hartmann 1989). The effects of both line-mixing and the finite collision duration are thus taken into account by this approach, but for the considered band wings region only. In the absence of precise and available data for other spectral region, the same χ-factor correction is generally used for all other CO_2 bands. In addition to this approximation, the effect of line mixing in the band center is not taken into account by the χ-factor correction. The second approach, based on the use of the impact and the Energy Corrected Sudden approximations (Tran et al. 2011 and references therein), takes line mixing into account but not the effect of finite duration of collisions. This model, self-consistent for all bands, leads to satisfactory agreement with laboratory measurements for various bands, at different pressure and temperature conditions (Tran et al., 2011). Very accurate predictions are obtained in the central regions of the bands with discrepancies that may increase together with the breakdown of the impact approximation (Hartmann et al., 2008), when going far away in the wings. The line mixing and the χ-factor approaches are thus fully different and rely on completely different approximations. Yet, they can both be used to model broad band CO_2 absorption spectra. Ozak et al. (2016) (hereafter, OZ16) explored the effect of using the line mixing (hereafter, LM) approach in CO_2-dominated atmospheres, typical of the early Martian environment (see review by Forget et al. 2013). They found that, using a 1D radiative-convective model, the use

of the LM approach results in colder early Mars surface temperatures than those obtained with the χ-factor approach. Note that, as mentioned above, LM effects on the line wings are already taken into account in the spectral calculations using the χ-factor approach, therefore, one cannot state that these calculations correspond to the case of'no line mixing', as done in OZ16. For instance, for a pure CO_2 atmosphere with a surface pressure of 2 bar, OZ16 reported that surface temperatures could be lowered by about 15 K compared to previous studies (Wordsworth et al., 2010a) in which the χ-factor approach was used. Such a result would have profound implications for the early Mars enigma (Wordsworth, 2016; Haberle et al., 2017), making the formation of ancient valley networks and lakes even more difficult to explain. However, here we show that this cooling is due to an improper choice of the LM model. OZ16 used the updated version (Lamouroux et al., 2010) of the LM approach database and software package of Niro et al. (2005), built for Earth atmosphere studies, i.e. for CO_2 broadened by air and not for pure CO_2, as needed for the case of early Mars. Here we instead use the LM package devoted to pure CO_2, developed by Tran et al. (2011) and updated in Kassi et al. (2015) to calculate absorption spectra of pure CO_2 under various pressure and temperature conditions typical of the early Martian environment. An example of our calculated spectra is shown in Fig. 10.1 in which those obtained by OZ16 are also reported for comparison. As in OZ16, we performed two calculations: the first with the LM approach but using the package of Tran et al. (2011) and Kassi et al. (2015) for pure CO_2 (hereafter denoted by pure CO_2 LM, in red). In the second calculation, the χ-factor approach for pure CO_2 (Perrin and Hartmann, 1989) was used (in blue). Note that the latter is the widely-adopted procedure to calculate absorptions for early Martian CO_2-dominated atmospheres (Wordsworth et al., 2010a; Mischna et al., 2012). Finally, we also calculated spectra, as done by OZ16, with CO_2-in-air LM by using the package of Niro et al. (2005) and Lamouroux et al. (2010) (in green). Figure 10.1 calls for two remarks. Firstly, our calculations with CO_2-in-air LM and with the pure CO_2 χ-factor approach agree very well with those of OZ16. The second and very important remark is that when using the correct collision partner, i.e. pure CO_2 LM, the obtained spectrum (red) is closer to that calculated with the pure CO_2 χ factor approach (blue), with respect to the CO_2-in-air LM calculation (green). Using the LMD Generic model (in 1D time-marching radiative-convective mode) parameterized following OZ16, with the two spectral calculation approaches for pure CO_2 (i.e., LM and χ factor), we performed numerical simulations of pure CO_2 atmospheres of various thicknesses (from 0.1 to 2 bar), under Noachian Mars conditions as in OZ16. Pure CO_2 continuum was taken into account in the two calculations. Specifically, the CO_2-CO_2 far infrared Collision Induced Absorptions (CIA) from Gruszka and Borysow (1997) and CIA and dimer absorptions from Baranov et al. (2004) were used and extrapolated for the whole spectral range, as widely done by previous studies and in particular by Wordsworth et al. (2010a). Fig. 10.2 shows the equilibrium surface temperatures obtained with (red) pure CO_2 LM and with (blue) the pure CO_2 χ-factor approach. For comparison, the results obtained by OZ16 using CO_2-in-air LM (green) and those obtained in Wordsworth et al. (2010a) (black) in which χ factors were used, were also plotted. In addition, we also performed simulations using CO_2-in-air LM. For this case, two calculations were made. In the first (solid orange line), pure CO_2 continuum was calculated as mentioned above, i.e. extrapolated for the whole spectral range. In the second, the same data were used but were truncated at 250 cm-1 for far infrared CIA and between 1200 and 1600 cm-1 for CIA and dimer absorptions from Baranov et al. (2004), respectively, as done in OZ16 (dashed orange line). As can be observed in Fig. 10.2, the result of this latter is in very good agreement with that of OZ16, indicating that the 1-D radiative-convective version of our LMD Generic Model agrees well with the one developed by OZ16.

The correlated-k radiative transfer model of OZ16 is thus not concerned by our comment and could be used for radiative transfer in planetary atmospheres.

Firstly, as can be observed, our simulations with the χ-factor approach (blue) agree well ($\pm$2K) with those of Wordsworth et al. (2010a) confirming the calculation procedure we used. The remaining difference is likely due to the spectroscopic data used in the two calculations. Wordsworth et al. (2010a) used data from HITRAN 2004 (Rothman et al., 2005) while in our calculations, HITRAN 2012 was used (Rothman et al., 2013). Secondly, surface temperatures obtained with pure CO_2 LM and pure CO_2 χ factors are very close to each other, the differences being always smaller than 2 K for all considered surface pressures. This is consistent with the fact that absorptions calculated with pure CO_2 LM are very close to those calculated with the χ factors in the most relevant infrared spectral regions for early Mars, as shown in Fig. 10.1. This is also consistent with the fact that LM effects on the line wings are by nature already taken into account in the χ factor approach. In the opposite, high resolution spectra with CO_2-in-air LM (green, see Fig. 10.1) being more transparent in infrared regions, surface temperatures obtained in this case can be much lower (up to 10 K, solid orange line on Fig. 10.2). Note that in addition to the effect of the wrong broadening species, due to the effect of pure CO_2 continuum truncation, OZ16 obtained even lower surface temperature (dashed orange and green lines on Fig. 10.2). In summary, the significant cooling reported in (Ozak et al., 2016) is mostly due to a wrong choice of broadening species (air instead of CO_2). Moreover, we show that early Mars surface temperatures calculated when using the proper LM model are very close to those obtained from spectra calculations based on the 'usual' χ factor approach, their differences being smaller than 2 K, and thus within the uncertainty of usual early Mars radiative transfer calculations (Figure 2 in Ozak et al. 2016). This very good agreement thus justifies the use of the usual χ-factor approach for early Mars climate studies. This work also stresses the need for accurate spectroscopic data for early Mars pressure and temperature conditions, as well as for their careful use.

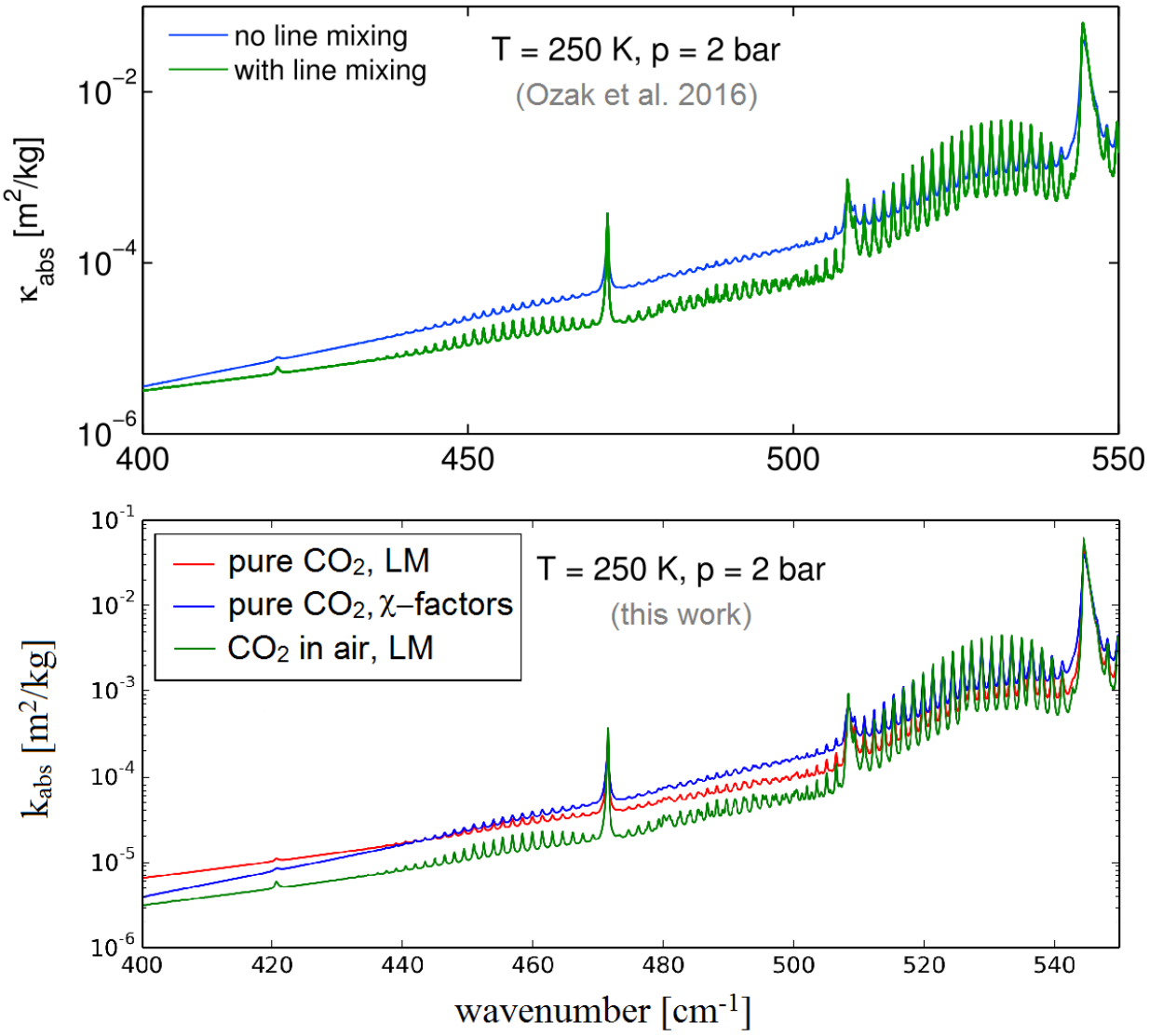

Figure 10.1: Line-by-line absorption spectra of a pure CO_2 atmosphere, at a temperature of 250K and a pressure of 2 bar. Upper panel: Figure directly imported from OZ16, calculated with their χ factors corrections (blue) or with their (green) inclusion of CO_2-in-air line mixing (LM). For comparison, we plotted in the lower panel 3 spectra calculated under the same pressure and temperature condition: in blue is the calculation with our χ factors, in green calculation with our CO_2-in-air line mixing, which both match the curves of OZ16, and in red our pure CO_2 line mixing. Absorption coefficient unit is in m^2 kg^{-1}, as in OZ16. Note that contribution of pure CO_2 continuum is not included here.

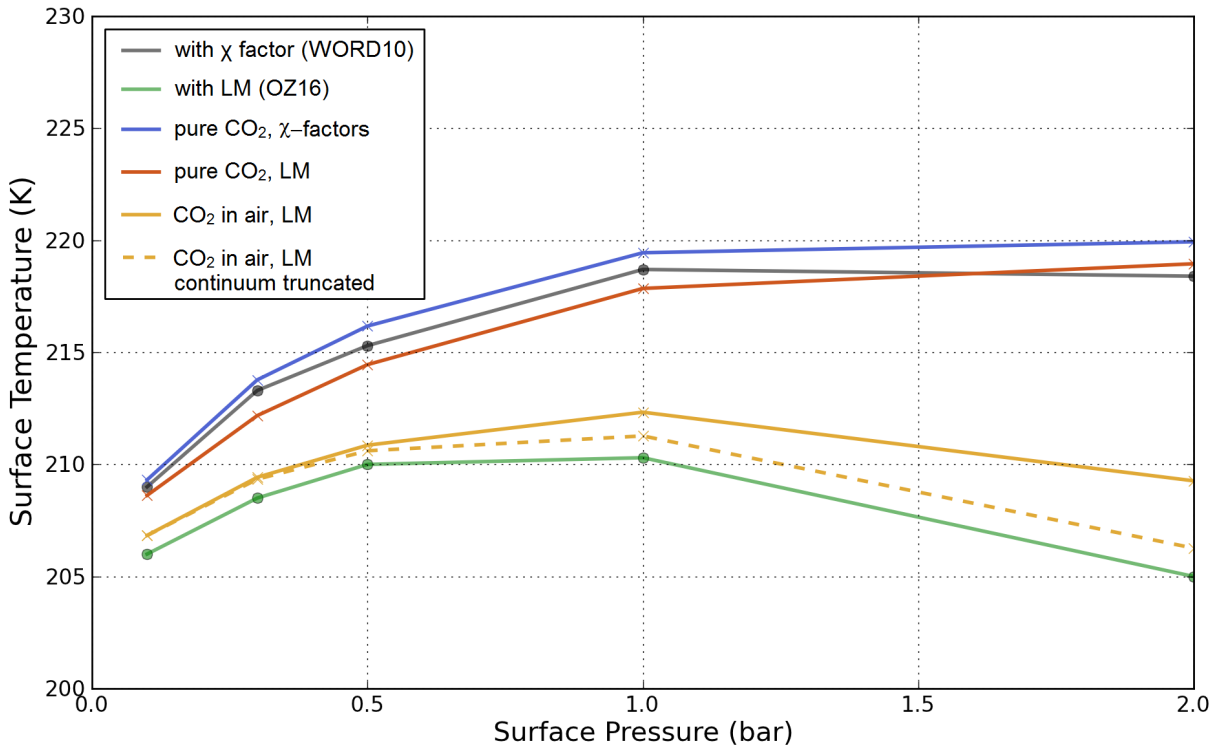

Figure 10.2: Temperatures at the surface of a pure CO_2 atmosphere of various thicknesses, exposed to early Mars conditions, and computed with the LMD Generic model, with pure CO_2 LM (red), and with the χ factors corrections (blue). Orange lines correspond to calculations using CO_2-in-air LM with pure CO_2 continuum truncated (dashed line) or not (solid line). For comparison, we plotted in black the original curve from Wordsworth et al. (2010a) (χ factors), and in green the one from OZ16 (with CO_2-in-air LM). Calculations include CO_2 condensation. Mean incident flux at the top of atmosphere is 442 W m^{-2}.

Chapter 11

Far infrared measurements of absorptions by CH_4+CO_2 and H_2+CO_2 mixtures

Contents

11.1 Preamble

I showed in Chapter 9 that one of the most promising solution for the early Mars enigma is the greenhouse warming by reducing gases, in particular H_2 and CH_4.

Greenhouse warming by reducing gases on early Mars is thought to be dominated by the collision-induced absorption (CIA) of CO_2-H_2 and CO_2-CH_4. Yet, as of 2018, the only information we have on the intensity and shape of these CIA absorptions comes from ab-initio theoretical calculations (Wordsworth et al., 2017), calling for further experimental validation.

With the help of my colleagues Jean-Michel Hartmann and Ha Tran, I demonstrated using transmission calculations that if the predictions of Wordsworth et al. (2017) were correct, we should be able to measure them experimentally with the AILES experiment, located in the SOLEIL synchrotron

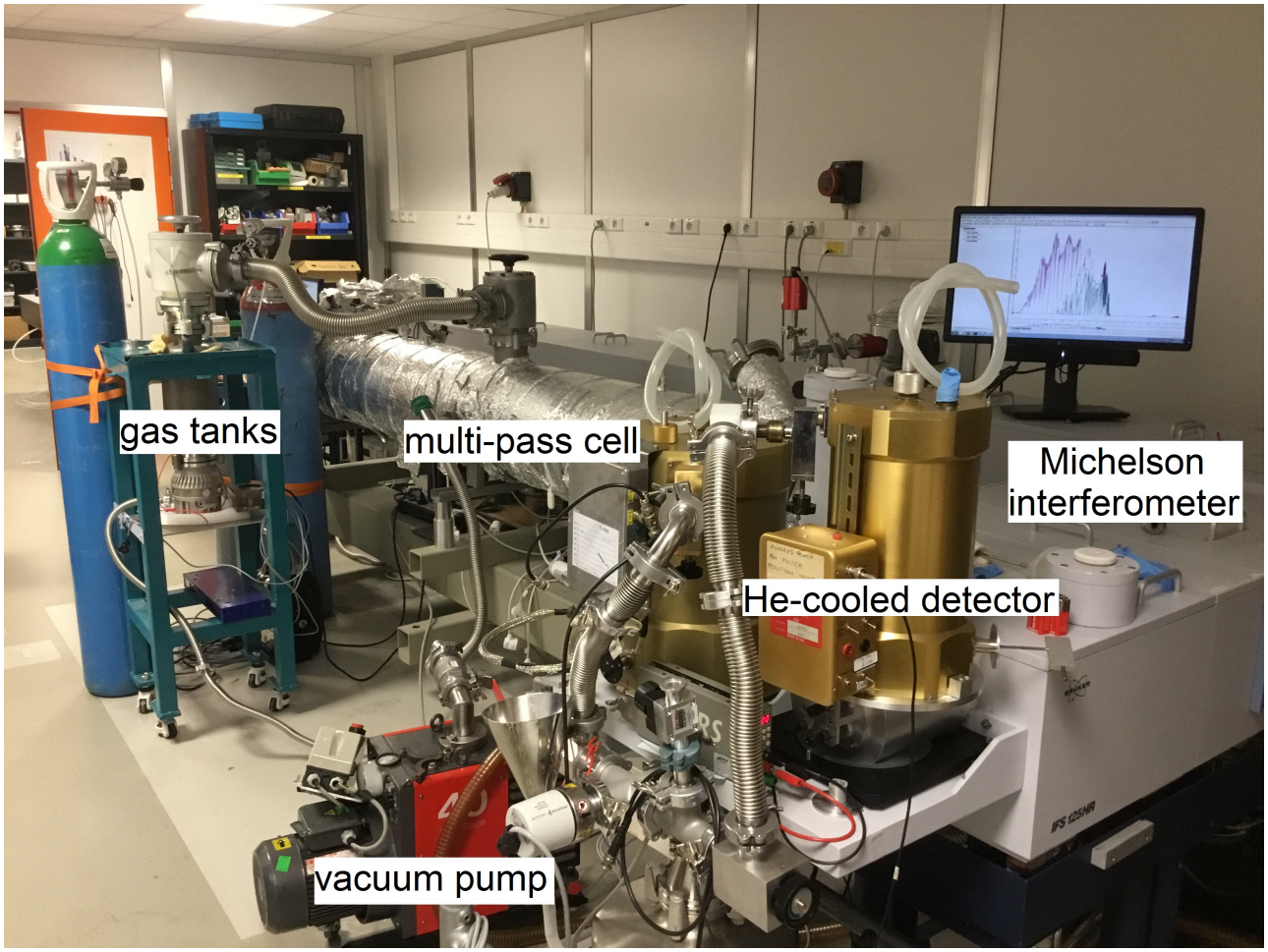

Figure 11.1: Experimental setup of the AILES experiment located at the SOLEIL synchrotron facility.

facility (located in the Paris area, in France). We then wrote a successful proposal to get a one-week period during which we used the AILES experiment (see Fig. 11.1) to record the CO_2-H_2 and CO_2-CH_4 CIAs. This experiment is equipped with a Fourier transform spectrometer and a detector cooled down to 4.2 K by liquid helium, thus allowing measurements in the far infrared, where CO_2-H_2 and CO_2-CH_4 CIAs are predicted by theoretical calculations to be the dominant sources of absorption (Wordsworth et al., 2017).

I present in this chapter the first experimental measurements of the CO_2-H_2 and CO_2-CH_4 collision-induced absorptions.

This chapter is based on a paper submitted to Icarus in May 2018. The full reference is: Martin Turbet, Ha Tran, Olivier Pirali, Francois Forget, Christian Boulet, & Jean-Michel Hartmann, **"Far infrared measurements of absorptions by CH_4+CO_2 and H_2+CO_2 mixtures and implications for greenhouse warming on early Mars"** (http://adsabs.harvard.edu/abs/2018arXiv180502595T).

11.2 Abstract

We present an experimental study of the absorption, between 40 and 640 cm^{-1}, by CO_2, CH_4 and H_2 gases as well as by H_2+CO_2 and CH_4+CO_2 mixtures at room temperature. A Fourier transform spectrometer associated to a multi-pass cell, whose optics were adjusted to obtain a 152 m pathlength, were used to record transmission spectra at total pressures up to about 0.98 bar. These measurements provide information concerning the collision-induced absorption (CIA) bands as well as about the wing of the CO_2 15 μm band. Our results for the CIAs of pure gases are, within uncertainties, in agreement with previous determinations, validating our experimental and data analysis procedures. We then consider the CIAs by H_2+CO_2 and CH_4+CO_2 and the low frequency wing of the pure CO_2 15 μm band, for which there are, to our knowledge, no previous measurements. We confirm experimentally the theoretical prediction of Wordsworth et al. (2017) that the H_2+CO_2 and CH_4+CO_2 CIAs are significantly stronger in the 50-550 cm^{-1} region than those of H_2+N_2 and CH_4+N_2, respectively. However, we find that the shape and the strength of these recorded CIAs differ from the aforementioned predictions. For the pure CO_2 line-wings, we show that both the χ- factor deduced from measurements near 4 μm and a line-mixing model very well describe the observed strongly sub-Lorentzian behavior in the 500-600 cm^{-1} region. These experimental results open renewed perspectives for studies of the past climate of Mars and extrasolar analogues.

11.3 Introduction

It is well known that, in the atmospheres of many planets, the far wings (FWs) of molecular absorption lines (e.g. those of CO_2 in Venus, of CH_4 in Titan and Jupiter) and collision-induced absorptions (CIAs, e.g. that by CO_2 pairs in Venus; of N_2 pairs in Titan; of H_2 pairs in Jupiter) significantly participate to the radiative budgets. This has motivated numerous experimental and theoretical laboratory studies of the CIA of various molecular systems, from the visible to the far infrared (see reviews in Frommhold (2006); Hartmann et al. (2008); Richard et al. (2012); Hartmann et al. (2018b); Karman et al. (2018). The same remark stands for the FWs, but the latter were essentially studied for H_2O and CO_2 only (see Hartmann et al. 2008, 2018b and references therein).

Understanding how the early Martian climate could have been warm enough for liquid water to flow on the surface remains one of the major enigmas of planetary science (Wordsworth, 2016; Haberle et al., 2017) and no consensus scenario has yet been reached. Thick, CO_2-dominated atmospheres do not provide the necessary greenhouse effect to warm the surface of early Mars above the melting point of water (Forget et al., 2013; Wordsworth et al., 2013). In this case, longwave radiation losses essentially occur in the 200-600 cm^{-1} region (Wordsworth et al., 2010a) where absorption and emission are dominated by the CO_2 roto-translational CIA and the FWs of the intense 15 μm-band lines. The radiative budget in this spectral region is significantly affected by the assumption made on the shape of these FWs (Turbet and Tran, 2017), and no measurements are, to our knowledge, available to constrain it.

In reducing atmosphere conditions, absorptions can arise from the CIAs of H_2-CO_2 and CH_4-CO_2 pairs. Up to now, the modelings of these two contributions were based, due to lack of relevant data, on the CIAs of H_2-N_2 and CH_4 -N_2 pairs, respectively (e.g. Ramirez et al. (2014a)). Wordsworth et al. (2017) recently calculated that the collision-induced absorptions by H_2+CO_2 and CH_4+CO_2 mixtures should be significantly stronger than those for H_2+N_2 and CH_4+N_2, respectively. These

calculations have important implications for our understanding of the climate of early Mars, at the time when valley networks were carved by liquid water. Indeed, with these new CIAs, only a few % of CH_4 and/or H_2 in a CO_2-dominated atmosphere could suffice to warm early Mars enough for surface liquid water to become stable (Wordsworth et al., 2017; Ramirez, 2017). These calculated CIAs, if confirmed by laboratory experiments, have the power to reconcile the Martian geology and mineralogy with our knowledge on atmospheric sciences.

The remainder of this paper is organized as follows. Section 11.4 describes the experiments and the way the recorded spectra of CO_2, CH_4, H_2, H_2+CO_2 and CH_4+CO_2 were analyzed. The results obtained for the CIAs and for the low frequency wings of the pure CO_2 lines are presented in Sections 11.5 and 11.6, respectively. Discussions of the results and the consequences for studies of the past climate of Mars are the subject of Section 11.7. Final conclusions and possible directions for future studies are given in Section 11.8.

11.4 Experiments and their analysis

11.4.1 Spectra recordings

The spectra used in this study have been recorded at the AILES line of the Soleil synchrotron facility in a way similar to that used in Pirali et al. (2009); Hartmann et al. (2011). A Bruker IFS 125HR Fourier transform spectrometer (FTS) and a 2.5 m long multi-pass cell with 60 μm thick polypropylene windows, were used. The globar source inside the FTS was used, together with a 6 μm thick mylar beam splitter, a band-pass filter, and a Si bolometer detector cooled down to 4.2 K by liquid helium. Measurements were made at room temperature ($\sim$ 296 K) for a path length of 151.75 m, with an unapodized spectral resolution of 1 cm^{-1}. In total, 1000 scans were co-added to generate each of the spectra. Due to the optics and detector used, the signal is significant and reliable between 40 and 680 cm^{-1}. Within this range, each recording provides about 2650 spectral values with a step of 0.24 cm^{-1}. The pressures were measured and continuously monitored with both a 1000 millibar (Pfeifer) and a 1000 Torr (Edwards) gauges. Their readings agreed in all cases to better than 1 %. CO_2, H_2 and CH_4 gases provided by Air Liquide were used for the recording of pure samples as well as mixtures. The latter were made by first introducing H_2 (or CH_4) and then adding CO_2 up to a total pressure of about 0.9 bar. After recording a first spectrum, the pressure of each initial gas sample was progressively reduced with a vacuum pump to yield spectra of the same mixture (or pure gas) at several lower pressures. In addition, reference (100% transmission) spectra were obtained for similar pressures by introducing pure argon into the cell. The list of recorded spectra and their conditions are given in Appendix 11.9.1.

Note that we had to limit the total pressure in the cell to slightly below 1 bar in order to avoid possible damage of the cell and/or of its windows since they are not designed to go above atmospheric pressure. The product of the path length and gas densities is thus limited to about 1.3×10^4 cm amagat^2 (1 amagat corresponds to 2.69×10^{19} molec/cm^3) for studies of pure gases and 0.33×10^4 cm amagat^2 for mixtures, which induces large uncertainties on the determination of weak CIAs, as shown in Secs. 11.5 and 11.6. We also draw the reader attention to the fact that the SOLEIL-AILES facility is extremely sought and busy and that we only had access to it for a few days, limiting the number of spectra we could record in this first study of the CIAs by H_2-CO_2 and CH_4-CO_2 pairs. We hope that this will stimulate further thorough experimental investigations, hopefully under more absorbing conditions.

11.4.2 Spectra treatments

The raw spectra recordings were treated using the five steps procedure detailed below.

Step 1: For all samples, the recorded spectra show absorption by water vapor lines due to small amounts of H_2O present in the gases used. The first step of the treatment of the collected data was thus to remove their contributions. For this, H_2O transmissions were computed and used, as explained in Appendix 11.9.2, in order to remove the absorption features due to water lines from the raw spectra and obtain "dried out" spectra.

Step 2: For a given sample, the transmission spectrum was then obtained by dividing the associated recording cleared from the H_2O contribution by a pure argon spectrum, also cleared of the H_2O lines. Among the various recorded pure Ar spectra (see Appendix 11.9.1), we chose a linear combination of two Ar spectra for which the broad-band features resulting from the absorption and interference patterns generated by the propylene windows are the closest to those observed in the sample gas spectrum. Indeed, since these features are different from one spectrum to another (likely because of changes of the temperature and/or window curvature induced by pressure), rationing adapted recordings is essential to minimize the residual broad-band oscillations in the resulting transmission spectrum. However, baseline variations due to changes of the globar source emission, bolometer responsivity and mechanical deformations of the multipass cell itself may also occur from one recording to another. This introduces an error on the 100% transmission level which directly affects the weak and broad-band absorption continua searched for. The way we dealt with this difficulty is described in step 5 below.

Step 3: For the part of this study devoted to the collision-induced absorption continua discussed in Sec. 11.5 (but not to the far line wings discussed in Sec. 11.6), the third step was to remove the contributions of the local lines of CO_2 and CH_4. These contributions were computed as explained in Appendix 11.9.2, yielding the associated transmission by local lines by which the spectrum obtained from steps 1 and 2 is divided so that only the CIA remains.

Step 4: The transmissions obtained from the preceding treatments show a few sharp features (outliers) essentially found close to the local lines (of H_2O, CH_4 and CO_2) that have been removed in steps 1 and 3. Analysis shows that this is due to small differences between the measurements and the calculation of these narrow features. In order to "clean" the spectra from these outliers, we performed the following procedure. First, a moving average of each spectrum over 5 cm^{-1} was computed. Then, the mean distance between this averaged spectrum and the original one was computed at each wavelength. All data points of the original spectrum that are further away from the averaged spectrum than half of this mean distance were rejected.

Step 5: Starting from each transmission spectrum obtained from steps 1-4, we compute the negative value of its natural logarithm and divide the result by the optical path length (15175 cm). This provides the measured absorption coefficient $\alpha^{\text{meas}}(\sigma,\mathrm{P_X},\mathrm{P_{CO_2}})$ at wave number σ that, since local line contributions have been removed and only CIA remains, should be equal to:

$$\alpha^{\text{calc}}(\sigma, P_{\mathrm{X}}, P_{\mathrm{CO_2}}) \;=\; P_{\mathrm{CO_2}}^2\; C_{\mathrm{CO_2-CO_2}}(\sigma) + P_{\mathrm{X}}\; P_{\mathrm{CO_2}}\; C_{\mathrm{CO_2}-X}(\sigma) + P_{\mathrm{X}}^2\; C_{\text{X-X}}(\sigma) \qquad (11.1)$$

where $C_{\mathrm{CO_2}-X}(\sigma)$ is the pressure-normalized binary collision-induced absorption coefficient for CO_2-X pairs. In order to determine its spectral values, two procedures have been used:

In the first procedure, we assume that the 100% transmission baseline is correct. For pure gases, we determine $C_{\text{X-X}}(\sigma_{\mathrm{i}})$ from a simultaneous least square fit of all spectra, by minimizing the

quantity

$$\sum_{P_X}\sum_{\sigma_i}\Big(\alpha^{meas}(\sigma_i,P_X)-P_X^2\ C_{X\text{-}X}(\sigma_i)\Big)^2$$

. For CO_2-X mixtures, we minimize:

$$\sum_{P_X}\sum_{P_{CO_2}}\sum_{\sigma_i}\Big(\Big[\alpha^{meas}(\sigma_i,P_X,P_{CO_2})-P_X^2\ C_{X\text{-}X}(\sigma_i)-P_{CO_2}^2\ C_{CO_2-CO_2}(\sigma_i)\Big]-\Big[P_X\ P_{CO_2}\ C_{CO_2-X}(\sigma_i)\Big]\Big)^2$$

by floating the values of the $C_{CO_2-X}(\sigma_i)$, those of $C_{X\text{-}X}(\sigma_i)$ and $C_{CO_2-CO_2}(\sigma_i)$ being fixed. For the latter, we used the data of Ho et al. (1971) for pure CO_2, of Codastefano et al. (1985) for pure CH_4 and of Abel et al. (2011) for pure H_2, because they are more precise than the ones determined in the present study. These least square fits also provide the 1-σ statistical (rms) uncertainties on the fitted parameters [$C_{X\text{-}X}(\sigma_i)$ and $C_{CO_2-X}(\sigma_i)$]. Note that 2-σ was adopted for the error bars displayed in the figures below.

In the second procedure, we introduce a baseline correction as a linear function of wave number. This function is assumed to be the same for a series of consecutive spectra at different pressures (i.e. those for a given mixture or a pure gas). In this case, for pure gases, we minimize the quantity:

$$\sum_{P_X}\sum_{\sigma_i}\Big(\alpha^{meas}(\sigma_i,P_X)-A-B\ \sigma_i-P_X^2\ C_{X\text{-}X}(\sigma_i)\Big)^2$$

by floating the values of A, B and $C_{X\text{-}X}(\sigma_i)$. For CO_2-X mixtures, since we recorded spectra at several pressures for each sample composition (i.e. each value of $\frac{P_X}{P_{CO_2}}$, see Table 1), we minimize the quantity

$$\sum_{P_X}\sum_{P_{CO_2}}\sum_{\sigma_i}\Big(\Big[\alpha^{meas}(\sigma_i,P_X,P_{CO_2})-P_X^2\ C_{X\text{-}X}(\sigma_i)-P_{CO_2}^2\ C_{CO_2-CO_2}(\sigma_i)-A(\frac{P_X}{P_{CO_2}})-B(\frac{P_X}{P_{CO_2}})\ \sigma_i\Big]$$

$$-\Big[P_X\ P_{CO_2}\ C_{CO_2-X}(\sigma_i)\Big]\Big)^2$$

by floating the values of A($\frac{P_X}{P_{CO_2}}$) , B($\frac{P_X}{P_{CO_2}}$) , and $C_{CO_2-X}(\sigma_i)$. We thus assume here that A and B have a unique value for each mixture relative composition. Note that there are about 1400 points in each fitted spectrum and that, for each mixture, nine spectra (3 pressures for each one of the three mixtures, see Table 1) were recorded. We thus have a total number of ∼12600 absorbance values. They provide enough information to deduce, from their adjustments, the ∼1400 pressure-normalized absorptions $C_{CO_2-X}(\sigma_i)$ and the 6 baseline parameters A($\frac{P_X}{P_{CO_2}}$) and B($\frac{P_X}{P_{CO_2}}$).

11.5 The Collision-Induced Absorptions (CIAs)

11.5.1 The test cases of the CIAs of pure CO_2, CH_4 and H_2

Although measuring the CIAs of pure gases is not the objective of this study since several measurements and calculations have been made before (see below), we measured them to test and evaluate the accuracy of our experimental and data analysis procedures. Indeed, since the previous experimental studies have been made under much more favorable conditions (stronger absorptions thanks to higher pressures), they are likely more accurate than our determinations.

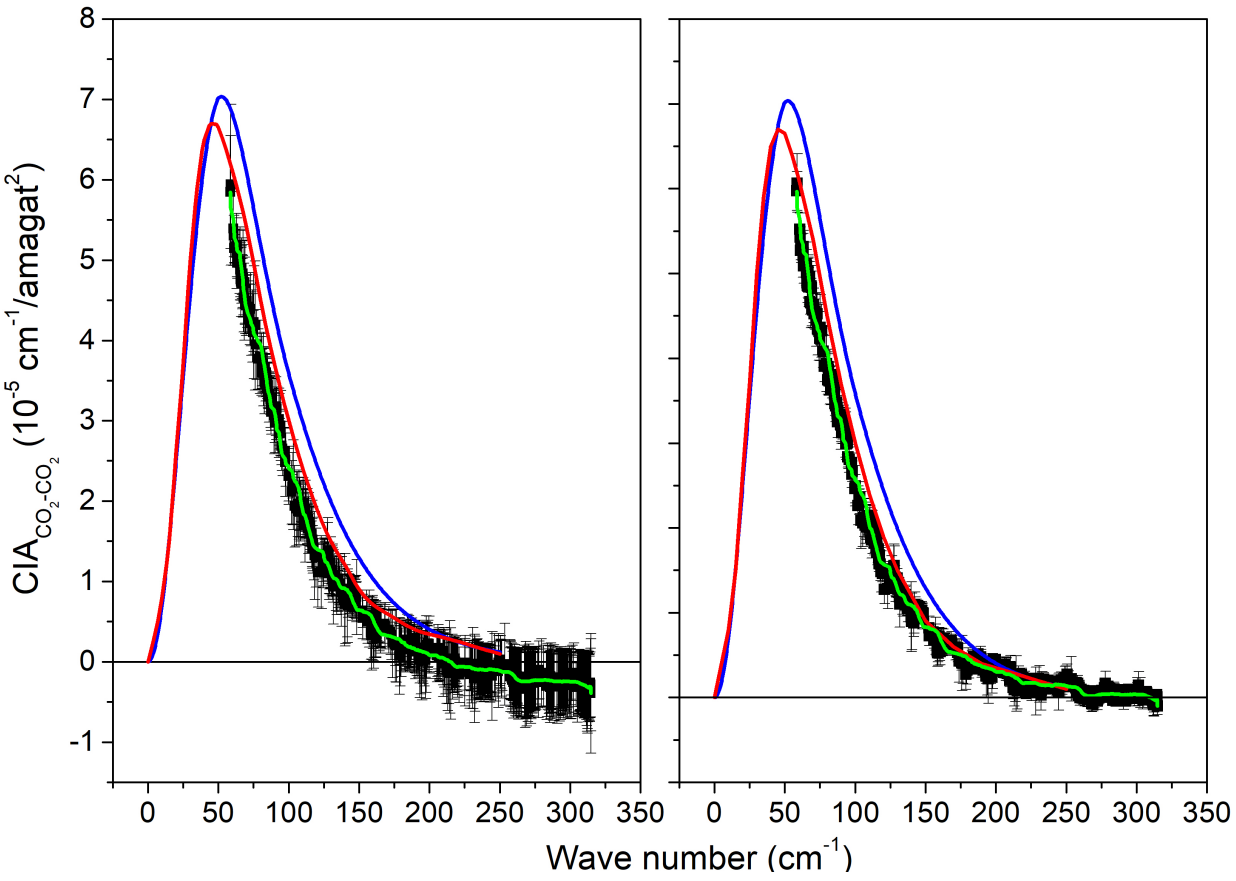

Figure 11.2: Pure CO_2 CIAs at room temperature. The symbols with error bars are the present measurements, the green line is a moving average of the latter over 10 cm^{-1}, the red line represents the measurements of Ho et al. (1971) (digitized from Fig. 1 of this reference), and the blue curve denotes the calculated values from Gruszka and Borysow (1997) which are available in the HITRAN CIA database section (Richard et al., 2012). The results in the left and right hand-side panels have been obtained without and with the baseline adjustment, respectively.

For the pure CO_2 CIA, measurements were reported in Harries (1970); Ho et al. (1971); Hartmann et al. (2011), for instance, and theoretical calculations can be found in Gruszka and Borysow (1997, 1998); Hartmann et al. (2011). A comparison of our results, obtained from fits of the five spectra at pressures from about 0.20 to 0.95 bar with and without introduction of a baseline, with the measured values of Ho et al. (1971) (uncertainty stated as better than 10 %) and the calculated results of Gruszka and Borysow (1997) is plotted in Fig. 1. As can be seen, adjusting a baseline in the fit significantly reduces the error bars (and rms of the fit), corrects for the negative values in the high frequency wing, and improves the agreement between our results and the previous determinations. In this case, the area obtained from the integration of our results between 60 and 250 cm^{-1} is 2.74±0.32 × 10^{-3} cm^{-2}/amagat^2 (the uncertainty given here being directly obtained from the error bars in Fig. 1) while 3.11±0.31 × 10^{-3} cm^{-2}/amagat^2 is obtained from the measurements of Ho et al. (1971), and 3.73 × 10^{-3} cm^{-2}/amagat^2 from the calculated values of Gruszka and Borysow (1997). Our determination thus agrees, within uncertainties, with the previous measurement of Ho et al. (1971). Note that, when compared to the other gas samples discussed below, the pure CO_2 case is the most favorable since, for the most optically thick sample investigated (at ∼0.95 bar), the transmission is 55% at the peak near 50 cm^{-1}.

The CIA of pure CH_4 was investigated experimentally in Codastefano et al. (1985, 1986); Birnbaum (1975); Dagg et al. (1986). El-Kader and Maroulis (2012); Borysow and Frommhold (1987b,a) provide examples of theoretical calculations. A comparison between some of these previous data and the results obtained from our three spectra (pressures between ∼0.60 and 0.98 bar) is plotted in Fig. 2. As for pure CO_2, introducing a baseline in the fit reduces the uncertainties (and rms), improves the CH_4-CH_4 CIA high frequency wing, and leads to a better agreement with previous determinations. In this case, the area obtained from the integration of our results between 70 and 600 cm^{-1} is 2.2±0.2 × 10^{-3} cm^{-2}/amagat^2. It is slightly lower than the experimental value of 2.97±0.31 × 10^{-3} cm^{-2}/amagat^2 from Codastefano et al. (1985). Note that, for the most optically thick sample investigated (at ∼0.98 bar), the peak absorption in our measurements is significantly smaller than for pure CO_2 with a transmission of about 90% near 250 cm^{-1}.

The CIA of pure H_2 was investigated experimentally in Birnbaum (1978); Bachet et al. (1983). Theoretical calculations were made in Birnbaum et al. (1996); Gustafsson et al. (2003); Abel et al. (2011); Karman et al. (2015b), and references therein. A comparison between some of these previous data and the results of our measurements is plotted in Fig. 3. Note that in this case, the treatment applied to the spectra was slightly different from that used for all other samples. In fact, a quick look at the transmissions obtained after step 4 revealed that they differed from unity at small wave numbers (where the absorption should be negligible (Birnbaum, 1978) for our recording conditions) with significant inconsistencies between the three spectra. This explains the very large uncertainties and negative values of the CIA obtained when no base line is introduced in the fit (see the left panel of Fig. 3). Therefore, we pre-treated each transmission spectrum by dividing it by the averaged value at about 100 cm^{-1} where the absorbance under our conditions should be nearly zero. Then, the procedure described in step 5 of Sec. 11.4 was applied with the fit of a single base line for all spectra. This leads to the results plotted in the right hand side panel of Fig. 3 which show several obvious improvements with respect to those in the left hand side panel. However, significant differences with previous determinations remain. These differences can be likely explained by the fact that, for the most optically thick sample investigated (i.e. about 0.95 bar of H_2), the peak absorption is very small with a transmission of about 94% near 600 cm^{-1} (according to the values of Birnbaum 1978).

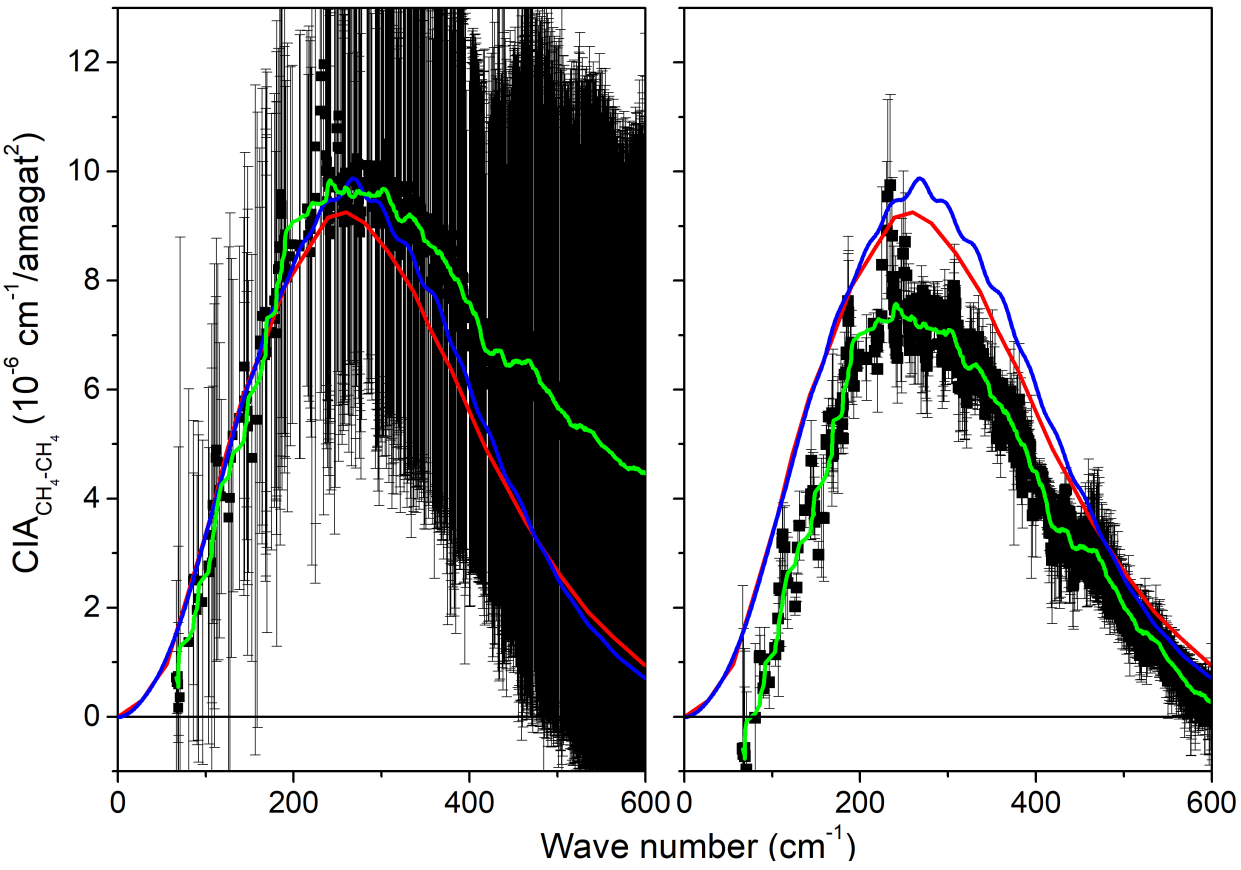

Figure 11.3: Pure CH_4 CIAs at room temperature. The symbols with error bars are the present measurements, the green line is a moving average of the latter over 10 cm^{-1}, the red line represents the measurements of Codastefano et al. (1985) (digitized from Fig. 1 of this reference), and the blue curve denotes the calculated values from Borysow and Frommhold (1987b) which are available in the HITRAN CIA database section (Richard et al., 2012). The results in the left and right hand-side panels have been obtained without and with adjustment of the baseline, respectively.

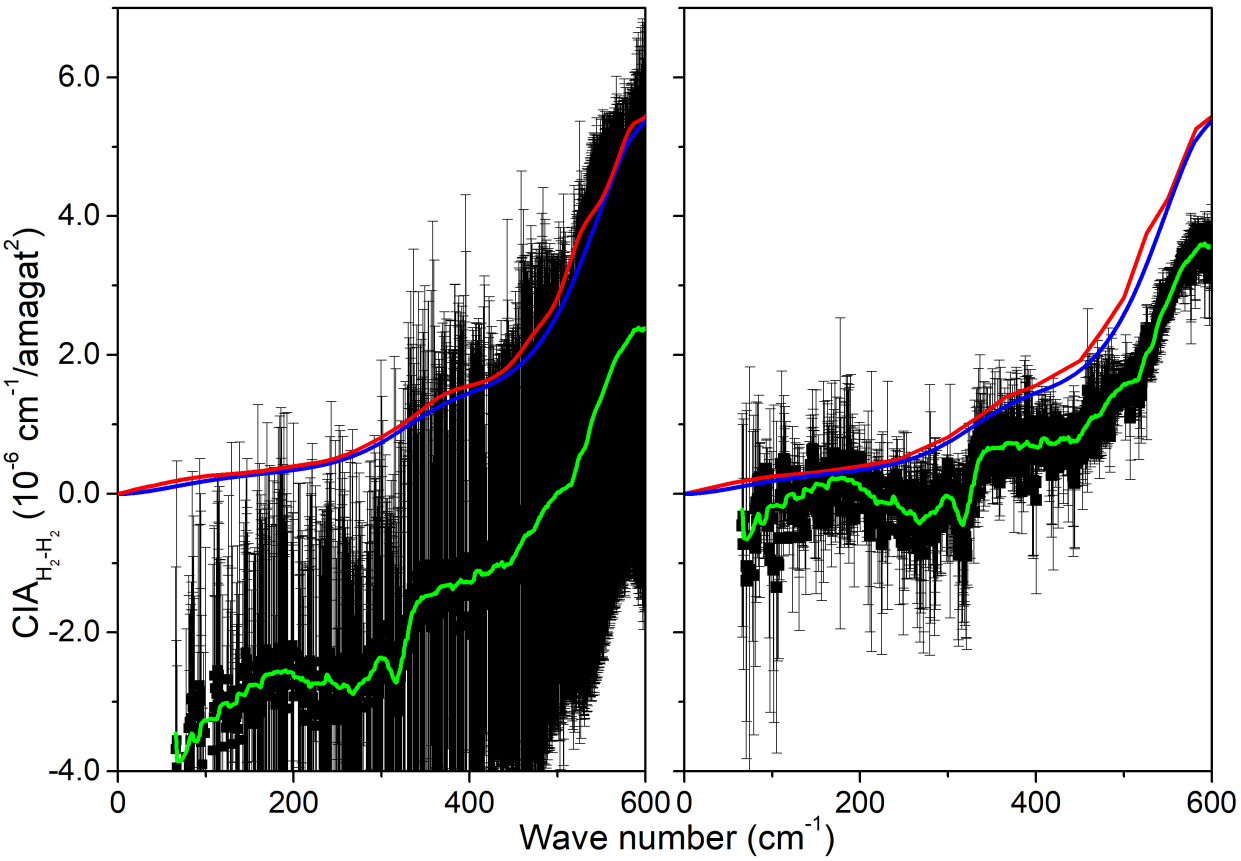

Figure 11.4: Pure H_2 CIA at room temperature. The symbols are the present measurements, the green line is a moving average of the latter over 10 cm^{-1}, the red line represents the measurements of Birnbaum (1978) (digitized from Fig. 2 of this reference), and the blue curve denotes the calculated values from Abel et al. (2011) which are available in the HITRAN CIA database section (Richard et al., 2012).

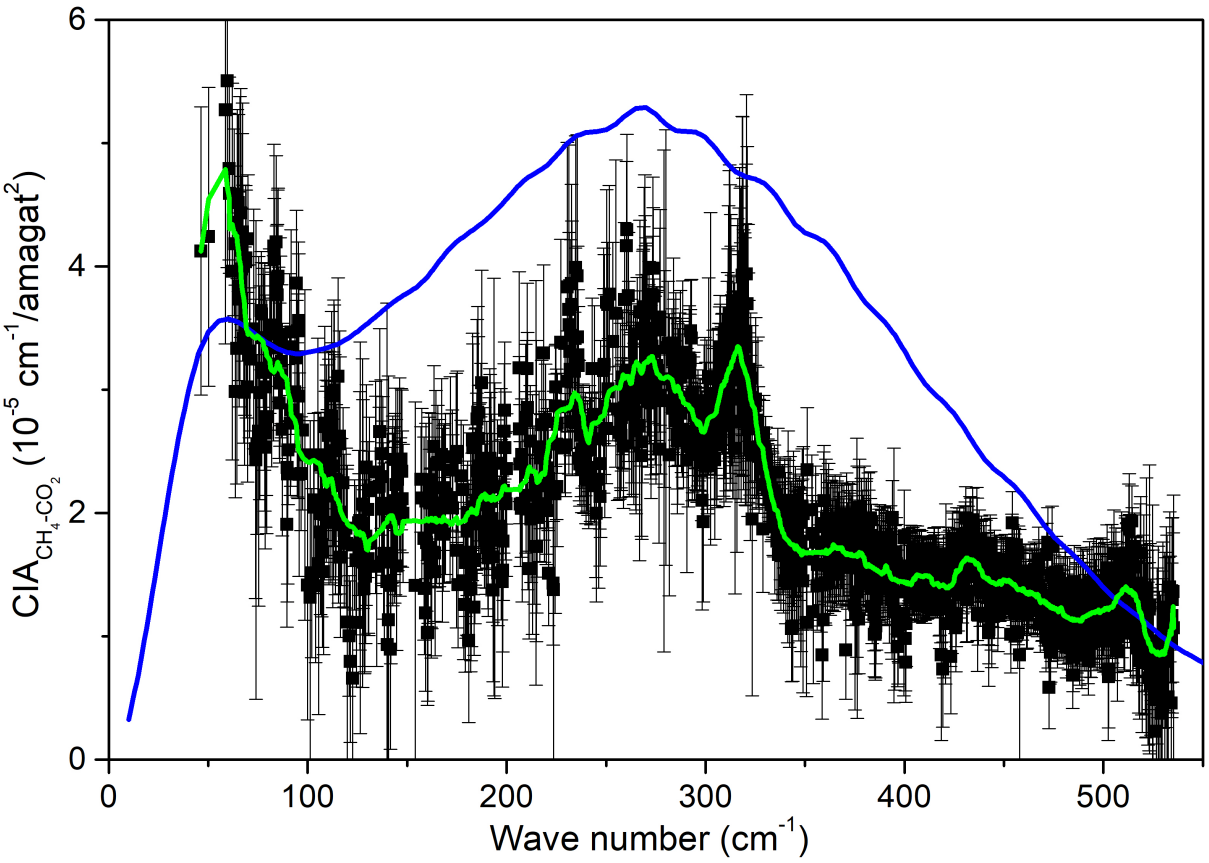

Figure 11.5: CH_4+CO_2 CIAs at room temperature. The symbols with error bars are the present measurements, the green line is a moving average of the latter over 10 cm^{-1}, the blue line represents the calculated values of Wordsworth et al. (2017).

11.5.2 The CIAs of CH_4+CO_2 and H_2+CO_2 mixtures

Now that the comparisons between our results for pure gases and previous determinations have validated our experimental and data analysis procedure (at least when the peak absorption is large enough, thus excluding the pure H_2 case) we consider the mixtures for which no other measurements are available. Note that, while squared pressures up to ∼1 bar^2 could be used for pure gases, the case of mixtures is much less favorable since P_X P_{CO_2} is now limited to ∼0.25 bar^2. Finally, since the results of Sec. 11.4 show that adjusting a linear baseline correction leads to significant improvements, only the results obtained with this approach are presented below. However, for the two considered mixtures, results obtained without adjustment of baselines are fully consistent when error bars are considered. The CIA of CH_4+CO_2 has never been measured before, but theoretical predictions have been made (Wordsworth et al., 2017). A comparison between these predictions and the results of our measurements is plotted in Fig. 4. We measure a significant CO_2-CH_4 CIA in the 50-500 cm^{-1} spectral range that has, as predicted (Wordsworth et al., 2017), two peaks around 50 and 270 cm^{-1}. However,

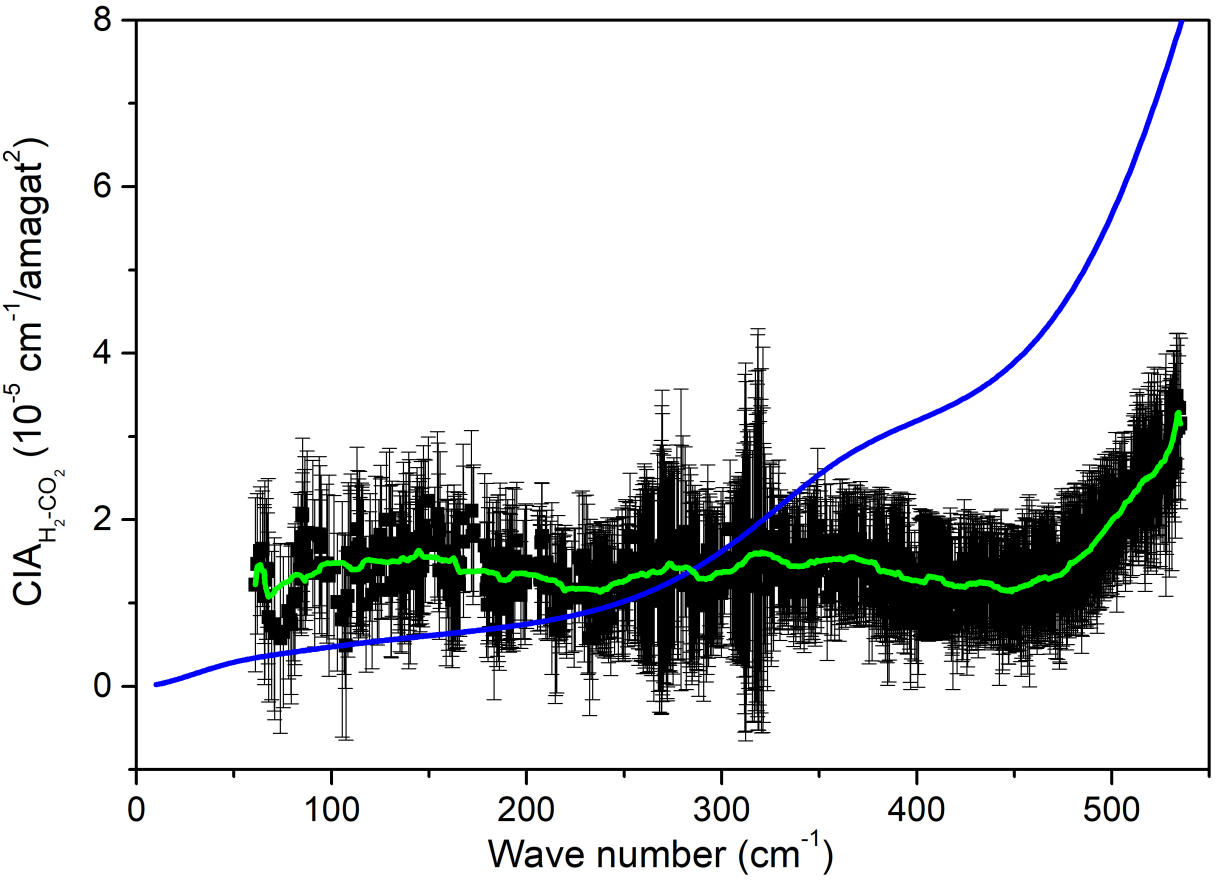

Figure 11.6: H_2+CO_2 CIAs at room temperature. The symbols with error bars are the present measurements, the green line is a moving average of the latter over 10 cm^{-1}, the blue line represents the calculated values of Wordsworth et al. (2017).

our experiments lead, on average, to significantly smaller values with an area between 50 and 500 cm^{-1} of 9.9±2.7 × 10^{-3} cm^{-2}/amagat^2, about 1.73 times smaller than that obtained from the prediction of Wordsworth et al. (2017). Despite the rather large uncertainties, the experimental results show that the theoretical prediction of Wordsworth et al. (2017) overestimates this CIA. Indeed, our CH_4+CO_2 CIA leads to peak absorbances for the optically thickest conditions investigated (∼0.47 bar of CH_4 + ∼0.47 bar of CO_2) of 0.16 and 0.10, corresponding to a transmission of about 85 % and 90 % near 50 and 270 cm^{-1} respectively, which gives relatively "comfortable" conditions.

As for the CIA of CH_4+CO_2, that of H_2+CO_2 has never been measured before, but theoretical predictions have also been made (Wordsworth et al., 2017). These calculated data and the results of our experiments are plotted in Fig. 5. We measure a significant CIA throughout the entire spectral range (corresponding to an absorbance of ∼0.07 for the optically thickest conditions) which increases with wavenumber at high frequencies, as predicted in Wordsworth et al. (2017). However, large differences can be observed in Fig. 5 between our measurements and the predictions, both for the shape and magnitude, for which we have no explanation at this step. Finally note that our determinations are

limited to wavenumbers lower than 550 cm^{-1} because of the strong contribution of CO_2 absorption lines beyond this frequency (see Fig. 6). In addition, it is possible that a part of the absorption that we measure comes from the H_2-broadened wings of the 15 μm CO_2 band lines, whose contributions are, as the CIA, proportional to P_{H_2} P_{CO_2}.

In order to generate "the best" datasets of measured CH_4+CO_2 and H_2+CO_2 CIAs we started from the values with error bars in Figs. 4 and 5. For the mean values, we computed a moving average over 25 cm^{-1} and tabulated its values with a step of 5 cm^{-1}. Determining the uncertainties is, as it is well known, a very difficult task, even in cases where numerous measurements have been made for reliable statistics. In the present study, we computed the moving average, over 25 cm^{-1}, of the error bars plotted in Figs. 4 and 5. The obtained results were then multiplied by 1.5 in order to take into account other sources of uncertainties (mostly due to base line stability within the same recording series). Since the error bars in Figs. 4 and 5 already correspond to the 2-σ value (95% confidence interval), we believe that the total uncertainty estimated this way is (very) conservative considering the measured data at our disposal. The final set of data for the CH_4+CO_2 and H_2+CO_2 CIAs are given in Table 2 of Appendix C of Turbet et al. (2018b). We recall the reader that these should be used with great care as their uncertainties are rather large.

11.6 The low frequency wing of the CO_2 ν_2 band

The recorded pure CO_2 spectra enable to study the absorption in the low frequency wing of the intense ν_2 band (centered at 667 cm^{-1}), from about 500 to 600 cm^{-1}. While there are, to our knowledge, no previous measurements available, comparisons with calculations are possible. Indeed, the spectra can be predicted using the line-mixing model of Tran et al. (2011) or Voigt profiles corrected in the wings by using a χ-factor. Three sets of such factors have been proposed, deduced from measurements in the high frequency wings of the ν_2 ($\sigma > 750$ cm^{-1}) (Tran et al., 2011) and ν_3 ($\sigma > 2400$ cm^{-1}) (Perrin and Hartmann, 1989; Tran et al., 2011) bands. Note that the line-mixing model of Tran et al. (2011) and the χ-factor of Perrin and Hartmann (1989) were used in Turbet and Tran (2017) for radiative transfer calculations in the far infrared for rich CO_2 atmospheres but that they had not been validated in this spectral region yet. Comparisons between measured transmissions and those computed with the four models mentioned above and by using purely Voigt profiles (no line-mixing and no χ-factor correction, i.e. $\chi(\Delta\sigma) = 1$] are plotted in Fig. 6, calling for the following remarks. The first is that calculations with pure Voigt line shapes (blue) lead to very large errors showing the strongly sub-Lorentzian behavior of the line wings. The second is that the three χ-factors used (red curves) lead to indiscernible results on this plot, all in very good agreement with the measured spectrum, except in a narrow interval around the Q branch centered at 545 cm^{-1}. This local effect of line-mixing is very nicely reproduced by the line-mixing model of Tran et al. (2011) which is also in excellent agreement with the χ-factor predictions (as also shown in Turbet and Tran 2017) and the measured spectra throughout the entire spectral range.

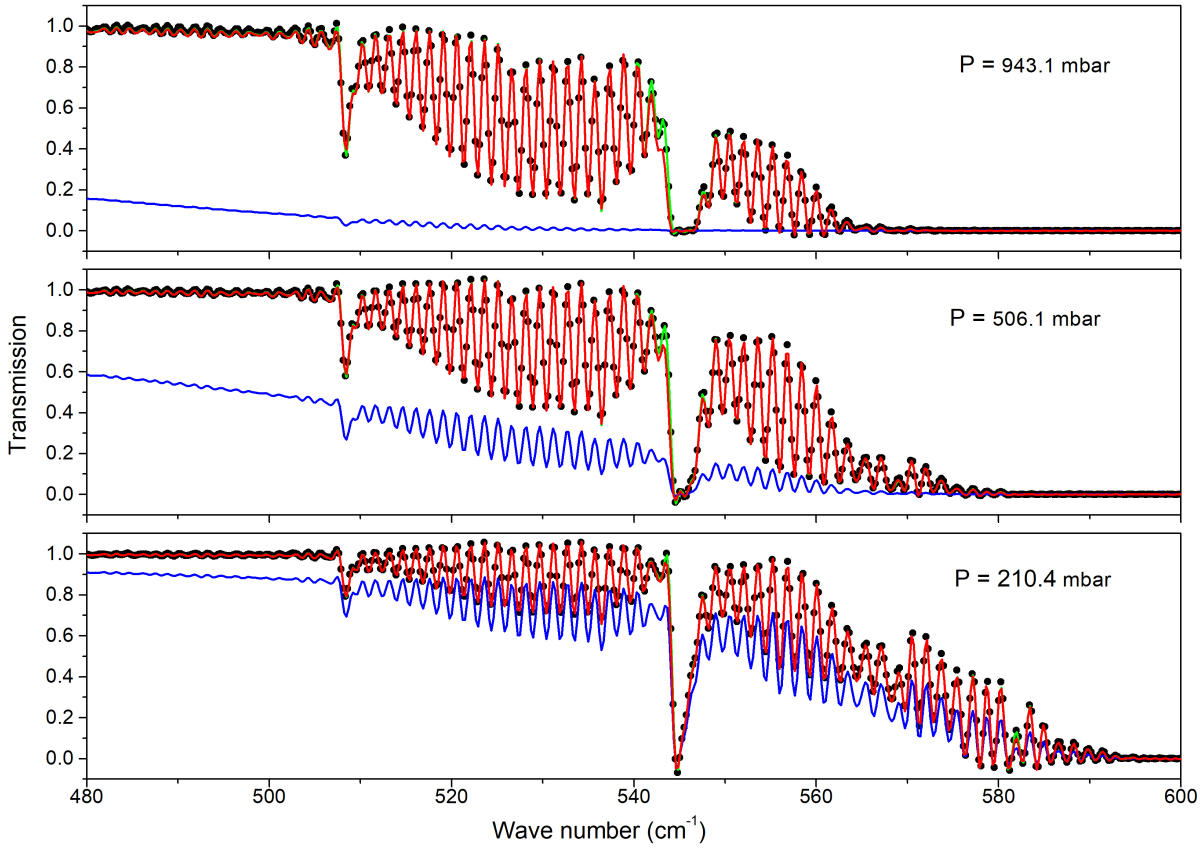

Figure 11.7: Pure CO_2 transmission spectra for three pressures. The black circle denotes the measured values (not all plotted). The red lines are the (indistinguishable) results obtained with the three χ-factors (see text). The blue line is obtained with purely Voigt line shapes ($\chi = 1$). The green line denotes the results of calculations obtained with the pure CO_2 line-mixing model of Tran et al. (2011).

11.7 Discussion

11.7.1 On the CIAs of CH_4+CO_2 and H_2+CO_2

A comparison between our final experimental determinations of the CH_4+CO_2 and H_2+CO_2 CIAs and the corresponding predictions of Wordsworth et al. (2017) as well as with the CIAs when CO_2 is replaced by N_2 is plotted in Fig. 7.

First, both our measurements and the predictions indicate that the effect of interactions of CH_4 and H_2 with CO_2 induce much stronger absorptions than with N_2. This could actually be expected by simply considering the long range induction mechanisms which are likely dominant here and are governed by the isotropic polarizability and the electric quadrupole moment (of N_2 or CO_2). As shown by the data given in Li et al. (1998), the values of all these parameters are, for CO_2, from 1.5 to nearly 3 times greater than for N_2. Reminding that the square of the dipole is involved, and even though the intermolecular potential and its anisotropy also play a role, it is quite obvious that the X-CO_2 should be significantly larger than the X-N_2 CIA.

For the differences between our measurements and the predictions of Wordsworth et al. (2017), which are significant and concern both the magnitude and the shape of the CIAs, we have no explanation at this step. Trying to understand their origin(s) is beyond the scope of the present paper. Obviously, independent checks of our results by new measurements are needed, if possible under more absorbing conditions in order to reduce the uncertainties resulting from a poor knowledge of the 100% transmission level. Ideally, we recommend performing future investigations of CO_2-CH_4 and CO_2-H_2 CIAs for products of the path length and gas densities up to at least 2 10^4 cm amagat^2. Furthermore, measurements at several temperatures (between at least 200 and 300 K) would be of considerable interest since they would provide the planetary science community with CIAs that can be used directly in numerical climate models. However, such experiments are difficult and there are not many (if any) existing setups suitable to carry them. In parallel, the approximations made for the predictions of Wordsworth et al. (2017) need to be investigated and this could be done by using various alternative theoretical approaches. These include fully classical computations based on molecular dynamics simulations (e.g. Gruszka and Borysow 1998; Hartmann et al. 2011, 2018a), semi-classical approaches based on line shapes (e.g. Birnbaum and Cohen 1976; Hunt and Poll 1978) and the so-called "isotropic approximation" (e.g. Leforestier et al. 2010; Hartmann et al. 2018a), and fully quantum scattering computations assuming isotropic intermolecular forces (e.g. Borysow and Frommhold 1986; Borysow and Tang 1993) or taking the intermolecular potential anisotropy into account (e.g. Karman et al. 2015a,b). Note that, in the absence of relevant measurements, theory may give information on the temperature dependences of the CO_2-CH_4 and CO_2-H_2 CIAs which are, as mentioned above, crucially needed.

11.7.2 Implications for the climate of early Mars

Although our measurements have large uncertainties, we can discuss their implications for the climate of early Mars. In the 200-600 cm^{-1} spectral window of early Mars, our measurements confirm that the CO_2-CH_4 and CO_2-H_2 CIA are much stronger than those of N_2-CH_4 and N_2-H_2 pairs, respectively. However, they also show that the calculations of Wordsworth et al. (2017) overestimate on average the CO_2-CH_4 and CO_2-H_2 CIAs by a factor of about 1.6.

Our measurements indicate that Wordsworth et al. (2017) and Ramirez (2017) overestimated the

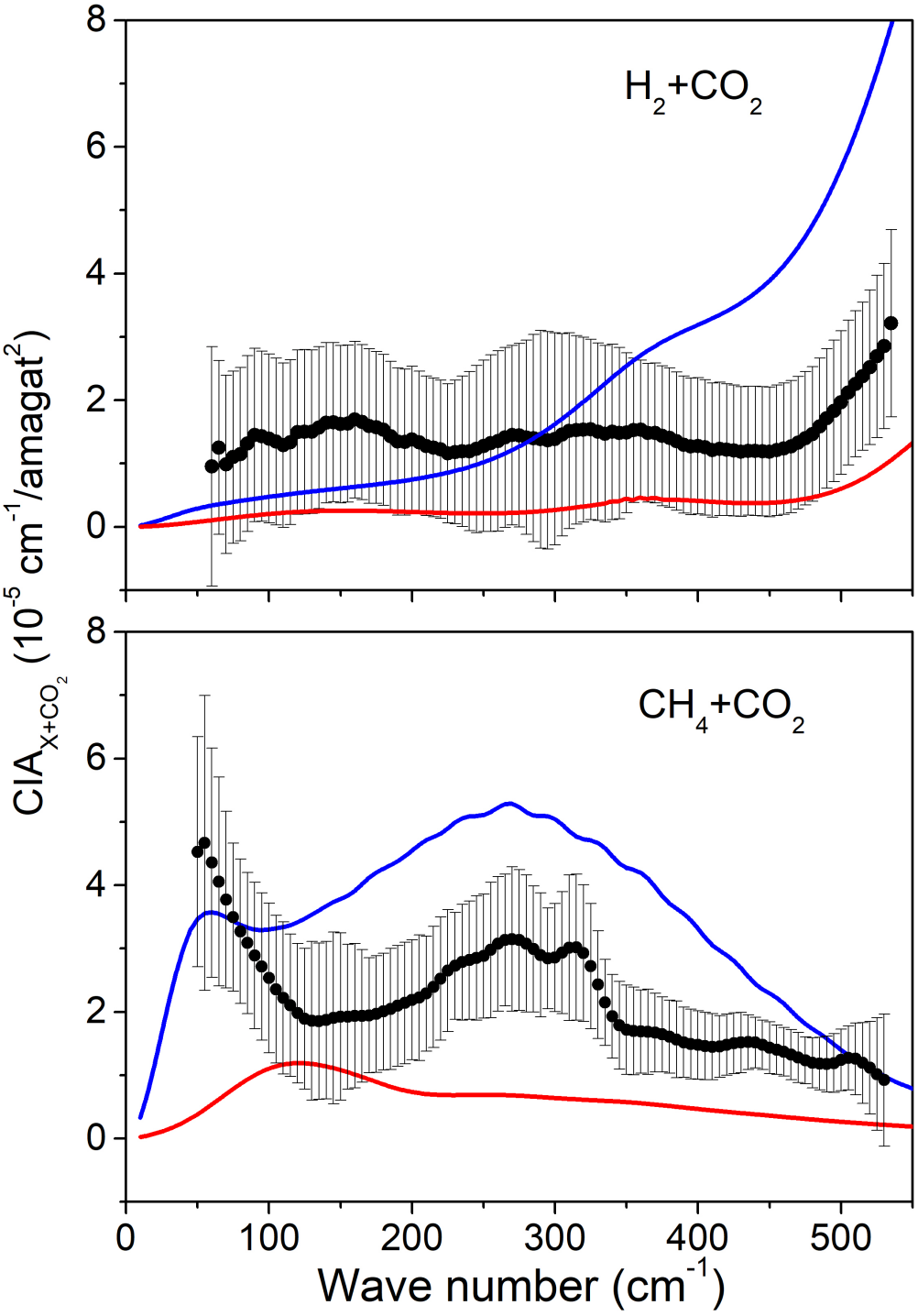

Figure 11.8: In black, H_2+CO_2 CIA (top panel) and CH_4+CO_2 CIA (bottom panel) measured at room temperature (symbols with error bars). The blue lines are the calculated valued of CO_2-H_2 and CO_2-CH_4, respectively, taken from Wordsworth et al. (2017). The red lines are the CIA of N_2-H_2 (Borysow and Frommhold, 1986) and N_2-CH_4 (Borysow and Tang, 1993), respectively, taken from the HITRAN CIA database section (Richard et al., 2012).

effect of these CIAs in their numerical climate simulations and that they therefore underestimated the amount of H_2 and CH_4 required to warm the surface of early Mars above the melting point of water, by a factor up to 2-3. Similarly, calculations of the boundaries of the Habitable Zone based on hydrogen (Ramirez and Kaltenegger, 2017) or methane (Ramirez and Kaltenegger, 2018) should be revised accordingly. Future experiments and calculations of these CIAs combined with numerical climate model simulations will eventually and hopefully better constrain these numbers.

11.8 Conclusion

We performed the first measurements of the far infrared CIAs of CO_2-CH_4 and CO_2-H_2 mixtures as well as of the absorption by the (low frequency) wings of the pure CO_2 15 μm band lines. We confirm the theoretical prediction of Wordsworth et al. (2017) that the H_2+CO_2 and CH_4+CO_2 CIAs are significantly stronger in the 40-600 cm^{-1} region than those of H_2+N_2 and CH_4+N_2, respectively. However, our results for H_2+CO_2 and CH_4+CO_2 significantly differ from the predictions, both in terms of the magnitude and shape of the CIAs. In the expected 200-600 cm^{-1} spectral window of early Mars, our measurements show that the calculations of Wordsworth et al. (2017) overestimate in average the CO_2-CH_4 and CO_2-H_2 CIAs by a factor of about 1.6. The amount of H_2 and CH_4 required to warm the surface of early Mars above the melting point of water should be revised accordingly. For the pure CO_2 15 μm-band line-wings, we show that both the χ-factor deduced from measurements near 4μm and a line-mixing model very well describe the observed strongly sub-Lorentzian behavior in the 500-600 cm^{-1} region. The results of this first experimental investigation obviously need confirmation by independent measurements and we hope that the results presented in this paper will stimulate new laboratory investigations. Similarly, it would be of great interest to compare the results of our measurements and of the only prediction available with those obtained from alternative models and calculations.

11.9 Appendix

11.9.1 Conditions of the recorded spectra

We performed various measurements of transmission spectra of Ar, CO_2, CH_4, H_2 as well as of H_2+CO_2 and CH_4+CO_2 mixtures at room temperature (23°C). In total, we recorded 39 spectra:

- 7 spectra of pure Argon between 100 and 950 mbar.
- 5 spectra of pure CO_2 between 200 and 950 mbar.
- 3 spectra of pure CH_4 between 600 and 980 mbar.
- 3 spectra of pure H_2 between 600 and 950 mbar.
- 9 spectra of CO_2+CH_4 between 500 and 950 mbar, for three different mixtures (30, 50 and 70% of CH_4).
- 10 spectra of CO_2+H_2 between 400 and 950 mbar, for three different mixtures (30, 50 and 70% of H_2).

The experimental conditions of the recorded spectra are detailed in Table 1 in Turbet et al. (2018b).

11.9.2 Removing the local lines of H_2O, CO_2 and CH_4

In order to remove the contribution of H_2O lines from the raw recorded spectra, the absorption coefficient of this species under the temperature, pressure and mixture compositions of the measurements was computed using Voigt line shapes with a cut-off 3 cm^{-1} away from the line center, using the kspectrum code (Eymet et al., 2016). We used the line positions and intensities from the 2012 edition of the HITRAN database (Rothman et al., 2013). For the pressure-broadening coefficients, we used data from Brown et al. (2007) for H_2O-CO_2, a factor of 1.14 applied to the air-broadening coefficients from HITRAN for H_2O-CH_4 (Nwaboh et al., 2014). For H_2- broadening coefficients of H_2O lines, a factor of 1 was used (Steyert et al., 2004), as well as for Ar- broadening. Note that the accuracy of the broadening coefficients used is not crucial since the spectral resolution of the measured spectra (1 cm^{-1}) is much larger than the line half-width (about 0.1 cm^{-1} at 1 atm). The transmission was then computed and convolved by the Fourier transform spectrometer instrument line shape (a cardinal sine function with a resolution of 1 cm^{-1}) and the relative H_2O amount was floated until the best agreement between measured and calculated absorptions around H_2O lines was obtained. The measured spectrum was then corrected by dividing it by the computed transmission of water vapor. Note that the retrieved H_2O relative amounts are small (between 1.2×10^{-6} and 8.0×10^{-6} mol/mol), making the contributions of the self and foreign water vapor continua (Mlawer et al., 2012; Ma and Tipping, 1992) fully negligible here. The same approach was used in order to remove the absorption by local CH_4 and CO_2 lines from the transmissions deduced from the spectra after their "cleaning" from the water vapor lines. CO_2 and CH_4 local lines were computed with the kspectrum code (Eymet et al., 2016) by using the HITRAN 2012 database (Rothman et al., 2013) and Voigt line shapes, with a cut-off 3 cm^{-1} away from the line center. We used the self and air-broadening coefficients from HITRAN 2012 for all mixtures, except for the pressure broadening of CH_4 by CO_2, where we applied a factor of 1.3 on the air-broadened Lorentzian half width at half maximum (deduced from Fissiaux

et al. 2014; Rothman et al. 2013). We used the known partial pressures of CH_4 and CO_2 to remove the local contributions of CH_4 and CO_2 lines from the recorded spectra because this yields a very good result. This good match validates the procedure used to make the gas mixtures and determine their compositions.

Chapter 12

Summary and perspectives

Contents

During this thesis, I explored various aspects of planetary habitability both inside and outside the solar system. I summarize below the main results that I obtained.

12.1 Planetary habitability outside the Solar System

In a first part of my PhD, I investigated the possibles climates and habitability of extrasolar planets.

The carbonate-silicate cycle and CO_2 surface condensation

The carbonate-silicate cycle is the main geochemical/geophysical thermostat of surface habitability on Earth, and possibly on other planets. In Chapter 2, I showed - using sophisticated 3-D global climate simulations taking into account both the water and carbon dioxide cycles - that this stabilizing cycle can become inefficient on planets that are distant from their star, because permanent CO_2 surface condensation can prevent distant planets from escaping glaciation periods. For an Earth-like planet orbiting a Sun-like star, permanent CO_2 surface condensation becomes a concern for planets that are at least 30% more distant than the Earth is from the Sun. Early Earth was irradiated enough that permanent condensation was likely avoided. Early Mars's low water content and chaotic obliquity disfavored the irreversible trapping of CO_2 on the surface. In Chapter 4, I showed that temperate, synchronous planets (e.g. rotating around M-stars) are also very sensitive to CO_2 atmospheric collapse on the nightside (here the cold trap).

Eventually, I evidenced in Chapters 2 and 4 the fact that CO_2 surface condensation is a major issue on water-rich planets, because CO_2 ice - denser than water ice - should sink below a water ice cover and could thus be lost permanently in the subsurface.

Possible atmospheres of temperate planets orbiting cool stars

I investigated in Chapters 3 and 4 the possible climates and the habitability of temperate planets orbiting cool stars, with a particular focus on Proxima Centauri b and the planets of the TRAPPIST-1 system. These planets are expected to be either in synchronous rotation or in very low-order resonance (Ribas et al., 2016; Turbet et al., 2018a).

I showed that it is not only difficult for such planets to accumulate CO_2 - because it easily condenses on the cold traps - but it is also difficult for them to accumulate CH_4, NH_3 and N_2. CH_4 and NH_3 are

sensitive to photochemical collapse, i.e. photodissociation by XUV photons emitted by the (active) cool host star and subsequent hydrogen escape to space. Similarly, N_2 (in a reducing atmosphere) can be photodissociated and lost in carbon/nitrile molecular chains as proposed in Chapter 4. This is a work in progress, in collaboration with Robin Wordsworth (from Harvard University). N_2 can also be rapidly lost through XUV-driven and stellar wind-driven atmospheric escapes around (active) M-stars (Airapetian et al., 2017; Garcia-Sage et al., 2017; Dong et al., 2017, 2018a).

Despite the difficulties that planets orbiting M-stars have to overcome to sustain (diverse) atmospheres, I showed that some of these planets are really good candidates for surface habitability. In Chapters 3 and 4, I showed in fact that Proxima b and TRAPPIST-1e should have surface liquid water for a broad range of atmospheric and water reservoir conditions. In particular, if these planets are (i) in synchronous rotation and (ii) water-rich (rich enough that water cannot be fully trapped on the nightside), then they should have surface liquid water - at least in the substellar region - whatever the composition and thickness of their atmosphere. I believe that this is a very important result because it suggests that there could be a lot of habitable planets around M-stars.

Future atmospheric characterization of Proxima Centauri b

In Chapter 3, I showed that Proxima b is a promising candidate for future atmosperic characterization. First, thermal phase curves could be attempted with the James Webb Space Telescope. Thermal phase curves could tell us if Proxima b has an atmosphere or not, and how thick the atmosphere (if present) is. Secondly, Proxima b is a unique (Earth-sized, temperate) target for direct imaging, due to its proximity (4 light years from us), with the next generation of ground-based telescopes (e.g. the European Extremely Large Telescope). Direct imaging could be used to produce reflexion phase curves that would provide us with measurements of the temporal variation of the visible/near-infrared albedo of Proxima b. Reflexion phase curves can thus bring useful information on the nature of the surface, the cloud distribution, etc. of Proxima b.

Proxima b may become the first potentially habitable planet to be characterized and thus has the potential to revolutionize all our knowledge on planetary habitability.

12.2 The early Mars enigmas

In a second part of my PhD, I investigated the possibles climates and habitability of early Mars.

Pure CO_2 atmospheres

Based on new spectroscopic calculations and measurements presented in Chapters 10 and 11 respectively, I confirmed that pure CO_2 atmospheres are unable to warm the surface of early Mars above the melting point of water. In Chapter 10, I showed that the χ-factor and the line-mixing approaches give similar results on the absorption in the low-frequency far wing of the ν_2 (or 15μm) CO_2 band lines. In Chapter 11, I presented the first measurements of CO_2 absorption around 17-20 μm, demonstrating that the widely used χ-factors of Perrin and Hartmann (1989) and Tran et al. (2011) (even though these χ-factors were calibrated with experimental data in other spectral regions) give satisfactory results to reproduce absorption in the far wing of the ν_2 CO_2 band. This reinforces the robustness of previous studies of CO_2-dominated atmospheres on early Mars (Wordsworth et al., 2010a; Forget et al., 2013; Wordsworth et al., 2013).

Therefore, other scenarios must be considered to explain the warming of the surface and the atmosphere of early Mars.

Catastrophic events

The first class of scenarios investigated in this thesis is the environmental effect of catastrophic events, such as outflow channel formation events and meteoritic impact events. For this, I employed a wide range of sophisticated numerical models (hydrocode, 3-D and 1-D climate models).

The first type of extreme events considered is outflow channel formation events, associated with large flows of liquid water on the slopes of the northern lowlands of Mars. I modeled in Chapter 5 the environmental effect of such liquid water flows on the climate of Hesperian Mars. I modeled the most extreme of these events, and I explored the role of various "external" parameters such as the initial CO_2 atmospheric pressure and the obliquity. Whatever the range of parameters considered, the duration of the outflow-triggered surface/atmospheric warming is short. Outflow waters would accumulate in the northern lowlands, forming an ocean. I showed that the lifetime of such transient ocean on Mars (e.g. fed by water released during outflow channel formation events) is geologically short, $\sim 10^3$ years before it is completely frozen, and $\sim 10^5$ years before water is completely transported to the cold traps of the planet.

The second type of extreme events considered in my thesis are meteoritic impact events. I first investigated in Chapter 7, using a hierarchy of climate models, the environmental effect of very large impactors, those that are large enough that they could vaporize tens of meters of precipitable water in the atmosphere of Mars. I showed that hot, runaway climate states reported by Segura et al. (2012) are not stable on early Mars. I confirmed with 1D numerical climate simulations that the water ice cloud greenhouse warming reported by Segura et al. (2008) and Urata and Toon (2013) is theoretically possible after impact events, but is unlikely to happen because it requires a long-lasting source of production of upper atmosphere water ice clouds to offset the gravitational sedimentation of ice particles. Eventually, I showed using 3-D numerical climate simulations that the nature of precipitation associated with large impact events (low amount of cumulated precipitation, deluge-style precipitation, precipitation uncorrelated with the valley network geographic patterns) make them poor candidates to explain the formation of the Late Noachian valley networks.

In Chapter 8, I explored the environmental effect of meteoritic impact of moderate sizes, combining the results of 2-D hydrocode simulations with 3-D global climate simulations. This combination of models is used to simulate the environmental effect of meteoritic impacts from $\sim$ second (following the impact) to multiple years timescales (to study the long-term environmental effect). I showed that the erosion by impact-induced precipitation is weak. Almost all the water vapour produced by the impact recondenses in the first few hours/days following the impact. Instead, the main source of erosion (induced by meteoritic impactors of moderate size) is likely produced by the melting of permanent surface ice reservoirs by the hot ejecta layer produced by the impact. Yet the maximum amount of liquid water that could be produced this way remains significantly lower than estimates of the minimum amount of water required to carve all the Martian valley networks (Luo et al., 2017).

More generally, I showed in Chapters 5, 7 and 8 that whatever the extreme event, whatever the epoch and whatever the external parameters, catastrophic events are poor candidates to explain the formation of the Martian valley networks. The induced hydrological cycle is always "one-shot", with almost no re-evaporation of precipitation. This negative result is in fact an important result because it suggests that a long-term warming solution - thus more favorable for life to emerge and develop - is

likely better suited to explain the formation of the valley networks.

Long-term greenhouse warming

The failure of catastrophic events to explain the Martian geology pushed me to investigate a second class of scenarios in my thesis: the long-term warming by greenhouse gases, in particular reducing gases such as methane (CH_4) and di-hydrogen (H_2).

In Chapter 11, I conducted the first far-infrared laboratory measurements of CO_2-CH_4 and CO_2-H_2 collision-induced absorptions. These measurements confirmed the theoretical prediction of Wordsworth et al. (2017) that the collision-induced absorptions (CIAs) of CO_2-X pairs are stronger than those of N_2-X pairs, but evidenced significant differences in the shapes of these CIAs. These measurements are important because they confirm that CO_2/CH_4/H_2 atmospheres can produce a strong greenhouse warming on early Mars.

In parallel, I set up in Chapter 9 3-dimensions global climate simulations of reducing atmospheres (CO_2+H_2-dominated atmospheres) assuming various surface water reservoirs. For this, I took into account feedbacks between geology, hydrology and climate, through the inclusion of the effect of impact crater lakes and oceans in the 3-D numerical climate model. I showed that the long-term warming produced by reducing greenhouse gases on early Mars is a promising way to explain the formation of the valley networks. In warm and wet simulations, (precipitation-induced) runoff patterns and lake positions coincide with the observed valley networks and impact crater lakes positions (in the high plateaux of Mars). The best match is found (1) assuming a pre-TPW topography (Bouley et al., 2016) and (2) by adapting the amount and position of large water reservoirs on Mars. However, the amount of di-hydrogen required to sustain such warm climates is much larger than what is required to warm the global mean surface temperature above the freezing point of water only.

12.3 What could we do next? A review of my perspectives

The redox state of terrestrial planets

The results of my work on early Mars suggest that the long-term warming by greenhouse gases is a promising scenario that deserves to be explored in more details in the future. Among the possible greenhouse gases, the best candidates are the reducing gases H_2 and CH_4, because (i) they provide a strong greenhouse warming in CO_2-dominated atmospheres, and (ii) their presence is compatible with the temporal redox (reduction-oxidation) evolution of planets, i.e. that the surface and atmosphere of planets get more and more oxidized with time (and thus more and more reduced back in time). This mainly results from the atmospheric escape of (light) hydrogen to space. This is coherent with the fact that distant planets/moons of the solar system (e.g. Titan, Pluto, Triton, etc.) have a surface/atmosphere that is now more reduced than inner planets[1]. Understanding all the processes that control the redox evolution of the surface and atmosphere of a planet is - in my opinion - a key direction to investigate. It is crucial to understand the redox state of the atmosphere/surface of any terrestrial planet, depending on its initial mass and composition, the distance to its host star and the type of the host star. Catastrophic processes such as large meteoritic impacts could transiently inject

[1] because outer planets/moons (i) are thought to be initially endowed with more volatiles (H_2O, CH4, NH_3, etc.) and (ii) lose less hydrogen to space, compared to inner planets.

reducing gases in the atmosphere and thus transiently affect the redox state of a planet (Haberle et al., 2017; Wordsworth et al., 2017). This process deserves more exploration.

Understanding the redox evolution of planets is crucial to understand the current differences of atmospheric compositions in the solar system, and assess the habitability of early Earth and Mars. It is also primordial to understand the future observations of temperate, Earth-sized planets, especially those around M-stars because these will be the first to be characterized. For instance, understanding the redox evolution of planets orbiting M stars is crucial to know whether or not oxygen could arise abiotically on these planets (Wordsworth et al., 2018), and thus could be considered as a biosignature or not.

The habitability of M-dwarfs

There are conflicting arguments against and for the surface habitability of planets orbiting M-dwarfs:

- **Against:** initial, extended period of runaway during the Pre Main Sequence phase of the star; higher atmospheric escape rates (due to a higher XUV flux and higher stellar wind) ; synchronous rotation (can lead to atmospheric collapse and/or the trapping of water as ice on the nightside).
- **For:** synchronous rotation (favorable insolation geometry that (i) makes planets more robust to glaciation and (ii) produces negative cloud feedbacks stabilizing the climate) and lowered albedo of ice, preventing planets from freezing.

I have shown during my thesis that surface habitability is very robust on TRAPPIST-1e and Proxima b, assuming they are (1) synchronously rotating and (2) water-rich. I believe that there is a large range of planets orbiting M-stars that could fit into this category, and this is definitely something that deserves to be explored in the future. I recently obtained a funding from the FACCTS (France And Chicago Collaborating in The Sciences) to study this idea - "how robust is surface habitability on synchronously-rotating, water-rich planets orbiting M-stars?" - in more details, with Dorian Abbot and Edwin Kite (from the University of Chicago).

To make progress in our understanding of planetary habitability, we need measurements: both laboratory and observational measurements.

We need laboratory measurements!

We need more spectroscopic measurements constraining regions of weak absorption, because these absorptions can play a major (radiative) role in thick atmospheres. The possible applications are twofold. First, it is crucial to better constrain the greenhouse warming produced in thick atmospheres, as illustrated with the case of dense CO_2 atmospheres on early Mars. Secondly, it is crucial to better constrain future measurements of thermal emission of extrasolar planets (e.g. through secondary eclipses or thermal phase curves). For instance, JWST observations of secondary eclipses of TRAPPIST-1b (with the MIRI instrument) are already planned in the Guaranteed Time Observer [GTO] (see `https://jwst-docs.stsci.edu/display/JSP/JWST+GTO+Observation+Specifications`). The maxima of the thermal emission of TRAPPIST-1b are expected to coincide with the atmospheric spectral windows of the planet. Understanding (and thus predict) thermal emission measurements of terrestrial planets require therefore a good knowledge of the spectroscopy in spectral regions of weak absorption.

We need observations!

We now have a nice list of temperate, Earth-sized planets that should be amenable to atmospheric characterization by the James Webb Space Telescope and by the next generation of extremely large ground-based telescopes. I showed in my thesis that Proxima b is a good candidate for that, but there are other very promising (transiting) targets such as the planets of the TRAPPIST-1 system or LHS1440b. This will be the first opportunity for us to directly characterize the atmosphere of potentially habitable extrasolar planets.

We can also learn a lot from highly irradiated, Earth-sized planets such as TRAPPIST-1b or GJ1132b, that are likely more favorable for most of the methods of atmospheric characterization (e.g. secondary eclipse). For example, we can learn whether or not planets orbiting active M-stars can keep an atmosphere or not. If any of these two planets have an atmosphere, then any Earth-sized planet orbiting a M-star could have an atmosphere. This would be a great discovery that would end the controversy about the potential habitability of planets orbiting M-stars.

More generally, we can learn a lot from understanding how the processes of planetary formation, atmospheric escape, interior/atmosphere exchanges, etc. shape the atmosphere and the surface of planets. We can learn a lot on theses processes from observing planets that are too hot, or too massive to be habitable - but that are much easier to characterize - and then apply what we learned on these objects to better constrain the evolution and thus the habitability of temperate, Earth-sized planets. ARIEL - a space mission that has been recently selected by ESA - will characterize the atmosphere of hundreds of these hot, large, massive planets (Tinetti et al., 2016) and will thus be crucial to better understand and constrain the processes that shape the (potentially habitable) planets.

In parallel, investigations of the geology and mineralogy of Mars must continue in order to better understand the history of the red planet and eventually solve the early Mars enigmas. Great progress could be made by obtaining better constraints on:

1. the (relative and absolute) ages of the Martian terrains. This is crucial to investigate if some events (e.g. meteoritic impacts and valley networks formation) are really correlated ... or not.

2. the redox evolution of the atmosphere/surface/mantle of Mars. Progress can hopefully be made based on Martian meteorites of different ages, or by in-situ analyses of Mars.

3. the geographic patterns of erosion of valley networks and impact crater lakes. For instance, is there any coherent trend (latitudinal? altitudinal?) of a differential erosion of valley networks?

Any progress made on any of these investigations will help to better constrain - directly or indirectly - the past habitability of Mars.

Appendix A

Publication List

Peer-reviewed Research Articles

17) **Martin Turbet**, V. Svetsov & F. Forget, "Exploring the environmental effect of medium-size meteoritic impacts on Early Mars combining hydrocode and global climate model simulations", in preparation, 2018.

16) **Martin Turbet** & F. Forget, "Influence of reducing greenhouse warming and water inventory on the climate of early Mars", in preparation, 2018.

15) **Martin Turbet**, B. Baudin, C. Gillmann, & F. Forget, "The environmental effect of very large meteoritic impacts on early Mars explored with a hierarchy of climate models", to be submitted, 2018.

14) **Martin Turbet** & F. Forget, "The paradoxes of the Late Hesperian Mars ocean", submitted to Nature Geoscience Perspectives, 2018.

13) **Martin Turbet**, H. Tran, O. Pirali, F. Forget, C. Boulet & J-M Hartmann, "Far infrared measurements of collision induced absorptions by CH_4+CO_2 and H_2+CO_2 mixtures and implications for greenhouse warming on early Mars", submitted to Icarus, 2018.

12) W. Pluriel, E. Marcq & **Martin Turbet**, "Modeling the albedo of Earth-like magma ocean planets with H_2O-CO_2 atmospheres", accepted for publication in Icarus, 2018.

11) S.L. Grimm, B-O. Demory, M. Gillon, C. Dorn, E. Agol, A. Burdanov, L. Delrez, M. Sestovic, A.H.M.J. Triaud, **Martin Turbet**, E. Bolmont, A. Caldas, J. de Wit, E. Jehin, J. Leconte, S.N. Raymond, V. Van Grootel, A.J. Burgasser, S. Carey, D. Fabrycky, K. Heng, D.M. Hernandez, J.G. Ingalls, S. Lederer, F. Selsis & D. Queloz, "The nature of the TRAPPIST-1 exoplanets", Astronomy & Astrophysics, vol. 613, 2018.

10) H. Tran, **Martin Turbet**, P. Chelin & X. Landsheere, "Measurements and modelling of absorption by CO_2+H_2O mixtures in the spectral region beyond the CO2 ν_3-band head", Icarus, vol. 306, 2018.

9) **Martin Turbet**, E. Bolmont, J. Leconte, F. Forget, F. Selsis, G. Tobie, A. Caldas, J. Naar & M. Gillon, "Modelling climate diversity, tidal dynamics and the fate of volatiles on TRAPPIST-1 planets", Astronomy & Astrophysics, vol. 612, 2018.

8) **Martin Turbet** & H. Tran, "Comment on 'Radiative transfer in CO2-rich atmospheres: 1. Collisional line mixing implies a colder early Mars'", JGR-Planets, vol. 122, 2017.

7) **Martin Turbet**, F. Forget, J. Leconte, B. Charnay & G. Tobie, "CO_2 condensation is a serious limit to the deglaciation of Earth-like planets", EPSL, vol. 476, 2017.

6) R. Luger, M. Sestovic, E. Kruse, S.L. Grimm, B-O. Demory, E. Agol, E. Bolmont, D. Fabrycky, C.S. Fernandes, V. Van Grootel, A. Burgasser, M. Gillon, J.G. Ingalls, E. Jehin, S.N. Raymond, F. Selsis, A.H.M.J. Triaud, T. Barclay, G. Barentsen, S.B. Howell, L. Delrez, J. de Wit, D. Foreman-Mackey, D.L. Holdsworth, J. Leconte, S. Lederer, **Martin Turbet**, Y. Almleaky, Z. Benkhaldoun, P. Magain, B. Morris, K. Heng, D. Queloz, "A seven-planet resonant chain in TRAPPIST-1", Nature Astronomy, vol. 1, 2017.

5) M. Gillon, A.H. M. J. Triaud, B-O. Demory, E. Jehin, E. Agol, K.M. Deck, S.M. Lederer, J. de Wit, A. Burdanov, J.G. Ingalls, E. Bolmont, J. Leconte, S.N. Raymond, F. Selsis, **Martin Turbet**, K. Barkaoui, A. Burgasser, M.R. Burleigh, S.J. Carey, A. Chaushev, C.M. Copperwheat, L. Delrez, C.S. Fernandes, D.L. Holdsworth, E.J. Kotze, V. Van Grootel, Y. Almleaky, Z. Benkhaldoun, P. Magain & D. Queloz, "Seven temperate terrestrial planets around the nearby ultracool dwarf star TRAPPIST-1", Nature, vol. 542, 2017.

4) **Martin Turbet**, F. Forget, J. Head & R. Wordsworth, "3D Global Climate Modelling of outflow channel formation events on Early Mars", Icarus, vol. 288, 2017.

3) **Martin Turbet**, J. Leconte, F. Selsis, E. Bolmont, F. Forget, I. Ribas, S.N. Raymond & G. Anglada-Escude, "The habitability of Proxima Centauri b II. Possible climates and Observability", Astronomy & Astrophysics, vol. 596, 2016.

2) I. Ribas, E. Bolmont, F. Selsis, A. Reiners, J. Leconte, S.N. Raymond, S.G. Engle, E.F. Guinan, J. Morin, **Martin Turbet**, F. Forget & G. Anglada-Escude, "The habitability of Proxima Centauri b. I. Irradiation, rotation and volatile inventory from formation to the present", Astronomy & Astrophysics, vol. 596, 2016.

1) S. Bouley, D. Baratoux, I. Matsuyama, F. Forget, A. Sejourne, **Martin Turbet** & F. Costard. "Late Tharsis formation and implications for early Mars". Nature, vol. 531, 2016.

Peer-reviewed Outreach Articles

1) C. Risi, V. Journe, J-L. Dufresne, J-Y. Grandpeix, P. Dubuisson & **Martin Turbet**. "Les couleurs du ciel". La Meteorologie, 2017.

Contributions to conference presentations

26) T. Fauchez, **Martin Turbet**, A. Mandell, R. Kopparapu, G. Arney & S.D. Domagal-Goldman. "Impact of clouds and hazes in the JWST simulated transmission spectra of TRAPPIST-1 planets in the habitable zone". CCTP3, 2018.

25) T. Fauchez, **Martin Turbet**, A. Mandell, R. Kopparapu, G. Arney & S.D. Domagal-Goldman. "Impact of clouds in the JWST and LUVOIR simulated transmission spectra of TRAPPIST-1 planets in the habitable zone". AAS Meeting, 2018.

24) J.W. Head, F. Forget, R. Wordsworth, **Martin Turbet**, J. Cassanelli & A. Palumbo. "Two Oceans on Mars?: History, Problems, and Prospects". LPSC, 2018.

23) D. Baratoux, S. Bouley, I. Matsuyama, F. Forget, A. Sejourne, **Martin Turbet** & F. Costard. "Global-scale hydrology on Mars and the timing of Tharsis". AGU, 2017.

22) F. Forget, **Martin Turbet**, F. Selsis & J. Leconte. "Definition and Characterization of the Habitable Zone". Habitable Worlds conference, 2017.

21) **Martin Turbet**, F. Forget, J. Leconte, G. Tobie, B. Charnay, F. Selsis & E. Bolmont. "Glaciation Escape on Earth-Like Planets Limited by CO2 Condensation". Habitable Worlds conference, 2017.

21) **Martin Turbet**, F. Forget, J. Leconte, F. Selsis & E. Bolmont. "Habitability and Observability of Proxima Cen and TRAPPIST-1 Planetary Systems". Habitable Worlds conference, 2017.

20) **Martin Turbet**, F. Forget, V. Svetsov, H. Tran, J-M. Hartmann, O. Karatekin, C. Gillmann, O. Popova & J.W. Head. "The Environmental Effect of Meteoritic Impacts on Early Mars with a Versatile 3-D Global Climate Model". 4th conference on Early Mars, 2017.

19) **Martin Turbet**, H. Tran, J-M. Hartmann & F. Forget. "Toward a more Accurate Spectroscopy of CO2/H2O-Rich Atmospheres: Implications for the Early Martian Atmosphere". 4th conference on Early Mars, 2017.

18) J.W. Head, R. Wordsworth, F. Forget & **Martin Turbet**. "Deciphering the Noachian Geological and Climate History of Mars - Part 2: A Noachian Stratigraphic View of Major Geologic Processes and Their Climatic Consequences". 4th conference on Early Mars, 2017.

17) J.W. Head, R. Wordsworth, F. Forget & **Martin Turbet**. "Deciphering the Noachian Geological and Climate History of Mars: A Stratigraphic, Geologic Process and Mineralogical Perspective - Part 1: Current Knowns and Unknowns". 4th conference on Early Mars, 2017.

16) F. Forget, **Martin Turbet**, E. Millour, L. Kerber, R. Wordsworth & J.W. Head. "On the Challenge of Simulating the Early Mars Environment with Climate Models". 4th conference on Early Mars, 2017.

15) **Martin Turbet**, F. Forget & C. Schott. "The LAPS Project: A tutorial, online model to simulate the atmosphere of any terrestrial planet". EPSC, 2017.

14) **Martin Turbet**, F. Forget, V. Svetsov, H. Tran, O. Karatekin, O. Popova & C. Gillmann. "The impact of meteoritic impacts on the early Martian environment". EPSC, 2017.

13) L. Rossi, D. Stam & **Martin Turbet**. "Retrieving the cloud coverage on Earth-like exoplanets using polarimetry". EPSC, 2017.

12) **Martin Turbet**, E. Bolmont, F. Forget, J. Leconte & F. Selsis. "Proxima Cen and TRAPPIST-1 exoplanetary systems: possible climates and observational constraints". EPSC, 2017.

11) **Martin Turbet**, F. Forget, J. Leconte, B. Charnay & G. Tobie. "CO2 condensation can seriously limit the deglaciation of Earth-like planets". EPSC, 2017.

10) W. Pluriel, E. Marcq, **Martin Turbet**, F. Forget & A. Salvador. "Modeling the albedo of magma ocean planets". EPSC, 2017.

9) **Martin Turbet**, F. Forget, V. Svetsov, O. Popova, C. Gillmann, O. Karatekin, Q. Wallemacq, J.W. Head & R. Wordsworth. "Catastrophic events: Possible solutions to the early Mars enigma(s)?". MAMO, 2017.

8) **Martin Turbet**. "How could Early Mars have been habitable?". SFR: FROM EARLY EARTH TO EXOPLANETS, 2016.

7) **Martin Turbet**, F. Forget & C. Schott. "The LAPS Project : A live 1D Radiative-Convective Model to explore the possible climates of terrestrial planets and exoplanets". DPS, 2016.

6) **Martin Turbet**, F. Forget, V. Svetsov, C. Gillmann, O. Karatekin, O. Popova & Q. Wallemacq. "3D Global Climate Modelling of the environmental effect of meteoritic impacts on Early Mars". DPS, 2016.

5) S. Bouley, D. Baratoux, I. Matsuyama, F. Forget, A. Sejourne, **Martin Turbet** & F. Costard. "Late Tharsis Formation and New Perspesctives for Early Mars". EGU, 2016.

4) E. Bolmont, A.S. Libert, J. Leconte, F. Selsis, **Martin Turbet** & F. Forget. "Habitability of planets on eccentric orbits : limits of the mean flux approximation". EGU, 2016.

3) **Martin Turbet**, F. Forget, R. Wordsworth & J.W. Head. "3D Modelling of the impact of outflow channel events on Late Hesperian Mars climate". EPSC, 2015.

2) **Martin Turbet**, F. Forget, J. Leconte & C. Schott. "The habitability of terrestrial exoplanets with a time-marching climate model : an educational tool". EPSC, 2015.

1) **Martin Turbet**, F. Forget, J. Leconte & C. Schott. "Exploring Earth-like planetary atmospheres with a real time 1D GCM : an educational tool". Pathways towards Habitable Planets II, 2015.

Bibliography

Abbot, D. S. (2016). Analytical Investigation of the Decrease in the Size of the Habitable Zone Due to a Limited CO_2 Outgassing Rate. *The Astrophysical Journal*, 827:117. (Cited on pages 22, 67 and 82.)

Abbot, D. S. and Pierrehumbert, R. T. (2010). Mudball: Surface dust and Snowball Earth deglaciation. *Journal of Geophysical Research (Atmospheres)*, 115:D03104. (Cited on page 74.)

Abbot, D. S. and Switzer, E. R. (2011). The Steppenwolf: A Proposal for a Habitable Planet in Interstellar Space. *The Astrophysical Journal Letters*, 735:L27. (Cited on pages 104 and 125.)

Abe, Y., Abe-Ouchi, A., Sleep, N. H., and Zahnle, K. J. (2011). Habitable Zone Limits for Dry Planets. *Astrobiology*, 11:443–460. (Cited on pages 18, 19, 24, 100 and 179.)

Abel, M., Frommhold, L., Li, X., and Hunt, K. L. C. (2011). Collision-Induced Absorption by H2Pairs: From Hundreds to Thousands of Kelvin. *Journal of Physical Chemistry A*, 115:6805–6812. (Cited on pages 318, 320 and 322.)

Airapetian, V. S., Glocer, A., Khazanov, G. V., Loyd, R. O. P., France, K., Sojka, J., Danchi, W. C., and Liemohn, M. W. (2017). How Hospitable Are Space Weather Affected Habitable Zones? The Role of Ion Escape. *The Astrophysical Journal Letters*, 836:L3. (Cited on pages 150 and 334.)

Andrews-Hanna, J. C. and Phillips, R. J. (2007). Hydrological modeling of outflow channels and chaos regions on Mars. *Journal of Geophysical Research*, 112. (Cited on pages 194, 196, 213 and 229.)

Anglada-Escudé, G., Amado, P. J., Barnes, J., Berdiñas, Z. M., Butler, R. P., Coleman, G. A. L., de La Cueva, I., Dreizler, S., Endl, M., Giesers, B., Jeffers, S. V., Jenkins, J. S., Jones, H. R. A., Kiraga, M., Kürster, M., López-González, M. J., Marvin, C. J., Morales, N., Morin, J., Nelson, R. P., Ortiz, J. L., Ofir, A., Paardekooper, S.-J., Reiners, A., Rodríguez, E., Rodríguez-López, C., Sarmiento, L. F., Strachan, J. P., Tsapras, Y., Tuomi, M., and Zechmeister, M. (2016). A terrestrial planet candidate in a temperate orbit around Proxima Centauri. *Nature*, 536:437–440. (Cited on pages 37, 38, 95, 96, 98, 104, 121 and 181.)

Arney, G., Domagal-Goldman, S. D., Meadows, V. S., Wolf, E. T., Schwieterman, E., Charnay, B., Claire, M., Hébrard, E., and Trainer, M. G. (2016). The Pale Orange Dot: The Spectrum and Habitability of Hazy Archean Earth. *Astrobiology*, 16:873–899. (Cited on pages 177 and 178.)

Arney, G. N. (2016). *Pulling Back the Veil: The Characterization and Habitability of Enshrouded Worlds*. PhD thesis, University of Washington. (Cited on page 177.)

Arney, G. N., Meadows, V. S., Domagal-Goldman, S. D., Deming, D., Robinson, T. D., Tovar, G., Wolf, E. T., and Schwieterman, E. (2017). Pale Orange Dots: The Impact of Organic Haze on the Habitability and Detectability of Earthlike Exoplanets. *The Astrophysical Journal*, 836:49. (Cited on pages 177 and 179.)

Asphaug, E. and Benz, W. (1996). Size, Density, and Structure of Comet Shoemaker-Levy 9 Inferred from the Physics of Tidal Breakup. *Icarus*, 121:225–248. (Cited on page 242.)

Asplund, M., Grevesse, N., Sauval, A. J., and Scott, P. (2009). The Chemical Composition of the Sun. *Annual Review of Astronomy & Astrophysics*, 47:481–522. (Cited on page 145.)

Auclair-Desrotour, P., Laskar, J., Mathis, S., and Correia, A. C. M. (2017a). The rotation of planets hosting atmospheric tides: from Venus to habitable super-Earths. *Astronomy & Astrophysics*, 603:A108. (Cited on page 16.)

Auclair-Desrotour, P., Laskar, J., Mathis, S., and Correia, A. C. M. (2017b). The rotation of planets hosting atmospheric tides: from Venus to habitable super-Earths. *Astronomy & Astrophysics*, 603:A108. (Cited on page 155.)

Bachet, G., Cohen, E. R., Dore, P., and Birnbaum, G. (1983). The translational-rotational absorption spectrum of hydrogen. *Canadian Journal of Physics*, 61:591. (Cited on page 320.)

Bahcall, J. N., Pinsonneault, M. H., and Basu, S. (2001). Solar models: Current epoch and time dependences, neutrinos, and helioseismological properties. *The Astrophysical Journal*, 555:990–1012. (Cited on page 200.)

Baker, V., Strom, R., Doh, J., Gulick, V., Kargel, J., Komatsu, G., Ori, G., and Rice, J. (1999). Mars - oceanus borealis, ancient glaciers, and the megaoutflo hypothesis. (Cited on page 229.)

Baker, V. R. (1982). *The channels of Mars*. University of Texas Press, Austin. (Cited on pages 193 and 194.)

Baker, V. R. (2001). Water and the martian landscape. *Nature*, pages 228–236. (Cited on page 194.)

Baker, V. R., Carr, M. H., Gulick, V. C., Williams, C. R., and Marley, M. S. (1992). *Channels and valley networks*, pages 493–522. University of Arizona Press, Tucson. (Cited on pages 28 and 194.)

Baker, V. R., Strom, R. G., Gulick, V. C., Kargel, J. S., Komatsu, G., and Kale, V. S. (1991). Ancient Oceans, ice sheets and the hydrological cycle on Mars. *Nature*, 352. (Cited on pages 193, 194, 197, 234 and 238.)

Baranov, Y. I. (2016). On the significant enhancement of the continuum-collision induced absorption in H_2O+CO_2 mixtures. *Journal of Quantitative Spectroscopy and Radiative Transfer*, 175:100–106. (Cited on page 60.)

Baranov, Y. I., Lafferty, W. J., and Fraser, G. T. (2004). Infrared spectrum of the continuum and dimer absorption in the vicinity of the O_2 vibrational fundamental in O_2/CO_2 mixtures. *Journal of Molecular Spectroscopy*, 228:432–440. (Cited on pages 59, 152, 182, 199, 251, 285 and 309.)

Barnhart, C. J., Howard, A. D., and Moore, J. M. (2009). Long-term precipitation and late-stage valley network formation: Landform simulations of Parana Basin, Mars. *Journal of Geophysical Research (Planets)*, 114:E01003. (Cited on page 269.)

Barstow, J. K. and Irwin, P. G. J. (2016). Habitable worlds with JWST: transit spectroscopy of the TRAPPIST-1 system? *Monthly Notices of the Royal Astronomical Society*, 461:L92–L96. (Cited on page 150.)

Batalha, N. E., Kopparapu, R. K., Haqq-Misra, J., and Kasting, J. F. (2016). Climate cycling on early Mars caused by the carbonate-silicate cycle. *Earth and Planetary Science Letters*, 455:7–13. (Cited on pages 22, 23 and 67.)

Bathurst, J. C. (1993). Flow resistance through the channel network. *Channel Network Hydrology*, pages 69–98. (Cited on page 195.)

Bazot, M., Christensen-Dalsgaard, J., Gizon, L., and Benomar, O. (2016). On the uncertain nature of the core of α Cen A. *Monthly Notices of the Royal Astronomical Society*, 460:1254–1269. (Cited on page 104.)

Belu, A. R., Selsis, F., Morales, J.-C., Ribas, I., Cossou, C., and Rauer, H. (2011). Primary and secondary eclipse spectroscopy with JWST: exploring the exoplanet parameter space. *Astronomy & Astrophysics*, 525:A83. (Cited on page 121.)

Berner, R. A. and Kothavala, Z. (2001). Geocarb iii: A revised model of atmospheric co2 over phanerozoic time. *American Journal of Science*, 301(2):182–204. (Cited on page 22.)

Berta-Thompson, Z. K., Irwin, J., Charbonneau, D., Newton, E. R., Dittmann, J. A., Astudillo-Defru, N., Bonfils, X., Gillon, M., Jehin, E., Stark, A. A., Stalder, B., Bouchy, F., Delfosse, X., Forveille, T., Lovis, C., Mayor, M., Neves, V., Pepe, F., Santos, N. C., Udry, S., and Wünsche, A. (2015). A rocky planet transiting a nearby low-mass star. *Nature*, 527:204–207. (Cited on page 38.)

Bertrand, T. and Forget, F. (2016). Observed glacier and volatile distribution on Pluto from atmosphere-topography processes. *Nature*, 540:86–89. (Cited on page 166.)

Bertrand, T. and Forget, F. (2017). 3D modeling of organic haze in Pluto's atmosphere. *Icarus*, 287:72–86. (Cited on page 48.)

Bézard, B., Tsang, C. C. C., Carlson, R. W., Piccioni, G., Marcq, E., and Drossart, P. (2009). Water vapor abundance near the surface of Venus from Venus Express/VIRTIS observations. *Journal of Geophysical Research (Planets)*, 114:E00B39. (Cited on pages 24 and 103.)

Bibring, J.-P., Langevin, Y., Mustard, J. F., Poulet, F., Arvidson, R., Gendrin, A., Gondet, B., Mangold, N., Pinet, P., and Forget, F. (2006). Global Mineralogical and Aqueous Mars History Derived from OMEGA/Mars Express Data. 312:400–404. (Cited on pages 27, 193, 197 and 246.)

Bills, B. G., Neumann, G. A., Smith, D. E., and Zuber, M. T. (2005). Improved estimate of tidal dissipation within Mars from MOLA observations of the shadow of Phobos. *Journal of Geophysical Research (Planets)*, 110:E07004. (Cited on page 154.)

Birnbaum, G. (1975). Far infrared collision-induced spectrum in gaseous methane. I. Band shape and temperature dependence. *The Journal of Chemical Physics*, 62:59–62. (Cited on page 320.)

Birnbaum, G. (1978). Far-infrared absorption in H2 and H2-He mixtures. *Journal of Quantitative Spectroscopy and Radiative Transfer*, 19:51–62. (Cited on pages 320 and 322.)

Birnbaum, G., Borysow, A., and Orton, G. S. (1996). Collision-Induced Absorption of H $_2$-H $_2$and H $_2$-He in the Rotational and Fundamental Bands for Planetary Applications. *Icarus*, 123:4–22. (Cited on page 320.)

Birnbaum, G. and Cohen, E. R. (1976). Theory of line shape in pressure-induced absorption. *Canadian Journal of Physics*, 54:593. (Cited on page 327.)

Bolmont, E., Libert, A.-S., Leconte, J., and Selsis, F. (2016a). Habitability of planets on eccentric orbits: Limits of the mean flux approximation. *Astronomy & Astrophysics*, 591:A106. (Cited on pages 48, 96, 151, 158 and 198.)

Bolmont, E., Raymond, S. N., and Leconte, J. (2011). Tidal evolution of planets around brown dwarfs. *Astronomy & Astrophysics*, 535:A94. (Cited on pages 153 and 154.)

Bolmont, E., Raymond, S. N., Leconte, J., Hersant, F., and Correia, A. C. M. (2015). Mercury-T: A new code to study tidally evolving multi-planet systems. Applications to Kepler-62. *Astronomy & Astrophysics*, 583:A116. (Cited on pages 153 and 158.)

Bolmont, E., Raymond, S. N., von Paris, P., Selsis, F., Hersant, F., Quintana, E. V., and Barclay, T. (2014). Formation, Tidal Evolution, and Habitability of the Kepler-186 System. *The Astrophysical Journal*, 793:3. (Cited on page 153.)

Bolmont, E., Selsis, F., Owen, J. E., Ribas, I., Raymond, S. N., Leconte, J., and Gillon, M. (2016b). Water loss from Earth-sized planets in the habitable zones of ultracool dwarfs: Implications for the planets of TRAPPIST-1. *ArXiv e-prints*. (Cited on page 118.)

Bolmont, E., Selsis, F., Owen, J. E., Ribas, I., Raymond, S. N., Leconte, J., and Gillon, M. (2017). Water loss from terrestrial planets orbiting ultracool dwarfs: implications for the planets of TRAPPIST-1. *Monthly Notices of the Royal Astronomical Society*, 464:3728–3741. (Cited on pages 147, 150 and 178.)

Bolmont, E., Selsis, F., Raymond, S. N., Leconte, J., Hersant, F., Maurin, A.-S., and Pericaud, J. (2013). Tidal dissipation and eccentricity pumping: Implications for the depth of the secondary eclipse of 55 Cancri e. *A&A*, 556:A17. (Cited on pages 153 and 158.)

Bonfils, X., Astudillo-Defru, N., Díaz, R., Almenara, J.-M., Forveille, T., Bouchy, F., Delfosse, X., Lovis, C., Mayor, M., Murgas, F., Pepe, F., Santos, N. C., Ségransan, D., Udry, S., and Wünsche, A. (2017). A temperate exo-Earth around a quiet M dwarf at 3.4 parsecs. *ArXiv e-prints*. (Cited on pages 37 and 38.)

Bonfils, X., Delfosse, X., Udry, S., Forveille, T., Mayor, M., Perrier, C., Bouchy, F., Gillon, M., Lovis, C., Pepe, F., Queloz, D., Santos, N. C., Segransan, D., and Bertaux, J.-L. (2013). The HARPS search for southern extra-solar planets. XXXI. The M-dwarf sample. *Astronomy & Astrophysics*, 549:A109. (Cited on page 34.)

Borucki, W. J., Koch, D., Basri, G., Batalha, N., Brown, T., Caldwell, D., Caldwell, J., Christensen-Dalsgaard, J., Cochran, W. D., DeVore, E., Dunham, E. W., Dupree, A. K., Gautier, T. N., Geary, J. C., Gilliland, R., Gould, A., Howell, S. B., Jenkins, J. M., Kondo, Y., Latham, D. W., Marcy, G. W., Meibom, S., Kjeldsen, H., Lissauer, J. J., Monet, D. G., Morrison, D., Sasselov, D., Tarter, J., Boss, A., Brownlee, D., Owen, T., Buzasi, D., Charbonneau, D., Doyle, L., Fortney, J., Ford, E. B., Holman, M. J., Seager, S., Steffen, J. H., Welsh, W. F., Rowe, J., Anderson, H., Buchhave, L., Ciardi, D., Walkowicz, L., Sherry, W., Horch, E., Isaacson, H., Everett, M. E., Fischer, D., Torres, G., Johnson, J. A., Endl, M., MacQueen, P., Bryson, S. T., Dotson, J., Haas, M., Kolodziejczak, J., Van Cleve, J., Chandrasekaran, H., Twicken, J. D., Quintana, E. V., Clarke, B. D., Allen, C., Li, J., Wu, H., Tenenbaum, P., Verner, E., Bruhweiler, F., Barnes, J., and Prsa, A. (2010). Kepler Planet-Detection Mission: Introduction and First Results. *Science*, 327:977. (Cited on page 34.)

Borysow, A. and Frommhold, L. (1986). Theoretical collision-induced rototranslational absorption spectra for modeling Titan's atmosphere - H2-N2 pairs. *The Astrophysical Journal*, 303:495–510. (Cited on pages 327 and 328.)

Borysow, A. and Frommhold, L. (1987a). Collision-induced rototranslational absorption spectra of binary methane complexes (CH4-CH4). *Journal of Molecular Spectroscopy*, 123:293–309. (Cited on page 320.)

Borysow, A. and Frommhold, L. (1987b). Collision-induced rototranslational absorption spectra of CH4-CH4 pairs at temperatures from 50 to 300 K. *The Astrophysical Journal*, 318:940–943. (Cited on pages 320 and 321.)

Borysow, A. and Tang, C. (1993). Far Infrared CIA Spectra of N $_2$-CH $_4$ Pairs for Modeling of Titan's Atmosphere. *Icarus*, 105:175–183. (Cited on pages 327 and 328.)

Boucher, O., Le Treut, H., and Baker, M. B. (1995). Precipitation and radiation modeling in a general circulation model: Introduction of cloud microphysical processes. *Journal of Geophysical Research*, 100:16. (Cited on pages 52, 153, 249 and 254.)

Bougher, S. W., Hunten, D. M., and Phillips, R. J., editors (1997). *Venus II*, volume 165. (Cited on pages 24 and 103.)

Bouley, S., Baratoux, D., Matsuyama, I., Forget, F., Séjourné, A., Turbet, M., and Costard, F. (2016). Late Tharsis formation and implications for early Mars. *Nature*, 531:344–347. (Cited on pages 28, 248, 253, 267, 269, 276, 286, 288, 297, 302, 303 and 336.)

Bourrier, V., Ehrenreich, D., Wheatley, P. J., Bolmont, E., Gillon, M., de Wit, J., Burgasser, A. J., Jehin, E., Queloz, D., and Triaud, A. H. M. J. (2017). Reconnaissance of the TRAPPIST-1 exoplanet system in the Lyman-α line. *Astronomy & Astrophysics*, 599:L3. (Cited on page 150.)

Boutle, I. A., Mayne, N. J., Drummond, B., Manners, J., Goyal, J., Hugo Lambert, F., Acreman, D. M., and Earnshaw, P. D. (2017). Exploring the climate of Proxima B with the Met Office Unified Model. *Astronomy & Astrophysics*, 601:A120. (Cited on page 181.)

Boyajian, T. S., von Braun, K., van Belle, G., McAlister, H. A., ten Brummelaar, T. A., Kane, S. R., Muirhead, P. S., Jones, J., White, R., Schaefer, G., Ciardi, D., Henry, T., López-Morales, M., Ridgway, S., Gies, D., Jao, W.-C., Rojas-Ayala, B., Parks, J. R., Sturmann, L., Sturmann, J., Turner, N. H., Farrington, C., Goldfinger, P. J., and Berger, D. H. (2012). Stellar Diameters and Temperatures. II. Main-sequence K- and M-stars. *The Astrophysical Journal*, 757:112. (Cited on pages 95 and 121.)

Brack, A. (1993). Liquid water and the origin of life. *Origins of Life and Evolution of the Biosphere*, 23:3–10. (Cited on page 4.)

Brantley, S. L. and Koepenick, K. W. (1995). Measured carbon dioxide emissions from Oldoinyo Lengai and the skewed distribution of passive volcanic fluxes. *Geology*, 23:933. (Cited on pages 82 and 173.)

Brogi, M., de Kok, R. J., Birkby, J. L., Schwarz, H., and Snellen, I. A. G. (2014). Carbon monoxide and water vapor in the atmosphere of the non-transiting exoplanet HD 179949 b. *Astronomy & Astrophysics*, 565:A124. (Cited on page 114.)

Brogi, M., Snellen, I. A. G., de Kok, R. J., Albrecht, S., Birkby, J., and de Mooij, E. J. W. (2012). The signature of orbital motion from the dayside of the planet τ Boötis b. *Nature*, 486:502–504. (Cited on pages 41 and 118.)

Brown, L. R., Humphrey, C. M., and Gamache, R. R. (2007). CO_2-broadened water in the pure rotation and ν_2 fundamental regions. *Journal of Molecular Spectroscopy*, 246:1–21. (Cited on pages 251 and 330.)

Burgasser, A. J. and Mamajek, E. E. (2017). On the Age of the TRAPPIST-1 System. *The Astrophysical Journal*, 845:110. (Cited on pages 38, 154 and 178.)

Cabrol, N. A. and Grin, E. A. (1999). Distribution, Classification, and Ages of Martian Impact Crater Lakes. *Icarus*, 142:160–172. (Cited on pages 25 and 246.)

Caldeira, K. and Kasting, J. F. (1992). The life span of the biosphere revisited. *Nature*, 360:721–723. (Cited on page 20.)

Campargue, A., Wang, L., Mondelain, D., Kassi, S., Bézard, B., Lellouch, E., Coustenis, A., Bergh, C. d., Hirtzig, M., and Drossart, P. (2012). An empirical line list for methane in the 1.26-1.71 μm region for planetary investigations (T = 80-300 K). Application to Titan. *Icarus*, 219:110–128. (Cited on page 152.)

Carone, L., Keppens, R., and Decin, L. (2015). Connecting the dots - II. Phase changes in the climate dynamics of tidally locked terrestrial exoplanets. *Monthly Notices of the Royal Astronomical Society*, 453:2412–2437. (Cited on pages 16 and 163.)

Carone, L., Keppens, R., and Decin, L. (2016). Connecting the dots - III. Nightside cooling and surface friction affect climates of tidally locked terrestrial planets. *Monthly Notices of the Royal Astronomical Society*, 461:1981–2002. (Cited on pages 16 and 163.)

Carr, M. H. (1990). D/H on Mars - Effects of floods, volcanism, impacts, and polar processes. *Icarus*, 87:210–227. (Cited on page 239.)

Carr, M. H. (1995). The Martain drainage system and the origin of valley networks and fretted channels. *Journal of Geophysical Research*, 100:7479–7507. (Cited on pages 25 and 246.)

Carr, M. H. (1996). *Water on Mars*. New York: Oxford University Press. (Cited on pages 193, 194, 197 and 207.)

Carr, M. H. and Head, J. W. (2003). Oceans on Mars: An assessment of the observational evidence and possible fate. *Journal of Geophysical Research (Planets)*, 108:5042. (Cited on page 238.)

Carr, M. H. and Head, J. W. (2015). Martian surface/near-surface water inventory: Sources, sinks, and changes with time. *Geophysical Research Letters*, 42:726–732. (Cited on pages 242, 299 and 301.)

Carter, J., Loizeau, D., Mangold, N., Poulet, F., and Bibring, J.-P. (2015). Widespread surface weathering on early Mars: A case for a warmer and wetter climate. *Icarus*, 248:373–382. (Cited on pages 27 and 246.)

Carter, J., Poulet, F., Bibring, J.-P., Mangold, N., and Murchie, S. (2013). Hydrous minerals on Mars as seen by the CRISM and OMEGA imaging spectrometers: Updated global view. *Journal of Geophysical Research (Planets)*, 118:831–858. (Cited on pages 27, 197 and 246.)

Cassanelli, J. P., Head, J. W., and Fastook, J. L. (2015). Sources of water for the outflow channels on Mars: Implications of the Late Noachian "icy highlands" model for melting and groundwater recharge on the Tharsis rise. *Planet. Space Sci.*, 108:54–65. (Cited on page 194.)

Cernicharo, J. and Crovisier, J. (2005). Water in Space: The Water World of ISO. *Space Science Reviews*, 119:29–69. (Cited on page 7.)

Chapman, S. and Lindzen, R. (1970). *Atmospheric tides. Thermal and gravitational*. (Cited on page 16.)

Charbonneau, D., Allen, L. E., Megeath, S. T., Torres, G., Alonso, R., Brown, T. M., Gilliland, R. L., Latham, D. W., Mandushev, G., O'Donovan, F. T., and Sozzetti, A. (2005). Detection of Thermal Emission from an Extrasolar Planet. *The Astrophysical Journal*, 626:523–529. (Cited on page 39.)

Charbonneau, D., Brown, T. M., Noyes, R. W., and Gilliland, R. L. (2002). Detection of an Extrasolar Planet Atmosphere. *The Astrophysical Journal*, 568:377–384. (Cited on page 39.)

Charnay, B. (2014). *Tropospheric dynamics and climatic evolution of Titan and the early Earth.* Theses, Universite Pierre et Marie Curie - Paris VI. (Cited on pages 48, 51, 53 and 248.)

Charnay, B., Forget, F., Tobie, G., Sotin, C., and Wordsworth, R. (2014). Titan's past and future: 3D modeling of a pure nitrogen atmosphere and geological implications. *Icarus*, 241:269–279. (Cited on page 48.)

Charnay, B., Forget, F., Wordsworth, R., Leconte, J., Millour, E., Codron, F., and Spiga, A. (2013). Exploring the faint young sun problem and the possible climates of the archean earth with a 3-d gcm. *Journal of Geophysical Research : Atmospheres*, 118:414–431. (Cited on pages 20, 47, 86, 96, 151, 152, 153, 198 and 289.)

Charnay, B., Le Hir, G., Fluteau, F., Forget, F., and Catling, D. C. (2017). A warm or a cold early Earth? New insights from a 3-D climate-carbon model. *Earth and Planetary Science Letters*, 474:97–109. (Cited on page 48.)

Charnay, B., Meadows, V., and Leconte, J. (2015a). 3D Modeling of GJ1214b's Atmosphere: Vertical Mixing Driven by an Anti-Hadley Circulation. *The Astrophysical Journal*, 813:15. (Cited on page 151.)

Charnay, B., Meadows, V., Misra, A., Leconte, J., and Arney, G. (2015b). 3D Modeling of GJ1214b Atmosphere: Formation of Inhomogeneous High Clouds and Observational Implications. *The Astrophysical Journal Letters*, 813:L1. (Cited on page 151.)

Chauvin, G., Desidera, S., Lagrange, A.-M., Vigan, A., Gratton, R., Langlois, M., Bonnefoy, M., Beuzit, J.-L., Feldt, M., Mouillet, D., Meyer, M., Cheetham, A., Biller, B., Boccaletti, A., D'Orazi, V., Galicher, R., Hagelberg, J., Maire, A.-L., Mesa, D., Olofsson, J., Samland, M., Schmidt, T. O. B., Sissa, E., Bonavita, M., Charnay, B., Cudel, M., Daemgen, S., Delorme, P., Janin-Potiron, P., Janson, M., Keppler, M., Le Coroller, H., Ligi, R., Marleau, G. D., Messina, S., Molliere, P., Mordasini, C., Muller, A., Peretti, S., Perrot, C., Rodet, L., Rouan, D., Zurlo, A., Dominik, C., Henning, T., Menard, F., Schmid, H.-M., Turatto, M., Udry, S., Vakili, F., Abe, L., Antichi, J., Baruffolo, A., Baudoz, P., Baudrand, J., Blanchard, P., Bazzon, A., Buey, T., Carbillet, M., Carle, M., Charton, J., Cascone, E., Claudi, R., Costille, A., Deboulbe, A., De Caprio, V., Dohlen, K., Fantinel, D., Feautrier, P., Fusco, T., Gigan, P., Giro, E., Gisler, D., Gluck, L., Hubin, N., Hugot, E., Jaquet, M., Kasper, M., Madec, F., Magnard, Y., Martinez, P., Maurel, D., Le Mignant, D., Moller-Nilsson, O., Llored, M., Moulin, T., Origne, A., Pavlov, A., Perret, D., Petit, C., Pragt, J., Puget, P., Rabou, P., Ramos, J., Rigal, R., Rochat, S., Roelfsema, R., Rousset, G., Roux, A., Salasnich, B., Sauvage, J.-F., Sevin, A., Soenke, C., Stadler, E., Suarez, M., Weber, L., Wildi, F., Antoniucci, S., Augereau, J.-C., Baudino, J.-L., Brandner, W., Engler, N., Girard, J., Gry, C., Kral, Q., Kopytova, T., Lagadec, E., Milli, J., Moutou, C., Schlieder, J., Szulagyi, J., Thalmann, C., and Wahhaj, Z. (2017). Discovery of a warm, dusty giant planet around HIP 65426. *Astronomy & Astrophysics*, 605:L9. (Cited on page 41.)

Chevrier, V., Poulet, F., and J.-P., B. (2007). Early geochemical environment of mars as determined from thermodynamics of phyllosilicates. 448:60–63. (Cited on page 197.)

Choblet, G., Tobie, G., Sotin, C., Kalousová, K., and Grasset, O. (2017). Heat transport in the high-pressure ice mantle of large icy moons. *Icarus*, 285:252–262. (Cited on page 6.)

Clifford, S. M. (1993). A model for the hydrologic and climatic behavior of water on mars. 98:10,973–11,016. (Cited on pages 29, 32, 190 and 194.)

Clifford, S. M. and Parker, T. (2001). The evolution of the martian hydrosphere: Implications for the fate of a primordial ocean and the current state of the northern plains. *Icarus*, 154:40–79. (Cited on pages 29, 32, 190, 194, 220 and 240.)

Clough, S. A., Shephard, M. W., Mlawer, E. J., Delamere, J. S., Iacono, M. J., Cady-Pereira, K., Boukabara, S., and Brown, P. D. (2005). Atmospheric radiative transfer modeling: a summary of the AER codes. *Journal of Quantitative Spectroscopy and Radiative Transfer*, 91:233–244. (Cited on pages 61, 86, 152, 199 and 285.)

Codastefano, P., Dore, P., and Nencini, L. (1985). *Far Infrared Absorption Spectra in Gaseous Methane from 138 to 296 K*, pages 119–128. Springer US, Boston, MA. (Cited on pages 318, 320 and 321.)

Codastefano, P., Dore, P., and Nencini, L. (1986). Temperature dependence of the far-infrared absorption spectrum of gaseous methane. *Journal of Quantitative Spectroscopy and Radiative Transfer*, 35:255–263. (Cited on page 320.)

Codron, F. (2012). Ekman heat transport for slab oceans. *Climate Dynamics*, 38:379–389. (Cited on pages 206, 244 and 289.)

Correia, A. C. M. and Laskar, J. (2001). The four final rotation states of Venus. *Nature*, 411:767–770. (Cited on page 16.)

Costard, F., Séjourné, A., Kelfoun, K., Clifford, S., Lavigne, F., Di Pietro, I., and Bouley, S. (2017). Modeling tsunami propagation and the emplacement of thumbprint terrain in an early Mars ocean. *Journal of Geophysical Research (Planets)*, 122:633–649. (Cited on pages 237, 238, 240, 241, 242, 243 and 244.)

Craddock, R. A. and Howard, A. D. (2002). The case for rainfall on a warm, wet early Mars. *Journal of Geophysical Research (Planets)*, 107:21–1. (Cited on pages 25, 26, 193 and 246.)

Craddock, R. A. and Maxwell, T. A. (1993). Geomorphic evolution of the Martian highlands through ancient fluvial processes. 98:3453–3468. (Cited on page 197.)

Crossfield, I. J. M., Hansen, B. M. S., Harrington, J., Cho, J. Y.-K., Deming, D., Menou, K., and Seager, S. (2010). A New 24 μm Phase Curve for upsilon Andromedae b. *The Astrophysical Journal*, 723:1436–1446. (Cited on page 121.)

Cuffey, K. and Paterson, W. (2010). *The physics of glaciers*. Academic Press. (Cited on page 79.)

Dagg, I. R., Anderson, A., Yan, S., Smith, W., and Joslin, C. G. (1986). Collision-induced absorption in gaseous methane at low temperatures. *Canadian Journal of Physics*, 64:763–767. (Cited on page 320.)

Davies, J. H. (2013). Global map of solid Earth surface heat flow. *Geochemistry, Geophysics, Geosystems*, 14:4608–4622. (Cited on page 82.)

Davies, J. H. and Davies, D. R. (2010). Earth's surface heat flux. *Solid Earth*, 1:5–24. (Cited on pages 104 and 160.)

De Wit, J., Wakeford, H. R., Gillon, M., Lewis, N. K., Valenti, J. A., Demory, B.-O., Burgasser, A. J., Burdanov, A., Delrez, L., Jehin, E., Lederer, S. M., Queloz, D., Triaud, A. H. M. J., and Van Grootel, V. (2016). A combined transmission spectrum of the Earth-sized exoplanets TRAPPIST-1 b and c. *Nature*, 537:69–72. (Cited on pages 147, 150 and 183.)

de Wit, J., Wakeford, H. R., Lewis, N. K., Delrez, L., Gillon, M., Selsis, F., Leconte, J., Demory, B.-O., Bolmont, E., Bourrier, V., Burgasser, A. J., Grimm, S., Jehin, E., Lederer, S. M., Owen, J. E., Stamenković, V., and Triaud, A. H. M. J. (2018). Atmospheric reconnaissance of the habitable-zone Earth-sized planets orbiting TRAPPIST-1. *Nature Astronomy*, 2:214–219. (Cited on page 147.)

Del Genio, A. D., Way, M. J., Amundsen, D. S., Aleinov, I., Kelley, M., Kiang, N. Y., and Clune, T. L. (2017). Habitable Climate Scenarios for Proxima Centauri b With a Dynamic Ocean. *ArXiv e-prints*. (Cited on pages 18 and 47.)

Delahaye, T., Landsheere, X., Pangui, E., Huet, F., Hartmann, J.-M., and Tran, H. (2016). Broadening of CO_2 lines in the 4.3 μm region by H_2O. *Journal of Molecular Spectroscopy*, 326:17–20. (Cited on page 251.)

Delrez, L., Gillon, M., Triaud, A. H. M. J., Demory, B.-O., de Wit, J., Ingalls, J. G., Agol, E., Bolmont, E., Burdanov, A., Burgasser, A. J., Carey, S. J., Jehin, E., Leconte, J., Lederer, S., Queloz, D., Selsis, F., and Van Grootel, V. (2018). Early 2017 observations of TRAPPIST-1 with Spitzer. *Monthly Notices of the Royal Astronomical Society*, 475:3577–3597. (Cited on page 38.)

Deming, D., Seager, S., Richardson, L. J., and Harrington, J. (2005). Infrared radiation from an extrasolar planet. *Nature*, 434:740–743. (Cited on page 39.)

Demory, B.-O., Gillon, M., de Wit, J., Madhusudhan, N., Bolmont, E., Heng, K., Kataria, T., Lewis, N., Hu, R., Krick, J., Stamenković, V., Benneke, B., Kane, S., and Queloz, D. (2016). A map of the large day-night temperature gradient of a super-Earth exoplanet. *Nature*, 532:207–209. (Cited on page 41.)

Demory, B.-O., Gillon, M., Seager, S., Benneke, B., Deming, D., and Jackson, B. (2012). Detection of Thermal Emission from a Super-Earth. *The Astrophysical Journal Letters*, 751:L28. (Cited on page 39.)

Demory, B.-O., Ségransan, D., Forveille, T., Queloz, D., Beuzit, J.-L., Delfosse, X., di Folco, E., Kervella, P., Le Bouquin, J.-B., Perrier, C., Benisty, M., Duvert, G., Hofmann, K.-H., Lopez, B., and Petrov, R. (2009). Mass-radius relation of low and very low-mass stars revisited with the VLTI. *Astronomy & Astrophysics*, 505:205–215. (Cited on pages 95 and 121.)

Dermott, S. F. (1979). Tidal dissipation in the solid cores of the major planets. *Icarus*, 37:310–321. (Cited on page 154.)

Di Achille, G. and Hynek, B. M. (2010). Ancient ocean on Mars supported by global distribution of deltas and valleys. *Nature Geoscience*, 3:459–463. (Cited on pages 25, 287, 299 and 301.)

Dicke, R. H. (1953). The Effect of Collisions upon the Doppler Width of Spectral Lines. *Physical Review*, 89:472–473. (Cited on page 57.)

Dittmann, J. A., Irwin, J. M., Charbonneau, D., Bonfils, X., Astudillo-Defru, N., Haywood, R. D., Berta-Thompson, Z. K., Newton, E. R., Rodriguez, J. E., Winters, J. G., Tan, T.-G., Almenara, J.-M., Bouchy, F., Delfosse, X., Forveille, T., Lovis, C., Murgas, F., Pepe, F., Santos, N. C., Udry, S., Wünsche, A., Esquerdo, G. A., Latham, D. W., and Dressing, C. D. (2017). A temperate rocky super-Earth transiting a nearby cool star. *Nature*, 544:333–336. (Cited on page 38.)

Dong, C., Jin, M., Lingam, M., Airapetian, V. S., Ma, Y., and van der Holst, B. (2018a). Atmospheric escape from the TRAPPIST-1 planets and implications for habitability. *Proceedings of the National Academy of Science*, 115:260–265. (Cited on pages 150 and 334.)

Dong, C., Lee, Y., Ma, Y., Lingam, M., Bougher, S., Luhmann, J., Curry, S., Toth, G., Nagy, A., Tenishev, V., Fang, X., Mitchell, D., Brain, D., and Jakosky, B. (2018b). Modeling Martian Atmospheric Losses over Time: Implications for Exoplanetary Climate Evolution and Habitability. *ArXiv e-prints*. (Cited on pages 197 and 294.)

Dong, C., Lingam, M., Ma, Y., and Cohen, O. (2017). Is Proxima Centauri b Habitable? A Study of Atmospheric Loss. *The Astrophysical Journal Letters*, 837:L26. (Cited on pages 150 and 334.)

Dorn, C., Venturini, J., Khan, A., Heng, K., Alibert, Y., Helled, R., Rivoldini, A., and Benz, W. (2017). A generalized Bayesian inference method for constraining the interiors of super Earths and sub-Neptunes. *Astronomy & Astrophysics*, 597:A37. (Cited on page 146.)

Dressing, C. D. and Charbonneau, D. (2013). The Occurrence Rate of Small Planets around Small Stars. *The Astrophysical Journal*, 767:95. (Cited on page 34.)

Dressing, C. D. and Charbonneau, D. (2015). The Occurrence of Potentially Habitable Planets Orbiting M Dwarfs Estimated from the Full Kepler Dataset and an Empirical Measurement of the Detection Sensitivity. *The Astrophysical Journal*, 807:45. (Cited on page 34.)

Durham, W. B., Kirby, S. H., and Stern, L. A. (1999). Steady-state flow of solid CO_2: Preliminary results. *Geophysical Research Letter*, 26:3493–3496. (Cited on pages 80, 82, 172 and 173.)

Durham, W. B. and Stern, L. A. (2001). Rheological Properties of Water Ice-Applications to Satellites of the Outer Planets. *Annual Review of Earth and Planetary Sciences*, 29:295–330. (Cited on pages 83 and 172.)

Durham, W. B., Stern, L. A., and Kirby, S. H. (2001). Rheology of ice I at low stress and elevated confining pressure. *Journal of Geophysical Research*, 106:11031–11042. (Cited on pages 83 and 172.)

Edson, A., Lee, S., Bannon, P., Kasting, J. F., and Pollard, D. (2011). Atmospheric circulations of terrestrial planets orbiting low-mass stars. *Icarus*, 212:1–13. (Cited on pages 16 and 163.)

Egbert, G. D. and Ray, R. D. (2000). Significant dissipation of tidal energy in the deep ocean inferred from satellite altimeter data. *Nature*, 405:775–778. (Cited on page 154.)

Egbert, G. D. and Ray, R. D. (2003). Semi-diurnal and diurnal tidal dissipation from TOPEX/Poseidon altimetry. *Geophys. Res. Lett.*, 30:1907. (Cited on page 154.)

Eggleton, P. P., Kiseleva, L. G., and Hut, P. (1998). The Equilibrium Tide Model for Tidal Friction. *ApJ*, 499:853–+. (Cited on page 153.)

Ehlmann, B. L., Mustard, J. F., Murchie, S. L., Bibring, J.-P., Meunier, A., Fraeman, A. A., and Langevin, Y. (2011). Subsurface water and clay mineral formation during the early history of Mars. *Nature*, 479:53–60. (Cited on pages 27, 193 and 246.)

El-Kader, M. S. A. and Maroulis, G. (2012). New insights into collision-induced rototranslational absorption and scattering spectra of gaseous methane at different temperatures. *Journal of Molecular Spectroscopy*, 281:28–39. (Cited on page 320.)

Emanuel, K. A. and Ivkovi-Rothman, M. (1999). Development and Evaluation of a Convection Scheme for Use in Climate Models. *Journal of Atmospheric Sciences*, 56:1766–1782. (Cited on pages 52 and 201.)

Evans, D. A., Beukes, N. J., and Kirschvink, J. L. (1997). Low-latitude glaciation in the palaeoproterozoic era. *Nature*, 386:262. (Cited on pages 21 and 69.)

Eymet, V., Coustet, C., and Piaud, B. (2016). kspectrum: an open-source code for high-resolution molecular absorption spectra production. *Journal of Physics Conference Series*, 676(1):012005. (Cited on pages 50, 86, 98, 152, 251 and 330.)

Fassett, C. I. and Head, J. W. (2008a). The timing of martian valley network activity: Constraints from buffered crater counting. *Icarus*, 195:61–89. (Cited on pages 25 and 197.)

Fassett, C. I. and Head, J. W. (2008b). Valley network-fed, open-basin lakes on Mars: Distribution and implications for Noachian surface and subsurface hydrology. *Icarus*, 198:37–56. (Cited on pages 25 and 301.)

Fastook, J. L. and Head, J. W. (2014). Amazonian mid- to high-latitude glaciation on Mars: Supply-limited ice sources, ice accumulation patterns, and concentric crater fill glacial flow and ice sequestration. *Planetary and Space Science*, 91:60–76. (Cited on page 221.)

Fastook, J. L. and Head, J. W. (2015). Glaciation in the Late Noachian Icy Highlands: Ice accumulation, distribution, flow rates, basal melting, and top-down melting rates and patterns. *Planetary and Space Science*, 106:82–98. (Cited on page 221.)

Fastook, J. L., Head, J. W., Marchant, D. R., Forget, F., and Madeleine, J.-B. (2012). Early Mars climate near the Noachian-Hesperian boundary: Independent evidence for cold conditions from basal melting of the south polar ice sheet (Dorsa Argentea Formation) and implications for valley network formation. *Icarus*, 219:25–40. (Cited on page 221.)

Fissiaux, L., Delière, Q., Blanquet, G., Robert, S., Vandaele, A. C., and Lepère, M. (2014). CO_2-broadening coefficients in the ν_4 fundamental band of methane at room temperature and application to CO_2-rich planetary atmospheres. *Journal of Molecular Spectroscopy*, 297:35–40. (Cited on page 330.)

Forget, F. (2013). On the probability of habitable planets. *International Journal of Astrobiology*, 12:177–185. (Cited on pages 5 and 111.)

Forget, F., Bertrand, T., Vangvichith, M., Leconte, J., Millour, E., and Lellouch, E. (2017). A post-new horizons global climate model of Pluto including the N_2, CH_4 and CO cycles. *Icarus*, 287:54–71. (Cited on pages 48, 163 and 198.)

Forget, F., Hourdin, F., Fournier, R., Hourdin, C., Talagrand, O., Collins, M., Lewis, S. R., Read, P. L., and Huot, J.-P. (1999). Improved general circulation models of the Martian atmosphere from the surface to above 80 km. *Journal of Geophysical Research*, 104:24155–24176. (Cited on pages 50, 151, 152, 153 and 285.)

Forget, F., Hourdin, F., and Talagrand, O. (1998). CO_2 snow fall on Mars: Simulation with a general circulation model. *Icarus*, 131:302–316. (Cited on page 201.)

Forget, F. and Lebonnois, S. (2013). Global Climate Models of the terrestrial planets. In Macwell S. J., Simon-Miller A. A., Harder J. W. and Bullock M . A., editor, *Comparative climatology of terrestrial planets*, pages 213–229. Space Sci. Series, Univ. of Arizona Press. (Cited on page 43.)

Forget, F. and Leconte, J. (2014). Possible climates on terrestrial exoplanets. *Philosophical Transactions of the Royal Society of London Series A*, 372:20130084–20130084. (Cited on pages 48, 150, 160 and 198.)

Forget, F. and Pierrehumbert, R. T. (1997). Warming early Mars with carbon dioxide clouds that scatter infrared radiation. *Science*, 278:1273–1276. (Cited on pages 14, 30, 31, 69, 74, 100, 101 and 153.)

Forget, F., Wordsworth, R., Millour, E., Madeleine, J.-B., Kerber, L., Leconte, J., Marcq, E., and Haberle, R. M. (2013). 3D modelling of the early martian climate under a denser CO_2 atmosphere: Temperatures and CO_2 ice clouds. *Icarus*, 222:81–99. (Cited on pages 14, 30, 31, 48, 52, 74, 86, 96, 100, 151, 152, 153, 182, 197, 198, 201, 203, 238, 243, 246, 247, 248, 249, 262, 284, 285, 289, 308, 315 and 334.)

Fowler, A. (2011). *Mathematical Geoscience*. Springer. (Cited on page 79.)

Fray, N. and Schmitt, B. (2009). Sublimation of ices of astrophysical interest: A bibliographic review. *Planetary and Space Science*, 57:2053–2080. (Cited on pages 161 and 164.)

Frommhold, L. (2006). *Collision-induced Absorption in Gases*. (Cited on page 315.)

Fu, Q. and Liou, K. N. (1992). On the correlated k-distribution method for radiative transfer in nonhomogeneous atmospheres. *Journal of Atmospheric Sciences*, 49:2139–2156. (Cited on pages 86, 98, 152, 199, 250 and 285.)

Fu, W. Q. (2006). 4 - radiative transfer1. In Wallace, J. M., , and Hobbs, P. V., editors, *Atmospheric Science (Second Edition)*, pages 113 – 152. Academic Press, San Diego, second edition edition. (Cited on page 50.)

Galperin, B., Kantha, L. H., Hassid, S., and Rosati, A. (1988). A Quasi-equilibrium Turbulent Energy Model for Geophysical Flows. *Journal of Atmospheric Sciences*, 45:55–62. (Cited on pages 50, 152, 198 and 248.)

Gamache, R. R., Farese, M., and Renaud, C. L. (2016). A spectral line list for water isotopologues in the 1100-4100 cm^{-1} region for application to CO_2-rich planetary atmospheres. *Journal of Molecular Spectroscopy*, 326:144–150. (Cited on page 251.)

Gamache, R. R., Roller, C., Lopes, E., Gordon, I. E., Rothman, L. S., Polyansky, O. L., Zobov, N. F., Kyuberis, A. A., Tennyson, J., Yurchenko, S. N., Csaszar, A. G., Furtenbacher, T., Huang, X., Schwenke, D. W., Lee, T. J., Drouin, B. J., Tashkun, S. A., Perevalov, V. I., and Kochanov, R. V. (2017). Total internal partition sums for 166 isotopologues of 51 molecules important in planetary atmospheres: Application to HITRAN2016 and beyond. *Journal of Quantitative Spectroscopy and Radiative Transfer*, 203:70–87. (Cited on page 56.)

Garcia-Sage, K., Glocer, A., Drake, J. J., Gronoff, G., and Cohen, O. (2017). On the Magnetic Protection of the Atmosphere of Proxima Centauri b. *The Astrophysical Journal Letters*, 844:L13. (Cited on pages 150 and 334.)

Gillon, M., Jehin, E., Lederer, S. M., Delrez, L., de Wit, J., Burdanov, A., Van Grootel, V., Burgasser, A. J., Triaud, A. H. M. J., Opitom, C., Demory, B.-O., Sahu, D. K., Bardalez Gagliuffi, D., Magain, P., and Queloz, D. (2016). Temperate Earth-sized planets transiting a nearby ultracool dwarf star. *Nature*, 533:221–224. (Cited on pages 38, 144 and 149.)

Gillon, M., Triaud, A. H. M. J., Demory, B.-O., Jehin, E., Agol, E., Deck, K. M., Lederer, S. M., de Wit, J., Burdanov, A., Ingalls, J. G., Bolmont, E., Leconte, J., Raymond, S. N., Selsis, F., Turbet, M., Barkaoui, K., Burgasser, A., Burleigh, M. R., Carey, S. J., Chaushev, A., Copperwheat, C. M., Delrez, L., Fernandes, C. S., Holdsworth, D. L., Kotze, E. J., Van Grootel, V., Almleaky, Y., Benkhaldoun, Z., Magain, P., and Queloz, D. (2017). Seven temperate terrestrial planets around the nearby ultracool dwarf star TRAPPIST-1. *Nature*, 542:456–460. (Cited on pages 37, 38, 144, 149, 150, 151, 158 and 181.)

Gold, T. and Soter, S. (1969). Atmospheric Tides and the Resonant Rotation of Venus. *Icarus*, 11:356–366. (Cited on page 16.)

Goldblatt, C., Robinson, T. D., Zahnle, K. J., and Crisp, D. (2013). Low simulated radiation limit for runaway greenhouse climates. *Nature Geoscience*, 6:661–667. (Cited on pages 12 and 20.)

Goldblatt, C. and Watson, A. J. (2012). The runaway greenhouse: implications for future climate change, geoengineering and planetary atmospheres. *Philosophical Transactions of the Royal Society of London Series A*, 370:4197–4216. (Cited on pages 254 and 262.)

Goldreich, P. and Peale, S. (1966). Spin-orbit coupling in the solar system. *The Astrophysical Journal*, 71:425–+. (Cited on pages 15 and 155.)

Goldsby, D. L. and Kohlstedt, D. L. (2001). Superplastic deformation of ice: Experimental observations. *Journal of Geophysical Research*, 106:11. (Cited on pages 83 and 172.)

Golombek, M. P., Grant, J. A., Crumpler, L., Greeley, R., Arvidson, R., Bell, J. F., Weitz, C. M., Sullivan, R., Christensen, P. R., Soderblom, L. A., and Squyres, S. W. (2006). Erosion rates at the Mars Exploration Rover landing sites and long-term climate change on Mars. *Journal of Geophysical Research*, 111. (Cited on page 197.)

Gómez-Leal, I., Pallé, E., and Selsis, F. (2012). Photometric Variability of the Disk-integrated Thermal Emission of the Earth. *The Astrophysical Journal*, 752:28. (Cited on page 118.)

Gough, D. O. (1981). Solar interior structure and luminosity variations. *Solar Phys.*, 74:21–34. (Cited on pages 74, 200 and 285.)

Gregory, D. (1995). A Consistent Treatment of the Evaporation of Rain and Snow for Use in Large-Scale Models. *Monthly Weather Review*, 123:2716. (Cited on pages 52, 249 and 258.)

Grimm, S. L., Demory, B.-O., Gillon, M., Dorn, C., Agol, E., Burdanov, A., Delrez, L., Sestovic, M., Triaud, A. H. M. J., Turbet, M., Bolmont, É., Caldas, A., de Wit, J., Jehin, E., Leconte, J., Raymond, S. N., Van Grootel, V., Burgasser, A. J., Carey, S., Fabrycky, D., Heng, K., Hernandez, D. M., Ingalls, J. G., Lederer, S., Selsis, F., and Queloz, D. (2018). The nature of the TRAPPIST-1 exoplanets. *ArXiv e-prints*. (Cited on pages 38, 144, 145, 146 and 147.)

Grott, M., Morschhauser, A., Breuer, D., and Hauber, E. (2011). Volcanic outgassing of CO_2 and H_2O on Mars. *Earth and Planetary Science Letters*, 308:391–400. (Cited on page 197.)

Grotzinger, J. P., Gupta, S., Malin, M. C., Rubin, D. M., Schieber, J., Siebach, K., Sumner, D. Y., Stack, K. M., Vasavada, A. R., Arvidson, R. E., Calef, F., Edgar, L., Fischer, W. F., Grant, J. A., Griffes, J., Kah, L. C., Lamb, M. P., Lewis, K. W., Mangold, N., Minitti, M. E., Palucis, M., Rice, M., Williams, R. M. E., Yingst, R. A., Blake, D., Blaney, D., Conrad, P., Crisp, J., Dietrich, W. E., Dromart, G., Edgett, K. S., Ewing, R. C., Gellert, R., Hurowitz, J. A., Kocurek, G., Mahaffy, P., McBride, M. J., McLennan, S. M., Mischna, M., Ming, D., Milliken, R., Newsom, H., Oehler, D., Parker, T. J., Vaniman, D., Wiens, R. C., and Wilson, S. A. (2015). Deposition, exhumation, and paleoclimate of an ancient lake deposit, Gale crater, Mars. *Science*, 350. (Cited on pages 27 and 246.)

Gruszka, M. and Borysow, A. (1997). Roto-Translational Collision-Induced Absorption of CO $_2$for the Atmosphere of Venus at Frequencies from 0 to 250 cm $^{-1}$, at Temperatures from 200 to 800 K. *Icarus*, 129:172–177. (Cited on pages 59, 152, 182, 199, 251, 309, 319 and 320.)

Gruszka, M. and Borysow, A. (1998). Computer simulation of the far infrared collision induced absorption spectra of gaseous co2. *Molecular Physics*, 93(6):1007–1016. (Cited on pages 59, 285, 320 and 327.)

Guerlet, S., Spiga, A., Sylvestre, M., Indurain, M., Fouchet, T., Leconte, J., Millour, E., Wordsworth, R., Capderou, M., Bezard, B., and Forget, F. (2014). Global climate modeling of Saturn's atmosphere. Part I: Evaluation of the radiative transfer model. *Icarus*, 238:110–124. (Cited on pages 48 and 198.)

Gulick, V. (2001). Origin of the valley networks on Mars: a hydrological perspective. *Geomorphology*, 37:241–268. (Cited on page 193.)

Gulick, V. C. (1998). Magmatic intrusions and a hydrothermal origin for fluvial valleys on Mars. *Journal of Geophysical Research*, 103:19365–19388. (Cited on page 193.)

Gulick, V. C. and Baker, V. R. (1989). Fluvial valleys and Martian palaeoclimates. *Nature*, 341:514–516. (Cited on page 193.)

Gulick, V. C. and Baker, V. R. (1990). Origin and evolution of valleys on Martian volcanoes. *Journal of Geophysical Research*, 95:14325–14344. (Cited on pages 28 and 193.)

Gulick, V. C., Tyler, D., McKay, C. P., Kargel, J. S., and Haberle, R. M. (1997). Episodic Ocean-Induced CO2 Greenhouse on Mars: Implications for Fluvial Valley Formation. *Icarus*, 130. (Cited on pages 193 and 197.)

Gustafsson, M., Frommhold, L., Bailly, D., Bouanich, J.-P., and Brodbeck, C. (2003). Collision-induced absorption in the rototranslational band of dense hydrogen gas. *Journal of Chemical Physics*, 119:12264–12270. (Cited on page 320.)

Haberle, R. M., Zahnle, K., and Barlow, N. (2017). Impact Delivery of Reduced Greenhouse Gases on Early Mars. In *Fourth International Conference on Early Mars: Geologic, Hydrologic, and Climatic Evolution and the Implications for Life*, volume 2014 of *LPI Contributions*, page 3022. (Cited on pages 246, 309, 315 and 337.)

Halevy, I. and Head, III, J. W. (2014). Episodic warming of early Mars by punctuated volcanism. *Nature Geoscience*, 7:865–868. (Cited on pages 30, 31 and 234.)

Halevy, I., Pierrehumbert, R. T., and Schrag, D. P. (2009). Radiative transfer in CO_2-rich paleoatmospheres. *Journal of Geophysical Research (Atmospheres)*, 114. (Cited on page 87.)

Hamano, K., Abe, Y., and Genda, H. (2013). Emergence of two types of terrestrial planet on solidification of magma ocean. *Nature*, 497:607–610. (Cited on page 24.)

Hamilton, D. P., Stern, S. A., Moore, J. M., Young, L. A., Binzel, R. P., Buie, M. W., Buratti, B. J., Cheng, A. F., Ennico, K., Grundy, W. M., Linscott, I. R., McKinnon, W. B., Olkin, C. B., Reitsema, H. J., Reuter, D. C., Schenk, P., Showalter, M. R., Spencer, J. R., Tyler, G. L., and Weaver, H. A. (2016). The rapid formation of Sputnik Planitia early in Pluto's history. *Nature*, 540:97–99. (Cited on page 166.)

Hansen, B. M. S. (2010). Calibration of Equilibrium Tide Theory for Extrasolar Planet Systems. *ApJ*, 723:285–299. (Cited on page 153.)

Hansen, J. E. and Travis, L. D. (1974). Light scattering in planetary atmospheres. *Space Science Reviews*, 16:527–610. (Cited on pages 86, 152 and 199.)

Haqq-Misra, J., Kopparapu, R. K., Batalha, N. E., Harman, C. E., and Kasting, J. F. (2016). Limit Cycles Can Reduce the Width of the Habitable Zone. *The Astrophysical Journal*, 827:120. (Cited on pages 22, 67 and 82.)

Haqq-Misra, J. D., Domagal-Goldman, S. D., Kasting, P. J., and Kasting, J. F. (2008). A Revised, Hazy Methane Greenhouse for the Archean Earth. *Astrobiology*, 8:1127–1137. (Cited on pages 32 and 284.)

Harries, J. E. (1970). The temperature variation of the far infrared absorption in compressed CO_2. *Journal of Physics B Atomic Molecular Physics*, 3:704–719. (Cited on page 320.)

Harrison, K. P. and Grimm, R. E. (2005). Groundwater-controlled valley networks and the decline of surface runoff on early Mars. *Journal of Geophysical Research*, 110. (Cited on page 197.)

Harrison, K. P. and Grimm, R. E. (2008). Multiple flooding events in Martian outflow channels. *Journal of Geophysical Research*, 113. (Cited on pages 194 and 229.)

Hartmann, J.-M., Boulet, C., and Jacquemart, D. (2011). Molecular dynamics simulations for CO_2 spectra. II. The far infrared collision-induced absorption band. *Journal of Chemical Physics*, 134(9):094316–094316. (Cited on pages 59, 60, 316, 320 and 327.)

Hartmann, J. M., Boulet, C., and Robert, D. (2008). Collisional effects on molecular spectra, laboratory experiments, consequences for applications, jean-michel hartmann, christian boulet, daniel robert, elsevier, amsterdam. price: 190 usd, 155 eur, 110 gbp. 110:173–174. (Cited on pages 58, 61, 62, 63, 308 and 315.)

Hartmann, J.-M., Boulet, C., Tran, D. D., Tran, H., and Baranov, Y. (2018a). Effect of humidity on the absorption continua of CO_2 and N_2 near 4 μm: Calculations, comparisons with measurements, and consequences for atmospheric spectra. *The Journal of Chemical Physics*, 148(5):054304. (Cited on pages 60 and 327.)

Hartmann, J.-M., Tran, H., Armante, R., Boulet, C., Campargue, A., Forget, F., Gianfrani, L., Gordon, I., Guerlet, S., Gustafsson, M., Hodges, J., Kassi, S., Lisak, D., Thibault, F., and Toon, G. (2018b). Recent advances in collisional effects on spectra of molecular gases and their practical consequences. *Journal of Quantitative Spectroscopy and Radiative Transfer*, 213:178 – 227. (Cited on page 315.)

Hartmann, W. K. (2005). Martian cratering 8: Isochron refinement and the chronology of Mars. *Icarus*, 174:294–320. (Cited on page 280.)

Hartmann, W. K. and Neukum, G. (2001). Cratering Chronology and the Evolution of Mars. *Space Science Reviews*, 96:165–194. (Cited on page 193.)

Hayashi, C. (1981). Structure of the Solar Nebula, Growth and Decay of Magnetic Fields and Effects of Magnetic and Turbulent Viscosities on the Nebula. *Progress of Theoretical Physics Supplement*, 70:35–53. (Cited on page 8.)

Head, J. W., Forget, F., Wordsworth, R., Turbet, M., Cassanelli, J., and Palumbo, A. (2018). Two Oceans on Mars?: History, Problems, and Prospects. In *Lunar and Planetary Science Conference*, volume 49 of *Lunar and Planetary Inst. Technical Report*, page 2194. (Cited on pages 27 and 238.)

Head, J. W., Kreslavsky, M. A., and Pratt, S. (2002). Northern lowlands of Mars: Evidence for widespread volcanic flooding and tectonic deformation in the Hesperian Period. *Journal of Geophysical Research (Planets)*, 107:3–1. (Cited on page 234.)

Head, J. W., Marchant, D. R., and Ghatan, G. J. (2004). Glacial deposits on the rim of a Hesperian-Amazonian outflow channel source trough: Mangala Valles, Mars. *Geophys. Res. Lett.*, 31:L10701. (Cited on page 193.)

Head, J. W. and Pratt, S. (2001). Extensive Hesperian-aged south polar ice sheet on Mars: Evidence for massive melting and retreat, and lateral flow and ponding of meltwater. *Journal of Geophysical Research*, 106:12275–12300. (Cited on page 28.)

Heng, K. and Kitzmann, D. (2017). Analytical Models of Exoplanetary Atmospheres. IV. Improved Two-stream Radiative Transfer for the Treatment of Aerosols. *The Astrophysical Journal Supplement Series*, 232:20. (Cited on page 31.)

Henning, W. G. and Hurford, T. (2014). Tidal Heating in Multilayered Terrestrial Exoplanets. *Astrophys. J.*, 789:30. (Cited on page 154.)

Ho, W., Birnbaum, G., and Rosenberg, A. (1971). Far-Infrared Collision-Induced Absorption in CO_2. I. Temperature Dependence. *The Journal of Chemical Physics*, 55:1028–1038. (Cited on pages 59, 318, 319 and 320.)

Hoffman, N. (2000). White Mars: A new model for Mars' surface and atmosphere based in CO2. *Icarus*, 146:326–342. (Cited on page 194.)

Hoffman, P. F., Kaufman, A. J., Halverson, G. P., and Schrag, D. P. (1998). A neoproterozoic snowball Earth. *Science*, 281:1342–1346. (Cited on pages 21 and 69.)

Hoffman, P. F. and Schrag, D. P. (2002). The snowball earth hypothesis : Testing the limits of global change. *Terra Nova*, 14:129–155. (Cited on pages 21 and 69.)

Hoke, M. R. T., Hynek, B. M., and Tucker, G. E. (2011). Formation timescales of large Martian valley networks. *Earth and Planetary Science Letters*, 312:1–12. (Cited on page 282.)

Hourdin, F., Le Van, P., Forget, F., and Talagrand, O. (1993). Meteorological variability and the annual surface pressure cycle on Mars. 50:3625–3640. (Cited on pages 53 and 198.)

Hourdin, F., Musat, I., Bony, S., Braconnot, P., Codron, F., Dufresne, J.-L., Fairhead, L., Filiberti, M.-A., Friedlingstein, P., Grandpeix, J.-Y., Krinner, G., Levan, P., Li, Z.-X., and Lott, F. (2006). The LMDZ4 general circulation model: climate performance and sensitivity to parametrized physics with emphasis on tropical convection. *Climate Dynamics*, 27:787–813. (Cited on pages 86, 96, 151, 198 and 285.)

Housen, K. R., Schmidt, R. M., and Holsapple, K. A. (1983). Crater ejecta scaling laws - Fundamental forms based on dimensional analysis. *Journal of Geophysical Research*, 88:2485–2499. (Cited on page 274.)

Howard, A. D. (2007). Simulating the development of Martian highland landscapes through the interaction of impact cratering, fluvial erosion, and variable hydrologic forcing. *Geomorphology*, 91:332–363. (Cited on pages 290 and 301.)

Hu, Y. and Yang, J. (2014). Role of ocean heat transport in climates of tidally locked exoplanets around M dwarf stars. *Proceedings of the National Academy of Science*, 111:629–634. (Cited on pages 18, 47 and 109.)

Hunt, J. L. and Poll, J. D. (1978). Lineshape analysis of collision induced spectra of gases. *Canadian Journal of Physics*, 56:950. (Cited on page 327.)

Hut, P. (1981). Tidal evolution in close binary systems. *Astronomy & Astrophysics*, 99:126–140. (Cited on page 153.)

Hynek, B. M., Beach, M., and Hoke, M. R. T. (2010). Updated global map of Martian valley networks and implications for climate and hydrologic processes. *Journal of Geophysical Research (Planets)*, 115:E09008. (Cited on pages 25, 190, 246, 269 and 301.)

Ingersoll, A. P. (1969). The Runaway Greenhouse: A History of Water on Venus. *Journal of Atmospheric Sciences*, 26:1191–1198. (Cited on pages 12, 118 and 262.)

Ivanov, M. A. and Head, J. W. (2001). Chryse Planitia, Mars : Topographic configuration, outflow channel continuity and sequence, and tests for hypothesized ancient bodies of water using Mars Orbiter Laser Altimeter (MOLA) data. *Journal of Geophysical Research*, 106:3275–3295. (Cited on pages 194, 195 and 197.)

Jakosky, B. M., Lin, R. P., Grebowsky, J. M., Luhmann, J. G., Mitchell, D. F., Beutelschies, G., Priser, T., Acuna, M., Andersson, L., Baird, D., Baker, D., Bartlett, R., Benna, M., Bougher, S., Brain, D., Carson, D., Cauffman, S., Chamberlin, P., Chaufray, J.-Y., Cheatom, O., Clarke, J., Connerney, J., Cravens, T., Curtis, D., Delory, G., Demcak, S., DeWolfe, A., Eparvier, F., Ergun, R., Eriksson, A., Espley, J., Fang, X., Folta, D., Fox, J., Gomez-Rosa, C., Habenicht, S., Halekas, J., Holsclaw, G., Houghton, M., Howard, R., Jarosz, M., Jedrich, N., Johnson, M., Kasprzak, W., Kelley, M., King, T., Lankton, M., Larson, D., Leblanc, F., Lefevre, F., Lillis, R., Mahaffy, P., Mazelle, C., McClintock, W., McFadden, J., Mitchell, D. L., Montmessin, F., Morrissey, J., Peterson, W., Possel, W., Sauvaud, J.-A., Schneider, N., Sidney, W., Sparacino, S., Stewart, A. I. F., Tolson, R., Toublanc, D., Waters, C., Woods, T., Yelle, R., and Zurek, R. (2015). The Mars Atmosphere and Volatile Evolution (MAVEN) Mission. *Space Science Reviews*, 195:3–48. (Cited on page 9.)

Jarrard, R. D. (2003). Subduction fluxes of water, carbon dioxide, chlorine, and potassium. *Geochemistry, Geophysics, Geosystems*, 4:1. (Cited on pages 82 and 173.)

Johnson, R. E., Oza, A., Young, L. A., Volkov, A. N., and Schmidt, C. (2015). Volatile Loss and Classification of Kuiper Belt Objects. *The Astrophysical Journal*, 809:43. (Cited on page 179.)

Joshi, M. M. and Haberle, R. M. (2012). Suppression of the Water Ice and Snow Albedo Feedback on Planets Orbiting Red Dwarf Stars and the Subsequent Widening of the Habitable Zone. *Astrobiology*, 12:3–8. (Cited on pages 74, 98, 109, 152 and 182.)

Kadoya, S. and Tajika, E. (2014). Conditions for Oceans on Earth-like Planets Orbiting within the Habitable Zone: Importance of Volcanic CO_2 Degassing. *The Astrophysical Journal*, 790:107. (Cited on page 22.)

Kalas, P., Graham, J. R., Chiang, E., Fitzgerald, M. P., Clampin, M., Kite, E. S., Stapelfeldt, K., Marois, C., and Krist, J. (2008). Optical Images of an Exosolar Planet 25 Light-Years from Earth. *Science*, 322:1345. (Cited on page 41.)

Kaltenegger, L., Selsis, F., Fridlund, M., Lammer, H., Beichman, C., Danchi, W., Eiroa, C., Henning, T., Herbst, T., Léger, A., Liseau, R., Lunine, J., Paresce, F., Penny, A., Quirrenbach, A., Röttgering, H., Schneider, J., Stam, D., Tinetti, G., and White, G. J. (2010). Deciphering Spectral Fingerprints of Habitable Exoplanets. *Astrobiology*, 10:89–102. (Cited on page 7.)

Kane, S. R. (2018). The Impact of Stellar Distances on Habitable Zone Planets. *The Astrophysical Journal Letters*, 861:L21. (Cited on page 38.)

Karman, T., Baranov, Y., RL, K., Sun, K., Sung, K., Wishnow, E., Wordsworth, R., Vigasin, A., Volkamer, R., Van Der Zande, W., Rothman, L., and Gordon, I. (2018). Update of the hitran collision-induced absorption section. *in preparation*. (Cited on page 315.)

Karman, T., Miliordos, E., Hunt, K. L. C., Groenenboom, G. C., and van der Avoird, A. (2015a). Quantum mechanical calculation of the collision-induced absorption spectra of N_2-N_2 with anisotropic interactions. *The Journal of Chemical Physics*, 142(8):084306. (Cited on page 327.)

Karman, T., van der Avoird, A., and Groenenboom, G. C. (2015b). Collision-induced absorption with exchange effects and anisotropic interactions: Theory and application to H_2 - H_2. *The Journal of Chemical Physics*, 142(8):084305. (Cited on pages 320 and 327.)

Kasper, M., Verinaud, C., and Mawet, D. (2013). Roadmap for PCS, the Planetary Camera and Spectrograph for the E-ELT. In Esposito, S. and Fini, L., editors, *Proceedings of the Third AO4ELT Conference*, page 8. (Cited on page 114.)

Kaspi, Y. and Showman, A. P. (2015). Atmospheric Dynamics of Terrestrial Exoplanets over a Wide Range of Orbital and Atmospheric Parameters. *The Astrophysical Journal*, 804:60. (Cited on pages 76 and 101.)

Kassi, S., Campargue, A., Mondelain, D., and Tran, H. (2015). High pressure Cavity Ring Down Spectroscopy: Application to the absorption continuum of CO_2 near 1.7 μm. *Journal of Quantitative Spectroscopy and Radiative Transfer*, 167:97–104. (Cited on page 309.)

Kasting, J. F. (1988). Runaway and moist greenhouse atmospheres and the evolution of earth and Venus. *Icarus*, 74:472–494. (Cited on pages 12, 44 and 45.)

Kasting, J. F. (1991). CO2 condensation and the climate of early Mars. *Icarus*, 94:1–13. (Cited on page 45.)

Kasting, J. F. and Ackerman, T. P. (1986). Climatic consequences of very high carbon dioxide levels in the earth's early atmosphere. *Science*, 234:1383–1385. (Cited on page 20.)

Kasting, J. F. and Harman, C. E. (2013). Extrasolar planets: Inner edge of the habitable zone. *Nature*, 504:221–223. (Cited on page 18.)

Kasting, J. F., Pollack, J. B., and Ackerman, T. P. (1984). Response of earth's atmosphere to increases in solar flux and implications for loss of water from Venus. *Icarus*, 57:335–355. (Cited on page 250.)

Kasting, J. F., Whitmire, D. P., and Reynolds, R. T. (1993). Habitable Zones around Main Sequence Stars. *Icarus*, 101:108–128. (Cited on pages 10, 11, 13, 44, 45, 67, 69, 95, 112, 149 and 254.)

Kerber, L., Forget, F., and Wordsworth (2015). Sulfur in the early martian atmosphere revisited : Experiments with a 3-D Global Climate Model. *Icarus*, 261:133–148. (Cited on pages 31, 48 and 234.)

Khare, B. N., Sagan, C., Arakawa, E. T., Suits, F., Callcott, T. A., and Williams, M. W. (1984). Optical constants of organic tholins produced in a simulated Titanian atmosphere - From soft X-ray to microwave frequencies. *Icarus*, 60:127–137. (Cited on pages 177 and 179.)

Kieffer, H. H., Titus, T. N., Mullins, K. F., and Christensen, P. R. (2000). Mars south polar spring and summer behavior observed by TES: Seasonal cap evolution controlled by frost grain size. *Journal of Geophysical Research*, 105:9653–9700. (Cited on pages 74 and 87.)

Kislyakova, K. G., Noack, L., Johnstone, C. P., Zaitsev, V. V., Fossati, L., Lammer, H., Khodachenko, M. L., Odert, P., and Guedel, M. (2017). Magma oceans and enhanced volcanism on TRAPPIST-1 planets due to induction heating. *Nature Astronomy*. (Cited on page 160.)

Kite, E. S., Gao, P., Goldblatt, C., Mischna, M. A., Mayer, D. P., and Yung, Y. L. (2017a). Methane bursts as a trigger for intermittent lake-forming climates on post-Noachian Mars. *Nature Geoscience*, 10:737–740. (Cited on pages 240 and 246.)

Kite, E. S., Michaels, T. I., Rafkin, S., Manga, M., and Dietrich, W. E. (2011a). Localized precipitation and runoff on Mars. *Journal of Geophysical Research*, 116. (Cited on pages 193, 200, 219 and 223.)

Kite, E. S., Mischna, M. A., Gao, P., and Yung, Y. L. (2017b). Climate optimum on Mars initiated by atmospheric collapse. *ArXiv e-prints*. (Cited on page 240.)

Kite, E. S., Rafkin, S., Michaels, T. I., Dietrich, W. E., and Manga, M. (2011b). Chaos terrain, storms, and past climate on Mars. *Journal of Geophysical Research*, 116. (Cited on page 200.)

Kite, E. S., Williams, J. P., Lucas, A., and Aharonson, O. (2014). Low palaeopressure of the martian atmosphere estimated from the size distribution of ancient craters. *Nature Geoscience*, 7:335–339. (Cited on pages 197 and 294.)

Kitzmann, D. (2016). Revisiting the Scattering Greenhouse Effect of CO_2 Ice Clouds. *The Astrophysical Journal Letters*, 817. (Cited on pages 14, 31, 74 and 100.)

Kitzmann, D. (2017). Clouds in the atmospheres of extrasolar planets. V. The impact of CO_2 ice clouds on the outer boundary of the habitable zone. *Astronomy & Astrophysics*, 600:A111. (Cited on page 153.)

Kitzmann, D., Alibert, Y., Godolt, M., Grenfell, J. L., Heng, K., Patzer, A. B. C., Rauer, H., Stracke, B., and von Paris, P. (2015). The unstable CO_2 feedback cycle on ocean planets. *Monthly Notices of the Royal Astronomical Society*, 452:3752–3758. (Cited on page 23.)

Kleinhans, M. G. (2005). Flow discharge and sediment transport models for estimating a minimum timescale of hydrological activity and channel and delta formation on Mars. *Journal of Geophysical Research*, 110. (Cited on page 194.)

Knudsen, J. G. and Katz, D. L. (1958). *Fluid Dynamics and Heat Transfer*. McGraw-Hill, New-York. (Cited on page 195.)

Knutson, H. A., Charbonneau, D., Allen, L. E., Fortney, J. J., Agol, E., Cowan, N. B., Showman, A. P., Cooper, C. S., and Megeath, S. T. (2007). A map of the day-night contrast of the extrasolar planet HD 189733b. *Nature*, 447:183–186. (Cited on page 41.)

Kodama, T., Nitta, A., Genda, H., Takao, Y., O'ishi, R., Abe-Ouchi, A., and Abe, Y. (2018). Dependence of the Onset of the Runaway Greenhouse Effect on the Latitudinal Surface Water Distribution of Earth-Like Planets. *Journal of Geophysical Research (Planets)*, 123:559–574. (Cited on page 19.)

Komatsu, G. and Baker, V. R. (1997). Paleohydrology and flood geomorphology of Ares Valles. *Journal of Geophysical Research*, 102. (Cited on page 194.)

Komatsu, G., Kargel, J. S., Baker, V. R., Strom, R. G., Ori, G. G., C., M., and L., T. K. (2000). A chaotic terrain formation hypothesis: Explosive outgas and outlow by dissociation of clathrate on Mars. (Cited on page 194.)

Kopparapu, R. K. (2013). A Revised Estimate of the Occurrence Rate of Terrestrial Planets in the Habitable Zones around Kepler M-dwarfs. *The Astrophysical Journal Letters*, 767:L8. (Cited on page 34.)

Kopparapu, R. K., Ramirez, R., Kasting, J. F., Eymet, V., Robinson, T. D., Mahadevan, S., Terrien, R. C., Domagal-Goldman, S., Meadows, V., and Deshpande, R. (2013). Habitable Zones around Main-sequence Stars: New Estimates. *The Astrophysical Journal*, 765:131. (Cited on pages 10, 12, 13, 20, 30, 69, 85, 95, 147, 149, 179, 182, 254, 262 and 297.)

Kopparapu, R. K., Ramirez, R. M., SchottelKotte, J., Kasting, J. F., Domagal-Goldman, S., and Eymet, V. (2014). Habitable Zones around Main-sequence Stars: Dependence on Planetary Mass. *The Astrophysical Journal Letters*, 787:L29. (Cited on pages 76, 95, 101, 182, 254 and 262.)

Kopparapu, R. K., Wolf, E. T., Arney, G., Batalha, N. E., Haqq-Misra, J., Grimm, S. L., and Heng, K. (2017). Habitable Moist Atmospheres on Terrestrial Planets near the Inner Edge of the Habitable Zone around M Dwarfs. *The Astrophysical Journal*, 845:5. (Cited on page 12.)

Kopparapu, R. K., Wolf, E. T., Haqq-Misra, J., Yang, J., Kasting, J. F., Meadows, V., Terrien, R., and Mahadevan, S. (2016). The Inner Edge of the Habitable Zone for Synchronously Rotating Planets around Low-mass Stars Using General Circulation Models. *The Astrophysical Journal*, 819:84. (Cited on pages 17, 95, 147, 149 and 179.)

Krasnopolsky, V. A. (2009). A photochemical model of Titan's atmosphere and ionosphere. *Icarus*, 201:226–256. (Cited on page 178.)

Krasnopolsky, V. A. (2014). Chemical composition of Titan atmosphere and ionosphere: Observations and the photochemical model. *Icarus*, 236:83–91. (Cited on page 178.)

Krawczynski, M. J., Behn, M. D., Das, S. B., and Joughin, I. (2009). Constraints on the lake volume required for hydro-fracture through ice sheets. *Geophysical Research Letters*, 36:L10501. (Cited on page 83.)

Kreslavsky, M. A. and Head, J. W. (2002). Mars: Nature and evolution of young latitude-dependent water-ice-rich mantle. 29(15):1719. (Cited on pages 194, 207, 221 and 238.)

Kump, L. R., Brantley, S. L., and Arthur, M. A. (2000). Chemical weathering, atmospheric co2 and climate. *Annu. Rev. Earth Planet. Sci.*, 28:611. (Cited on page 69.)

Lainey, V., Arlot, J.-E., Karatekin, Ö., and van Hoolst, T. (2009). Strong tidal dissipation in Io and Jupiter from astrometric observations. *Nature*, 459:957–959. (Cited on page 154.)

Lainey, V., Jacobson, R. A., Tajeddine, R., Cooper, N. J., Murray, C., Robert, V., Tobie, G., Guillot, T., Mathis, S., Remus, F., Desmars, J., Arlot, J.-E., De Cuyper, J.-P., Dehant, V., Pascu, D., Thuillot, W., Le Poncin-Lafitte, C., and Zahn, J.-P. (2017). New constraints on Saturn's interior from Cassini astrometric data. *Icarus*, 281:286–296. (Cited on page 154.)

Lammer, H., Bredehöft, J. H., Coustenis, A., Khodachenko, M. L., Kaltenegger, L., Grasset, O., Prieur, D., Raulin, F., Ehrenfreund, P., Yamauchi, M., Wahlund, J.-E., Grießmeier, J.-M., Stangl, G., Cockell, C. S., Kulikov, Y. N., Grenfell, J. L., and Rauer, H. (2009). What makes a planet habitable? *The Astronomy & Astrophysics Review*, 17:181–249. (Cited on pages 5 and 111.)

Lamouroux, J., Tran, H., Laraia, A. L., Gamache, R. R., Rothman, L. S., Gordon, I. E., and Hartmann, J.-M. (2010). Updated database plus software for line-mixing in CO_2 infrared spectra and their test using laboratory spectra in the 1.5-2.3 μm region. *Journal of Quantitative Spectroscopy and Radiative Transfer*, 111:2321–2331. (Cited on page 309.)

Laskar, J., Correia, A. C. M., Gastineau, M., Joutel, F., Levrard, B., and Robutel, P. (2004). Long term evolution and chaotic diffusion of the insolation quantities of Mars. *Icarus*, 170:343–364. (Cited on pages 198 and 248.)

Lawson, P. R., Poyneer, L., Barrett, H., Frazin, R., Caucci, L., Devaney, N., Furenlid, L., Gładysz, S., Guyon, O., Krist, J., Maire, J., Marois, C., Mawet, D., Mouillet, D., Mugnier, L., Pearson, I., Perrin, M., Pueyo, L., and Savransky, D. (2012). On advanced estimation techniques for exoplanet detection and characterization using ground-based coronagraphs. In *Adaptive Optics Systems III*, volume 8447 of *Proceedings of the SPIE*, page 844722. (Cited on page 112.)

Le Deit, L., Hauber, E., Fueten, F., Pondrelli, M., Rossi, A. P., and Jaumann, R. (2013). Sequence of infilling events in Gale Crater, Mars: Results from morphology, stratigraphy, and mineralogy. *Journal of Geophysical Research (Planets)*, 118:2439–2473. (Cited on page 28.)

Le Treut, H. and Li, Z. X. (1991). Sensitivity of an atmospheric general circulation model to prescribed SST changes: Feedback effects associated with the simulation of cloud optical properties. *Climate Dynamics*, 5:175–187. (Cited on pages 53 and 206.)

Lebonnois, S., Eymet, V., Lee, C., and Vatant d'Ollone, J. (2015). Analysis of the radiative budget of the Venusian atmosphere based on infrared Net Exchange Rate formalism. *Journal of Geophysical Research (Planets)*, 120:1186–1200. (Cited on page 118.)

Lecar, M., Podolak, M., Sasselov, D., and Chiang, E. (2006). On the Location of the Snow Line in a Protoplanetary Disk. *The Astrophysical Journal*, 640:1115–1118. (Cited on page 8.)

Leconte, J., Forget, F., Charnay, B., Wordsworth, R., and Pottier, A. (2013a). Increased insolation threshold for runaway greenhouse processes on Earth-like planets. *Nature*, 504:268–280. (Cited on pages 12, 20, 48, 51, 95, 96, 151, 152, 153, 198, 201, 248, 249 and 257.)

Leconte, J., Forget, F., Charnay, B., Wordsworth, R., Selsis, F., and Millour, E. (2013b). 3D climate modeling of close-in land planets: Circulation patterns, climate moist bistability and habitability. *Astronomy.and Astrophysics, in press.* (Cited on pages 48, 95, 96, 100, 104, 106, 125, 151, 170, 179 and 198.)

Leconte, J., Wu, H., Menou, K., and Murray, N. (2015). Asynchronous rotation of Earth-mass planets in the habitable zone of lower-mass stars. *Science*, 347:632–635. (Cited on pages 16, 155 and 158.)

Leforestier, C., Tipping, R. H., and Ma, Q. (2010). Temperature dependences of mechanisms responsible for the water-vapor continuum absorption. II. Dimers and collision-induced absorption. *Journal of Chemical Physics*, 132(16):164302–164302. (Cited on page 327.)

Li, X., Champagne, M. H., and Hunt, K. L. C. (1998). Long-range, collision-induced dipoles of T_d-D_h molecule pairs: Theory and numerical results for CH_4 or CF_4 interacting with H_2, N_2, CO_2, or CS_2. *Journal of Chemical Physics*, 109:8416–8425. (Cited on page 327.)

Liang, M.-C., Heays, A. N., Lewis, B. R., Gibson, S. T., and Yung, Y. L. (2007). Source of Nitrogen Isotope Anomaly in HCN in the Atmosphere of Titan. *The Astrophysical Journal Letters*, 664:L115–L118. (Cited on page 178.)

Lide, D. (2004). *CRC Handbook of Chemistry and Physics: A Ready-reference Book of Chemical and Physical Data 85th ed.* CRC Press. (Cited on pages 83 and 174.)

Lillis, R. J., Deighan, J., Fox, J. L., Bougher, S. W., Lee, Y., Combi, M. R., Cravens, T. E., Rahmati, A., Mahaffy, P. R., Benna, M., Elrod, M. K., McFadden, J. P., Ergun, R. E., Andersson, L., Fowler, C. M., Jakosky, B. M., Thiemann, E., Eparvier, F., Halekas, J. S., Leblanc, F., and Chaufray, J.-Y. (2017). Photochemical escape of oxygen from Mars: First results from MAVEN in situ data. *Journal of Geophysical Research (Space Physics)*, 122:3815–3836. (Cited on pages 197 and 294.)

Longhi, J. (2005). Phase equilibria in the system CO $_2$-H $_2$O I: New equilibrium relations at low temperatures. *Geochimica et Cosmochimica Acta*, 69:529–539. (Cited on pages 84 and 174.)

Lorenz, R. D. (2000). Microtektites on Mars: Volume and Texture of Distal Impact Ejecta Deposits. *Icarus*, 144:353–366. (Cited on page 274.)

Lorenz, R. D. and Lunine, J. I. (1996). Erosion on Titan: Past and Present. *Icarus*, 122:79–91. (Cited on page 178.)

Lorenz, R. D., Lunine, J. I., and McKay, C. P. (1997). Titan under a red giant sun: A new kind of 'habitable' moon. *Geophysical Research Letters*, 24:2905. (Cited on page 177.)

Lorenz, R. D., Mitchell, K. L., Kirk, R. L., Hayes, A. G., Aharonson, O., Zebker, H. A., Paillou, P., Radebaugh, J., Lunine, J. I., Janssen, M. A., Wall, S. D., Lopes, R. M., Stiles, B., Ostro, S., Mitri, G., and Stofan, E. R. (2008). Titan's inventory of organic surface materials. *Geophysical Research Letters*, 35:L02206. (Cited on page 178.)

Lovis, C. and Fischer, D. (2010). *Radial Velocity Techniques for Exoplanets*, pages 27–53. (Cited on page 36.)

Lovis, C., Snellen, I., Mouillet, D., Pepe, F., Wildi, F., Astudillo-Defru, N., Beuzit, J.-L., Bonfils, X., Cheetham, A., Conod, U., Delfosse, X., Ehrenreich, D., Figueira, P., Forveille, T., Martins, J. H. C., Quanz, S. P., Santos, N. C., Schmid, H.-M., Ségransan, D., and Udry, S. (2017). Atmospheric characterization of Proxima b by coupling the SPHERE high-contrast imager to the ESPRESSO spectrograph. *Astronomy & Astrophysics*, 599:A16. (Cited on pages 41, 112 and 114.)

Luger, R. and Barnes, R. (2015). Extreme Water Loss and Abiotic O2Buildup on Planets Throughout the Habitable Zones of M Dwarfs. *Astrobiology*, 15:119–143. (Cited on pages 150 and 178.)

Luger, R., Lustig-Yaeger, J., and Agol, E. (2017a). Planet-Planet Occultations in TRAPPIST-1 and Other Exoplanet Systems. *The Astrophysical Journal*, 851:94. (Cited on page 39.)

Luger, R., Sestovic, M., Kruse, E., Grimm, S. L., Demory, B.-O., Agol, E., Bolmont, E., Fabrycky, D., Fernandes, C. S., Van Grootel, V., Burgasser, A., Gillon, M., Ingalls, J. G., Jehin, E., Raymond, S. N., Selsis, F., Triaud, A. H. M. J., Barclay, T., Barentsen, G., Howell, S. B., Delrez, L., de Wit, J., Foreman-Mackey, D., Holdsworth, D. L., Leconte, J., Lederer, S., Turbet, M., Almleaky, Y., Benkhaldoun, Z., Magain, P., Morris, B. M., Heng, K., and Queloz, D. (2017b). A seven-planet resonant chain in TRAPPIST-1. *Nature Astronomy*, 1:0129. (Cited on pages 144, 151, 154, 158, 160, 166, 178 and 183.)

Lunine, J. I. (2017). Ocean worlds exploration. *Acta Astronautica*, 131:123–130. (Cited on page 8.)

Luo, W., Cang, X., and Howard, A. D. (2017). New Martian valley network volume estimate consistent with ancient ocean and warm and wet climate. *Nature Communications*, 8:15766. (Cited on pages 269, 282 and 335.)

Ma, Q. and Tipping, R. H. (1992). A far wing line shape theory and its application to the foreign-broadened water continuum absorption. III. *Journal of Chemical Physics*, 97:818–828. (Cited on pages 251 and 330.)

Madeleine, J.-B. (2011). *Dust and clouds on Mars: Remote sensing, modeling of climate feedbacks and paleoclimate applications*. Theses, Université Pierre et Marie Curie - Paris VI. Manuscrit soumis aux rapporteurs le 15 Décembre 2010 et accepté sans modification majeures. La version finale ne comporte que des changements mineurs. (Cited on pages 49, 52, 55 and 249.)

Makarov, V. V. and Efroimsky, M. (2013). No Pseudosynchronous Rotation for Terrestrial Planets and Moons. *ApJ*, 764:27. (Cited on page 154.)

Malin, M. C. and Edgett, K. S. (1999). Oceans or seas in the Martian northern lowlands: High resolution imaging tests of proposed coastlines. *Geophysical Research Letters*, 26:3049–3052. (Cited on page 238.)

Malin, M. C. and Edgett, K. S. (2003). Evidence for Persistent Flow and Aqueous Sedimentation on Early Mars. *Science*, 302:1931–1934. (Cited on pages 25 and 246.)

Manabe, S. (1969). Climate and the Ocean CIRCULATION1. *Monthly Weather Review*, 97:739. (Cited on page 286.)

Manabe, S. and Wetherald, R. (1967). Thermal equilibrium of the atmosphere with a given distribution of relative humidity. 24:241–259. (Cited on pages 200 and 248.)

Mangold, N., Adeli, S., Conway, S., Ansan, V., and Langlais, B. (2012). A chronology of early Mars climatic evolution from impact crater degradation. *Journal of Geophysical Research (Planets)*, 117:E04003. (Cited on pages 25 and 246.)

Mangold, N. and Ansan, V. (2006). Detailed study of an hydrological system of valleys, a delta and lakes in the Southwest Thaumasia region, Mars. *Icarus*, 180:75–87. (Cited on pages 25 and 246.)

Mangold, N., Quantin, C., Ansan, V., Delacourt, C., and Allemand, P. (2004). Evidence for Precipitation on Mars from Dendritic Valleys in the Valles Marineris Area. *Science*, 305:78–81. (Cited on pages 190, 193 and 200.)

Marcq, E., Salvador, A., Massol, H., and Davaille, A. (2017). Thermal radiation of magma ocean planets using a 1-D radiative-convective model of H_2O-CO_2 atmospheres. *Journal of Geophysical Research (Planets)*, 122:1539–1553. (Cited on page 254.)

Marois, C., Macintosh, B., Barman, T., Zuckerman, B., Song, I., Patience, J., Lafrenière, D., and Doyon, R. (2008). Direct Imaging of Multiple Planets Orbiting the Star HR 8799. *Science*, 322:1348. (Cited on page 41.)

Matsubara, Y., Howard, A. D., and Drummond, S. A. (2011). Hydrology of early Mars: Lake basins. *Journal of Geophysical Research (Planets)*, 116:E04001. (Cited on pages 289, 290, 291, 292, 293 and 301.)

Maurin, A. S., Selsis, F., Hersant, F., and Belu, A. (2012). Thermal phase curves of nontransiting terrestrial exoplanets. II. Characterizing airless planets. *Astronomy & Astrophysics*, 538:A95. (Cited on page 121.)

Mayor, M. and Queloz, D. (1995). A Jupiter-mass companion to a solar-type star. *Nature*, 378:355–359. (Cited on page 34.)

McEwen, A. S., Dundas, C. M., Mattson, S. S., Toigo, A. D., Ojha, L., Wray, J. J., Chojnacki, M., Byrne, S., Murchie, S. L., and Thomas, N. (2014). Recurring slope lineae in equatorial regions of Mars. *Nature Geoscience*, 7:53–58. (Cited on page 25.)

McEwen, A. S., Ojha, L., Dundas, C. M., Mattson, S. S., Byrne, S., Wray, J. J., Cull, S. C., Murchie, S. L., Thomas, N., and Gulick, V. C. (2011). Seasonal Flows on Warm Martian Slopes. *Science*, 333:740. (Cited on page 25.)

McKay, C. P. (2016). Titan as the Abode of Life. *Life*, 6:8. (Cited on page 5.)

McKay, C. P., Pollack, J. B., and Courtin, R. (1991). The greenhouse and antigreenhouse effects on Titan. *Science*, 253:1118–1121. (Cited on page 177.)

Mellor, G. L. and Yamada, T. (1982). Development of a turbulence closure model for geophysical fluid problems. *Reviews of Geophysics and Space Physics*, 20:851–875. (Cited on pages 50, 152, 198 and 248.)

Menou, K. (2013). Water-trapped Worlds. *The Astrophysical Journal*, 774. (Cited on pages 79, 104 and 173.)

Menou, K. (2015). Climate stability of habitable Earth-like planets. *Earth and Planetary Science Letters*, 429:20–24. (Cited on pages 22, 23, 67, 69 and 82.)

Menoux, V., Le Doucen, R., Boissoles, J., and Boulet, C. (1991). Line shape in the low frequency wing of self- and N2-broadened nu3 CO2 lines - Temperature dependence of the asymmetry. *Atomic and Molecular Physics*, 30:281–286. (Cited on page 60.)

Mignard, F. (1979). The evolution of the lunar orbit revisited. I. *Moon and Planets*, 20:301–315. (Cited on page 153.)

Millour, E., Forget, F., Diez, B., and Montabone, L. (2009). Simulating the Martian CO2 Cycle with the LMD Global Climate Model. In *Third International Workshop on Mars Polar Energy Balance and the CO2 Cycle*, volume 1494 of *LPI Contributions*, pages 41–42. (Cited on page 53.)

Millour, E., Forget, F., Spiga, A., Navarro, T., Madeleine, J.-B., Montabone, L., Pottier, A., Lefevre, F., Montmessin, F., Chaufray, J.-Y., Lopez-Valverde, M. A., Gonzalez-Galindo, F., Lewis, S. R., Read, P. L., Huot, J.-P., Desjean, M.-C., and MCD/GCM development Team (2015). The Mars Climate Database (MCD version 5.2). *European Planetary Science Congress 2015*, 10:EPSC2015–438. (Cited on page 100.)

Milton, D. J. (1974). Carbon dioxide hydrate and floods on Mars. *Science*, 183:654–656. (Cited on page 194.)

Mischna, M. A., Baker, V., Milliken, R., Richardson, M., and Lee, C. (2013). Effects of obliquity and water vapor/trace gas greenhouses in the early martian climate. *Journal of Geophysical Research (Planets)*, 118:560–576. (Cited on page 31.)

Mischna, M. A., Lee, C., and Richardson, M. (2012). Development of a fast, accurate radiative transfer model for the Martian atmosphere, past and present. *Journal of Geophysical Research (Planets)*, 117:E10009. (Cited on page 309.)

Mlawer, E. J., Payne, V. H., Moncet, J.-L., Delamere, J. S., Alvarado, M. J., and Tobin, D. C. (2012). Development and recent evaluation of the MT_CKD model of continuum absorption. *Philosophical Transactions of the Royal Society of London Series A*, 370:2520–2556. (Cited on pages 61, 251 and 330.)

Moore, J. M., Howard, A. D., Dietrich, W. E., and Schenk, P. M. (2003). Martian Layered Fluvial Deposits: Implications for Noachian Climate Scenarios. *Geophysical Research Letters*, 30:2292. (Cited on pages 25 and 246.)

Moore, J. M., McKinnon, W. B., Spencer, J. R., Howard, A. D. Schenk, P. M., Beyer, R. A., Nimmo, F., Singer, K. N., Umurhan, O. M., White, O. L., Stern, S. A., Ennico, K. Olkin, C. B., Weaver, H. A., Young, L. A., Binzel, R. P., Buie, M. W., Buratti, B. J., Cheng, A. F., Cruikshank, D. P., Grundy, W. M., Linscott, I. R., Reitsema, H. J., Reuter, D. C. Showalter, M. P., Bray, V. J., Chavez, C. L., Howett, C. J. A., Lauer, T. R., Lisse, C. M., Parker, A. H., Porter, S. B. Robbins, S. J., Runyon, K., Stryk, T., Throop, H. B. Tsang, C. C. C., Verbiscer, A. J., Zangari, A. M. Chaikin, A. L., and Wilhelms, D. E. (2016). The geology of Pluto and Charon through the eyes of New Horizons . *Science*, 351:1284. (Cited on page 106.)

Morley, C. V., Kreidberg, L., Rustamkulov, Z., Robinson, T., and Fortney, J. J. (2017). Observing the Atmospheres of Known Temperate Earth-sized Planets with JWST. *The Astrophysical Journal*, 850:121. (Cited on page 150.)

Mouginot, J., Pommerol, A., Beck, P., Kofman, W., and Clifford, S. M. (2012). Dielectric map of the Martian northern hemisphere and the nature of plain filling materials. *Geophysical Research Letters*, 39. (Cited on page 221.)

Mustard, J. F., Murchie, S. L., Pelkey, S. M., Ehlmann, B. L., Milliken, R. E., Grant, J. A., Bibring, J.-P., Poulet, F., Bishop, J., Dobrea, E. N., Roach, L., Seelos, F., Arvidson, R. E., Wiseman, S., Green, R., Hash, C., Humm, D., Malaret, E., McGovern, J. A., Seelos, K., Clancy, T., Clark, R., Marais, D. D., Izenberg, N., Knudson, A., Langevin, Y., Martin, T., McGuire, P., Morris, R., Robinson, M., Roush, T., Smith, M., Swayze, G., Taylor, H., Titus, T., and Wolff, M. (2008). Hydrated silicate minerals on Mars observed by the Mars Reconnaissance Orbiter CRISM instrument. *Nature*, 454:305–309. (Cited on pages 27 and 246.)

Nakajima, S., Hayashi, Y.-Y., and Abe, Y. (1992). A study on the 'runaway greenhouse effect' with a one-dimensional radiative-convective equilibrium model. *Journal of Atmospheric Sciences*, 49:2256–2266. (Cited on pages 12, 254 and 262.)

Neron de Surgy, O. and Laskar, J. (1997). On the long term evolution of the spin of the Earth. *Astronomy & Astrophysics*, 318:975–989. (Cited on pages 154, 155 and 156.)

Niemann, H. B., Atreya, S. K., Bauer, S. J., Carignan, G. R., Demick, J. E., Frost, R. L., Gautier, D., Haberman, J. A., Harpold, D. N., Hunten, D. M., Israel, G., Lunine, J. I., Kasprzak, W. T., Owen, T. C., Paulkovich, M., Raulin, F., Raaen, E., and Way, S. H. (2005). The abundances of constituents of Titan's atmosphere from the GCMS instrument on the Huygens probe. *Nature*, 438:779–784. (Cited on page 175.)

Niro, F., Jucks, K., and Hartmann, J.-M. (2005). Spectra calculations in central and wing regions of CO_2 IR bands. IV: software and database for the computation of atmospheric spectra. *Journal of Quantitative Spectroscopy and Radiative Transfer*, 95:469–481. (Cited on page 309.)

Nwaboh, J. A., Werhahn, O., and Ebert, V. (2014). Line strength and collisional broadening coefficients of H_2O at 2.7 μm for natural gas quality assurance applications. *Molecular Physics*, 112:2451–2461. (Cited on page 330.)

Nye, J. F., Durham, W. B., Schenk, P. M., and Moore, J. M. (2000). The Instability of a South Polar Cap on Mars Composed of Carbon Dioxide. *Icarus*, 144:449–455. (Cited on pages 80 and 173.)

Ojha, L., Wilhelm, M. B., Murchie, S. L., McEwen, A. S., Wray, J. J., Hanley, J., Massé, M., and Chojnacki, M. (2015). Spectral evidence for hydrated salts in recurring slope lineae on Mars. *Nature Geoscience*, 8:829–832. (Cited on page 25.)

Ozak, N., Aharonson, O., and Halevy, I. (2016). Radiative transfer in CO_2-rich atmospheres: 1. Collisional line mixing implies a colder early Mars. *Journal of Geophysical Research (Planets)*, 121:965–985. (Cited on pages 307, 308 and 310.)

Palumbo, A. M., Head, J. W., and Wordsworth, R. D. (2018). Late Noachian Icy Highlands climate model: Exploring the possibility of transient melting and fluvial/lacustrine activity through peak annual and seasonal temperatures. *Icarus*, 300:261–286. (Cited on page 247.)

Paradise, A. and Menou, K. (2017). GCM Simulations of Unstable Climates in the Habitable Zone. *The Astrophysical Journal*, 848:33. (Cited on page 22.)

Paradise, A., Menou, K., Valencia, D., and Lee, C. (2018). Habitable Snowballs: Generalizing the Habitable Zone. *ArXiv e-prints*. (Cited on page 23.)

Parker, T. J., Saunders, R. S., and Schneeberger, D. M. (1989). Transitional morphology in west Deuteronilus Mensae, Mars - Implications for modification of the lowland/upland boundary. *Icarus*, 82:111–145. (Cited on page 238.)

Peale, S. J. (1977). Rotation histories of the natural satellites. In Burns, J. A., editor, *IAU Colloq. 28: Planetary Satellites*, pages 87–111. (Cited on page 15.)

Perrin, M. Y. and Hartmann, J. M. (1989). Temperature-dependent measurements and modeling of absorption by CO2-N2 mixtures in the far line-wings of the 4.3-micron CO2 band. *Journal of Quantitative Spectroscopy and Radiative Transfer*, 42:311–317. (Cited on pages 59, 152, 182, 251, 308, 309, 325 and 334.)

Perron, J. T., Mitrovica, J. X., Manga, M., Matsuyama, I., and Richards, M. A. (2007). Evidence for an ancient martian ocean in the topography of deformed shorelines. *Nature*, 447:840–843. (Cited on page 238.)

Petrenko, V. F. and Whitworth, R. W. (2002). *Physics of Ice*. (Cited on page 125.)

Phillips, R. J., Zuber, M. T., Solomon, S. C., Golombek, M. P., Jakosky, B. M., Banerdt, W. B., Smith, D. E., Williams, R. M. E., Hynek, B. M., Aharonson, O., and Hauck, S. A. (2001). Ancient Geodynamics and Global-Scale Hydrology on Mars. *Science*, 291:2587–2591. (Cited on pages 28 and 198.)

Pierrehumbert, R. and Gaidos, E. (2011). Hydrogen Greenhouse Planets Beyond the Habitable Zone. *The Astrophysical Journal Letters*, 734:L13. (Cited on page 19.)

Pierrehumbert, R. T. (1995). Thermostats, Radiator Fins, and the Local Runaway Greenhouse. *Journal of Atmospheric Sciences*, 52:1784–1806. (Cited on page 257.)

Pierrehumbert, R. T. (2005). Climate dynamics of a hard snowball Earth. *Journal of Geophysical Research (Atmospheres)*, 110. (Cited on pages 68 and 69.)

Pierrehumbert, R. T. (2010). *Principles of Planetary Climate*. (Cited on page 9.)

Pierrehumbert, R. T. (2011). A Palette of Climates for Gliese 581g. *The Astrophysical Journal Letters*, 726:L8. (Cited on pages 95, 109, 181 and 183.)

Pierrehumbert, R. T., Abbot, D. S., Voigt, A., and Koll, D. (2011). Climate of the Neoproterozoic. *Annual Review of Earth and Planetary Sciences*, 39:417–460. (Cited on pages 68, 69 and 87.)

Piqueux, S. and Christensen, P. R. (2009). A model of thermal conductivity for planetary soils: 1. Theory for unconsolidated soils. *Journal of Geophysical Research (Planets)*, 114:E09005. (Cited on page 286.)

Pirali, O., Vervloet, M., Mulas, G., Malloci, G., and Joblin, C. (2009). High-resolution infrared absorption spectroscopy of thermally excited naphthalene. Measurements and calculations of anharmonic parameters and vibrational interactions. *Physical Chemistry Chemical Physics (Incorporating Faraday Transactions)*, 11:3443. (Cited on page 316.)

Poliakow, E. (2005). Numerical modelling of the paleotidal evolution of the Earth-Moon System. In Knežević, Z. and Milani, A., editors, *IAU Colloq. 197: Dynamics of Populations of Planetary Systems*, pages 445–452. (Cited on page 154.)

Pollack, J. B., Dalton, J., Grinspoon, D., Wattson, R. B., Freedman, R., Crisp, D., Allen, D. A., Bezard, B., DeBergh, C., Giver, L. P., Ma, Q., and Tipping, R. (1993). Near-infrared light from venus' nightside: A spectroscopic analysis. *Icarus*, 103(1):1 – 42. (Cited on page 251.)

Pollack, J. B., Kasting, J. F., Richardson, S. M., and Poliakoff, K. (1987). The case for a wet, warm climate on early Mars. *Icarus*, 71:203–224. (Cited on page 67.)

Popp, M., Schmidt, H., and Marotzke, J. (2016). Transition to a Moist Greenhouse with CO_2 and solar forcing. *Nature Communications*, 7:10627. (Cited on page 12.)

Poulet, F., Bibring, J.-P., Mustard, J. F., Gendrin, A., Mangold, N., Langevin, Y., Arvidson, R. E., Gondet, B., and Gomez, C. (2005). Phyllosilicates on Mars and implications for early martian climate. *Nature*, 438:623–627. (Cited on pages 27 and 246.)

Pruppacher, H. and Klett, J. (1996). *Microphysics of Clouds and Precipitation*. Atmospheric and Oceanographic Sciences Library. Springer Netherlands. (Cited on page 262.)

Quantin, C., Allemand, P., Mangold, N., Dromart, G., and Delacourt, C. (2005). Fluvial and lacustrine activity on layered deposits in Melas Chasma, Valles Marineris, Mars. *Journal of Geophysical Research*, 110. (Cited on page 193.)

Quantin, C., Craddock, R. A., Dubuffet, F., Lozac'h, L., and Martineau, M. (2015). Long-term evolution of the erosion rates during early mars. In *European Planetary Science Congress 2015*. (Cited on pages 25 and 197.)

Quintana, E. V., Barclay, T., Raymond, S. N., Rowe, J. F., Bolmont, E., Caldwell, D. A., Howell, S. B., Kane, S. R., Huber, D., Crepp, J. R., Lissauer, J. J., Ciardi, D. R., Coughlin, J. L., Everett, M. E., Henze, C. E., Horch, E., Isaacson, H., Ford, E. B., Adams, F. C., Still, M., Hunter, R. C., Quarles, B., and Selsis, F. (2014). An Earth-Sized Planet in the Habitable Zone of a Cool Star. *Science*, 344:277–280. (Cited on page 34.)

Rackham, B. V., Apai, D., and Giampapa, M. S. (2018). The Transit Light Source Effect: False Spectral Features and Incorrect Densities for M-dwarf Transiting Planets. *The Astrophysical Journal*, 853:122. (Cited on page 145.)

Ragozzine, D. and Holman, M. J. (2010). The Value of Systems with Multiple Transiting Planets. *ArXiv e-prints*. (Cited on page 39.)

Rajpurohit, A. S., Reylé, C., Allard, F., Homeier, D., Schultheis, M., Bessell, M. S., and Robin, A. C. (2013). The effective temperature scale of M dwarfs. *Astronomy & Astrophysics*, 556:A15. (Cited on pages 98 and 152.)

Ramirez, R. M. (2017). A warmer and wetter solution for early Mars and the challenges with transient warming. *Icarus*, 297:71–82. (Cited on pages 284, 294, 299, 303, 316 and 327.)

Ramirez, R. M. and Craddock, R. A. (2018). The geological and climatological case for a warmer and wetter early Mars. *Nature Geoscience*, 11:230–237. (Cited on pages 294 and 297.)

Ramirez, R. M. and Kaltenegger, L. (2017). A Volcanic Hydrogen Habitable Zone. *The Astrophysical Journal Letters*, 837:L4. (Cited on pages 19 and 329.)

Ramirez, R. M. and Kaltenegger, L. (2018). A methane extension to the classical habitable zone. *The Astrophysical Journal*, 858(2):72. (Cited on page 329.)

Ramirez, R. M. and Kasting, J. F. (2017). Could cirrus clouds have warmed early Mars? *Icarus*, 281:248–261. (Cited on pages 31, 235, 240, 246, 247, 250, 263, 264 and 265.)

Ramirez, R. M., Kopparapu, R., Zugger, M. E., Robinson, T. D., Freedman, R., and Kasting, J. F. (2014a). Warming early Mars with CO_2 and H_2. *Nature Geoscience*, 7:59–63. (Cited on pages 30, 32, 240, 246, 262, 283, 284, 285, 293 and 315.)

Ramirez, R. M., Kopparapu, R. K., Lindner, V., and Kasting, J. F. (2014b). Can Increased Atmospheric CO2 Levels Trigger a Runaway Greenhouse? *Astrobiology*, 14:714–731. (Cited on pages 20 and 254.)

Read, P. and Lewis, S. R. (2004). *The Martian Climate Revisited*. (Cited on page 100.)

Remus, F., Mathis, S., Zahn, J.-P., and Lainey, V. (2015). The surface signature of the tidal dissipation of the core in a two-layer planet. *Astronom. Astrophys.*, 573:A23. (Cited on page 154.)

Riaud, P. and Schneider, J. (2007). Improving Earth-like planets' detection with an ELT: the differential radial velocity experiment. *Astronomy & Astrophysics*, 469:355–361. (Cited on page 41.)

Ribas, I. (2010). The Sun and stars as the primary energy input in planetary atmospheres. In Kosovichev, A. G., Andrei, A. H., and Rozelot, J.-P., editors, *Solar and Stellar Variability: Impact on Earth and Planets*, volume 264 of *IAU Symposium*, pages 3–18. (Cited on page 19.)

Ribas, I., Bolmont, E., Selsis, F., Reiners, A., Leconte, J., Raymond, S. N., Engle, S. G., Guinan, E. F., Morin, J., Turbet, M., Forget, F., and Anglada-Escudé, G. (2016). The habitability of Proxima Centauri b. I. Irradiation, rotation and volatile inventory from formation to the present. *Astronomy & Astrophysics*, 596:A111. (Cited on pages 95, 96, 100, 104, 107, 112, 123, 155 and 333.)

Richard, C., Gordon, I. E., Rothman, L. S., Abel, M., Frommhold, L., Gustafsson, M., Hartmann, J.-M., Hermans, C., Lafferty, W. J., Orton, G. S., Smith, K. M., and Tran, H. (2012). New section of the HITRAN database: Collision-induced absorption (CIA). *Journal of Quantitative Spectroscopy and Radiative Transfer*, 113:1276–1285. (Cited on pages 86, 98, 152, 315, 319, 321, 322 and 328.)

Robbins, S. J. and Hynek, B. M. (2012). A new global database of Mars impact craters greater or equal to 1 km: 1. Database creation, properties, and parameters. *Journal of Geophysical Research (Planets)*, 117:E05004. (Cited on page 33.)

Roder, H. M. (1978). The molar volume (density) of solid oxygen in equilibrium with vapor. *Journal of Physical and Chemical Reference Data*, 7:949–958. (Cited on page 164.)

Rodriguez, J. A. P., Fairén, A. G., Tanaka, K. L., Zarroca, M., Linares, R., Platz, T., Komatsu, G., Miyamoto, H., Kargel, J. S., Yan, J., Gulick, V., Higuchi, K., Baker, V. R., and Glines, N. (2016). Tsunami waves extensively resurfaced the shorelines of an early Martian ocean. *Scientific Reports*, 6:25106. (Cited on pages 237, 238, 240 and 242.)

Rodriguez, J. A. P., Platz, T., Gulick, V., Baker, V. R., Fairen, A. G., Kargel, J., Yan, J., Miyamoto, H., and Glines, N. (2015). Did the martian outflow channels mostly form during the Amazonian Period? *Icarus*, 257:387–395. (Cited on page 28.)

Ros, K. and Johansen, A. (2013). Ice condensation as a planet formation mechanism. *Astronomy & Astrophysics*, 552:A137. (Cited on page 8.)

Rossow, W. B. (1978). Cloud microphysics - Analysis of the clouds of Earth, Venus, Mars, and Jupiter. *Icarus*, 36:1–50. (Cited on pages 52, 153, 249 and 254.)

Rothman, L. S., Gordon, I. E., Babikov, Y., Barbe, A., Chris Benner, D., Bernath, P. F., Birk, M., Bizzocchi, L., Boudon, V., Brown, L. R., Campargue, A., Chance, K., Cohen, E. A., Coudert, L. H., Devi, V. M., Drouin, B. J., Fayt, A., Flaud, J.-M., Gamache, R. R., Harrison, J. J., Hartmann, J.-M., Hill, C., Hodges, J. T., Jacquemart, D., Jolly, A., Lamouroux, J., Le Roy, R. J., Li, G., Long, D. A., Lyulin, O. M., Mackie, C. J., Massie, S. T., Mikhailenko, S., Müller, H. S. P., Naumenko, O. V., Nikitin, A. V., Orphal, J., Perevalov, V., Perrin, A., Polovtseva, E. R., Richard, C., Smith, M. A. H., Starikova, E., Sung, K., Tashkun, S., Tennyson, J., Toon, G. C., Tyuterev, V. G., and Wagner, G. (2013). The HITRAN2012 molecular spectroscopic database. *Journal of Quantitative Spectroscopy and Radiative Transfer*, 130:4–50. (Cited on pages 86, 152, 182, 199, 251, 310, 330 and 331.)

Rothman, L. S., Gordon, I. E., Barbe, A., Benner, D. C., Bernath, P. F., Birk, M., Boudon, V., Brown, L. R., Campargue, A., Champion, J.-P., Chance, K., Coudert, L. H., Dana, V., Devi, V. M., Fally, S., Flaud, J.-M., Gamache, R. R., Goldman, A., Jacquemart, D., Kleiner, I., Lacome, N., Lafferty, W. J., Mandin, J.-Y., Massie, S. T., Mikhailenko, S. N., Miller, C. E., Moazzen-Ahmadi, N., Naumenko, O. V., Nikitin, A. V., Orphal, J., Perevalov, V. I., Perrin, A., Predoi-Cross, A., Rinsland, C. P., Rotger, M., Šimečková, M., Smith, M. A. H., Sung, K., Tashkun, S. A., Tennyson, J., Toth, R. A., Vandaele, A. C., and Vander Auwera, J. (2009). The HITRAN 2008 molecular spectroscopic database. *Journal of Quantitative Spectroscopy and Radiative Transfer*, 110:533–572. (Cited on pages 98 and 285.)

Rothman, L. S., Jacquemart, D., Barbe, A., Chris Benner, D., Birk, M., Brown, L. R., Carleer, M. R., Chackerian, C., Chance, K., Coudert, L. H., Dana, V., Devi, V. M., Flaud, J.-M., Gamache, R. R., Goldman, A., Hartmann, J.-M., Jucks, K. W., Maki, A. G., Mandin, J.-Y., Massie, S. T., Orphal, J., Perrin, A., Rinsland, C. P., Smith, M. A. H., Tennyson, J., Tolchenov, R. N., Toth, R. A., Vander Auwera, J., Varanasi, P., and Wagner, G. (2005). The HITRAN 2004 molecular spectroscopic database. *Journal of Quantitative Spectroscopy and Radiative Transfer*, 96:139–204. (Cited on page 310.)

Rothschild, L. J. and Mancinelli, R. L. (2001). Life in extreme environments. *Nature*, 409:1092–1101. (Cited on page 4.)

Rotto, S. L. and Tanaka, K. L. (1992). Chryse Planitia region, Mars: Channeling history, flood volume estimates, and scenarios for bodies of water in the northern plains. Lunar and Planet. Inst., Houston, Tex. Workshop on the Martian Surface and Atmosphere Through Time. (Cited on page 194.)

Rotto, S. L. and Tanaka, K. L. (1995). Geologic/geomorphologic map of the Chryse Planitia region of Mars. (Cited on page 28.)

Ruiz, J., McGovern, P. J., Jimenez-Diaz, A., Lopez, V., Williams, J.-P., Hahn, B. C., and Tejero, R. (2011). The thermal evolution of Mars as constrained by paleo-heat flows. *Icarus*, 215:508–517. (Cited on page 239.)

Sagan, C. (1977). Reducing greenhouses and the temperature history of earth and Mars. *Nature*, 269:224–226. (Cited on page 283.)

Sagan, C. and Mullen, G. (1972). Earth and Mars: Evolution of Atmospheres and Surface Temperatures. *Science*, 177:52–56. (Cited on page 20.)

Santiago, D. L., Colaprete, A., Kreslavsky, M., Kahre, M. A., and Asphaug, E. (2012). Cloud Formation and Water Transport on Mars After Major Outflow Events. volume 43 of *Lunar and Planetary Science Conference*. (Cited on page 193.)

Scanlon, K. E., Head, J. W., Fastook, J. L., and Wordsworth, R. D. (2018). The Dorsa Argentea Formation and the Noachian-Hesperian climate transition. *Icarus*, 299:339–363. (Cited on page 28.)

Schaake, J. C., Koren, V. I., Duan, Q.-Y., Mitchell, K., and Chen, F. (1996). Simple water balance model for estimating runoff at different spatial and temporal scales. *Journal of Geophysical Research: Atmospheres*, 101:7461–7475. (Cited on page 286.)

Schmitt, B., De Bergh, C., and Festou, M. (1997). *Solar system ices*. Kluwer Academic. (Cited on pages 88, 89, 164, 169 and 172.)

Schopf, J. W., Kudryavtsev, A. B., Czaja, A. D., and Tripathi, A. B. (2007). Evidence of Archean life: Stromatolites and microfossils. *Precambrian Research*, 158:141–155. (Cited on page 20.)

Seager, S. (2013). Exoplanet Habitability. *Science*, 340:577–581. (Cited on page 19.)

Seager, S., Kuchner, M., Hier-Majumder, C. A., and Militzer, B. (2007). Mass-Radius Relationships for Solid Exoplanets. *The Astrophysical Journal*, 669:1279–1297. (Cited on page 76.)

Segura, T. L., McKay, C. P., and Toon, O. B. (2012). An impact-induced, stable, runaway climate on Mars. *Icarus*, 220:144–148. (Cited on pages 32, 245, 246, 247, 262, 267 and 335.)

Segura, T. L., Toon, O. B., and Colaprete, A. (2008). Modeling the environmental effects of moderate-sized impacts on Mars. *Journal of Geophysical Research (Planets)*, 113:E11007. (Cited on pages 32, 245, 246, 247, 254, 263, 265, 268 and 335.)

Segura, T. L., Toon, O. B., Colaprete, A., and Zahnle, K. (2002). Environmental Effects of Large Impacts on Mars. *Science*, 298:1977–1980. (Cited on pages 32, 245, 246, 247, 251, 253, 254, 263 and 267.)

Selsis, F., Maurin, A.-S., Hersant, F., Leconte, J., Bolmont, E., Raymond, S. N., and Delbo', M. (2013). The effect of rotation and tidal heating on the thermal lightcurves of super Mercuries. *Astronomy & Astrophysics*, 555:A51. (Cited on page 121.)

Selsis, F., Wordsworth, R. D., and Forget, F. (2011). Thermal phase curves of nontransiting terrestrial exoplanets. I. Characterizing atmospheres. *Astronomy & Astrophysics*, 532:A1. (Cited on pages 114 and 121.)

Shields, A. L., Bitz, C. M., Meadows, V. S., Joshi, M. M., and Robinson, T. D. (2014). Spectrum-driven Planetary Deglaciation due to Increases in Stellar Luminosity. *The Astrophysical Journal Letters*, 785:L9. (Cited on page 111.)

Shields, A. L., Meadows, V. S., Bitz, C. M., Pierrehumbert, R. T., Joshi, M. M., and Robinson, T. D. (2013). The Effect of Host Star Spectral Energy Distribution and Ice-Albedo Feedback on the Climate of Extrasolar Planets. *Astrobiology*, 13:715–739. (Cited on page 152.)

Showman, A. P. and Polvani, L. M. (2011). Equatorial Superrotation on Tidally Locked Exoplanets. *The Astrophysical Journal*, 738:71. (Cited on page 100.)

Shuvalov, V. (2009). Atmospheric erosion induced by oblique impacts. *Meteoritics and Planetary Science*, 44:1095–1105. (Cited on page 271.)

Shuvalov, V. V. (1999). Multi-dimensional hydrodynamic code SOVA for interfacial flows: Application to the thermal layer effect. *Shock Waves*, 9:381–390. (Cited on page 271.)

Shuvalov, V. V. and Artemieva, N. A. (2002). Numerical modeling of Tunguska-like impacts. *Planetary and Space Science*, 50:181–192. (Cited on page 271.)

Sing, D. K., Fortney, J. J., Nikolov, N., Wakeford, H. R., Kataria, T., Evans, T. M., Aigrain, S., Ballester, G. E., Burrows, A. S., Deming, D., Désert, J.-M., Gibson, N. P., Henry, G. W., Huitson, C. M., Knutson, H. A., Lecavelier Des Etangs, A., Pont, F., Showman, A. P., Vidal-Madjar, A., Williamson, M. H., and Wilson, P. A. (2016). A continuum from clear to cloudy hot-Jupiter exoplanets without primordial water depletion. *Nature*, 529:59–62. (Cited on page 39.)

Sleep, N. H. and Zahnle, K. (1998). Refugia from asteroid impacts on early Mars and the early Earth. *Journal of Geophysical Research*, 103:28529–28544. (Cited on page 274.)

Sloan, E. (1998). *Clathrate hydrates of natural gases, 2nd ed.* CRC Press. (Cited on pages 84 and 174.)

Smith, D. E., Zuber, M. T., and 17 coauthors (1999). The global topography of Mars and implication for surface evolution. *Science*, 284:1495–1503. (Cited on pages 198, 248, 287, 288 and 302.)

Smith, D. E., Zuber, M. T., Frey, H. V., Garvin, J. B., Head, J. W., Muhleman, D. O., Pettengill, G. H., Phillips, R. J., Solomon, S. C., Zwally, H. J., Banerdt, W. B., Duxbury, T. C., Golombek, M. P., Lemoine, F. G., Neumann, G. A., Rowlands, D. D., Aharonson, O., Ford, P. G., Ivanov, A. B., Johnson, C. L., McGovern, P. J., Abshire, J. B., Afzal, R. S., and Sun, X. (2001). Mars Orbiter Laser Altimeter: Experiment summary after the first year of global mapping of Mars. 106:23689–23722. (Cited on pages 198, 248, 287, 288 and 302.)

Snellen, I., de Kok, R., Birkby, J. L., Brandl, B., Brogi, M., Keller, C., Kenworthy, M., Schwarz, H., and Stuik, R. (2015). Combining high-dispersion spectroscopy with high contrast imaging: Probing rocky planets around our nearest neighbors. *Astronomy & Astrophysics*, 576:A59. (Cited on pages 41 and 118.)

Snellen, I. A. G., Brandl, B. R., de Kok, R. J., Brogi, M., Birkby, J., and Schwarz, H. (2014). Fast spin of the young extrasolar planet β Pictoris b. *Nature*, 509:63–65. (Cited on pages 41 and 118.)

Snellen, I. A. G., de Kok, R. J., de Mooij, E. J. W., and Albrecht, S. (2010). The orbital motion, absolute mass and high-altitude winds of exoplanet HD209458b. *Nature*, 465:1049–1051. (Cited on pages 41 and 118.)

Solomon, S. C. and Head, J. W. (1991). Fundamental issues in the geology and geophysics of Venus. *Science*, 252:252–260. (Cited on page 24.)

Solomon, S. C., Head, J. W., Kaula, W. M., McKenzie, D., Parsons, B., Phillips, R. J., Schubert, G., and Talwani, M. (1991). Venus tectonics - Initial analysis from Magellan. *Science*, 252:297–312. (Cited on page 24.)

Sotin, C., Tobie, G., Wahr, J., and McKinnon, W. B. (2009). *Tides and Tidal Heating on Europa*, page 85. (Cited on page 154.)

Soto, A., Mischna, M., Schneider, T., Lee, C., and Richardson, M. (2015). Martian atmospheric collapse: Idealized GCM studies. *Icarus*, 250:553–569. (Cited on page 169.)

Span, R. and Wagner, W. (1996). A New Equation of State for Carbon Dioxide Covering the Fluid Region from the Triple-Point Temperature to 1100 K at Pressures up to 800 MPa. *Journal of Physical and Chemical Reference Data*, 25:1509–1596. (Cited on pages 83, 84 and 174.)

Sparks, W. B. and Ford, H. C. (2002). Imaging Spectroscopy for Extrasolar Planet Detection. *The Astrophysical Journal*, 578:543–564. (Cited on page 41.)

Spencer, J. R., Rathbun, J. A., Travis, L. D., Tamppari, L. K., Barnard, L., Martin, T. Z., and McEwen, A. S. (2000). Io's Thermal Emission from the Galileo Photopolarimeter- Radiometer. *Science*, 288:1198–1201. (Cited on pages 9 and 104.)

Spiga, A., Guerlet, S., Meurdesoif, Y., Indurain, M., Millour, E., Dubos, T., Sylvestre, M., Leconte, J., and Fouchet, T. (2015). Waves and eddies simulated by high-resolution global climate modeling of saturn's troposphere and stratosphere. In *European Planetary Science Congress 2015*. (Cited on pages 48 and 198.)

Spiga, A., Guerlet, S., Millour, E., Meurdesoif, Y., Indurain, M., Dubos, T., Sylvestre, M., Cabanes, S., Boissinot, A., and Fouchet, T. (2017). High-resolution Global Climate Modeling of Saturn's and Jupiter's tropospheric and stratospheric circulations. *European Planetary Science Congress*, 11:EPSC2017–295. (Cited on page 48.)

Stefani, S., Piccioni, G., Snels, M., Grassi, D., and Adriani, A. (2013). Experimental CO_2 absorption coefficients at high pressure and high temperature. *Journal of Quantitative Spectroscopy and Radiative Transfer*, 117:21–28. (Cited on page 251.)

Stern, S. A., Bagenal, F., Ennico, K., Gladstone, G. R., Grundy, W. M., McKinnon, W. B., Moore, J. M., Olkin, C. B., Spencer, J. R., Weaver, H. A., Young, L. A., Andert, T., Andrews, J., Banks, M., Bauer, B., Bauman, J., Barnouin, O. S., Bedini, P., Beisser, K., Beyer, R. A., Bhaskaran, S., Binzel, R. P., Birath, E., Bird, M., Bogan, D. J., Bowman, A., Bray, V. J., Brozovic, M., Bryan, C., Buckley, M. R., Buie, M. W., Buratti, B. J., Bushman, S. S., Calloway, A., Carcich, B., Cheng, A. F., Conard, S., Conrad, C. A., Cook, J. C., Cruikshank, D. P., Custodio, O. S., Dalle Ore, C. M., Deboy, C., Dischner, Z. J. B., Dumont, P., Earle, A. M., Elliott, H. A., Ercol, J., Ernst, C. M., Finley, T., Flanigan, S. H., Fountain, G., Freeze, M. J., Greathouse, T., Green, J. L., Guo, Y., Hahn, M., Hamilton, D. P., Hamilton, S. A., Hanley, J., Harch, A., Hart, H. M., Hersman, C. B., Hill, A., Hill, M. E., Hinson, D. P., Holdridge, M. E., Horanyi, M., Howard, A. D., Howett, C. J. A., Jackman, C., Jacobson, R. A., Jennings, D. E., Kammer, J. A., Kang, H. K., Kaufmann, D. E., Kollmann, P., Krimigis, S. M., Kusnierkiewicz, D., Lauer, T. R., Lee, J. E., Lindstrom, K. L., Linscott, I. R., Lisse, C. M., Lunsford, A. W., Mallder, V. A., Martin, N., McComas, D. J., McNutt, R. L., Mehoke, D., Mehoke, T., Melin, E. D., Mutchler, M., Nelson, D., Nimmo, F., Nunez, J. I., Ocampo, A., Owen, W. M., Paetzold, M., Page, B., Parker, A. H., Parker, J. W., Pelletier, F., Peterson, J., Pinkine, N., Piquette, M., Porter, S. B., Protopapa, S., Redfern, J., Reitsema, H. J., Reuter, D. C., Roberts, J. H., Robbins, S. J., Rogers, G., Rose, D., Runyon, K., Retherford, K. D., Ryschkewitsch, M. G., Schenk, P., Schindhelm, E., Sepan, B., Showalter, M. R., Singer, K. N., Soluri, M., Stanbridge, D., Steffl, A. J., Strobel, D. F., Stryk, T., Summers, M. E., Szalay, J. R.,

Tapley, M., Taylor, A., Taylor, H., Throop, H. B., Tsang, C. C. C., Tyler, G. L., Umurhan, O. M., Verbiscer, A. J., Versteeg, M. H., Vincent, M., Webbert, R., Weidner, S., Weigle, G. E., White, O. L., Whittenburg, K., Williams, B. G., Williams, K., Williams, S., Woods, W. W., Zangari, A. M., and Zirnstein, E. (2015). The Pluto system: Initial results from its exploration by New Horizons. *Science*, 350:aad1815. (Cited on page 179.)

Stevenson, D. J. (1999). Life-sustaining planets in interstellar space? *Nature*, 400:32. (Cited on pages 19 and 183.)

Steyert, D. W., Wang, W. F., Sirota, J. M., Donahue, N. M., and Reuter, D. C. (2004). Hydrogen and helium pressure broadening of water transitions in the 380-600cm-1 region. *Journal of Quantitative Spectroscopy & Radiative Transfer*, 83:183–191. (Cited on page 330.)

Stofan, E. R., Elachi, C., Lunine, J. I., Lorenz, R. D., Stiles, B., Mitchell, K. L., Ostro, S., Soderblom, L., Wood, C., Zebker, H., Wall, S., Janssen, M., Kirk, R., Lopes, R., Paganelli, F., Radebaugh, J., Wye, L., Anderson, Y., Allison, M., Boehmer, R., Callahan, P., Encrenaz, P., Flamini, E., Francescetti, G., Gim, Y., Hamilton, G., Hensley, S., Johnson, W. T. K., Kelleher, K., Muhleman, D., Paillou, P., Picardi, G., Posa, F., Roth, L., Seu, R., Shaffer, S., Vetrella, S., and West, R. (2007). The lakes of Titan. *Nature*, 445:61–64. (Cited on page 106.)

Strughol, H. (1955). The Ecosphere of the Sun. *Avia. Med.*, 26:323–328. (Cited on page 10.)

Sung, K., Brown, L. R., Toth, R. A., and Crawford, T. J. (2009). Fourier transform infrared spectroscopy measurements of H2O-broadened half-widths of CO2at 4.3 μmThis article is part of a Special Issue on Spectroscopy at the University of New Brunswick in honour of Colan Linton and Ron Lees. *Canadian Journal of Physics*, 87:469–484. (Cited on page 251.)

Svetsov, V. (2011). Cratering erosion of planetary embryos. *Icarus*, 214:316–326. (Cited on page 271.)

Svetsov, V. V. (2007). Atmospheric erosion and replenishment induced by impacts of cosmic bodies upon the Earth and Mars. *Solar System Research*, 41:28–41. (Cited on page 271.)

Svetsov, V. V. and Shuvalov, V. V. (2016). Silicate impact-vapor condensate on the Moon: Theoretical estimates versus geochemical data. *Geochimica et Cosmochimica Acta*, 173:50–63. (Cited on page 271.)

Tajika, E. (2003). Faint young Sun and the carbon cycle: implication for the Proterozoic global glaciations. *Earth and Planetary Science Letters*, 214:443–453. (Cited on page 22.)

Tajika, E. (2007). Long-term stability of climate and global glaciations throughout the evolution of the Earth. *Earth, Planets, and Space*, 59:293–299. (Cited on page 22.)

Tasker, E. (2017). pages 27–53. (Cited on page 10.)

Tian, F., Claire, M. W., Haqq-Misra, J. D., Smith, M., Crisp, D. C., Catling, D., Zahnle, K., and Kasting, J. F. (2010). Photochemical and climate consequences of sulfur outgassing on early Mars. *Earth and Planetary Science Letters*, 295:412–418. (Cited on pages 31 and 234.)

Tian, F., Kasting, J. F., and Zahnle, K. (2011). Revisiting HCN formation in Earth's early atmosphere. *Earth and Planetary Science Letters*, 308:417–423. (Cited on page 178.)

Tinetti, G., Drossart, P., Eccleston, P., Hartogh, P., Heske, A., Leconte, J., Micela, G., Ollivier, M., Pilbratt, G., Puig, L., Turrini, D., Vandenbussche, B., Wolkenberg, P., Pascale, E., Beaulieu, J.-P., Gudel, M., Min, M., Rataj, M., Ray, T., Ribas, I., Barstow, J., Bowles, N., Coustenis, A., Coude du Foresto, V., Decin, L., Encrenaz, T., Forget, F., Friswell, M., Griffin, M., Lagage, P. O., Malaguti, P., Moneti, A., Morales, J. C., Pace, E., Rocchetto, M., Sarkar, S., Selsis, F., Taylor, W., Tennyson, J., Venot, O., Waldmann, I. P., Wright, G., Zingales, T., and Zapatero-Osorio, M. R. (2016). The science of ARIEL (Atmospheric Remote-sensing Infrared Exoplanet Large-survey). In *Space Telescopes and Instrumentation 2016: Optical, Infrared, and Millimeter Wave*, volume 9904 of *Proceedings of the SPIE*, page 99041X. (Cited on page 338.)

Tinetti, G., Vidal-Madjar, A., Liang, M.-C., Beaulieu, J.-P., Yung, Y., Carey, S., Barber, R. J., Tennyson, J., Ribas, I., Allard, N., Ballester, G. E., Sing, D. K., and Selsis, F. (2007). Water vapour in the atmosphere of a transiting extrasolar planet. *Nature*, 448:169–171. (Cited on page 39.)

Tobie, G., Lunine, J. I., and Sotin, C. (2006). Episodic outgassing as the origin of atmospheric methane on Titan. *Nature*, 440:61–64. (Cited on page 178.)

Toon, O. B., McKay, C. P., Ackerman, T. P., and Santhanam, K. (1989). Rapid calculation of radiative heating rates and photodissociation rates in inhomogeneous multiple scattering atmospheres. *Journal of Geophysical Research*, 94:16287–16301. (Cited on pages 86, 152 and 199.)

Toon, O. B., Segura, T., and Zahnle, K. (2010). The Formation of Martian River Valleys by Impacts. *Annual Review of Earth and Planetary Sciences*, 38:303–322. (Cited on pages 27, 32, 245, 246 and 251.)

Tran, H., Boulet, C., Stefani, S., Snels, M., and Piccioni, G. (2011). Measurements and modelling of high pressure pure CO_2 spectra from 750 to 8500 cm^{-1}. I - central and wing regions of the allowed vibrational bands. *Journal of Quantitative Spectroscopy and Radiative Transfer*, 112:925–936. (Cited on pages 62, 251, 308, 309, 325, 326 and 334.)

Tran, H., Turbet, M., Chelin, P., and Landsheere, X. (2018). Measurements and modeling of absorption by CO_2+ H_2O mixtures in the spectral region beyond the CO_2 ν_3-band head. *Icarus*, 306:116–121. (Cited on pages 58, 60 and 251.)

Trowbridge, A. J., Melosh, H. J., Steckloff, J. K., and Freed, A. M. (2016). Vigorous convection as the explanation for Pluto polygonal terrain. *Nature*, 534:79–81. (Cited on page 164.)

Turbet, M., Bolmont, E., Leconte, J., Forget, F., Selsis, F., Tobie, G., Caldas, A., Naar, J., and Gillon, M. (2018a). Modeling climate diversity, tidal dynamics and the fate of volatiles on TRAPPIST-1 planets. *Astronomy & Astrophysics*, 612:A86. (Cited on pages 48, 74, 86, 147 and 333.)

Turbet, M., Forget, F., Head, J. W., and Wordsworth, R. (2017a). 3D modelling of the climatic impact of outflow channel formation events on early Mars. *Icarus*, 288:10–36. (Cited on pages 48, 53, 86, 96, 151, 153, 238, 239, 243, 247, 249, 253, 254, 285, 290 and 296.)

Turbet, M., Forget, F., Leconte, J., Charnay, B., and Tobie, G. (2017b). CO_2 condensation is a serious limit to the deglaciation of Earth-like planets. *Earth and Planetary Science Letters*, 476:11–21. (Cited on pages 23, 48, 96, 101, 151, 153, 165, 167, 169, 170, 172 and 198.)

Turbet, M., Leconte, J., Selsis, F., Bolmont, E., Forget, F., Ribas, I., Raymond, S. N., and Anglada-Escudé, G. (2016). The habitability of Proxima Centauri b. II. Possible climates and observability. *Astronomy & Astrophysics*, 596:A112. (Cited on pages 48, 86, 151, 152, 153, 166, 181 and 198.)

Turbet, M. and Tran, H. (2017). Comment on "radiative transfer in co2-rich atmospheres: 1. collisional line mixing implies a colder early mars". *Journal of Geophysical Research: Planets*, 122(11):2362–2365. 2017JE005373. (Cited on pages 30, 60, 182, 262, 315 and 325.)

Turbet, M., Tran, H., Hartmann, J.-M., and Forget, F. (2017c). Toward a more Accurate Spectroscopy of CO2/H2O-Rich Atmospheres: Implications for the Early Martian Atmosphere. *LPI Contributions*, 2014:3063. (Cited on pages 58 and 251.)

Turbet, M., Tran, H., Pirali, O., Forget, F., Boulet, C., and Hartmann, J.-M. (2018b). Far infrared measurements of absorptions by CH4+CO2 and H2+CO2 mixtures and implications for greenhouse warming on early Mars. *ArXiv e-prints*. (Cited on pages 240, 325 and 330.)

Turbo-King, M., Tang, B. R., Habeertable, Z., Chouffe, M. C., Exquisit, B., and Keg-beer, L. (2017). A revolution is brewing: observations of TRAPPIST-1 exoplanetary system fosters a new biomarker. *ArXiv e-prints*. (Cited on page 10.)

Turcotte, D. L. and Schubert, G. (2001). *Geodynamics, 2nd ed.* Cambridge Univ. Press. (Cited on pages 82 and 172.)

Umurhan, O. M., Howard, A. D., Moore, J. M., Earle, A. M., White, O. L., Schenk, P. M., Binzel, R. P., Stern, S. A., Beyer, R. A., Nimmo, F., McKinnon, W. B., Ennico, K., Olkin, C. B., Weaver, H. A., and Young, L. A. (2017). Modeling glacial flow on and onto Pluto's Sputnik Planitia. *Icarus*, 287:301–319. (Cited on pages 163 and 164.)

Unterborn, C. T., Desch, S. J., Hinkel, N. R., and Lorenzo, A. (2018). Inward migration of the TRAPPIST-1 planets as inferred from their water-rich compositions. *Nature Astronomy*, 2:297–302. (Cited on pages 146 and 147.)

Urata, R. A. and Toon, O. B. (2013). Simulations of the martian hydrologic cycle with a general circulation model: Implications for the ancient martian climate. *Icarus*, 226:229–250. (Cited on pages 31, 234, 245, 247, 265, 268, 280 and 335.)

Van Grootel, V., Fernandes, C. S., Gillon, M., Jehin, E., Manfroid, J., Scuflaire, R., Burgasser, A. J., Barkaoui, K., Benkhaldoun, Z., Burdanov, A., Delrez, L., Demory, B.-O., de Wit, J., Queloz, D., and Triaud, A. H. M. J. (2018). Stellar Parameters for Trappist-1. *The Astrophysical Journal*, 853:30. (Cited on page 38.)

Van Leeuwen, F. (2007). Validation of the new Hipparcos reduction. *Astronomy & Astrophysics*, 474:653–664. (Cited on page 95.)

Villanueva, G. L., Mumma, M. J., Novak, R. E., Kaufl, H. U., Hartogh, P., Encrenaz, T., Tokunaga, A., Khayat, A., and Smith, M. D. (2015). Strong water isotopic anomalies in the martian atmosphere: Probing current and ancient reservoirs. *Science*, 348:218–221. (Cited on pages 299 and 301.)

Vinatier, S., Rannou, P., Anderson, C. M., Bézard, B., de Kok, R., and Samuelson, R. E. (2012). Optical constants of Titan's stratospheric aerosols in the 70-1500 cm^{-1} spectral range constrained by Cassini/CIRS observations. *Icarus*, 219:5–12. (Cited on pages 177 and 179.)

von Paris, P., Grenfell, J. L., Hedelt, P., Rauer, H., Selsis, F., and Stracke, B. (2013a). Atmospheric constraints for the CO_2 partial pressure on terrestrial planets near the outer edge of the habitable zone. *Astronomy & Astrophysics*, 549:A94. (Cited on page 170.)

von Paris, P., Selsis, F., Kitzmann, D., and Rauer, H. (2013b). The Dependence of the Ice-Albedo Feedback on Atmospheric Properties. *Astrobiology*, 13:899–909. (Cited on page 152.)

Wagner, W., Saul, A., and Pruss, A. (1994). International Equations for the Pressure Along the Melting and Along the Sublimation Curve of Ordinary Water Substance. *Journal of Physical and Chemical Reference Data*, 23:515–527. (Cited on page 125.)

Walker, J. C. G. (1985). Carbon dioxide on the early earth. *Origins of Life*, 16:117–127. (Cited on pages 84 and 170.)

Walker, J. C. G., Hays, P. B., and Kasting, J. F. (1981). A negative feedback mechanism for the long term stabilization of the earth's surface temperature. *Journal of Geophysical Research*, 86:9776–9782. (Cited on pages 21, 22, 67, 69 and 123.)

Walker, J. C. G. and Zahnle, K. J. (1986). Lunar nodal tide and distance to the moon during the Precambrian. *Nature*, 320:600–602. (Cited on page 74.)

Wang, F., Cheruy, F., and Dufresne, J.-L. (2016). The improvement of soil thermodynamics and its effects on land surface meteorology in the IPSL climate model. *Geoscientific Model Development*, 9:363–381. (Cited on pages 286 and 287.)

Wang, S., Wu, D.-H., Barclay, T., and Laughlin, G. P. (2017). Updated Masses for the TRAPPIST-1 Planets. *ArXiv e-prints*. (Cited on pages 150, 151 and 181.)

Warren, S. G. (1984). ReviewImpurities in snow: effects on albedo and snowmelt. *Annals of Glaciology*, 5:177–179. (Cited on pages 98 and 152.)

Warren, S. G. and Wiscombe, W. J. (1980). A Model for the Spectral Albedo of Snow. II: Snow Containing Atmospheric Aerosols. *Journal of Atmospheric Sciences*, 37:2734–2745. (Cited on pages 98, 152 and 182.)

Way, M. J., Del Genio, A. D., Kiang, N. Y., Sohl, L. E., Grinspoon, D. H., Aleinov, I., Kelley, M., and Clune, T. (2016). Was Venus the first habitable world of our solar system? *Geophysical Research Letters*, 43:8376–8383. (Cited on page 24.)

Weiss, D. K. and Head, J. W. (2016). Impact ejecta-induced melting of surface ice deposits on Mars. *Icarus*, 280:205–233. (Cited on page 274.)

Weitz, C. M., Milliken, R. E., Grant, J. A., McEwen, A. S., Williams, R. M. E., and Bishop, J. L. (2008). Light-toned strata and inverted channels adjacent to Juventae and Ganges chasmata, Mars. *Geophysical Research Letters*, 35. (Cited on page 193.)

Wheatley, P. J., Louden, T., Bourrier, V., Ehrenreich, D., and Gillon, M. (2017). Strong XUV irradiation of the Earth-sized exoplanets orbiting the ultracool dwarf TRAPPIST-1. *Monthly Notices of the Royal Astronomical Society*, 465:L74–L78. (Cited on pages 150 and 177.)

Wieczorek, M. A., Correia, A. C. M., Le Feuvre, M., Laskar, J., and Rambaux, N. (2012). Mercury's spin-orbit resonance explained by initial retrograde and subsequent synchronous rotation. *Nature Geoscience*, 5:18–21. (Cited on page 166.)

Williams, J. G., Turyshev, S. G., and Boggs, D. H. (2014). The past and present Earth-Moon system: the speed of light stays steady as tides evolve. *Planetary Science*, 3:2. (Cited on page 154.)

Williams, R. M. E., Grotzinger, J. P., Dietrich, W. E., Gupta, S., Sumner, D. Y., Wiens, R. C., Mangold, N., Malin, M. C., Edgett, K. S., Maurice, S., and et al. (2013). Martian Fluvial Conglomerates at Gale Crater. *Science*, 340:1068–1072. (Cited on pages 27 and 246.)

Wilson, L., Ghatan, G. J., Head, J. W., and Mitchell, K. L. (2004). Mars outflow channels: A reappraisal of the estimation of water flow velocities from water depths, regional slopes, and channel floor properties. *Journal of Geophysical Research*, 109. (Cited on page 195.)

Winn, J. N. (2010). Transits and Occultations. *ArXiv e-prints*. (Cited on page 37.)

Wolf, E. T. (2017). Assessing the Habitability of the TRAPPIST-1 System Using a 3D Climate Model. *The Astrophysical Journal Letters*, 839:L1. (Cited on page 182.)

Wolf, E. T. and Toon, O. B. (2010). Fractal Organic Hazes Provided an Ultraviolet Shield for Early Earth. *Science*, 328:1266. (Cited on page 179.)

Wolf, E. T. and Toon, O. B. (2013). Hospitable Archean Climates Simulated by a General Circulation Model. *Astrobiology*, 13:656–673. (Cited on page 182.)

Wolf, E. T. and Toon, O. B. (2015). The evolution of habitable climates under the brightening Sun. *Journal of Geophysical Research (Atmospheres)*, 120:5775–5794. (Cited on pages 12 and 20.)

Wood, E. F., Lettenmaier, D. P., and Zartarian, V. G. (1992). A land-surface hydrology parameterization with subgrid variability for general circulation models. *Journal of Geophysical Research: Atmospheres*, 97:2717–2728. (Cited on page 286.)

Wordsworth, R., Forget, F., and Eymet, V. (2010a). Infrared collision-induced and far-line absorption in dense CO $_2$ atmospheres. *Icarus*, 210:992–997. (Cited on pages 30, 86, 98, 152, 182, 199, 262, 285, 307, 309, 310, 312, 315 and 334.)

Wordsworth, R., Forget, F., Millour, E., Head, J. W., Madeleine, J.-B., and Charnay, B. (2013). Global modelling of the early martian climate under a denser CO_2 atmosphere: Water cycle and ice evolution. *Icarus*, 222:1–19. (Cited on pages 30, 47, 48, 86, 96, 151, 152, 153, 198, 199, 200, 201, 203, 221, 238, 239, 243, 246, 247, 248, 249, 250, 253, 262, 269, 270, 276, 284, 285, 290, 297, 299, 301, 302, 315 and 334.)

Wordsworth, R., Kalugina, Y., Lokshtanov, S., Vigasin, A., Ehlmann, B., Head, J., Sanders, C., and Wang, H. (2017). Transient reducing greenhouse warming on early Mars. *Geophysical Research Letters*, 44:665–671. (Cited on pages 32, 240, 246, 284, 285, 293, 313, 314, 315, 316, 323, 324, 327, 328, 329, 336 and 337.)

Wordsworth, R. D. (2016). The Climate of Early Mars. *Annual Review of Earth and Planetary Sciences*, 44:381–408. (Cited on pages 246, 269, 297, 299, 301, 309 and 315.)

Wordsworth, R. D., Forget, F., Selsis, F., Madeleine, J.-B., Millour, E., and Eymet, V. (2010b). Is Gliese 581d habitable? Some constraints from radiative-convective climate modeling. *Astronomy & Astrophysics*, 522:A22. (Cited on page 182.)

Wordsworth, R. D., Forget, F., Selsis, F., Millour, E., Charnay, B., and Madeleine, J.-B. (2011). Gliese 581d is the First Discovered Terrestrial-mass Exoplanet in the Habitable Zone. *The Astrophysical Journal Letters*, 733:L48. (Cited on pages 48, 86, 95, 96, 101, 151, 152, 153 and 198.)

Wordsworth, R. D., Kerber, L., Pierrehumbert, R. T., Forget, F., and Head, J. W. (2015). Comparison of "warm and wet" and "cold and icy" scenarios for early Mars in a 3-D climate model. *Journal of Geophysical Research (Planets)*, 120:1201–1219. (Cited on pages 48, 96, 151, 243, 247, 284, 285, 287, 301, 302 and 303.)

Wordsworth, R. D. and Pierrehumbert, R. T. (2013). Water Loss from Terrestrial Planets with CO_2-rich Atmospheres. *The Astrophysical Journal*, 778:154. (Cited on page 112.)

Wordsworth, R. D., Schaefer, L. K., and Fischer, R. A. (2018). Redox Evolution via Gravitational Differentiation on Low-mass Planets: Implications for Abiotic Oxygen, Water Loss, and Habitability. *The Astronomical Journal*, 155:195. (Cited on page 337.)

Yang, J., Cowan, N. B., and Abbot, D. S. (2013). Stabilizing Cloud Feedback Dramatically Expands the Habitable Zone of Tidally Locked Planets. *The Astrophysical Journal Letters*, 771:L45. (Cited on pages 16, 95, 118, 123, 149 and 179.)

Yang, J., Liu, Y., Hu, Y., and Abbot, D. S. (2014). Water Trapping on Tidally Locked Terrestrial Planets Requires Special Conditions. *The Astrophysical Journal Letters*, 796:L22. (Cited on page 108.)

Yoder, C. F., Konopliv, A. S., Yuan, D. N., Standish, E. M., and Folkner, W. M. (2003). Fluid Core Size of Mars from Detection of the Solar Tide. *Science*, 300:299–303. (Cited on page 154.)

Yung, Y. L., Allen, M., and Pinto, J. P. (1984). Photochemistry of the atmosphere of Titan - Comparison between model and observations. *The Astrophysical Journal Supplement Series*, 55:465–506. (Cited on page 178.)

Zahnle, K. and Walker, J. C. G. (1987). A constant daylength during the precambrian era? *Precambrian Research*, 37:95–105. (Cited on page 74.)

Zahnle, K. J. and Catling, D. C. (2017). The Cosmic Shoreline: The Evidence that Escape Determines which Planets Have Atmospheres, and what this May Mean for Proxima Centauri B. *The Astrophysical Journal*, 843:122. (Cited on page 9.)

Ziethe, R. and Spohn, T. (2007). Two-dimensional stokes flow around a heated cylinder: A possible application for diapirs in the mantle. *Journal of Geophysical Research (Solid Earth)*, 112:B09403. (Cited on pages 83 and 173.)

Zuber, M. T., Smith, D. E., Lemoine, F. G., and Neumann, G. A. (1994). The Shape and Internal Structure of the Moon from the Clementine Mission. *Science*, 266:1839–1843. (Cited on page 106.)